Geology, lithogeochemistry, age, and genesis of the Zn-Pb-Cu-Ag-(Au)-barite AG volcanogenic massive sulfide (VMS) deposit, Haines, Alaska.

by

© Kei Quinn

A Thesis Submitted to the School of Graduate Studies

in partial fulfillment of the requirements for the degree of

Master of Science

in the

Department of Earth Sciences

Memorial University of Newfoundland

St. John's, Newfoundland, Canada

March 2024

Abstract

The AG volcanogenic massive sulfide (VMS) deposit is hosted within the Late Triassic (Hyd and Tats Group) bimodal volcanic rocks of the Alexander Triassic metallogenic belt (ATMB). The AG deposit is composed of both exhalative- and replacement-style, barite-rich VMS mineralization with an inferred resource of 4.3 Mt grading 4.64% Zn, 0.12% Cu, 0.96% Pb, 119.5 g/t Ag, 0.53 g/t Au and 34.8% $BaSO_4$. The volcanic sequence that hosts the AG deposit includes: (1) enriched mid-ocean ridge basalt (EMORB)-like pillowed flows of tholeiitic basalts, (2) effusive flows of ferroandesites (FeA) and FIIIa ferrodacites (FeD) that are capped by FIIIa ferrorhyolitic lapilli tuffs (FeR), all of which have weak "arc-like" geochemical signatures and mixed tholeiitic/calc-alkaline affinities (3) EMORB-like pillowed flows of FeTi-rich, variolitic basalts (Z-FeTiB) that are intercalated with barite clast-bearing heterolithic fragmental rocks, (4) pyroclastic deposits of EMORB-like, FeTi-rich, hanging wall (HW) basalts (HW-FeTiB), and (5) syn-volcanic sills of FIIIb high-silica rhyolites (HSR).

The AG deposit is a bimodal-mafic deposit with a flow-dominated stratigraphic footwall and a volcaniclastic-dominated hangingwall. Most of the AG deposit formed at the contact of the Fe-rich, intermediate to felsic rocks with weak "arc-like" geochemical signatures and the EMORB-like FeTi-rich basalts. Mineralization is intercalated with FeTi-rich, variolitic pillowed basalts and heterolithic fragmental rocks. The heterolithic fragmental rocks are considered debris flow deposits that were emplaced along an interpreted syn-volcanic fault, the Finch fault. The Finch fault also controlled the distribution of HSR sills, sharp lateral changes in hydrothermal alteration intensity, the thicknesses and facies of units, and VMS mineralization.

Litho- and chemo-stratigraphic reconstruction of the volcanic environment suggests the rocks hosting the AG VMS deposit formed in a propagating intra-arc rift associated with basin

development where high temperature (> 900 ºC), shallow (< 10 km) magmatic processes included basaltic underplating, crystal fractionation, assimilation of arc crust, and periodic magmatic replenishment. The tectono-magmatic conditions that were essential for initiating and sustaining the hydrothermal convection required to form the AG VMS deposit are both physically and chemically reflected in the AG volcanic sequence.

Zircons from the FeR and HSR yield new chemical abrasion isotope dilution thermal ionization mass spectrometry (CA-ID-TIMS) U-Pb crystallization dates of 210.35 ± 0.27, and 210.52 ± 0.08 Ma, respectively (Fig. 2.17; Table 2.4, Table 2.5) that constrain the timing (210.60 Ma to 210.08 Ma) of the AG mineralization and corroborate the Norian (ca. 227–208.5 Ma) conodonts in the Tats Group rocks that host the Windy Craggy VMS deposit and the timing of VMS mineralization at the Palmer deposit (213 ± 5 Ma; Hyd Group).

The AG volcanic rocks have geochemical and geologic features that are like assemblages documented in Neoarchean VMS-hosting rocks in the Abitibi greenstone belt, suggesting that the tectono-magmatic processes responsible for forming the AG volcanic rocks in the Late Triassic may have been operative in the Neoarchean.

Acknowledgments

My graduate school journey and the completion of this thesis have greatly benefitted from many. First and foremost, I want to thank my supervisor, Prof. Stephen Piercey for the privilege and opportunity. Through his intuitive mentorship, patience, and unwavering support, I became a better critical thinker and a more effective communicator. These skills have allowed me to grow both professionally and personally. I will forever appreciate Prof. Piercey's knack for connecting with and inspiring those around him. His light-hearted references to the Trailer Park Boys softened the moments when I was in throes of it.

Additionally, I would like to thank Prof. Luke Beranek for being on my supervisory committee and reviewing this manuscript. External reviewers, Prof. Graham Layne and Dr. Steven Hollis provided constructive recommendations that greatly improved this thesis. I would like to express my gratitude for Dr. Wanda Aylward for her guidance at MUN's TERRA facility. Jim Crowley and his team at the Boise State University Isotope Geology Laboratory in Idaho are applauded for their preparation of and analytical work on the geochronologic samples in this study. A special thanks to Charlie Greig who allowed me to use his microscope when the world shut down during the Covid-19 pandemic. Many thanks to my friends on the Piercey research team who were so welcoming and supportive, from the classroom to the local watering hole and everywhere in between. I wouldn't have been Screeched in properly without them.

This research was made possible by the encouragement, logistical backing, and financial support of Constantine Metal Resources Ltd. and Dowa Metals & Mining Ltd. In addition to the many incredibly talented and dedicated workers and consultants who have made exploration programs at the Palmer Project possible, I would specifically like to thank Garfield MacVeigh, Darwin Green, Liz Cornejo, Ian Cunningham-Dunlop, Nathan Steeves, Allegra Cairns, and Conor McKinley. Funding for the geochronology work was provided by a HighGold Mining Ltd. bursary, an Alaska Geological Society scholarship, and an NSERC Discovery Grant to Prof. Piercey. Financial support was also provided by a Society of Economic Geologists' Graduate Student Fellowship, a Memorial University's School of Gradaute F.A. Aldrich Fellowship, an Association of Professional Engineers and Geoscientists Past Presidents' Geoscience Scholarship, and a Young Mining Professional's Atlantic Canada Student in Mining Scholarship sponsored by Anaconda Mining.

Finally, I thank my friends and family for being the most steadfast support system. My Grandma Carol and Grandpa Lorne both passed during the writing of this thesis, but I feel Grandma's uninhibited curiosity paired with Grandpa's joyful and mindful approach flow through me and this work. To my immediate pack – Zack, our dog Yuki, and our cat Finch, I am forever grateful for your unconditional love and support. I hope that I have found and corrected any extraneous characters that Finch may have contributed to this thesis by her frequent visits to my keyboard. One really must pay attention to Finch's faults.

This thesis is dedicated to all those who have chipped away at understanding our Earth. Pictured here is the late Bruce Hickock, Kennecott geologist, rock sampling at the Nunatak prospect (AG deposit area) next to the Saksaia Glacier circa mid 1980s. Permission to use this photo granted courtesy of the photographer, Lance Miller.

Table of Contents

Abstract ii
Acknowledgments iv
Table of Contents vii
List of Tables x
List of Figures xi
List of Acronyms xiii

Chapter 1. Introduction to the AG VMS deposit 1
1.1. Introduction 1
1.2. Regional setting 2
1.2.1. Alexander terrane 2
1.2.2. Alexander Triassic metallogenic belt (ATMB) 3
1.3. Local setting - the Palmer VMS Project 5
1.3.1. Previous studies and exploration history 5
1.3.2. District Geology 6
Regional metamorphism and deformation 9
1.4. AG Deposit Geology 10
1.5. VMS Deposits 11
1.5.1. VMS model 11
1.5.2. Classification 13
1.5.3. Tectono-magmatic associations 14
1.5.4. Using geochemistry for VMS exploration 15
1.6. Fundamental research questions and approaches 16
1.7. Research goals and organization of the thesis 17
Chapter 1 References 18
Chapter 1 Tables 31
Chapter 1 Figures 32

Chapter 2. Geology, lithogeochemistry, age, and genesis of the AG VMS deposit 39
2.1. Abstract 39
2.2. Introduction 40
2.3. Geological setting 43
2.3.1. Regional geology 43
2.3.2. Palmer property geology 44
2.4. Geology and lithostratigraphy of the AG deposit 44
2.4.1. Methodology 44
2.4.2. Geology of AG deposit 46
Alteration and metamorphism 47
Deformation 47
The Nunatak panel 48

The JAG panel 49
Sequence 1 – Footwall basalts and ferrobasalts 50
Sequence 2 – Footwall Fe-rich silicic rocks 51
Sequence 3 – The zone FeTi basalts and heterolithic fragmental rocks 52
Sequence 4 – The hangingwall FeTi basalts 54
Sequence 5 – The high-silica rhyolites 57
Sequence 6 – Argillite 58
Mineralization 58
2.5. Primary lithogeochemistry 60
2.5.1. Analytical methods 60
2.5.2. Lithogeochemical methods 61
2.5.3. Results 64
The footwall basalt suite (FW-B and FW-FeB) 65
The Fe-rich silicic suite (FeA, FeD, and FeR) 66
The FeTi basalt suite (Z-FeTiB and HW-FeTiB) 68
The high silica rhyolite suite (HSR) 69
2.6. U-Pb zircon geochronology 70
2.6.1. Sample selection 70
2.6.2. Analytical methodology 71
2.6.3. Results 71
2.7. Discussion 72
2.7.1. Volcanic controls on AG VMS mineralization 72
2.7.2. Petrogenesis of the AG volcanic rocks 76
Petrogenesis of the footwall basalt suite 76
Petrogenesis of the Fe-rich silicic suite 77
Petrogenesis of the FeTi basalt suite 80
Petrogenesis of the HSR suite 82
2.7.3. Tectonic controls on the AG VMS deposit genesis 84
2.7.4. Age of the AG VMS deposit and implications for the timing of hydrothermal activity in the ATMB 87
2.7.5. The association of VMS deposits with Fe-rich volcanic rocks and high-silica rhyolites – comparisons to the Neoarchean Blake River Group, Abitibi greenstone belt 89
2.8. Conclusions 92
Chapter 2 References 95
Chapter 2 Tables 125
Chapter 2 Figures 132

Chapter 3. Summary and future research 153
3.1. Directions for future consideration 155

Appendix 1. Supplementary photographs of the AG deposit geology 159

Appendix 2. Petrographic descriptions, microphotographs, and backscattered electron (BSE) images 171
W605013 – Iron Formation 172
W605041 - HSR 175
S039314 – HW-FeTiB 178
S039313 – HW-FeTiB 181
94-31 – HW-FeTiB 187
W600919 – HW-FeTiB 190
109-185 – HW-FeTiB 193
99-49 – HW-FeTiB 198
S037015 – Z-FeTiB 202
W605318 – FeR 209
99-362 – FW-FeB 219

Appendix 3. Whole rock geochemical data 224

Appendix 4. Quality control and quality assurance (QAQC) 229
Appendix 4 References 237

Appendix 5. U-Pb geochronology 238
Sample collection 239
Analytical methodology 239
    LA-ICPMS methodology 239
    CA-ID-TIMS U-Pb geochronology method 241
Results 244
Appendix 5 References 256

Appendix 6. Electron probe microanalyzer data 258
Analytical methods 259
Results 260
Appendix 6 References 280

List of Tables

Table 1.1 Summary of significant VMS deposits in the ATMB.. 31

Table 2.1 Summary of criteria used to select the least altered samples. 125

Table 2.2 Whole rock lithogeochemical data of twenty-two representative, least-altered samples of the eight geochemical volcanic units of the AG deposit. 126

Table 2.3 Summary of significant element ratios of the least altered AG volcanic rocks. 130

Table 2.4 Chemical abrasion isotope dilution thermal ionization mass spectrometry (CA-ID-TIMS) U-Pb zircon isotopic data for felsic rocks in the AG stratigraphy. 131

Table 2.5 Summary of U-Pb geochronology results. 131

List of Figures

Fig. 1.1 Terrane map of the northwestern Cordillera. 32

Fig. 1.2 Schematic stratigraphic section through the Alexander Triassic metallogenic belt (ATMB). 33

Fig. 1.3 Palmer property VMS occurrences, prospects, and deposits location map.. 34

Fig. 1.4 Regional geology near the Palmer property. 35

Fig. 1.5 VMS convective hydrothermal system and components. 36

Fig. 1.6 Lithostratigraphic classification of VMS deposits shown with their respective stratigraphic relationships and associated petrochemical assemblages by Piercey (2011). 36

Fig. 1.7 Tectonic settings where VMS deposits form. 37

Fig. 1.8 Extension-related magmatic plumbing system. 38

Fig. 2.1 Location and regional geology of the Alexander terrane. 133

Fig. 2.2 Geology maps of the Palmer property and AG deposit area 134

Fig. 2.3 Graphic logs for four representative drill holes through the JAG panel. 135

Fig. 2.4 Oblique section across the AG deposit map area and cross sections highlighting the JAG panel stratigraphy. 136

Fig. 2.5 Photographs and microphotographs of the ferrorhyolites (FeR). 137

Fig. 2.6 Photos of the Zone FeTi basalts (Z-FeTiB) and associated heterolithic fragmental rocks. 138

Fig. 2.7 Outcrop and drill core photographs and microphotographs of the hangingwall FeTi basalts (HW-FeTiB). 139

Fig. 2.8 Outcrop photographs, hand sample photograph, and microphotographs of the FIIIb high-silica rhyolites (HSR). 140

Fig. 2.9 Major and trace element discrimination plots for the mafic and felsic rocks of the AG stratigraphy. 141

Fig. 2.10 Variation diagrams of Nb versus selected major and trace elements for the AG volcanic rocks. 142

Fig. 2.11 Multi-element primitive mantle normalized plots for the eight volcanic units. 143

Fig. 2.12 Rare Earth element (REE) chondrite normalized plots for the eight volcanic units. 144

Fig. 2.13 Tectono-magmatic plots. 145

Fig. 2.14 Felsic tectono-magmatic discrimination diagrams. 146

Fig. 2.15 Zr versus Nb_{pm}/Th_{pm} (A) and La_{pm}/Sm_{pm} versus Nb_{pm}/Th_{pm} (B). (C) Zr_{pm}/Sm_{pm} and Hf_{pm}/Sm_{pm} versus Nb_{pm}/Th_{pm}. (D) SiO_2 versus TiO_2 plot. 147

Fig. 2.16 Nb/Yb versus Th/Yb plots. 148

Fig. 2.17 Concordia diagrams displaying CA-ID-TIMS U-Pb dates from zircon grains in the felsic rocks of the AG stratigraphy 149

Fig. 2.18 Idealized schematic illustrating the tectnono-magmatic evolution of the AG volcanic sequence 150

Fig. 2.19 Generalized stratigraphic columns of Greens Creek, Palmer, AG, and Windy Craggy. 151
Fig. 2.20 Comparison of the multi-element primitive mantle normalized signatures of some volcanic samples from the Kam Kotia mine and some of the least altered samples in the AG volcanic stratigraphy.. 152

List of Acronyms

% RD	Percent relative difference
% RSD	Percent relative standard deviation
2D	Two dimensions
3D	Three dimensions
Ab	Albite
ACC	Average continental crust
AFC	Assimilation fractional crystallization
Aln	Allanite
AMC	Axial magma chamber
Amp	Amphibole
Ank	Ankerite
Ap	Apatite
ATMB	Alexander Triassic metallogenic belt
BAB	Back-arc basin
BABB	Back-arc basin basalt
BC	British Columbia
BCGS	British Columbia Geological Survey
Brt	Barite
BSE	Backscatter electron
BSU IGL	Boise State University Isotope Geology Laboratory
Bt	Biotite
CAB	Calc-alkaline basalt
Cal	Calcite
CA-ID-TIMS	Chemical abrasion isotope dilution thermal ionization mass spectrometry
Ccp	Chalcopyrite
Chl	Chlorite
CL	Cathodoluminescence
cm	Centimeter
cn	Chondrite
CV_{avg}	Average coefficient of variation
EDS	Energy dispersive spectrometer
EMORB	Enriched mid-ocean ridge basalt
Ep	Epidote
EPMA	Electron probe microanalyzer
F	Batch melting
FC	Fractional crystallization
$Fe_2O_3^T$	Total Fe expressed as Fe_2O_3
FeA	Ferroandesites
FeD	Ferrodacites
FeO^T	Total Fe expressed as FeO
FeR	Ferrorhyolites
Fig(s)	Figure(s)
FOV	Field of view

Fsp	Feldspar
FW	Footwall (stratigraphic)
FW-B	Footwall basalts
FW-FeB	Footwall ferrobasalts
g/t	Grams per ton
Gn	Galena
HC	Hydrothermal convection
Hem	Hematite
HFSE	High field strength elements
HREE	Heavy rare earth elements
HSR	High-silica rhyolites
HW	Hangingwall (stratigraphic)
HW-FeTiB	Hangingwall FeTi basalts
IAB	Island arc basalt
IAT	Island arc tholeiite
ICP-AES	Inductively coupled plasma - atomic emission spectroscopy
ICP-MS	Inductively coupled plasma - mass spectrometry
Ilm	Ilmenite
IR	infrared spectroscopy
km	Kilometer
LA-ICPMS	Laser ablation inductively coupled mass spectrometry
LFSE	Low field strength elements
LIP	Large igneous province
LOD	Limit of detection
LOI	Loss on ignition
LREE	Light rare earth elements
m	Meter
Ma	Million years ago
Mag	Magnetite
mm	Milometer
Mnz	Monazite
MORB	Mid-ocean ridge basalt
MREE	Middle rare earth elements
Ms	Muscovite
Mt	Million tonne
n	number of samples
nm	Nanometer
NMORB	Normal mid-ocean ridge basalt
OIB	Ocean island basalt
pH	Potential hydrogen
Pl	Plagioclase
pm	Primitive mantle
ppm	Parts per million
Py	Pyrite
QAQC	Quality assurance and quality control
Qz	Quartz

R	Replenishment
Rt	Rutile
SEM	Scanning electron microscope
Sp	Sphalerite
SRM	Standard reference material
SZ	Subduction zone
TB	Tholeiitic basalt
Ti-mag	Titanomagnetite
USGS	United States Geological Survey
VAB	Volcanic arc basalt
VMS	Volcanogenic massive sulfide
WPB	Within plate basalt
WPT	Within plate tholeiite
Wt %	Weight percent
XRF	X-Ray fluorescence spectroscopy
Z-FeTiB	Zone FeTi basalts
Zrn	Zircon
μm	Micrometer

Chapter 1. Introduction to the AG VMS deposit

1.1. Introduction

The rocks of the Alexander Triassic metallogenic belt (ATMB) in the North American Cordillera are well endowed with volcanogenic massive sulfide (VMS) deposits, including the supergiant (~300 Mt) Cu-Co Windy Craggy deposit, the Ag-rich Greens Creek deposit, and the polymetallic (Zn-Cu-Pb-Ag-Au-Ba) Palmer deposit (Figs. 1.1, 1.2; Taylor et al., 2008). Despite the economic significance of the ATMB, it remains understudied compared to other global VMS districts (such as those reviewed by Allen et al., 2002; Franklin et al., 2005; Monecke et al., 2017a). The most recent discovery (2017) in the ATMB, the AG VMS deposit, is located 3 km from the 10 Mt Palmer deposit on Constantine Mining LLC's advanced stage Palmer VMS Project (Fig. 1.4). It is hosted in bimodal volcanic rocks and is composed of both exhalative- and replacement-style, barite-rich VMS mineralization with an inferred resource of 4.3 Mt grading 4.64% Zn, 0.12% Cu, 0.96% Pb, 119.5 g/t Ag, 0.53 g/t Au and 34.8% $BaSO_4$ (Gray and Cunningham-Dunlop, 2018). No detailed study of the deposit-scale stratigraphy, lithogeochemistry, and structural architecture exists for this deposit.

The focus of this thesis is to integrate observations from geologic mapping, core logging, petrography, lithogeochemistry, and U-Pb zircon geochronology to: (1) reconstruct the AG volcanic architecture, (2) improve our understanding of the relationships between the magmatic, tectonic, and hydrothermal processes that formed the AG VMS deposit, and (3) constrain the timing of VMS formation at AG.

Much of our understanding of VMS genesis arises from exploration and studies of numerous ancient deposits and studies of modern analogues on the seafloor (Allen et al., 2002;

Franklin et al., 2005; Galley et al., 2007; Gibson et al., 2007). The goal of this thesis is to better understand the setting and genesis of the AG deposit to guide future exploration efforts, facilitate correlations with nearby VMS occurrences on the Palmer property, and contribute to the growing knowledge of Late Triassic VMS systems in the ATMB and VMS systems worldwide.

1.2. Regional setting

1.2.1. Alexander terrane

The Alexander terrane spans the Saint Elias Mountains in southwestern Yukon and northwestern British Columbia (BC), most of the Alexander Archipelago in southeastern Alaska, and a minor part of western BC near Prince Rupert (Fig. 1.1). It has a nearly complete rock record beginning from at least the Ediacaran (a felsic metavolcanic with a U-Pb zircon date of 595 ± 20 Ma; Gehrels et al., 1996) and spanning until it was accreted to the North American continental margin during the Middle Jurassic to Late Cretaceous (Berg et al., 1972; Plafker and Berg, 1994; Nelson et al., 2013b). The Alexander terrane is composed of the Craig and Admiralty subterranes, which are crustal fragments that are differentiated based on their pre-Permian stratigraphy (Gehrels and Saleeby, 1987; Karl et al., 2010; Beranek et al., 2014) and the recently proposed Saint Elias subterrane, which has a pericratonic signature (Nelson et al., 2013a). The Alexander terrane originated in the paleo-Arctic during the Neoproterozoic (Beranek et al., 2012; Nelson et al., 2013b; White et al., 2016), and faunal and isotopic evidence suggests that it had low latitude affinities with Siberia or Baltica in the late Silurian to Early Devonian (Soja and Antoshkina, 1997). In general, the tectonic evolution of the terrane included: (1) Neoproterozoic to Silurian oceanic arc magmatism, including the formation of Neoproterozoic and Ordovician to Silurian VMS deposits (Ayuso et al., 2005; Slack et al., 2007; Beranek et al., 2012; Nelson et al., 2013a), (2) a period of quiescence during the Devonian to Permian with the Alexander and its subterranes joined to the Wrangellia-Peninsular super-terrane by the late Permian (Capitanian) (Karl et al., 2010; Beranek et al., 2014; Israel et al., 2014; Sack et al., 2016), (3) the formation of the economically significant Late Triassic VMS deposits during extension along the eastern edge of the Alexander terrane in a 200-800m thick sequence of rocks known as the Alexander Triassic metallogenic belt (ATMB) (Gehrels and Saleeby, 1987; Gehrels and Berg H.C., 1994; Newberry et al., 1997; Katvala and Stanley, 2008; Taylor et al., 2008; Steeves et al., 2016; Steeves, 2018), and (4) accretion of the composite Alexander-Wrangellia-Peninsular superterrane to the North American continental margin during the Middle Jurassic to Late Cretaceous, as marked by Gravina (and related) overlap assemblages (Berg et al., 1972; Plafker and Berg, 1994; Nelson et al., 2013b).

1.2.2. Alexander Triassic metallogenic belt (ATMB)

Late Triassic rifting of the Alexander terrane coincided with the deposition of volcanic and sedimentary rocks and VMS deposit formation in a northwest-trending belt - the Alexander Triassic metallogenic belt (ATMB) (Fig. 1.2; Taylor et al., 2008). These rocks formed in an asymmetrical back-arc or intra-arc rift and are discontinuously exposed over a strike length of ~750 km along the eastern margin of the Alexander terrane in southeastern Alaska and northwestern BC (Taylor et al., 2008). The ATMB includes the Hyd Group in Alaska (Loney, 1964; Muffler, 1967; Wilson et al., 2015) and the Tats Group (MacIntyre et al., 1992; Cui et al., 2017) in northwestern BC. The Randall Formation (Woodsworth and Orchard, 1985) on Randall Island in BC near Prince Rupert may also be equivalent to the Hyd Group.

The most complete lithostratigraphic and biostratigraphic section through the ATMB is in Keku Strait (Muffler, 1967; Katvala and Stanley, 2008). The ATMB stratigraphy includes a basal conglomerate overlain by a lower volcanic section, a middle sedimentary section, and a thick mafic volcanic cap (Loney, 1964; Taylor et al., 2008; Sack et al., 2016). Regionally, the lower volcanic section is rhyolite-dominant in the southeast (e.g., the Keku Inlet (KI) section) and thins and transitions to bimodal and mafic-dominant in the northwest (Taylor et al., 2008; Fig. 1.2).

In addition to the AG deposit, the ATMB hosts three other significant VMS deposits (Table 1.1). The ~300 Mt Cu-Co Windy Craggy deposit is the world's largest known Besshi (pelitic-mafic)-type deposit though it is protected from production by BC provincial park status (Peter and Scott, 1997). The 24.2 Mt Greens Creek deposit, with 13.9% Zn, 5.1% Pb, 658 g/t Ag, and 5.1 g/t Au, is consistently among the top ten Ag producers worldwide (Bennett, 2016; Steeves, 2018). The 10 Mt Cu-Zn-Ag-Au-Ba Palmer deposit is 3 km from the AG deposit on the Palmer property (Fig. 1.4; Goodwin et al., 2019).

The ATMB also hosts the small, past-producing, 0.75 Mt, Ba-rich Castle Island deposit in the Duncan Canal area. Several VMS-related prospects on the Cornwallis Peninsula at the north end of Kuiu Island are proximal to the 150–200 ton Ag-Pb-Zn Kuiu prospect, which was mined between 1937–1938 (Still et al., 2002). On Annette Island, the Sylburn Peninsula hosts several VMS-related prospects and drilling results from 1976, combined with soil geochemical anomalies, defined a ~1–2 Mt ore body averaging 32% barite and 2-3% combined Pb and Zn (Taylor, 1993).

Several authors (Karl et al., 2010; White et al., 2016) suggest that restoring the ~180 km post-middle Cretaceous and pre-Holocene (Hudson et al., 1982) dextral movement along the Chatham Strait fault would place the Palmer property deposits approximately 30-50 km from Greens Creek (Fig. 1.2). The Greens Creek deposit formed after the emplacement of a Hyd Group rhyolite with a chemical abrasion isotope dilution-thermal ionization mass spectrometry (CA-ID-TIMS) U-Pb zircon date of 226.86 ± 0.24 Ma (Sack et al., 2011; Sack et al., 2016) interpreted to stratigraphically underlie argillites that hosts the Greens Creek deposit (Steeves, 2018). These argillites contain conodonts assigned to the Carnian-Norian boundary (~227 Ma) (Premo et al., 2010; Steeves, 2018). Previous conodont studies on the Palmer property confirmed that the host rocks for VMS mineralization are Late Triassic (Norian to Rhaetian; Green, 2001; Green et al., 2003) and an ID-TIMS U-Pb zircon date of 213 ± 5 Ma from a hydrothermally altered rhyolite constrains the timing of mineralization at the Palmer deposit (Green, 2001). These geochronologic constraints suggest that the Palmer deposit could be at least 10 – 15 million years younger than the Greens Creek deposit.

1.3. Local setting - the Palmer VMS Project

The Palmer volcanogenic massive sulfide (VMS) project is an advanced-stage Cu-Zn-Au-Ag VMS exploration project located within the ATMB near Haines, Alaska (Goodwin et al., 2019). The Palmer VMS project includes both the Palmer and AG VMS deposits as well as several other VMS prospects and occurrences (Fig. 1.3; Fig. 1.4). The Palmer VMS deposit contains 4.7 Mt of indicated resources grading 5.23 % Zn, 1.49 % Cu, 30.8 g/t Ag, 0.30 gt Au, 23.9 % $BaSO_4$ and 5.3 Mt of inferred resources grading 5.20 % Zn, 0.96 % Cu, 29.2 g/t Ag, 0.28 g/t Au, 22.0 % $BaSO_4$ (Goodwin et al., 2019). The AG VMS deposit contains 4.3 Mt of inferred resources grading 4.64 % Zn, 0.12 % Cu, 0.96 % Pb, 119.5 g/t Ag, 0.53 g/t Au, 34.8 % $BaSO_4$ (Goodwin et al., 2019).

1.3.1. Previous studies and exploration history

The Palmer property is in the Porcupine Mining Area within the Skagway B-4 Quadrangle. Active mining in the area began in 1898 with the discovery of placer gold in Porcupine Creek and Glacier Creek (Still, 1991). In 1969, a local prospector, Merrill Palmer, first discovered VMS-style massive barite and base-metal sulfides in the Glacier Creek prospect area. Since then, several VMS-related mineral occurrences and prospects, and two VMS deposits hosted within Upper Triassic volcanic rocks have been identified on the property (Figs. 1.4, 1.3).

The geology of the property has been established through the regional mapping and geochemical sampling efforts of MacKevett Jr. et al. (1974), Redman et al. (1985), Forbes et al. (1989), and Still (1991). Since 1979, 206 drill holes totaling ~76,900 m have been drilled on the property. Various operators conducted drilling programs between 1979-1989, including Anaconda (1979), Bear Creek Mining/Kennecott Exploration (1984 and 1985), Granges Exploration Inc. (1989), and Newmont Exploration Ltd. (1987-1989). In 1999, Rubicon Minerals Corporation drilled the Palmer deposit discovery hole into the RW zone. In 2007, Constantine drilled the discovery hole into the Southwall zone. Between 2006 and 2022, Constantine explored and defined the Palmer deposit, which consists of the Southwall and RW zones (Green et al., 2003; Steeves et al., 2016). In 2017, Constantine drilled the AG discovery hole and subsequent drilling and mapping to 2018 resulted in the definition of the first inferred resource (Gray and Cunningham-Dunlop, 2018).

Two Master of Sciences theses (Green, 2001; Steeves, 2013), two research projects associated with applied Master of Sciences programs (Doherty, 2018; Transburg, 2020), one undergraduate honors thesis (Miller, 2015), and many generations of internal company reports are the basis of the geological knowledge base of the Palmer Project area.

1.3.2. District Geology

The Palmer property is underlain by Paleozoic to Mesozoic marine metavolcanic and metasedimentary rocks that are intruded by Mesozoic granodiorite plutons (MacKevett Jr. et al., 1974; Macintyre and Schroeter, 1985; Redman et al., 1985; Still, 1991; Green et al., 2003; Wilson et al., 2015; Proffett, 2019). Figure 1.4 highlights the distribution of regional geologic units as compiled by Wilson et al. (2015). Geochronologic data includes fossils (Green et al., 2003), U-Pb zircon dates from the Palmer rhyolite (213 Ma) (Green, 2001), and U-Pb dates from detrital zircons (Karl et al., 2020). The locations of radiometric data from Green (2001) and Karl et al. (2020) are presented in Figure 1.4.

Thinly bedded limestone and marble of the Devonian basement rocks are in depositional contact with the overlying, informally-named Porcupine slates (Redman et al., 1985; Karl et al., 2010). The Porcupine slates are likely correlative with the Devonian to Early Permian Cannery Formation (Karl et al., 2010; Wilson et al., 2015). The Porcupine slates and Cannery Formation consist of cherty graywacke and argillite with subordinate conglomerate, limestone, and volcanic interbeds (Redman et al., 1985; Karl et al., 2010; Wilson et al., 2015). The youngest Paleozoic rocks are Early Permian and contain brachiopods in limestone that were documented in 1904 by C.W. Wright at a poorly referenced location along Porcupine Creek (Karl et al., 2010).

The Permian-Triassic boundary at Palmer is not easily distinguishable. Thick sequences of pillowed basalt of the Hyd Group provide the best indication of Triassic stratigraphy. Locally, Permian argillite is in contact with Triassic argillite but is often challenging to differentiate. Elsewhere in the Alexander terrane, the Permian-Triassic boundary is unconformable and marked by a distinct polymictic conglomerate (or breccia) containing locally derived Paleozoic clasts (Loney, 1964; Muffler, 1967; Taylor et al., 2008; Karl et al., 2010). At Greens Creek, mineralization is hosted in Upper Triassic sedimentary rocks directly above the Permian-Triassic unconformity, and is an economically significant contact regionally (Taylor et al., 2010; Steeves, 2018).

Geologic mapping and petrography by Proffett (2019) helped characterize the Permian-Triassic boundary near the headwaters of Sara Creek immediately to the north of the Jurassic argillites that are immediately north of the Palmer deposit (Fig. 1.4). Proffett (2019) identified marble clast-bearing conglomerates unconformably overlying marbles and greenstones of probable Paleozoic age; petrographic evidence also suggested the clasts were derived from underlying marbles and greenstones. Stratigraphically above the conglomerates are black limestone and a thick pile of pillowed basalts. An older foliation in the marbles and greenstones is truncated by the marble-clast conglomerate contact and crenulated by the main foliation observed in the rocks stratigraphically above the conglomerates (Proffett, 2019). Proffett's (2019) observations suggest that the marble-clast conglomerates occur at the Permian-Triassic boundary. Similar but more deformed marble clast conglomerates were documented by the author in 2018 on the hillsides flanking the eastern margin of the Jarvis Glacier; they may also represent the unconformable Triassic-Permian boundary, but more evidence is needed to test this hypothesis.

Lower to Middle Triassic rocks are not documented on the property and are mostly absent from the rock record in the Alexander terrane; an Anisian (Middle Triassic) conodont fossil from a limestone debris flow found east of Keku Strait is the only known pre-Late Triassic fossil in the Alexander terrane (Katvala and Stanley, 2008). Volcanogenic massive sulfide mineralization is hosted within Upper Triassic mafic-dominated, bimodal volcanic sequences with associated volcaniclastic rocks and minor fine-grained sedimentary and tuffaceous interbeds (Green et al., 2003; Steeves et al., 2016). The age of mineralization at Palmer is constrained by a U-Pb age of 213 +/- 5 Ma from a hydrothermally altered rhyolite at the Palmer deposit with stratiform mineralization above and below (Green et al., 2003).

The Triassic section is capped by volcanic breccias at the top of Mt. Morlan (Green et al., 2003), near the Palmer deposit, and black argillites that occupy a syncline (Proffett, 2019) to the north of the Palmer deposit. The igneous crystallization age for the volcanic breccia is ~195 Ma based on U-Pb zircon dates (Karl et al., 2020), and the black argillites have a young population of detrital zircons with U-Pb zircon dates of ~144 Ma (Karl et al., 2020).

Regional metamorphism and deformation

Mid-Cretaceous deformation of the Alexander terrane (Karl et al., 1999; Nelson et al., 2013b) resulted in four main deformation events (D1 to D4) that affected the rocks in the Palmer area (Lewis, 1998; Green et al., 2003). A north-south contractional deformation event (D1) is characterized by south-verging folds and thrust faults and slatey cleavage (S1) (Lewis, 1998; Green et al., 2003). It is best displayed by the deposit-scale geometry of Palmer, consisting of a south-verging, overturned anticline with ~200m displacement along a thrust fault proximal to the axial surface of the anticline (Green et al., 2003; Steeves et al., 2016). D2 is marked by tight to open, north-northwest-plunging folds (Green et al., 2003). D3 is weakly manifested as NE-striking crenulation cleavage in some rocks (Lewis, 1998; Green et al., 2003). D4 consists of poorly understood, late, SW- and NW-striking, high-angle brittle faults related to the post-middle Cretaceous and pre-Holocene (Hudson et al., 1982) dextral transpression that formed the Chatham Strait fault system (Karl et al., 1999; Steeves et al., 2016). Proffett (2019) documented an older foliation (pre-D1) in rocks of apparent Paleozoic age compared to the overlying Mesozoic rocks. Peak, lower to mid-greenschist facies, regional metamorphism (Green et al., 2003) was reached before the emplacement of non-metamorphosed granitic rocks with cooling ages between 110-120 Ma (Forbes et al., 1989). Reverse faults, normal faults (Lewis, 1998; Wasteneys, 2009), strike-slip faults (Proffett, 2016), and south-verging thrusts (Green et al., 2003) occur on the Palmer property.

1.4. AG Deposit Geology

The AG deposit is a tabular, steeply northeast dipping barite- and sulfide-rich lens underlain predominantly by coherent mafic flows and subordinate rhyolite (Gray and Cunningham-Dunlop, 2018). The immediate stratigraphic footwall to the deposit is comprised of rhyolitic lapilli tuffs and most mineralization is associated with these felsic tuffs and with basalts that contain distinctive white ovoid features that company geologists have called spherulites (Gray and Cunningham-Dunlop, 2018). The deposit is overlain by mafic volcaniclastic rocks that are overlain by argillite (Gray and Cunningham-Dunlop, 2018).

Based on the metal tenor, the AG deposit is divided into the “Main,” “Zinc,” “Hinge,” and “Upper” zones (Gray and Cunningham-Dunlop, 2018). Barite is a major phase, especially in the exhalative-style ores, and also occurs within veins (“stringers”) that are commonly sulfide-bearing (Doherty, 2018). Pyrite, sphalerite, galena, sulfosalts, and rare chalcopyrite are present as disseminated, vein, semi-massive, and massive sulfide facies (Doherty, 2018). Hydrothermal alteration assemblages in the stratigraphic footwall are dominated by pervasive fine-grained white mica (colloquially referred to as sericite), disseminated pyrite, and variable pervasive to selective quartz (Gray and Cunningham-Dunlop, 2018). Hyperspectral imaging of white micas shows that short wave infrared Al-OH feature absorption wavelengths range from 2190 nm to 2215 nm, indicating the presence of paragonite (2,195 nm), muscovite (2,200 nm) and phengite (2,210 nm), however these data were insufficient to document the distribution of mica species in the deposit area (Transburg, 2020).

1.5. VMS Deposits

Volcanogenic massive sulfide (VMS) deposits are stratiform concentrations of sulfide minerals that precipitate on or near the seafloor from hydrothermal fluids that form by the convective circulation of seawater through ocean crust in thermally driven, submarine, extensional regimes (Fig. 1.6; Franklin et al., 2005; Hannington et al., 2005; Galley et al., 2007). Volcanogenic massive sulfide deposits are syngenetic and stratigraphic setting exerts a first-order control on their formation. Structures and permeability of substrate control the migration of hydrothermal fluids and can influence deposit morphology (Gibson et al., 1999). Further, the volcano-sedimentary sequences that host VMS deposits are diverse and can reflect complex and dynamic volcanic, sedimentary, tectonic, and alteration processes, which can influence metal tenor, size, geometry, mineralization styles, and preservation.

1.5.1. VMS model

Extensional submarine environments and high-temperature magmatism are essential components for the formation of VMS deposits (Lesher et al., 1986; Hart et al., 2004; Franklin et al., 2005; Hannington et al., 2005; Galley et al., 2007; Piercey, 2010). Rift environments contain extensional faults that serve as fluid pathways for hydrothermal convective cells and provide void space for upwelling high-temperature magmas (Fig. 1.6; Galley et al., 2007; Piercey, 2011). Mantle-derived, high-temperature magmatism within shallow (3–10 km) crustal levels initiates and sustains hydrothermal convective cell(s) by drawing seawater (with dissolved Cl^- and SO_4^{2-}) down through the brittle section of crust (1–3 km) where it is modified by a series of high-temperature fluid-rock chemical reactions to become a high-temperature (250–400°C), acidic fluid (Fig. 1.6; Franklin et al., 2005; Herzig and Hannington, 2006; Galley et al., 2007; Gibson et al., 2007; Hannington, 2013). This highly reactive fluid can leach metals (such as Li, K, Rb, Ca, Ba, Fe, Mn, Cu, Zn, Au, Ag, and some Si) from the wall rock putting them into solution as chloride complexes (Herzig and Hannington, 2006). In some systems, magmatic fluids and gases may also contribute metals to the hydrothermal fluids (Hannington et al., 2005; Piercey et al., 2015). These hot, metalliferous fluids above high-level magma chambers are buoyant and migrate through the crust to the seafloor, preferentially along major structures, but they can also migrate laterally through porous substrates. The abrupt change in conditions at or near the seafloor causes sulfide or sulfate minerals to precipitate as the hydrothermal fluids mix with ambient seawater (~2^{o}C). The complete convective cycle of seawater through the crust occurs within an estimated three years or less (Herzig and Hannington, 2006). Volcanogenic massive sulfide mineralization emplaced within the existing seafloor substrate is replacement-style, whereas mineralization formed by exhalation on the seafloor is exhalative-style (Doyle and Allen, 2003; Piercey, 2015). Black smokers on the modern seafloor, modern analogs to some ancient VMS deposits, are the physical expressions of exhalative-style mineralization. They result from the venting of hydrothermal fluids (generally >300^{o}C to 400^{o}C) containing sufficient metal and sulfur to precipitate iron sulfide and iron oxide particles, whereas white smokers result from the venting of cooler (<10^{o}C to 50^{o}C) hydrothermal fluids that are not capable of transporting significant dissolved metals and instead produce minerals such as anhydrite, barite, or siliceous Fe-oxyhydroxides, Mn-oxides and silica (Herzig and Hannington, 2006). Chemical sedimentary rocks that are products of exhalative processes have been referred to by many names depending on their character (e.g., barite-rich rocks, chert, jasper, Algoma-type iron formations) and all can broadly be termed "exhalites" (James, 1954; Gross, 1983; Spry et al., 2000; Peter, 2003). Because they are genetically linked to hydrothermal fluids they can be spatially and temporally associated with VMS deposits (Peter, 2003).

Many factors influence the size, geometry, and metal endowment of VMS deposits, including host substrate composition (Barrie and Hannington, 1999) and texture/permeability (Gibson et al., 1999), tectonic spreading rates (Hannington et al., 2005; Patten et al., 2016), redox conditions (Herzig and Hannington, 2006), or presence of a sediment pile (Herzig and Hannington, 2006). These factors are not critical to forming VMS deposits but can account for unique features observed between deposits (Franklin et al., 2005).

The growth of a VMS deposit requires a period of volcanic quiescence to allow for the undisturbed deposition of metals. Larger and higher-grade deposits generally have more complex growth patterns and result from "zone refinement" processes (Piercey et al., 2015). Zone refinement is the redistribution of metals in the massive sulfide mound caused by the progressive dissolution and sequential precipitation of metals in response to decreasing temperature and increasing pH during mixing with cold seawater (Eldridge et al., 1983; Lydon, 1988; Gibson et al., 2007). The sulfide mound can trap metals before they are diluted and dispersed at the vent site. This process is especially important in the genesis of Zn-rich VMS deposits (Piercey et al., 2015). Finally, the preservation of a deposit relies on shielding from natural submarine erosion and weathering processes, generally through subsequent burial.

1.5.2. Classification

Several classification schemes for VMS deposits have been proposed based mainly on ore composition or host-rock lithology (Franklin et al., 1981). The most widely-used classification is non-genetic, based on the pre-alteration host-rock lithologies and geodynamic setting, and includes mafic, mafic siliciclastic, bimodal mafic, bimodal felsic and felsic siliciclastic (Barrie and Hannington, 1997; Franklin et al., 2005; Galley et al., 2007; Piercey, 2011; Piercey et al., 2015). Piercey (2011) summarizes the petrochemical associations and tectonic implications of these end-member classes (Fig. 1.6) and shows that some volcanic successions have progressive geochemical variations throughout their stratigraphy that reflect shifting geodynamic regimes. As such, this classification scheme is closely linked to the tectonic setting of formation.

1.5.3. Tectono-magmatic associations

Volcanogenic massive sulfide deposits form in extensional environments that range from primitive to more evolved (continental) settings, including mid-ocean ridges (ophiolites), intra-oceanic arc rifts, back-arc basins, evolved rifted arcs, rifted continental margins, or intra-continental rifts (Fig. 1.8; Barrett and MacLean, 1999; Galley et al., 2007; Piercey, 2010). Each tectonic setting is associated with distinct suites of igneous rocks that reflect magmatic source(s), melting depth(s), degree(s) of melting, melt temperature(s), and mantle flow regimes.

In an extensional environment, two important things happen:

(1) the crust attenuates, causing a decrease in lithostatic pressure, which may induce upwelling of the mantle and associated adiabatic melting; and

(2) networks of extensional faults develop to accommodate brittle deformation and serve as fluid pathways for the hydrothermal convective cell and, in some cases, for ascending magmas (Piercey, 2011).

Hot, mafic melts derived from the mantle are generally not buoyant in the crust, resulting in ponding at the base of the crust in a process referred to as basaltic underplating (Fig. 1.9; Galley et al., 2007; Winter, 2010; Piercey, 2011). The thermal input of these ponded basalts is essential to induce crustal, partial melting resulting in the formation of intermediate to silicic melts (Huppert and Sparks, 1988). The mechanisms that drive VMS formation and the nuances specific to each tectonic setting of formation are geochemically and petrologically reflected in the overall volcanic successions that host these deposits.

1.5.4. Using geochemistry for VMS exploration

Geochemistry can be used to investigate precursor composition, alteration, and ore-bearing potential of host rocks to VMS mineralization. Primary igneous lithogeochemical signatures provide insight into an assemblage's tectonic and petrologic history (Lesher et al., 1986; Hart et al., 2004; Piercey, 2010; Piercey, 2011). Immobile elements are unaffected by metasomatism and, therefore, can be used to investigate magmatic processes, precursor composition, and tectonic setting (e.g., Pearce et al., 1984; Lesher et al., 1986; Hart et al., 2004; Piercey, 2010; Ross and Bédard, 2009; Piercey, 2010; Pearce, 2014). Common immobile elements include Al_2O_3, TiO_2, high field strength elements (HFSE; Zr, Hf, Nb, Ta, Y, Sc, Ti, V), and rare earth elements (REE) (Piercey, 2010). The Cann (1970) correlation method can be applied to test the mobility of elements in any given suite of rocks prior to lithogeochemical determinations that rely on the assumptions of immobility.

Altered rocks near VMS deposits may include hydrothermal alteration products, diagenesis, seafloor weathering and oxidation, and regional metamorphism (Gifkins et al., 2005). Hydrothermally altered rocks in VMS systems reflect the large-scale convective cell that drives fluid circulation associated with ore deposition and the associated redistribution of elements (Galley, 1993; Gifkins et al., 2005). Major element ratios, normative calculations, alteration indices, and mass balance calculations can be used to evaluate hydrothermal alteration (Barrett and MacLean, 1994; Large et al., 2001; Mathieu, 2018). Establishing that a hydrothermal system is present, understanding the chemical reactions that produce alteration mineral assemblages, and then quantifying the intensity and extent of the alteration provides insight into the genesis of a deposit and guides exploration efforts.

1.6. Fundamental research questions and approaches

This thesis aims to use detailed mapping, core logging, petrography, geochemistry, and geologic modeling to reconstruct the volcanic environment hosting the AG deposit and to develop a genetic model for the AG deposit. Furthermore, geochronologic studies will help to understand the timing of hydrothermal mineralization. This research will also set the framework for future detailed studies on other aspects of the deposit.

This thesis aims to:

1. Characterize the lithostratigraphy by:
    a. logging drill core at a scale of 1:400.
    b. geologic mapping near the AG zone deposit at a scale of 1:1,000.
    c. collecting hand samples from the surface and drill core
    d. describing the mineralogy, mineral assemblages, and textures of the rocks.
    e. conducting petrographic analysis using both transmitted and reflected light microscopy.
    f. identifying textures and minerals that are indistinguishable by transmitted and reflected light microscopy methods using:
        i. a scanning electron microscope (SEM); and
        ii. an electron probe microanalyzer (EPMA),
2. Establish the tectono-magmatic framework of the deposit by:

    a. distinguishing and interpreting volcano-sedimentary facies using geologic mapping and petrographic techniques; and
    b. investigating the lithogeochemistry using immobile element ratios, discrimination diagrams, multi-element normalized diagrams, and other geochemical and geostatistical methods.
3. Present an updated geologic map and associated cross-section interpretations by:
    a. incorporating core logging observations, surface geological mapping, lithogeochemical analyses, and structural observations into 2D
    b. modeling the chemostratigraphy in LeapFrog Geo 3D software
4. Constrain the timing of VMS mineralization with a combination of:
    a. laser ablation inductively coupled plasma mass spectrometry (LA-ICPMS) U-Pb zircon geochronology,
    b. and chemical abrasion isotope dilution thermal ionization mass spectrometry (CA-ID-TIMS) U-Pb zircon geochronology

1.7. Research goals and organization of the thesis

This research project aims to understand how the AG deposit formed and the main controls on this formation, the chemostratigraphy of volcanic units, their petrogenetic history and tectonic settings, the volcanic facies of these units, and their emplacement, and inter-relationships between units. Further, it will evaluate the structural architecture of the deposit and whether syn-volcanic faults can be identified. This research will also evaluate the age of mineralization at AG and compare when it formed with other VMS mineralization on the Palmer Property and in the ATMB. Further, petrogenetic information from both mafic and felsic igneous rocks may provide insight into the relationship of magmatism and tectonics to the formation of bimodal VMS deposits, and provide insight into the evolution of the ATMB.

This thesis includes three chapters with accompanying appendices. Chapter one provides background information and the research objectives. Chapter two is written as a scientific paper intended for publication and contains the lithologic descriptions, chemostratigraphic observations, geochronologic results, and a genetic model for the AG deposit based on mapping, core logging, petrography, lithogeochemical techniques, and U-Pb geochronology. Chapter three summarizes the research conclusions and proposes future research ideas. The appendices contain photographs of the AG deposit host stratigraphy, petrographic descriptions, geochemical data, geochronologic data, and electron probe microanalyzer (EPMA) data.

Chapter 1 References

Allen, R.L., Weihed, P., Blundell, D., Crawford, T., Davidson, G., Galley, A., Gibson, H., Hannington, M., Herzig, P., Large, R., Lentz, D., Maslennikov, V., McCutcheon, S., Peter, J., et al., 2002, Global comparisons of volcanic-associated massive sulphide districts: Geological Society of London, Special Publications, v. 204, p. 13–37.

Ayuso, R.A., Karl, S.M., Slack, J.F., Haeussler, P.J., Bittenbender, P.E., Wandless, G.A., and Colvin, A.S., 2005, Oceanic Pb-isotopic sources of Proterozoic and Paleozoic volcanogenic massive sulfide deposits on prince of Wales Island and vicinity, southeastern Alaska: U.S. Geological Survey Professional Paper 1732-E, 20 p.

Barrett, T.J., and MacLean, W.H., 1994, Mass changes in hydrothermal alteration zones associated with VMS deposits of the Noranda area: Exploration and Mining Geology, v. 3, p. 131–160.

Barrett, T.J., and MacLean, W.H., 1999, Volcanic sequences, lithogeochemistry, and hydrothermal alteration in some bimodal volcanic-associated massive sulfide systems: Reviews in Economic Geology, v. 8, p. 101–132.

Barrie, C.T., and Hannington, M.D., 1999, Classification of volcanic-associated massive sulfide deposits based on host-rock composition: Reviews in Economic Geology, v. 8, p. 1–12.

Bennett, S.M., 2016, 2016 Minerals Yearbook: Silver: U.S. Geological Survey, p. 68.1-68.13.

Beranek, L.P., van Staal, C.R., Gordee, S.M., McClelland, W.C., Israel, S., and Mihalynuk, M., 2012, Tectonic significance of Upper Cambrian-Middle Ordovician mafic volcanic rocks on the Alexander terrane, Saint Elias Mountains, northwestern Canada: Journal of Geology, v. 120, p. 293–314.

Beranek, L.P., van Staal, C.R., McClelland, W.C., Joyce, N., and Israel, S., 2014, Late Paleozoic assembly of the Alexander-Wrangellia-Peninsular composite terrane, Canadian and Alaskan Cordillera: Geological Society of America Bulletin, v. 126, p. 1531–1550.

Berg, H.C., Jones, D.L., and Richter, D.H., 1972, Gravina-Nutzotin Belt: Tectonic significance of an Upper Mesozoic sedimentary and volcanic sequence in southern and southeastern Alaska: U.S. Geological Survey Professional Paper 800-D, p. D1–D24.

Cann, J.R., 1970, Rb, Sr, Y, Zr and Nb in some ocean floor basaltic rocks: Earth and Planetary Science Letters, v. 10, p. 7–11.

Cui, Y., Miller, D., Schiarizza, P., and Diakow, L.J., 2017, British Columbia digital geology: British Columbia Ministry of Energy, Mines and Petroleum Resources, British Columbia Geological Survey Open File 2017-8, 9p. Data version 2019-12-19.

Doherty, J., 2018, The mineralogy, ore mineral chemistry, and geochemistry of the Nunatak prospect AG Zone: a new Zn-Pb-Cu-Ag (Au)-barite VMS discovery outside of Haines, Alaska: Report synthesizing applied M.Sc. program research, Kingston, Canada, Queen's University: 83 p.

Doyle, M.G., and Allen, R.L., 2003, Subsea-floor replacement in volcanic-hosted massive sulfide deposits: Ore Geology Reviews, v. 23, p. 183–222.

Eldridge, C.S., Barton Jr., P.B., and Ohmoto, H., 1983, Mineral textures and their bearing on formation of the Kuroko orebodies: Economic Geology Monograph, v. 5, p. 241–281.

Forbes, R.B., Gilbert, W.., and Redman, E., 1989, Geologic setting and petrology of the metavolcanic rocks in the northwestern part of the Skagway B-4 Quadrangle, southeastern Alaska: Alaska Division of Geological & Geophysical Surveys Public Data File 89-14, 46 p.

Franklin, J.M., Lydon, J.W., and Sangster, D.F., 1981, Volcanic-associated massive sulfide deposits: Economic Geology, 75th Anniversary Volume, p. 485–627.

Franklin, J.M., Gibson, H.L., Jonasson, I.R., and Galley, A.G., 2005, Volcanogenic massive sulfide deposits: Economic Geology, 100th Anniversary Volume, p. 523–560.

Galley, A.G., 1993, Characteristics of semi-conformable alteration zones associated with volcanogenic massive sulphide districts: Journal of Geochemical Exploration, v. 48, p. 175–200.

Galley, A.G., Hannington, M.D., and Jonasson, I.R., 2007, Volcanogenic massive sulphide deposits: Geological Association of Canada, Special Publication, v. 5, p. 141–161.

Gehrels, G.E., Butler, R.F., and Bazard, D.R., 1996, Detrital zircon geochronology of the Alexander terrane, southeastern Alaska. Geological Society of America Bulletin 108, p. 722–734.

Gehrels, G.E., and Berg H.C., 1994, Geology of southeastern Alaska: Geological Society of America, v. G-1, p. 451–467.

Gehrels, G.E., and Saleeby, J.B., 1987, Geologic framework, tectonic evolution, and displacement history of the Alexander terrane: Tectonics, v. 6, p. 151–173.

Gibson, H.L., Morton, R.L., and Hudak, G.J., 1999, Submarine volcanic processes, deposits, and environments favorable for the location of volcanic-associated massive sulfide deposits: Reviews in Economic Geology, v. 8, p. 13–52.

Gibson, H.L., Allen, R.L., Riverin, G., and Lane, T.E., 2007, The VMS model: advances and application to exploration targeting: Proceedings of Exploration: Fifth Decennial International Conference on Mineral Exploration, v. 7, p. 713–730.

Gifkins, C., Herrmann, W., and Large, R., 2005, Altered volcanic rocks: a guide to description and interpretation: Hobart, Australia, Centre for Ore Deposit Research University of Tasmania, 275 p.

Goodwin, R., Mcleod, K., Levy, M., DiMarchi, J.J., Gray, J.N., and Casey, J., 2019, Palmer project Alaska, USA: NI 43-101 Report for Constantine Metal Resources Ltd. June 3, 2019, 326 p.

Gray, J.N., and Cunningham-Dunlop, I.R., 2018, Updated resource estimate to include the AG zone resource estimate for the Palmer exploration project, Porcupine Mining District, Southeast Alaska, USA: NI 43-101 Report for Constantine Metal Resources Ltd. December 18, 2018, 233 p.

Green, D., 2001, Geology of volcanogenic massive sulphide prospects of the Palmer property, Haines area, southeastern Alaska: M.Sc. thesis, Ottawa, Canada, Carleton University: 255 p.

Green, D., MacVeigh, J.G., Palmer, M., Watkinson, D.H., and Orchard, M.J., 2003, Stratigraphy and geochemistry of the RW Zone, a new discovery at the Glacier Creek VMS prospect, Palmer property, Porcupine Mining District, southeastern Alaska: Division of Geological & Geophysical Surveys Professional Report 120, p. 35–51.

Gross, G.A., 1983, Tectonic systems and the deposition of iron-formation: Precambrian Research, v. 20, p. 171–187.

Hannington, M.D., 2014, Volcanogenic massive sulfide deposits: Treatise on Geochemistry 2, Oxford, England, Elsevier, v. 13, p. 463–488.

Hannington, M.D., De Ronde, C.E.J., and Petersen, S., 2005, Sea-floor tectonics and submarine hydrothermal systems: Economic Geology, 100th Anniversary Volume, p. 111–141.

Hart, T.R., Gibson, H.L., and Lesher, C.M., 2004, Trace element geochemistry and petrogenesis of felsic volcanic rocks associated with volcanogenic massive Cu-Zn-Pb sulfide deposits: Economic Geology, v. 99, p. 1003–1013.

Herzig, P.M., and Hannington, M.D., 2006, Input from the deep: Hot vents and cold seeps: Marine Geochemistry, Berlin, Germany, Springer, p. 457–479.

Hudson, T., Plafker, G., and Dixon, K., 1982, Horizontal offset history of the Chatham Strait fault: U.S. Geological Survey Circular 844, p. 128–131.

Huppert, H.E., and Sparks, R.S.J., 1988, The generation of granitic magmas by intrusion of basalt into continental crust: Journal of Petrology, v. 29, p. 599–624.

Israel, S., Beranek, L., Friedman, R.M., and Crowley, J.L., 2014, New ties between the Alexander terrane and Wrangellia and implications for North America Cordilleran evolution: Lithosphere, v. 6, p. 270–276.

James, H.L., 1954, Sedimentary facies of iron-formation: Economic Geology, v. 49, p. 235–293.

Karl, B.S.M., Haeussler, P.J., and Mccafferty, A., 1999, Reconnaissance geologic map of the Duncan Canal-Zarembo Island area, southeastern Alaska: U.S. Geological Survey Open-File Report 99-168, p. 1–29.

Karl, S., Steeves, N., Quinn, K., Proffett, J., O'Sullivan, P.B., McMillan, J., and Jones, J. V, 2020, Lower Jurassic volcanic and sedimentary rocks depositionally overlie Upper Triassic host rocks at the Palmer VMS property in the Alexander Triassic metallogenic belt, southeast Alaska: Geological Society of America, Abstracts with Programs, v. 52, doi:10.1130/abs/2020AM-357716.

Karl, S.M., Layer, P.W., Harris, A.G., Haeussler, P.J., and Murchey, B.L., 2010, The Cannery Formation—Devonian to Early Permian arc-marginal deposits within the Alexander terrane, southeastern Alaska: U.S. Geological Survey Professional Paper 1776-B, 45 p.

Katvala, E.C., and Stanley, G.D., 2008, Conodont biostratigraphy and facies correlations in a Late Triassic island arc, Keku Strait, southeast Alaska: Geological Society of America, Special Paper 442, p. 181–226.

Large, R.R., Gemmell, J.B., and Paulick, H., 2001, The alteration box plot: A simple approach to understanding the relationship between alteration mineralogy and lithogeochemistry associated with volcanic-hosted massive sulfide deposits: Economic Geology, v. 96, p. 957–971.

Lesher, C.M., Goodwin, A.M., Campbell, I.H., and Gorton, M.P., 1986, Trace-element geochemistry of ore-associated and barren, felsic metavolcanic rocks in the Superior Province, Canada: Canadian Journal of Earth Sciences, v. 23, p. 222–237.

Lewis, P., 1998, Palmer Project preliminary field report: Structural and stratigraphic setting of mineral occurrences, Glacier and Jarvis Creek area, Haines, Alaska: Unpublished consulting report for Rubicon Minerals Corporation, 11 p.

Loney, R.A., 1964, Stratigraphy and petrography of the Pybus-Gambier area, Admiralty Island, Alaska: U.S. Geological Survey Bulletin 1178, 2 sheets, scale 1:63,360, 103 p.

Lydon, J.W., 1988, Volcanogenic massive sulphide deposits Part 2: Genetic models: Geoscience Canada, v. 15, p. 43–65.

Macintyre, D.G., and Schroeter, T.G., 1985, Mineral occurrences in the Mount Henry Clay area: British Columbia Ministry of Energy, Mines and Petroleum Resources, Geological Fieldwork Paper 1985-1, p. 365–379.

MacIntyre, D.G., Mihalynuk, M.G., Smith, M.T., Schiarizza, P., and Deschênes, M. Timmerman, J., 1992, Tats Lake map area geology: Northwest Tatshenshini River map area, northwestern British Columbia: British Columbia Ministry of Energy, Mines and Petroleum Resources, Open File 1993-13, 6 sheets.

MacKevett Jr., E.M., Robertson, E.C., and Winkler, G.R., 1974, Geology of the Skagway B-3 and B-4 quadrangles, southeastern Alaska: U.S. Geological Survey Professional Paper 832, 33 p.

Mathieu, L., 2018, Quantifying hydrothermal alteration: a review of methods: Geosciences, v. 8, doi: 10.3390/geosciences8070245.

Miller, L., 2015, Stratigraphy, structure, and volcanic rock geochemistry in the Little Jarvis area of the Palmer Property, southeast Alaska: B.A. senior thesis, Vermont, USA, Middlebury College: 81 p.

Monecke, T., Mercier-Langevin, P., and Dube, B., 2017, Archean base and precious metal deposits, southern Abitibi greenstone belt: Reviews in Economic Geology, v. 19, p. 1–5.

Muffler, L.P., 1967, Stratigraphy of the Keku Islets and neighboring parts of Kuiu and Kupreanof Islands, southeastern Alaska: U.S. Geological Survey Bulletin 1241–C, 1 pl., scale 1:63,360, 52 p.

Nelson, J., Diakow, L., van Staal, C., and Chipley, D., 2013a, Ordovician volcanogenic sulphides in the southern Alexander terrane, coastal NW British Columbia: Geology, Pb isotopic signature, and a case for correlation with Appalachian and Scandinavian deposits: British Columbia Ministry of Energy, Mines and Natural Gas Geological Survey Paper 2013-1, p. 13–34.

Nelson, J.L., Colpron, M., and Israel, S., 2013b, The Cordillera of British Columbia, Yukon, and Alaska: tectonics and metallogeny: Society of Economic Geologists, Special Publication, v. 17, p. 53–109.

Newberry, R.J., Crafford, T.C., Newkirk, S.R., Young, L.E., Nelson, S.W., and Duke, N.A., 1997, Volcanogenic massive sulfide deposits of Alaska: Economic Geology Monograph, v. 9, p. 120–150.

Patten, C., Pitcairn, I., Teagle, D., and Harris, M., 2016, Mobility of Au and related elements during the hydrothermal alteration of the oceanic crust: implications for the sources of metals in VMS deposits: Mineralium Deposita, v. 51, p. 179–200.

Pearce, J.A., 2014, Immobile element fingerprinting of ophiolites: Elements, v. 10, p. 101–108.

Pearce, J.A., Harris, N.B.W., and Tindle, A.G., 1984, Trace element discrimination diagrams for the tectonic interpretation of granitic rocks: Journal of Petrology, v. 25, p. 956–983.

Peter, J.M., 2003, Ancient iron formations: Their genesis and use in the exploration for stratiform base metal sulphide deposits, with examples from the Bathurst mining camp: Geological Association of Canada, GeoText, v. 4, p. 145–176.

Peter, J.M., and Scott, S.D., 1997, Windy Craggy, northwestern British Columbia: The world's largest Besshi-type deposit: Reviews in Economic Geology, v. 8, p. 261–296.

Peter, J.M., Leybourne, M.I., Scott, S.D., and Gorton, M.P., 2014, Geochemical constraints on the tectonic setting of basaltic host rocks to the Windy Craggy Cu-Co- Au massive sulphide deposit, northwestern British Columbia: International Geology Review, v. 56, p. 1484–1503.

Piercey, S.J., 2010, An overview of petrochemistry in the regional exploration for volcanogenic massive sulphide (VMS) deposits: Geochemistry: Exploration, Environment, Analysis, v. 10, p. 1–18.

Piercey, S.J., 2011, The setting, style, and role of magmatism in the formation of volcanogenic massive sulfide deposits: Mineralium Deposita, v. 46, p. 449–471.

Piercey, S.J., 2015, A semipermeable interface model for the genesis of subseafloor replacement-type volcanogenic massive sulfide (VMS) deposits: Economic Geology, Special Publication, v. 110, p. 1655–1660.

Piercey, S.J., Peter, J.M., and Herrington, R.J., 2015, Zn-rich volcanogenic massive sulphide (VMS) deposits: Irish Association for Economic Geology, Special Publication, p. 37–57.

Plafker, G., and Berg, H.C., 1994, Overview of the geology and tectonic evolution of Alaska: Geological Society of America, v. G-1, p. 989–1021.

Premo, W.R., Taylor, C.D., Snee, L.W., and Harris, A.G., 2010, Microfossil and radioisotopic geochronological studies of the Greens Creek host rocks: U.S. Geological Survey Professional Paper 1763, p. 287–333.

Proffett, J., 2016, Review of the Kudo fault and adjacent area, Glacier Creek deposit, Palmer Prospect, southeastern Alaska: Unpublished consulting report for Constantine Metal Resources Ltd., 14 p.

Proffett, J., 2019, Results of geological mapping at the Palmer Project, Alaska: Unpublished consulting report for Constantine Metal Resources Ltd., 2 sheets, map scale 1:2,000, 24 p.

Redman, E.C., Gilbert, W.G., Jones, B.K., Rosenkrans, D.S., and Hickok, B.D., 1985, Preliminary bedrock-geologic map of the Skagway B-4 Quadrangle, Alaska: Alaska Division of Geological and Geophysical Surveys Report of Investigations 85–6, 1 sheet, scale 1:40,000.

Ross, P.S., and Bédard, J.H., 2009, Magmatic affinity of modern and ancient subalkaline volcanic rocks determined from trace-element discriminant diagrams: Canadian Journal of Earth Sciences, v. 46, p. 823–839.

Sack, P., 2009, Characterization of footwall lithologies to the Greens Creek volcanic-hosted massive sulfide (VHMS) deposit , Alaska, USA: Ph.D. thesis, Hobart, Australia, University of Tasmania: 415 p.

Sack, P.J., Berry, R.F., Gemmell, J.B., Meffre, S., and West, A., 2016, U-Pb zircon geochronology from the Alexander terrane, southeast Alaska: implications for the Greens Creek massive sulphide deposit: Canadian Journal of Earth Sciences, v. 53, p. 1458–1475.

Slack, J.F., Shanks, W.C., Karl, S.M., Gemery, P.A., Bittenbender, P.E., and Ridley, W.I., 2007, Geochemical and sulfur-isotopic signatures of volcanogenic massive sulfide deposits on Prince of Wales Island and vicinity, southeastern Alaska: U.S. Geological Survey Professional Paper 1732 C, p. 1–37.

Soja, C.M., and Antoshkina, A.I., 1997, Coeval development of Silurian stromatolite reefs in Alaska and the Ural Mountains: implications for paleogeography of the Alexander terrane: Geology, v. 25, p. 539–542.

Spry, P.G., Peter, J.M., and Slack, J.F., 2000, Meta-exhalites as exploration guides to ore: Reviews in Economic Geology, v. 11, p. 163–201.

Steeves, N.J., 2013, Mineralization and alteration of the Late Triassic Glacier Creek Cu-Zn VMS deposit, Palmer project, Alexander terrane, Southeast Alaska: M.Sc. thesis, Ottawa, Canada, University of Ottawa: 365 p.

Steeves, N.J., 2018, Mineralization and genesis of the Greens Creek volcanogenic massive sulfide (VMS) deposit, Alaska, USA: Ph.D. thesis, Hobart, Australia, University of Tasmania: 416 p.

Steeves, N.J., Hannington, M.D., Gemmell, J.B., Green, D., and Mcveigh, G., 2016, The Glacier Creek Cu-Zn VMS deposit, southeast Alaska: an addition to the Alexander Triassic metallogenic belt: Economic Geology, v. 111, p. 151–178.

Still, J.C., 1991, Mineral investigations in the Juneau mining district, Alaska, 1984-1988: U.S. Bureau of Mines Special Publication, v. 2A, 9 sheets, 214 p.

Still, J.C., Bittenbender, P.E., Bean, K.W., and Gensler, E.G., 2002, Mineral assessment of the Stikine area, central southeast Alaska: U.S. Bureau of Land Management Technical Report 51, p. 560.

Taylor, C.D., 1993, Summary of geochemical data; Annette Islands Reserve, southeast Alaska: U.S. Geological Survey Special Symposium, p. 77–82.

Taylor, C.D., Premo, W.R., Meier, A.L., and Taggart, J.E.J., 2008, The metallogeny of Late Triassic rifting of the Alexander terrane in southeastern Alaska and northwestern British Columbia: Economic Geology, v. 103, p. 89–115.

Taylor, C.D., Philpotts, J., Premo, W.R., Meier, A.L., and Taggart, J.E., 2010, The Late Triassic metallogenic setting of the Greens Creek massive sulfide deposit in southeastern Alaska: U.S. Geological Survey Professional Paper 1763, p. 13–59.

Transburg, F.W., 2020, Alteration characteristics of the newly discovered AG zone deposit volcanogenic massive sulfide prospect, Palmer property, southeast Alaska: Alaska Mining

Association Conference, Program with Abstract, p. 13.

Wasteneys, H., 2009, Geology of the Palmer map area: interpretation to accompany ArcGIS 9.3 compilation map for Constantine Metal Resources Ltd.: Unpublished consulting report for Constantine Metal Resources Ltd., geodatabase, 21 p.

White, C., Gehrels, G.E., Pecha, M., Giesler, D., Yokelson, I., McClelland, W.C., and Butler, R.F., 2016, U-Pb and Hf isotope analysis of detrital zircons from Paleozoic strata of the southern Alexander terrane (southeast Alaska): Lithosphere, v. 8, p. 83–96.

Wilson, F.H., Hults, C.P., Mull, C.G., and Karl, S.M., 2015, Geologic map of Alaska: U.S. Geological Survey Scientific Investigations map 3340, 2 sheets, geodatabase, 1 pamphlet, 196 p.

Winter, J.D., 2010, An introduction to igneous and metamorphic petrology: Upper Saddle River, USA, Pearson Prentice Hall, 702 p.

Woodsworth, G.J., and Orchard, M.J., 1985, Upper Paleozoic to Lower Mesozoic strata and their conodonts, western Coast Plutonic Complex, British Columbia: Canadian Journal of Earth Sciences, v. 22, p. 1329–1344.

Chapter 1 Tables

Table 1.1 Summary of significant VMS deposits in the ATMB. The VMS classifications are based on Barrie and Hannington (1997). Data for Windy Craggy are from Peter and Scott (1997) and Peter et al. (2014); data for Greens Creek are from Premo et al. (2010), Steeves (2018), Sack (2009) and Sack et al. (2016); data for the Palmer deposit are from Goodwin et al. (2019), Green (2001), and Steeves et al., (2016); data for the AG deposit are from Goodwin et al. (2019) and [1]this thesis.

	Windy Craggy deposit	Greens Creek deposit	Palmer deposit	AG deposit
Classification	Pelitic-mafic; Besshi type	Mafic of pelitic-mafic VMS; hybrid VMS-SEDEX	Bimodal-mafic; Kuroko type	Bimodal-mafic; Kuroko type
Main Commodities	Cu-Co-Au-Ag	Zn-Pb-Ag-Au	Zn-Cu-Ag-Au-$BaSO_4$	Zn-Pb-Ag-Au-$BaSO_4$
Tonnage	297.4 Mt	24.2 Mt	10.0 Mt	4.3 Mt
Grade	1.38% Cu, 0.07% Co, 0.2 g/t Au, 3.8 g/t Ag	13.9% Zn, 5.1% Pb, 658 g/t Ag, 5.1 g/t Au	4.7 Mt indicated resource grading 5.23 % Zn, 1.49 % Cu, 30.8 g/t Ag, 0.30 gt Au, 23.9 % $BaSO_4$ 5.3 Mt inferred resrouce grading 5.20 % Zn, 0.96 % Cu, 29.2 g/t Ag, 0.28 g/t Au, 22.0 % $BaSO_4$	4.64 % Zn, 0.12 % Cu, 0.96 % Pb, 119.5 g/t Ag, 0.53 g/t Au, 34.8 % $BaSO_4$ (inferred)
Host rocks	Argillites and alkalic basaltic flows and dikes/sills	Graphitic argillite, dolomite, and sedimentary breccias; footwall Mississipian (340 - 330 Ma) tholeiitic mafic volcanic rocks and phyllites (volcaniclastic rocks mixed with graphitic sedimentary component)	Tholeiitic plagioclase-phyric basalt, volcaniclastic rocks, rhyolite, tuffaceous rocks, argillites	Tholeiitic basalts including FeTi basalts, ferro-andesites, ferro-dacites, FIIIa ferro-rhyolites, FIIIb high-silica rhyolites, volcaniclastic rocks, minor argillites[1]
Age	Early Norian (~225 Ma) based on conodonts collected within sedimentary beds hosting the deposit.	Younger than (1) a Hyd Group rhyolite with a CA-ID-TIMS U-Pb zircon date of 226.86 ± 0.24 Ma and (2) argillite with Norian-Carnian (227 ± 4.4 Ma) conodonts. These argillites are intruded by gabbros with a LA-ICP-QMS U-Pb zircon date of 219 ± 8 Ma. Possibly coeval with nearby altered mafic-ultramafic intrusions that have fuchsite with a $^{40}Ar/^{39}Ar$ plateau age of 210.3 ± 0.3 Ma.	Coeval with rhyolite that has a ID-TIMS U-Pb zircon date of 213 ± 5 Ma.	Between 210.60 Ma to 210.08 Ma based on coeval rhyolites with CA-ID-TIMS U-Pb zircon dates of 210.35 ± 0.27, and 210.52 ± 0.08 Ma.[1]

Chapter 1 Figures

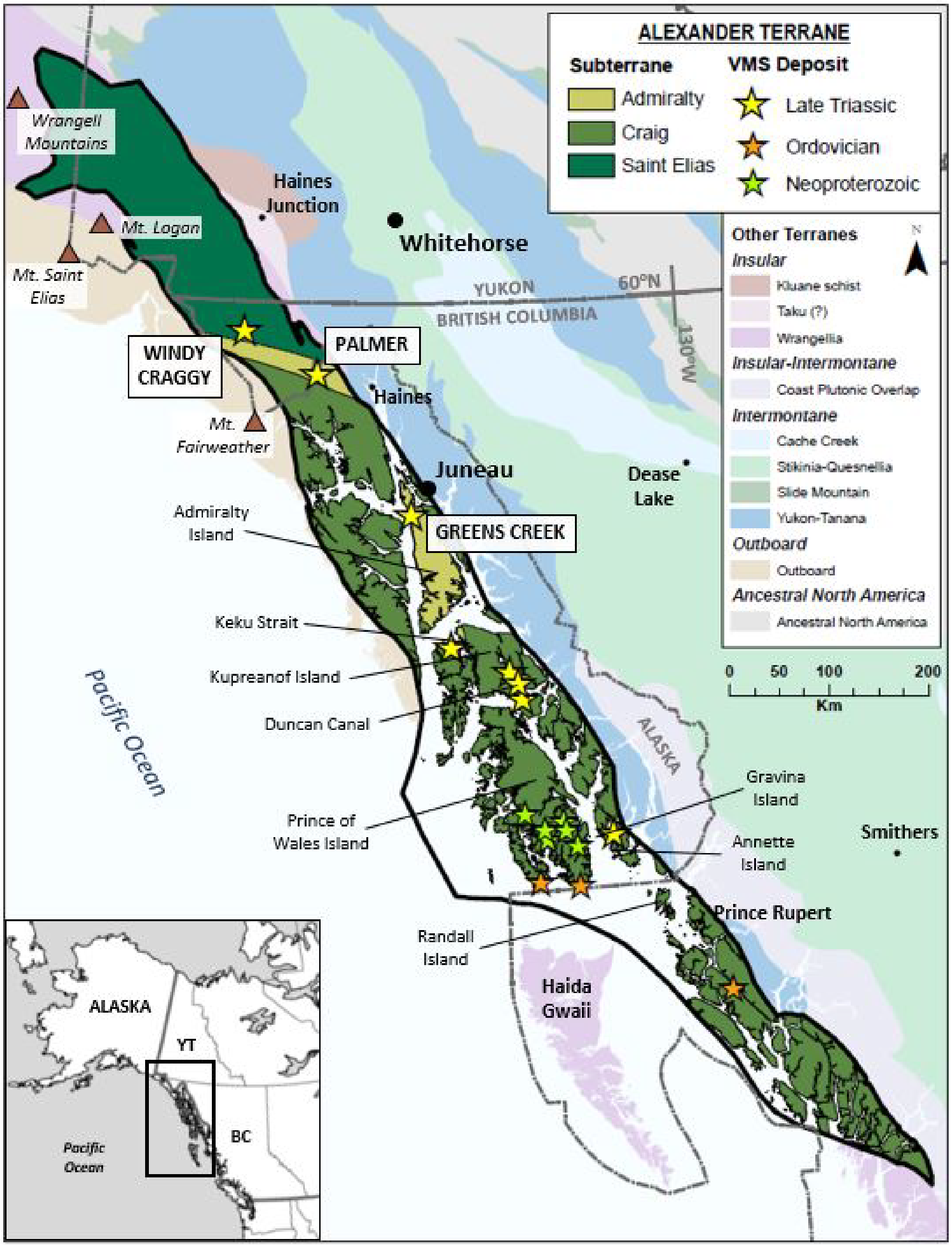

Fig. 1.1 Terrane map of the northwestern Cordillera highlighting the Alexander terrane and subterranes. Pre-Triassic VMS deposits are from Slack et al. (2007) and Nelson et al. (2013b). Terrane boundaries are from Colpron and Nelson (2011).

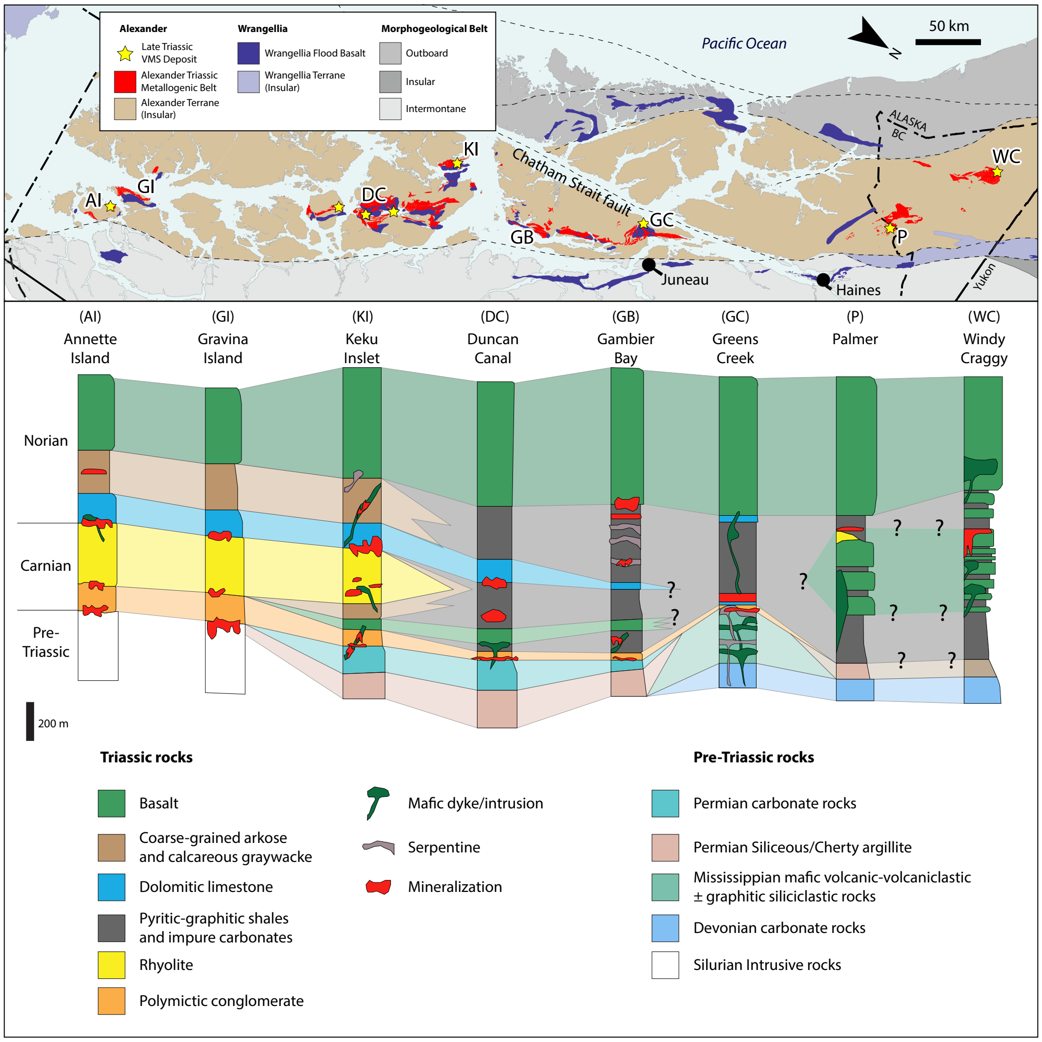

Fig. 1.2 Schematic stratigraphic section from southeast to northwest (left to right) through the Alexander Triassic metallogenic belt (ATMB) modified after Steeves (2018) and Taylor et al. (2008). The corresponding map at the top shows the Alexander Triassic Metallogenic Belt (ATMB; red) and the Wrangellia Flood Basalts (WFB; dark blue). Terrane boundaries are from Colpron and Nelson (2011), the ATMB is derived from digital files of the USGS (Wilson et al., 2015) and the WFB are from the digital files of Greene et al. (2010).

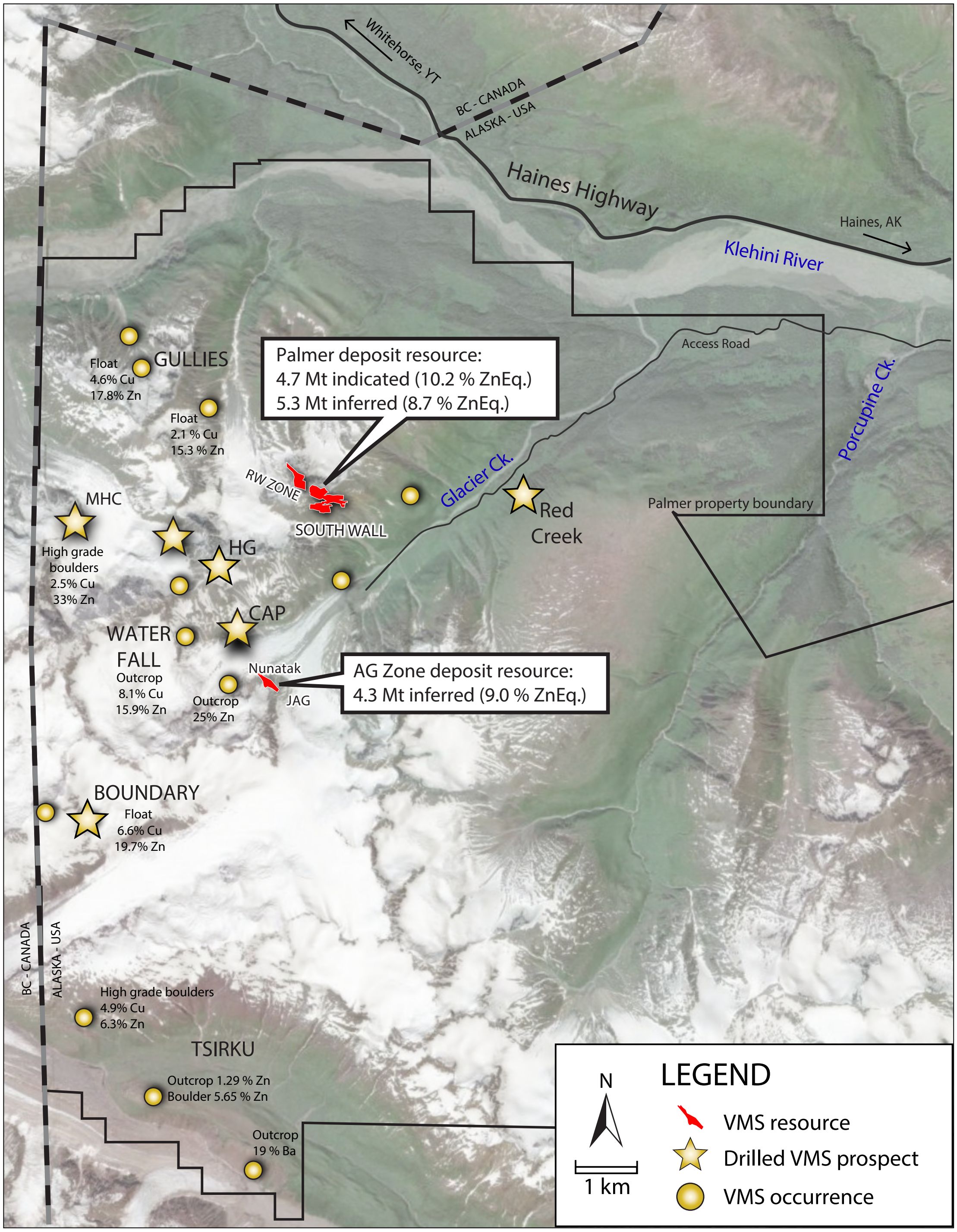

Fig. 1.3 Palmer property VMS occurrences, prospects, and deposits location map.

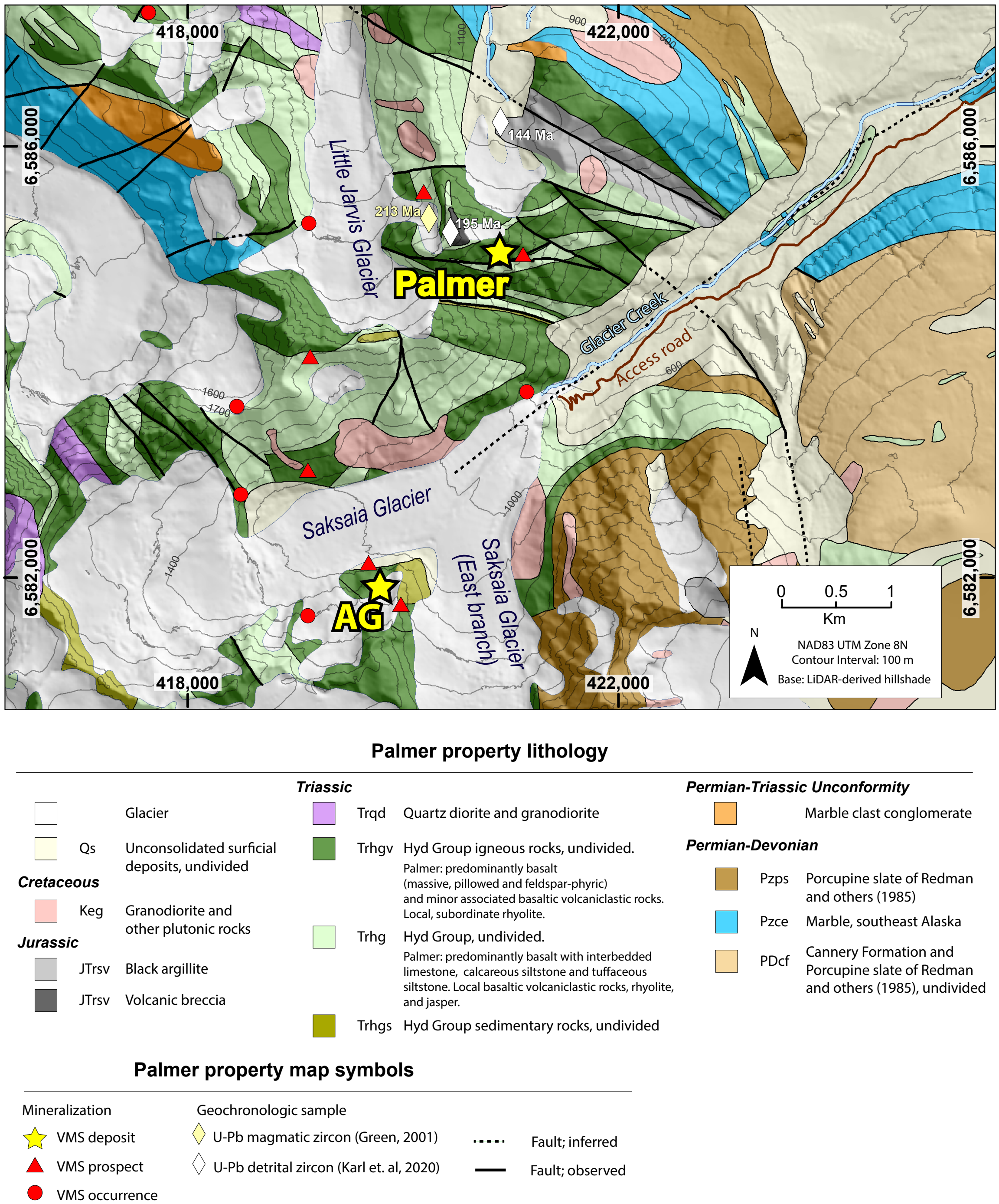

Fig. 1.4 Regional geology near the Palmer property based on the Alaska digital geology compilation by the USGS (Wilson et al., 2015). The locations of the Palmer and AG VMS deposits and several VMS prospects are shown. Geochronologic data includes a U-Pb zircon date of 213 Ma from the Palmer rhyolite (Green, 2001) and U-Pb dates from detrital zircons (Karl et al., 2020).

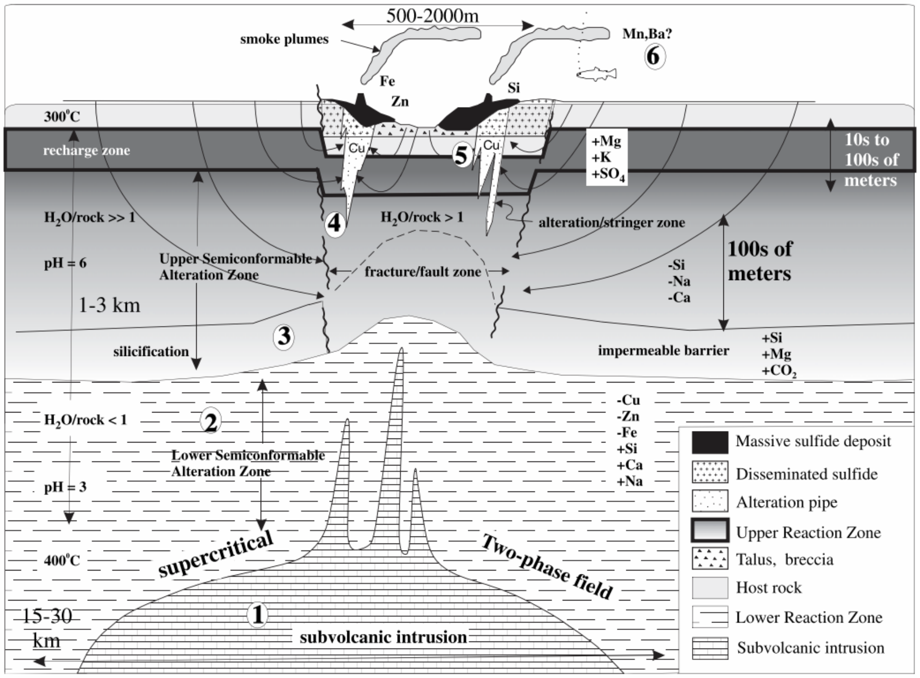

Fig. 1.5 VMS convective hydrothermal system and components from Franklin et al. (2005) after Galley (1993) and Gibson et al. (2007). The numbers reflect (1) a heat source, (2) a high-temperature reaction zone, (3) synvolcanic faults and fissures, (4) a footwall alteration zone, (5) massive sulfide deposits, and (6) distal hydrothermal products that may be mixed with background sedimentation.

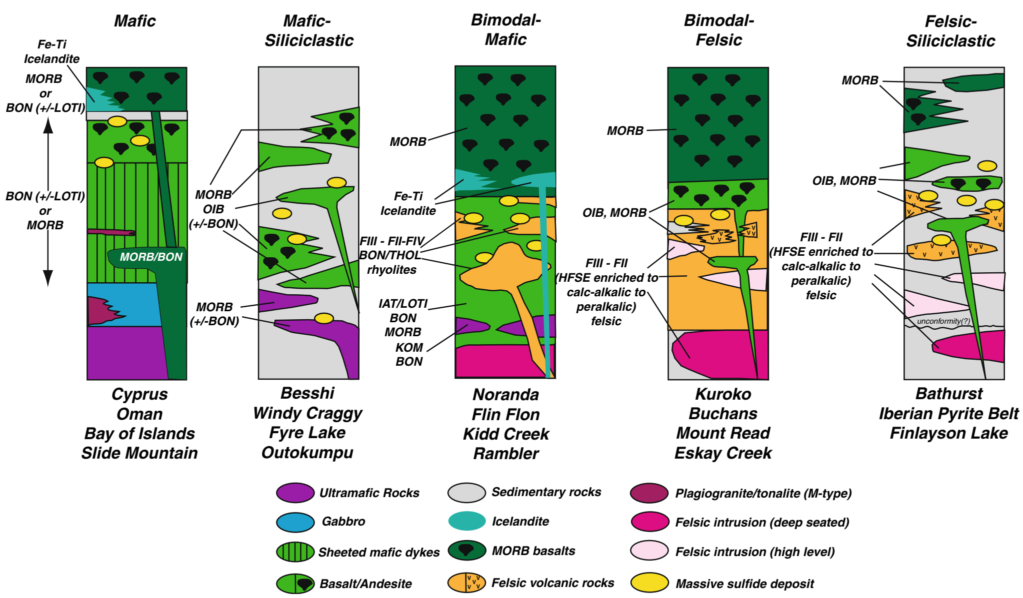

Fig. 1.6 Lithostratigraphic classification of VMS deposits shown with their respective stratigraphic relationships and associated petrochemical assemblages by Piercey (2011).

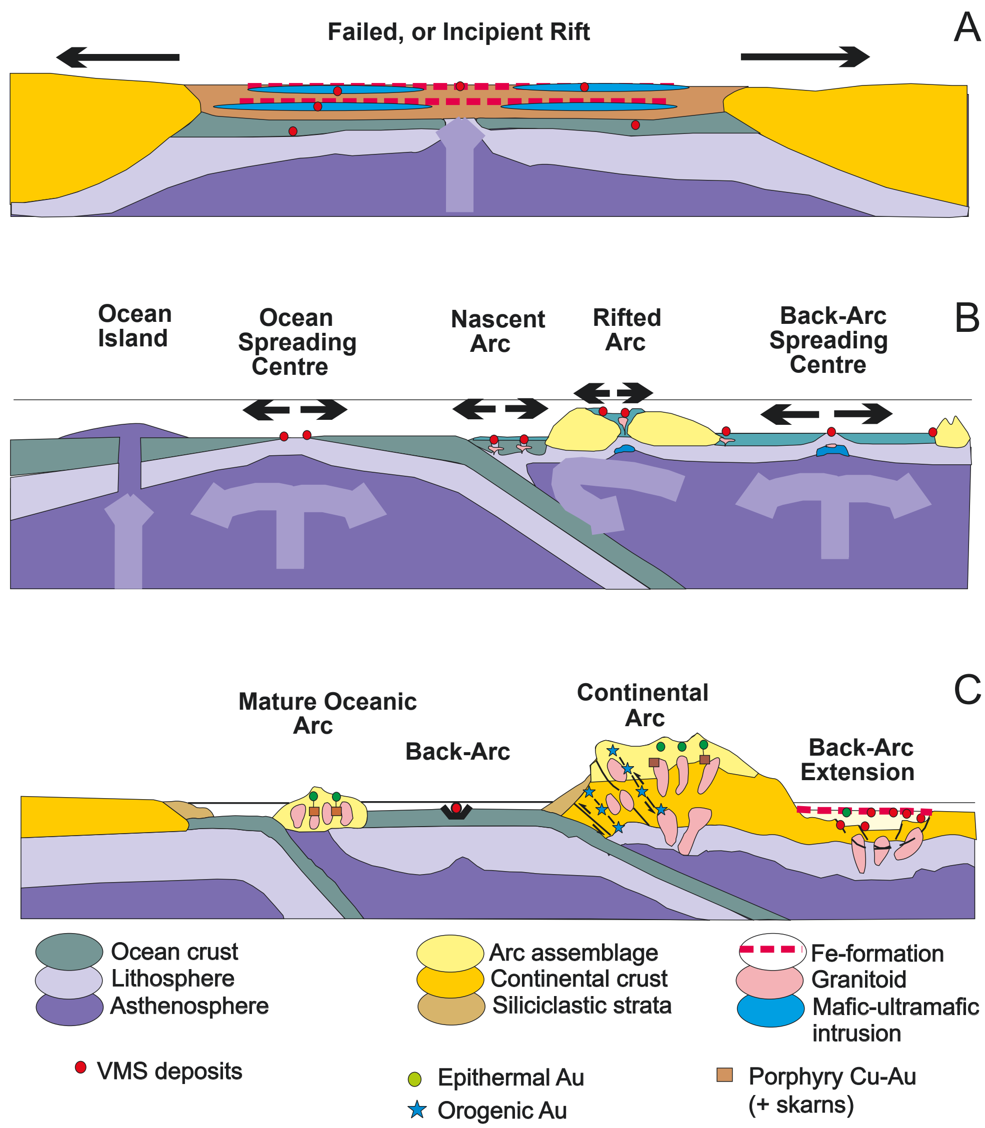

Fig. 1.7 Tectonic settings where VMS deposits form with black arrows showing extension direction and pale arrows showing mantle movement from Galley et al. (2007). A) Incipient rift environments such as those formed from vigorous mantle plume activity in early Earth evolution or those formed in the Phanerozoic during transpressional, back-arc rifting. B) Mafic-dominated deposits form in ocean spreading centers. The formation of oceanic arcs at subduction zones commonly coincides with extension in the arc or back-arc parts of the system were bimodal mafic, bimodal felsic, and mafic-dominated VMS deposits form. C) Felsic-dominated and bimodal siliciclastic VMS deposits form in more evolved settings such as mature oceanic back-arc basins and continental back-arc basins.

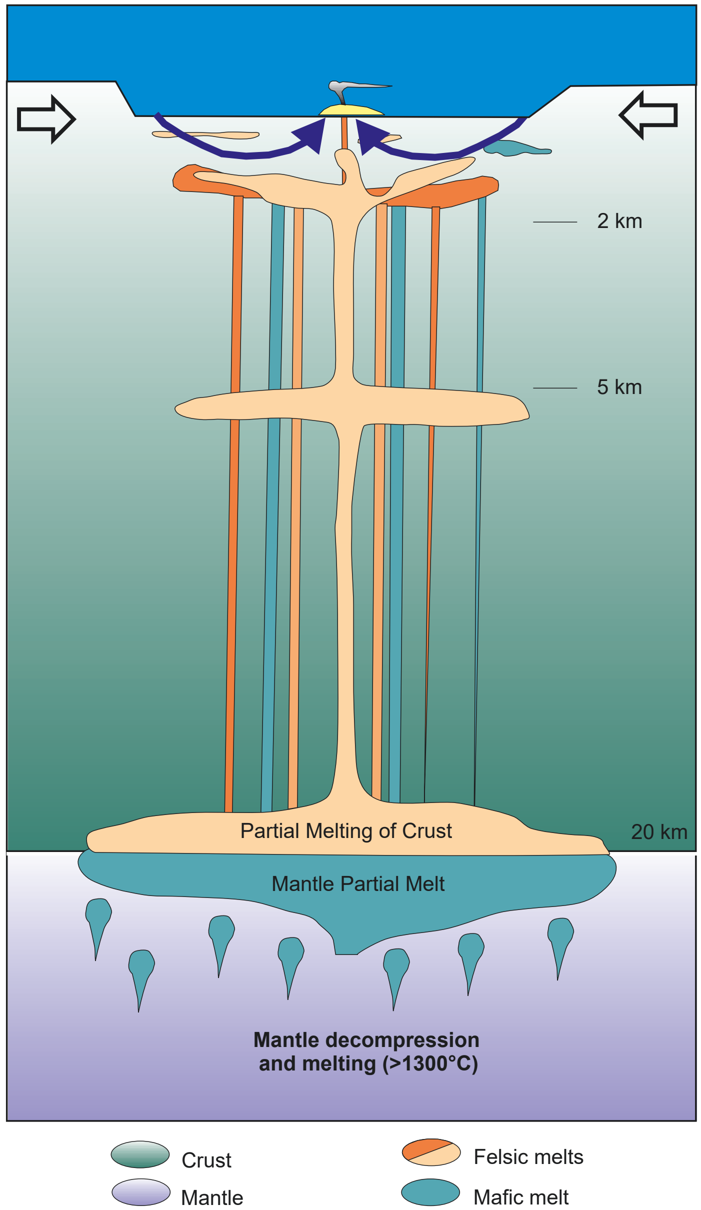

Fig. 1.8 Extension-related magmatic plumbing system including crustal thinning, mantle decompression melting, the generation of basaltic melts that underplate the crust, and the generation of felsic melts by partially melting the crust. From Galley et al. (2007).

Chapter 2. Geology, lithogeochemistry, age, and genesis of the AG VMS deposit, Alaska

2.1. Abstract

The 4.3 Mt, bimodal-mafic AG volcanogenic massive sulfide (VMS) deposit contains both exhalative- and replacement-style, barite-rich, Zn-Ag-Pb-Cu-Au VMS mineralization hosted by Late Triassic (Hyd Group) volcano-sedimentary rocks of the Alexander Triassic metallogenic belt (ATMB) near Haines, Alaska. The immediate stratigraphic footwall consists of coherent to volcaniclastic Fe-rich, intermediate to felsic rocks with weak "arc-like" geochemical signatures, including FIIIa felsic rocks that were derived from high-temperature (T > 900ºC) melts that were generated at shallow (< 10 km) depths in the crust. Mineralization is intercalated with FeTi-rich, enriched mid-ocean ridge basalt (EMORB)-like, variolitic pillowed basalts and heterolithic fragmental rocks. The heterolithic fragmental rocks are considered debris flow deposits that were emplaced along an interpreted syn-volcanic fault. This syn-volcanic structure also controlled the distribution of FIIIb high-silica rhyolite (HSR) sills, sharp lateral changes in hydrothermal alteration intensity, the thicknesses and facies of units, and VMS mineralization. The AG deposit is capped by volcaniclastic, FeTi-rich basalts that are interpreted to be products of explosive submarine volcanism.

Two new high-precision chemical abrasion isotope dilution thermal ionization mass spectrometry (CA-ID-TIMS) U-Pb geochronology dates from zircons of hydrothermally altered FIIIa ferrorhyolite lapilli tuffs (FeR), 210.35 ± 0.27 Ma, and FIIIb HSR, 210.52 ± 0.08 Ma, constrain the timing of the AG hydrothermal activity.

Litho- and chemo-stratigraphic reconstruction of the volcanic environment suggests the AG VMS deposit formed in a propagating intra-arc rift associated with basin development where high temperature, shallow magmatic processes included basaltic underplating, crystal fractionation, assimilation of arc crust, and periodic magmatic replenishment. The AG volcanic rocks have geochemical and geologic features that are like assemblages documented in Neoarchean VMS-hosting rocks in the Abitibi greenstone belt, suggesting that the tectono-magmatic processes responsible for forming the AG volcanic rocks in the Late Triassic may have been operative in the Neoarchean.

2.2. Introduction

Volcanogenic massive sulfide (VMS) deposits are synvolcanic, stratiform concentrations of sulfide minerals that form in submarine, rifted environments associated with high-temperature magmatism (Franklin et al., 2005; Galley et al., 2007; Gibson et al., 2007; Piercey, 2011). Reconstructing the physical volcanic environment is critical to identify favorable intervals that may host VMS deposits and to map out primary structures (e.g., syn-volcanic faults, rift basins, and calderas) that may control the siting of mineralization (Gibson et al., 1999; Allen et al., 2002). Additionally, the geochemical signatures of VMS-hosting volcanic sequences can be used to evaluate petrogenetic settings and predict VMS-favorable successions (Lesher et al., 1986; Kerrich and Wyman, 1996; Lentz, 1998; Barrett and MacLean, 1999; Barrie and Hannington, 1999; Hart et al., 2004; Piercey, 2010; Piercey, 2011). Combining the physical volcanology with litho- and chemo-stratigraphy of VMS-hosting volcanic sequences provides an opportunity to understand the interplay between the magmatic, tectonic, and hydrothermal processes that form these deposits.

The Alexander terrane in the North American Cordillera contains abundant volcanogenic massive sulfide (VMS) deposits in the Late Triassic rift-related intra-oceanic island arc rocks of the Alexander Triassic metallogenic belt (ATMB) (Fig. 2.1; Taylor et al., 2008). The belt contains the supergiant (~300 Mt) Cu-Co Windy Craggy deposit (Peter and Scott, 1997), the Ag-rich Greens Creek deposit (Taylor et al., 2010), and the 10 Mt polymetallic (Zn-Cu-Pb-Ag-Au-Ba) Palmer deposit (Green et al., 2003; Steeves et al., 2016); however, there are limited studies detailing the geodynamics of individual deposits within the ATMB (Taylor et al., 2008; Sack, 2009; Peter et al., 2014). Chemostratigraphic reconstructions at Greens Creek have been difficult because the VMS mineralization is hosted in highly deformed sedimentary rocks located directly above a regional unconformity (Sack, 2009; Steeves, 2018). The Windy Craggy deposit is hosted in mafic rocks intercalated with voluminous sedimentary rocks (Peter and Scott, 1997) and is postulated to have formed in a subduction zone setting associated with a slab window (Peter et al., 2014). The rocks at the Palmer property provide an opportunity to improve our understanding of the tectonostratigraphic, magmatic, and hydrothermal evolution of VMS deposits in the ATMB as they contain well-preserved and well-exposed mafic and felsic rocks, which have only undergone greenschist facies metamorphism and minimal deformation, with stratigraphy well preserved in structural panels.

Massive barite outcrops were first discovered at the Nunatak prospect in the 1970s that eventually led to the drill discovery of the AG deposit in 2017; the AG deposit is located 3 km from the 10 Mt Palmer deposit on the Palmer property (Fig. 2.2). Drilling and geologic mapping data up to 2018 was used to calculate an inferred resource for AG of 4.3 Mt grading 4.64% Zn, 0.12% Cu, 0.96% Pb, 119.5 g/t Ag, 0.53 g/t Au and 34.8% $BaSO_4$ (Gray and Cunningham-Dunlop, 2018). Diamond drilling programs between 2017-2019 have totaled 12,000 m. Over 800 whole rock geochemical samples from the AG stratigraphy were collected from the surface and drill core between 2014-2021. The systematic sampling programs paired with high-quality, modern analytical data provide a unique opportunity to apply lithogeochemical methods to understand the evolution of the volcanic succession that hosts this deposit. The Palmer deposit has been the focus of deposit-scale studies published on the Palmer property (Green et al., 2003; Steeves et al., 2016); descriptions of the geology in the vicinity of the AG deposit have only been documented in a few company reports and technical documents (Gray and Cunningham-Dunlop, 2018). This contribution represents the first comprehensive description of the AG deposit geology. It aims to integrate observations from geologic mapping, core logging, petrography, lithogeochemistry, and U-Pb zircon geochronology to: (1) reconstruct the volcanic stratigraphy through facies analysis and chemostratigraphic correlation, (2) evaluate the petrogenesis of the AG volcanic units, (3) propose a model for the genesis of the AG deposit, and (4) constrain the timing of the formation of the AG deposit.

This study highlights the importance of the Late Triassic intra-arc rifting that: (1) formed the geochemically distinct syn-rift felsic and mafic volcanic rocks hosting the AG deposit and (2) led to the development of syn-volcanic structures and rift basins where replacement- and exhalative-style VMS mineralized bodies were localized. The relationships of the tectono-magmatic evolution of the host rocks to the AG deposit and the deposit genesis can potentially improve future exploration efforts at the Palmer property, the ATMB, and in other analogous VMS environments globally.

2.3. Geological setting

2.3.1. Regional geology

The AG deposit is in southeast Alaska and occurs within the Alexander terrane (Fig. 2.1). The Alexander terrane includes a near complete Ediacaran to Late Cretaceous rock record (Muffler, 1967; Saleeby, 1983; Gehrels and Saleeby, 1987; Gehrels and Berg, 1994; Gehrels et al., 1996, Nelson et al., 2013b) and radiogenic isotopic signatures of the contained rocks suggest it formed in a wholly oceanic realm (Samson and Patchett, 1991; Peter and Scott, 1997; Peter et al., 2014; Steeves et al., 2016). The early geologic history of the terrane includes Ediacaran to Silurian intraoceanic arc magmatism followed by deposition of Devonian to Permian shallow marine carbonate and minor greenstone rocks (Gehrels and Saleeby, 1987; Gehrels et al., 1996; Plafker and Berg, 1994; Taylor et al., 2008). From the Pennsylvanian to the earliest Permian, the Alexander terrane had a shared geologic history with the Wrangellia and Peninsular terranes, forming the Alexander-Wrangellia-Peninsular superterrane (Gardner et al., 1988; Beranek et al., 2014; Israel et al., 2014). The Middle Triassic was marked by renewed volcanism in the Alexander-Wrangellia-Peninsular superterrane and thick accumulations of tholeiitic basalts that formed the Wrangellia flood basalts (or large igneous province) during the middle Ladinian to Norian (239 – 225 Ma) (Nelson et al., 2013b). Late Triassic island arc rifting coincided with the deposition of the Hyd (Loney, 1964; Muffler, 1967; Wilson et al., 2015) and Tats Group (MacIntyre et al., 1992) volcanic and sedimentary rocks that host numerous metal occurrences and deposits in a ~750 km northwest-trending belt: the Alexander Triassic metallogenic belt (ATMB) (Fig. 2.1; Taylor et al., 2008). Significant VMS deposits in the ATMB include the supergiant Windy Craggy deposit, the Ag-rich Greens Creek deposit, and the polymetallic Palmer deposit (Fig. 2.1).

2.3.2. Palmer property geology

The Palmer property contains the AG and Palmer VMS deposits along with fifteen VMS prospects hosted within a Late Triassic mafic-dominated bimodal volcanic belt that contains associated volcaniclastic rocks and minor fine-grained sedimentary and tuffaceous interbeds (Fig. 2.2A; Redman et al., 1985; Green et al., 2003; Wilson et al., 2015). In places, a marble clast-bearing conglomerate marks the base of the Late Triassic rocks on the Palmer property and is interpreted to be a Permian-Triassic unconformity (Proffett, 2019). The timing of mineralization at the Palmer deposit is constrained by an isotope dilution-thermal ionization mass spectrometry (ID-TIMS) U-Pb zircon date of 213 ± 5 Ma from a hydrothermally altered rhyolite (Green, 2001). Jurassic volcanic breccias and black argillites cap the Triassic section; the igneous crystallization age for the volcanic breccia is ~195 Ma based on U-Pb zircon dates from the tuffaceous matrix of the volcanic breccia, and the black argillites have a young population of detrital zircons with U-Pb zircon dates of ~144 Ma (Karl et al., 2020). Rocks at the Palmer property have undergone multiple phases of deformation, greenschist facies metamorphism, and local contact metamorphism (Forbes et al., 1989; Lewis, 1998; Green et al., 2003; Steeves et al., 2016), yet are remarkably well-preserved and contain primary stratigraphic and volcanic textures, despite these overprints.

2.4. Geology and lithostratigraphy of the AG deposit

2.4.1. Methodology

Geologic bedrock mapping (1:1,000) and core logging was utilized to document volcanic textures and lithofacies, contact relationships, and hydrothermal alteration mineral assemblages. Nine drill holes totaling about 3,700 m were relogged, but all core logs and photos for the

~12,000 m of available drill core were reviewed. Appendix 1 contains additional photographs of the AG deposit geology. The volcanic rocks are broadly categorized as coherent or volcaniclastic (McPhie et al., 1993). The volcaniclastic rocks are classified using the non-genetic, granulometric terms of tuff, lapilli, and block/bomb of Fisher (1966) with the transport- and depositional-focused descriptive terminology of White and Houghton (2006).

Petrographic analyses using transmitted and reflected light microscopy were completed on polished thin sections. A subset was further investigated using a JEOL JSM 7100F scanning electron microscope (SEM) operating at 15 kV at Memorial University. Textures were identified with backscatter electron (BSE) imaging, whereas mineral chemistry was explored with semi-quantitative energy dispersive spectrometer (EDS) point analysis. See Appendix 2 for petrographic descriptions, including microphotographs and BSE images. Quantitative analysis of plagioclase and FeTi oxide mineral chemistry was investigated using a JEOL JXA-8230 electron probe microanalyzer (EPMA) equipped with four energy dispersive spectrometers (EDS) at Memorial University. The EPMA analytical methods and results are summarized in Appendix 6.

Prior to this study, only basalt and rhyolite compositions were identified in the stratigraphy. Lithogeochemical investigations of the volcanic rocks were critical to identify geochemically unique units (including basaltic, andesitic, dacitic, and rhyolitic compositions), to recognize genetically related units, and to reconstruct the volcanic stratigraphy. All samples were classified with lithogeochemical techniques (section 2.5) using ioGAS 8.0 software and then explored in Seequent's Leapfrog Geo 6.0 software to visualize their distribution in 2D and 3D space. There is a strong correlation between stratigraphic position and the primary geochemistry of the volcanic rocks (section 2.5), so new geochemical nomenclature for the units was created and is used throughout for consistency and to highlight chemostratigraphic relationships. Some units are readily identified in the field, but most volcanic units in the stratigraphic footwall, especially where strongly hydrothermally altered, are typically only distinguishable with lithogeochemistry. The reconstruction of the AG volcanic stratigraphy was an iterative process involving mapping, core logging, lithogeochemical classification, and 2D to 3D visualization. A new geologic bedrock map at a scale of 1:1,000 reflects the distribution of the newly identified geologic units and other geologic features (Fig. 2.2B). Graphic logs and associated cross-section interpretations are consistent with the updated geologic bedrock map and are presented in Figures 2.3 and 2.4, respectively.

2.4.2. Geology of AG deposit

The AG deposit is a tabular, steeply northeast dipping barite- and sulfide-rich lens that varies in thickness from tens of centimeters to 15 m and that extends for ~600 m along strike (see Fig. 2.2B) and ~100–250 m downdip. It is underlain by locally mineralized coherent volcanic and volcaniclastic rocks. Most mineralization is along strike of and intercalated with basalts with a distinct variolitic texture, referred to as the Zone FeTi basalts (Z-FeTiB) (Figs. 2.3, 2.4, 2.6). Local heterolithic fragmental rocks and minor, thin (typically sub-meter or thinner) discontinuous beds of argillite and chemical sedimentary rocks (e.g., jasper-magnetite and chert) are also spatially associated with mineralization. The immediate footwall is comprised of rhyolitic lapilli tuffs, referred to as the ferrorhyolites (FeR), that also locally host replacement-style VMS mineralization (Fig. 2.5). Most of the footwall consists of basalt, andesite, and dacite flows. Mafic volcaniclastic rocks, termed the hangingwall FeTi basalts (HW-FeTiB; Fig. 2.7), overlie the deposit and are capped by argillite.

Alteration and metamorphism

The footwall volcanic rocks locally contain hydrothermal alteration assemblages dominated by pervasive fine-grained white mica (colloquially referred to as sericite), disseminated pyrite, and variable pervasive to selective quartz. Hydrothermal alteration extends up to at least ~200 m into the footwall. The Z-FeTiB and the HW-FeTiB locally contain alteration assemblages composed of chlorite, Fe- and Ca-carbonate, magnetite, quartz, hematite, and sericite. In places, hydrothermal alteration is present tens of meters into the hanging wall basalts (the HW-FeTiB). The rocks have undergone regional greenschist facies metamorphism, and metamorphic assemblages of chlorite, calcite, quartz, and epidote are typical where rocks are less impacted by hydrothermal alteration. Local, intense epidote-garnet-chlorite-biotite is present in some units proximal to Mesozoic intrusions and is interpreted to have formed from contact metamorphism. Although the volcanic rocks are affected by metamorphism and VMS-related alteration, primary textures, and lithologic contacts are well-preserved in much of the stratigraphy. The “meta” prefix is not attached to the rock names, but it is implied.

Deformation

Mapping (Fig. 2.2B), core logging (Fig. 2.3), cross-section interpretations (Fig. 2.4), and chemostratigraphic studies (section 2.5) show that the stratigraphic sequence is folded along a deposit-scale syncline. The axial trace of the syncline is consistent with northwest-oriented schistose foliation that is best developed in strongly hydrothermally altered rocks and may be related to the north-south contractional deformation event (D1) displayed by the geometry of the Palmer deposit (3 km to the north) (Fig. 2.2A), consisting of a south-verging overturned anticline disrupted by a thrust fault (Lewis, 1998; Green et al., 2003; Steeves et al., 2016). Local occurrences of northeast striking schistosity at AG suggest that the axial traces of the D1 folds were broadly warped by a later deformation event (D2), though interference patterns are poorly understood.

Hanging wall sedimentary rocks are well exposed along a prominent north-south ridge in the northeast part of the deposit mapping area (Fig. 2.2B). This sedimentary package has widely varied bedding orientations and a major fault, the “Main” fault, which divides two structural domains, herein referred to as the “Jag panel” and the “Nunatak panel,” which host the Jag and Nunatak prospects, respectively. The Main fault is a steep (~70º dip), north-northeast dipping (~22º dip-azimuth), 0.5–1 m wide recessively-weathered reverse fault composed of sheared rock and gouge that roughly parallels the hinge of the deposit-scale syncline between the JAG and Nunatak prospects. The Main fault may be related to other, poorly understood late, SW- and NW-striking, high-angle brittle faults on the property referred to as D4 events (Lewis, 1998; Green et al., 2003) attributed to the post-middle Cretaceous and pre-Holocene (Hudson et al., 1982) dextral transpression that formed the Chatham Strait fault system (Karl et al., 1999; Steeves et al., 2016). The stratigraphy to the south of the Main fault within the JAG panel is upright and steeply north-dipping. The stratigraphy north of the Main fault within the Nunatak panel is parasitically folded within the hinge of the deposit-scale syncline (Fig. 2.2B and 2.4). It is also faulted.

The Nunatak panel

The Nunatak prospect consists of two massive barite beds layered with pyrite, sphalerite, galena, and sulfosalts on talus-dominated north-facing slopes. The more northern exposures (at elevations 1140 m and 1162 m) are within a steeply south-dipping bed between strongly hydrothermally altered ferroandesitic (FeA) volcanic rocks to the south and a chloritic, strongly foliated undifferentiated mafic volcanic unit to the north (Fig. 2.2B). The southern exposures crop out at 1222 m. They are folded in a tight syncline marked by fragmental basalts (HW-FeTiB) in the core of the syncline and strongly hydrothermally altered rhyolitic fragmental rocks (FeR) underlying the moderately south-dipping limb. Stratigraphic reconstruction of the Nunatak panel has been hindered by chaotic folding, poorly understood faulting, intense hydrothermal alteration, and limited drilling in this area. Most of the Nunatak outcrops are strongly quartz-sericite-pyrite altered, and lithogeochemistry is critical in determining protolith composition.

The JAG panel

The JAG panel hosts the bulk of the AG deposit, including its surface expression at the JAG prospect on an east-facing cliff between elevations 1310 m to 1410 m (Fig. 2.2B). Here, upright, steeply NNW-dipping beds of baritic massive sulfide with laminations of pyrite, sphalerite, sulfosalts, and galena overlie strongly hydrothermally altered rhyolite (FeR) and are overlain by basalt flows (Z-FeTiB) with intense chlorite, carbonate, and magnetite alteration (Fig. 2.5C). Cross-section interpretations show that the northeastern extent of the AG deposit, where mineralization is the thickest, is truncated by the Finch fault (Fig. 2.4). The Finch fault is only identified on the JAG panel. It dips ~64º towards the southwest, strikes ~145º, and projects to the surface beneath the talus between the JAG prospect and East AG (Fig. 2.2B). The Finch fault is defined by the complete discontinuation of units (e.g., the barite-rich beds and heterolithic fragmental rocks), the sharp changes in the thickness of units (particularly the Z-FeTiB), and the repetition of units (e.g., drill hole 120; Fig. 2.4) as defined by chemostratigraphic patterns (section 2.5). Intrusive felsic rocks, chemically defined as high-silica rhyolites (HSR; section 2.5), are localized on the southwestern side of this fault and taper in thickness away from this structure (Fig. 2.4). In drill core, the Finch fault is obscured by intrusive rocks interpreted to post-date mineralization.

Compared to the Nunatak panel, the JAG panel contains a more densely drilled and straightforward section of ~ 400 m of stratigraphy that occupies the steeply northeast-dipping, upright limb of the northeast closing deposit-scale syncline (Fig. 2.4). Based mainly on the intact JAG panel, the AG succession is herein divided into six informal litho- and chemo-stratigraphic sequences that are presented from the base to the top of the section and include the: (1) footwall basalts (FW-B) and ferrobasalts (FW-FeB), (2) footwall Fe-rich silicic rocks including ferroandesites (FeA), ferrodacites (FeD), and ferrorhyolites (FeR), (3) Zone FeTi basalts (Z-FeTiB) and associated fragmental rocks, (4) hangingwall FeTi basalts (HW-FeTiB), (5) High silica rhyolites (HSR), and (6) argillite. Most mineralization is hosted in Sequence 3, but Sequence 2 is an important host for replacement-style mineralization. The entire succession, particularly sequence 6, is intruded by various undifferentiated dykes and sills (e.g., Fig. 2.3), which are not described herein.

Sequence 1 – Footwall basalts and ferrobasalts

In Figure 2.2B, the footwall basalts (FW-B) and ferrobasalts (FW-FeB) are merged into one lithologic unit, described together as the footwall basalts because they have similar field characteristics, occur laterally along strike from each other, and have similar geochemical signatures (section 2.5). The FW-B are more abundant in the west, and the FW-FeB are more common in the east part of the study area. They are the lowermost stratigraphic sequence with a thickness of >150 m. Their lower contact is not intersected in drilling. They comprise predominantly pillowed, amygdaloidal flows that locally grade into flow-margin breccias such as hyaloclastite and autoclastite (monomictic, locally jigsaw-fit, matrix-poor breccias) and pillow breccias. They have a fine-grained dark grey to green groundmass commonly metamorphosed to chlorite, calcite, quartz, albite, and epidote. Sparse plagioclase-phenocrysts (up to ~5 mm in length) are selectively replaced by muscovite.

Sequence 2 – Footwall Fe-rich silicic rocks

Sequence 2 is composed predominantly of coherent ferroandesite (FeA) and ferrodacite (FeD) flows and is capped by lesser ferrorhyolitic lapilli tuffs (FeR). The FeD are discontinuous, up to 40 m thick, and dominated by sparsely amygdaloidal pillowed to lobate flows with an aphanitic, grey groundmass. They have some monomictic brecciated facies associated with intense chlorite alteration, which occur along the margins of individual pillows and flow margins, including at their upper contacts with the base of the FeA. The FeA are predominantly massive and contain minor amygdules and sparse feldspar phenocrysts that locally form glomerocrysts in a fine-grained, green chloritic groundmass. The FeA unit reaches thicknesses exceeding ~30m, but in some places, it is less than 8 m thick. Monomictic breccias with local jigsaw-fit textures up to 3 m thick are common at their flow margins and contacts with other units. They commonly underlie the FeR lapilli tuffs (e.g., at the JAG prospect; Fig. 2.5C), but where the FeR are absent, they directly underlie the Z-FeTiB. They share their lower contacts with any of the FeD, footwall basalts, or the HSR.

The ferrorhyolitic (FeR) lapilli tuffs locally host replacement-style mineralization (Fig. 2.5G) and generally immediately underlie exhalites, including massive baritic sulfides, chert, and jasper-magnetite (Fig. 2.5B-C). In some places, they underlie the Z-FeTiB. They vary in thickness from 1–25 m. They are exclusively fragmental and dominated by poorly sorted, matrix-supported lapilli tuffs (Fig. 2.5A-B, E-H). In general, they are non-stratified, although sparse sections (< 50 cm thick) are composed of laminated tuffs (Fig. 2.5E). Where discernable, fragments include subangular chloritic clasts (primary glassy fragments?), lapilli with ragged to winged margins or wispy to fiamme-like textures (Fig. 2.5A-B, E-H). Some fiamme-like clasts are locally aligned and define a foliation (Fig. 2.5A-B). Clasts with abundant 1 – 5 mm ovoid features (typically composed of quartz but locally sulfides) may represent original pumice clasts that have had their vesicles later filled by quartz and sulfides (Fig. 2.5G). In thin section, the FeR have muscovite-rich matrices that are presumably altered tuffaceous material (Fig. 2.5E). In some places, especially where pyrite is absent, they contain disseminated euhedral magnetite (~2%) (Fig. 2.5F). Accessory euhedral zircon crystals up to 170 μm are typically fractured (see Appendix 2). Backscattered electron (BSE) images combined with semi-quantitative EDS point analyses show that allanite is an accessory phase and that the FeR contain globular features ("globules") up to 150 μm in diameter composed of random and disorganized arrangements of anhedral rutile masses intergrown with variably anhedral to euhedral sub-micrometer zircon and monazite, and rare apatite (Fig. 2.5E). Based on: (1) their ubiquitous fragmental character and lack of an association with an effusive facies (Figs. 2.3, 2.4, 2.5), (2) the presence of wispy and fiamme-like fragments, and pumice (Figs. 2.5A-B, E-I) that could by pyroclasts (White and Houghton, 2006), (3) their tuffaceous-rich matrices (devitrified mainly to muscovite; Fig. 2.5E-I) and (4) their lithofacies consisting dominantly of massive, poorly sorted, matrix-supported lapilli tuffs with rare laminated tuffaceous sections (Fig. 2.5E-I), the FeR may be subaqueous pyroclastic flow deposits (Gibson et al., 1999).

Sequence 3 – The zone FeTi basalts and heterolithic fragmental rocks

Sequence 3 hosts most of the AG exhalative- and replacement-style VMS mineralization (Fig. 2.3 and 2.4) and consists of the Zone FeTi basalts (Z-FeTiB) (2.6A-E) and heterolithic fragmental rocks (Fig. 2.6F-G). In some places, the Z-FeTiB directly underlie exhalative massive sulfides (e.g., drill hole 109; Fig. 2.3 and 2.4), and in some areas, they directly overlie exhalative massive sulfides (e.g., at the JAG prospect or drill hole 128; Fig. 2.4 and Fig. 2.5C). Some of the thickest intersections of mineralization occur near accumulations of hydrothermally altered heterolithic fragmental rocks that have sharp lateral transitions into thick sequences of relatively less altered Z-FeTiB flows that help define the Finch fault (Fig. 2.3 and 2.4). Sequence 3 is dominantly clastic southwest of the Finch fault, but flow-dominant northeast of the Finch fault.

The Z-FeTiB pillowed (up to 3 m in diameter) flows reach total accumulated thicknesses of up to 90 m. Individual flows can be less than a few meters thick and are marked by matrix-poor, flow margin breccias that have monomictic cuspate to winged clasts (0.5 – 10 cm) with local jigsaw-fit textures (Fig. 2.6C). They contain a grey-green, fine-grained groundmass consisting of plagioclase microlites set in a mesostasis of intersertal, cryptocrystalline biotite, chlorite, lesser epidote, and minor apatite, amphibole, and quartz (Fig. 2.6D-E). Disseminated magnetite and ilmenite reach combined modal abundances of >10%. Sparse, lath-shaped plagioclase phenocrysts up to 1.5 mm are partially replaced by albite, muscovite, chlorite, biotite, and minor epidote (Appendix 2). Abundant (up to 30%) leucocratic varioles (see Fowler et al., 2002) are a distinguishing feature of the Z-FeTiB (Fig. 2.6 B-E). They are white (dominated by quartz and plagioclase), 0.5–5 mm in diameter, locally coalesce to form wormy trains, and have sharp mineral phase boundaries with the groundmass (Fig. 2.6 B-E). The varioles are commonly zoned with an outer rim of recrystallized polycrystalline quartz and cores that are typically composed of plagioclase partially to wholly replaced by muscovite, epidote, and minor chlorite, biotite, and amphibole (Fig. 2.6 B, D-E). Greenschist facies metamorphism has obscured the primary textures and mineralogy of the distinct leucocratic varioles. However, some varioles have preserved features that are consistent with spherulitic crystallization, including: (1) fibrous plagioclase crystals radiating from a somewhat lath-shaped plagioclase core with interstitial mafic phases that could have been primary glassy components that later recrystallized (Fig. 2.6E), and (2) the coalescence of varioles to form wormy trains (Fig. 2.6D; Lofgren, 1974; Philpotts, 1977; McPhie et al., 1993; Fowler et al., 2002). Further detailed evidence for spherulitic crystallization is discussed in Appendix 6.

The heterolithic fragmental rocks are intercalated with the Z-FeTiB and vary in thickness from ~5–50 m. At the surface adjacent to the hanging glacier above the Nunatak prospect near an elevation of 1350 m (Fig. 2.2B; intersected by section line D-D'), the fragmental rocks are a chaotic mixture of subrounded to subangular volcanic, exhalite, and minor sedimentary fragments supported in a fine-grained chloritic matrix with patchy Fe-carbonate alteration (Fig. 2.6F-G). Most fragments are 3–50 cm in apparent maximum dimension, but some larger blocks and bombs are greater than 1 m. Some elongate fragments are aligned, defining a crude foliation. The fragments are mainly white, siliceous, aphyric, subangular to subround rhyolite (?), or highly altered basalt (?) that locally contain abundant ovoid features that may be amygdules or varioles. Some green-colored blocks of the Z-FeTiB are recognized based on their distinct variolitic texture. Subround to oval-shaped, massive barite clasts are up to 30 cm long and are commonly rimmed with Fe-carbonate, magnetite, and pyrite (Fig. 2.6G). Minor discontinuous and deformed lenses (~10 cm x ~50 cm) of argillite are minor. Fragments of jasper and chert are rare but present. Irregular-shaped gossanous patches are undifferentiated hydrothermally altered fragments (Fig. 2.6E). In places (e.g., drill hole 110), strong hydrothermal alteration obscures the identification of the heterolithic fragmental rocks. They can be recognized by chaotic, brecciated intervals with variable fine-grained silica, pyrite, and sericite matrix that contain amygdaloidal(?) volcanic fragments with variable chlorite to sericite alteration, lesser pale grey-white cherty fragments, and local tuffaceous parts. A few clasts have been geochemically identified as Z-FeTiB, FeR, and chert, suggesting the clasts are of local origin (e.g., samples W812865 and W812866 in Appendix 3).

Sequence 4 – The hangingwall FeTi basalts

The 40–80 m thick HW-FeTiB were the last major volcanic rocks to erupt in the AG stratigraphy. They overlie Z-FeTiB flows, exhalative massive sulfides (e.g., Nunatak prospect;

drill hole 109), and thin beds of pelagic sedimentary rocks, and they are not appreciably offset by the Finch fault (Figs. 2.3, 2.4). Their lower contact is typically sharp and locally chaotic. Their upper contacts are poorly understood because they are often obscured by abundant dykes (Fig. 2.3). The HW-FeTiB have exclusively volcaniclastic textures with diverse particle sizes, components, and lithofacies (Figs. 2.7). They have two generalized facies that include: (1) a thick (> 30 m) basal section of monolithic, locally crystal-bearing, massive lapilli tuffs with minor bombs (Fig. 2.7A-E, H), and (2) a thinner (< 10 m) capping sequence of laminated tuffs with sparse lapilli (Fig. 2.7F-G, I-K).

The basal lapilli tuffs lack internal structures except for local, crude foliations defined by aligned lapilli to bombs. The tuffaceous matrix contains recrystallized chlorite, magnetite, quartz, calcite, ankerite, and muscovite (Fig. 2.7H). The abundance of fragments ranges from 20 to 60 %. Most are subangular to subround green, grey, or black, strongly magnetic basalt lapilli that are locally plagioclase-phyric. Some contain abundant ovoid features that may be amygdules, indicating that these are potentially scoria. Clasts vary in form and can be wispy with cuspate to ragged margins (Fig. 2.7C-D) or have ameboidal (Fig. 2.7E) to fiamme-like shapes (Fig. 2.7H). Ovoid basaltic bombs up to 10 cm long occur, especially in the more matrix-rich facies, and some have pale alteration fronts along their margins (Fig. 2.7A). Juvenile plagioclase crystals occur in varied abundances and are typically wholly replaced by quartz, muscovite, and lesser calcite and chlorite (Fig. 2.7C-D). Selective alteration of clasts locally imparts an apparent heterolithic texture. Generally, the larger lapilli and bombs with more abundant ovoid features are more strongly altered to quartz, carbonate, and muscovite, imparting variable pale grey, tan, to pale pink colors. Some basalt clasts are partially to wholly replaced by bright red jasper-magnetite (Fig. 2.7C, E).

The basalt lapilli tuffs gradationally transition into medium-bedded tuffs with sparse lapilli overlain by laminated tuffs (Fig. 2.7F-G, I-K). The medium-bedded tuffs typically have pale tan-brownish tuffaceous matrices recrystallized to quartz, magnetite, muscovite, and chlorite (Fig. 2.7I). They have up to 10% disseminated lapilli composed of recrystallized magnetite. Some lapilli with honeycomb textures outlined by FeTi oxide minerals have deformed and stretched-out appearances and could be tube-scoria fragments (Fig. 2.7I). The laminated tuffs have sharp, planar, chlorite- and magnetite-rich laminations alternating with beige-tan-pink, predominantly quartz and muscovite laminations (Fig. 2.7G). Some laminated tuffs are strongly altered to chlorite, carbonate, and FeTi oxide minerals, resembling Algoma-type iron formations (Spry et al., 2000). Some tuff-rich layers contain abundant cuspate, Y- to X-shaped (McPhie et al., 1993, p.28) shards (Fig. 2.7K) and microscopically-identified concentrically zoned accretionary lapilli (Fig. 2.7J).

Like the FeR, the HW-FeTiB have many features consistent with pyroclastic origins, including their: (1) ubiquitous fragmental character and lack of an association with effusive facies, (2) abundance and variety of pyroclastic particles like shards, wispy/fiamme-like lapilli, scoria, bombs with ameboidal to fluidal margins, plagioclase crystals, and rare accretionary lapilli (Fig. 2.7; White and Houghton, 2006), (3) tuffaceous-rich matrices (devitrified to quartz, calcite, magnetite, ankerite, muscovite, and chlorite) that locally contain shards (Fig. 2.7), and (4) their internal organization of unstratified, poorly-sorted, matrix-supported lapilli tuffs overlain by laminated tuffs that is similar to stratigraphic patterns described for deposits of pyroclastic density currents (Figs. 2.3, 2.4; McPhie et al., 1993; Gibson et al., 1999).

Sequence 5 – The high-silica rhyolites

The high-silica rhyolites (HSR) are strongly siliceous, aphyric, pale grey-white, massive lens-like bodies that occupy multiple stratigraphic levels (Fig. 2.4 and 2.8). They vary in thickness from 0.1 – 125 m, but they may reach estimated true thicknesses greater than 200 m where their lower contacts were not intersected in drilling beneath AG west (Fig. 2.2, 2.4, and 2.8B). Thick occurrences of the HSR are localized along the Finch fault. They taper with distance from this structure (Fig. 2.4). They are interpreted as a sill complex because they are generally massive with a distinct homogeneous-texture (Fig. 2.8C) and have intrusive relationships observed in several locations, including: (1) a swarm of 10-50 cm dykes with sharp, chilled margins that intruded the footwall basalts in drill hole 109 (Figs. 2.3 and 2.4), (2) their sharp contacts that bound the FeD flows in drill hole 114 (Fig. 2.4), and (3) a 15 m thick tabular body with sharp contacts with the Z-FeTiB and underlying FeR at East AG (Fig. 2.8A). They contain some monomictic in-situ brecciated facies with subangular clasts up to 6 cm in a matrix that resembles the composition of the clasts, but this does not preclude them from being intrusive, as brecciated margins have been documented on some felsic cryptodomes (e.g., Goto and McPhie, 1998). Based on cross-cutting relationships, some HSR bodies are at least younger than the Z-FeTiB. The relative timing between the emplacement of the HSR and the HW-FeTiB is uncertain because no contact relationships were observed between these two units. Because the HSR locally contain hydrothermal chlorite, pyrite, and muscovite, hydrothermal activity is interpreted to have occurred following their emplacement. However, they are typically less altered than the HW-FeTiB, suggesting that they may post-date the HW-FeTiB. In thin section, the HSR groundmass is dominated by fine-grained muscovite and quartz (Fig. 2.8D-E). Quartz is interstitial, and some grains are rounded and composed of a single quartz crystal (up to 0.3 mm in diameter) that may be quartz eyes. Accessory epidote locally has allanite cores with Ce, La, and Nd (as deduced from

EDS spectra); other accessory minerals include magnetite, zircon, apatite, and rutile (Fig. 2.8D-E). Rare microscopic grains of disseminated rutile contain minor Nb (as deduced from EDS spectra; Appendices 2, 6).

Sequence 6 – Argillite

The capping sequence to the volcanic stratigraphy includes a 5–20 m section of undifferentiated tuffs thinly interbedded with pelagic sedimentary rocks (argillite) that gradationally transitions into a ~60 m section of argillite. The tuffs are laminated to thinly bedded and range in color from pale grey, light to medium green, and pale brown to maroon. They are commonly calcareous. The argillite unit comprises laminated to thinly bedded siliciclastic mudstone, siltstone, and rare sandstone. The sedimentary sequences vary from pale grey to black, locally have water escape structures including flames, and resemble distal turbidite formations (Bouma and Ravenne, 2004). Most of the argillite is calcareous, although it is darker grey, non-calcareous, and siliceous in a few places. Rare oval-shaped fossils composed of calcium carbonate occur in a few sandier beds and are interpreted as Late Triassic sponges called *Heterastridium?* (Appendix 1; Karl et al., 2020). This entire unit was intruded by mafic to felsic dykes and pale hornfels is common in the wall rocks along the intrusive contacts.

Mineralization

The AG deposit comprises exhalative-, replacement-, and minor vein-style mineralization (e.g., Doyle and Allen, 2003; Piercey, 2015). Barite is a major phase, especially in the exhalative-style ores, and occurs within veins (“stringers”) that are commonly sulfide-bearing. Pyrite, sphalerite, galena, sulfosalts, and sparse chalcopyrite are disseminated, vein, semi-massive, and massive sulfide facies. Silver is mainly hosted in freibergite-tetrahedrite-tennantite solid solution minerals, whereas the residency of gold is undetermined except for being hosted in a rare visible electrum grain (Doherty, 2018).

Exhalative-style mineralization occurs in beds that vary in approximate true thickness from tens of centimeters to greater than 15 m. Surface exposures of exhalative-style mineralization are located at the JAG and Nunatak prospects where sub-meter to 4 m thick massive barite beds with lesser quartz contain minor laminations of pyrite, sphalerite, galena, and sulfosalts (Fig. 2.2B and 2.5C). Exhalative mineralization consists of sulfide- and sulfosalt-bearing massive barite (Fig. 2.5D) and mineralized chert is a minor mineralization type, which is typically more Ag- and Au-rich than replacement-style mineralization (Gray and Cunningham-Dunlop, 2018). Exhalative mineralization contains laminated to diffusely layered sulfide, sulfate, and silicate minerals that likely reflects a combination of primary bedding, post-depositional zone refining processes, and possibly tectonic foliations (Lydon, 1988; Gibson et al., 2007; Lafrance et al., 2020). Deposition on the seafloor is supported by: (1) the presence of chemical sedimentary rocks, such as jasper- and magnetite-rich iron formations, along strike or directly overlying the massive barite- and sulfide-rich beds (Fig. 2.5B-C), (2) the local accumulation of fine-grained, laminated pelagic sedimentary rocks at or near these horizons (e.g., drill hole 110; Fig. 2.3), and (3) significantly more intense hydrothermal alteration of the stratigraphic footwall rocks compared to the hangingwall sequences (e.g., Doyle and Allen, 2003).

Underlying the exhalative style mineralization is mineralization interpreted to be subseafloor replacement-style based on the presence of relict volcanic facies such as pumice-bearing felsic lapilli tuffs (FeR) that have tuffaceous matrices replaced by sericite, barite and pyrite and pumice clasts replaced by quartz, barite, sphalerite, galena, and sulfosalts (Fig. 2.5G). The heterolithic fragmental rocks are locally mineralized, especially near the Finch fault and gradually become less altered with distance from the Finch fault, consistent with a subseafloor-type replacement model where replacement fronts are a diagnostic feature (Doyle and Allen, 2003). The felsic lapilli tuffs (FeR) and heterolithic fragmental rocks are the predominant hosts to replacement-style mineralization.

2.5. Primary lithogeochemistry

2.5.1. Analytical methods

Between 2014 to 2021, 661 drill core and 122 surface rock samples were prepared and analyzed by Constantine Metals at the ALS Minerals laboratory in North Vancouver, BC using the complete characterization package (ALS code CCP-PKG-03). As part of this study, an additional 22 drill core samples were collected and analyzed using the same methods and laboratory. Three of these samples were duplicates of samples in the company database used to assess the reproducibility of the company's whole rock dataset. In addition, six standard reference materials ("SRM"; three samples each of LK-NIP-1 diabase and ORCA-1 rhyolite) were analyzed to monitor analytical accuracy and precision. The whole rock lithogeochemical data for the 22 drill core samples and six SRM are provided in Appendix 3. An assessment of the accuracy and precision is provided in Appendix 4. The geochemical results presented in this section include only samples of volcanic and syn-volcanic rocks (n = 428) that represent the stratigraphic sequence hosting the AG deposit. Intrusive rocks interpreted to post-date the VMS-hosting volcanic sequence are not presented here.

Rock samples were crushed in an oscillating steel jaw crusher (>70% of the sample passing through a 6 mm screen), followed by a riffle split of 250 grams using a Boyd crusher/rotary splitter combination, then pulverized in a carbon steel ring mill (>85% of the sample passing through a 75 µm screen). A 1g sample was ignited in a furnace at 1000°C, cooled, and weighed to determine loss on ignition (LOI). Major oxides (Al_2O_3, BaO, CaO, Cr_2O_3, Fe_2O_3, K_2O, MgO, MnO, Na_2O, P_2O_5, SiO_2, SrO, and TiO_2) were obtained by fusing a prepared sample (0.66g) with a lithium tetraborate and lithium metaborate flux and creating a disk that was then analyzed by X-ray fluorescence (XRF). The "total" presented is the combination of the major/minor element oxides and LOI. Sulfur and carbon were determined using combustion and a LECO infrared spectroscopy analyzer. Chalcophile and siderophile elements (Ag, Cd, Co, Cu, Mo, Ni, Pb, Zn) and lithophile elements (Li and Sc) were determined by 4-acid digestion with an inductively coupled plasma - atomic emission spectroscopy (ICP-AES) analytical finish. Volatile elements (As, Bi, Hg, In, Sb, Se, Tl, Te, Re) were determined by aqua regia digestion and an inductively coupled plasma - mass spectrometry (ICP-MS) analytical finish. The high field strength elements (HFSE; Ga, Y, Zr, Nb, Hf, and Ta), the low field strength elements (LFSE; Rb, Sr, Cs, and Ba), rare earth elements (REE; La, Ce, Pr, Nd, Sm, Eu, Gd, Tb, Dy, Ho, Er, Tm, Yb, and Lu), transition elements (V and Cr) and other elements (Ge, Sn, and W) were determined by a lithium borate fusion technique followed by a 3-acid (HF-HNO_3-HCl) dissolution and ICP-MS analytical finish.

2.5.2. Lithogeochemical methods

The AG host volcanic rocks have been variably affected by ocean floor metamorphism, local hydrothermal alteration, regional greenschist facies metamorphism, and local intrusion-related metamorphism. Under these conditions, many major elements (Na, Mg, Si, K, Ca, Mn, Fe) and LFSE (Ba, Sr, Rb) are mobile (Cann, 1970; MacLean, 1990; Jenner, 1996; Barrett and MacLean, 1999), and cannot be relied upon for use in traditional volcanic rock classification schemes (e.g., Peacock, 1931; Irvine and Baragar, 1971; Peccerillo and Taylor, 1976; Le Bas et al., 1986; Le Maitre, 2002). Common immobile elements in VMS settings include Al +/- P, HFSE (Y, Sc, Th, Zr, Hf, Ti, Nb, Ta) and REE, and some transitional elements (+/-V, +/- Cr, +/- Ni)(Pearce and Cann, 1973; MacLean and Kranidiotis, 1987; Barrett and Maclean, 1994; Barrett and MacLean, 1999; Piercey, 2010). However, some traditionally immobile elements can be mobile under certain conditions (e.g., high fluid-to-rock ratio or in the presence of dissolved species such as CO_2 or F) or in proximity to major structures (Finlow-Bates and Stumpfl, 1981; Campbell et al., 1984; Humphris, 1984; MacLean, 1988; Rubin et al., 1993; Liaghat and MacLean, 1995; Pearce, 1996; Polat and Hofmann, 2003). Identifying compositionally uniform volcanic units and establishing element immobility was accomplished using bivariate plots of potentially immobile elements and their ratios (Cann, 1970; MacLean, 1990; Maclean and Barrett, 1993; Barrett and Maclean, 1994; Gifkins et al., 2005). This method confirmed that the most highly immobile elements in the AG dataset are Al_2O_3, TiO_2, Nb, Zr, Th, and the HREE, especially Gd and Yb. The LREE are mainly immobile except in the most intensely hydrothermally altered samples. Yttrium, Sc, V, and P_2O_5 showed variable mobility. The most immobile elements were used to classify and interpret the petrogenesis of the volcanic rocks in the AG suite; some plots based on mobile elements supplement the immobile element observations (Figs. 2.9 to 2.16). Niobium was selected as a fractionation monitor because it is highly resistant to the most intense alteration (Mathieu, 2018), and it behaves incompatibly for all units (Fig. 2.10). To improve all classifications, the least altered samples representative of each unit were identified by visual observation, textural characteristics and using several geochemical criteria (Table 2.1; Spitz and Darling, 1978; Campbell et al., 1984; Barrett and MacLean, 1994; Large et al., 2001; Gifkins et al., 2005; Mathieu, 2018; Rollinson and Pease, 2021). Coherent facies were preferentially selected over fragmental facies for representative least altered samples, but the FeR and HW-FeTiB are exclusively clastic and are included herein. All samples of the

FeR and the HW-FeTiB are moderately altered, likely owing to their volcaniclastic nature, so the least-altered samples do not meet the criteria of Table 2.1, but the best, least altered candidates were selected. Many samples of the FW-B are monomictic breccias with considerable amounts of glassy components (hyaloclastite) and breccia cement. These samples typically had major element abundances that totaled more than 100%; they were omitted from plots in favor of the more crystalline and homogeneous samples for this unit. Any samples with visible weathering or oxidation were also omitted.

The major and trace element whole rock lithogeochemical data for 22 representative, least altered samples are presented in Table 2.2, and significant element ratios are summarized in Table 2.3. The least altered samples are depicted as the largest symbols on all lithogeochemical plots, whereas smaller symbols represent variably altered samples (Figs. 2.9 to 2.16). Major elements in the lithogeochemical plots are presented as original values and have not been recalculated on a volatile-free basis. Iron is reported as $Fe_2O_3^T$, denoting total iron expressed as Fe_2O_3. The fractionations of Nb, Zr, Ti, and Eu compared to their neighboring elements on pm-normalized diagrams (Nb anomaly = Nb/Nb^*_{pm}; Zr anomaly = Zr/Zr^*_{pm}; Ti anomaly = Ti/Ti^*_{pm}; Eu anomaly = Eu/Eu^*_{cn}) were quantified using geometric means following the method outlined in McLennan and Taylor (2012) (Table 2.3). Unless otherwise specified, normalizing reference values for primitive mantle (pm) and chondrite (cn) are from Sun and McDonough (1989). Plots with the reference mantle reservoirs, pm, enriched mid-ocean ridge basalt (EMORB), normal mid-ocean ridge basalt (NMORB), and ocean island basalt (OIB) are from Sun and McDonough (1989). The average continental crust (ACC) is from Rudnick and Gao (2014).

2.5.3. Results

The AG volcanic rocks show a mainly bimodal distribution on the Nb/Y versus Zr/Ti plot, where they cluster predominantly in the basalt and rhyolite fields (Fig. 2.9A) with the exception of a tight cluster of samples in the basaltic-andesite field and a more dispersed population of samples that plot across the basaltic-andesite to rhyolite-dacite boundary (Fig. 2.9A). Most samples are subalkaline (Nb/Y < 0.7), except one population of rhyolites (the HSR), and some altered FeTi basalts (Fig. 2.9A). Immobile element plots involving Al_2O_3, TiO_2, and Zr demonstrate that these elements are highly immobile and suggest that there are eight compositionally homogeneous populations in the AG stratigraphy (Fig. 2.9B): footwall basalts (FW-B; n = 32), footwall ferrobasalts (FW-FeB; n = 41), ferroandesites (FeA; n = 63), ferrodacites (FeD; n = 25), ferrorhyolites (FeR; n = 49), zone FeTi basalts (Z-FeTiB; n = 81), hangingwall FeTi basalts (HW-FeTiB; n = 84), and high-silica rhyolites (HSR; n = 53). Based on empirical diagrams (Figs. 2.9, 2.13–2.16), fractionation trends of the least altered samples (Fig. 2.10), ratios of HFSE (Table 2.3), and pm- and cn-normalized signatures (Figs. 2.11 and 2.12), these units are grouped into four distinct magmatic suites: footwall basalt suite (FW-B and FW-FeB), Fe-rich silicic suite (FeA, FeD, and FeR), FeTi basalt suite (Z-FeTiB and HW-FeTiB) and high silica rhyolite suite (HSR). These geochemical suites are highly correlated with stratigraphic position (see section 2.4). The FW-B, FW-FeB, and FeA are indistinguishable in the field, especially where strongly hydrothermally altered. The FeD can be confused with altered basalts without geochemical classification. The FeTi-rich basalts and the two unique rhyolites (FeR and HSR) have distinct lithological and petrographic features (see section 2.4). However, where strongly hydrothermally altered, the FeR lapilli tuffs can be confused with altered fragmental basalts or heterolithic fragmental rocks. Strongly hydrothermally altered Z-FeTiB can be misclassified without the aid of lithogeochemistry.

The footwall basalt suite (FW-B and FW-FeB)

The pillowed flows of this suite have basaltic Zr/Ti ratios and subalkaline Nb/Y ratios (Fig. 2.9A; Pearce, 1996). Ratios of Zr/Al_2O_3 and Al_2O_3/TiO_2 indicate that the footwall basalts (FW-B) and ferrobasalts (FW-FeB) are two compositionally homogeneous units (Fig. 2.9B). The FW-FeB are more evolved than the FW-B and have lower Al_2O_3, Ni, Sc and higher Fe_2O_3, TiO_2, P_2O_5, and ΣREE (Fig. 2.10) and exhibit a typical tholeiitic magmatic trend (Maclean and Barrett, 1993; Koepke et al., 2018). The FW-FeB have $Fe_2O_3^T > 14.32$ wt.% and $TiO_2 < 1.9$ wt.% (Table 2.3) and are classified as ferrobasalts ($FeO^T > 12$ wt % and $TiO_2 < 2$ wt %; Perfit et al., 1999; Christie et al., 2005). The Fe-rich nature of the FW-FeB is reflected by their classification as high-Fe tholeiitic basalts on the Jensen (1976) cation plot, whereas the FW-B plot on the boundary between calc-alkaline basalts and tholeiitic andesites (Fig. 2.9C). In addition to their Fe-enrichment trends, the FW-B and the FW-FeB have tholeiitic Zr/Y versus Th/Yb ratios (Fig. 2.9D; Ross and Bédard, 2009) and within plate tholeiite (WPT) Th-Zr-Nb signatures (Fig. 2.13; Wood, 1980).

The FW-B and FW-FeB have similar typical non-arc EMORB-like (Sun and McDonough, 1989) signatures on pm- and cn-normalized plots (Figs. 2.11 and 2.12), with: (1) LREE enrichment compared to HREE and MREE, (2) flat HREE patterns, (3) no significant Nb or Zr anomalies, and (4) slight negative Ti anomalies (Table 2.3). They also have EMORB-like Zr-Th-Nb-Yb-TiO_2 systematics on several tectono-magmatic discrimination diagrams (Figs. 2.13A-C, 2.16). They have MORB/back-arc basin basalt (BABB) Ti/V ratios (Fig. 2.13D; Vermeesch, 2006; Shervais, 2022).

The Fe-rich silicic suite (FeA, FeD, and FeR)

These units have subalkaline Nb/Y ratios (except one least altered FeR sample has Nb/Y = 0.72) and Zr/Ti ratios indicative of andesitic, dacitic, and rhyolitic compositions (Fig. 2.9A; Pearce, 1996). The three compositionally homogeneous units are also differentiated based on ratios of Zr/Al_2O_3 and Al_2O_3/TiO_2 (Fig. 2.9B). These units are interpreted to be more evolved than the footwall basalts that precede them in the stratigraphy based on their fractionation trends (Fig. 2.10). Relative to the footwall basalts, they show decreasing Fe and Ti with fractionation, typical of intermediate compositions fractionating FeTi phases in either tholeiitic or calc-alkaline magmatic systems (Juster et al., 1989; Barrett and MacLean, 1999; Frost and Frost, 2011; Charlier et al., 2013; Koepke et al., 2018). The least altered FeA have Al-Mg-Ti-Fe contents like high-Fe tholeiitic basalts (Fig. 2.9C; Jensen, 1976), reflecting their relatively high concentrations of TiO_2 (TiO_2 = 1.5–1.7 wt.%) and $Fe_2O_3^T$ ($Fe_2O_3^T$ = 12.7–16.8 wt.%) compared to typical orogenic andesites ($Fe_2O_3^T$ < 12 wt.% and typically $Fe_2O_3^T$ is closer to 8.5 to 9 wt.% and TiO_2 = 0.8–1.0 wt.%; Gill, 1981). This suggests that they are Fe- and Ti-rich andesites, also known as ferroandesites or icelandites (Gill, 1981; Gibson et al., 2007). Their high P_2O_5 contents (P_2O_5 = 0.52–0.57 wt.%) are also consistent with their classification in the icelandite/ferroandesite family, as typical orogenic andesites have P_2O_5 = 0.05–0.30 wt.% (Gill, 1981, p. 112). The FeD have Al-Mg-Ti-Fe contents like tholeiitic andesites (Fig. 2.9C; Jensen, 1976), reflecting their relatively high concentrations of TiO_2 (TiO_2 wt.% = 0.82–0.85 %) and $Fe_2O_3^T$ ($Fe_2O_3^T$ wt.% = 8.9–11.1) compared to typical dacites (e.g., $Fe_2O_3^T$ ~4.75 % and TiO_2 ~0.60 %; Mathieu, 2018), suggesting that they are FeTi-rich dacites, or ferrodacites (Barrett and MacLean, 1999). The FeR have Al-Mg-Ti-Fe contents like tholeiitic dacites to andesites (Fig. 2.9C; Jensen, 1976) reflecting their relatively average TiO_2 (TiO_2 = 0.26–0.36 wt.%) and high concentrations of $Fe_2O_3^T$ ($Fe_2O_3^T$ = 8.19–8.64 wt.%) compared to typical rhyolites (e.g., $Fe_2O_3^T$ ~ 2.71 wt.% and TiO_2 ~ 0.36 wt.%;

Mathieu, 2018), suggesting that they are ferrorhyolites. Most of the FeR and FeD samples have ferroan ("tholeiitic") SiO_2 versus Fe* signatures, but some of the least altered samples plot within the magnesian ("calc-alkaline") field near the ferroan-magnesian boundary (Fig. 2.14B; Frost et al., 2001). The Fe-rich nature of the FeA, FeD, and FeR lithologies, combined with the FIIIa-like signatures (Fig. 2.14A; Hart et al., 2004) of the felsic units strongly supports that they are tholeiitic. Furthermore, the A-type affinities (Fig. 2.14B, D; Pearce et al., 1984; Frost et al., 2001) of the felsic units (FeD and FeR) shows that they have characteristically high Fe/(Fe + Mg) (Bonin, 2007; Frost and Frost, 2011); a feature more typical of the tholeiites. However, the FeA have transitional to nearly calc-alkaline Th-Yb-Zr-Y affinities (Fig. 2.9D; Ross and Bédard, 2009), and the FeD and FeR have calc-alkaline Th-Yb-Zr-Y signatures (Fig. 2.9D; Ross and Bédard, 2009). Furthermore, the FeD have subalkaline Zr contents, and the FeR have peralkaline Zr abundances (Table 2.3; Fig. 2.14C; Leat et al., 1986; Piercey, 2010).

The FeA, FeD, and FeR have similar, irregular signatures on pm- and cn-normalized plots (Figs. 2.11 and 2.12), with: (1) LREE enrichment relative to HREE and MREE (2) relatively flat HREE patterns, (3) negative Nb, Ti, and Eu anomalies, and (4) positive Zr anomalies (Table 2.3). The intensity of their LREE-enrichments and the magnitudes of their Nb, Ti, Eu, and Zr anomalies increase as the rock types become more evolved from andesitic (FeA), to dacitic (FeD), to rhyolitic (Fer) compositions. These pm-normalized signatures are more typical of arc-related rocks (Kerrich and Wyman, 1996). Arc-like influences are also supported by tectono-magmatic discrimination diagrams that show that they are enriched in Th relative to Nb (Figs. 2.13A-B, 2.15A-C, 2.16; Wood, 1980; Condie, 2005; Pearce, 2008).

The FeTi basalt suite (Z-FeTiB and HW-FeTiB)

These units have basaltic Zr/Ti ratios and subalkaline Nb/Y ratios (Fig. 2.9A; Pearce, 1996). Ratios of Zr/Al_2O_3 and Al_2O_3/TiO_2 indicate that the Z-FeTiB and HW-FeTiB are two compositionally homogeneous units (Fig. 2.9B). The Z-FeTiB are more evolved than the HW-FeTiB based on their lower Al_2O_3 and Ni and higher TiO_2, P_2O_5, and ΣREE relative to Nb (Fig. 2.10) and exhibit typical tholeiitic magmatic trends (Maclean and Barrett, 1993; Koepke et al., 2018). Relative to the footwall basalts, both the Z-FeTiB and the HW-FeTiB show extreme Fe- and Ti-enrichment trends and relatively high concentrations of TiO_2 (Z-FeTiB TiO_2 = 2.78–3.16 wt.% and HW-FeTiB TiO_2 = 2.38–2.68 wt.%) and Fe_2O_3 (Z-FeTiB $Fe_2O_3{}^T$ = 13.05–22.19 wt.% and HW-FeTiB $Fe_2O_3{}^T$ = 17.04–20.00 wt.%), typical of FeTi basalts (FeO^T > 12 wt % and TiO_2 > 2 wt %; Byerly et al., 1976; Perfit et al., 1999; Christie et al., 2005). Their tholeiitic, Fe-rich nature is also supported by their classification as high-Fe tholeiitic basalts on the Jensen (1976) cation plot (Fig. 2.9C) and their within plate tholeiite (WPT) Th-Zr-Nb signatures (Fig. 2.13; Wood, 1980). However, the FeTi basalts have tholeiitic to transitional affinities based on the trace elements Zr, Y, Th, and Yb (Fig. 2.9D; Ross and Bédard, 2009).

The FeTi basalts have similar typical non-arc EMORB-like (Sun and McDonough, 1989) signatures on pm- and cn-normalized plots (Figs. 2.11 and 2.12), with: (1) LREE enrichment compared to HREE and MREE, (2) relatively flat HREE patterns, (3) no significant Nb or Zr anomalies, and (4) slight negative Ti and Eu anomalies (Table 2.3). They also have EMORB-like Zr-Th-Nb-Yb-TiO_2 systematics on several tectono-magmatic discrimination diagrams (Figs. 2.13A-C, 2.16). They typically plot within (Fig. 2.13C) or slightly above (2.16A-B) MORB-ocean island basalt (OIB) arrays. The Z-FeTiB have OIB-like Ti/V ratios and the HW-FeTiB have MORB/BABB- to OIB-like Ti/V ratios (Fig. 2.13C-D; Vermeesch, 2006; Shervais, 2022). Compared to all other mafic units, the HW-FeTiB have the most fractionated HREE patterns

(Gd_{pm}/Yb_{pm} = 1.42–1.48), but these are still closer to EMORB (Gd_{pm}/Yb_{pm} = 1.04) than OIB (Gd_{pm}/Yb_{pm} = 2.92) (Sun and McDonough, 1989). They also have TiO_2-Yb-Nb signatures that straddle the boundary between EMORB and OIB (Fig. 2.13C). Compared to the footwall basalt suite, the FeTi basalts are slightly more Th-enriched relative to Nb (Figs. 2.13A-B, 2.15A-C).

The high silica rhyolite suite (HSR)

Both the large HSR bodies and thinner dykes and sills have rhyolitic Zr/Ti ratios and plot within the alkali rhyolite field on the modified Floyd-Winchester volcanic discrimination plot (Fig. 2.9A; Pearce,1996). They form a tight cluster on the Al_2O_3/TiO_2 versus Zr/Al_2O_3 plot (Fig. 2.9B). The least altered HSR have 71.26–75.06 SiO_2 wt % (Table 2.2), extreme HFSE-REE enrichments (Figs. 2.11, 2.12), flat REE patterns with negative Eu anomalies (Fig. 2.12), Y > 108.5 ppm, La_{cn}/Yb_{cn} = 2.62–5.5 (Fig. 2.14A), and anomalously low Zr/Hf ratios (Table 2.3; Fig. 2.10), consistent with other high-silica rhyolites (Barrie et al., 1993; Barrie and Pattison, 1999; Galley, 2003; Claiborne et al., 2018); they are the most evolved of all units (Fig. 2.10).

Although they plot in the alkali rhyolite field (Fig. 2.9A) and have Th-Zr-Nb systematics that more closely resemble those of alkali basalts (Fig. 2.13A-B), their Nb/Y (Nb/Y = 0.43–0.59), Zr/Y (Zr/Y = 2.09–2.50), and La_{cn}/Yb_{cn} (La_{cn}/Yb_{cn} = 2.6–5.6) ratios, and Zr abundances (Zr = 271–378 ppm; Fig. 2.14C) are more akin to tholeiitic felsic magmas (Nb/Y < 0.7; Zr/Y = 2–7; $La_{cn}/Yb_{cn} < 6$; Zr = 200–500 ppm) as opposed to alkaline (Nb/Y >> 0.7; Zr/Y > 7; $La_{cn}/Yb_{cn} >> 6$; Zr > 500 ppm) or calc-alkaline (Nb/Y <0.7; Zr/Y > 7; $La_{cn}/Yb_{cn} > 6$; Zr < 500 ppm) felsic magmas (see Lentz, 1998). Furthermore, their A-type (Fig. 2.14B, D) and FIIIb affinities (Fig. 2.14A) are more typical of tholeiitic melts (Hart et al., 2004; Fassbender et al., 2022). However, they have tholeiitic to transitional Th-Yb-Zr-Y affinities (Fig. 2.9D; Ross and Bédard, 2009). Furthermore, the least altered HSR have calc-alkaline major element signatures and plot near tholeiitic/calc-alkaline dividing boundaries (Fig. 2.9C, Jensen, 1976; Fig. 2.14B; Frost et al., 2001). In summary, their magmatic affinity is undetermined due to these varied classifications based on major and trace element signatures; a common trait of A-type felsic rocks (Bonin, 2007).

The HSR have irregular signatures on pm- and cn-normalized plots (Figs. 2.11 and 2.12), with: (1) LREE enrichment relative to HREE and MREE (2) relatively flat HREE patterns, and (4) weak negative Nb anomalies, strong negative Zr and Eu anomalies, and very strong negative Ti anomalies (Table 2.3); typical of arc-related rocks (Kerrich and Wyman, 1996). Arc-like influences are also supported by their Th-enrichment relative to Nb; they are much more Th-enriched relative to Nb compared to all the basalts but less so compared to the Fe-rich silicic suite (Figs. 2.13A-B, 2.15A-C, 2.16).

2.6. U-Pb zircon geochronology

2.6.1. Sample selection

Two samples of felsic rocks from the AG stratigraphy were collected from drill hole 110 to constrain the timing of VMS mineralization at AG based on their stratigraphic location, lithology, and geochemical attributes (Fig. 2.3 and 2.4). Sample 110-322 is a hydrothermally altered FeR lapilli tuff located along the strike of exhalative VMS mineralization and underlies hydrothermally altered and mineralized heterolithic fragmental rocks. Sample 110-368 is massive high-silica rhyolite (HSR) with patchy chlorite, calcite, and epidote alteration that intrudes FeA flows downhole of the FeR lapilli tuffs. The samples were analyzed at the Boise State University Isotope Geology Laboratory (BSU IGL) in Idaho. Mineral separation and extraction, imaging, laser ablation inductively coupled plasma mass spectrometry (LA-ICPMS), and chemical abrasion isotope dilution thermal ionization mass spectrometry (CA-ID-TIMS) were all performed at the BSU IGL. The results presented here are adapted from an internal BSU IGL report presented in Appendix 4.

2.6.2. Analytical methodology

Individual zircon grains were separated and prepared using standard techniques. Cathodoluminescence (CL) images were obtained with a JEOL JSM-300 scanning electron microscope (SEM) and Gatan MiniC (Fig. A5. 3, Fig. A5. 4). Laser ablation was performed on each zircon grain using a Teledyne Photon Machines Analyte Excite+ 193 nm excimer laser ablation system with HelEx II Active two-volume ablation cell. An iCAP RQ Quadrupole ICP-MS was used to analyze the ablated material for U-Th-Pb isotopic ratios and trace element concentrations. A selected subset of zircon grains were removed from the epoxy mounts for CA-ID-TIMS dating based on the CL images and LA-ICPMS ages. Chemical abrasion was performed on individual grains following methods modified after Mattinson (2005) that are detailed in Appendix 4. Isotopic measurements for U and Pb were made on a GV Isoprobe-T or IsotopX Phoenix multi-collector TIMS equipped with an ion-counting Daly detector. More in-depth details on sample preparation, analytical methods, quality assurance, quality control, and data reduction calculations are provided in Appendix 4.

2.6.3. Results

A total of 11 and 49 zircon grains were analyzed by LA-ICPMS for samples 110-322 and 110-368, respectively. In sample 110-322, the zircons were difficult to recover due to the presence of pyrite and the eleven recovered anhedral to subhedral grains were small; they yielded LA-ICPMS $^{206}Pb/^{238}U$ dates of 212 ± 6 to 194 ± 5 Ma. Sample 110-368 contained abundant euhedral, prismatic, and oscillatory-zoned zircon grains; they yielded LA-ICPMS $^{206}Pb/^{238}U$ dates of 213 ± 5 to 189 ± 4 Ma. The LA-ICP MS U-Pb geochronologic analyses and trace element concentrations are provided in Appendix 4.

A total of seven and six zircon grains were analyzed by CA-ID-TIMS for samples 110-322 and 110-368, respectively. Four older grains in 110-322 yielded $^{206}Pb/^{238}U$ dates of 211.03 ± 0.32 to 210.68 ± 0.17 Ma and are interpreted as containing inherited components. The three youngest zircon grains from 110-322 yielded a weighted mean $^{206}Pb/^{238}U$ date of 210.35 ± 0.27 Ma, the interpreted igneous crystallization age. The six zircon grains analyzed by CA-ID-TIMS from sample 110-368 yielded a weighted mean $^{206}Pb/^{238}U$ date of 210.52 ± 0.08, the interpreted igneous crystallization age. The CA-ID-TIMS U-Pb zircon isotopic data is presented in Table 2.4. Concordia diagrams displaying CA-ID-TIMS U-Pb dates are shown in Figure 2.17. The U-Pb geochronology results are summarized in Table 2.5.

2.7. Discussion

2.7.1. Volcanic controls on AG VMS mineralization

The location, style and hydrothermal alteration footprints of VMS deposits are influenced by the types of volcanic rocks that host them (Gibson et al., 1999). In flow-dominated host successions, hydrothermal fluid pathways are typically restricted to syn-volcanic normal faults (Sillitoe, 1982; Gibson et al., 1999; Lafrance et al., 2020) and VMS-style mineralization is precipitated immediately below the seafloor in stringer and replacement zones and at the seafloor as exhalative mineralization (Gibson et al., 1999). In the rock record, syn-volcanic faults can be recognized by sharp lateral changes in volcanic lithofacies, discontinuous units, local thickening of units, and offset stratigraphy (Nelson, 1998; Gibson et al., 1999; Allen et al., 2002; Lafrance et al., 2020). In volcaniclastic-dominated successions, hydrothermal fluid migration is less restricted, favoring the formation of subseafloor replacement-style deposits associated with pervasive, widespread stratigraphy-parallel alteration zones and the development of multiple, coalescing vent sites at the seafloor (Gibson et al., 1999; Piercey, 2015). Whether VMS deposits are hosted by flow- or volcaniclastic-dominated substrates, a commonality is that they form in proximal (near-vent) environments that can be recognized by distinct lithofacies associations (McPhie et al., 1993; Gibson et al., 1999; Allen et al., 2002).

At AG, the footwall rocks are dominated by effusive flows. However, the main mineralized succession includes a mix of volcaniclastic (FeR, heterolithic fragmental rocks) and coherent volcanic rocks (Z-FeTiB), and minor sedimentary units (Fig. 2.4). The pumice-bearing FeR lapilli tuffs are especially thick (up to 25 m) where they underlie the first barite- and sulfide-rich exhalite at AG (e.g., drill hole 109; Figs. 2.3, 2.4). This may indicate that the thickest parts of the FeR represent a proximal volcanic center (Gibson et al., 1999) and that the location of some VMS mineralization at AG coincided with the same structures that may have fed the FeR eruptions. Further, most VMS mineralization is focused along the southwest side of the Finch fault (Figs. 2.3, 2.4), where the heterolithic fragmental rocks are thickest (Fig. 2.4, 2.6F-H) and coincide with barite-rich beds layered with sulfides and minor argillite suggesting that the localization of both volcaniclastic rocks and mineralization here is because they are basin-filling sequences and that the Finch fault was a synvolcanic fault. The above units are locally underlain by Z-FeTiB and they sharply transition laterally into a thick package of Z-FeTiB flows, suggesting that the Z-FeTiB were likely uplifted and eroded during basin subsidence along the rift shoulder of the Finch fault (Figs. 2.3, 2.4). In other words, the Finch fault is interpreted to have been a topographic scarp that formed after the emplacement of the Z-FeTiB and was present at the time of VMS deposition (Fig 2.18F). Further, based on their lithofacies, clast components, and volcano-stratigraphic relationships, the heterolithic fragmental rocks that were deposited proximal to the Finch fault may be debris flow deposits that reworked some of the previously deposited units (Z-FeTiB, FeR, massive barite) (Fig. 2.18E-F) during synvolcanic faulting (e.g., McPhie et al., 1993; Hampton et al., 1996; Hughes et al., 2021). Following the emplacement of the heterolithic fragmental rocks, the thickest deposits of barite- and sulfide-rich exhalites accumulated adjacent to the Finch fault, suggesting that the Finch fault provided the pathways for hydrothermal fluids to reach the seafloor (Fig. 2.4). In addition, the heterolithic fragmental rocks are strongly hydrothermally altered to quartz, sericite, and pyrite, and locally mineralized adjacent to the Finch fault and the alteration intensity dissipates with distance from this structure, further supporting that this fault is synvolcanic (Fig. 2.2). Minor, thin flows of Z-FeTiB were emplaced between the deposition of the barite- and sulfide-rich exhalites, but in general, volcanism was subdued, and allowed for VMS mineralization and background pelagic sedimentation to accumulate.

The mineralized sequences are overlain by the HW-FeTiB, whose upper contacts are not appreciably offset at the Finch fault, further supporting that this is a synvolcanic structure (Gibson et al., 1999). These units are also thick (up to 80m), and have features including their (1) abundance and variety of pyroclastic particles like shards, wispy/fiamme-like lapilli, scoria, bombs with ameboidal to fluidal margins, plagioclase crystals, and rare accretionary lapilli (Fig. 2.7; White and Houghton, 2006), and (2) their internal organization of unstratified, poorly-sorted, matrix-supported lapilli tuffs overlain by laminated tuffs that suggest the HW-FeTiB are also pyroclastic flow deposits (Figs. 2.3, 2.4; McPhie et al., 1993; Gibson et al., 1999) and given their proximity to the synvolcanic Finch fault, they were likely emplaced in a proximal volcanic center (Gibson et al., 1999). Their field relationships suggest they may have filled the paleo AG basin and spilled over its walls, thus capping the AG deposit and likely helping to preserve the exhalative parts of the deposit from erosion and oxidation on the seafloor (Figs.2.4, 2.18G).

The HSR intrusions are interpreted as the last phase of magmatism in the AG volcanic succession. Because felsic magmas are viscous, their occurrence, especially where they form thick flows or abundant intrusions, typically mark vent-proximal locations and synvolcanic faults (McPhie et al., 1993; Gibson et al., 1999; Franklin et al., 2005) The thickest parts of the HSR intrusions are localized along the Finch fault and they taper in thickness with distance from it, implying this fault acted as the conduit for HSR emplacement. The HSR intrusions likely plugged this conduit, impeded hydrothermal fluid flow, or redirected it and potential VMS mineralization elsewhere. This is supported by the absence of VMS mineralization within or above the HW-FeTiB.

In the sequence (FeR → Z-FeTiB → heterolithic fragmental rocks → HW-FeTiB → HSR) that hosts the AG deposit, rift-related features (the Finch fault and the heterolithic fragmental rocks), basin-filling sequences (exhalites, minor sedimentary rocks, HW-FeTiB), and vent-proximal volcanic deposits (FeR, HW-FeTiB, and HSR) demonstrate that AG formed in a rift basin near an active volcanic center. The flow-dominated footwall sequence (FW-B, FW-FeB, FeD, and FeA) includes relatively impermeable host-rocks that restricted hydrothermal fluids to permeable synvolcanic structures (e.g., Gibson et al., 1999), such as the Finch fault, that controlled the siting of most of the AG mineralization. The HSR intrusions may have ultimately quenched the hydrothermal system by plugging crustal structures and hindering hydrothermal fluid flow.

2.7.2. Petrogenesis of the AG volcanic rocks

Petrogenesis of the footwall basalt suite

The footwall basalts (FW-B) and ferrobasalts (FW-FeB) were the first to erupt in the volcanic sequence in the AG deposit. Their EMORB signatures (Figs. 2.11, 2.12) and Zr-Nb-Yb-Ti systematics (Figs. 2.13A-C, 2.16) indicate they were derived from an HFSE-REE-enriched mantle and have not been influenced by subducted slab fluids (Pearce, 2008; Pearce, 2014). Their TiO_2/Yb ratios (Fig. 2.13C) and relatively flat HREE patterns (Figs. 2.11 and 2.12) show that garnet was not a residual phase, typical of shallow (< 2.5 Gpa; < 80 km) melts (Pearce, 2008; Pearce, 2014). The FW-B and the FW-FeB are interpreted to be related to one another by fractional crystallization based on their decreasing Al_2O_3, Ni, Sc, and increasing Fe_2O_3, TiO_2, P_2O_5, and ΣREE relative to Nb (Fig. 2.10). These are typical major and trace element fractionation trends for low pressure, shallow-level fractional crystallization in tholeiitic magmas that are dominated by Fe-poor and Al-rich mineral phases such as plagioclase, olivine (Ni-bearing), and clinopyroxene (Sc-bearing), creating residual melts that become increasingly Fe-Ti-P-rich and Al-Ni-Sc-poor at somewhat constant SiO_2 during fractionation (Juster et al., 1989; Perfit et al., 1999; Charlier et al., 2013; Grove and Brown, 2018; Koepke et al., 2018). Fractionating tholeiitic melts also exhibit steadily increasing HFSE and REE concentrations (Brophy, 2009) without a change in the pattern of their primitive mantle-normalized signatures, except for total concentrations of said elements (Maclean and Barrett, 1993), a trend observed from the FW-B to the FW-FeB. Their non-arc, within-plate EMORB signatures (Figs. 2.11, 2.12, 2.13A-C, 2.16) and MORB/BABB-like Ti/V ratios (Fig. 2.13D) are also consistent with their formation in an extensional setting like a mid-ocean ridge (MOR) or back-arc basin (BAB) where thinned crust allowed enriched asthenosphere to upwell and partially melt by decompression (Fig. 2.18B; Sun and McDonough, 1989; Kerrich and Wyman, 1996; Pearce, 1996). These basaltic magmas probably rapidly intruded cold crust and likely cooled quickly, favoring fractional crystallization processes (e.g., Christie and Sinton, 1981; Huppert and Sparks, 1988).

Petrogenesis of the Fe-rich silicic suite

The Fe-rich silicic suite was emplaced following the footwall basalt suite. They are tholeiitic (Fig. 2.9C) and have Nb/Yb ratios that are comparable to the footwall basalt suite, suggesting derivation from similarly enriched mantle sources (Fig.2.16; Pearce, 2008). Similar mantle sources are also supported by the comparable Nb/Ta (Table 2.3) for both suites that more closely resemble the mantle (Nb/Ta ~ 17.5) than crustal values (Nb/Ta ~ 11–12) (Green, 1995). However, the Fe-rich silicic rocks have trace element signatures (Fig. 2.9, 2.13A-B, 2.16) and distinctly negative Nb and Ti anomalies (Fig. 2.11; Table 2.3) that are more typical of arc-like volcanic rocks (Saunders et al., 1980; Pearce and Peate, 1995; Elliott, 2004; Pearce and Stern, 2006; Pearce, 2008). The FIIIa-type signatures of the felsic rocks (Fig. 2.14A), suggests they formed within the upper 10 km of the crust at low pressure (< 0.5 GPa) and high temperatures (1,100–900°C) (Hart et al., 2004). Their high abundances of REE and HFSE (Fig. 2.11, 2.12, Table 2.2) also indicate that they were anomalously hot, depolymerized melts, such that they could accommodate these highly incompatible elements (e.g., Zr > 200 ppm; Fig. 2.14C) (Leat et al., 1986; Lentz, 1998; Hart et al., 2004; Piercey, 2011). These geochemical features, combined with their within plate (A-type) signatures (Fig. 2.14B, D), are typical of tholeiitic felsic rocks derived from extension-related magmatism, such as those that form in intra-oceanic back arcs and arc-related rifts (Lesher et al., 1986; Hart et al., 2004; Piercey, 2011; Fassbender et al., 2022). The arc-like Fe-rich silicic suite is stratigraphically bound by non-arc, EMORB-like basalts (discussed above and below) providing strong evidence that the AG succession formed in an arc-related extensional setting since both arc-like and MOR-like rocks can be spatially and temporally juxtaposed in these environments (Pearce and Stern, 2006).

The origin of extension-related intermediate to felsic lavas in oceanic arc settings has been attributed to: (1) fractional crystallization of a basaltic parent (Fretzdorff et al., 2006; Haase et al., 2011; Beier et al., 2015; Ma et al., 2017), (2) partially melting mixed MORB-like (dry) and arc-like (wet) mantle sources (Stern et al., 1990; Arai and Dunn, 2014; Caratori Tontini et al., 2019), (3) partially melting arc crust (Haraguchi et al., 2017), typically by basaltic underplating (Lesher et al., 1986; Lentz, 1998; Hart et al., 2004; Piercey, 2011) - these partial melts may further contaminate the basaltic intrusions (Kent et al., 2002), or (4) a combination of these processes, such as assimilation fractional crystallization (AFC) (DePaolo, 1981; Kondo et al., 2000; Marty et al., 2001).

Fractional crystallization is inefficient at changing incompatible element ratios (O'Neill and Jenner, 2012) and so the Fe-rich silicic suite cannot be related to the footwall basalt suite by fractional crystallization because the Fe-rich silicic suite has distinct Th-enrichment relative to Nb, Zr-Hf enrichments relative to Sm, and they have more fractionated LREE patterns compared to the footwall basalt suite (Table 2.3, Fig. 2.11, 2.15A-C). Their weak negative Nb anomalies could be explained by melts derived from mixed MORB-like and arc-like mantle sources in a back-arc setting (Stern et al., 1990; Pearce and Stern, 2006), but this contradicts their consistent positive Zr anomalies (Table 2.3, Fig. 2.11) since subduction-related melts typically have negative (or flat) Zr anomalies (Kelemen et al., 1993; Pearce and Peate, 1995; Kerrich and Wyman, 1996; Niu et al., 1999; Pearce and Stern, 2006). Even though the FeA, FeD, and FeR could be related to each other by fractional crystallization based on decreasing Al-Ti-Fe-Sc-P (plagioclase, FeTi oxide, clinopyroxene, and apatite fractionation) and increasing ΣREE as Nb increases (Fig. 2.10), this process alone cannot account for why the magnitudes of $(La/Sm)_{pm}$, the negative Nb anomalies, and the positive Zr anomalies that increase from andesitic (FeA), to dacitic (FeD), to rhyolitic (FeR) compositions. Instead, contamination by arc crust is likely why this suite shows these systematic compositional trends, consistent with AFC processes (Fig.2.16; DePaolo, 1981; Pearce, 2008). For example, the FeA, FeD, and FeR show a negative compositional trend of increasing $(La/Sm)_{pm}$ and Zr with decreasing $(Nb/Th)_{pm}$ (Fig. 2.15A-B), typical of rocks derived from crustal contamination (e.g., Piercey et al., 2006; Ordóñez-Calderón et al., 2016). Assimilating arc crust into a fractionating tholeiitic magma also resolves why this Fe-rich, tholeiitic suite has trace element patterns that are transitional between tholeiitic and calc-alkaline (Fig. 2.9D). To explain their enrichments in Zr-Hf relative to Sm, the crustal contaminant could have been partially melted hydrated mafic crust, since the decoupling of Zr-Hf relative to Sm is a feature shared by silicic melts experimentally-derived from partially melted mafic rocks under conditions (low pressure, high temperature, hydrous, and highly oxidizing) simulating the tops of magma chambers beneath spreading centers (France et al., 2010; France et al., 2014). This argument is supported by the SiO_2-TiO_2 systematics (Fig. 2.15D; Koepke et al., 2007) of the FeR and FeD and their FIIIa signatures (Hart et al., 2004), which are consistent with derivation from hydrous partial melting of mafic crust. The distribution of the FeA, FeD, and FeR across the fields of MORB differentiation and hydrous partial melting suggests that fractional crystallization was an important process, but assimilation was especially significant for the more felsic melts (Fig. 2.15D). The interpretation that the Fe-rich silicic suite is made up of contaminated tholeiites mirrors that proposed for hybrid tholeiitic/calc-alkaline rocks associated with VMS deposits in the Archean Abitibi greenstone belt (Gélinas and Ludden, 1984; Laflèche et al., 1992a). It may also explain why the FeR have distinct Ti-rich globules observed in thin section (Fig. 2.5I); perhaps these are disequilibrium features derived from mixed magmatic sources. For example, quenched mafic globules in felsic tuffs from the Kamiskotia VMS area in the Abitibi greenstone belt have been interpreted as evidence that mafic and felsic liquids co-existed in a subvolcanic magma chamber (Barrie et al., 1993).

Basaltic underplating beneath a rifted arc can best explain the geochemical features of the Fe-rich silicic suite. In this model, thinned island arc crust promoted the upwelling of hot asthenosphere to shallow depths beneath the rift where it partially melted by decompression and these melts intruded the arc crust (Lesher et al., 1986; Huppert and Sparks, 1988; Lentz, 1998; Hart et al., 2004; Shukuno et al., 2006; Galley et al., 2007; Piercey, 2011). The basaltic melts may have been sourced from a similarly enriched type of mantle to the footwall basalt suite (e.g., Fig. 2.16). The thermal input of fractionating, tholeiitic, mafic magmas in the arc crust likely caused the geothermal gradient to increase and induced partial melting of the arc crust. The silicic, partial melts of arc crust were assimilated by the Fe-rich basaltic intrusions, forming the Fe-rich silicic suite with mixed crust-mantle signatures (Fig. 2.18C; Huppert and Sparks, 1988; Galley et al., 2007; Piercey, 2011). The most felsic compositions were formed by basaltic intrusions that assimilated the highest amounts of crustal contaminants. Since assimilation requires sustained, anomalous heat at crustal levels (Grove and Brown, 2018), it can be surmised that the Fe-rich silicic suite formed in a thermally anomalous geodynamic setting, a feature that is critical in the development of hydrothermal systems (Maclennan et al., 2005; Piercey, 2011). The Fe-rich silicic suite immediately precedes the emplacement of the first beds of barite- and sulfide-rich exhalite and it is interpreted that the heat necessary to form the Fe-rich silicic suite also drove the hydrothermal system that formed the AG deposit.

Petrogenesis of the FeTi basalt suite

A volcanic hiatus between the emplacement of the Fe-rich silicic suite and the Z-FeTiB is indicated by exhalative massive sulfides that locally marks the contact between them (Figs. 2.3, 2.4). Because both the Z-FeTiB and HW-FeTiB (the FeTi basalts) have EMORB-like Zr-Nb-Y-Ti systematics (Figs. 2.13A-C, 2.16A-B; Pearce, 2008; Pearce, 2014) and smooth primitive mantle-normalized signatures that are more similar to the footwall basalts (Fig. 2.11), it is possible that they were derived from similar shallow, extension-related, enriched magmatic sources as the footwall basalts. However, their unique primitive mantle-normalized signatures relative to the preceding Fe-rich silicic suite suggests that these suites probably formed in separate magma chambers from that suite (Figs. Fig. 2.11, 2.18D). The FeTi basalts likely evolved by extensive fractional crystallization given their extreme enrichments in Fe_2O_3, TiO_2, P_2O_5, ΣREE relative to Nb (Fig. 2.10). The FeTi basalts have slightly lower Nb/Th (Figs. 2.13A-C, 2.15A-C, 2.16) compared to the footwall basalts, indicating that their enriched mantle sources also had slight additions from subducted slab-related fluids (Pearce, 2008). Further, because the FeTi basalts have lower Nb_{pm}/Th_{pm} relative to other monitors of crustal contamination, like La_{pm}/Sm_{pm} and Zr, than the footwall basalt suite (Fig 2.15A-B; e.g., Piercey et al., 2006; Ordóñez-Calderón et al., 2016), their Th-enrichment relative to Nb is interpreted to represent minor crustal contamination. These interpretations are consistent with petrologic studies that have shown that the formation of FeTi basalts is primarily attributed to extensive low-pressure (<1-3 kbars) fractional crystallization of typical MORB (Byerly et al., 1976; Juster et al., 1989) and some studies have shown that, in addition, minor assimilation of oceanic crustal material is also important in their genesis (Perfit et al., 1999). The Z-FeTiB were emplaced synchronous with rifting and VMS mineralization (as discussed above) and fractional crystallization was important in their formation. Collectively, these features suggest that hydrothermal convective circulation was efficient at transferring heat (and metals) from the crust to the seafloor when they formed (Fig. 2.18D; e.g., Maclennan et al., 2005; Liu and Lowell, 2011), also promoting VMS formation. By association, Fe- and Ti-rich mafic rocks like the Z-FeTiB may be prospective for VMS in other districts. In fact, Fe- and Ti-rich basalts are associated with several VMS deposits and districts globally including in the Abitibi greenstone belt (Matagami, Kamiskotia, and Noranda camps), the Wawa subprovince greenstone belts (Geco, Nama Creek, and Winston Lake deposits), the

Uchi subprovince greenstone belts (South Bay deposit), and the Flin Flon belt (Cuprus and White Lake deposits) (Barrie and Pattison, 1999; Gibson et al., 2007; Kerrich et al., 2008 and references therein; Syme et al., 2000).

The HW-FeTiB were the last to erupt in the AG host sequence (Figs. 2.3, 2.4). They have highly correlated Nb/Th values to the Z-FeTiB (Figs. 2.13A-C, 2.16), suggesting these units had similar levels of crustal contamination. However, the HW-FeTiB do not follow expected AFC fractionation vectors relative to the Z-FeTiB (Fig. 2.16A-B). The HW-FeTiB are less evolved than the Z-FeTiB based on their higher Al_2O_3-Sc-Ni and lower TiO_2-P_2O_5-ΣREE relative to Nb (Fig. 2.10); they have Ni and P_2O_5 abundances that are comparable to the FW-B (Table 2.2). These geochemical trends suggest that the HW-FeTiB cannot be related to the Z-FeTiB by crystal fractionation or AFC processes. They could, however, be derived from the same magma chamber that was replenished by influxes of new mafic magmas that could have reset the residual melts, resulting in lower TiO_2-Fe_2O_3-P_2O_5 and higher Al_2O_3-Ni-Sc relative to Nb. If the replenishing magmas were derived from a slightly deeper or more enriched source, this would help explain why the HW-FeTiB trend toward slightly more alkaline compositions (Fig. 2.16) and why they have a more intermediate depth signatures (Fig. 2.13C) and somewhat more fractionated HREE patterns (Figs. 2.11, 2.12). Furthermore, magmatic replenishment provides a mechanism to trigger explosive eruptions (Sparks et al., 1977; Fujibayashi and Sakai, 2003; Head and Wilson, 2003; Cassidy et al., 2016; Leeman and Smith, 2018) consistent with the pyroclastic textures exhibited by the HW-FeTiB.

Petrogenesis of the HSR suite

The HSR are the most evolved of all the units based on their high silica contents (Fig. 2.15), FIIIb classifications (Fig.2.14), and their most extreme abundances of HFSE and REE

(Figs.2.10, 2.11, 2.12; Table 2.2). They are interpreted to be a sill complex and based on cross-cutting relationships - some of the HSR sills are younger than the Z-FeTiB (Figs. 2.2B, 2.8A) but their timing of emplacement relative to the HW-FeTiB is uncertain. They have Nb/Yb and Nb/Ta ratios that are comparable to the HW-FeTiB (Table 2.3), suggesting derivation from similar mantle sources, however, they plot above the MORB-OIB array, indicating that they have been modified by subduction zone-related influences (Fig.2.16).

The formation of FIIIb high-silica rhyolites like the HSR has been attributed to extensive fractional crystallization of a basaltic parent (Lesher et al., 1986), or shallow (< 10 km), high-temperature (1,100º–900ºC) hydrous partial melting of mafic crust where clinopyroxene is more stable than amphibole (Lesher et al., 1986; Barrie et al., 1993; Barrie and Pattison, 1999; Hart et al., 2004). Plagioclase, clinopyroxene, and titanite could have been fractionating phases as indicated by negative Eu anomalies, low Sc contents (Sc < 1 ppm), and extreme negative Ti anomalies, respectively, in the HSR suite (Table 2.3, Fig. 2.11). Furthermore, the HSR have anomalously low Zr/Hf (Zr/Hf = 24.20–28.21) relative to chondritic meteorites (Zr/Hf = 34.08–37.09) and the primitive mantle (Zr/Hf = 34.17 – 37.10) (Sun and McDonough, 1989; Mcdonough and Sun, 1995; Palme and O'Neill, 2014) that could also be explained by the fractionation of zircon, clinopyroxene, or titanite (Linnen and Keppler, 2002; Claiborne et al., 2018). Zircon fractionation is also supported by their accessory euhedral zircon crystals (Fig. 2.8D-E) including grains recovered from the geochronologic sample 110-368 (Table 2.5; Appendix 4) that were interpreted as igneous and not inherited grains.

Their extremely low Fe and Ti, high Si nature, and high abundance of HREE could also reflect hydrous partial melting of mafic crust (Table 2.3; Fig. 2.15D, Koepke et al., 2007; Wanless et al., 2010; Fassbender et al., 2022). Their elevated Th/Nb (Fig. 2.13A-B, 2.15A-C, 2.16) relative to the footwall basaltic and FeTi basalt suites suggests that mafic arc crust was the likely contaminant. Derivation from mixed crust-mantle sources best explains their variable tholeiitic (Fig.2.14A,C) and calc-alkaline (Figs. 2.9C, 2.14B) major and trace element signatures. Some of their transitional (Figs. 2.9D) to alkaline (Figs. 2.9A, 2.13A-B) trace element signatures may not be reliable since Zr behaved compatibly during zircon fractionation. For example, they have higher Nb relative to Zr compared to the FeR (Fig. 2.14C). The HSR probably formed by high-temperature, low-pressure crustal partial melting followed by fractional crystallization since they: (1) have relatively constant compositions, (2) are hosted in a bimodal volcanic succession, and (3) none of the other volcanic suites are related to each other purely by fractional crystallization suggesting the absence of a single, large, fractionating magma chamber (e.g., Hart et al., 2004).

Magmatic replenishment by slightly deeper (or possibly somewhat more alkaline) sources was invoked to relate the HW-FeTiB to the Z-FeTiB (described above). Perhaps such an influx of hot mafic magma into the crust may have promoted crustal melting to generate the HSR. Once the HSR melts were generated, they may have further evolved by fractional crystallization. These petrogenetic interpretations are consistent with those postulated for some high silica rhyolites with FIIIb signatures elsewhere (Barrie et al., 1993; Barrie and Pattison, 1999; Hart et al., 2004), including some high Zr/Ti felsic composite intrusions that postdate the main VMS-forming events in Precambrian VMS camps (Galley, 2003); the HSR are interpreted to postdate the main AG VMS-forming period.

2.7.3. Tectonic controls on the AG VMS deposit genesis

In the ancient rock record an estimated 80% of all VMS deposits are interpreted to have formed in rifted arc settings (Hannington et al., 2005). The VMS deposits of the ATMB are postulated to have formed in a propagating intra-arc rift (Taylor et al., 2008) and radiogenic isotopic signatures of rocks in the Alexander terrane suggest it formed in a wholly oceanic realm (Samson and Patchett, 1991; Peter and Scott, 1997; Peter et al., 2014; Steeves et al., 2016). Rifting is the first stage in arc extension that may occur over several millions of years before true ocean floor spreading allows mantle material to upwell passively in a back-arc basin (Barrett and MacLean, 1999; Hannington et al., 2005; Stern, 2010). The rifting stage is typically geochemically and spatially disorganized (Gill et al., 2021). In sufficiently wide (~ 200 km) back-arc basins with true seafloor spreading (Hannington et al., 2005), volcanism is dominated by monotonous piles of effusive MORB-like basalts with minimal felsic to intermediate rocks and especially minor volcaniclastic facies (Syme et al., 2000). Given that the AG volcanic stratigraphy includes diverse rock compositions, especially highly evolved compositions (e.g., FeTi basalts, andesitic through rhyolitic compositions including high-silica rhyolites) with variable MOR-like to arc-like geochemical features, and volcaniclastic facies (FeR, heterolithic fragmental rocks, HW-FeTiB) are volumetrically significant in the AG suite, an intra-arc rift is the preferred tectonic setting (Fig. 2.19). Intra-arc rifting is the most common cause of mantle enrichment, with enriched compositions typically migrating into the space beneath the rift during and immediately after arc rifting (Hawkins, 2003; Hochstaedter et al., 1990; Pearce and Peate, 1995; Gill et al., 2021), consistent with the enriched mantle signatures of the AG units. The FIIIa signatures of the FeR and FeD are also common in felsic rocks associated with rifted intraoceanic island arcs (Fassbender et al., 2022).

Evolved basalts enriched in Fe and Ti, like the Z-FeTiB and HW-FeTiB, are not common on the seafloor, but in arc settings, many have been sampled in association with ridge discontinuities such as propagating rifts, transform faults, and overlapping spreading centers (Sinton et al., 1993; Pearce et al., 1994; Caroff and Fleutelot, 2003; Sinton et al., 2003; Fleutelot et al., 2005; Fretzdorff et al., 2006). The formation of evolved lavas by AFC processes in intraoceanic island arc settings, such as the Fe-rich silicic suite and the HSR, has also been linked to propagating rift tips (Fassbender et al., 2022), where the opportunities for these melt-generating processes are highest (Pearce and Stern, 2006). The lithogeochemical associations with propagating rift tips reflect the unique tectonic, thermal, and magmatic regimes at ridge discontinuities governed by episodic magmatic supply rates that favor the formation of isolated magma chambers where fractional crystallization processes dominate (Sinton et al., 1983; Pearce et al., 1994) but where assimilation can also occur (Pearce and Stern, 2006), especially following magmatic replenishment cycles (Grove and Brown, 2018). A propagating intra-arc rift provides the mechanism for basin development where upwelling asthenosphere brings heat to crustal levels. The injection of asthenosphere-derived partial melts into cold crust favors fractional crystallization processes (e.g., Christie and Sinton, 1981; Huppert and Sparks, 1988), generating basalts like the footwall basalt suite (Fig. 2.18B). High heat flow from basaltic intrusions in rifted crust also initiates hydrothermal convective circulation and induces partial crustal melting to create geochemically distinct units like the Fe-rich silicic suite and the HSR (Fig. 2.19C, H). Ridge discontinuities may result in the development of disconnected magma chambers that are cut off from magmatic replenishment (Sinton et al., 1983), favoring fractional crystallization processes and the development of highly evolved basalts, like the FeTi basalts. The cooling of these isolated magma chambers may be enhanced in rifted basins that create conduits for hydrothermal fluids to efficiently transfer heat (and metals) from the crust to the seafloor (e.g., Maclennan et al., 2005; Liu and Lowell, 2011), a process critical in the development of VMS deposits.

The formation of the AG deposit in a propagating intra-arc rift agrees with previous interpretations for the VMS deposits of the ATMB (Taylor et al., 2008) and this tectonic setting is common for bimodal-mafic VMS deposits globally (Allen et al., 2002; Galley et al., 2007; Piercey, 2011). The thermally anomalous, extension-related tectono-magmatic processes at propagating intra-arc rifts are conducive to VMS formation, and furthermore, the volcanic rocks that form in these settings have distinct lithogeochemical associations that can be used to guide VMS exploration.

2.7.4. Age of the AG VMS deposit and implications for the timing of hydrothermal activity in the ATMB

Generalized stratigraphic columns with geochronologic data for Greens Creek, Palmer, AG, and Windy Craggy are provided in Fig. 2.19. Previous conodont studies on the Palmer property confirmed that the host rocks for VMS mineralization are Late Triassic (Norian to Rhaetian; Green, 2001; Green et al., 2003) and an ID-TIMS U-Pb zircon date of 213 ± 5 Ma from a hydrothermally altered rhyolite constrains the timing of mineralization at the Palmer deposit (Green, 2001). Zircons from the FeR and HSR at AG yield new CA-ID-TIMS U-Pb crystallization dates of 210.35 ± 0.27, and 210.52 ± 0.08 Ma, respectively (Fig. 2.17; Table 2.4, Table 2.5) that are in agreement with these previous age constraints on the Palmer property. The FeR crystallized at 210.35 ± 0.27 Ma, marking a break in volcanism, the onset of hydrothermal activity, and the accumulation of exhalative massive barite laminated with sulfides. Therefore, this date provides a reasonable constraint on the age of hydrothermal activity at AG. The HSR are interpreted to be emplaced as high-level intrusions, some of which were emplaced after the Z-FeTiB when VMS mineralization was interpreted to be at a maximum. They are locally hydrothermally altered, suggesting they were emplaced synchronously with hydrothermal activity. The HSR sill that intrudes the FeA in drill hole 110 crystallized at 210.52 ± 0.08 Ma. This date also provides a reliable constraint on the age of hydrothermal activity at AG. The HSR sill is interpreted to have formed after the FeR, based on their stratigraphic relationship. The overlapping date ranges for the FeR and the HSR suggest that the immediate volcanic hosts to the AG deposit (FeR, Z-FeTiB, HSR) were emplaced within less than million years of each other and that the deposit formed sometime between 210.60 Ma (oldest limit of HSR) to 210.08 Ma (youngest limit of FeR).

It has been suggested that Greens Creek mineralization formed mainly by subseafloor replacement on a 100 million year unconformity (Steeves, 2018) and occurred after the deposition of argillite containing conodonts assigned to the Norian-Carnian boundary (220.7 ± 4.4 Ma; Premo et al., 2010). According to the current Norian-Carnian boundary (227 Ma; Walker et al., 2018), the argillite is estimated to have been deposited around 227 Ma (Steeves, 2018). A Hyd Group rhyolite interpreted to be stratigraphically above the argillite and post-dating the Greens Creek mineralization returned a CA-ID-TIMS U-Pb zircon date of 226.86 ± 0.24 Ma (Sack et al., 2011; Sack et al., 2016) suggesting that the AG deposit could be at least 15 million years younger than the Greens Creek deposit. However, field mapping and structural interpretations suggest that this Hyd Group rhyolite is actually structurally above the argillite in an overturned sequence, making it stratigraphically older than the argillite and thus older than Greens Creek mineralization (Steeves, 2018). The argillites are intruded by gabbros with a LA-ICP quadrupole mass spectrometry (QMS) U-Pb zircon date of 219 ± 8 Ma. Hydrothermal mineralization at Greens Creek may be linked to mafic-ultramafic intrusions emplaced between 215 and 211 Ma in Gambier Bay (Premo et al., 2010). Fuchsite from one of these altered ultramafic bodies has a $^{40}Ar/^{39}Ar$ plateau age of 210.3 ± 0.3 Ma, representing the time that the intrusion cooled to below 300^{o}C and when hydrothermal activity is interpreted to have ceased (Premo et al., 2010). Furthermore, a mineralized sample at Greens Creek yielded a LA-ICP-MS U-Pb age of 209 ± 9.4 Ma from hydrothermal monazite, however, this age was deemed unreliable due to Pb contamination from sulfides and also possible Pb loss from later metamorphism (Steeves, 2018).

The age of mineralization at AG is very similar to the interpreted age of hydrothermal activity near Greens Creek based on the mafic-ultramafic intrusions (Premo et al., 2010). This is significant because the Palmer property that hosts the AG and Palmer deposits may have formed only 30-50 km from Greens Creek after restoring the ~180 km post-middle Cretaceous and pre-Holocene dextral movement along the Chatham Strait fault (Hudson et al., 1982). The overlapping ages of interpreted hydrothermal activity at AG and near Greens Creek suggests that the AG and Greens Creek deposits could be broadly coeval. This differs from previous interpretations that suggest that the AG and Palmer deposits formed from two different hydrothermal events approximately 10–15 million years apart (Sack et al., 2016). Until the timing of mineralization at Greens Creek can be determined with higher confidence, the possibility that AG and Greens Creek could be coeval remains valid and testable.

2.7.5. The association of VMS deposits with Fe-rich volcanic rocks and high-silica rhyolites – comparisons to the Neoarchean Blake River Group, Abitibi greenstone belt

Fe-rich volcanic rocks and high-Si rhyolites are common in many bimodal-mafic settings, including the Archean Abitibi greenstone belt, which hosts world-class VMS deposits in various similar sequences, many of which are within the Blake River Group (“BRG”) in Ontario and Quebec (Barrett and MacLean, 1999; Barrie and Pattison, 1999; Franklin et al., 2005; Gibson et al., 2007; Hathway et al., 2008; Kerrich et al., 2008). The BRG rocks have many similarities to the AG volcanic stratigraphy, including: (1) variolitic, Fe-rich basalts (Gélinas et al., 1976; Gélinas et al., 1984; Fowler et al., 1987), (2) Fe-rich volcanic rocks of varied compositions, including some with hybrid tholeiitic to calc-alkaline affinities (Dimroth et al., 1982; Gélinas et al., 1984; Gélinas and Ludden, 1984; Fowler and Jensen, 1989; Gibson, 1990; Barrett et al., 1991; Laflèche et al., 1992b; Barrie et al., 1993), (3) FIII-type high-silica rhyolites and FeTi-rich mafic rocks with VMS mineralization (Lesher et al., 1986; Barrie and Pattison, 1999; Hart et al., 2004; Hathway et al., 2008), (4) pyroclastic deposits within VMS-hosting stratigraphy (Barrie and Pattison, 1999; Ross et al., 2011), and (5) formation in rifted arc geodynamic settings (Laflèche et al., 1992b; Wyman, 2003). The stratigraphy of the Aldermac VMS deposit (2700.2 ± 0.9 Ma; McNicoll et al., 2014) is similar to AG, mineralization formed at the end of an andesite, dacite, and Fe-rich rhyolite extrusive cycle and was followed by the emplacement of a large dome of mainly massive to brecciated high-Si rhyolite and high-Ti andesite (Barrett et al., 1991). In the Kamiskotia volcanic complex, the Kam Kotia VMS deposit occurs along strike from FeTi basalts and they occur in the immediate stratigraphic hangingwall; mixed basalt-rhyolite lapilli tuffs are broadly synchronous with mineralization; and the deposit is both underlain and overlain by high-silica rhyolites (Barrie and Pattison, 1999). The spatial association of FeTi-rich mafic rocks, FIII-type high-silica rhyolites, and volcaniclastic rocks with VMS mineralization at Kam Kotia are like some of the AG units (Fig. 2.20).

The similarities between the AG volcanic stratigraphy and sequences hosting VMS deposits in the BRG indicate the Late Triassic intra-oceanic island arc rift processes proposed to have formed the AG rocks may have also been operative in the Neoarchean. Interestingly, it has been suggested that the BRG may have formed by plume-arc interaction (Wyman, 2003). By association, could mantle plume events or the products of plume events, such as oceanic plateaus and large igneous provinces (LIP), be linked to the formation of the ATMB? In the Alexander-Wrangellia-Peninsular composite super-terrane, thick (> 6,000 m) accumulations of plume-related Ladinian to Norian (239–225 Ma; Nelson et al., 2013b) tholeiitic basalts were deposited in the Wrangellia flood basalt province (Lassiter et al., 1995; Greene et al., 2008; Greene et al., 2009), immediately prior to the emplacement of the rhyolite (226.86 ± 0.24 Ma; Sack et al., 2011; Sack et al., 2016) postulated to be in the Greens Creek stratigraphic footwall (Steeves, 2018) and about 15 million years before the AG deposit formed (between 210.60 to 210.08; this study) in the rifted arc rocks of the ATMB. The interaction of mantle plumes or products of mantle plumes (e.g., LIP) with intra-oceanic island arc systems has been documented in some modern settings, such as the Tonga-Lau intraoceanic arc system (Ewart et al., 1998; Falloon et al., 2007; Lupton et al., 2012; Price et al., 2014; Timm et al., 2014; Lupton et al., 2015; Gill et al., 2021) and the New Hebrides Island arc system (Anderson et al., 2016). Large igneous provinces can plug subduction zones, cause subduction zone reversals, initiate rifting, impact the dynamics of ridge segmentation, and subduction of these LIPs can enhance magmatism (Hall, 2002; Stern, 2004; de Ronde et al., 2007; Hastie and Kerr, 2010; Anderson, 2018). Peter et al. (2014) combined observations from geochemistry, isotope studies, and geological relationships to infer that the Late Triassic ATMB Windy Craggy deposit hosted by argillite and alkalic basalts formed in a back-arc setting associated with a slab window; similar tectonic configurations are proposed in the northern Lau basin in the southwest Pacific (Regelous et al., 2008; Lupton et al., 2009; Price et al., 2014) where seismic evidence suggests that there is a tear in the Pacific plate associated with the hotspot volcanism of the Samoan Islands (Millen and Hamburger, 1998). It is possible that the Wrangellia flood basalt events imparted complex and heterogeneous stresses to the Late Triassic Alexander intra-oceanic arc system that eventually rifted to form the ATMB (e.g., Nelson et al., 2013b). Furthermore, these thick, buoyant masses may have helped to preserve the VMS-hosting crust during terrane accretion. FIIIb rhyolites like the HSR at AG are much more common in the Archean (Hart et al., 2004; Piercey, 2011), possibly because the mantle was hotter in the Archean (Abbott et al., 1994), but it could also reflect the low preservation potential of mid-ocean ridge or mature back-arc basin oceanic crust where FIIIb rhyolites are mainly formed today (Fassbender et al., 2022). Complex microplate configurations associated with buoyant crust (e.g., LIP such as the Wrangellia flood basalts) may have been critical to initiate arc rifting in the ATMB and preserve it from subduction (Dilek and Furnes, 2014).

2.8. Conclusions

Reconstruction of the AG volcanic architecture with the aid of lithogeochemical investigations indicates that the AG deposit is a bimodal-mafic VMS deposit hosted by FIII-type rhyolites and FeTi-rich basalts. The primary geochemical signatures of the volcanic rocks are highly correlated with their stratigraphic position; chemostratigraphic patterns show that most of the deposit formed at the contact between the Fe-rich silicic suite and the FeTi basalt suite. Field relationships, geochemical observations, and geochronologic evidence suggest that the AG deposit formed in a propagating intra-arc rift sometime between 210.60 to 210.08 million years ago. A propagating intra-arc rift provided the mechanism for basin development where:

1. Thinned arc crust promoted enriched asthenosphere to upwell and partially melt by decompression, forming the pillowed, footwall basalt suite that have tholeiitic, EMORB-like geochemical signatures.
2. Fractionating tholeiitic basaltic intrusions at shallow (< 10 km from surface) levels in the arc crust induced partial crustal melting and assimilated those crustal melts to create the Fe-rich silicic suite, including FIIIa- and A-type felsic rocks, which have mixed tholeiitic and calc-alkaline geochemical signatures. The high heat flow required to sustain assimilation processes was also critical in the development of hydrothermal convective circulation. Barite- and sulfide-rich exhalites accumulated above the thickest parts of the FeR lapilli tuffs that have a crystallization age of 210.35 ± 0.27 Ma.
3. Propagating rift tectonics allowed the development of a disconnected magma chamber that could evolve by extensive fractional crystallization and minor crustal assimilation to form

the EMORB-like Z-FeTiB. The cooling of the Z-FeTiB magma chamber may have been enhanced in a rifted basin where synvolcanic structures created conduits for hydrothermal fluids to efficiently transfer heat from the crust to the seafloor. The Z-FeTiB variolitic, pillowed flows were emplaced synchronous with rift-related heterolithic fragmental rocks and VMS mineralization. One synvolcanic fault, the Finch fault, was responsible for the sharp lateral changes in the thicknesses and facies of units and the focus of VMS mineralization.

4. Magma recharge in the same crustal magma chamber that fed the Z-FeTiB may have triggered the explosive volcanic eruption of the volcaniclastic HW-FeTiB that cap the AG deposit, and likely helped to preserve the exhalative parts of the deposit.
5. The influx of mafic magma related to the HW-FeTiB is interpreted to have promoted high-temperature (1,100º–900ºC), low-pressure (< 10 km) crustal melting followed by fractional crystallization (e.g., zircon fractionation) to generate the FIIIb HSR. The HSR intrusions were the last magmatic phase in the AG volcanic succession and crystallized at 210.52 ± 0.08 Ma. They were emplaced as intrusions along the Finch fault, and they likely plugged this conduit, possibly quenched the hydrothermal system, or redirected it elsewhere.

Collectively, the FIIIa FeR, Z-FeTiB, and heterolithic fragmental rocks are the most important hosts to VMS mineralization at AG. Hydrothermal mineralization was intimately associated with basin development in a rifted arc environment near an active volcanic center. Volcanic rocks with weak arc-like geochemical signatures that are derived from AFC processes, such as the Fe-rich silicic suite and the HSR, signify a thermally anomalous geodynamic setting; a feature that is critical in the development of hydrothermal systems. Fe- and Ti-rich basalts, like the Z-FeTiB and HW-FeTiB are also prospective for VMS because they may coincide with rifted settings governed by efficient heat transfer from the crust to the seafloor.

The lithostratigraphic and geochemical features of the AG host volcanic rocks help to elucidate the tectono-magmatic conditions governing the formation of the AG VMS deposit. These insights can help to improve our understanding of how VMS deposits form. They can also identify VMS-favorable successions and guide exploration at the property- to belt-scale and in similar intra-arc rift settings globally, from the Neo-Archean to the present.

Chapter 2 References

Abbott, D., Burgess, L., Longhi, J., and Smith, W.H.F., 1994, An empirical thermal history of the Earth's upper mantle: Journal of Geophysical Research, v. 99, p. 13835–13850.

Allen, R.L., Weihed, P., Blundell, D., Crawford, T., Davidson, G., Galley, A., Gibson, H., Hannington, M., Herzig, P., Large, R., Lentz, D., Maslennikov, V., McCutcheon, S., Peter, J., et al., 2002, Global comparisons of volcanic-associated massive sulphide districts: Geological Society of London, Special Publications, v. 204, p. 13–37.

Anderson, M., 2018, Relationships between tectonics, volcanism, and hydrothermal venting in the New Hebrides and Mariana back-arc basins, Western Pacific: Ph.D. thesis, Ottawa, Canada, University of Ottawa: 1021 p.

Anderson, M.O., Hannington, M.D., Haase, K., Schwarz-Schampera, U., Augustin, N., McConachy, T.F., and Allen, K., 2016, Tectonic focusing of voluminous basaltic eruptions in magma-deficient backarc rifts: Earth and Planetary Science Letters, v. 440, p. 43–55.

Arai, R., and Dunn, R.A., 2014, Seismological study of Lau back arc crust: mantle water, magmatic differentiation, and a compositionally zoned basin: Earth and Planetary Science Letters, v. 390, p. 304–317.

Barrett, T.J., and Maclean, W.H., 1994, Chemostratigraphy and hydrothermal alteration in exploration for VHMS deposits in greenstones and younger volcanic rocks: Geological Association of Canada, Short Course Notes, v. 11, p. 433–467.

Barrett, T.J., and MacLean, W.H., 1994, Mass changes in hydrothermal alteration zones associated with VMS deposits of the Noranda area: Exploration and Mining Geology, v. 3,

p. 131–160.

Barrett, T.J., and MacLean, W.H., 1999, Volcanic sequences, lithogeochemistry, and hydrothermal alteration in some bimodal volcanic-associated massive sulfide systems: Reviews in Economic Geology, v. 8, p. 101–132.

Barrett, T.J., Cattalani, S., Chartrand, F., and Jones, P., 1991, Massive sulfide deposits of the Noranda area, Quebec. II. The Aldermac mine: Canadian Journal of Earth Sciences, v. 28, p. 1301–1327.

Barrie, C.T., and Hannington, M.D., 1999, Classification of volcanic-associated massive sulfide deposits based on host-rock composition: Reviews in Economic Geology, v. 8, p. 1–12.

Barrie, C.T., and Pattison, J., 1999, Fe-Ti basalts, high silica rhyolites, and the role of magmatic heat in the genesis of the Kam-Kotia volcanic-associated massive sulfide deposit, Western Abitibi Subprovince, Canada: Economic Geology Monograph, v. 10, p. 577–592.

Barrie, C.T., Ludden, J.N., and Green, T.H., 1993, Geochemistry of volcanic rocks associated with Cu-Zn and Ni-Cu deposits in the Abitibi Subprovince: Economic Geology, v. 88, p. 1341–1358.

Le Bas, M.J., Le Maitre, R.W., Streckeisen, A., and Zanettin, B., 1986, A chemical classification of volcanic rocks based on the total alkali-silica diagram: Journal of Petrology, v. 27, p. 745–750.

Beier, C., Bach, W., Turner, S., Niedermeier, D., Woodhead, J., Erzinger, J., and Krumm, S., 2015, Origin of silicic magmas at spreading centres—An example from the South East Rift, Manus basin: Journal of Petrology, v. 56, p. 255–272.

Beranek, L.P., van Staal, C.R., McClelland, W.C., Joyce, N., and Israel, S., 2014, Late Paleozoic assembly of the Alexander-Wrangellia-Peninsular composite terrane, Canadian and Alaskan Cordillera: Geological Society of America Bulletin, v. 126, p. 1531–1550.

Bonin, B., 2007, A-type granites and related rocks: Evolution of a concept, problems and prospects: Lithos, v. 97, p. 1–29.

Bouma, A.H., and Ravenne, C., 2004, The Bouma Sequence (1962) and the resurgence of geological interest in the French Maritime Alps (1980s): the influence of the Grès d'Annot in developing ideas of turbidite systems: Geological Society of London, Special Publications, v. 221, p. 27–38.

Brophy, J.G., 2009, La-SiO_2 and Yb-SiO_2 systematics in mid-ocean ridge magmas: implications for the origin of oceanic plagiogranite: Contributions to Mineralogy and Petrology, v. 158, p. 99–111.

Byerly, G.R., Melson, W.G., and Vogt, P.R., 1976, Rhyodacites, andesites, ferro-basalts and ocean tholeiites from the Galapagos spreading center: Earth and Planetary Science Letters, v. 30, p. 215–221.

Campbell, I.H., Lesher, C.M., Coad, P., Franklin, J.M., Gorton, M.P., and Thurston, P.C., 1984, Rare-earth element mobility in alteration pipes below massive Cu-Zn-sulfide deposits: Chemical Geology, v. 45, p. 181–202.

Cann, J.R., 1970, Rb, Sr, Y, Zr and Nb in some ocean floor basaltic rocks: Earth and Planetary Science Letters, v. 10, p. 7–11.

Caratori Tontini, F., Bassett, D., de Ronde, C.E.J., Timm, C., and Wysoczanski, R., 2019, Early evolution of a young back-arc basin in the Havre trough: Nature Geoscience, v. 12, p. 856–862.

Caroff, M., and Fleutelot, C., 2003, The north-south propagating spreading center of the north Fiji basin. Modeling of the geochemical evolution in periodically replenished and tapped magma chambers: Mineralogy and Petrology, v. 79, p. 203–224.

Cas, R., 1992, Submarine volcanism: eruption styles, products, and relevance to understanding the host-rock successions to volcanic-hosted massive sulfide deposits: Economic Geology, v. 87, p. 511–541.

Cas, R., and Wright, J., 1987, Volcanic successions: Modern and ancient: A geological approach to processes, products and successions: London, Allen & Unwin Ltd., 528 p.

Cassidy, M., Castro, J.M., Helo, C., Troll, V.R., Deegan, F.M., Muir, D., Neave, D.A., and Mueller, S.P., 2016, Volatile dilution during magma injections and implications for volcano explosivity: Geology, v. 44, p. 1027–1030.

Charlier, B., Namur, O., and Grove, T.L., 2013, Compositional and kinetic controls on liquid immiscibility in ferrobasalt-rhyolite volcanic and plutonic series: Geochimica et Cosmochimica Acta, v. 113, p. 79–93.

Christie, D.M., and Sinton, J.M., 1981, Evolution of abyssal lavas along propagating segments of the Galapagos spreading center: Earth and Planetary Science Letters, v. 56, p. 321–335.

Christie, D.M., Werner, R., Hauff, F., Hoernle, K., and Hanan, B.B., 2005, Morphological and geochemical variations along the eastern Galápagos spreading center: Geochemistry, Geophysics, Geosystems, v. 6, article Q01006.

Claiborne, L.L., Miller, C.F., Walker, B.A., Wooden, J.L., Mazdab, F.K., and Bea, F., 2018, Tracking magmatic processes through Zr/Hf ratios in rocks and Hf and Ti zoning in zircons: an example from the Spirit Mountain batholith, Nevada: Journal of Petrology, v. 70, p. 517–543.

Colpron, M., and Nelson, J., 2011, A digital atlas of terranes for the northern Cordillera: British Columbia Ministry of Energy, Mines and Natural Gas, BCGS GeoFile 2011-11.

Condie, K.C., 2005, High field strength element ratios in Archean basalts: a window to evolving sources of mantle plumes? Lithos, v. 79, p. 491–504.

Cui, Y., Miller, D., Schiarizza, P., and Diakow, L.J., 2017, British Columbia digital geology: British Columbia Ministry of Energy, Mines and Petroleum Resources, British Columbia Geological Survey Open File 2017-8, 9p. Data version 2019-12-19.

DePaolo, D.J., 1981, Trace element and isotopic effects of combined wallrock assimilation and fractional crystallization: Earth and Planetary Science Letters, v. 53, p. 189–202.

Dilek, Y., and Furnes, H., 2014, Ophiolites and their origins: Elements, v. 10, p. 93–100.

Dimroth, E., Imreh, L., Rocheleau, M., and Goulet, N., 1982, Evolution of the south-central part of the Archean Abitibi belt, Quebec. Part I: stratigraphy and paleogeographic model: Canadian Journal of Earth Sciences, v. 19, p. 1729–1758.

Doherty, J., 2018, The mineralogy, ore mineral chemistry, and geochemistry of the Nunatak prospect AG Zone: a new Zn-Pb-Cu-Ag (Au)-barite VMS discovery outside of Haines, Alaska: Report synthesizing applied M.Sc. program research, Kingston, Canada, Queen’s University: 83 p.

Doyle, M.G., and Allen, R.L., 2003, Subsea-floor replacement in volcanic-hosted massive sulfide deposits: Ore Geology Reviews, v. 23, p. 183–222.

Elliott, T., 2004, Tracers of the slab: American Geophysical Union Monograph, v. 138, p. 23–45.

Ewart, A., Collerson, K.D., Regelous, M., Wendt, J.I., and Niu, Y., 1998, Geochemical evolution within the Tonga-Kermadec-Lau arc-back-arc systems: the role of varying mantle wedge composition in space and time: Journal of Petrology, v. 39, p. 331–368.

Falloon, T.J., Danyushevsky, L. V., Crawford, T.J., Maas, R., Woodhead, J.D., Eggins, S.M., Bloomer, S.H., Wright, D.J., Zlobin, S.K., and Stacey, A.R., 2007, Multiple mantle plume components involved in the petrogenesis of subduction-related lavas from the northern termination of the Tonga arc and northern Lau basin: evidence from the geochemistry of arc and backarc submarine volcanics: Geochemistry, Geophysics, Geosystems, v. 8, article Q09003.

Fassbender, M.L., Hannington, M., Stewart, M., Brandl, P.A., Baxter, A.T., and Diekrup, D., 2022, Geochemical signatures of felsic volcanic rocks in modern oceanic settings and implications for Archean greenstone belts: Economic Geology, v. 118, p. 319–345.

Finlow-Bates, T., and Stumpfl, E.F., 1981, The behaviour of so-called immobile elements in hydrothermally altered rocks associated with volcanogenic submarine-exhalative ore deposits: Mineralium Deposita, v. 16, p. 319–328.

Fisher, R. V, 1966, Rocks composed of volcanic fragments and their classification: Earth-Science Reviews, v. 1, p. 287–298.

Fleutelot, C., Fleutelot, C., Eissen, J.-P., Eissen, J.-P., Dosso, L., Dosso, L., Juteau, T., Juteau, T., Launeau, P., Launeau, P., Bollinger, C., Bollinger, C., Cotten, J., Cotten, J., et al., 2005, Petrogenetic variability along the north–south propagating spreading center of the north Fiji basin: Mineralogy and Petrology, v. 83, p. 55–86.

Forbes, R.B., Gilbert, W.., and Redman, E., 1989, Geologic setting and petrology of the metavolcanic rocks in the northwestern part of the Skagway B-4 Quadrangle, southeastern Alaska: Alaska Division of Geological & Geophysical Surveys Public Data File 89-14, 46 p.

Fowler, A.D., and Jensen, L.S., 1989, Quantitative trace-element modelling of the crystallization history of the Kinojévis and Blake River groups, Abitibi greenstone belt, Ontario: Canadian Journal of Earth Sciences, v. 26, p. 1356–1367.

Fowler, A.D., Jensen, L.S., and Peloquin, S.A., 1987, Varioles in Archean basalts: products of spherulitic crystallization: The Canadian Mineralogist, v. 25, p. 275–289.

Fowler, A.D., Berger, B., Shore, M., Jones, M.I., and Ropchan, J., 2002, Supercooled rocks: development and significance of varioles, spherulites, dendrites and spinifex in Archaean volcanic rocks, Abitibi greenstone belt, Canada: Precambrian Research, v. 115, p. 311–328.

France, L., Koepke, J., Ildefonse, B., Cichy, S.B., and Deschamps, F., 2010, Hydrous partial melting in the sheeted dike complex at fast spreading ridges: experimental and natural observations: Contributions to Mineralogy and Petrology, v. 160, p. 683–704.

France, L., Koepke, J., MacLeod, C.J., Ildefonse, B., Godard, M., and Deloule, E., 2014, Contamination of MORB by anatexis of magma chamber roof rocks: constraints from a geochemical study of experimental melts and associated residues: Lithos, v. 202–203, p. 120–137.

Franklin, J.M., Gibson, H.L., Jonasson, I.R., and Galley, A.G., 2005, Volcanogenic massive sulfide deposits: Economic Geology, 100th Anniversary Volume, p. 523–560.

Fretzdorff, S., Schwarz-Schampera, U., Gibson, H.L., Garbe-Schönberg, C.-D., Hauff, F., and Stoffers, P., 2006, Hydrothermal activity and magma genesis along a propagating back-arc basin: Valu Fa ridge (southern Lau basin): Journal of Geophysical Research, v. 111, article B08205.

Frost, B.R., Barnes, C.G., Collins, W.J., Arculus, R.J., Ellis, D.J., and Frost, C.D., 2001, A geochemical classification for granitic rocks: Journal of Petrology, v. 42, p. 2033–2048.

Frost, C.D., and Frost, B.R., 2011, On ferroan (A-type) granitoids: their compositional variability and modes of origin: Journal of Petrology, v. 52, p. 39–53.

Fujibayashi, N., and Sakai, U., 2003, Vesiculation and eruption processes of submarine effusive and explosive rocks from the Middle Miocene Ogi basalt, Sado Island, Japan: American Geophysical Union Monograph, v. 140, p. 259–272.

Galley, A.G., 2003, Composite synvolcanic intrusions associated with Precambrian VMS-related hydrothermal systems: Mineralium Deposita, v. 38, p. 443–473.

Galley, A.G., Hannington, M.D., and Jonasson, I.R., 2007, Volcanogenic massive sulphide deposits: Geological Association of Canada, Special Publication, v. 5, p. 141–161.

Gardner, M.C., Bergman, S.C., Cushing, G.W., MacKevett, J., Plafker, G., Campbell, R.B., Dodds, C.J., McClelland, W.C., and Mueller, P.A., 1988, Pennsylvanian pluton stitching of Wrangellia and the Alexander terrane, Wrangell Mountains, Alaska: Geology, v. 16, p. 967–971.

Gehrels, G.E., Butler, R.F., and Bazard, D.R., 1996, Detrital zircon geochronology of the Alexander terrane, southeastern Alaska. Geological Society of America Bulletin 108, p. 722–734.

Gehrels, G.E., and Berg H.C., 1994, Geology of southeastern Alaska: Geological Society of America, v. G-1, p. 451–467.

Gehrels, G.E., and Saleeby, J.B., 1987, Geologic framework, tectonic evolution, and displacement history of the Alexander terrane: Tectonics, v. 6, p. 151–173.

Gélinas, L., and Ludden, J.N., 1984, Rhyolitic volcanism and the geochemical evolution of an Archaean central ring complex: the Blake River Group volcanics of the southern Abitibi belt, Superior province: Physics of the Earth and Planetary Interiors, v. 35, p. 77–88.

Gélinas, L., Brooks, C., and Trzcienski W. E., J., 1976, Archean variolites; quenched immiscible liquids: Canadian Journal of Earth Sciences, v. 13, p. 210–230.

Gélinas, L., Trudel, P., and Hubert, C., 1984, Chemostratigraphic division of the Blake River Group, Rouyn-Noranda area, Abitibi, Quebec: Canadian Journal of Earth Sciences, v. 21, p. 220–231.

Gibson, H.L., 1990, The mine sequence of the central Noranda Volcanic Complex: geology, alteration, massive sulphide deposits and volcanological reconstruction: Ph.D. thesis, Ottawa, Ontario, Carleton University: 715 p.

Gibson, H.L., Morton, R.L., and Hudak, G.J., 1999, Submarine volcanic processes, deposits, and environments favorable for the location of volcanic-associated massive sulfide deposits: Reviews in Economic Geology, v. 8, p. 13–52.

Gibson, H.L., Allen, R.L., Riverin, G., and Lane, T.E., 2007, The VMS model: advances and application to exploration targeting: Proceedings of Exploration: Fifth Decennial International Conference on Mineral Exploration, v. 7, p. 713–730.

Gifkins, C., Herrmann, W., and Large, R., 2005, Altered volcanic rocks: a guide to description and interpretation: Hobart, Australia, Centre for Ore Deposit Research University of Tasmania, 275 p.

Gill, J., Hoernle, K., Todd, E., Hauff, F., Werner, R., Timm, C., Garbe-Schönberg, D., and Gutjahr, M., 2021, Basalt geochemistry and mantle flow during early backarc basin evolution: Havre trough and Kermadec arc, southwest Pacific: Geochemistry, Geophysics, Geosystems, v. 22, article e2020GC009339.

Gill, J.B., 1981, Orogenic andesites and plate tectonics: Berlin, Germany, Springer-Verlag, 392 p.

Goto, Y., and McPhie, J., 1998, Endogenous growth of a Miocene submarine dacite cryptodome, Rebun Island, Hokkaido, Japan: Journal of Volcanology and Geothermal Research, v. 84, p. 273–286.

Gray, J.N., and Cunningham-Dunlop, I.R., 2018, Updated resource estimate to include the AG zone resource estimate for the Palmer exploration project, Porcupine Mining District, Southeast Alaska, USA: NI 43-101 Report. December 18, 2018, 233 p.

Green, D., 2001, Geology of volcanogenic massive sulphide prospects of the Palmer property, Haines area, southeastern Alaska: M.Sc. thesis, Ottawa, Canada, Carleton University: 255 p.

Green, D., MacVeigh, J.G., Palmer, M., Watkinson, D.H., and Orchard, M.J., 2003, Stratigraphy and geochemistry of the RW Zone, a new discovery at the Glacier Creek VMS prospect, Palmer property, Porcupine Mining District, southeastern Alaska: Division of Geological & Geophysical Surveys Professional Report 120, p. 35–51.

Green, T.H., 1995, Significance of Nb/Ta as an indicator of geochemical processes in the crust-mantle system: Chemical Geology, v. 120, p. 347–359.

Greene, A.R., Scoates, J.S., and Weis, D., 2008, Wrangellia flood basalts in Alaska: A record of plume-lithosphere interaction in a Late Triassic accreted oceanic plateau: Geochemistry, Geophysics, Geosystems, v. 9, article Q12004.

Greene, A.R., Scoates, J.S., Weis, D., Nixon, G.T., and Kieffer, B., 2009, Melting history and magmatic evolution of basalts and picrites from the accreted Wrangellia oceanic plateau, Vancouver Island, Canada: Journal of Petrology, v. 50, p. 467–505.

Greene, A. R., Scoates, J. S., Weis, D., Katvala, E. C., Israel, S., and Nixon, G. T., 2010, The architecture of oceanic plateaus revealed by the volcanic stratigraphy of the accreted Wrangellia oceanic plateau: Geosphere, v. 6, p. 47–73.

Grove, T.L., and Brown, S.M., 2018, Magmatic processes leading to compositional diversity in igneous rocks: Bowen (1928) revisited: American Journal of Science, v. 318, p. 1–28.

Haase, K.M., Krumm, S., Regelous, M., and Joachimski, M., 2011, Oxygen isotope evidence for the formation of silicic Kermadec island arc and Havre-Lau backarc magmas by fractional crystallisation: Earth and Planetary Science Letters, v. 309, p. 348–355.

Hall, R., 2002, Cenozoic geological and plate tectonic evolution of SE Asia and the SW Pacific: computer-based reconstructions, model and animations: Journal of Asian Earth Sciences, v. 20, p. 353–431.

Hampton, M.A., Lee, H.J., and Locat, J., 1996, Submarine landslides: Journal of Geophysical Research, v. 34, p. 33–59.

Hannington, M.D., De Ronde, C.E.J., and Petersen, S., 2005, Sea-floor tectonics and submarine hydrothermal systems: Economic Geology, 100th Anniversary Volume, p. 111–141.

Haraguchi, S., Kimura, J.I., Senda, R., Fujinaga, K., Nakamura, K., Takaya, Y., and Ishii, T., 2017, Origin of felsic volcanism in the Izu arc intra-arc rift: Contributions to Mineralogy and Petrology, v. 172, doi: 10.1007/s00410-017-1345-1.

Hart, T.R., Gibson, H.L., and Lesher, C.M., 2004, Trace element geochemistry and petrogenesis of felsic volcanic rocks associated with volcanogenic massive Cu-Zn-Pb sulfide deposits: Economic Geology, v. 99, p. 1003–1013.

Hastie, A.R., and Kerr, A.C., 2010, Mantle plume or slab window?: physical and geochemical constraints on the origin of the Caribbean oceanic plateau: Earth-Science Reviews, v. 98, p. 283–293.

Hathway, B., Hudak, G., and Hamilton, M.A., 2008, Geologic setting of volcanic-associated massive sulfide deposits in the Kamiskotia area, Abitibi subprovince, Canada: Economic Geology, v. 103, p. 1185–1202.

Hawkins, J. W., 2003, Geology of supra-subduction zones – implciations for the origin of ophiolites: Geological Society of America, Special Paper 373, p. 227–268.

Head, J.W., and Wilson, L., 2003, Deep submarine pyroclastic eruptions: theory and predicted landforms and deposits: Journal of Volcanology and Geothermal Research, v. 121, p. 155–193.

Hochstaedter, A.G., Gill, J.B., and Morris, J.D., 1990, Volcanism in the Sumisu rift, II. Subduction and non-subduction related components: Earth and Planetary Science Letters, v. 100, p. 195–209.

Hudson, T., Plafker, G., and Dixon, K., 1982, Horizontal offset history of the Chatham Strait fault: U.S. Geological Survey Circular 844, p. 128–131.

Hughes, A., Escartín, J., Olive, J.A., Billant, J., Deplus, C., Feuillet, N., Leclerc, F., and Malatesta, L., 2021, Quantification of gravitational mass wasting and controls on submarine scarp morphology along the Roseau fault, Lesser Antilles: Journal of Geophysical Research, v. 126, article e2020JF005892.

Humphris, S.E., 1984, The mobility of the rare earth elements in the crust: Rare Earth Element Geochemistry, Amsterdam, Netherlands, Elsevier, v. 2, p. 317–342.

Huppert, H.E., and Sparks, R.S.J., 1988, The generation of granitic magmas by intrusion of basalt into continental crust: Journal of Petrology, v. 29, p. 599–624.

Irvine, T.N., and Baragar, W.R.A., 1971, A guide to the chemical classification of the common volcanic rocks: Canadian Journal of Earth Sciences, v. 8, p. 523–548.

Israel, S., Beranek, L., Friedman, R.M., and Crowley, J.L., 2014, New ties between the Alexander terrane and Wrangellia and implications for North America Cordilleran evolution: Lithosphere, v. 6, p. 270–276.

Jenner, G., 1996, Trace element geochemistry of igneous rocks: geochemical nomenclature and analytical geochemistry: Geological Association of Canada, Short Course Notes, v. 12, p. 51–77.

Jensen, L.S., 1976, A new cation plot for classifying subalkalic volcanic rocks: Ontario Division of Mines, Miscellaneous Paper 66, 22 p.

Juster, T.C., Grove, T.L., and Perfit, M.R., 1989, Experimental constraints on the generation of FeTi basalts, andesites, and rhyodacites at the Galapagos Spreading Center, 85°W and 95°W: Journal of Geophysical Research, v. 94, p. 9251–9274.

Karl, B.S.M., Haeussler, P.J., and Mccafferty, A., 1999, Reconnaissance geologic map of the Duncan Canal-Zarembo Island area, southeastern Alaska: U.S. Geological Survey Open-File Report 99-168, 1 pamphlet, 29 p.

Karl, S., Steeves, N., Quinn, K., Proffett, J., O'Sullivan, P.B., McMillan, J., and Jones, J. V, 2020, Lower Jurassic volcanic and sedimentary rocks depositionally overlie Upper Triassic host rocks at the Palmer VMS property in the Alexander Triassic metallogenic belt, southeast Alaska: Geological Society of America, Abstracts with Programs, v. 52, doi: 10.1130/abs/2020AM-357716.

Kelemen, P.B., Shimizu, N., and Dunn, T., 1993, Relative depletion of niobium in some arc magmas and the continental crust: partitioning of K, Nb, La and Ce during melt/rock reaction in the upper mantle: Earth and Planetary Science Letters, v. 120, p. 111–134.

Kent, A.J.R., Peate, D.W., Newman, S., Stolper, E.M., and Pearce, J.A., 2002, Chlorine in submarine glasses from the Lau Basin: seawater contamination and constraints on the composition of slab-derived fluids: Earth and Planetary Science Letters, v. 202, p. 361–377.

Kerrich, R., and Wyman, D.A., 1996, The trace element systematics of igneous rocks in mineral exploration: an overview: Geological Association of Canada, Short Course Notes, v. 12, p.

1–50.

Kerrich, R., Polat, A., and Xie, Q., 2008, Geochemical systematics of 2.7 Ga Kinojevis Group (Abitibi), and Manitouwadge and Winston Lake (Wawa) Fe-rich basalt-rhyolite associations: backarc rift oceanic crust? Lithos, v. 101, p. 1–23.

Koepke, J., Berndt, J., Feig, S.T., and Holtz, F., 2007, The formation of SiO_2-rich melts within the deep oceanic crust by hydrous partial melting of gabbros: Contributions to Mineralogy and Petrology, v. 153, p. 67–84.

Koepke, J., Botcharnikov, R.E., and Natland, J.H., 2018, Crystallization of late-stage MORB under varying water activities and redox conditions: implications for the formation of highly evolved lavas and oxide gabbro in the ocean crust: Lithos, v. 323, p. 58–77.

Kondo, H., Shuto, K., and Fukase, M., 2000, An AFC (assimilation and fractional crystallization) process as the petrogenesis of andesites from the Pliocene Myojin-iwa Formation, the back-arc side of the northeast Japan: combined major-and trace-element and Sr-Nd isotope constraints: The Journal of the Geological Society of Japan, v. 106, p. 426–441.

Laflèche, M.R., Dupuy, C., and Bougault, H., 1992a, Geochemistry and petrogenesis of Archean mafic volcanic rocks of the southern Abitibi belt, Québec: Precambrian Research, v. 57, p. 207–241.

Laflèche, M.R., Dupuy, C., and Dostal, J., 1992b, Tholeiitic volcanic rocks of the late Archean Blake River Group, southern Abitibi greenstone belt: origin and geodynamic implications: Canadian Journal of Earth Sciences, v. 29, p. 1448–1458.

Lafrance, B., Gibson, H.L., and Stewart, M.S., 2020, Internal and external deformation and modification of volcanogenic massive sulfide deposits: Reviews in Economic Geology, v. 21, p. 147–171.

Large, R.R., Gemmell, J.B., and Paulick, H., 2001, The alteration box plot: a simple approach to understanding the relationship between alteration mineralogy and lithogeochemistry associated with volcanic-hosted massive sulfide deposits: Economic Geology, v. 96, p. 957–971.

Lassiter, J.C., Depaolo, D.J., and Mahoney, J.J., 1995, Geochemistry of the Wrangellia flood basalt province: implications for the role of continental and oceanic lithosphere in flood basalt genesis: Journal of Petrology, v. 36, p. 983–1009.

Leat, P.T., Jackson, S.E., Thorpe, R.S., and Stillman, C.J., 1986, Geochemistry of bimodal basalt-subalkaline/peralkaline rhyolite provinces within the southern British Caledonides: Journal of the Geological Society, v. 143, p. 259–273.

Leeman, W.P., and Smith, D.R., 2018, The role of magma mixing, identification of mafic magma inputs, and structure of the underlying magmatic system at Mount St. Helens: American Mineralogist, v. 103, p. 1925–1944.

Lentz, D.R., 1998, Petrogenetic evolution of felsic volcanic sequences associated with Phanerozoic volcanic-hosted massive sulphide systems: the role of extensional geodynamics: Ore Geology Reviews, v. 12, p. 289–327.

Lesher, C.M., Goodwin, A.M., Campbell, I.H., and Gorton, M.P., 1986, Trace-element geochemistry of ore-associated and barren, felsic metavolcanic rocks in the Superior Province, Canada: Canadian Journal of Earth Sciences, v. 23, p. 222–237.

Lewis, P., 1998, Palmer Project preliminary field report: structural and stratigraphic setting of mineral occurrences, Glacier and Jarvis Creek area, Haines, Alaska: Unpublished consulting report for Rubicon Minerals Corporation, 11 p.

Liaghat, S., and MacLean, H., 1995, Lithogeochemistry of altered rocks at the New Insco VMS deposit, Noranda, Quebec: Journal of Geochemical Exploration, v. 52, p. 333–350.

Linnen, R.L., and Keppler, H., 2002, Melt composition control of Zr/Hf fractionation in magmatic processes: Geochimica et Cosmochimica Acta, v. 66, p. 3293–3301.

Liu, L., and Lowell, R.P., 2011, Modeling heat transfer from a convecting, crystallizing, replenished silicic magma chamber at an oceanic spreading center: Geochemistry, Geophysics, Geosystems, v. 12, article Q09010.

Lofgren, G., 1974, An experimental study of plagioclase crystal morphology; isothermal crystallization: American Journal of Science, v. 274, p. 243–273.

Loney, R.A., 1964, Stratigraphy and petrography of the Pybus-Gambier area, Admiralty Island, Alaska: U.S. Geological Survey Bulletin 1178, 2 sheets, scale 1:63,360, 103 p.

Lupton, J., Rubin, K.H., Arculus, R., Lilley, M., Butterfield, D., Resing, J., Baker, E., and Embley, R., 2015, Helium isotope, C/^{3}He, and Ba-Nb-Ti signatures in the northern Lau Basin: Distinguishing arc, back-arc, and hotspot affinities: Geochemistry, Geophysics, Geosystems, v. 16, p. 1133–1155.

Lupton, J.E., Arculus, R.J., Greene, R.R., Evans, L.J., and Goddard, C.I., 2009, Helium isotope variations in seafloor basalts from the northwest Lau backarc basin: Mapping the influence of the Samoan hotspot: American Geophysical Union, Geophysical Research Letters, v. 36, article L17313.

Lupton, J.E., Arculus, R.J., Evans, L.J., and Graham, D.W., 2012, Mantle hotspot neon in basalts from the northwest Lau back-arc basin: Geophysical Research Letters, v. 39, article L08308.

Lydon, J.W., 1988, Volcanogenic massive sulphide deposits Part 2: genetic models: Geoscience Canada, v. 15, p. 43–65.

Ma, Y., Zeng, Z., Chen, S., Yin, X., and Wang, X., 2017, Origin of the volcanic rocks erupted in the eastern Manus basin: basaltic andesite-andesite-dacite associations: Journal of Oceanic and Coastal Sea Research, University of China, v. 16, p. 389–402.

Macintyre, D.G., and Schroeter, T.G., 1985, Mineral occurrences in the Mount Henry Clay area: British Columbia Ministry of Energy, Mines and Petroleum Resources, Geological Fieldwork Paper 1985-1, p. 365–379.

MacIntyre, D.G., Mihalynuk, M.G., Smith, M.T., Schiarizza, P., and Deschênes, M. Timmerman, J., 1992, Tats Lake map area geology: Northwest Tatshenshini River map area, northwestern British Columbia: British Columbia Ministry of Energy, Mines and Petroleum Resources, Open File 1993-13, 6 sheets.

MacKevett Jr., E.M., Robertson, E.C., and Winkler, G.R., 1974, Geology of the Skagway B-3 and B-4 quadrangles, southeastern Alaska: U.S. Geological Survey Professional Paper 832, 33 p.

Maclean, W., and Barrett, T., 1993, Lithogeochemical techniques using immobile elements: Journal Of Geochemical Exploration, v. 48, p. 109–133.

MacLean, W., 1990, Mass change calculations in altered rock series: Mineralium Deposita, v. 25, p. 44–49.

MacLean, W.H., 1988, Rare earth element mobility at constant inter-REE ratios in the alteration zone at the Phelps Dodge massive sulphide deposit, Matagami, Quebec: Mineralium Deposita, v. 23, p. 38.

MacLean, W.H., and Kranidiotis, P., 1987, Alteration: Phelps Dodge massive sulfide deposit, Matagami, Quebec: Economic Geology, v. 82, p. 1898–1911.

Maclennan, J., Hulme, T., and Singh, S.C., 2005, Cooling of the lower oceanic crust: Geology, v. 33, p. 357–360.

Le Maitre, R.W., 2002, Igneous rocks: A classification and glossary of terms: International Union of Geological Sciences Subcommission on the Systematics of Igneous Rocks, Cambridge, England, Cambridge University Press, p. 33–38.

Marty, B., Sano, Y., and France-Lanord, C., 2001, Water-saturated oceanic lavas from the Manus basin: volatile behaviour during assimilation-fractional crystallisation-degassing (AFCD): Journal of Volcanology and Geothermal Research, v. 108, p. 1–10.

Mathieu, L., 2018, Quantifying hydrothermal alteration: a review of methods: Geosciences, v. 8, doi: 10.3390/geosciences8070245.

Mattinson, J.M., 2005, Zircon U-Pb chemical abrasion (“CA-TIMS”) method: combined annealing and multi-step partial dissolution analysis for improved precision and accuracy of zircon ages: Chemical Geology, v. 220, p. 47–66.

Mcdonough, W.F., and Sun, S.S., 1995, The composition of the Earth: Chemical Geology, v. 120, p. 223–253.

McLennan, S.M., and Taylor, S.R., 2012, Geology, geochemistry and natural abundances: Encyclopedia of Inorganic and Bioinorganic Chemistry, Hoboken, USA, John Wiley & Sons, Ltd., doi: 10.1002/9781119951438.eibc2004.

McNicoll, V., Goutier, J., Dubé, B., Mercier-Langevin, P., Ross, P.S., Dion, C., Monecke, T., Legault, M., Percival, J., and Gibson, H., 2014, U-Pb geochronology of the Blake River Group, Abitibi greenstone belt, Quebec, and implications for base metal exploration: Economic Geology, v. 109, p. 27–59.

McPhie, J., Doyle, M., and Allen, R.L., 1993, Volcanic textures: a guide to the interpretation of textures in volcanic rocks: Hobart, Australia, Centre for Ore Deposit Research University of Tasmania, 198 p.

Millen, D.W., and Hamburger, M.W., 1998, Seismological evidence for tearing of the Pacific plate at the northern termination of the Tonga subduction zone: Geology, v. 26, p. 659–662.

Muffler, L.P., 1967, Stratigraphy of the Keku Islets and neighboring parts of Kuiu and Kupreanof Islands, southeastern Alaska: U.S. Geological Survey Bulletin 1241–C, 1 pl., scale 1:63,360, 52 p.

Nakamura, N., 1974, Determination of REE, Ba, Fe, Mg, Na and K in carbonaceous and ordinary chondrites: Geochimica et Cosmochimica Acta, v. 38, p. 757–775.

Nelson, J., 1998, The quiet counter-revolution: structural control of syngenetic deposits: Geoscience Canada, v. 24, p. 91–98.

Nelson, J.L., Colpron, M., and Israel, S., 2013, The Cordillera of British Columbia, Yukon, and Alaska: tectonics and metallogeny: Society of Economic Geologists, Special Publication, v. 17, p. 53–109.

Niu, Y., Collerson, K.D., Batiza, R., Wendt, J.I., and Regelous, M., 1999, Origin of enriched-type mid-ocean ridge basalt at ridges far from mantle plumes: the East Pacific Rise at 11°20′N: Journal of Geophysical Research, v. 104, p. 7067–7087.

O'Neill, H.S.C., and Jenner, F.E., 2012, The global pattern of trace-element distributions in ocean floor basalts: Nature, v. 491, p. 698–704.

Ordóñez-Calderón, J.C., Lafrance, B., Gibson, H.L., Schwartz, T., Pehrsson, S.J., and Rayner, N.M., 2016, Petrogenesis and geodynamic evolution of the Paleoproterozoic (∼1878 Ma) Trout Lake volcanogenic massive sulfide deposit, Flin Flon, Manitoba, Canada: Economic Geology, v. 111, p. 817–847.

Palme, H., and O'Neill, H., 2014, Cosmochemical estimates of mantle composition: Treatise on Geochemistry 2, Oxford, England, Elsevier, v. 3, p. 1–39.

Peacock, M.A., 1931, Classification of igneous rock series: The Journal of Geology, v. 39, p. 54–67.

Pearce, J., 1996, A user's guide to basalt discrimination diagrams: Geological Association of Canada, Short Course Notes, v. 12, p. 79–113.

Pearce, J.A., 2008, Geochemical fingerprinting of oceanic basalts with applications to ophiolite classification and the search for Archean oceanic crust: Lithos, v. 100, p. 14–48.

Pearce, J.A., 2014, Immobile element fingerprinting of ophiolites: Elements, v. 10, p. 101–108.

Pearce, J.A., and Cann, J.R., 1973, Tectonic setting of basic volcanic rocks determined using trace element analyses: Earth and Planetary Science Letters, v. 19, p. 290–300.

Pearce, J.A., and Peate, D.W., 1995, Tectonic implications of the composition of volcanic arc magmas: Annual Review of Earth and Planetary Sciences, v. 23, p. 251–285.

Pearce, J.A., and Stern, R.J., 2006, Origin of back-arc basin magmas: trace element and isotope perspectives: Geophysical Monograph Series, v. 166, p. 63–86.

Pearce, J.A., Harris, N.B.W., and Tindle, A.G., 1984, Trace element discrimination diagrams for the tectonic interpretation of granitic rocks: Journal of Petrology, v. 25, p. 956–983.

Pearce, J.A., Ernewein, M., Bloomer, S.H., Parson, L.M., Murton, B.J., and Johnson, L.E., 1994, Geochemistry of Lau basin volcanic rocks: influence of ridge segmentation and arc proximity: Geological Society of London, Special Publications, v. 81, p. 53–75.

Peccerillo, A., and Taylor, S.R., 1976, Geochemistry of Eocene calc-alkaline volcanic rocks from the Kastamonu area, northern Turkey: Contributions to Mineralogy and Petrology, v. 58, p. 63–81.

Perfit, M.R., Ridley, I., and Jonasson, I.R., 1999, Geologic, petrologic and geochemical relationships between magmatism and massive sulfide mineralization along the eastern Galapagos spreading center: Reviews in Economic Geology, v. 8, p. 75–100.

Peter, J.M., and Scott, S.D., 1997, Windy Craggy, northwestern British Columbia: the world's largest Besshi-type deposit: Reviews in Economic Geology, v. 8, p. 261–296.

Peter, J.M., Leybourne, M.I., Scott, S.D., and Gorton, M.P., 2014, Geochemical constraints on the tectonic setting of basaltic host rocks to the Windy Craggy Cu-Co- Au massive sulphide deposit, northwestern British Columbia: International Geology Review, v. 56, p. 1484–1503.

Philpotts, A.R., 1977, Archean variolites - quenched immiscible liquids: discussion: Canadian Journal of Earth Sciences, v. 14, p. 139–144.

Piercey, S.J., 2010, An overview of petrochemistry in the regional exploration for volcanogenic massive sulphide (VMS) deposits: Geochemistry: Exploration, Environment, Analysis, v. 10, p. 1–18.

Piercey, S.J., 2011, The setting, style, and role of magmatism in the formation of volcanogenic massive sulfide deposits: Mineralium Deposita, v. 46, p. 449–471.

Piercey, S.J., 2015, A semipermeable interface model for the genesis of subseafloor replacement-type volcanogenic massive sulfide (VMS) deposits: Economic Geology, Special Publication, v. 110, p. 1655–1660.

Piercey, S.J., Road, R.L., Nelson, J.L., Colpron, M., Dusel-bacon, C., and Roots, C.F., 2006, Paleozoic magmatism and crustal recycling along the ancient Pacific margin of North America, northern Cordillera: Geological Association of Canada Special Paper, v. 45, p. 281–322.

Plafker, G., and Berg, H.C., 1994, Overview of the geology and tectonic evolution of Alaska: Geological Society of America, v. G-1, p. 989–1021.

Polat, A., and Hofmann, A.W., 2003, Alteration and geochemical patterns in the 3.7-3.8 Ga Isua greenstone belt, west Greenland: Precambrian Research, v. 126, p. 197–218.

Premo, W.R., Taylor, C.D., Snee, L.W., and Harris, A.G., 2010, Microfossil and radioisotopic geochronological studies of the Greens Creek host rocks: U.S. Geological Survey Professional Paper 1763, p. 287–333.

Price, A., Jackson, M.G., Blichert-Toft, J., Hall, P.S., Sinton, J.M., Kurz, M.D., and Blusztajn, J., 2014, Evidence for a broadly distributed Samoan-plume signature in the northern Lau and North Fiji Basins: Geochemistry, Geophysics, Geosystems, v. 15, p. 986–1008.

Proffett, J., 2019, Results of geological mapping at the Palmer Project, Alaska: Unpublished consulting report for Constantine Metal Resources Ltd., 2 sheets, map scale 1:2,000, 24 p.

Redman, E.C., Gilbert, W.G., Jones, B.K., Rosenkrans, D.S., and Hickok, B.D., 1985, Preliminary bedrock-geologic map of the Skagway B-4 Quadrangle, Alaska: Alaska Division of Geological and Geophysical Surveys Report of Investigations 85–6, 1 sheet, scale 1:40,000.

Regelous, M., Turner, S., Falloon, T.J., Taylor, P., Gamble, J., and Green, T., 2008, Mantle dynamics and mantle melting beneath Niuafo'ou Island and the northern Lau back-arc basin: Contributions to Mineralogy and Petrology, v. 156, p. 103–118.

Rollinson, H.R., 1993, Using geochemical data: evaluation, presentation, interpretation: Harlow, England, Longman, 352 p.

Rollinson, H.R., and Pease, V., 2021, Using geochemical data to understand geological processes: Cambridge, England, Cambridge University Press, 346 p.

de Ronde, C.E.J., Baker, E.T., Massoth, G.J., Lupton, J.E., Wright, I.C., Sparks, R.J., Bannister, S.C., Reyners, M.E., Walker, S.L., Greene, R.R., Ishibashi, J., Faure, K., Resing, J.A., and Lebon, G.T., 2007, Submarine hydrothermal activity along the mid-Kermadec arc, New Zealand: large-scale effects on venting: Geochemistry, Geophysics, Geosystems, v. 8, article Q07007.

Ross, P.S., and Bédard, J.H., 2009, Magmatic affinity of modern and ancient subalkaline volcanic rocks determined from trace-element discriminant diagrams: Canadian Journal of Earth Sciences, v. 46, p. 823–839.

Ross, P.S., Goutier, J., Mercier-Langevin, P., and Dubé, B., 2011, Basaltic to andesitic volcaniclastic rocks in the Blake River Group, Abitibi greenstone belt: 1. Mode of emplacement in three areas: Canadian Journal of Earth Sciences, v. 48, p. 728–756.

Rubin, J.N., Henry, C.D., and Price, J.G., 1993, The mobility of zirconium and other "immobile" elements during hydrothermal alteration: Chemical Geology, v. 110, p. 29–47.

Rudnick, R.L., and Gao, S., 2014, Composition of the continental crust: Treatise on Geochemistry 2, Oxford, England, Elsevier, v. 4, p. 1–51.

Sack, P., 2009, Characterization of footwall lithologies to the Greens Creek volcanic-hosted massive sulfide (VHMS) deposit , Alaska, USA: Ph.D. thesis, Hobart, Australia, University of Tasmania: 415 p.

Sack, P.J., Berry, R.F., Meffre, S., Falloon, T.J., Gemmell, J.B., and Friedman, R.M., 2011, In situ location and U-Pb dating of small zircon grains in igneous rocks using laser ablation-inductively coupled plasma-quadrupole mass spectrometry: Geochemistry, Geophysics, Geosystems, v. 12, article Q0AA14.

Sack, P.J., Berry, R.F., Gemmell, J.B., Meffre, S., and West, A., 2016, U-Pb zircon geochronology from the Alexander terrane, southeast Alaska: implications for the Greens Creek massive sulphide deposit: Canadian Journal of Earth Sciences, v. 53, p. 1458–1475.

Saleeby, J.B., 1983, Accretionary tectonics of the north American Cordillera: Annual Review of Earth and Planetary Sciences, v. 2, p. 45–73.

Samson, S.D., and Patchett, P.J., 1991, The Canadian Cordillera as a modern analogue of Proterozoic crustal growth: Australian Journal of Earth Sciences, v. 38, p. 595–611.

Saunders, A.D., Tarney, J., and Weaver, S.D., 1980, Transverse geochemical variations across the Antarctic peninsula: implications for the genesis of calc-alkaline magmas: Earth and Planetary Science Letters, v. 46, p. 344–360.

Shervais, J.W., 1982, Ti-V plots and the petrogenesis of modern and ophiolitic lavas: Earth and Planetary Science Letters, v. 59, p. 101–118.

Shervais, J.W., 2022, The petrogenesis of modern and ophiolitic lavas reconsidered: Ti-V and Nb-Th: Geoscience Frontiers, v. 13, article 101319.

Shukuno, H., Tamura, Y., Tani, K., Chang, Q., Suzuki, T., and Fiske, R.S., 2006, Origin of silicic magmas and the compositional gap at Sumisu submarine caldera, Izu-Bonin arc, Japan: Journal of Volcanology and Geothermal Research, v. 156, p. 187–216.

Sillitoe, R.H., 1982, Extensional habitats of rhyolite-hosted massive sulfide deposits: Geology, v. 10, p. 403–407.

Sinton, J.M., Wilson, D.S., Christie, D.M., Hey, R.N., and Delaney, J.R., 1983, Petrologic consequences of rift propagation on oceanic spreading ridges: Earth and Planetary Science Letters, v. 62, p. 193–207.

Sinton, J.M., Price, R.C., Johnson, K.T.M., Staudigel, H., and Zindler, A., 1993, Petrology and geochemistry of submarine lavas from the Lau and north Fiji back-arc basins: Circum-Pacific Council for Energy and Mineral Resources, Earth Science Series, v. 15, p. 119–135.

Sinton, J.M., Ford, L.L., Chappell, B., and McCulloch, M.T., 2003, Magma genesis and mantle heterogeneity in the Manus back-arc basin, Papua New Guinea: Journal of Petrology, v. 44, p. 159–195.

Sparks, S.R.J., Sigurdsson, H., and Wilson, L., 1977, Magma mixing: a mechanism for triggering acid explosive eruptions: Nature, v. 267, p. 315–318.

Spitz, G., and Darling, R., 1978, Major and minor element lithogeochemical anomalies surrounding the Louvem copper deposit, Val d'Or, Quebec: Canadian Journal of Earth Sciences, v. 15, p. 1161–1169.

Spry, P.G., Peter, J.M., and Slack, J.F., 2000, Meta-exhalites as exploration guides to ore: Reviews in Economic Geology, v. 11, p. 163–201.

Steeves, N.J., 2018, Mineralization and genesis of the Greens Creek volcanogenic massive sulfide (VMS) deposit, Alaska, USA: Ph.D. thesis, Hobart, Australia, University of Tasmania: 416 p.

Steeves, N.J., Hannington, M.D., Gemmell, J.B., Green, D., and Mcveigh, G., 2016, The Glacier Creek Cu-Zn VMS deposit, southeast Alaska: an addition to the Alexander Triassic metallogenic belt: Economic Geology, v. 111, p. 151–178.

Stern, R.J., 2004, Subduction initiation: spontaneous and induced: Earth and Planetary Science Letters, v. 226, p. 275–292.

Stern, R.J., 2010, The anatomy and ontogeny of modern intra-oceanic arc systems: Geological Society of London, Special Publications, v. 338, p. 7–34.

Stern, R.J., Lin, P.-N., Morris, J.D., Jackson, M.C., Fryer, P., Bloomer, S.H., and Ito, E., 1990, Enriched back-arc basin basalts from the northern Mariana trough: implications for the magmatic evolution of back-arc basins: Earth and Planetary Science Letters, v. 100, p. 210–225.

Still, J.C., 1991, Mineral investigations in the Juneau mining district, Alaska, 1984-1988: U.S. Bureau of Mines Special Publication, v. 2A, 9 sheets, 214p.

Sun, S.S., and McDonough, W.F., 1989, Chemical and isotopic systematics of oceanic basalts: implications for mantle composition and processes: Geological Society of London, Special Publications, v. 42, p. 313–345.

Syme, E.C., Lucas, S.B., Bailes, A.H., and Stern, R.A., 2000, Contrasting arc and MORB-like assemblages in the Paleoproterozoic Flin Flon belt, Manitoba, and the role of intra-arc extension in localizing volcanic-hosted massive sulphide deposits: Canadian Journal of Earth Sciences, v. 36, p. 1767–1788.

Taylor, C.D., Premo, W.R., Meier, A.L., and Taggart, J.E.J., 2008, The metallogeny of Late Triassic rifting of the Alexander terrane in southeastern Alaska and northwestern British Columbia: Economic Geology, v. 103, p. 89–115.

Taylor, C.D., Philpotts, J., Premo, W.R., Meier, A.L., and Taggart, J.E., 2010, The Late Triassic metallogenic setting of the Greens Creek massive sulfide deposit in southeastern Alaska: U.S. Geological Survey Professional Paper 1763, p. 13–59.

Timm, C., Davy, B., Haase, K., Hoernle, K.A., Graham, I.J., De Ronde, C.E.J., Woodhead, J., Bassett, D., Hauff, F., Mortimer, N., Seebeck, H.C., Wysoczanski, R.J., Caratori-Tontini, F., and Gamble, J.A., 2014, Subduction of the oceanic Hikurangi plateau and its impact on the Kermadec arc: Nature Communications, v. 5, article 4923.

Vermeesch, P., 2006, Tectonic discrimination diagrams revisited: Geochemistry, Geophysics, Geosystems, v. 7, article Q06017.

Walker, J.D., Geissman, J.W., Bowring, S.A., and Babcock, L.E., compilers, 2018,

Geologic Time Scale v. 5.0: Geological Society of America.

Wanless, V.D., Perfit, M.R., Ridley, W.I., and Klein, E., 2010, Dacite petrogenesis on mid-ocean ridges: evidence for oceanic crustal melting and assimilation: Journal of Petrology, v. 51, p. 2377–2410.

White, J.D.L., and Houghton, B.F., 2006, Primary volcaniclastic rocks: Geology, v. 34, p. 677–680.

Wilson, F.H., Hults, C.P., Mull, C.G., and Karl, S.M., 2015, Geologic map of Alaska: U.S. Geological Survey Scientific Investigations map 3340, 2 sheets, geodatabase, 1 pamphlet, 196 p.

Winchester, J.A., and Floyd, P.A., 1977, Geochemical discrimination of different magma series and their differentiation products using immobile elements: Chemical Geology, v. 20, p. 325–343.

Wood, D.A., 1980, The application of a Th–Hf–Ta diagram to problems of tectonomagmatic classification and to establishing the nature of crustal contamination of basaltic lavas of the British Tertiary Volcanic Province: Earth and Planetary Science Letters, v. 50, p. 11–30.

Wyman, D.A., 2003, Upper mantle processes beneath the 2.7 Ga Abitibi belt, Canada: a trace element perspective: Precambrian Research, v. 127, p. 143–165.

Chapter 2 Tables

Table 2.1 Summary of criteria used to select the least altered samples.

Alteration test	Least altered sample criteria	Rationale	Reference
Visual Assessment	Absence of abundant hydrothermal minerals (sulphides, brt, qz, sericite, chl, carbonate, and ep). Absence of abundant contact metamorphism minerals (bt, grt, chl and ep).	Fresh volcanic rocks are not hydrothermally altered and haven't undergone contact metamorphism.	Barrett and Maclean (1994)
Na_2O (wt %)	1.5 to 5	Na_2O wt % for average fresh volcanic rocks from basaltic to rhyolitic compositions varies from 2.56% to 3.87%. Na-depletion is characteristic of sericite- or chlorite-alteration.	Mathieu (2018)
Al_2O_3 (wt %)	> 10	Al_2O_3 wt % for average, fresh volcanic rocks from basaltic to rhyolitic compositions varies from 13.24% to 16.67%	Mathieu (2018)
Al_2O_3/Na_2O	< 10	Monitors Na-depletion caused by feldspar destruction while Al is conserved. Ideal for samples containing plagioclase. Felsdspars break down into sericite and quartz.	Spitz-Darling (1978)
Ishikawa alteration index (AI)	20 - 60	The principal rock-forming elements that are gained and lost during sericite and chlorite alteration (MgO, K_2O, Na_2O, CaO) define the AI.	Large et al. (2001)
Chlorite-carbonate-pyrite Index (CCPI)	15 - 85	The increase in MgO and FeO associated with chlorite, Mg-Fe-carbonate, pyrite, magnetite or hematite alteration defines the CCPI.	Large et al. (2001)
Loss on ignition (LOI)	< 7 %	LOI is a proxy for volatile phases such as H_2O, CO_2, sulfur oxides and fluorine. Altered rocks typically contain more volatile phases than fresh volcanic rocks. Many variables can impact LOI and its significance should be interpreted with caution.	Gifkins et al. (2005)
LREE signatures on multi-element normalized diagrams	Absence of extreme depletion in LREE compared to neighbouring HFSE	LREE can be mobile under high fluid to rock ratio, for example, in fluid upflow zones. U-shaped patterns signifying strong depletion compared to neighbouring elements.	Campbell et al. (1984)
Zn (ppm)	< 300		
Cu (ppm)	< 100		
Pb (ppm)	< 10	Enriched by hydrothermal fluids	
Ag (g/t)	< 0.5		
BaO (%)	< 0.2		
S (%)	< 0.75	High S in the presence of sulfides/sulfates	
C (%)	< 1.6	High C may be attributed to presence of CO_2 for example, in carbonate mineral.	
Total (%)	98-102	Analysis reliability indicator - major element oxides should total to about 100%	Rollinson and Pease (2021)

Table 2.2 Whole rock lithogeochemical data of twenty-two representative, least-altered samples of the eight geochemical volcanic units of the AG deposit.

	FeTi basalts					
	Hangingwall			Zone-equivalent		
Sample	S039241	W605535	W814293	S037015	W420988	W420983
Unit	HW-FeTiB	HW-FeTiB	HW-FeTiB	Z-FeTiB	Z-FeTiB	Z-FeTiB
Texture	Tuff	Lapilli tuff	Lapilli tuff	Pillowed, variolitic	Pillowed	Variolitic
Type	DDH	DDH	DDH	Outcrop	DDH	DDH
SiO_2 (wt %)	45.43	50.87	47.31	56.71	47.11	41.94
Al_2O_3	13.02	14.84	15.19	13.87	12.68	14.12
Fe_2O_3	17.36	20	17.04	13.05	22.19	15.82
TiO_2	2.38	2.61	2.68	3.16	2.78	3.06
MnO	0.1	0.01	0.14	0.11	0.08	0.21
MgO	5.07	2.19	5.53	3.14	3.31	3.7
CaO	4.35	0.61	4.74	3.12	3.45	7.42
K_2O	3.49	5.34	2.04	1.53	4.26	3.57
Na_2O	0.11	0.71	0.09	3.42	1.51	1.94
P_2O_5	0.25	0.2	0.28	0.64	0.4	1.07
BaO	0.13	0.05	0.2	0.06	0.06	0.07
Cr_2O_3	<0.01	<0.01	0.01	<0.01	<0.01	<0.01
SrO	0.02	0.01	0.04	0.04	0.03	0.03
S	0.04	<0.01	0.23	0.45	0.01	0.01
C	1.54	0.09	0.41	0.01	0.44	1.46
LOI	7.3	1.97	4.34	1.04	2.05	6.7
Total	99.26	99.52	100.45	101.2	100.05	99.81
Se (ppm)	0.5	<0.2	0.6	0.9	0.3	<0.2
Li	20	20	20	20	20	10
Sc	32	31	38	36	33	36
V	479	257	572	343	329	367
Cr	30	40	40	10	10	20
Co	29	36	55	35	21	31
Ni	21	25	34	11	12	11
Cu	11	<1	67	59	1	3
Zn	208	121	189	136	181	233
Ga	19.4	24.2	23.4	22.2	21.8	23.9
Ge	<5	<5	<5	<5	7	<5
As	26.9	3.9	7.5	0.6	1	1.3
Mo	<1	<1	1	3	1	1
Ag	<0.5	<0.5	<0.5	<0.5	<0.5	<0.5
Cd	0.7	<0.5	<0.5	<0.5	<0.5	<0.5
In	0.031	0.013	0.015	0.009	0.043	0.052
Sn	1	2	2	2	1	2
Sb	4.21	3.28	2.91	0.08	0.27	0.49
Te	<0.01	<0.01	0.02	0.04	<0.01	<0.01
W	2	1	1	<1	1	1
Re	<0.001	<0.001	0.002	0.004	<0.001	<0.001
Hg	0.012	<0.005	<0.005	0.006	<0.005	<0.005
Tl	4.51	1.5	1.81	0.25	0.47	0.22
Bi	0.02	0.02	0.02	0.05	0.01	0.02
Rb	100	170	40.7	36.5	138.5	96.7
Sr	185	100.5	353	375	269	281
Cs	3.09	5.24	1.09	1.1	4.78	2.43
Ba	1180	438	1735	488	631	652
Pb	<2	7	17	<2	7	<2
Th	1.73	2.11	2	2.06	2.16	2.38
U	1.74	0.23	2.65	1.64	0.86	1.77
Y	37.2	34.9	34.2	51.2	59.5	95.3
Zr	152	176	160	176	197	194
Nb	15.5	17.5	18.6	18.8	19.1	20.1
Hf	3.8	4.5	4.1	4.3	5	5.2
Ta	0.9	1	1.1	1.2	1	1.1
La	20.2	20	18.1	22.3	21.3	25.2
Ce	40.8	44.7	42.8	46.5	48.9	53.2
Pr	5.58	5.64	5.54	5.78	6.74	7.34
Nd	23.6	25.7	25.5	27.4	30.4	32.6
Sm	6.02	6.37	7	7.29	8.2	8.83
Eu	2.07	1.98	2.16	2.03	2.71	2.87
Gd	7.04	6.26	7.2	8.2	9.73	10.95
Tb	1.18	0.95	1.26	1.51	1.72	1.92
Dy	7.44	6.58	7.13	9.45	11.15	12.9
Ho	1.57	1.32	1.57	2.05	2.37	3.04
Er	4.48	3.78	4.22	5.66	6.46	8.64
Tm	0.61	0.51	0.63	0.82	0.97	1.37
Yb	4.06	3.5	4.18	5.7	6.12	8.54
Lu	0.58	0.51	0.65	0.83	0.99	1.42

	Ferro-basalts		Basalts		High-silica rhyolites (HSR)	
	Footwall		Footwall		Multiple stratigraphic levels	
Sample	W600902	W605561	W604981	W604985	W605034	W605521
Unit	FW-FeB	FW-FeB	FW-B	FW-B	HSR	HSR
Texture	Massive; feldspar-phyric	Massive; feldspar-phyric	Pillowed; hyaloclastic	Hyaloclastic	Massive	Massive
Type	Outcrop	DDH	DDH	DDH	DDH	DDH
SiO_2 (wt %)	47.66	48.71	53.84	51.59	71.26	75.06
Al_2O_3	13.29	14.28	14.36	14.84	14	12.08
Fe_2O_3	14.32	14.95	10.2	9.76	3.58	2.31
TiO_2	1.81	1.9	1.17	1.2	0.14	0.12
MnO	0.28	0.23	0.18	0.15	0.02	0.03
MgO	2.88	2.66	4.02	4.06	1.14	0.56
CaO	7.95	7.02	8.77	9.4	1.34	1.98
K_2O	0.22	0.28	1.83	2.18	3.3	2.69
Na_2O	4.24	4.46	2.5	3.01	2.26	2.27
P_2O_5	0.31	0.36	0.27	0.33	0.03	0.04
BaO	0.02	0.03	0.07	0.06	0.13	0.1
Cr_2O_3	<0.01	0.01	0.01	0.01	<0.01	<0.01
SrO	0.04	0.04	0.04	0.02	0.02	0.01
S	0.12	0.17	0.26	0.5	0.06	0.49
C	1.49	0.91	0.43	0.75	0.09	0.42
LOI	6.01	3.97	2.22	3.32	1.57	2.28
Total	99.44	99.5	100.3	101.25	99.02	100.45
Se (ppm)	0.2	0.5	0.7	0.5	0.5	0.2
Li	10	10	10	10	10	10
Sc	37	39	43	44	1	1
V	327	347	325	340	6	8
Cr	10	10	30	40	<10	<10
Co	40	45	25	55	1	2
Ni	8	8	13	29	<1	<1
Cu	30	36	31	61	5	6
Zn	170	158	110	132	73	33
Ga	18	18.5	16.9	17.2	35.6	32.2
Ge	<5	<5	<5	<5	<5	<5
As	2.8	1.6	2.2	5.6	0.4	1.2
Mo	2	11	1	2	1	1
Ag	<0.5	<0.5	<0.5	<0.5	<0.5	<0.5
Cd	0.5	<0.5	0.7	0.7	<0.5	<0.5
In	0.021	0.015	0.015	0.011	0.036	0.029
Sn	1	1	<1	<1	9	7
Sb	0.11	0.77	0.19	0.2	0.15	0.13
Te	<0.01	0.01	0.01	0.03	0.01	0.01
W	1	1	1	1	1	1
Re	0.001	0.003	<0.001	0.006	0.001	0.001
Hg	0.009	0.005	<0.005	<0.005	<0.005	0.011
Tl	0.04	0.03	0.72	0.83	0.3	0.04
Bi	0.01	<0.01	0.02	0.02	0.02	0.02
Rb	3.3	4.5	51	50	43.4	32.2
Sr	385	302	319	196.5	164.5	100.5
Cs	0.3	0.27	1.78	1.56	1.4	0.33
Ba	112	252	534	513	1325	932
Pb	3	2	8	4	7	8
Th	0.94	1.12	0.85	0.92	12.6	11.2
U	0.47	0.56	0.99	3.1	3.51	2.49
Y	36.5	40.3	26.4	29.4	180.5	108.5
Zr	111	125	69	74	378	271
Nb	9.3	11	8.8	9.2	77.1	64.5
Hf	3.2	3.4	1.7	1.9	13.4	11.2
Ta	0.5	0.7	0.6	0.5	4.4	3.8
La	10.5	12.6	9.6	10	91.8	97.8
Ce	23.8	27.1	19.5	21.6	193.5	202
Pr	3.35	3.77	2.5	2.76	24.5	24.3
Nd	15.7	18	11.4	13.5	95.6	98.9
Sm	4.62	5.15	3.09	3.56	22.5	22.3
Eu	1.41	1.74	1.03	1.06	3.93	3.64
Gd	5.37	6.48	4	4.64	25	22.4
Tb	1.11	1.21	0.81	0.83	4.59	3.5
Dy	6.6	7.15	5.01	5.27	30.6	22.1
Ho	1.41	1.62	0.98	1.13	7.67	4.39
Er	4.07	4.55	3.05	3.43	22.8	12.25
Tm	0.65	0.66	0.46	0.48	3.59	1.78
Yb	4.24	4.36	2.96	3.08	23.4	11.75
Lu	0.62	0.67	0.4	0.48	3.19	1.61

Ferro-andesites (FeA)

	Footwall					
Sample	W420955	W605563	W812314	W812316	W812317	W813093
Unit	FeA	FeA	FeA	FeA	FeA	FeA
Texture	Massive; sparse FP	Massive; sparse FP	Massive; sparse FP	Massive; sparse FP	Massive; sparse FP	Massive; sparse FP
Type	DDH	DDH	DDH	DDH	DDH	DDH
SiO_2 (wt %)	52.42	52.82	55.36	54.36	55.28	50.57
Al_2O_3	13.46	11.71	12.99	13.23	13.02	13.52
Fe_2O_3	16.79	12.69	14.27	14.65	14.52	15.29
TiO_2	1.74	1.51	1.62	1.64	1.73	1.66
MnO	0.25	0.15	0.14	0.23	0.14	0.17
MgO	4.72	3.42	5.43	4.23	4.67	5.03
CaO	2.98	7.35	3.04	4	3.1	5.26
K_2O	1.39	1.38	0.84	1.4	1.31	2
Na_2O	3.91	2.81	3.13	3.57	3.73	2.41
P_2O_5	0.55	0.57	0.53	0.55	0.52	0.53
BaO	0.04	0.06	0.04	0.04	0.04	0.05
Cr_2O_3	<0.01	<0.01	<0.01	<0.01	<0.01	<0.01
SrO	0.03	0.04	0.03	0.04	0.05	0.04
S	0.15	0.3	0.16	0.13	0.14	0.56
C	0.01	1.07	0.06	0.03	0.03	0.08
LOI	1.59	4.45	2.26	0.99	1.22	2.08
Total	100.35	99.75	100.2	99.36	99.79	100.3
Se (ppm)	0.3	0.7	0.6	1.6	0.5	0.5
Li	20	10	20	10	10	20
Sc	25	20	22	23	25	24
V	181	151	159	160	192	169
Cr	10	<10	10	10	10	10
Co	34	27	29	29	32	31
Ni	6	5	3	5	5	5
Cu	31	26	26	29	32	23
Zn	137	126	138	143	127	113
Ga	18.7	18.2	21.2	20.6	19.9	20.6
Ge	<5	<5	<5	<5	<5	<5
As	1.4	2.6	0.8	1.2	1	1.4
Mo	<1	1	<1	1	1	1
Ag	<0.5	<0.5	<0.5	<0.5	<0.5	<0.5
Cd	<0.5	<0.5	<0.5	0.7	0.6	0.8
In	0.02	0.009	0.021	0.032	0.03	0.009
Sn	2	2	2	2	2	2
Sb	0.16	0.13	0.18	0.24	0.21	0.17
Te	0.03	<0.01	0.01	0.03	0.02	0.03
W	1	1	1	1	1	1
Re	<0.001	0.002	0.001	0.001	0.001	0.005
Hg	<0.005	0.005	<0.005	<0.005	<0.005	<0.005
Tl	0.25	0.38	0.14	0.31	0.37	0.4
Bi	0.02	0.01	0.01	0.03	0.03	0.01
Rb	29.8	30.2	18.9	31.4	39.3	50
Sr	225	303	225	313	420	290
Cs	3.28	1.42	1.61	4.01	3.36	2.01
Ba	365	588	274	307	267	434
Pb	<2	5	5	6	8	3
Th	3.52	3.57	3.93	4.1	3.51	3.92
U	1.8	3.54	2.31	3.42	2	2.3
Y	52.3	53.8	54.3	55.7	57.3	54.8
Zr	220	238	263	253	216	261
Nb	14.3	15.2	16.2	20.1	16.1	16.4
Hf	5.5	5.6	6.4	6.3	5.1	6.2
Ta	0.7	0.9	1.1	1	0.9	1.1
La	20.9	26.9	23.3	24.4	22	21.7
Ce	43.7	51.3	49.8	52.5	47.2	47.6
Pr	5.69	6.41	6.14	6.43	5.97	6.38
Nd	24.6	27.3	28.3	29.6	26.9	27.5
Sm	6.25	7.36	6.92	7.73	6.92	7.04
Eu	1.88	1.92	1.95	2.05	1.82	1.87
Gd	7.53	8.35	8.63	8.55	8.29	8.56
Tb	1.38	1.44	1.48	1.54	1.43	1.46
Dy	8.57	8.9	9.15	9.78	9.26	9.36
Ho	1.92	2.01	1.97	2.13	2.03	2.07
Er	5.4	5.74	5.68	6.54	6.43	6.12
Tm	0.85	0.95	0.89	0.96	0.99	0.94
Yb	5.51	6.55	6.32	6.4	6.2	5.99
Lu	0.89	0.95	0.94	1.03	0.92	0.91

	Ferro-dacites (FeD)		Ferro-rhyoiltes (FeR)	
	Footwall		Footwall	
Sample	W605416	W812877	W601175	W813071
Unit	FeD	FeD	FeR	FeR
Texture	Pillowed; hyaloclastite	Pillowed; amygdaloidal	Lapilli tuff	Lapilli tuff
Type	DDH	DDH	DDH	DDH
SiO_2 (wt %)	59.48	65.63	64.2	69.08
Al_2O_3	12.65	11.79	14.54	11.62
Fe_2O_3	11.1	8.93	8.64	8.19
TiO_2	0.82	0.85	0.36	0.26
MnO	0.18	0.1	0.04	0.03
MgO	1.76	2.14	2.26	2.2
CaO	6.75	3.44	2.05	1.32
K_2O	1.72	1.04	4.47	3.21
Na_2O	1.97	3.71	0.72	0.16
P_2O_5	0.28	0.32	0.05	0.04
BaO	0.01	0.03	0.14	0.1
Cr_2O_3	<0.01	<0.01	0.01	0.005
SrO	0.03	0.03	0.02	0.03
S	0.01	0.07	0.17	0.07
C	0.65	0.25	0.05	0.17
LOI	3.53	1.6	1.9	2.37
Total	100.35	99.85	99.9	99.1
Se (ppm)	0.3	0.2	0.9	0.2
Li	10	10	20	10
Sc	10	10	11	2
V	8	18	79	21
Cr	<10	10	20	10
Co	10	9	8	6
Ni	<1	<1	4	14
Cu	5	16	13	1520
Zn	110	101	100	1145
Ga	21.2	18.5	25.6	22
Ge	<5	<5	5	2.5
As	0.5	0.9	1.4	2.3
Mo	2	2	<1	0.5
Ag	<0.5	<0.5	<0.5	6
Cd	<0.5	<0.5	<0.5	0.7
In	0.015	0.007	0.014	0.084
Sn	4	4	7	28
Sb	0.16	0.18	0.21	2.06
Te	<0.01	<0.01	0.01	0.02
W	1	1	1	1
Re	0.001	<0.001	0.001	0.0005
Hg	<0.005	<0.005	<0.005	0.008
Tl	0.18	0.17	0.7	0.15
Bi	0.01	0.01	0.02	0.14
Rb	33	28.4	93.3	65.9
Sr	277	332	222	158.5
Cs	0.92	0.99	2.61	1.23
Ba	249	231	1205	935
Pb	8	5	4	115
Th	6.69	6.41	15.25	12.1
U	2.99	2.96	5.45	4.33
Y	60.4	56.7	108	52
Zr	339	335	627	516
Nb	20.3	19	42.6	37.3
Hf	8.1	8	15.7	12.4
Ta	1.1	1.2	2.5	2.2
La	28.1	27.9	67.5	46.5
Ce	60.6	57.2	141	98.1
Pr	7.53	6.87	16.5	11.2
Nd	30.6	27.3	69.1	47.3
Sm	7.89	6.99	15.85	11.25
Eu	1.9	1.61	2.46	1.71
Gd	8.64	7.56	16.15	11.4
Tb	1.58	1.4	3.1	1.93
Dy	10.2	9.31	19.5	12.2
Ho	2.26	2.08	4.2	2.3
Er	6.7	6.9	12.15	6.73
Tm	1.06	1.04	1.9	0.96
Yb	6.47	7.22	11.95	6.97
Lu	1.02	1.06	1.74	1.01

Table 2.3 Summary of significant element ratios of the least altered AG volcanic rocks.

	FeTi basalts		Footwall basalts		Fe-rich silicic suite			High-silica rhyolites
	HW-FeTiB	Z-FeTiB	FW-FeB	FW-B	FeA	FeD	FeR	HSR
Zr/Ti	0.01	0.01	0.01	0.01	0.02 - 0.03	0.07	0.28 - 0.33	0.38 - 0.45
Nb/Y	0.42 - 0.54	0.21 - 0.37	0.25 - 0.27	0.31 - 0.33	0.27 - 0.36	0.34	0.39 - 0.72	0.43 - 0.59
Al_2O_3/ TiO_2	5.47 - 5.69	4.39 - 4.61	7.34 - 7.52	12.27 - 12.37	7.74 - 8.14	13.87 - 15.43	40.39 - 44.69	100.00 - 100.67
Zr/Al_2O_3	10.53 -11.86	12.69 - 15.54	8.35 - 8.75	4.81 - 4.99	16.34 - 20.25	26.80 - 28.41	43.12 - 44.41	22.43 - 27.00
Ti/V	28.09 - 60.88	49.99 - 55.23	32.83 - 33.18	21.16 - 21.58	54.02 - 61.45	283.10 - 614.50	27.32 - 74.22	89.93 - 139.89
La/Yb	4.33 - 5.71	2.95 - 3.91	2.48 - 2.89	3.24 - 3.25	3.55 - 4.11	3.86 - 4.34	5.65 - 6.67	3.92 - 8.32
Zr/Y	4.09 - 5.04	2.04 - 3.44	3.04 - 3.10	2.52 - 2.61	3.77 - 4.84	5.61 - 5.91	5.81 - 9.92	2.09 - 2.50
Th/Yb	1.47 - 1.65	1.50 - 1.62	1.39 - 1.40	1.32 - 1.37	2.80 - 3.37	4.52 - 4.62	1.28 - 1.74	2.24 - 2.38
Nb/Zr	0.10 - 0.12	0.10 - 0.11	0.08 - 0.09	0.12 - 0.13	0.06 - 0.08	0.06	0.06 - 0.07	0.20 - 0.24
Th/Zr	0.01	0.01	0.01	0.01	0.01 - 0.02	0.02	0.02	0.03 - 0.04
Th/Nb	0.11 - 0.12	0.11 - 0.12	0.10	0.10	0.20 - 0.25	0.33 - 0.34	0.32 - 0.36	0.16 - 0.17
La/Th	9.05 - 11.68	9.86 - 10.83	11.17 - 11.25	10.87 - 11.29	5.54 - 7.54	4.20 - 4.35	3.84 - 4.43	7.29 - 8.73
Nb/Yb	3.82 - 5.00	2.35 - 3.30	2.19 - 2.52	2.97 - 2.99	2.32 - 3.14	2.63 - 3.14	3.56 - 5.35	3.29 - 5.49
TiO_2/Yb	0.59 - 0.75	0.36 - 0.55	0.43 - 0.44	0.39 - 0.40	0.23 - 0.32	0.12 - 0.13	0.03	0.01
Nb/Ta	16.91 - 17.50	15.67 - 19.10	15.71 - 18.60	14.67 - 18.40	14.73 - 20.43	15.83 - 18.45	16.95 - 17.04	16.97 - 17.52
Zr/Hf	39.02 - 40.00	37.31 - 40.93	34.69 - 36.76	38.95 - 40.59	40.00 - 42.50	41.85 - 41.88	39.93 - 41.61	24.20 - 28.21
$(Hf/Sm)_{pm}$	0.84 - 1.02	0.85 - 0.86	0.95 - 1.00	0.77 - 0.79	1.06 - 1.33	1.48 - 1.64	1.42 - 1.58	0.72 - 0.86
$(Zr/Sm)_{pm}$	0.91 - 1.10	0.87 - 0.95	0.95 - 0.96	0.82 - 0.89	1.24 - 1.51	1.70 - 1.90	1.57 - 1.82	0.48 - 0.67
$(La/Yb)_{pm}$	3.11 - 4.10	2.12 - 2.81	1.78 - 2.07	2.33	2.55 - 2.95	2.77 - 3.12	4.05 - 4.78	2.82 - 5.97
$(La/Sm)_{pm}$	1.67 - 2.17	1.68 - 1.98	1.47 - 1.58	1.82 - 2.01	1.99 - 2.36	2.30 - 2.58	2.67 - 2.75	2.64 - 2.83
$(Gd/Yb)_{pm}$	1.42 - 1.48	1.06 - 1.32	1.05 - 1.23	1.12 - 1.25	1.05 - 1.18	0.87 - 1.10	1.12 - 1.35	0.88 - 1.58
$(Nb/Nb^*)_{pm}$	0.89 - 1.05	0.88 - 0.95	0.99 - 1.00	1.03 - 1.04	0.53 - 0.68	0.48 - 0.50	0.45 - 0.53	0.66 - 0.77
$(Zr/Zr^*)_{pm}$	1.04 - 1.28	0.91 - 1.05	0.99 - 1.02	0.84 - 0.90	1.31 - 1.56	1.89 - 2.12	1.80 - 2.09	0.56 - 0.73
$(Ti/Ti^*)_{pm}$	0.87 - 0.90	0.74 - 0.97	0.78 - 0.86	0.70 - 0.79	0.46 - 0.60	0.24 - 0.28	0.05	0.01
$(Eu/Eu^*)_{cn}$	0.93 - 0.97	0.80 - 0.93	0.87 - 0.92	0.80 - 0.90	0.73 - 0.84	0.68 - 0.70	0.46 - 0.47	0.50 - 0.51
Th_N/Nb_N	1.47 - 1.65	1.50 - 1.62	1.39 - 1.40	1.32 - 1.37	2.80 - 3.37	4.52 - 4.62	4.45 - 4.91	2.24 - 2.38
ΣREE	125.23 - 127.94	145.52 - 178.82	83.45 - 95.06	64.79 - 71.82	135.07 - 159.64	164.44 - 174.55	259.56 - 383.10	528.72 - 552.67
AI	61.05 - 85.08	41.66 - 60.42	20.27 - 20.39	33.46 - 34.17	32.09 - 50.4	28.52 - 30.78	28.52 - 30.78	43.33 - 55.22
CCPI	76.94 - 90.74	75.04 - 80.14	77.27 - 77.95	71.22 - 75.30	77.79 - 82.15	68.17 - 76.10	68.17 - 76.10	34.72 - 43.96
Al_2O_3/Na_2O	20.90 - 168.78	4.06 - 8.40	3.13 - 3.20	4.93 - 5.74	3.44 - 5.61	3.18 - 6.42	20.19 - 72.63	5.32 - 6.19

Table 2.4 Chemical abrasion isotope dilution thermal ionization mass spectrometry (CA-ID-TIMS) U-Pb zircon isotopic data for felsic rocks in the AG stratigraphy.

			Compositional parameters							**Radiogenic Isotope Ratios**								**Isotopic Dates**					
CA-TIMS label (a)	mass spectrometer	LA-ICPMS label	Th/U (b)	$^{206}Pb^*$ x10^{-13} mol (c)	mol % $^{206}Pb^*$ (c)	Pb* (pg) (c)	Pb_c (pg) (c)	Pb*/Pb_c (c)	$^{206}Pb/^{204}Pb$ (d)	$^{208}Pb/^{206}Pb$ (e)	$^{207}Pb/^{206}Pb$ (e)	% err (f)	$^{207}Pb/^{235}U$ (e)	% err (f)	$^{206}Pb/^{238}U$ (e)	% err (f)	corr. coef.	$^{207}Pb/^{206}Pb$ (g)	± (f)	$^{207}Pb/^{235}U$ (g)	± (f)	$^{206}Pb/^{238}U$ (g)	± (f)
Sample 110-322																							
z6	Phoenix	222	0.396	0.1296	98.01%	3.1	0.22	14.4	904	0.126	0.050	0.745	0.231	0.817	0.033	0.153	0.547	214.99	17.24	211.36	1.56	211.03	0.32
z9	Isoprobe-T	217	0.369	0.0915	97.01%	2.2	0.23	9.4	602	0.117	0.050	0.963	0.230	1.044	0.033	0.105	0.802	199.40	22.35	209.95	1.98	210.89	0.22
z5	Phoenix	215	0.324	0.1122	97.69%	2.7	0.22	12.1	779	0.103	0.050	0.634	0.230	0.698	0.033	0.097	0.700	207.74	14.69	210.56	1.33	210.81	0.20
z4	Phoenix	213	0.397	0.2343	98.85%	5.7	0.23	25.1	1564	0.126	0.050	0.394	0.230	0.444	0.033	0.084	0.656	202.86	9.15	210.04	0.84	210.68	0.17
z7	Isoprobe-T	214	0.422	0.0795	97.41%	1.9	0.18	11.1	696	0.134	0.050	0.927	0.230	1.005	0.033	0.130	0.641	205.21	21.51	210.08	1.91	210.51	0.27
z8	Isoprobe-T	219	0.300	0.0719	97.23%	1.7	0.17	10.0	652	0.095	0.050	0.902	0.230	0.978	0.033	0.118	0.679	203.48	20.93	209.82	1.85	210.38	0.24
z1	Phoenix	221	0.344	0.2088	98.79%	5.0	0.21	23.5	1488	0.109	0.050	0.392	0.230	0.443	0.033	0.082	0.679	209.63	9.09	210.23	0.84	210.28	0.17
Sample 110-368																							
z2	Phoenix	225	0.421	1.3891	99.75%	33.9	0.29	116.0	7127	0.134	0.050	0.128	0.231	0.181	0.033	0.073	0.819	215.25	2.97	211.05	0.34	210.67	0.15
z6	Phoenix	233	0.416	1.1943	99.72%	29.1	0.28	105.1	6473	0.132	0.050	0.117	0.231	0.172	0.033	0.071	0.863	212.41	2.70	210.70	0.33	210.54	0.15
z1	Phoenix	251	0.408	1.0170	99.33%	24.8	0.57	43.4	2692	0.130	0.050	0.168	0.231	0.220	0.033	0.071	0.803	213.26	3.90	210.73	0.42	210.50	0.15
z4	Phoenix	228	0.397	1.1534	99.62%	28.0	0.36	77.2	4781	0.126	0.050	0.174	0.230	0.220	0.033	0.075	0.726	211.55	4.03	210.58	0.42	210.50	0.15
z3	Phoenix	249	0.369	1.6959	99.71%	40.8	0.41	99.5	6208	0.117	0.050	0.153	0.231	0.199	0.033	0.074	0.735	214.18	3.55	210.79	0.38	210.48	0.15
z5	Phoenix	246	0.423	1.4452	99.60%	35.3	0.48	73.9	4544	0.134	0.050	0.140	0.231	0.192	0.033	0.073	0.809	215.22	3.24	210.82	0.37	210.43	0.15

(a) z1, z2, etc. are labels for analyses composed of single zircon grains that were annealed and chemically abraded. Red, bold labels denote grains used in weighted mean date calculations.

(b) Model Th/U ratio calculated from radiogenic $^{208}Pb/^{206}Pb$ ratio and $^{207}Pb/^{235}U$ date.

(c) Pb* and Pb_c are radiogenic and common Pb, respectively. mol % $^{206}Pb^*$ is with respect to radiogenic and blank Pb.

(d) Measured ratio corrected for spike and fractionation only. Pb fractionation correction is 0.18 ± 0.03 (1 sigma) %/amu (atomic mass unit) for single-collector Daly analyses done on Isoprobe-T mass spectrometer and 0.24 ± 0.03 (1 sigma) %/amu (atomic mass unit) for single-collector Daly analyses done on the Phoenix mass spectrometer, both based on recent analyses of EARTHTIME ^{202}Pb-^{205}Pb ET2535 tracer solution.

(e) Corrected for fractionation and spike. Common Pb in zircon analyses is assigned to procedural blank with composition of $^{206}Pb/^{204}Pb$ = 18.04 ± 0.61%; $^{207}Pb/^{204}Pb$ = 15.54 ± 0.52%; $^{208}Pb/^{204}Pb$ = 37.69 ± 0.63% (1 sigma). $^{206}Pb/^{238}U$ and $^{207}Pb/^{206}Pb$ ratios corrected for initial disequilibrium in $^{230}Th/^{238}U$ using a D(Th/U) of 0.20 ± 0.05 (1 sigma).

(f) Errors are 2 sigma, propagated using algorithms of Schmitz and Schoene (2007) and Crowley et al. (2007).

(g) Calculations based on the decay constants of Jaffey et al. (1971). $^{206}Pb/^{238}U$ and $^{207}Pb/^{206}Pb$ dates corrected for initial disequilibrium in $^{230}Th/^{238}U$ using a D(Th/U) of 0.20 ± 0.05 (1 sigma).

Table 2.5 Summary of U-Pb geochronology results.

Sample Attributes					**LA-ICPMS**		**CA-TIMS**				
Sample	**Lithology**	**Location description**	**Drillhole ID**	**Sample depth in core (m)**	**Number of zircon grains analyzed**	**$^{206}Pb/^{238}U$ dates (Ma)**	**Number of zircon grains analysed**	**Number of analyses used in weighted mean**	**Mean square of weighted deviates (MSWD)**	**Probability of fit**	**Weighted mean $^{206}Pb/^{238}U$ date (Ma)**
110-322	FIIIa Ferro-rhyolite (FeR) lapilli tuff	Stratigraphically underlying hydrothermally altered heterolithic fragmental unit and along strike of exhalative VMS mineralization.	CMR18-110	322	11	212 ± 6 to 194 ± 5	7	3	1.1	0.32	210.35 ± 0.27
110-368	Massive FIIIb High-silica rhyolite (HSR)	Suspect this is a high-level, syn-volcanic intrusion. Intrudes ferro-andesite (FeA) flows.	CMR18-110	368	49	213 ± 5 to 189 ± 4	6	6	1.2	0.29	210.52 ± 0.08

Chapter 2 Figures

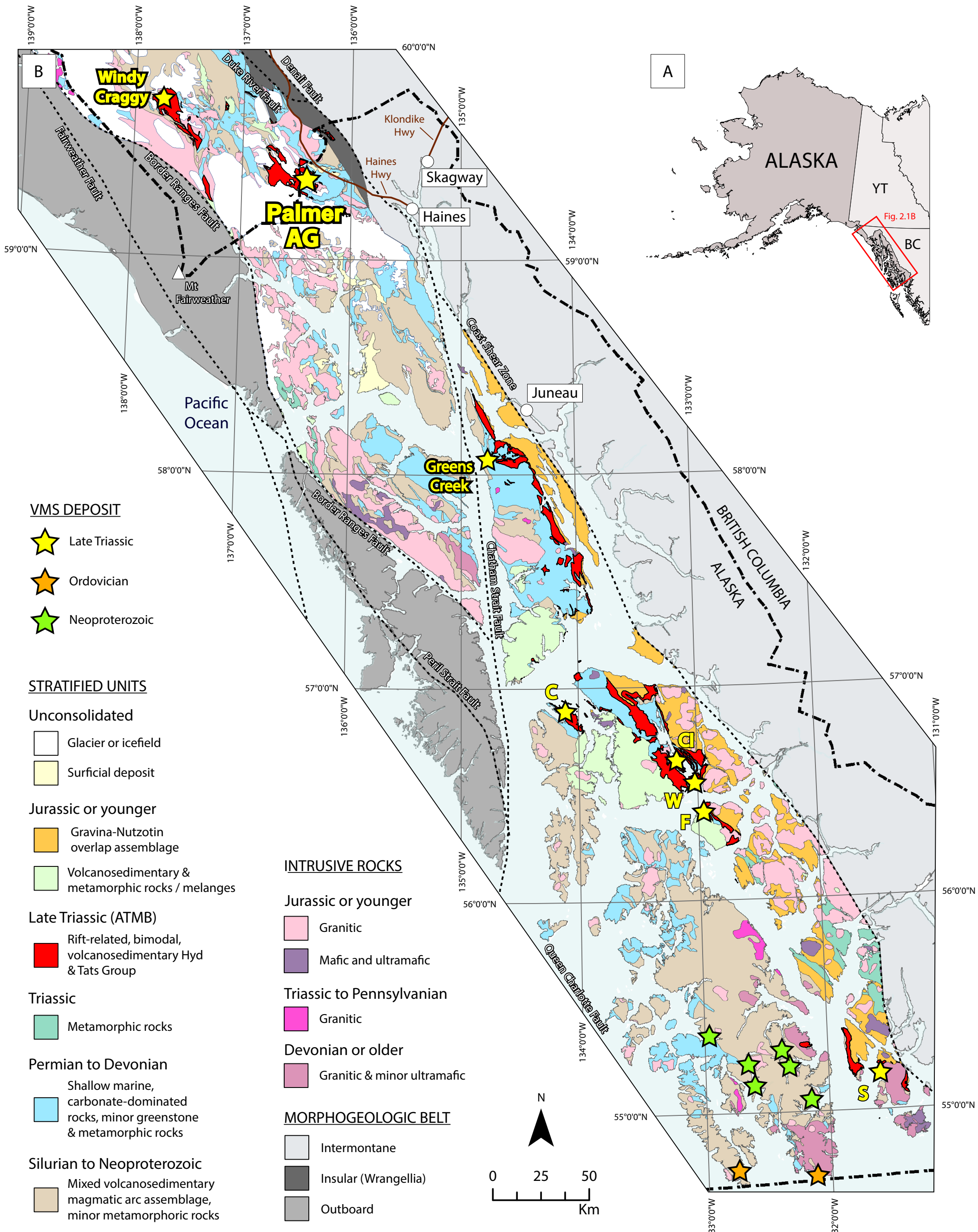

Fig. 2.1 (A) Location of the Alexander terrane. (B) Regional geology of the Alexander terrane in southeastern Alaska and northwestern British Columbia. Stratified units and intrusive rocks of Alaska and British Columbia are based on digital files from the USGS (Wilson et al., 2015) and the BCGS (Cui et al., 2017), respectively. They are grouped to reflect the generalized tectonic environments of the terrane (Gehrels and Saleeby, 1987). The terrane boundaries are from Colpron and Nelson (2011). The Alexander Triassic metallogenic belt (ATMB) hosts several VMS deposits, including Windy Craggy, Palmer and AG, Greens Creek, C: Cornwallis Peninsula (Kuiu), CI: Castle Island, WI: Woewodski Island, F: Frenchie, and S: Sylburn Peninsula.

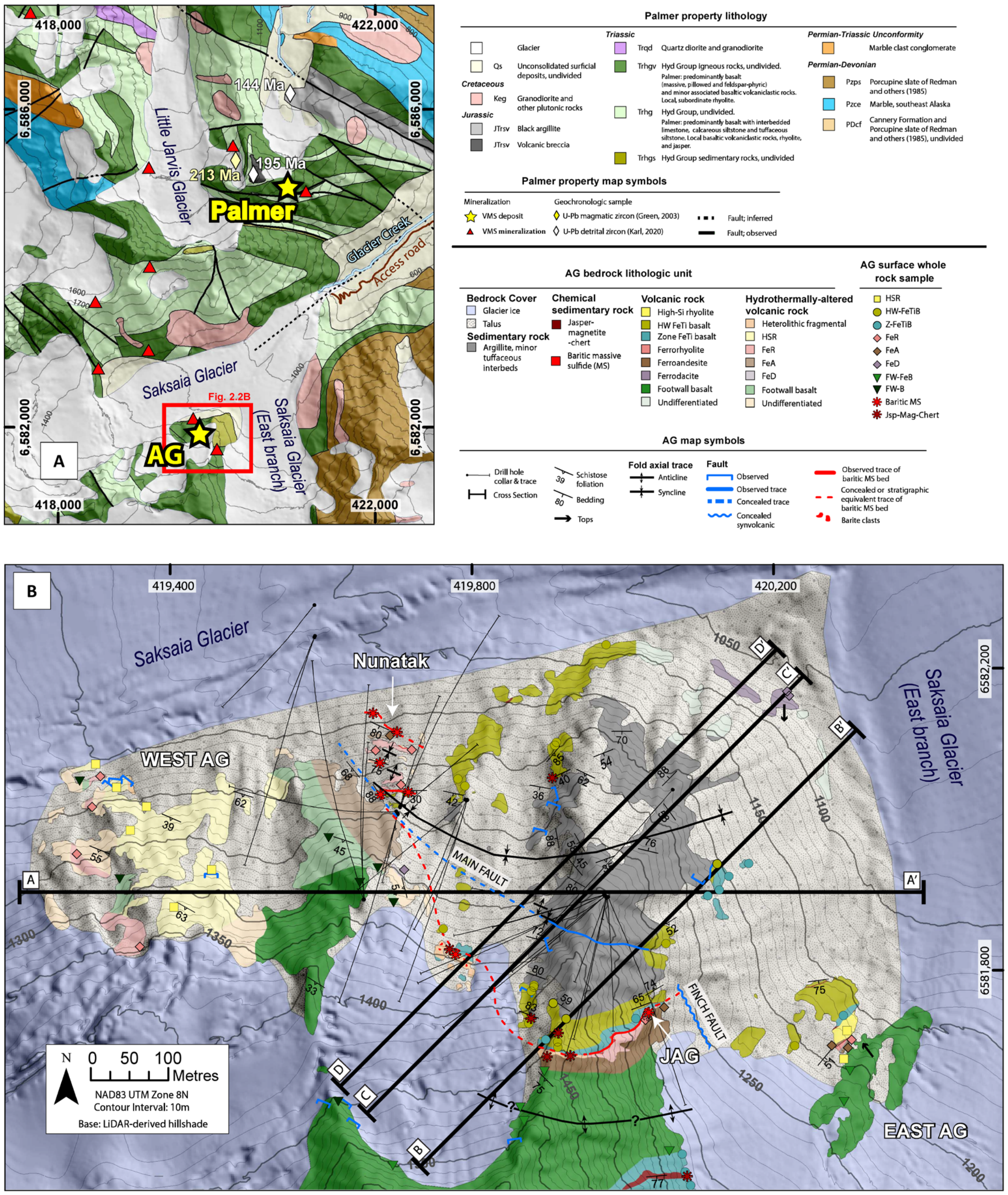

Fig. 2.2 (A) Regional geology of the Palmer property modified from the Alaska digital geology compilation (Wilson et al., 2015). The locations of the Palmer and AG VMS deposits and several VMS prospects are shown. Geochronologic data includes one U-Pb zircon date from the Palmer rhyolite (213 Ma) (Green, 2001) and U-Pb dates from detrital zircons (Karl et al., 2020). (B) Bedrock geology in the vicinity of the AG deposit. Map units coincide with the new chemostratigraphic nomenclature developed in this study from surface mapping, drill core logging, and lithogeochemical studies. The locations of the oblique section (A-A') and cross sections (B-B', C-C', and D-D') shown in Fig. 2.4 are displayed.

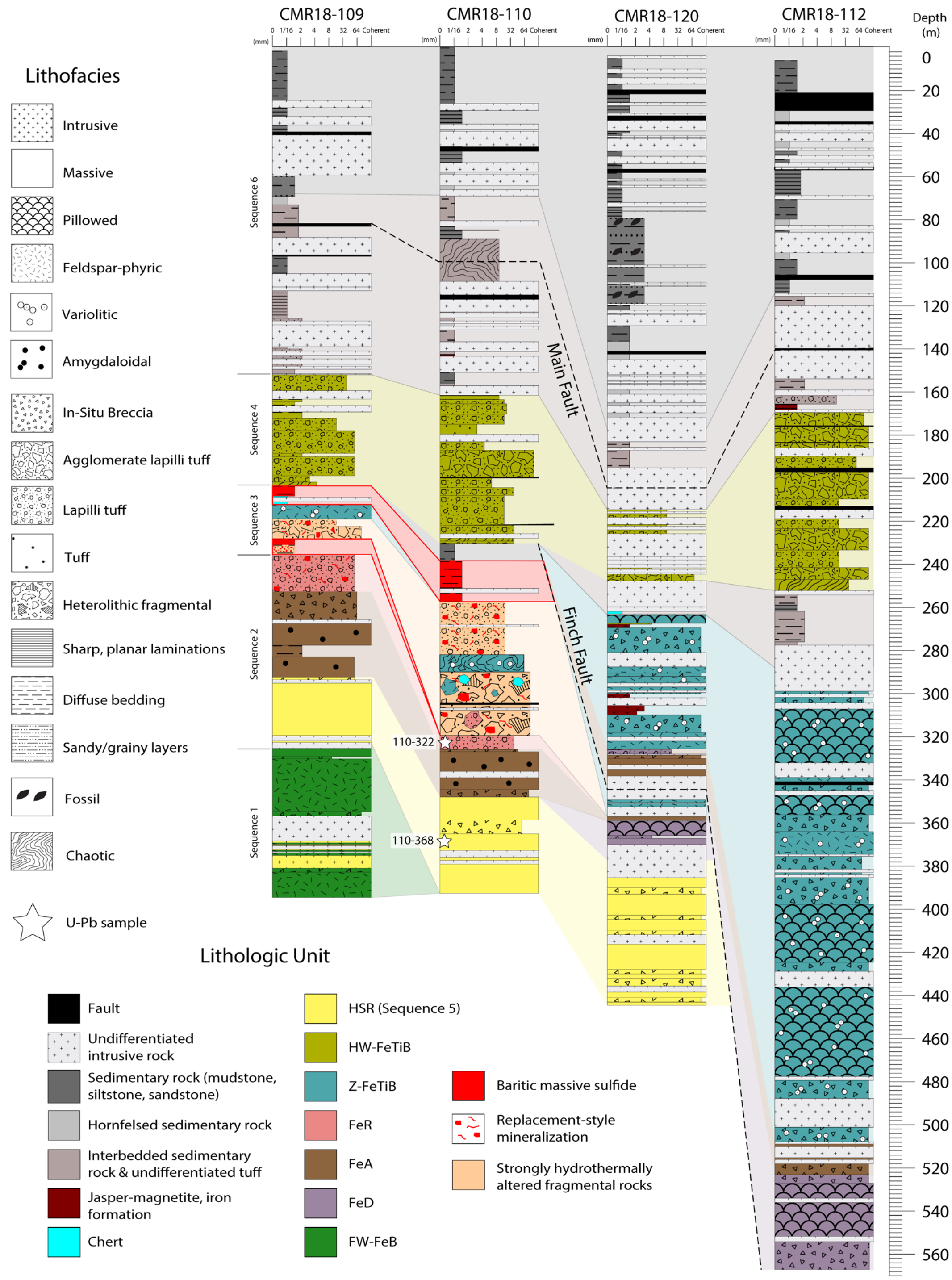

Fig. 2.3 Graphic logs for four representative drill holes through the JAG panel that coincide with the cross-section, C-C', shown in Fig. 2.4. Note that sequence 5, the HSR, is an intrusive sill complex that has massive and brecciated facies.

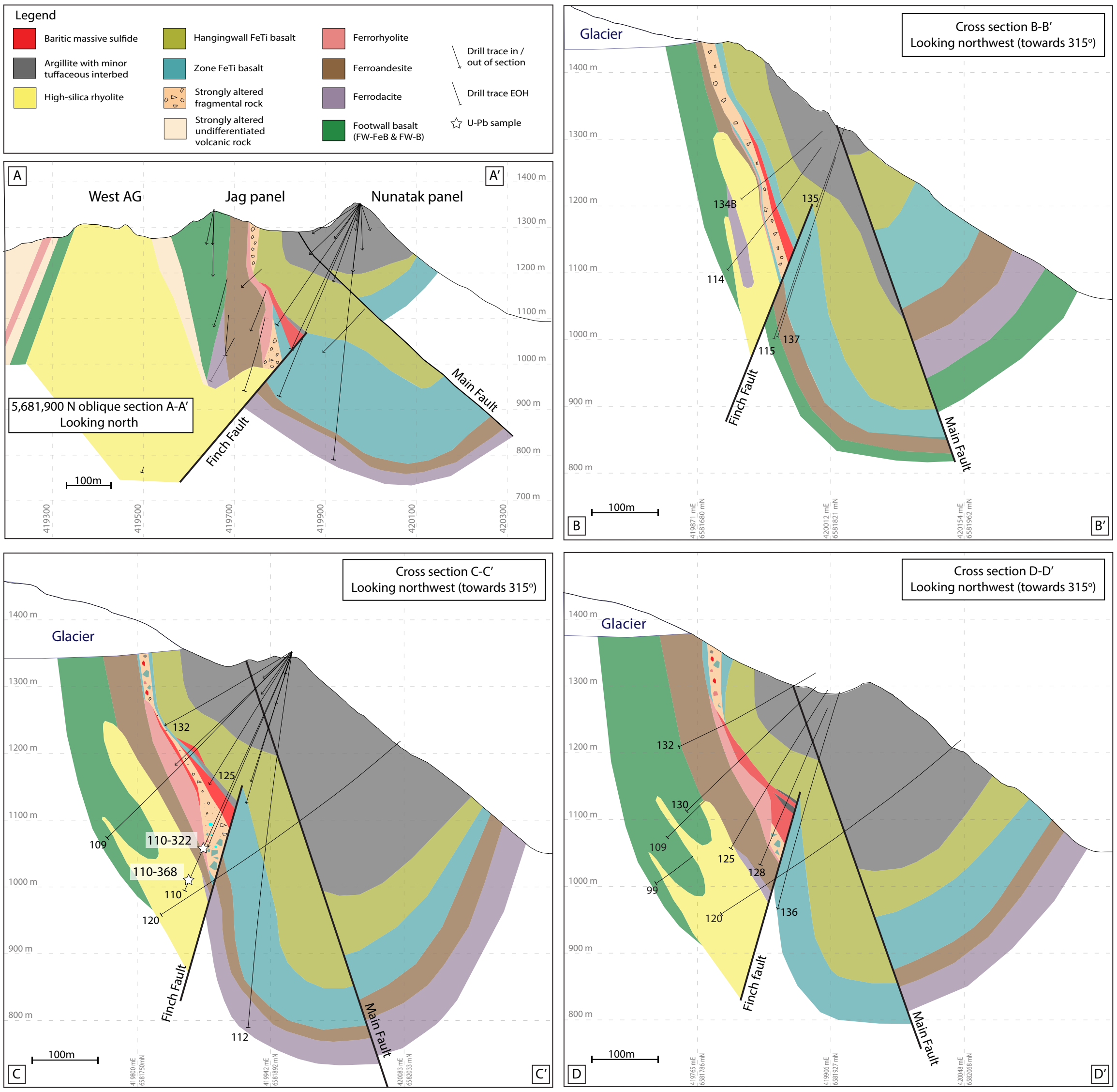

Fig. 2.4 Oblique section (A-A') across the AG deposit map area and cross sections (B-B', C-C', and D-D') highlighting the JAG panel stratigraphy. Section locations are shown in Fig. 2.2B. Detailed graphic logs associated with section C-C' are displayed in Fig. 2.3.

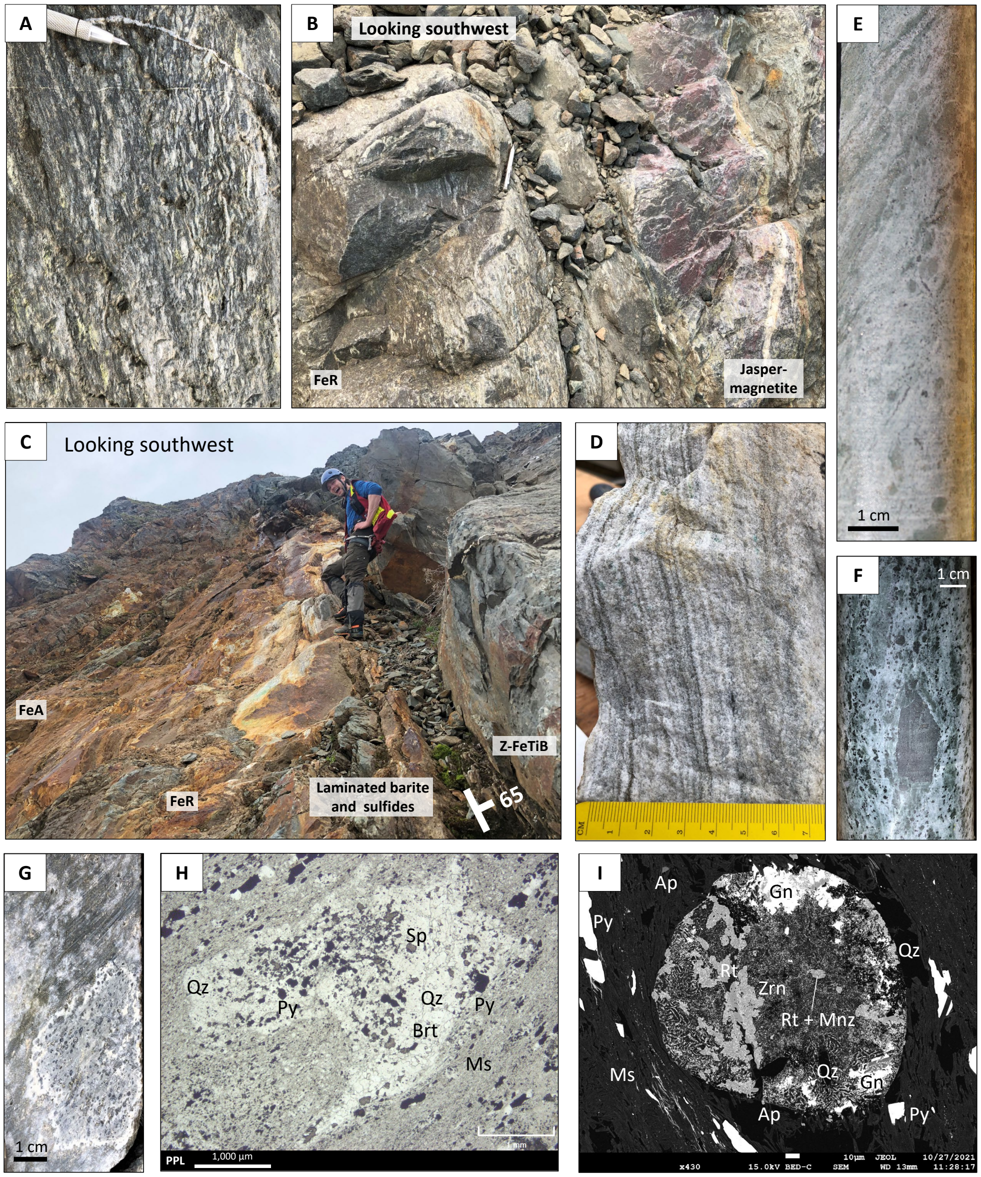

Fig. 2.5 Photographs (A-C; E-G) and microphotographs (H-I) of the ferrorhyolites (FeR). (A-B) At East AG, the FeR lapilli tuff is foliated and contains lighter-colored fiamme-like lapilli in a magnetic, dark grey matrix. A bed of jasper-magnetite conformably overlies the FeR. (C-D) The JAG prospect consists of upright, steeply north-dipping massive barite with minor laminations of pyrite, sphalerite, galena, and sulfosalts (hand sample shown in D). The exhalative-style VMS mineralization is underlain by strongly hydrothermally altered ferrorhyolites (FeR) and ferroandesites (FeA) and is overlain by Zone FeTi basalt (Z-FeTiB) flows. (E) FeR lapilli tuff grading into laminated tuffaceous facies. (F) Subround to subangular glassy felsic lapilli altered to chlorite supported in a muscovite-quartz-chlorite-magnetite matrix (devitrified tuff?). (G) Pumice (?) clast reaction rim around ragged margins contains abundant amygdules (?) composed of galena, sphalerite, and sulfosalts. Patchy barite and very fine-grained muscovite-pyrite replace the tuffaceous matrix. (H) Microphotograph in plane-polarized light (PPL) of the FeR lapilli tuff in PPL showing a wispy clast with cuspate and winged margins. The clast is predominantly quartz with minor muscovite and contains barite, sphalerite, and pyrite. The matrix surrounding the clast comprises very fine-grained, aligned muscovite (defining foliation), disseminated pyrite, and minor quartz. (I) Back scattered electron (BSE) image of a 150 µm globular feature ("globule") composed of anhedral masses and symplectic intergrowths of rutile, zircon, and monazite in the FeR. Abbreviations: Qz = quartz, py = pyrite, sp = sphalerite, ms = muscovite, brt = barite, ap = apatite, zrn = zircon, mnz = monazite, rt = rutile.

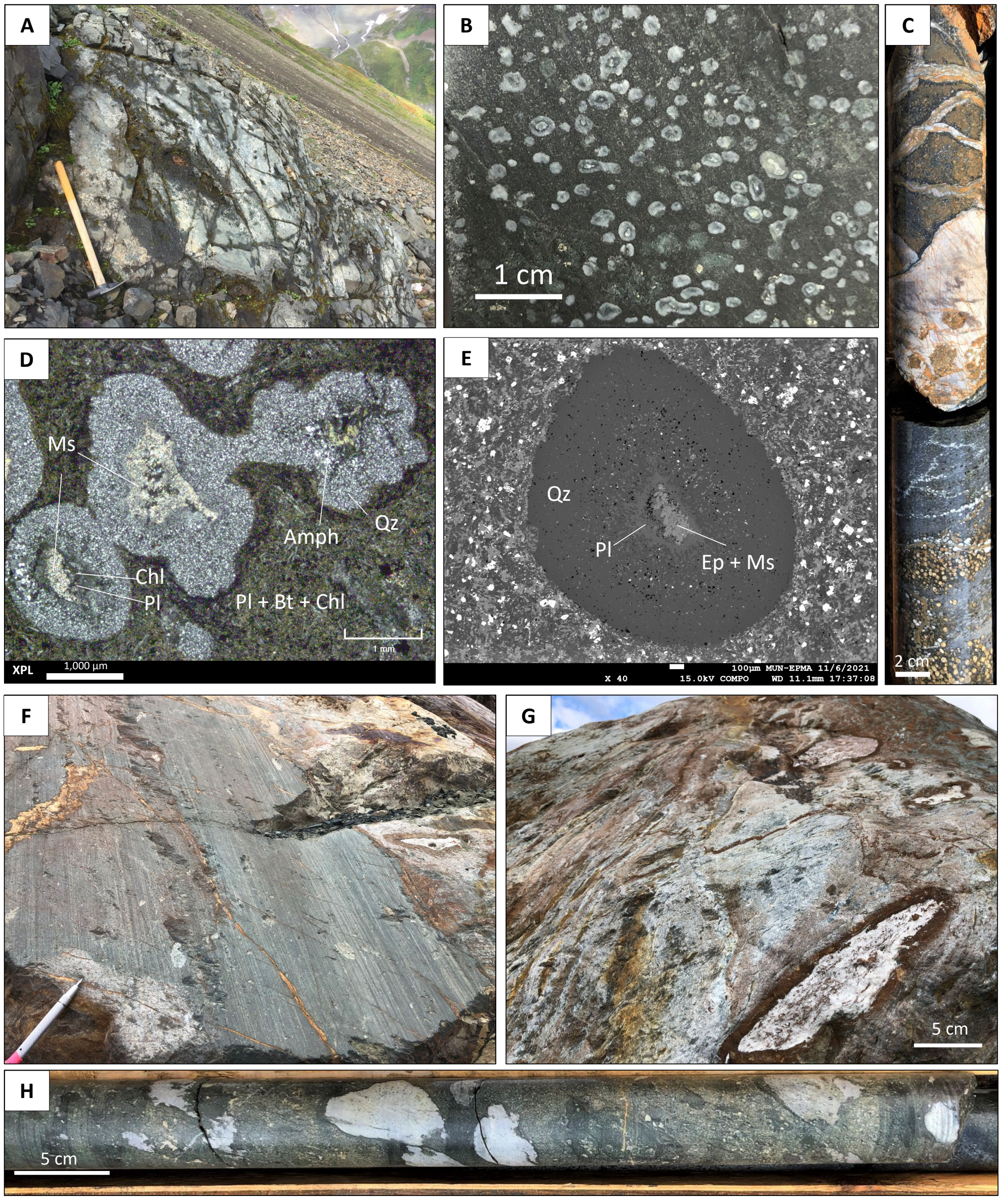

Fig. 2.6 Photos of the Zone FeTi basalts (Z-FeTiB) (A-E) and associated heterolithic fragmental rocks (F-H). (A) Variolitic, pillowed basalt flows of the Z-FeTiB in outcrop northeast of the JAG prospect. Some pillows have iron carbonate cores. (B) The varioles are concentrically zoned, 1–5 mm, leucocratic features composed of quartz and muscovite (C) Jigsaw-fit monomictic breccia texture at a pillow margin. The interpillow space is quartz with some magnetite and iron carbonate. Iron carbonate overprints the Z-FeTiB here. Varioles are composed of quartz, muscovite, and iron carbonate. (D) Microphotograph in cross-polarized light (XPL) of larger, coalescing varioles that have cores of plagioclase variably replaced by albite, muscovite, epidote, chlorite, amphibole, and biotite. The outer rims of the varioles are composed of recrystallized quartz (E) Back scattered electron (BSE) image of a variole with well-defined zoning from the plagioclase (partially replaced by epidote and muscovite) core. (F) Heterolithic fragmental with varied clasts, including pale grey, siliceous rhyolite(?), gossan patches, and barite clasts. (G) Close-up of oval-shaped massive barite clasts rimmed with magnetite and iron carbonate and set in a chloritic matrix. (H) Subround to ragged white, siliceous (felsic? Chert?) clasts and green (mafic?) lapilli supported in a green, chlorite- and carbonate-altered matrix. Abbreviations: Qz = quartz, pl = plagioclase, amph = amphibole, ms = muscovite, bt = biotite, chl = chlorite, ep = epidote.

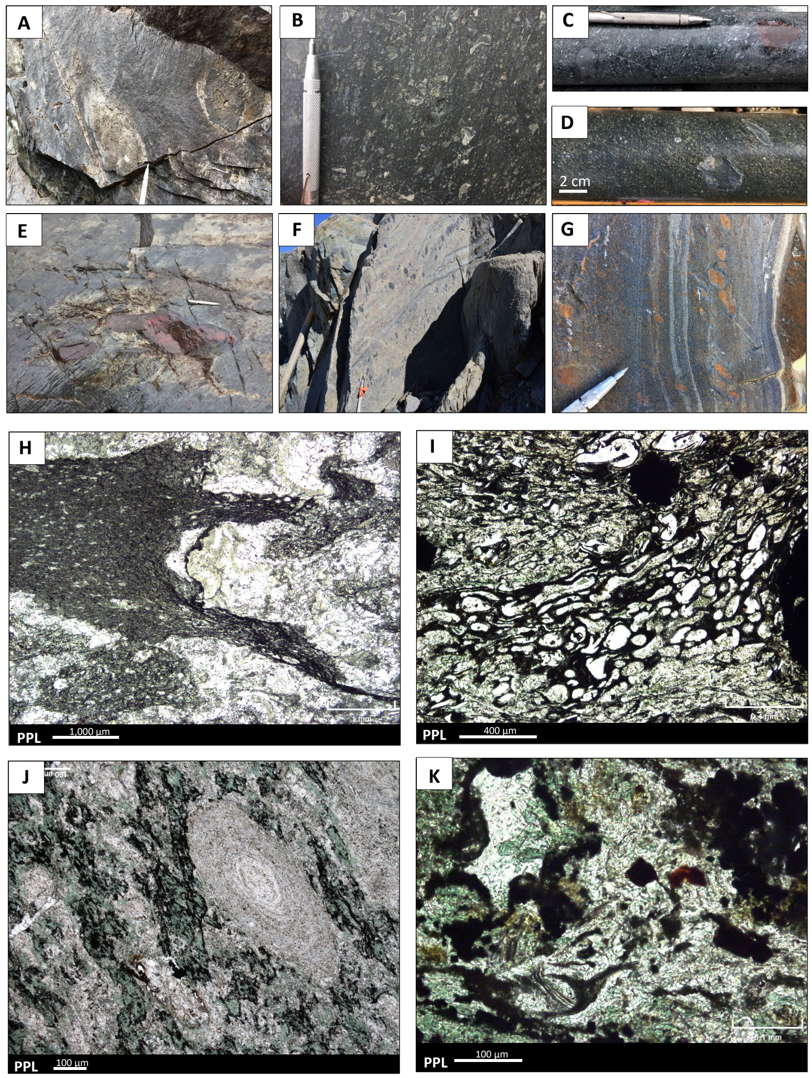

Fig. 2.7 Outcrop (A, B, E-G) and drill core (C-E) photographs and microphotographs (H-K) of the hangingwall FeTi basalts (HW-FeTiB). The laminated facies with sparse lapilli are shown in F-G and I-K. (A) Rounded bombs of basalt with distinct reaction rims on their margins supported in a tuffaceous basalt matrix. (B) Lapilli-rich facies with abundant cuspate particles. (C) Some grey basalt lapilli have relict plagioclase phenocrysts and are amygdaloidal. Some basalt clasts have jasper alteration. (D) Crystal-rich (plagioclase) lapilli tuff facies. (E) Fluidal clast of basalt altered to jasper and magnetite supported in a chloritic matrix. (F) Strongly quartz, muscovite, and magnetite-altered laminated tuffs with sparse lapilli that are wholly altered to magnetite. (G) Strongly chlorite-, iron carbonate- and magnetite-altered laminated tuffs with sparse lapilli. (H-K) Microphotographs (PPL) of different pyroclastic particles in the HW-FeTiB. (H) Scoriaceous lapilli with fiamme-like ("flame-like") textures. Lapilli are outlined by opaque magnetite. The tuffaceous matrix comprises aggregates of recrystallized very fine-grained calcite, quartz, ankerite, and chlorite with disseminated magnetite, rare pyrite, and chalcopyrite. (I) Stretched and deformed tube scoria fragments that resemble reticulite ("thread-lace scoria") with a honeycomb texture. Groundmass of scoria is mainly FeTi oxide minerals. Amygdules are quartz with minor muscovite. The matrix is very fine-grained muscovite, quartz, and chlorite. (J) An oval-shaped accretionary lapilli (2.8 mm long) has alternating quartz-rich and muscovite-rich layers that create a concentric zoning pattern. Matrix is recrystallized tuffaceous material composed of magnetite- and chlorite-rich domains and quartz-, calcite-, and muscovite-rich domains. (K) A Y-shaped shard composed of very fine-grained magnetite. The matrix is a mix of quartz, chlorite, magnetite, muscovite, and carbonate with patches of brown, grungy material. Some oxidized FeTi oxide minerals have a reddish-brown hue in PPL.

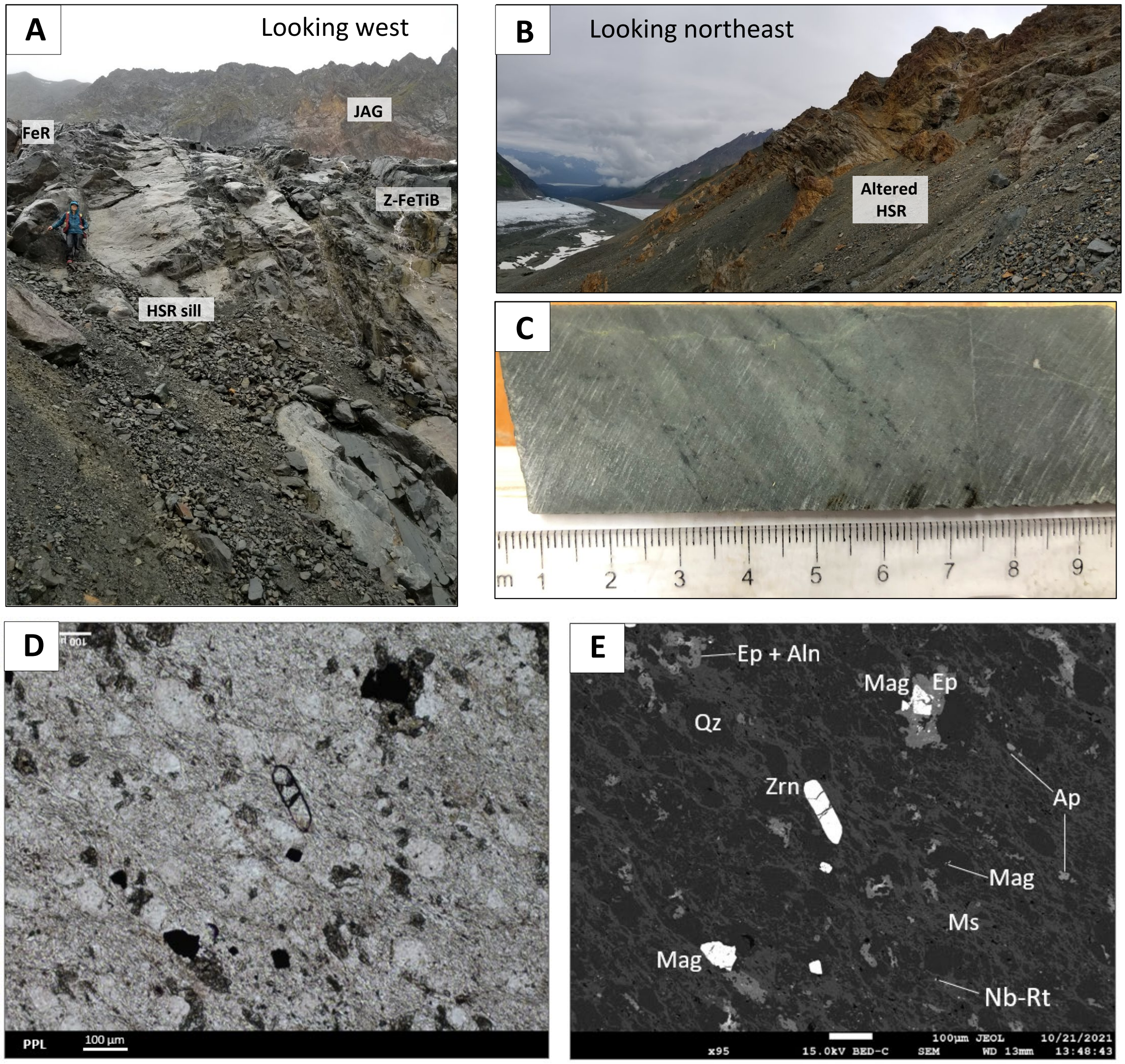

Fig. 2.8 Outcrop photographs (A-B), hand sample photograph (C), and microphotographs (D-E) of the FIIIb high-silica rhyolites (HSR). (A) At East AG, a 15 m thick HSR sill intrudes the contact between the Z-FeTiB and underlying FeR and FeA. (B) West AG has the most extensive exposure of HSR and consists of rusty-colored, rounded, bluff-forming outcrops that dominate the hillside. (C) Hand sample photograph of the massive HSR. (D-E) Microphotographs of the same area in PPL (D) and a backscattered electron image (BSE) image (E). A euhedral zircon crystal is within a groundmass of muscovite grains woven around rounded quartz domains (quartz eyes?) and disseminated epidote. Epidote locally has allanite cores (brighter in the BSE image) with Ce, La, and Nd spectra. Apatite and magnetite are accessory phases, and rare rutile grains with Nb spectra are disseminated. Abbreviations: Qz = quartz, ms = muscovite, mag = magnetite, ap = apatite, zrn = zircon, ep = epidote, aln = allanite, Nb-rt = rutile with Nb EDS spectra.

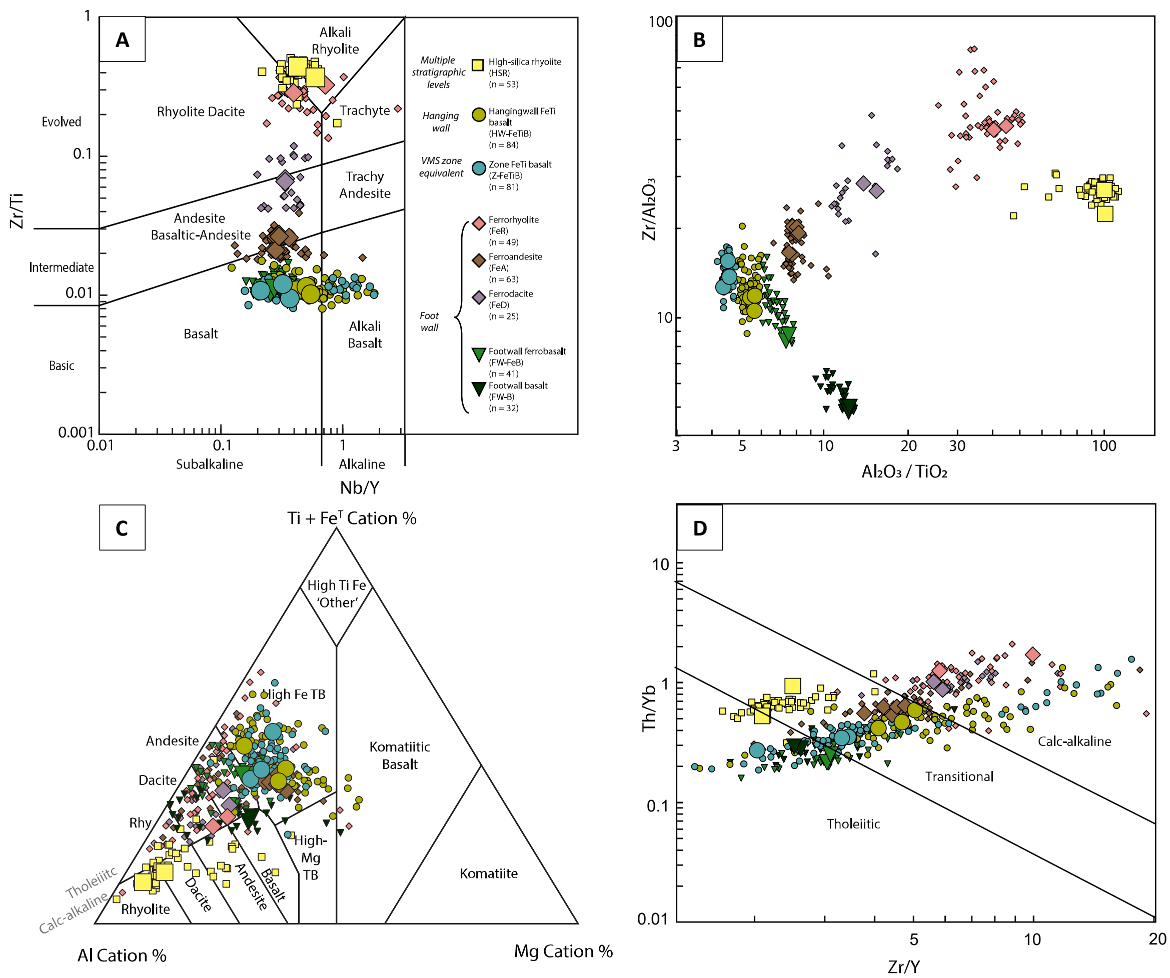

Fig. 2.9 Major and trace element discrimination plots for the mafic and felsic rocks of the AG stratigraphy. The largest symbols are the least altered samples, and rocks are color-coded by geochemical affinity. (A) The modified Winchester and Floyd (1977) volcanic rock discrimination diagram (Pearce, 1996). (B) Al_2O_3/TiO_2 versus Zr/ $Al2O_3$ ratios define eight geochemically distinct volcanic units. (C) The Jensen (1976) cation plot for classifying subalkaline rocks; TB = tholeiitic basalt. (D) Magmatic affinity diagram of Ross and Bédard (2009) modified from concepts in Maclean and Barrett (1993) and Barrett and MacLean (1999).

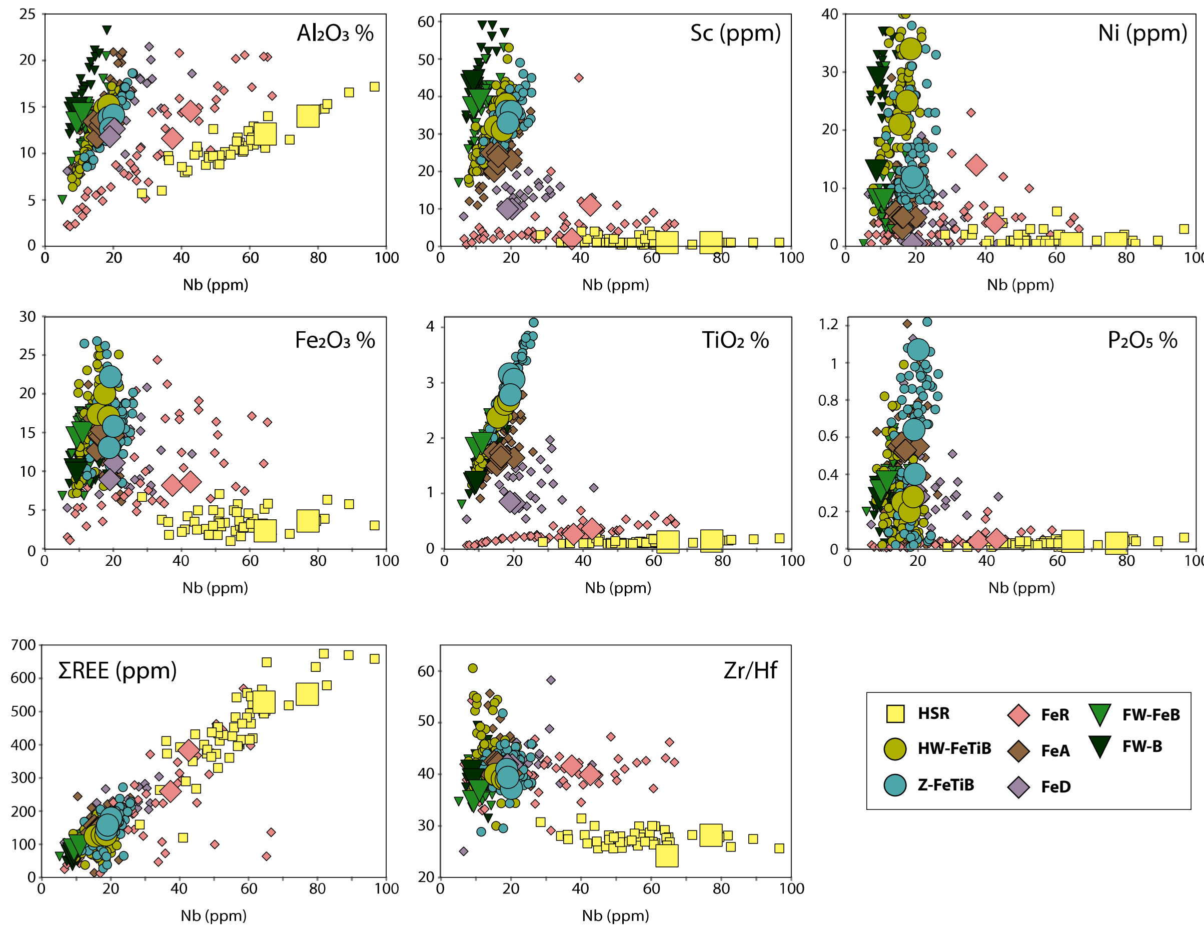

Fig. 2.10 Variation diagrams of Nb versus selected major and trace elements for the AG volcanic rocks.

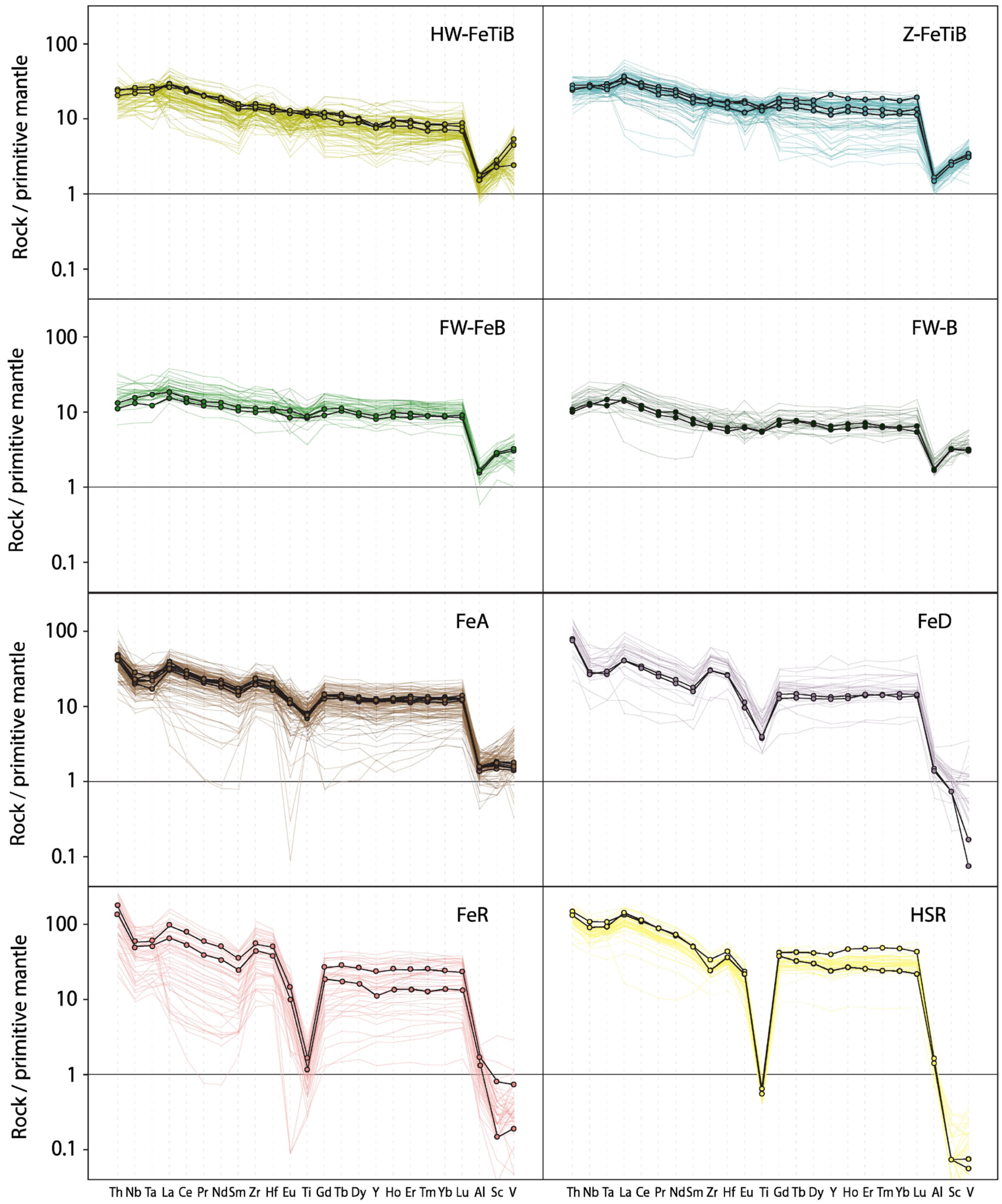

Fig. 2.11 Multi-element primitive mantle normalized plots for the eight volcanic units. The least altered samples are presented as bold lines with dots. The more altered samples are shown as thin-colored lines. Samples within each geochemical unit have parallel multi-element patterns that can be offset due to mass balance changes associated with the alteration. Note the REE mobility of some intensely altered samples as evidenced by the swooping, U-shaped LREE patterns. The normalizing factor is the primitive mantle (pm) from Sun and McDonough (1989).

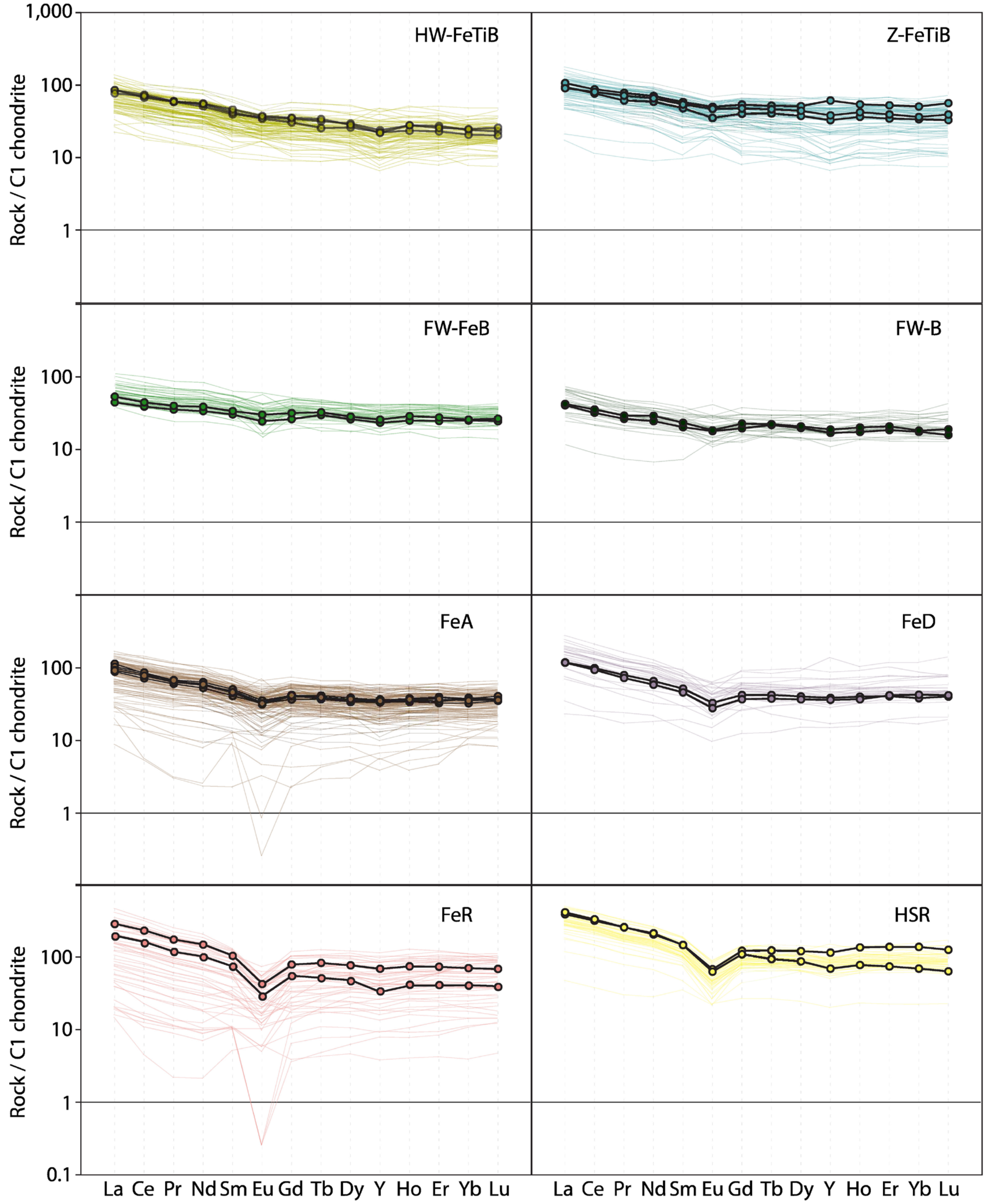

Fig. 2.12 Rare Earth element (REE) chondrite normalized plots for the eight volcanic units. The least altered samples are presented as bold lines with dots. The more altered samples are shown as thin-colored lines. The FeD, FeR, and HSR have strong negative Eu anomalies. Intensely altered samples have extreme negative Eu anomalies and mobile REE, especially LREE. The normalizing factor is the C1 chondrite (cn) from Sun and McDonough (1989).

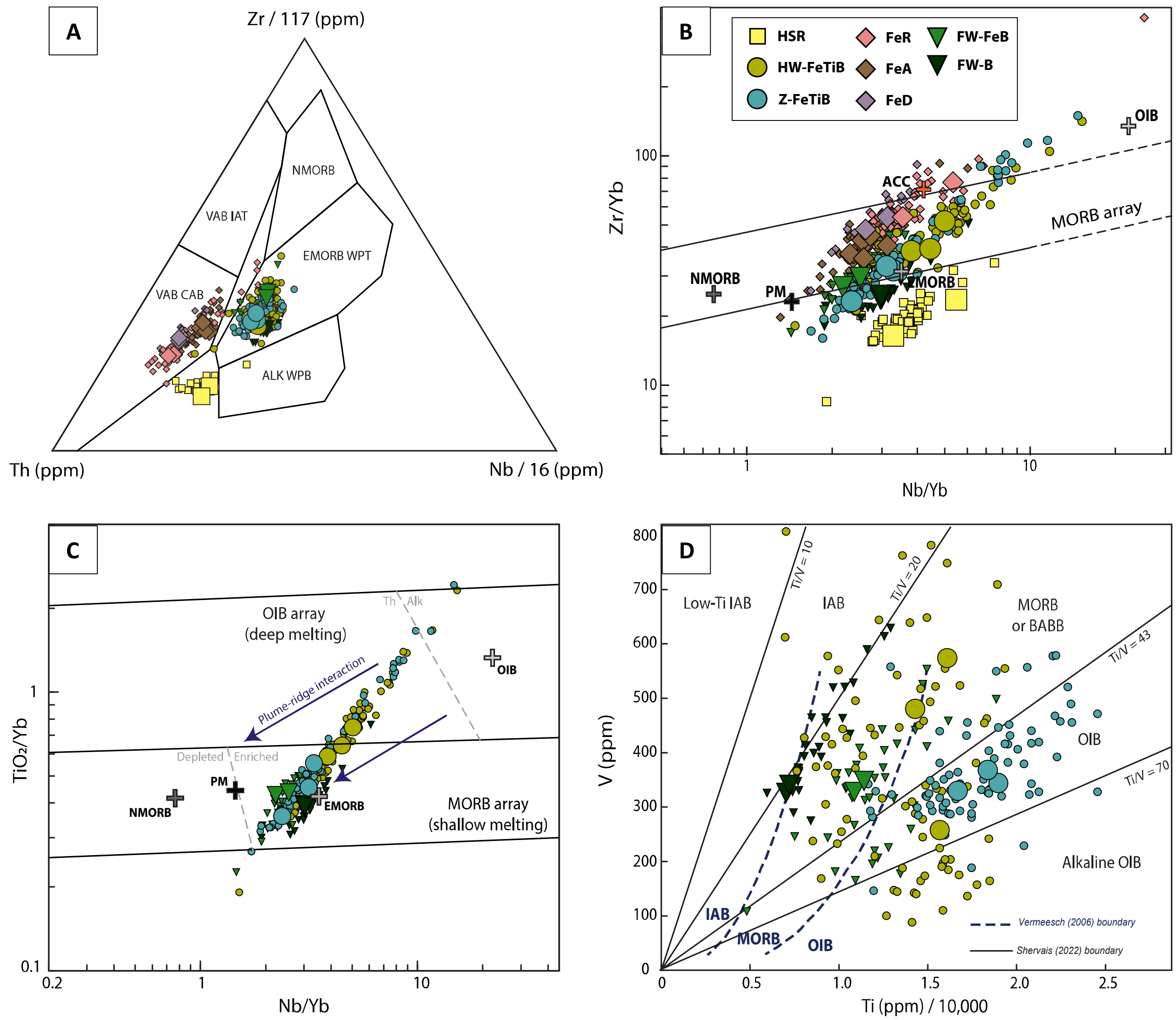

Fig. 2.13 Tectono-magmatic plots (A-D). (A) Th-Zr-Nb plot by Rollinson (1993; p. 182-185) after Wood (1980). (B) Nb/Th versus Zr/Nb (Condie, 2005). Vectors indicate the effects of subduction zone component (SZ) and batch melting (F). Isotopic mantle reservoirs EM2 and HIMU are from Condie (2005). (C) Nb/Yb versus TiO_2/Yb (Pearce, 2008) (D) The Ti-V basalt discrimination diagram of Shervais (2022) after Shervais (1982). The modified boundaries of Vermeesch (2006) are shown as dark blue dashed lines and labeled in dark blue in the lower left corner near the origin. Reference earth reservoir values are shown as crosses on some plots and include normal midocean ridge basalt (NMORB), enriched MORB (EMORB), and ocean island basalt (OIB) from Sun and McDonough (1989). Abbreviations: VAB - volcanic arc basalt; IAT - island arc tholeiite; CAB - calc-alkaline basalt; WPT – within plate tholeiite; WPB – within plate basalt; BABB – back-arc basin basalt; IAB – island arc basalt.

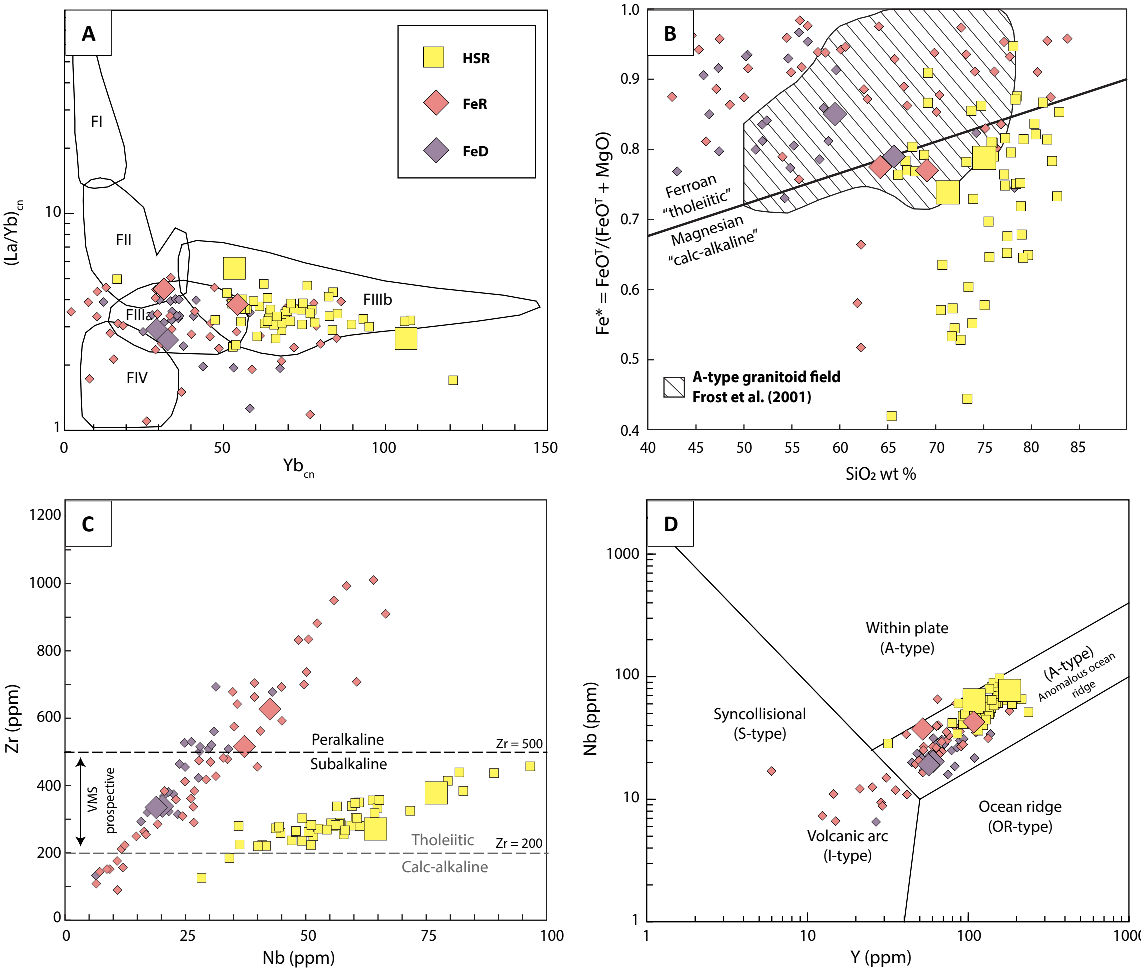

Fig. 2.14 Felsic tectono-magmatic discrimination diagrams (A-E). (A) Felsic volcanic fertility plot of Hart et al. (2004), where cn denotes chondrite-normalized values from Nakamura (1974). (B) The Fe* versus SiO_2 granitoid plot of Frost et al. (2001), showing the boundary between ferroan (tholeiitic) and magnesian (calc-alkaline) granitoids and the field for A-type granitoid rocks. (C) The Nb versus Zr VMS-prospective felsic diagram after Leat et al. (1986) and Piercey (2010). VMS-hosting felsic volcanic rocks are characterized by higher concentrations of HFSE (e.g., Zr > 200). Generally, tholeiitic felsic magmas have Zr between 200–500 ppm, and calc-alkaline felsic magmas have Zr < 200 ppm (Lentz, 1998). (D) The Y versus Nb granite discrimination diagram of Pearce et al. (1984b).

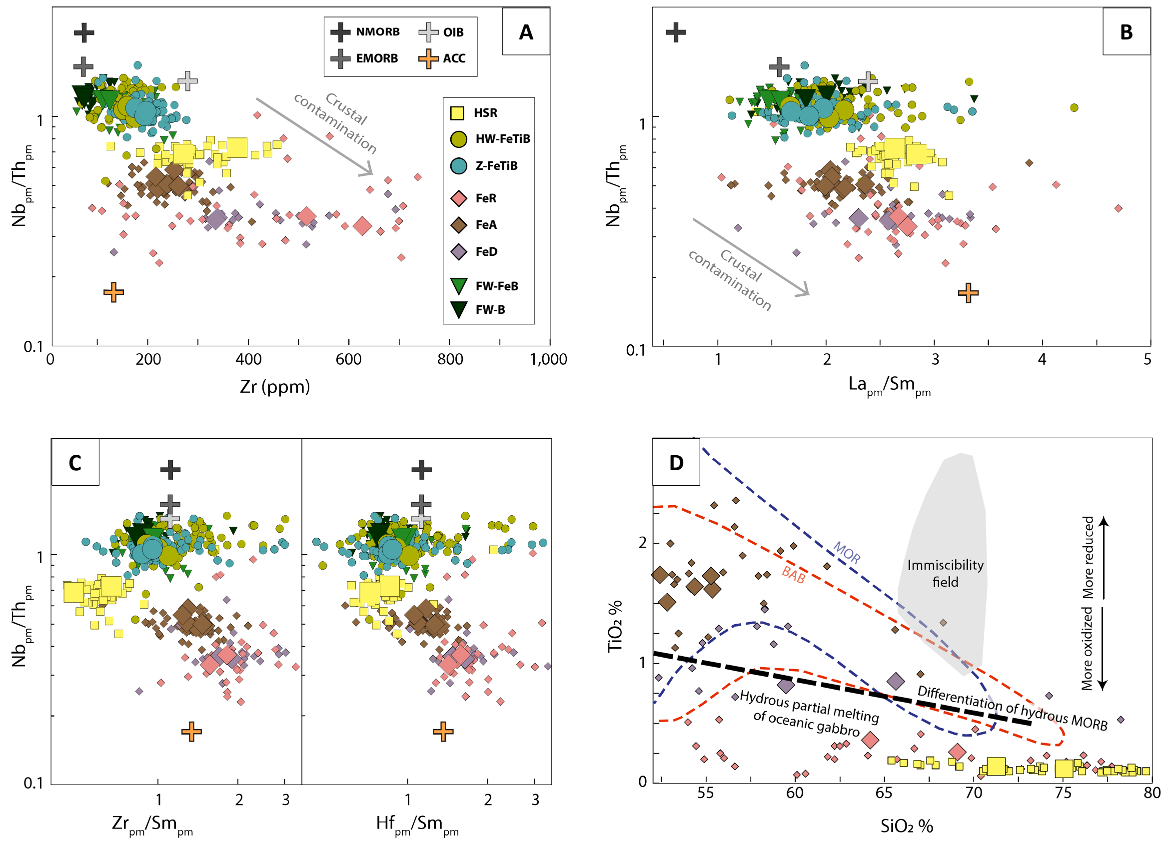

Fig. 2.15 Zr versus Nb_{pm}/Th_{pm} (A) and La_{pm}/Sm_{pm} versus Nb_{pm}/Th_{pm} (B) after Piercey et al. (2006) and Ordóñez-Calderón et al. (2016), indicating that crustal assimilation was minor for the FeTi basalts, but more significant for the silicic rocks. (C) Zr_{pm}/Sm_{pm} and Hf_{pm}/Sm_{pm} versus Nb_{pm}/Th_{pm}, showing that the Fe-rich silicic suite rocks have Zr and Hf enrichments relative to Sm. The HSR Hf_{pm}/Sm_{pm} values are like the basalts but have anomalously low Zr_{pm}/Sm_{pm}. For A-C, reference earth reservoir values are shown as crosses. Normal midocean ridge basalt (NMORB), enriched MORB (EMORB), and ocean island basalt (OIB) are from Sun and McDonough (1989). The average continental crust (ACC) is from Rudnick and Gao (2014). (D) SiO_2 versus TiO_2 plot of Koepke et al. (2007). The black dashed line marks the boundary between fields for Si-enriched volcanic melts experimentally derived from hydrous partial melting of oceanic gabbro versus those from fractional crystallization of hydrous MORB under oxidizing conditions. The field for Si-rich melts generated by liquid immiscibility is also shown. The fields for mid-ocean ridge (MOR) and back-arc basin (BAB) are from Koepke et al. (2007) and were constructed based on samples of Si-rich volcanic glasses collected from these settings.

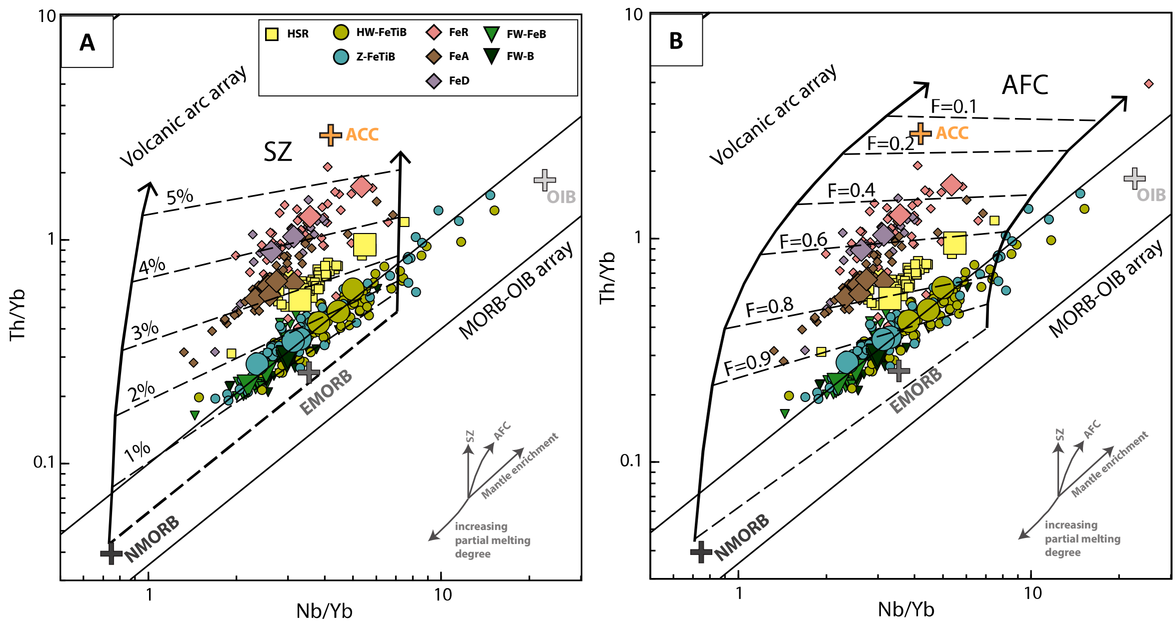

Fig. 2.16 Nb/Yb versus Th/Yb plots assessing magmatic differentiation trends and showing petrogenetic vectors (Pearce, 2008). (A) Vectors indicating the addition of subduction zone components (SZ) are given as a percentage. (B) Vectors indicating assimilation fractional crystallization (AFC) where F is the fraction of melt remaining after AFC based on r = 0.3 (assimilation rate relative to the crystallization rate). Reference earth reservoir values are shown as crosses. Normal midocean ridge basalt (NMORB), enriched MORB (EMORB), and ocean island basalt (OIB) are from Sun and McDonough (1989). The average continental crust (ACC) is from Rudnick and Gao (2014).

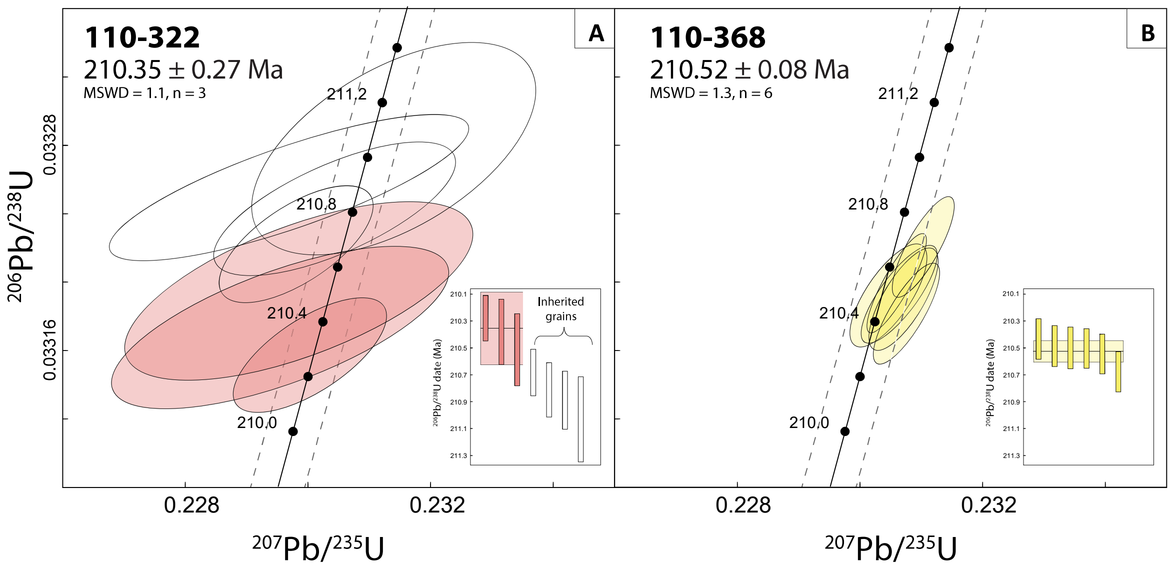

Fig. 2.17 Concordia diagrams displaying CA-ID-TIMS U-Pb dates from zircon grains in the felsic rocks of the AG stratigraphy. (A) FIIIa ferrorhyolite lapilli tuffs that underlie heterolithic fragmental rocks and are along strike of exhalative VMS mineralization. (B) Massive FIIIb high-silica rhyolites that intruded the ferroandesites (FeA) downhole of the ferrorhyolites. See Figs. 2.3 and 2.4 for sample locations. Colored ellipses and bars represent analyses used to calculate the weighted mean $^{206}Pb/^{238}U$ date. Each ellipse has uncertainties plotted at the 2σ error level. Dashed grey lines show the error due to the uncertainties in the U decay constants. Inset panels show the results of each single grain analysis and their 2σ error as vertical bars; the calculated weighted mean $^{206}Pb/^{238}U$ date is indicated by the horizontal solid black line and derived from the grains marked by colored bars; grains interpreted to be inherited in the FeR were not used to calculate the weighted mean $^{206}Pb/^{238}U$ date; the colored box behind the error bars indicates the weighted mean date. MSWD = mean square of the weighted deviates; n = the number of grains used to calculate the weighted mean $^{206}Pb/^{238}U$ date.

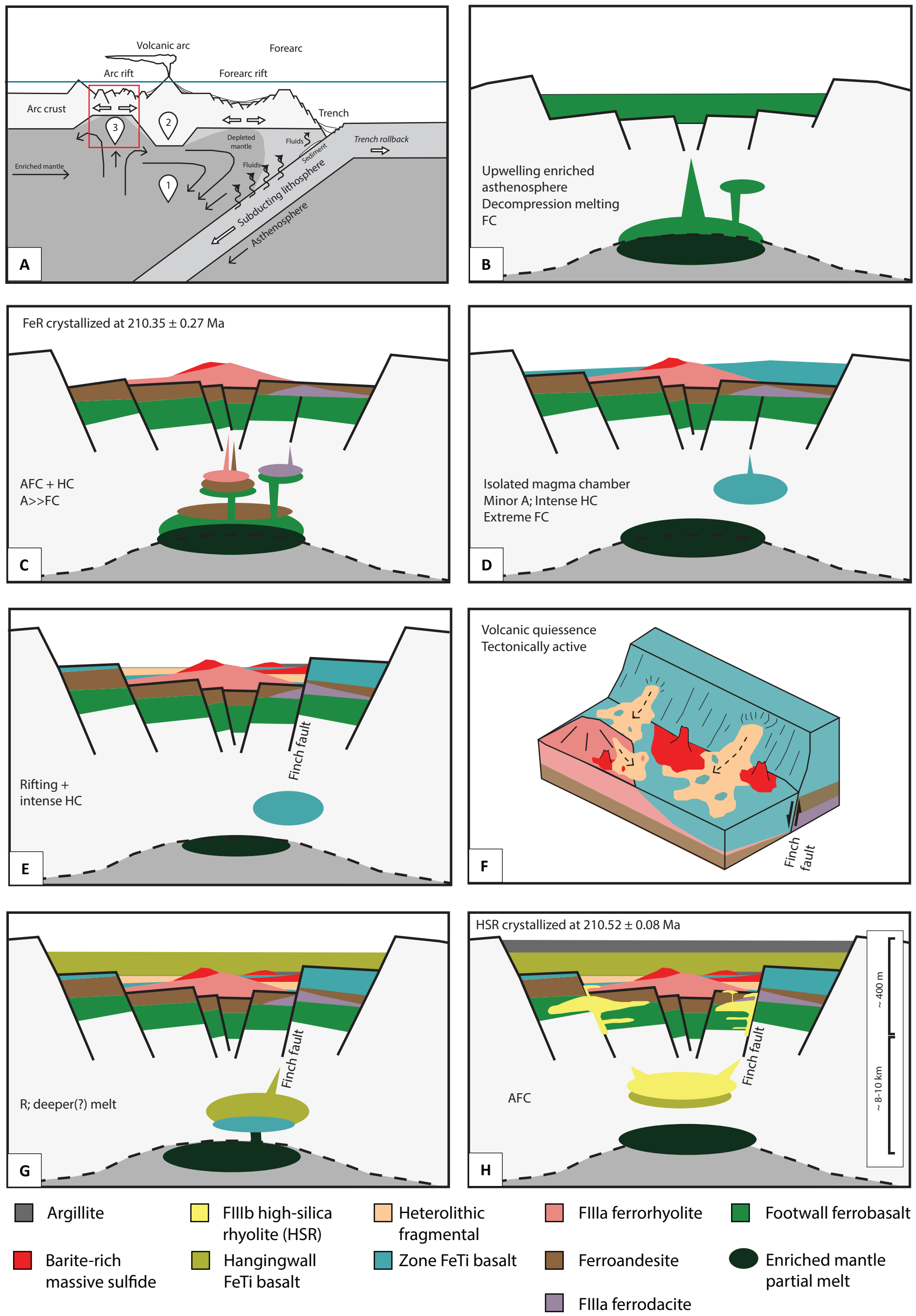

Fig. 2.18 Idealized schematic illustrating the tectono-magmatic evolution of the AG volcanic sequence (A-H). See text for details. (A) Schematic of an intra-oceanic island arc system after Stern (2010) and Hawkins (2003) showing melt generation in the metasomatized mantle wedge (1), within the arc crust (2), and at shallower levels in an unorganized rift basin beneath attenuated arc crust (3). The arc rift basin may eventually evolve to become a back-arc basin with true seafloor spreading. The red outline denotes the area represented by B-E and G-H. Abbreviations: A = assimilation, FC = fractional crystallization, R = replenishment, HC = hydrothermal circulation.

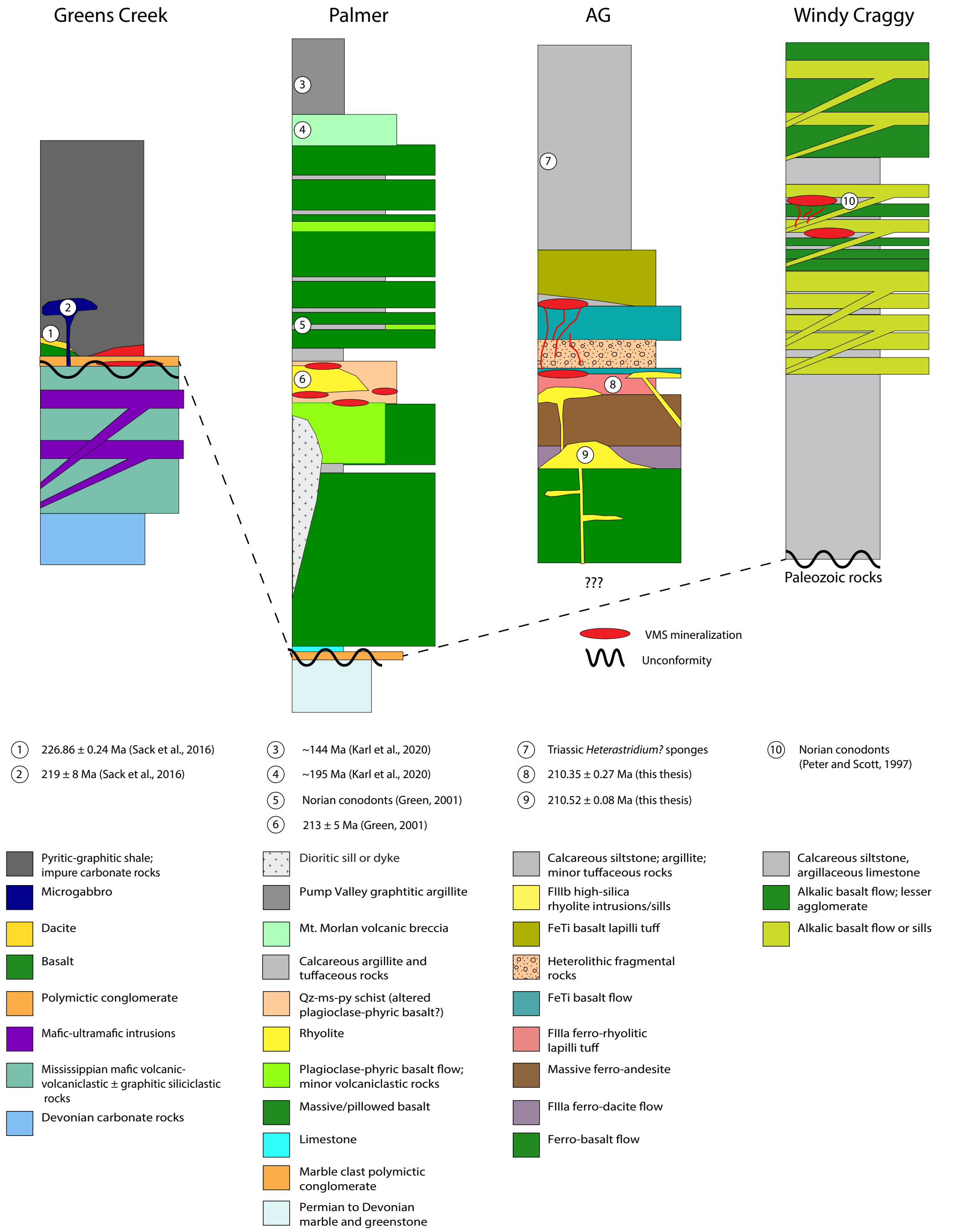

Fig. 2.19 Generalized stratigraphic columns of Greens Creek (unknown thickness), Palmer (~1,500–2,500 m), AG (~400 m), and Windy Craggy (~3,100–5,700 m). Data for Greens Creek are from Steeves (2018) and Sack et al. (2016); data for Palmer are from Green (2001), Steeves et al., (2016), Proffett (2019), and Karl et al. (2020); data for AG are from this study; data for Windy Craggy are from Peter and Scott (1997) and Peter et al. (2014).

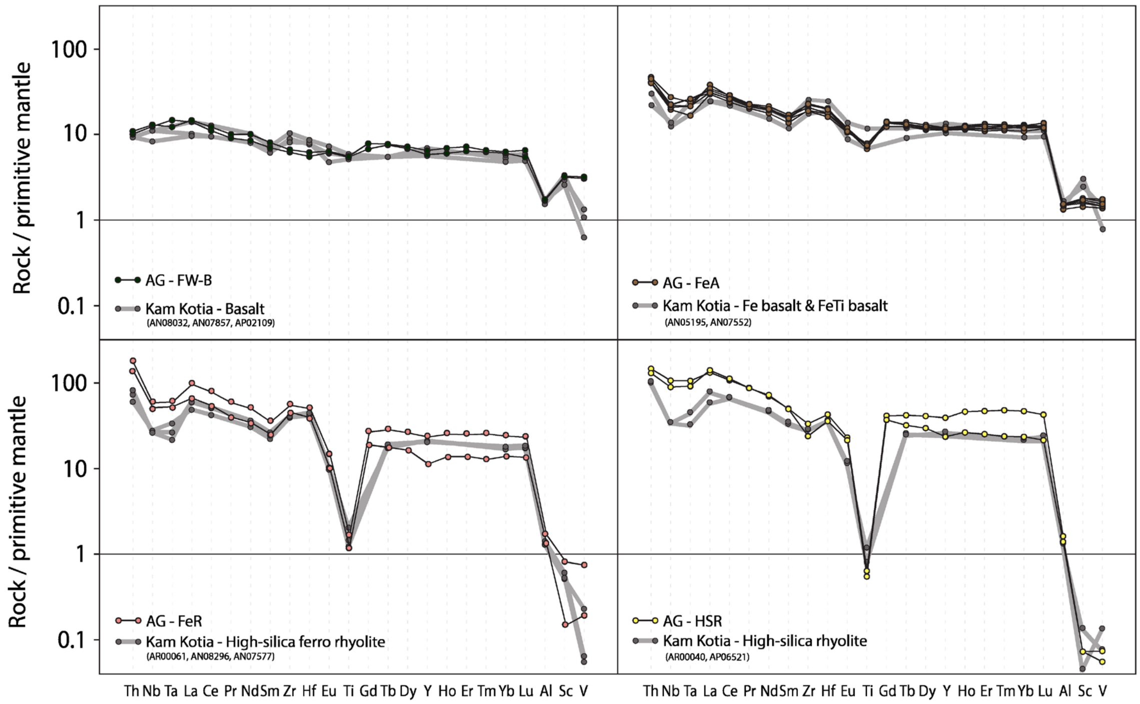

Fig. 2.20 Comparison of the multi-element primitive mantle normalized signatures of some volcanic samples from the Kam Kotia mine (Kamiskotia VMS camp; Upper Blake River Group) and some of the least altered samples in the AG volcanic stratigraphy. Kamiskotia samples are from Barrie and Pattison (1999), and sample ID labels are given on the plots. Primitive mantle (pm) values are from Sun and McDonough (1989).

Chapter 3. Summary and future research

The Late Triassic, bimodal-mafic polymetallic AG VMS deposit is hosted by FIII-type rhyolites and FeTi-rich basalts. The availability of a robust geochemical dataset (>800 whole rock geochemical samples) for the host rocks to the AG VMS deposit provided a unique opportunity to apply lithogeochemical methods to understand how its host volcanic succession formed. The integration of volcanic stratigraphy and lithogeochemical observations allowed for a greater understanding of the interplay between the magmatic, tectonic, and hydrothermal processes that formed the AG deposit. Furthermore, U-Pb geochronologic data has constrained the timing of VMS formation.

The major conclusions from this study include:

(1) Based on empirical diagrams, fractionation trends of the least altered samples, ratios of HFSE, and primitive mantle and chondrite normalized signatures, there are at least eight geochemically distinct volcanic units hosting the AG deposit that are grouped into four distinct magmatic suites: the footwall basalt suite (FW-B and FW-FeB), the Fe-rich silicic suite (FeA, FeD, and FeR), the FeTi basalt suite (Z-FeTiB and HW-FeTiB) and the high silica rhyolite suite (HSR). These geochemically defined magmatic suites are highly correlated with stratigraphic position allowing for chemostratigraphic reconstruction of the AG volcanic succession.

(2) From the base to the top of the stratigraphic section, the volcanic succession that hosts the AG deposit includes: (i) EMORB-like effusive pillowed flows of tholeiitic basalts, (ii) effusive flows of ferroandesites (FeA) and FIIIa ferrodacites (FeD), and FIIIa ferrorhyolite lapilli tuffs (FeR); all that have hybrid tholeiitic-calc-alkalic geochemical

signatures, (iii) pillowed flows of tholeiitic, FeTi-rich, variolitic basalts (Z-FeTiB) that are locally intercalated with heterolithic fragmental rocks, (iv) pyroclastic deposits of tholeiitic, FeTi-rich, basalts (HW-FeTiB). The volcanic succession is intruded by FIIIb high-silica rhyolite (HSR) syn-volcanic sills that occur at multiple stratigraphic levels.

(3) The footwall basalts formed by decompression melting of enriched asthenosphere and evolved by tholeiitic fractional crystallization. The Fe-rich silicic rocks were derived from ferrobasaltic magmas that assimilated partially melted arc crust and evolved by AFC processes. The Z-FeTiB formed by extensive tholeiitic fractional crystallization with minor crustal contamination. The HW-FeTiB are interpreted to be the products of pyroclastic eruptions triggered by magma recharge in a crustal magma chamber. The FIIIb HSR were derived from partially melted mafic arc crust and evolved further by fractional crystallization.

(4) Most of the AG deposit formed following the emplacement of the FIIIa FeR, followed by the Z-FeTiB and heterolithic fragmental rocks. The Finch fault is an important syn-volcanic structure that acted as a conduit for hydrothermal fluids and magmas. Most of the AG VMS mineralization is localized along this structure.

(5) The FeTi basalts and FIIIa FeR are identified as property- to belt-scale exploration targets. The FIIIb HSR sills and pyroclastic HW-FeTiB are locally hydrothermally altered, suggesting that they were also emplaced synchronous with hydrothermal activity and may also be important units to consider in exploration.

(6) The rocks hosting the AG VMS deposit probably formed in a propagating oceanic intra-arc rift associated with high temperature (T > 900ºC), shallow-level (<10 km from surface) magmatism where the development of synvolcanic structures, partial melting of enriched asthenosphere, extensive shallow-level crystal fractionation, assimilation of partially melted arc crust, and periodic magmatic replenishment were all important processes.

(7) The timing of the AG mineralization is constrained by two new high-precision CA-ID-TIMS U-Pb geochronology dates from hydrothermally altered FeR and HSR that have interpreted crystallization dates of at 210.35 ± 0.27 Ma and 210.52 ± 0.08 Ma, respectively. The overlapping date ranges suggest that the immediate volcanic host rocks to the AG deposit (FeR, Z-FeTiB, and HSR) were emplaced in less than one million years.

3.1. Directions for future consideration

This study has helped to provide a framework for future studies on other aspects of the AG deposit or for more in-depth studies on topics covered in this thesis. This research has successfully addressed many questions about the AG VMS deposit and, in doing so, has generated even more questions. Potential topics to explore in the future include:

(1) More detailed studies of each unique volcanic unit delineated in this study. Can the origins of the volcaniclastic units (FeR, heterolithic fragmental rocks, HW-FeTiB) be better understood by more detailed volcanic facies mapping? Understanding the origins of the volcaniclastic units would help to further refine the reconstructions of

the basin architecture. No petrographic work was done on the least altered samples of the FeA or FeD. If these are products of mantle-crust interaction, are any petrographic features preserved that would support this? These units immediately precede VMS mineralization at AG, and therefore they merit more detailed geologic descriptions than what was accomplished here. The HSR were interpreted as an intrusive complex, but is there any convincing evidence that some of the HSR could be extrusive? If so, this would have significant implications for how the tectono-magmatic evolution of the AG volcanic sequence is modeled. Sulfide-bearing argillite and exhalites like jasper and chert are spatially associated with VMS mineralization. What are their geochemical signatures like? What do these signatures tell us about their provenance and for the exhalites, the hydrothermal systems they originated from? How do their signatures compare to exhalites or metalliferous sedimentary rocks in other VMS districts?

(2) Application of chemostratigraphic and volcanic facies mapping studies to the larger AG deposit area. The stratigraphy on the Nunatak panel is parasitically folded and disrupted by several faults. Can the chemostratigraphic patterns of the JAG panel be used to unravel the complexities of the Nunatak panel? Within the general AG deposit map area, rocks in some outcrops remain undifferentiated and could be classified with the help of lithogeochemical investigations. Geochemistry in the West AG area has defined important units (HSR, FeR); perhaps the strongly altered volcanic stratigraphy in this area can be better mapped at the surface, knowing where some of these units occur. To the south of the JAG prospect, Z-FeTiB have been sampled in contact with exhalites like jasper. Could this bed of Z-FeTiB represent a limb of a north-closing anticline related to the deposit-scale syncline? AG West and AG East have prospective

units (HSR and FeR at AG West; FeR, HSR, and Z-FeTiB at AG East) that merit targeting with drill programs.

(3) More detailed alteration studies could help to map out alteration facies, identify fluid pathways, and unravel the geometry of the alteration zones (stinger, pipe, semi-concordant zone). These studies may help further refine the volcanic architecture model by highlighting vent sites. Furthermore, understanding the chemical reactions that produce alteration mineral assemblages and then quantifying the intensity and extent of the alteration to provide insight into the siting and style of the VMS mineralization and act as guides exploration efforts.

(4) Additional geochronologic studies. Dating the HSR sill at East AG that intruded the Z-FeTiB could provide a capping age of VMS mineralization. There are minor intermediate to felsic tuffs intercalated with sedimentary rocks above the HW-FeTiB that could also give a capping age of VMS mineralization. Acquiring high-precision U-Pb dates from zircons in these units may help to constrain how long it took for the AG VMS deposit to form. One rare sub-micrometer zircon was observed in a variole in the Z-FeTiB, so this unit is also a possible candidate for U-Pb dating. Re-analyzing the RW rhyolite in the Palmer deposit using modern U-Pb geochronology techniques, like CA-ID-TIMS, may help show if the AG and Palmer deposits are coeval or if VMS mineralization occurred at different times within the Palmer property stratigraphy.

(5) Application of chemostratigraphic and volcanic facies mapping studies to the entire Palmer property. Including the AG area, the Palmer property whole rock

lithogeochemical database includes ~ 2,700 samples analyzed by the same modern analytical techniques at the ALS laboratory in Vancouver (ALS code CCP-PKG03). Lithogeochemical studies at AG were critical to identify geochemically unique units, to recognize genetically related units, and to reconstruct the volcanic stratigraphy. The insights from this work could be used to train and test all other data on the property using machine learning methods. This may reveal what other types of rocks occur in the Triassic stratigraphy and if any volcanic successions at nearby prospects resemble the AG host stratigraphy. This could help to determine if VMS mineralization is confined to one stratigraphic level, or multiple. Using these insights could inform where to drill next to target new VMS mineralization or expand known VMS mineralization.

(6) Updated belt-scale studies that incorporate the insights gleaned from this thesis. Are FeTi basalts, FIIIa ferrorhyolites, and FIIIb high-silica rhyolites observed elsewhere in the ATMB? Can these belt-scale studies be used to identify potential VMS targets in the ATMB?

Appendix 1. Supplementary photographs of the AG deposit geology

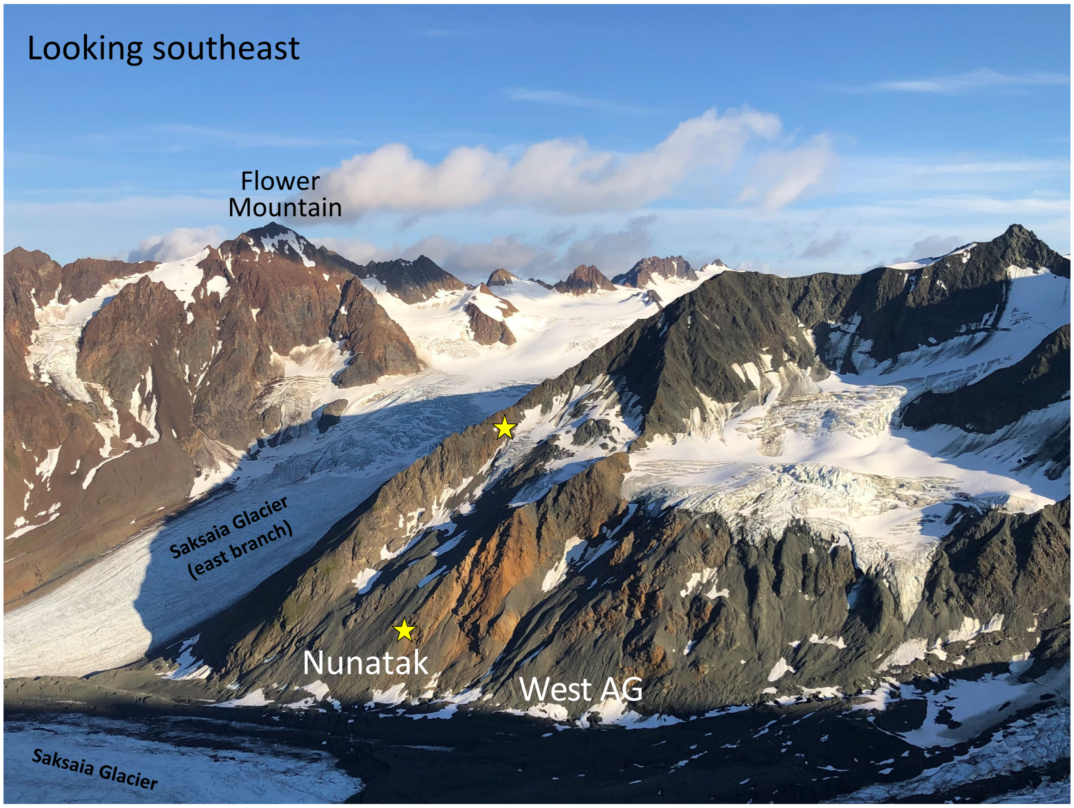

Fig. A1. 1 The AG deposit area (looking southeast). The yellow stars show the location of the Nunatak prospect (labeled) and the western continuation of the JAG prospect.

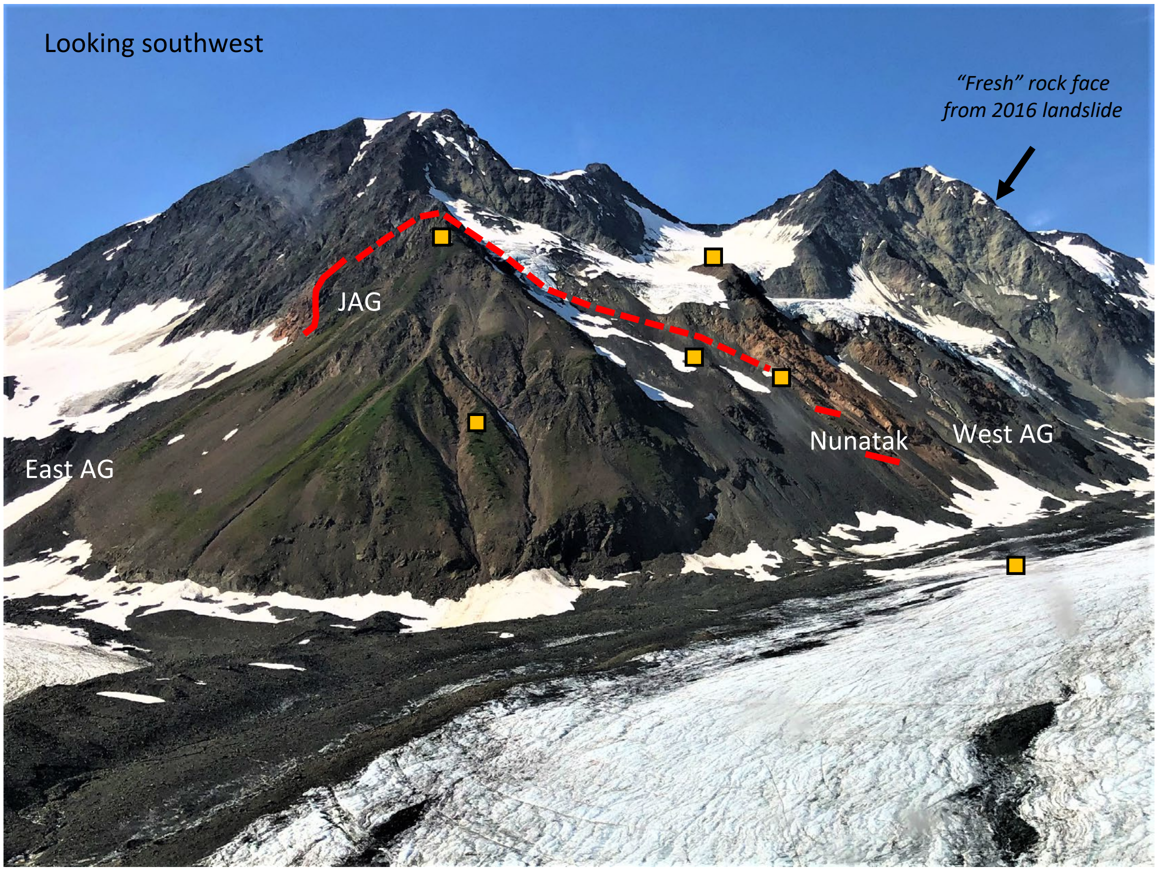

Fig. A1. 2 AG deposit area. Orange squares depict drill pad locations. The red line is the exhalative mineralization (solid) trace and concealed or equivalent stratigraphy to the mineralized zone (dashed).

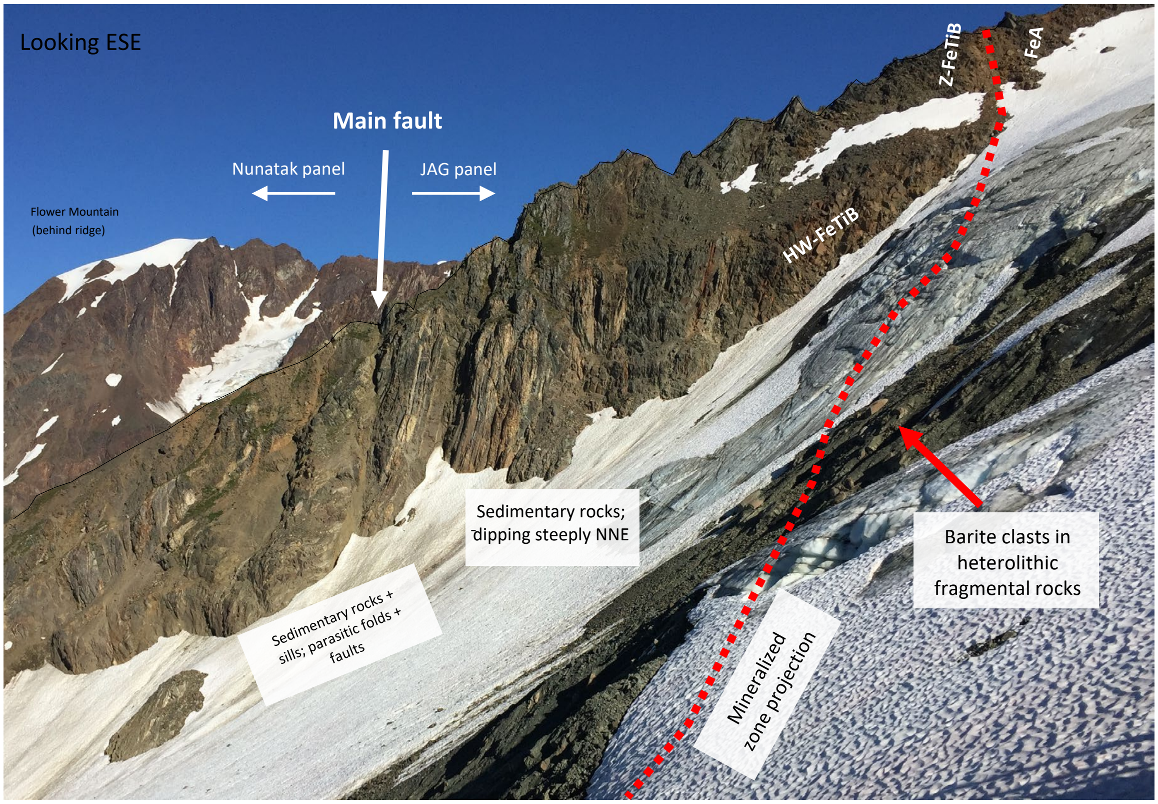

Fig. A1. 3 Ridgeline with exposures of folded and faulted sedimentary rocks in the capping sequence. The Main fault divides the Nunatak panel (north of the fault) from the JAG panel (south of the fault). Barite-clast-bearing heterolithic breccias are exposed in the glacially polished outcrops between glacial ice and talus and along strike of the Z-FeTiB.

Fig. A1. 4 Close-up photographs of the Main fault looking to the southeast.

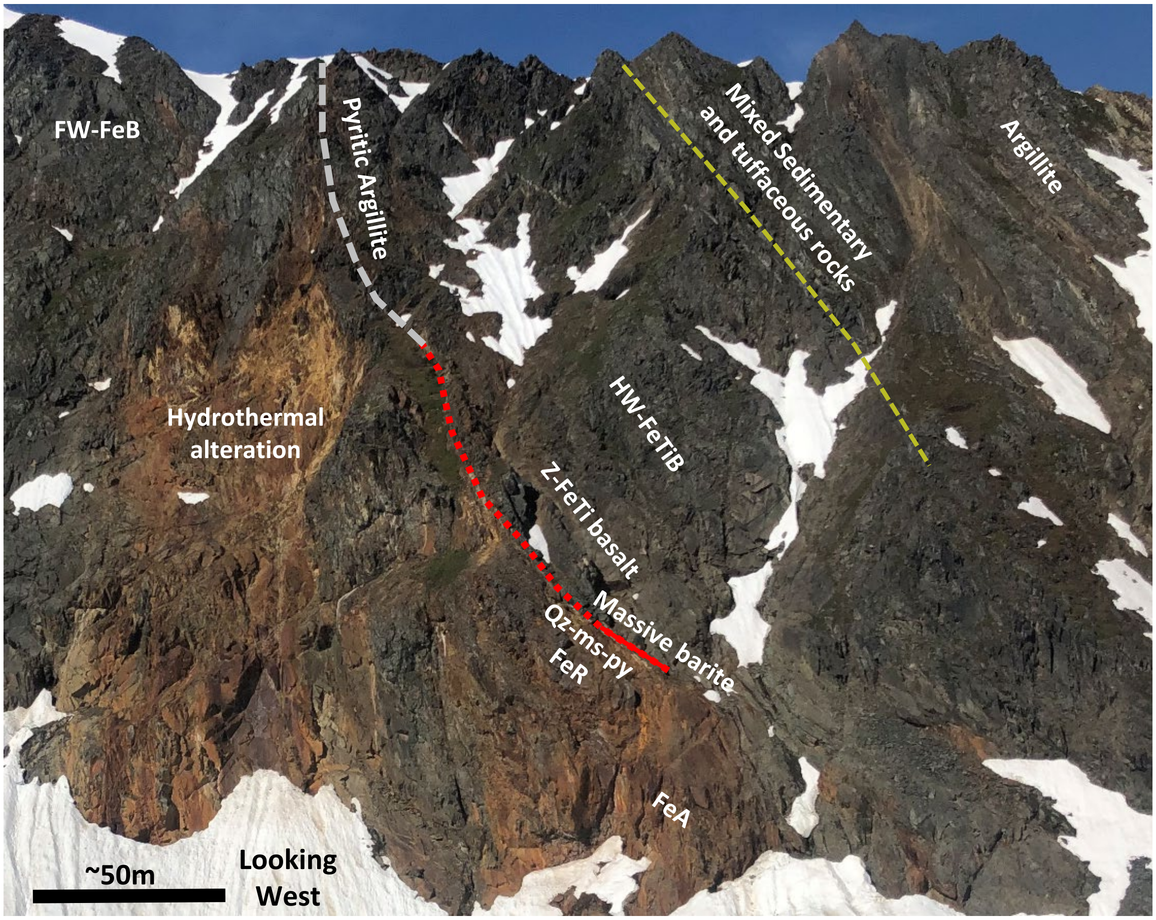

Fig. A1. 5 The JAG prospect geology.

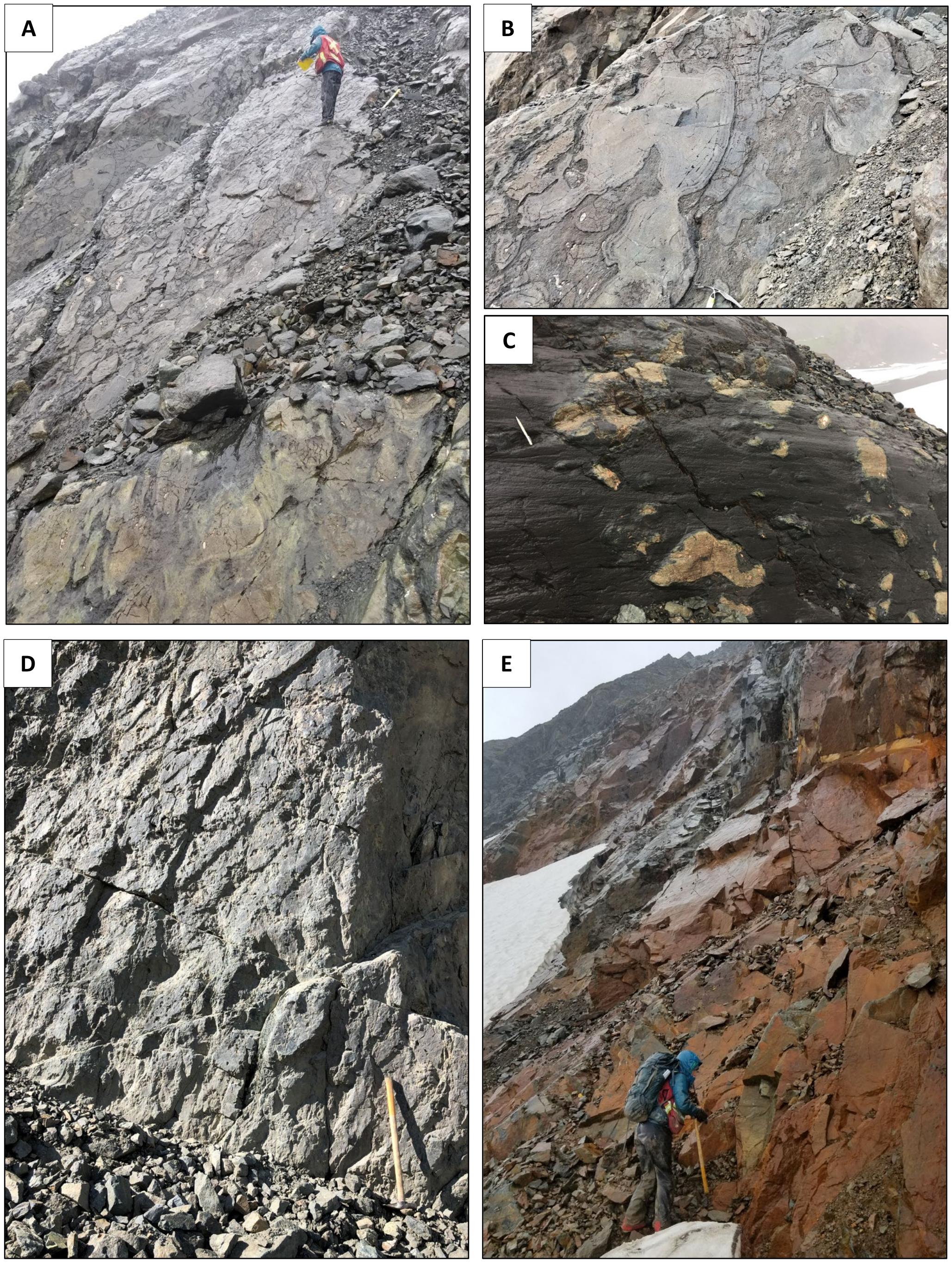

Fig. A1. 6 Outcrop photographs of coherent volcanic units in the stratigraphic footwall (A-E). (A-B) Pillowed ferrobasalts (FW-FeB) with tops to the north at East AG. Some of the FW-FeB have strong epidote. (C) The pillowed ferrobasalts grade into pillow breccias with pillow fragments that have quartz, chlorite, epidote, and locally garnet-bearing metamorphic assemblages. (D) Pillowed and lobate flows of the ferrodacites (FeD) located in the mapping area's northeast part. Pillowed tops are to the south. (E) Rust-stained cliffs of massive ferroandesites (FeA) in the stratigraphic footwall to the JAG prospect.

Fig. A1. 7 Drill core photograph of ferroandesite (FeA) with sparse feldspar phenocrysts. Sample W813093 in drill hole 112 @ 515.4 m.

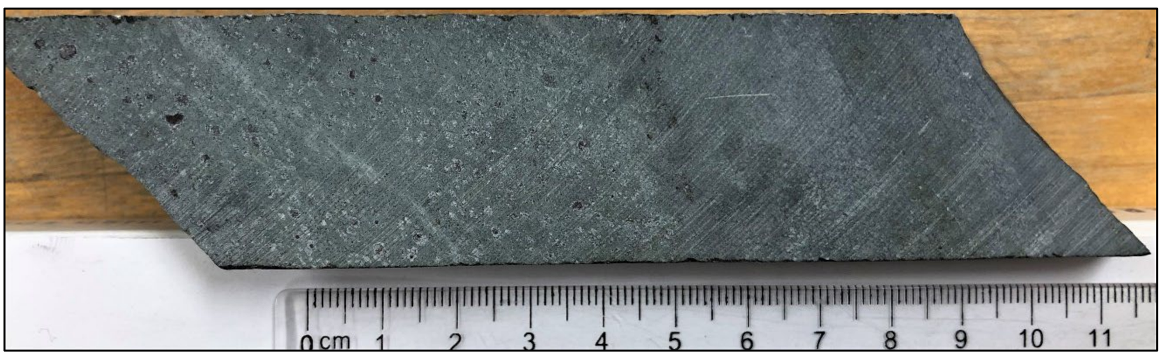

Fig. A1. 8 Drill core photograph of chlorite-altered, amygdaloidal ferroandesite (FeA). Sample W605024 in drill hole 120 @ 330.1 m.

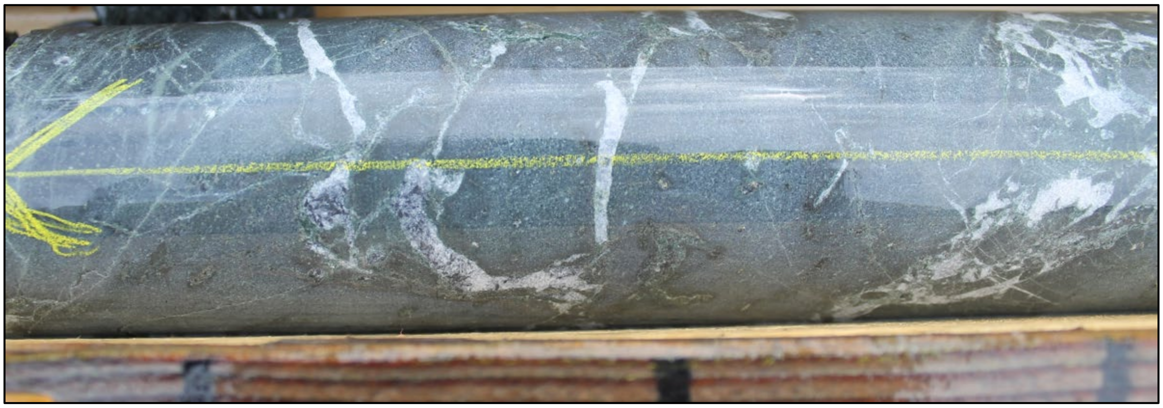

Fig. A1. 9 Drill core photograph of amygdaloidal ferrodacite (FeD). Sample W605516 in drill hole 114 @ 243.9 m.

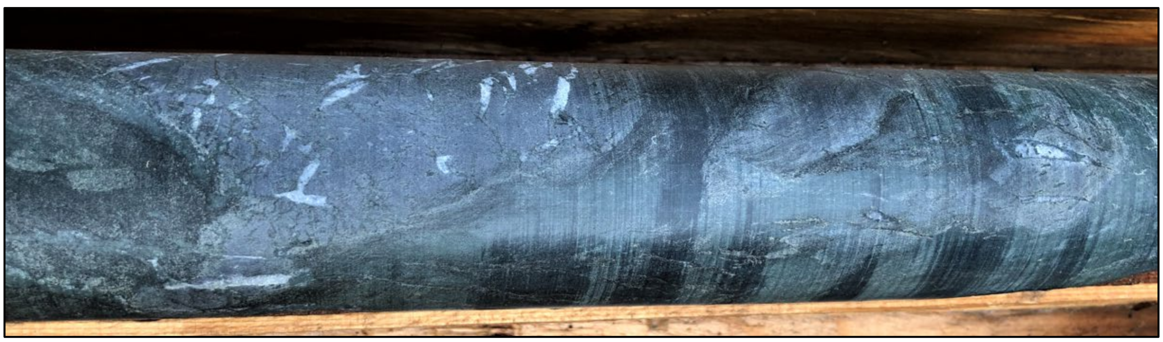

Fig. A1. 10 Pillowed textures of FeD with intense interpillow chlorite alteration. Photo taken in drill hole 112 @ 539 m.

Fig. A1. 11 High-silica rhyolite (HSR) dykes (pale grey) intrude weakly to moderately sericite- and pyrite-altered FW-FeB (medium to pale green, grey) in drill hole 109 @ 372.5 m. Both the HSR and FW-FeB are intruded by later green dykes.

Fig. A1. 12 Sharp contact between the HSR (paler color) and overlying FeA (darker) in drill hole 134B @ 207.5 m.

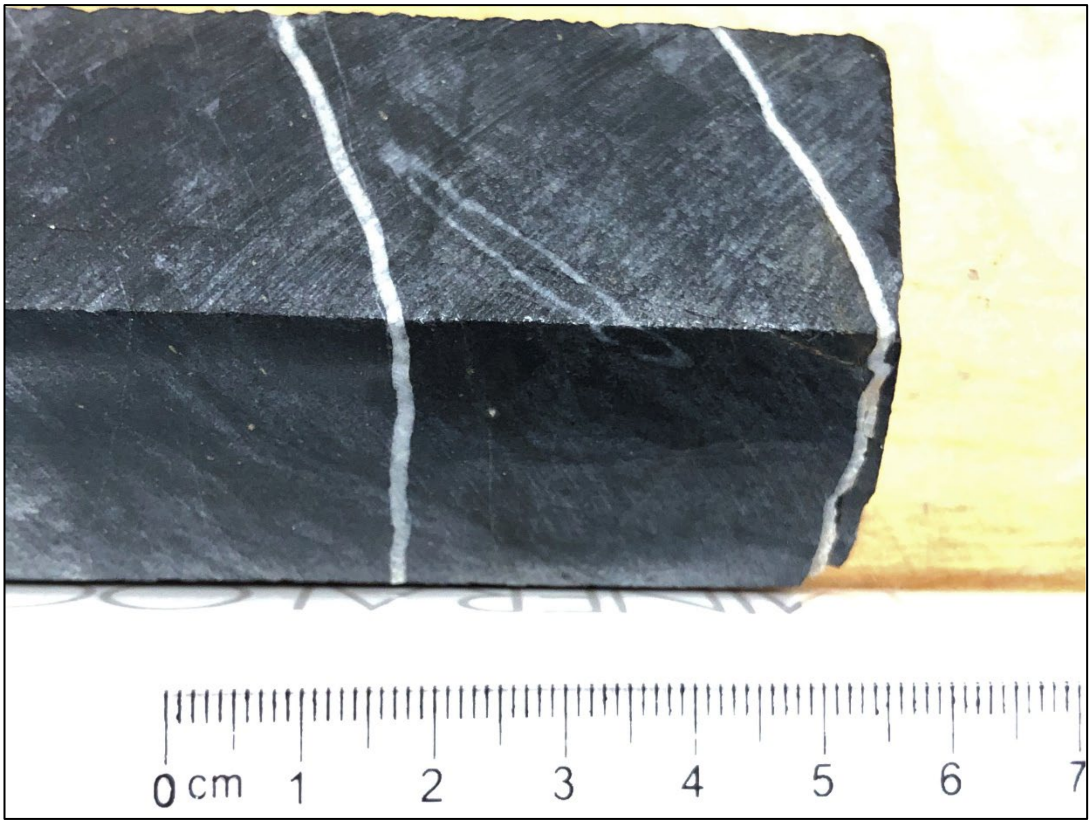

Fig. A1. 13 Argillite with rare oval-shaped fossil composed of calcium carbonate that is interpreted to be a Late Triassic sponge called *Heterastridium?* (drill hole 120 @ 87 m).

Fig. A1. 14 Exhalative-style barite-rich massive sulfide mineralization in drill hole 109 @ 206 m. Layers of honey-brown sphalerite contain disseminated sulfosalts and alternate with white, barite-rich layers.

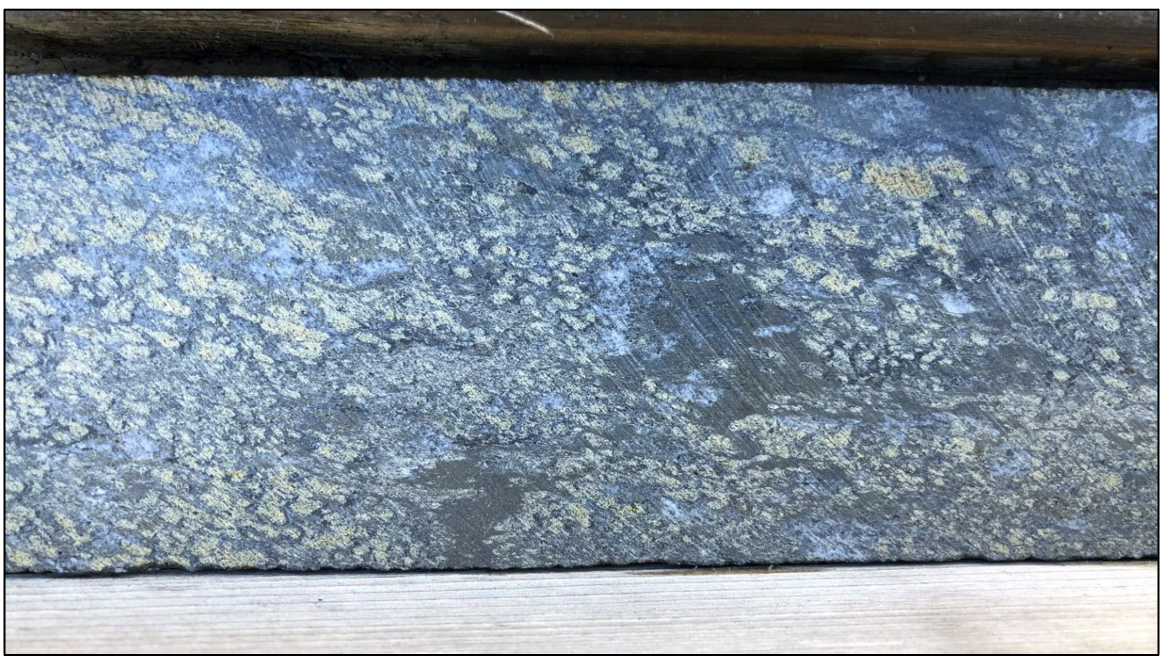

Fig. A1. 15 Replacement-style VMS mineralization in drill hole 110 @ 263.6 m. Blebby honey brown sphalerite and white barite replaced the tuffaceous matrix. Relic lapilli (darker shades) are replaced by very fine-grained sericite and pyrite.

Appendix 2. Petrographic descriptions, microphotographs, and backscattered electron (BSE) images

W605013 – Iron Formation

Sample ID: W605013

Drill hole: CMR18-120 **Drill hole depth (m):** 268.4 m

Rock Name: Jasper-clast bearing massive magnetite
Geochemical Suite: Chemical sediment/iron formation

Lithofacies and textures:
Clastic

Hand sample description:
60% dark grey vfg-fg massive magnetite. 40% red-white, subangular-subround jasper clasts 1 cm to >3 cm. Jsp clasts have "grainy" textures with vfg-cg 1-3mm, subround-round "grains". Tr cal vfg-fg blebs in clasts.

Petrographic description:
Euhedral grains (0.01-0.1mm) of mag and interstitial hematite with a "shreddy" appearance. Quartz and albite are interstitial. Rare barite and chlorite. Amoeboid jasper clast >2.5cm and composed of qz with up to 15% vfg specks of red translucent (PPL) mineral (Fe-ox?), that likely imparts red hue. Ovoid features within jasper amoeboid are 0.3-1 mm and composed of qz and outlined by mt – perhaps original colloidal gel-like features?

Mineral	Residence	%	Size max (μm)	Habit	Comments
Muscovite	Groundmass	50%	50?	Fibrous, platy	Aligned grains define moderate foliation, interconnected fibrous wisps weave around qz grains. Probably replacing all primary fsp.
Quartz	Groundmass, micropheno (qz-eye), vein	40%	320	Subround, qz-eyes, interstitial	Most grains are 0.05 - 0.1 mm. Some grains are rounded and may possibly be quartz eyes? Some of the more elongate grains are weakly aligned to foliation. Some qz is interstitial to muscovite.
Epidote	Groundmass, vein	5%	220	Subhedral, Tabular, lath, skeletal	Locally twinned crystal growth, up to 0.22mm, dirty appearance in PPL.
Allanite	Cores of epidote crystals	1%	40	Subhedral	Local cores of epidote crystals that mirror epidote crystal shape. Hosting LREE - spectra for La-Ce-Nd observed using the SEM.
Magnetite	Groundmass	1%	100	Euhedral-subhedral, equant	Probe work determined this to be stoichiometric magnetite with lower Ti-V compared to mag in basalt samples. Hydrothermal(?) or igneous (with low Ti-V reflecting low abundances in rhyolitic melt).
Apatite	Groundmass	Trace	20	Anhedral-subhedral	F-bearing spectra.
Zircon	Groundmass	Trace	160	Euhedral	Larger isolated euhedral xls (some cracked) or tiny clusters containing vfg xls.
Chlorite	Qz-eye?	Rare	100	Flakey	Within a qz-eye(?) associated with epidote. Typically, not in muscovite-rich part of groundmass.
Albite	Groundmass	Rare	10	Interstitial	10-micron area between muscovite identified with SEM.
Rutile	Groundmass	Rare	0.1	Anhedral-euhedral, acicular	Main Nb-host. Grains too small to get spectra free from interference (common to see Fe-Si from ep-qz). Vary from acicular to anhedral blebs.

Fig. A2. 1 Hand sample photograph (above) and thin section scan (below) of sample W605013.

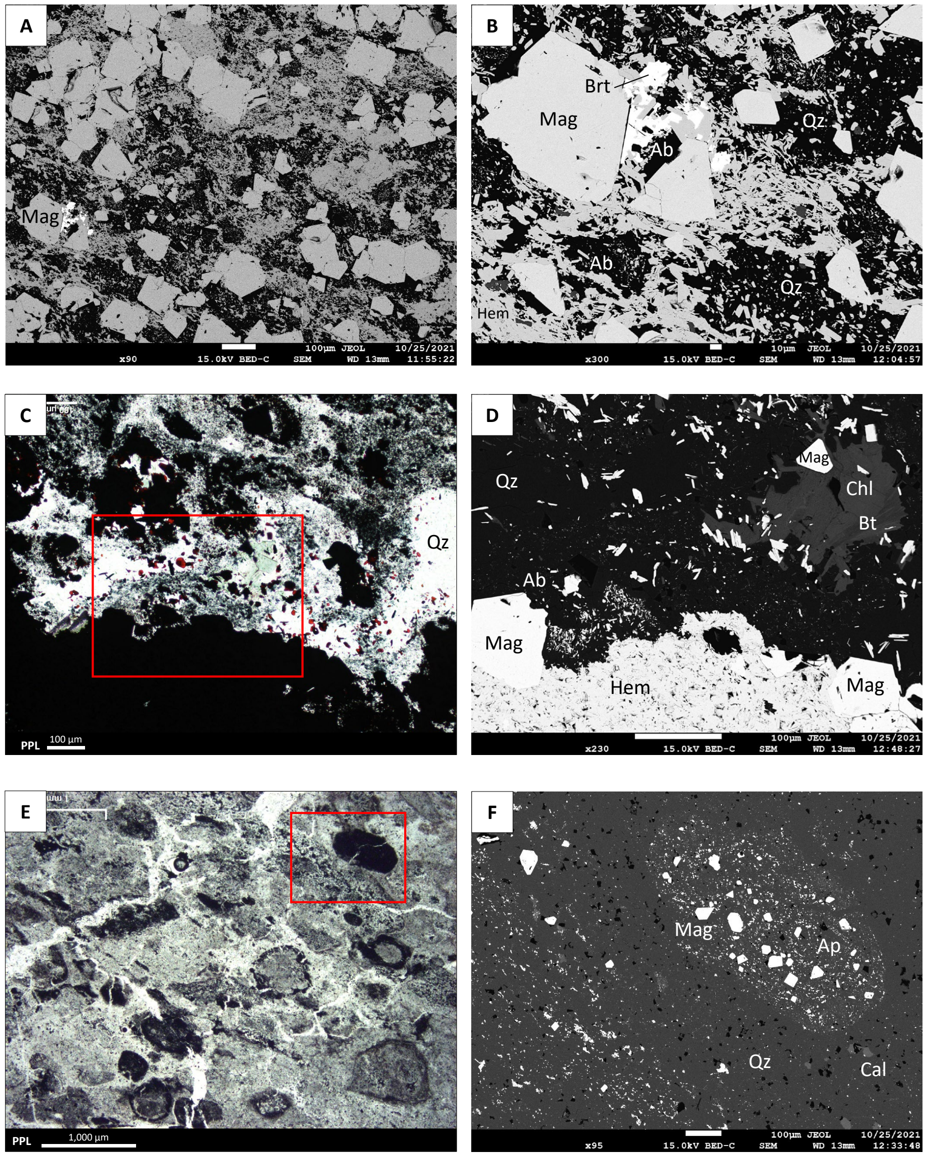

Fig. A2. 2 (A-F) Microphotographs of sample W605013. (A-B) BSE images of massive euhedral magnetite with albite, quartz, and shreddy-textured hematite in between the larger grains. Minor barite along some grain boundaries. (C-D) Edge of massive magnetite section where it contacts more quartz- and jasper-rich section in PPL (C) and an BSE image (D). The red box in (C) is the same area in (D). In PPL, oxidized FeTi oxide mineral (rutile?) are tiny red specks that impart red colour to jasper. (E-F) The jasper-rich section has ovoid features (colloidal gels?) shown in PPL (E) and one ovoid feature (outlined in red box) is shown in an BSE image in (F). The ovoid feature is made up of fine-grained magnetite, quartz, and sparse, very fine-grained apatite.

W605041 - HSR

Sample ID: W605041

Drill hole: CMR18-120 **Drill hole depth (m):** 443.4m

Rock Name: Ms-qz-ep, qz-eye bearing, massive rhyolite
Geochemical Suite: FIIIb High-silica rhyolite (HSR)

Lithofacies and textures:
Massive, foliated
Aphanitic, aphyric, qz-eyes (?)

Hand sample description:
Aphanitic light gray massive rhyolite with greenish hue imparted by ep. Sparse discontinuous greenish streaks of ep +/- chl. Tr fg-mg blebs of mt.

Petrographic description:
Groundmass is dominated by wispy vfg muscovite ("sericite") that weaves around vfg-fg qz grains, some of which are rounded and composed of a single qz crystal that may be qz-eyes. All fsp gone to ms, except rare interstitial albite. Epidote is the predominant mafic mineral, commonly skeletal with resorbed crystal edges and locally contains cores of allanite. Apatite is F-bearing.

Vein:
0.02-0.34mm quartz-epidote vein, pinches and swells, contains largest ep crystals

Mineral	Residence	%	Size max (μm)	Habit	Comments
Muscovite	Groundmass	50%	50?	Fibrous, platy	Aligned grains define moderate foliation, interconnected fibrous wisps weave around qz grains. Probably replacing all primary fsp.
Quartz	Groundmass, micropheno (qz-eye), vein	40%	320	Subround, qz-eyes, interstitial	Most grains are 0.05 - 0.1 mm. Some grains are rounded and may possibly be quartz eyes? Some of the more elongate grains are weakly aligned to foliation. Some qz is interstitial to muscovite.
Epidote	Groundmass, vein	5%	220	Subhedral, Tabular, lath, skeletal	Locally twinned crystal growth, up to 0.22mm, dirty appearance in PPL.
Allanite	Cores of epidote crystals	1%	40	Subhedral	Local cores of epidote crystals that mirror epidote crystal shape. Hosting LREE - spectra for La-Ce-Nd observed using the SEM.
Magnetite	Groundmass	1%	100	Euhedral-subhedral, equant	Probe work determined this to be stoichiometric magnetite with lower Ti-V compared to mag in basalt samples. Hydrothermal(?) or igneous (with low Ti-V reflecting low abundances in rhyolitic melt).
Apatite	Groundmass	Trace	20	Anhedral-subhedral	F-bearing spectra.
Zircon	Groundmass	Trace	160	Euhedral	Larger isolated euhedral xls (some cracked) or tiny clusters containing vfg xls.
Chlorite	Qz-eye?	Rare	100	Flakey	Within a qz-eye(?) associated with epidote. Typically, not in muscovite-rich part of groundmass.
Albite	Groundmass	Rare	10	Interstitial	10-micron area between muscovite identified with SEM.
Rutile	Groundmass	Rare	0.1	Anhedral-euhedral, acicular	Main Nb-host. Grains too small to get spectra free from interference (common to see Fe-Si from ep-qz). Vary from acicular to anhedral blebs.

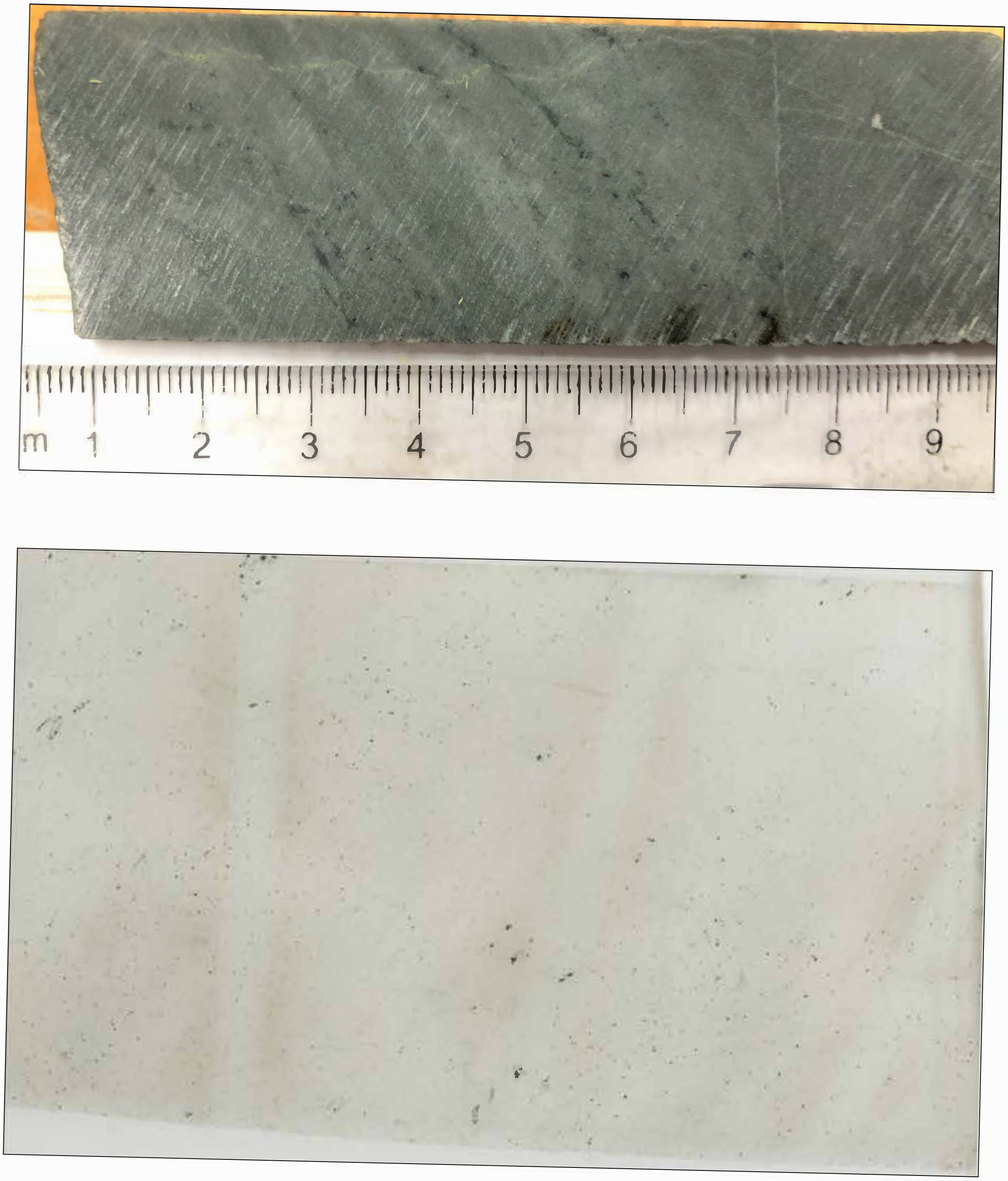

Fig. A2. 3 Hand sample photograph (above) and thin section scan (below) of sample W605041.

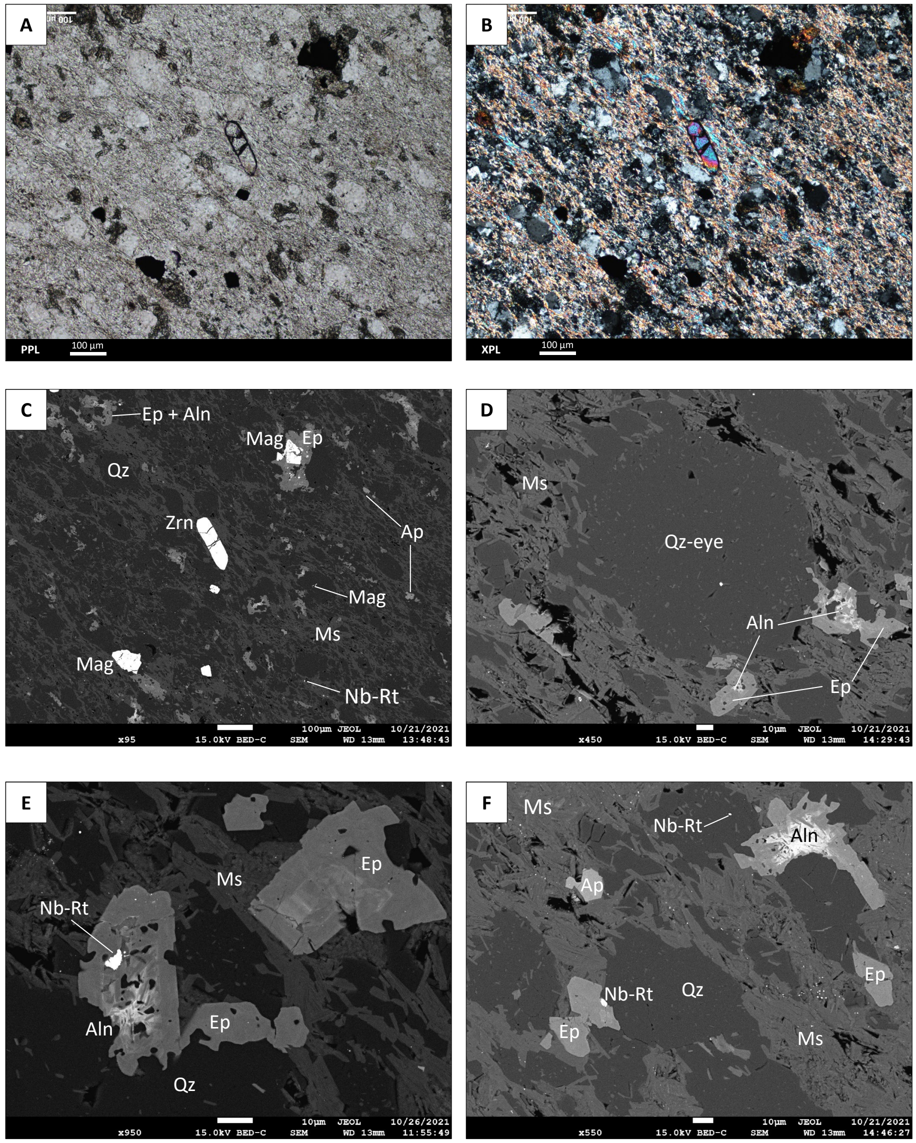

Fig. A2. 4 Microphotographs of sample W605041. (A-C) show the same area in PPL (A), XPL (B) and an BSE image (C). A euhedral zircon crystal is within a groundmass of muscovite with qz-eyes and disseminated epidote. Epidote locally has allanite cores (brighter in BSE image) with Ce, La, and Nd spectra. Apatite and magnetite are accessory phases. Trace Nb-rich rutile grains. (D) BSE image of a quartz eye surrounded by muscovite and quartz. A few epidote crystals have allanite cores. (E) BSE image of epidote crystals with zoned pattern and allanite (brighter shade) interiors. A bleb of rutile with Nb EDS spectra is within the epidote grain. (F) BSE image of muscovite and quartz groundmass with accessory phases of epidote and apatite. A Nb-bearing rutile grain is along the edge an epidote crystal, and another is within a quartz-rich part of the rock. The tiny, bright disseminated specks are zircon, and some are Nb-bearing rutile.

S039314 – HW-FeTiB

Sample ID: S039314

Surface Sample - UTM NAD 83 Zone 8N
Easting: 419917 m **Northing:** 6581736 m **Elevation:** 1436 m

Rock Name: Chl-mag-qz-bt-ms-carbonate, laminated tuff
Geochemical Suite: Hangingwall FeTi basalt (HW-FeTiB)

Lithofacies and textures:
Laminated, shards, crossbedding?

Hand sample description:
Laminated basaltic tuff. Dark green, chl- and mag-rich layers alternate w/ beige-tan-pinkish qz- and ms-rich layers. One lam w/ purplish hematite. Moderately pervasive fizzy.

Petrographic description:

Laminations are up to 1cm, and there are at least three differentiable compositions.

The dominant laminations are chl- and mag-rich. Chl (55%), qz (15%), mag (10%), bt (5%), carbonate (5%), ms (5%) and trace euhedral py with rare cpy blebs. Py is 0.08-1mm and mag generally less than 0.04mm. Some of the opaque features in PPL look like cuspate, Y-shaped to platy shards.

Creamy pink layers - Qz- and ms-rich layer with minor vfg mag (5%) wisps and patches of vfg brown crud. Minor chl.

Vfg reddish-brown layers: Two layers. One is 5mm and is vfg dark brownish crud (PPL) with 5% qz +/- ms+/- chl subround to subangular features and the other is a 2.1mm lam with wavy, deformed internal structure.

Mineral	Residence	%	Size max (µm)	Habit	Comments
Chlorite	Matrix	55		Anhedral, recrystallized	Recrystallized tuffaceous material?
Magnetite	Matrix, shards	10		Subhedral, euhedral	Some oxidized. Commonly outlines shapes of shards.
Quartz	Matrix	20		Anhedral	
Carbonate	Matrix	5			Recrystallized tuffaceous material?
Biotite	Matrix	5			Vfg cruddy brown material
Muscovite	Matrix	5			Cryptocrystalline
Pyrite	Disseminated	Trace		Subhedral to euhedral	Some spongey w/ ccp inclusions. Commonly rimmed by mag.
Chalcopyrite	Inclusions in py	Rare		Anhedral	Rare blebs as inclusions in spongey py grains

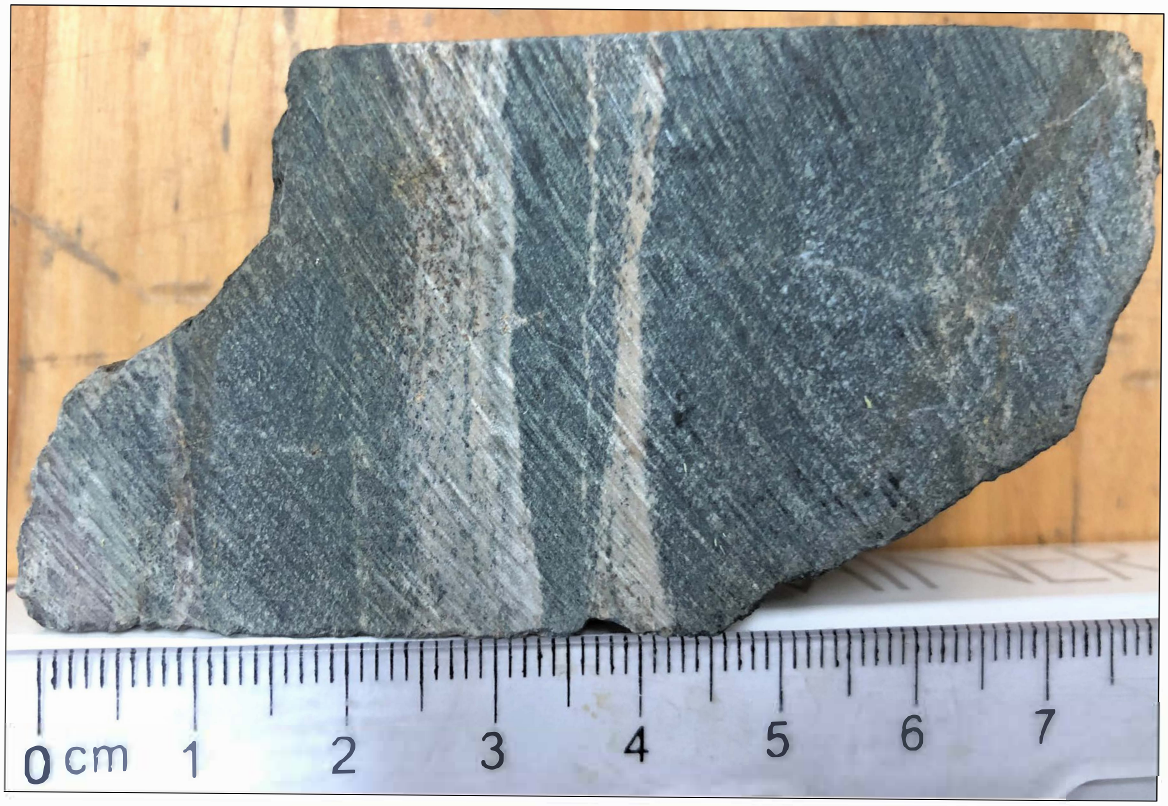

Fig. A2. 5 Hand sample photograph (above) and thin section scan (below) of sample S039314.

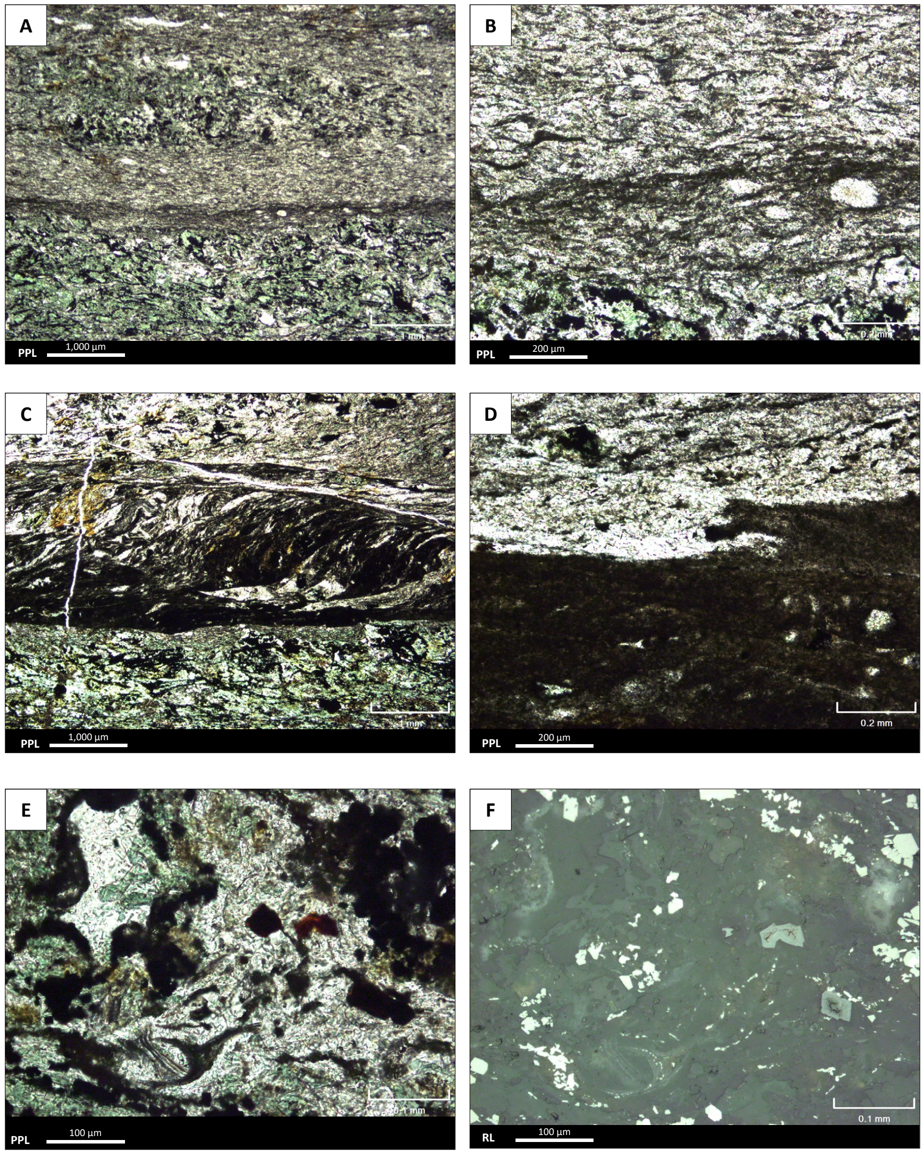

Fig. A2. 6 Microphotographs of sample S039314 (A-F). (A-B) The pinkish, very fine-grained, and smooth layers (middle layer in FOV in A) are composed of quartz, muscovite, and magnetite (PPL). (B) Close up of the pinkish layer with the more chlorite-, magnetite-, and carbonate-rich layer at bottom of FOV (PPL). Opaque minerals are FeTi oxides (probably magnetite) that outline Y-shaped shards. (C) A 2.1mm lamination of the reddish-brown layer with wavy, deformed internal structure that may be crossbedding? The layer below is chlorite rich. (D) Flame-like bedding structure between the quartz- and muscovite-rich lamination (top FOV) and the very fine-grained dark brown layer (bottom FOV). (E-F) Cuspate, 0.15mm Y-shaped shard in chlorite-rich layer is outlined by opaque minerals (FeTi oxides; probably magnetite). The matrix is quartz, chlorite, magnetite, muscovite, and carbonate with patches of brown, grungy material. Some oxidized FeTi oxides are reddish in PPL (E) and darker grey in RL (F).

S039313 – HW-FeTiB

Sample ID: S039313

Surface Sample - UTM NAD 83 Zone 8N
Easting: 419917 m **Northing:** 6581736 m **Elevation:** 1436 m

Rock Name: Qz-mag-ms-chl, laminated, tube pumice(?)-bearing basaltic lapilli tuff
Geochemical Suite: Hangingwall FeTi basalt (HW-FeTiB)

Lithofacies and textures:
Matrix-supported, poorly sorted, tube-pumice(?), scoria(?), shards

Hand sample description:
Laminated tan-brown-pink-orange tuff with 15% diss clots of massive mag up to 1cm. Some laminations are pinkish w/ more concentrated fg mag. Very weak pervasive calcite (fizzy). Some wormy chl-mag veinlets. Weak-mod pervasive very fine-grained muscovite (“sericite”).

Petrographic description:

The lighter tan layers are composed of ms-qz with minor chl. Some of these contain abundant cuspate (Y- to X-shaped) and platy shards. The shards were likely originally glassy and are devitrified to vfg FeTi-oxide minerals (magnetite and/or rutile). Layers with a pinkish hue have clusters of cryptocrystalline minerals with a deep reddish-brown hue in PPL. These brownish patches are mainly composed of a mixture of vfg chl-bt-qz and rutile, locally with some ms and dark blebs of glass. The BSE image reveals that rutile locally forms polygonal networks and is filled with qz-bt-chl.
The larger dark clots are predominantly composed of recrystallized, euhedral magnetite grains (commonly with vfg qz inclusions). They have spongey interiors composed mainly of qz, some Fe-Ti oxides and minor muscovite-chl. Lapilli (~3%) contain abundant ovoid qz +/- ms +/- chl +/- carbonate features rimmed by vfg mag. If the ovoid features are amygs, then these are scoria. Some of these abundant-ovoid lapilli between larger mag-clots have a stretched-out, ductile appearance and could possibly be tube-scoria fragments that resemble reticulite (“thread-lace scoria”) with a honeycomb texture. These ovoid-rich lapilli commonly warp around margins of the larger mag clots. The groundmass of the lapilli is rutile, mag, qz, chl, ms, apatite and rare epidote, allanite, and albite. The mag clots are likely primary lapilli that are strongly altered and recrystallized. Disseminated cubes of vfg-fg mag throughout all laminations, and especially abundant in the pinkish layers. Larger mag xls are commonly spongey. Magnetite is near stoichiometric endmember with ulvospinel content averaging 0.1 %. Rutile is Nb-bearing.

Mineral	Residence	%	Size max (µm)	Habit	Comments
Quartz	Matrix, clasts, ovoids	40		Anhedral, interstitial	
Magnetite	Clasts, matrix	20	500	Subhedral, euhedral	Recrystallized, spongey cubes in larger clots. In smaller lapilli, finer grained and can be intergrown with rutile and outline ovoid features. Generally stoichiometric, but a few grains have some Ti-enrichment, but not enough to be ilmenite. Some of the mag grains have more hematite-like chemistry at their rims. Possible hem in center of a few ovoids.

Muscovite	Matrix, clasts, ovoids	20		Fibrous	Intergrown w/ chl. Most abundant in matrix but can be in groundmass of lapilli and in ovoid features.
Chlorite	Matrix, clasts	7		Fibrous	
Biotite	Matrix, clasts	5		Fibrous	Intergrown w/ chl-ms.
Rutile	Clasts, matrix	5	20	Anhedral to euhedral	Blebby masses or acicular needles, most common in groundmass of lapilli. Imparts reddish-brown hue (PPL) to parts of tuffaceous matrix where intergrown w/ chl-ms-bt.
Ankerite	Matrix, clasts	1			Interstitial bits in matrix or in clasts.
Calcite	Matrix, clasts	1			Interstitial bits in matrix or in clasts.
Apatite	Clast	Trace			Most common as blebs intergrown w/ rutile in the groundmass of the lapilli surrounding ovoid features
Epidote	Clast	Trace			Rare in groundmass of lapilli
Allanite	Clast	Trace			Rare in groundmass of one lapilli. Has La, Ce, Nd in SEM spectra.
Albite	Clast	Trace			Some interstitial blebs in groundmass of one basaltic lapilli

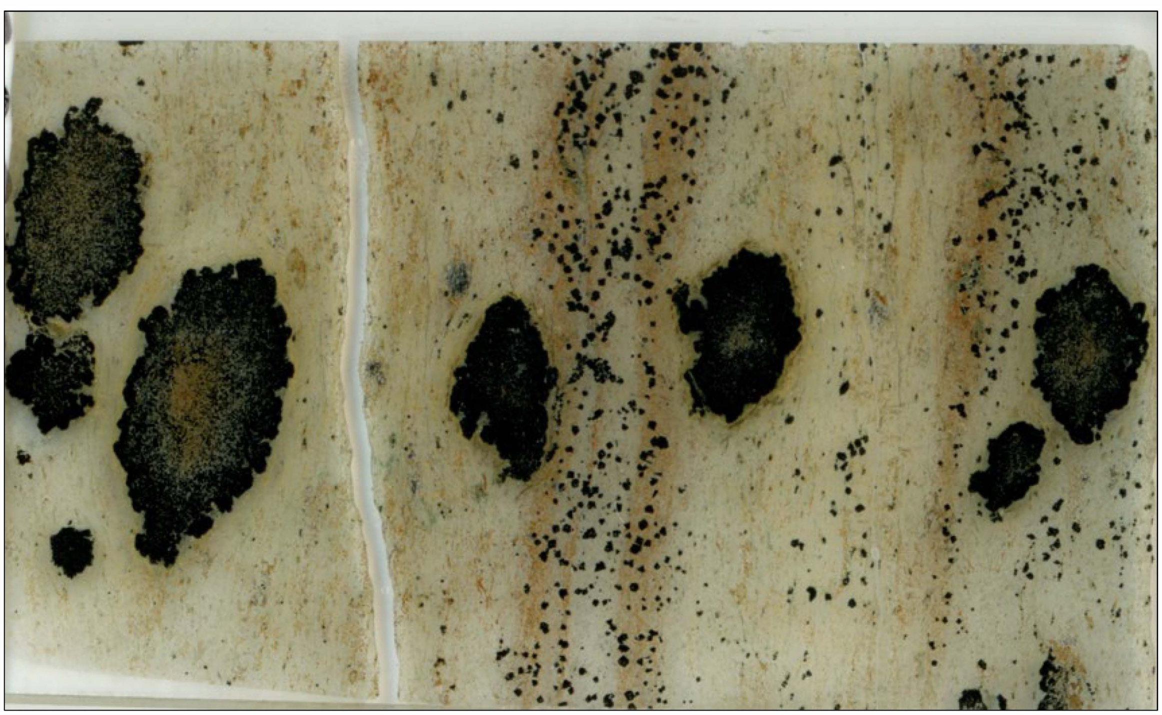

Fig. A2. 7 Hand sample photograph (above) and thin section scan (below) of sample S039313.

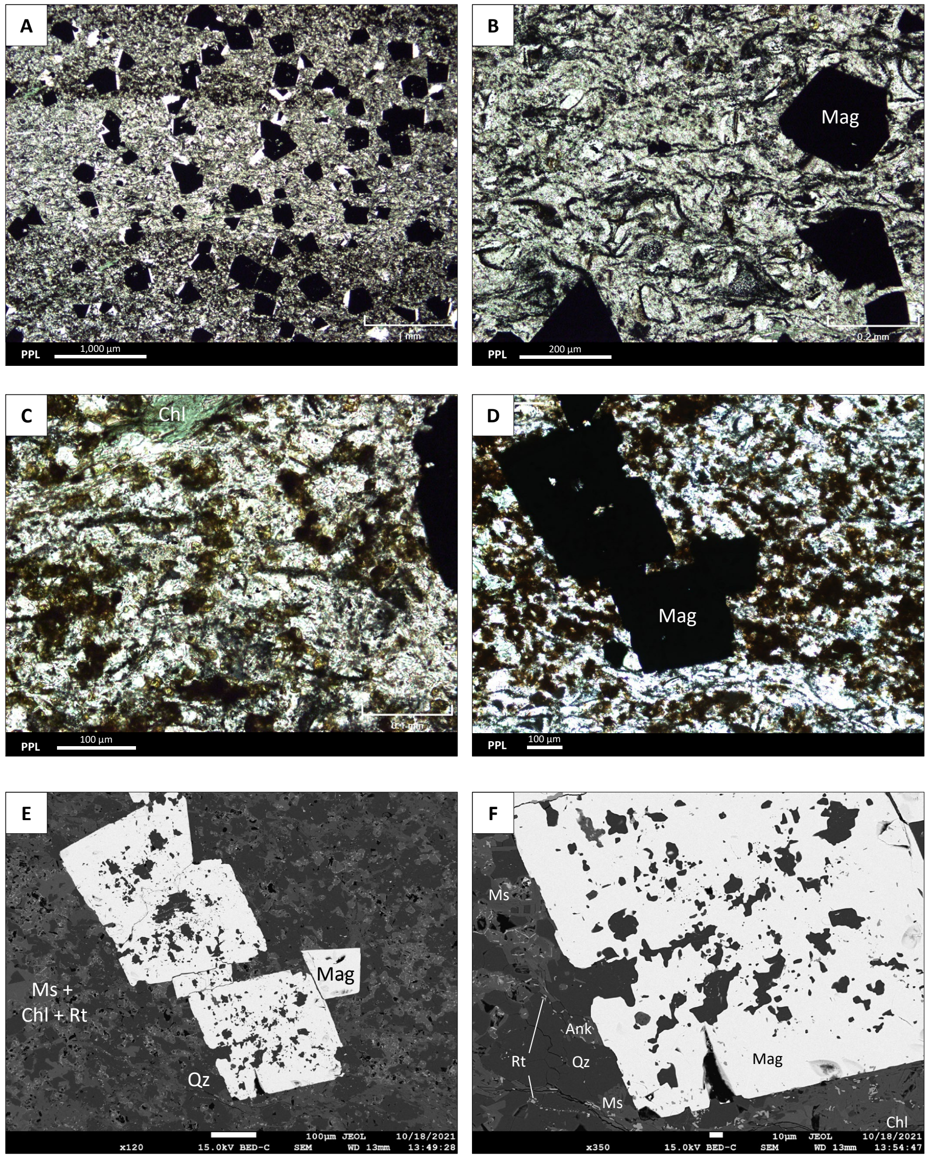

Fig. A2. 8 (A-E) Microphotographs of tuffaceous laminations with disseminated magnetite. (A) Layers with a pinkish hue in hand sample are the top and bottom layers in this FOV and contain more opaque rutile, and the paler tan-colored layer is in the middle and is more quartz- and muscovite-rich (PPL). (B) Cuspate (Y- and X-shaped) shards in the more tan-colored layer. (C-F) Microphotographs of the layers with a more pinkish hue. (C-D) In PPL, this layer has brownish-red patches. (E-F) BSE images reveal that the tuffaceous material is a mixture of very fine-grained rutile needles, muscovite, chlorite, and quartz. Euhedral magnetite crystals are spongey and contain inclusion of matrix minerals, like quartz.

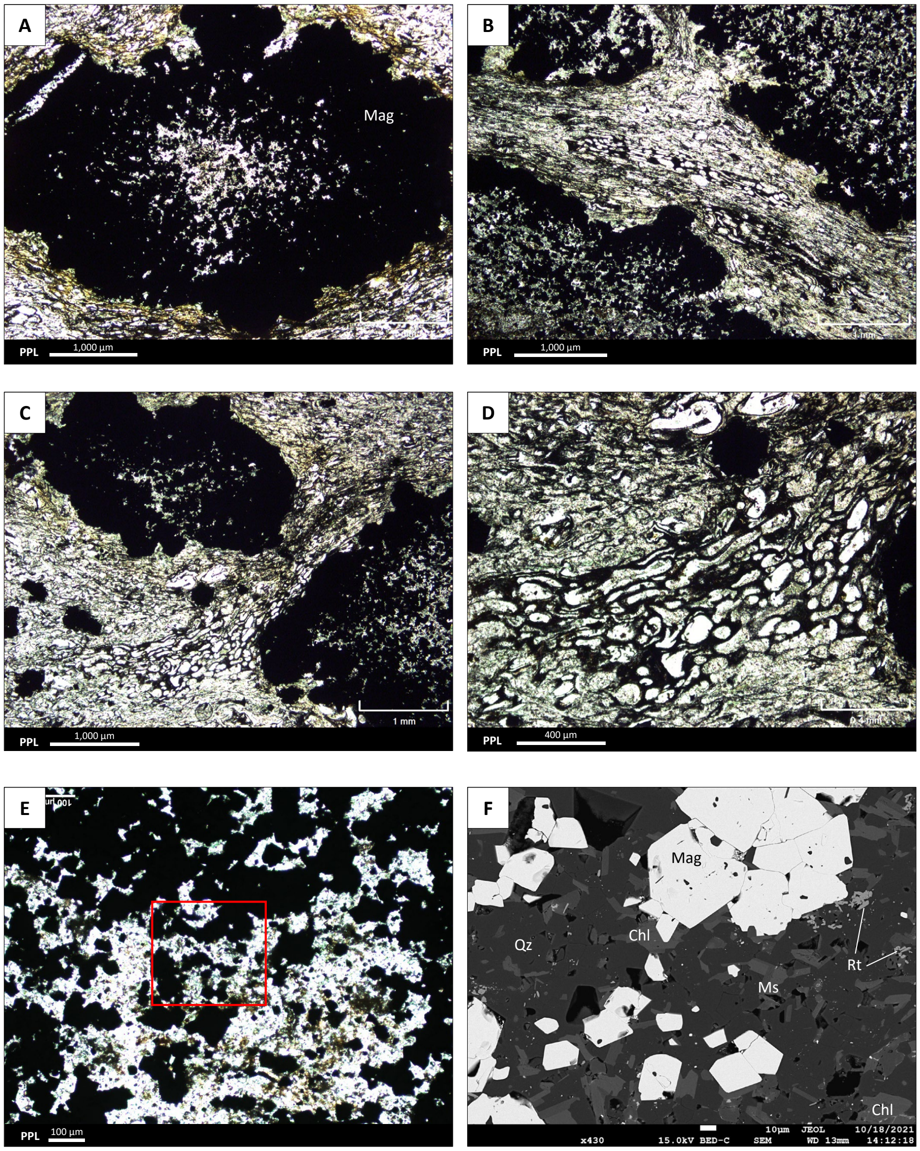

Fig. A2. 9 (A-E) Microphotographs of the larger magnetite-rich clots (likely recrystallized basaltic lapilli). (B-D) Between the larger magnetite-rich clots, there are deformed, stretched-out tuff to lapilli-sized fragments of basaltic material with abundant ovoid features (amygdules?) that may be tube pumice. (E-F) Microphotographs from the center of the magnetite-rich clots. The red box in (E) marks the location of the BSE image in (F). The center of the magnetite clot is composed of quartz, chlorite, and muscovite and has minor clusters of very fine-grained rutile needles.

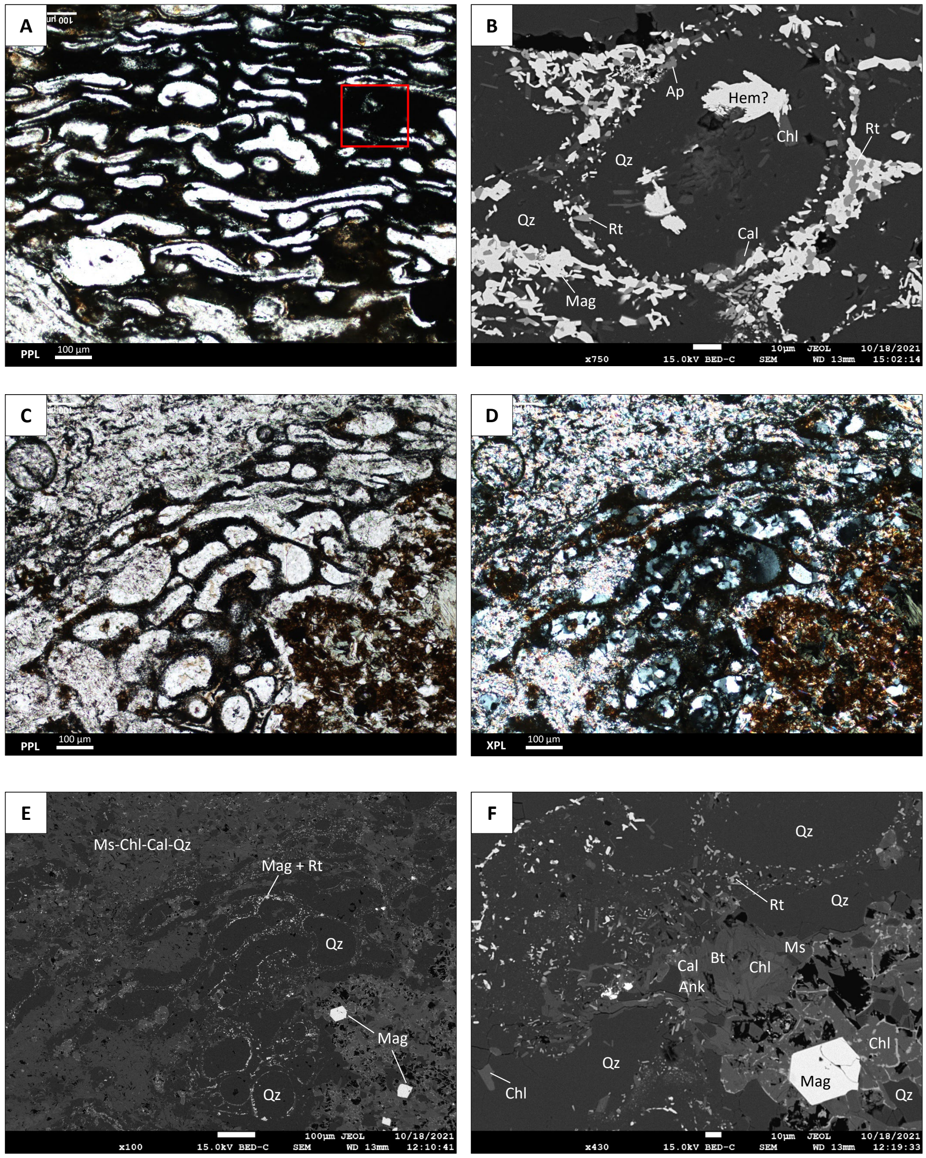

Fig. A2. 10 Microphotographs of some of the lapilli to tuff sized fragments that contain abundant ovoid features (amygdules?). (A) The opaque FeTi oxide minerals are magnetite and rutile with possible rare hematite that outline the ovoid features. The red box in (A) marks the location of the BSE image in (B). (C-D) Microphotographs of the ovoid-rich lapilli within a tuffaceous matrix composed of muscovite, chlorite, and quartz with some calcite. The ovoid features are quartz, and some have muscovite, chlorite. The brown cruddy material (PPL) is composed of very fine-grained intergrown biotite, chlorite, quartz, muscovite, and rutile. The rutile locally forms polygonal networks.

94-31 – HW-FeTiB

Sample ID: 94-31

Drill hole: CMR17-94 **Drill hole depth (m):** 31 m

Rock Name: Chl-qz-cal-mag basaltic tuff with sparse lapilli and fsp crystals (?)
Geochemical Suite: Hangingwall FeTi basalt (HW-FeTiB)

Lithofacies and textures:
Tuffaceous-rich, poorly-moderately sorted

Hand sample description:
Fg-mg, green, magnetic, tuffaceous-rich volcaniclastic with 20% chloritic, angular 0.5–2 mm grains, and 10% white, qz-rich, 1-2mm grains in a pale green (ms + chl?) finer-grained matrix. White cal interstitial. Rare dark grey vfg 2mm clast. Trace orange fecarb blebs associated with chloritic parts.

Petrographic description:
Distinguishing clast versus matrix is challenging due to tuffaceous nature of rock that has irregular, recrystallized chl-mag versus qz-ms-carbonate domains. A few convincing lapilli with distinct margins are either mainly qz-ms, or chl-mag (mixed lapilli compositions?) One chl- and mag-rich lapilli has irregular, winged, cuspate margins and a core composed of ankerite. Some mag-chl clasts have interconnected mag that outlines round chl features that could be relic amygs or spherulites. One 2.8 mm oval-shaped lapilli has alternating ms-rich and qz-rich layers that create a concentric zoning pattern reminiscent of armored lapilli. A few domains where shreddy muscovite is concentrated may represent relic pl xls. Magnetite is near stochiometric endmember, ulvospinel content averages 0.1 %. Rutile is Nb-bearing. Some of the muscovite has Ba spectra peak.

Mineral	Residence	%	Size max (µm)	Habit	Comments
Chlorite	Matrix, clasts	40		Anhedral	Anhedral masses of lapilli or tuffaceous patches
Magnetite	Matrix, clasts	10	40	Subhedral, euhedral	Associated w/ chl. Locally outlines lapilli
Quartz	Matrix, clasts	25			Associated w/ ms-carbonate tuffaceous domains. Recrystallized
Calcite	Matrix, clasts	15	100		Associated w/ qz-ms tuffaceous domains.
Muscovite	Matrix, clasts	10			Shreddy patches. Forms layers in the one concentrically zoned lapilli.
Ankerite	Matrix, clasts	Tr	100		Rare within core of chl-mag lapilli. Some blebs in tuffaceous matrix.
Rutile	Matrix, clasts	Tr	20		Disseminated
Apatite	Matrix, clasts	Tr	20		Disseminated
Epidote	Matrix	Tr	10	Subhedral, euhedral	Sparse clusters of xls in matrix

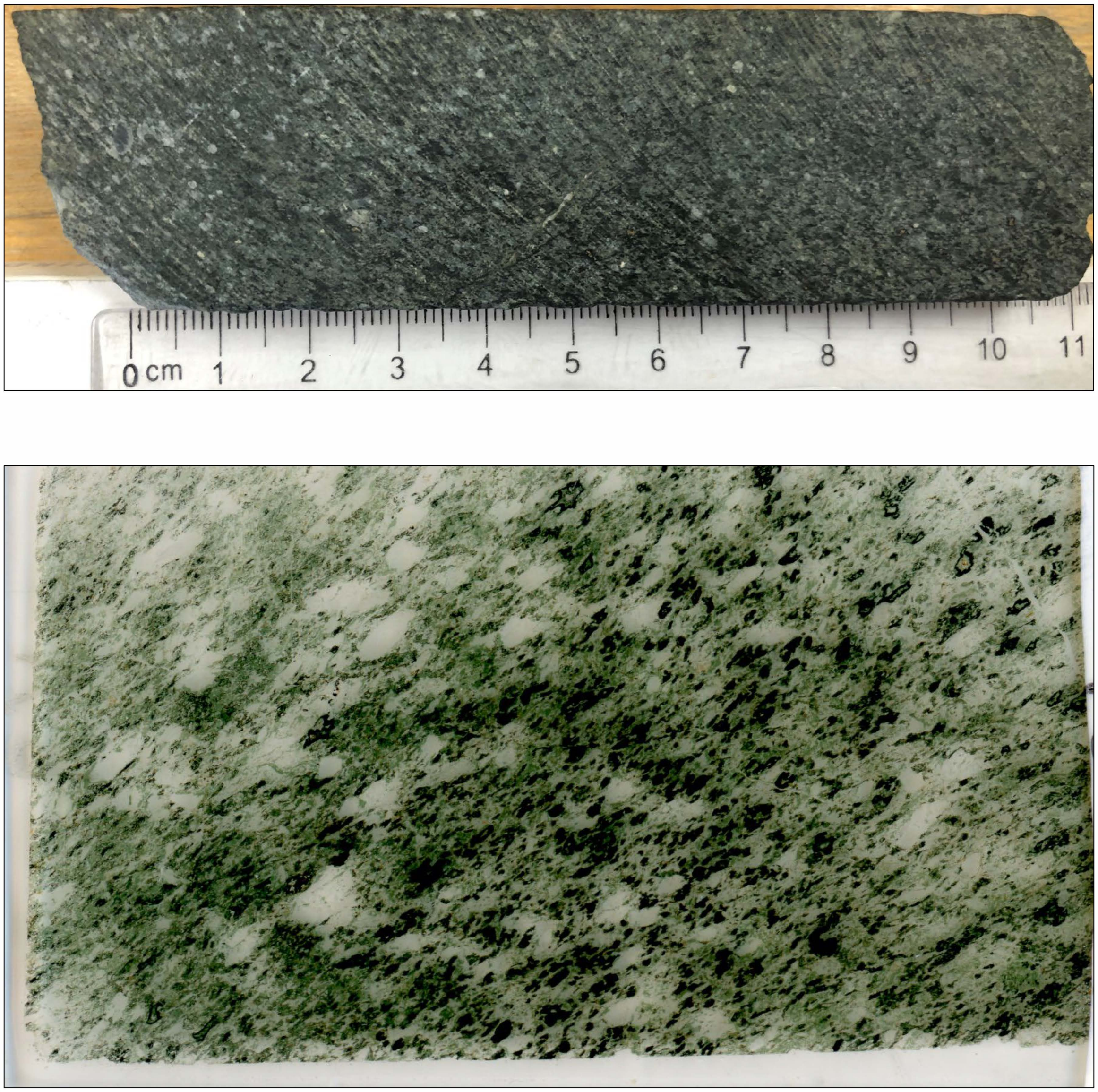

Fig. A2. 11 Hand sample photograph (above) and thin section scan (below) of sample 94-31.

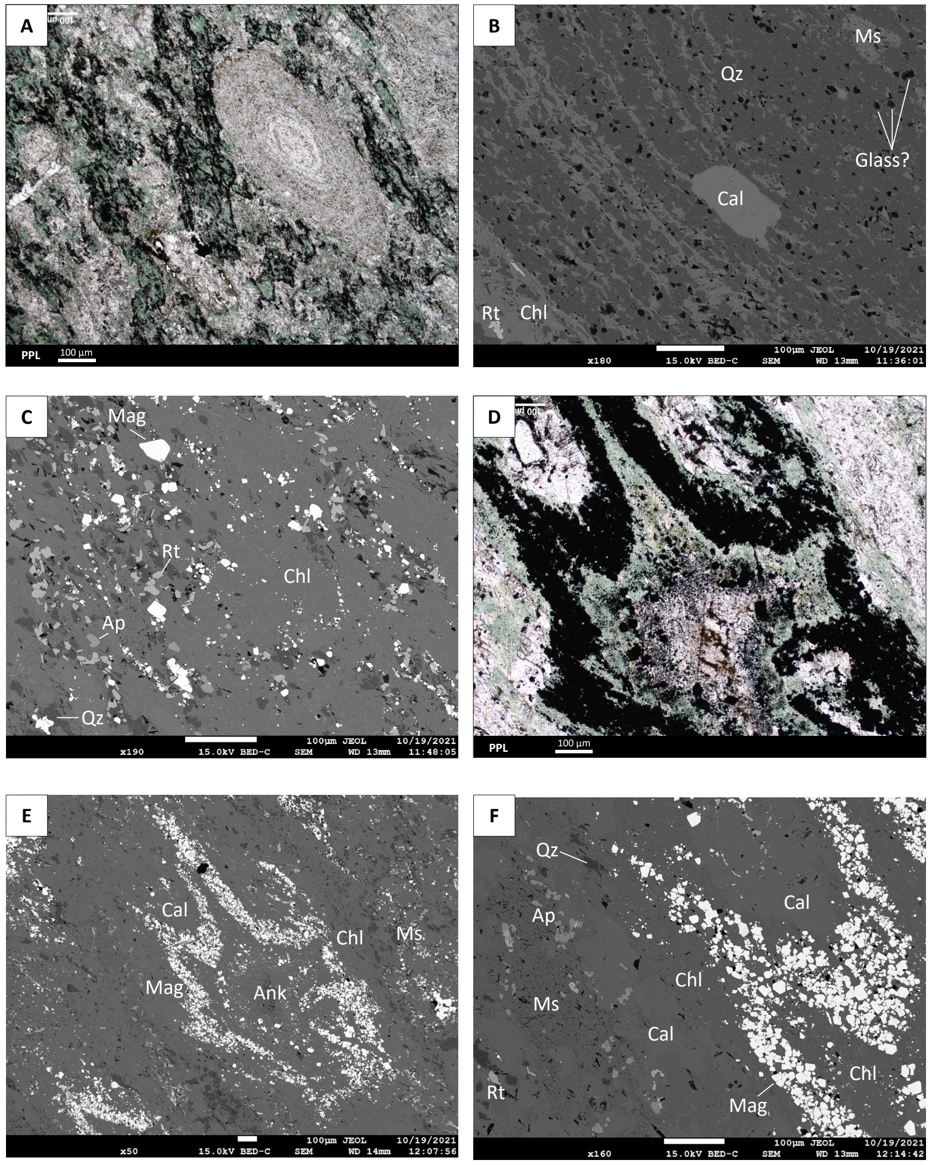

Fig. A2. 12 (A) Oval lapilli (2.8 mm long) has alternating quartz-rich and muscovite-rich layers that create a concentric zoning pattern reminiscent of accretionary lapilli (PPL). Matrix is recrystallized tuffaceous material composed of magnetite- and chlorite-rich domains and quartz-, calcite-, and muscovite-rich domains. (B) BSE image of part of the zoned lapilli showing the alternating quartz-rich and muscovite-rich layers, and larger euhedral calcite grain. The lapilli has abundant, very fine-grained dark blebs (glass?) with mixed Na-Mg-Al-Si-S-K-Ca-Ti-Fe spectra. (C) BSE image of the more mafic, chloritic tuffaceous part of the rock to the left of the lapilli in the FOV of (A). This is chlorite with minor interstitial quartz and disseminated apatite, rutile, and magnetite. (D-F) A chlorite- and magnetite-rich lapilli with irregular, winged, cuspate margins and a core composed of ankerite. Shown in PPL (D) and BSE images at different scales (E-F). Surrounded by mixed calcite, chlorite, muscovite tuffaceous material with disseminated apatite and rutile.

W600919 – HW-FeTiB

Sample ID: W600919

Surface Sample - UTM NAD 83 Zone 8N
Easting: 419876 m **Northing:** 6581777 m **Elevation:** 1377 m

Rock Name: Cal-qz-mag-chl, fiamme-bearing basaltic lapilli tuff.
Geochemical Suite: Hangingwall FeTi basalt (HW-FeTiB)

Lithofacies and textures:
Matrix-supported, poorly sorted, juvenile fiamme, monolithic, moderately foliated

Hand sample description:
Matrix-supported lapilli tuff. Matrix is chl, cal, ank. Dark grey lapilli are elongate and aligned (defining foliation), 0.2-2 cm, with ragged edges and fiamme-like shapes. Tr fg py.

Petrographic description:
Matrix is cryptocrystalline calcite, ankerite, qz, chl, with disseminated mag and rare py, and ccp. Clasts are subangular, commonly with ragged margins and fiamme-like shapes, and are aligned along foliation. Clasts have ovoid features (10-30%) that are cal, ms, qz. Groundmass of clasts if mainly vfg cal, qz, mag, and chl. Clasts are probably juvenile.

Mineral	Residence	%	Size max (µm)	Habit	Comments
Calcite	Matrix, ovoid features, replacing phenocrysts	40	500	Recrystallized	Predominant mineral in tuffaceous matrix, recrystallized and intimately intergrown w/ chl and qz. Wholly replaces some relic fsp phenocrysts in lapilli. Common in ovoid features w/ qz.
Quartz	Matrix, ovoid features	20		Recrystallized	Recrystallized in matrix. Ovoid features in lapilli.
Magnetite	Clasts, matrix	20	100	Subhedral	Most abundant in groundmass of clasts. Disseminated in matrix.
Ankerite	Matrix, ovoid features, replacing phenocrysts	10		Recrystallized	Imparts pumpkin-orange colour on weathered surface of hand sample.
Chlorite	Matrix, clasts	10	100	Subhedral, interstitial, fibrous	Aligned along foliation.
Pyrite	Matrix	Rare	10	Bleb	Connected w/ ccp blebs
Chalcopyrite	Matrix	Rare	10	Bleb	

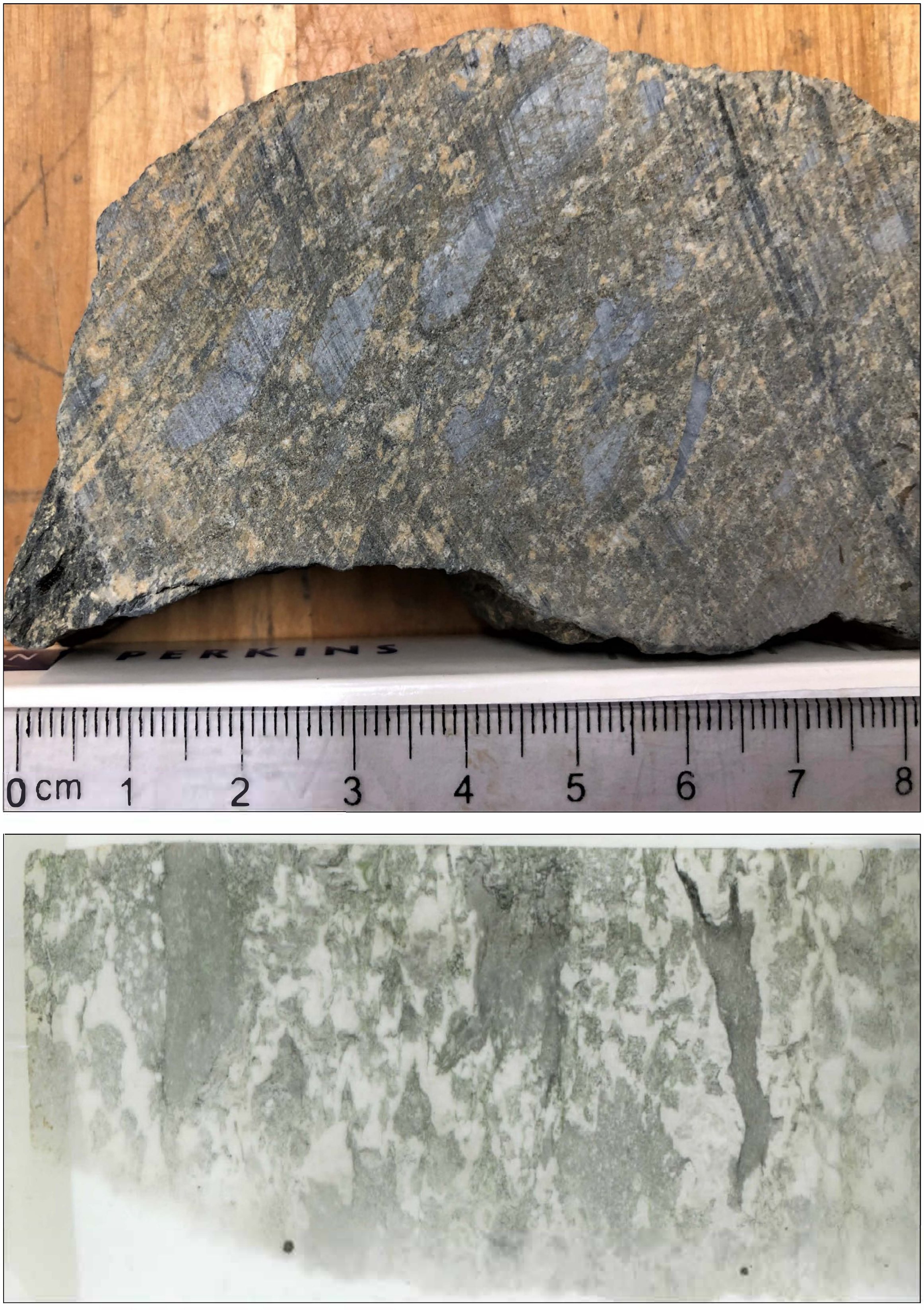

Fig. A2. 13 Hand sample photograph (above) and thin section scan (below) of sample W600919.

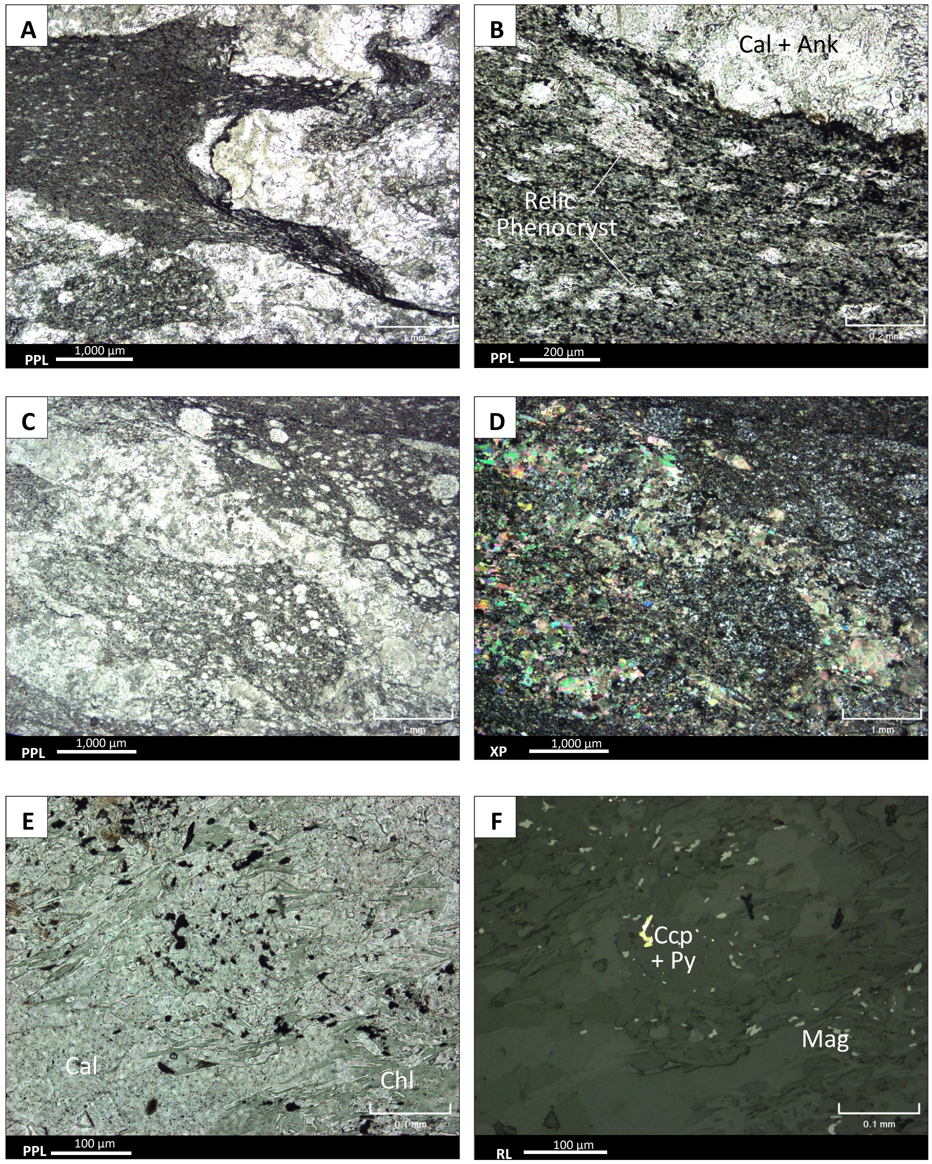

Fig. A2. 14 (A-E) Microphotographs of juvenile fiamme-like basaltic lapilli and associated calcite-rich tuffaceous matrix. Lapilli are outlined by opaque (PPL and XPL) magnetite (A-D) and tuffaceous matrix (A-E) has a dirty appearance and is composed of aggregates of recrystallized very fine-grained calcite, quartz, ankerite, and chlorite with disseminated magnetite and rare pyrite and chalcopyrite.

109-185 – HW-FeTiB

Sample ID: 109-185

Drill hole: CMR18-109 **Drill hole depth (m):** 185 m

Rock Name: Qz-cal-chl-ilm-ap, scoria (?)-bearing, monolithic, poorly sorted basaltic pl-crystal-poor lapilli tuff
Geochemical Suite: Hangingwall FeTi basalt (HW-FeTiB)

Lithofacies and textures:
Matrix supported, poorly sorted, monolithic

Hand sample description:
White qz-cal fg matrix w/ 25% green-chloritic clasts of basalt, that are 1-10 mm. Clasts have irregular margins including varied cuspate, curviplanar, ragged, and rounded textures. One clast has an appreciably rounded margin on one side and is quite ragged and cuspate on the side. Some clasts have cal-qz ovoid features (amygs?). Some clasts may be original glassy shards. Non-magnetic. Tr vfg py. Matrix supported, poorly sorted, monomictic.

Petrographic description:

Matrix is predominantly calcite-quartz with trace apatite and sparse vfg py. One plagioclase crystal fragment (>1.8mm) at edge of thin section is wholly replaced by qz-ms-cal-chl.

Clasts are volcanic (mafic) up to 1.4 cm. Groundmass of clasts is typically cryptocrystalline with a dirty brownish appearance in PPL. BSE imaging revealed the groundmass of the clasts is composed mainly of vfg ilm, chl, minor apatite and trace ep, ms, and qz. Ilmenite it typically restricted to the clasts. Some clasts have up to 30% ovoid features that are typically 0.1-0.2 mm and composed of chl with minor cal that may be relic amygs or varioles. Some larger ovoid features or amalgamated clusters (up to 1.8mm) are composed of more calcite + qz + chlorite. Rare larger amyg(?) with 0.7mm diameter has mag-(py)-ccp in core surrounded by calcite and then chlorite. Rare perfectly round wholly qz amyg?. Rare lath-shaped pl phenocryst (0.75 x 0.15 mm) in clasts, suggesting clast source is probably pl-phyric basalt. If majority of the chl-qz-carb ovoid features are amyg, then these are scoria clasts.

Mineral	Residence	%	Size max (µm)	Habit	Comments
Calcite	Matrix	35	200	Subhedral-euhedral	Probably recrystallized – aggregates w/ triple junctions.
Quartz	Matrix	30		Interstitial	Throughout matrix or replaces pl phenos
Chlorite	Clasts, matrix	20	100	Subhedral-anhedral, masses or fibers	Predominant in clasts, minor amounts in matrix. Some fibers are elongate, lath shaped. In ovoid features, chl is anhedral masses.
Ilmenite	Clasts	10	20	Subhedral, euhedral, acicular	Opaque (PPL) part of clasts is composed of vfg interconnected needles of ilmenite. In places, these trains of ilmenite outline the chl-qz-carbonate ovoid features
Apatite	Clasts, matrix	2	20	Anhedral-subhedral, blebs	Interconnected vfg xls in groundmass of clasts. Tr blebs in matrix.
Muscovite	Pl crystals, clasts	1		Fibrous	Replaces pl crystals (broken one in matrix), or microphenocrysts in clasts

Epidote +/- Allanite	Clast	Tr	40	Anhedral	Tr blebs typically only within clasts. Some have brighter specks that have noise in spectra (La-Nd-Ce) and are probably REE-bearing allanite.
Py	Matrix, amyg?	Tr	20	Anhedral-euhedral	Inclusions in rare mag grain within amyg. Rare cubes in matrix.
Mag	Amyg?	Rare	100	Cube	Inclusions of py
Ccp	Amyg?	Rare	10	Bleb	Rare bleb near mag grain within a qz-chl amyg(?)

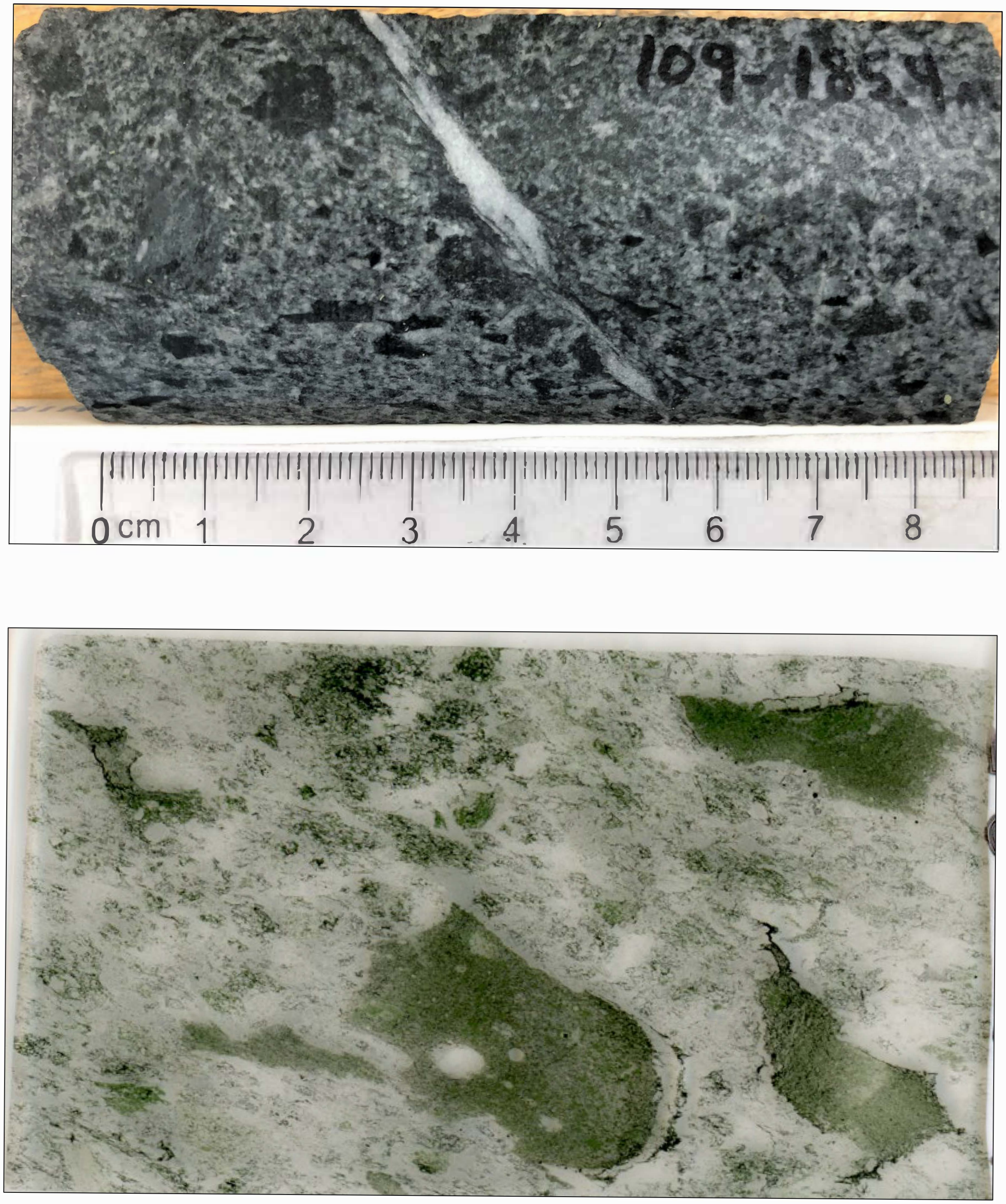

Fig. A2. 15 Hand sample photograph (A) and thin section scan (B) of sample 109-185.

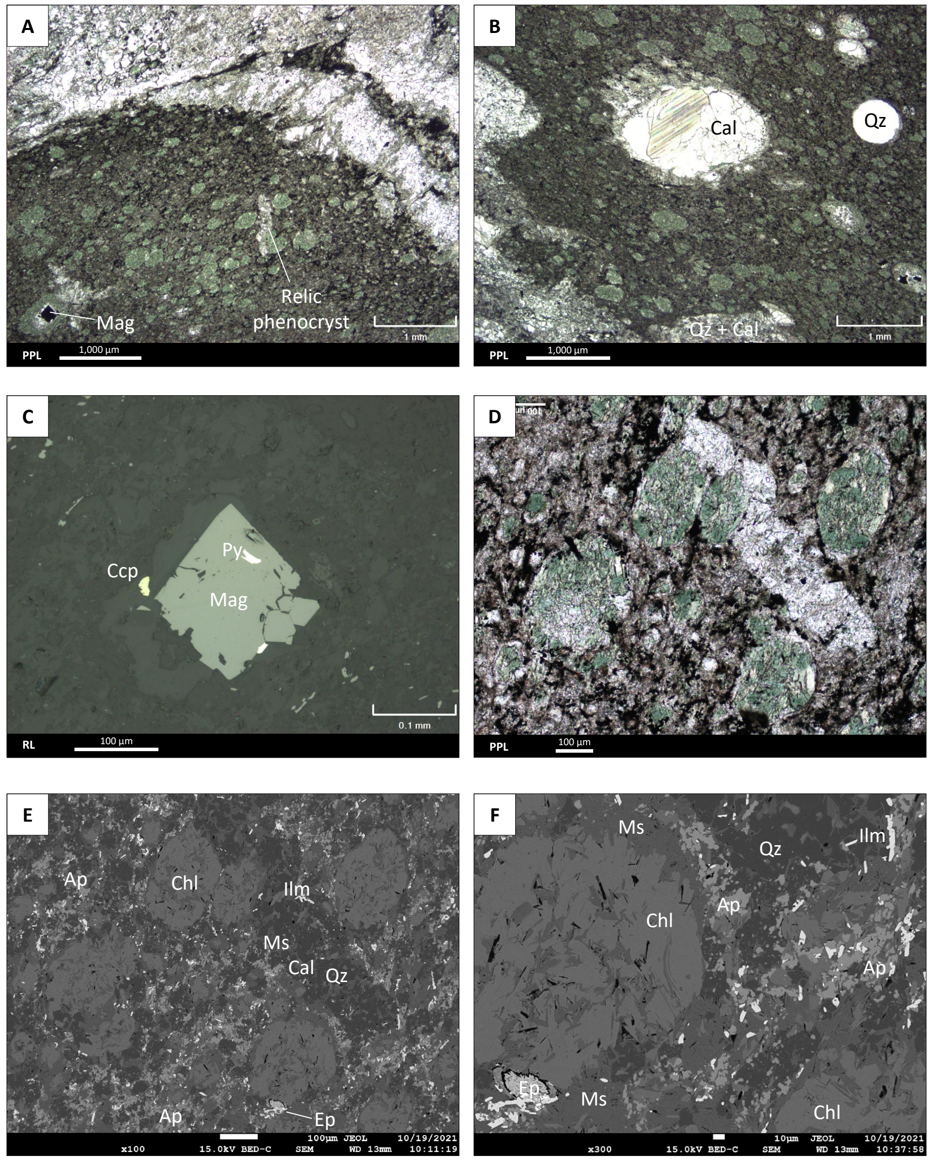

Fig. A2. 16 (A-E) Microphotographs of the largest basaltic lapilli fragment in the thin section. (A) Subround margin of clast next to qz-calcite dominant matrix (PPL). The clast groundmass has a dirty appearance in PPL and opaque FeTi oxide minerals are abundant. The clast contains abundant chlorite-rich ovoid features that may be amygdules (and so this would be a scoria clast) or they could be relic spherulites modified by later alteration and metamorphism. A magnetite crystal is in the center of one of the larger ovoid features. Lath shaped tabular features composed of quartz, muscovite, and minor calcite are wholly replaced plagioclase phenocrysts. (B) A more ragged, cuspate margin of the clast. A larger ovoid feature composed of polycrystalline calcite and a perfectly round ovoid feature composed of polycrystalline quartz may are markedly different from the green, chlorite-rich ovoid features dominant in the clast. Perhaps the chloritic features are spherulites and the larger qz-calcite dominant features are amygdules? (C) RL microphotograph of the magnetite crystal within a chlorite, quartz. Calcite ovoid feature labelled in (A). The magnetite crystal has an inclusion of pyrite. A bleb of chalcopyrite (yellowish hue) is nearby. (D-E) Close up of the relic plagioclase phenocryst labelled in (A), but the FOV is at a different orientation. In PPL (D), the groundmass has a dirty brown appearance. The BSE image (E) in the same FOV and a more close-up BSE image (F) show that the groundmass is composed of very fine-grained apatite, ilmenite, muscovite, and trace epidote. The ovoid features are chlorite with minor muscovite. The plagioclase phenocryst is wholly replaced by quartz, muscovite, and calcite.

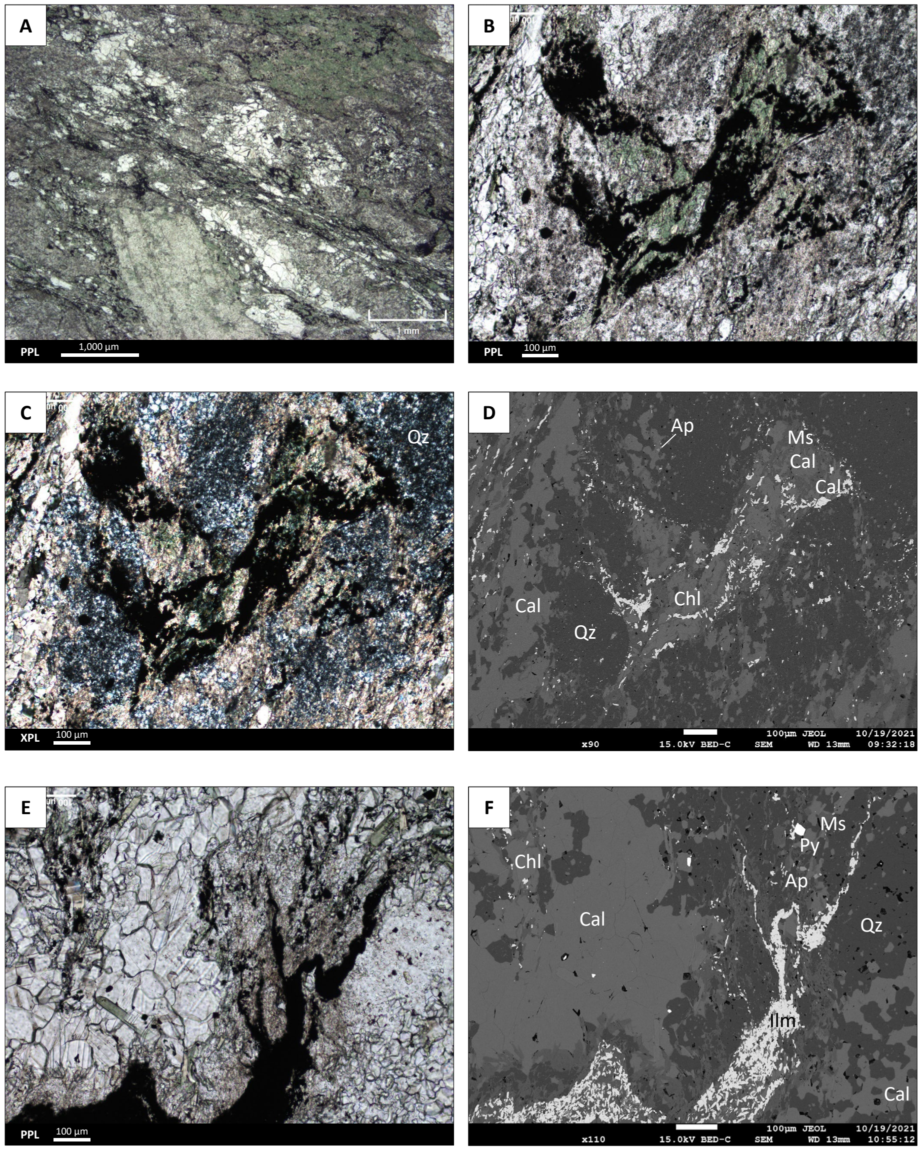

Fig. A2. 17 (A) Plagioclase crystal (> 1.8 mm) at the edge of the thin section is wholly replaced by muscovite with minor quartz and chlorite (PPL). Deformed, fiamme-like basaltic lapilli are darker green, black (chlorite- and ilmenite-rich) components amidst a calcite and quartz dominant matrix. (B-D) An irregular shaped lapilli fragment supported in a calcite and quartz matrix. Opaque minerals (PPL and XPL) are concentrated in the lapilli fragment and are very fine-grained interconnected acicular needles of ilmenite that outline ovoid chloritic features. (E-F) Deformed, ragged margin of a basaltic, ilmenite-rich lapilli in PPL (E) and an BSE image (F).

99-49 – HW-FeTiB

Sample ID: 99-49

Drill hole: CMR17-99 **Drill hole depth (m):** 49 m

Rock Name: Bt-mag-qz-cal-chl scoria(?)-bearing basaltic lapilli tuff
Geochemical Suite: Hangingwall FeTi basalt (HW-FeTiB)

Lithofacies and textures:
Matrix-supported, very poorly sorted, chaotic, monolithic?

Hand sample description:
Dark grey, strongly magnetic, matrix supported, very poorly sorted lapilli tuff with even more strongly magnetic clasts. One clast >3 cm consists of 3 discrete 0.5-2 cm pinkish sil-mt altd patches with 5% diss 1mm ovoid features (amygs?) composed of fg mt and these patches are separated but enclosed within an ameboidal grey to weakly buff colored grainy matrix w/ mag-qz-cal and rare 1mm Jsp bleb. This may have been a pumiceous clast that was only partly altered giving it an apparent clastic texture just within the clast. Other rounded clasts include amorphous, dark gray basalt with 0.5-1 mm cal amygs(?) that are similar color to matrix, just slightly finer-grained and markedly more magnetic than matrix. A thin lens of mag that is 1cm long may be a relic clast? A subtle, yet discrete ovoid 2 cm area of cal-mag-chl and minor hematite may be another altered clast. Sparse 6mm, irregular somewhat lath-like sericitic features may be fsp xls.

Petrographic description:
Matrix is cryptocrystalline bt-chl-qz-cal and sparse epidote with 4% 0.1-0.15mm euhedral disseminated mag grains. Overall matrix has a hectic deformed wavy texture, and some clast margins blend into matrix by alteration (local clusters of ovoid "amygs" may indicate clast). Sparse patches of chl.
Most clasts are predominantly composed of mag, making their groundmass opaque in PPL. One black basalt clast (2 cm) has subangular fragment with cuspate, irregular margins, locally embayed, with a discontinuous reaction rim up to 0.34m of calcite, biotite, epidote and qz. Fragment is composed of 30% vfg mag that masks identification of surrounding minerals by its opaqueness in PPL. Contains 25% ovoid features that are mostly 0.05-1 mm, composed of calcite +/- minor biotite-ep-qz. Largest ovoid is 1.5 mm and composed of calcite with sparse biotite and epidote. Some elongate, lath-like features are likely relic fsp phenocrysts that have been replaced by calcite and are aligned in the clast and define a foliation. The largest convincing lath-like feature is 0.6 mm.
One paler clast (>1.8 cm) has cryptocrystalline groundmass, but likely mix of qz-calcite and 5% vfg mag. Not as much of the vfg mag in groundmass compared to other clast, but mostly aggregates (10%) of larger grains, some up to 1 mm, but most ~0.5 mm. Ovoid features (20%) are up to 0.8 mm, most are 0.1mm, composed of calcite +/- qz and rare ep. Feld phenos (1%) are 0.04-0.18 mm, laths, replaced by qz.
This volcaniclastic rock is probably monolithic and the basalt clasts have differential alteration giving it a polylithic appearance.

Mineral	Residence	%	Size max (µm)	Habit	Comments

Biotite	Matrix, clasts	30	100	Cryptocrystalline	Vfg parts of matrix and clasts, and in some ovoid features.
Magnetite	Clasts, matrix	25	300	Subhedral, euhedral	Abundant in lapilli as vfg interconnected crystals that commonly outline ovoid (amyg?) shapes. Also disseminated cubes in matrix.
Quartz	Matrix, clasts	20		Cryptocrystalline	Vfg parts of matrix and clasts. Commonly wholly replaces relic fsp phenocrysts. Within ovoid features.
Calcite	Matrix, clasts	10	100	Cryptocrystalline	Vfg in matrix and groundmass of clasts. Common as slightly larger xls in ovoid features in clasts. Highly anomalous, washed-out interference colours in XPL.
Chlorite	Matrix, clasts	10		Cryptocrystalline	Vfg parts of matrix and clasts
Epidote	Matrix, clasts	2	300	Subhedral, euhedral	Disseminated in matrix and clasts.

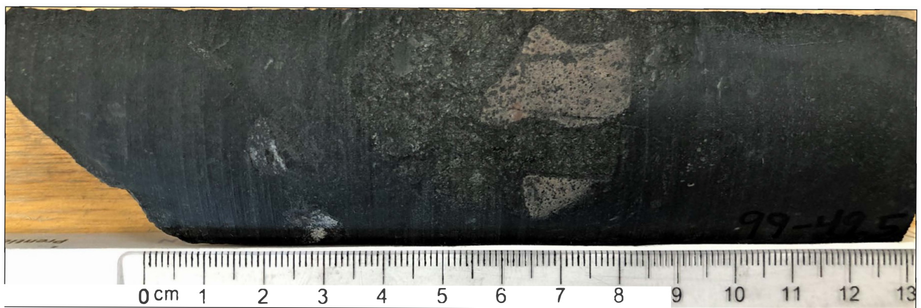

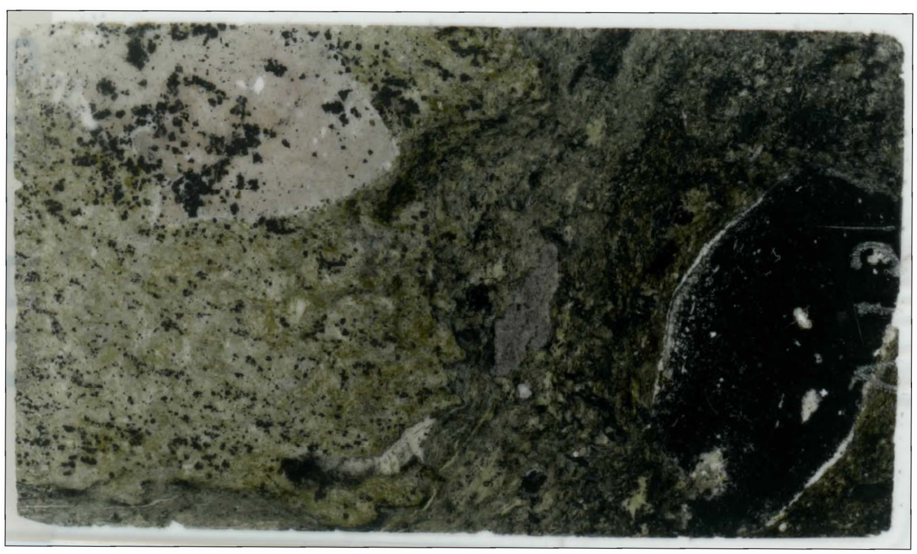

Fig. A2. 18 Hand sample photograph (above) and thin section scan (below) of sample 99-49.

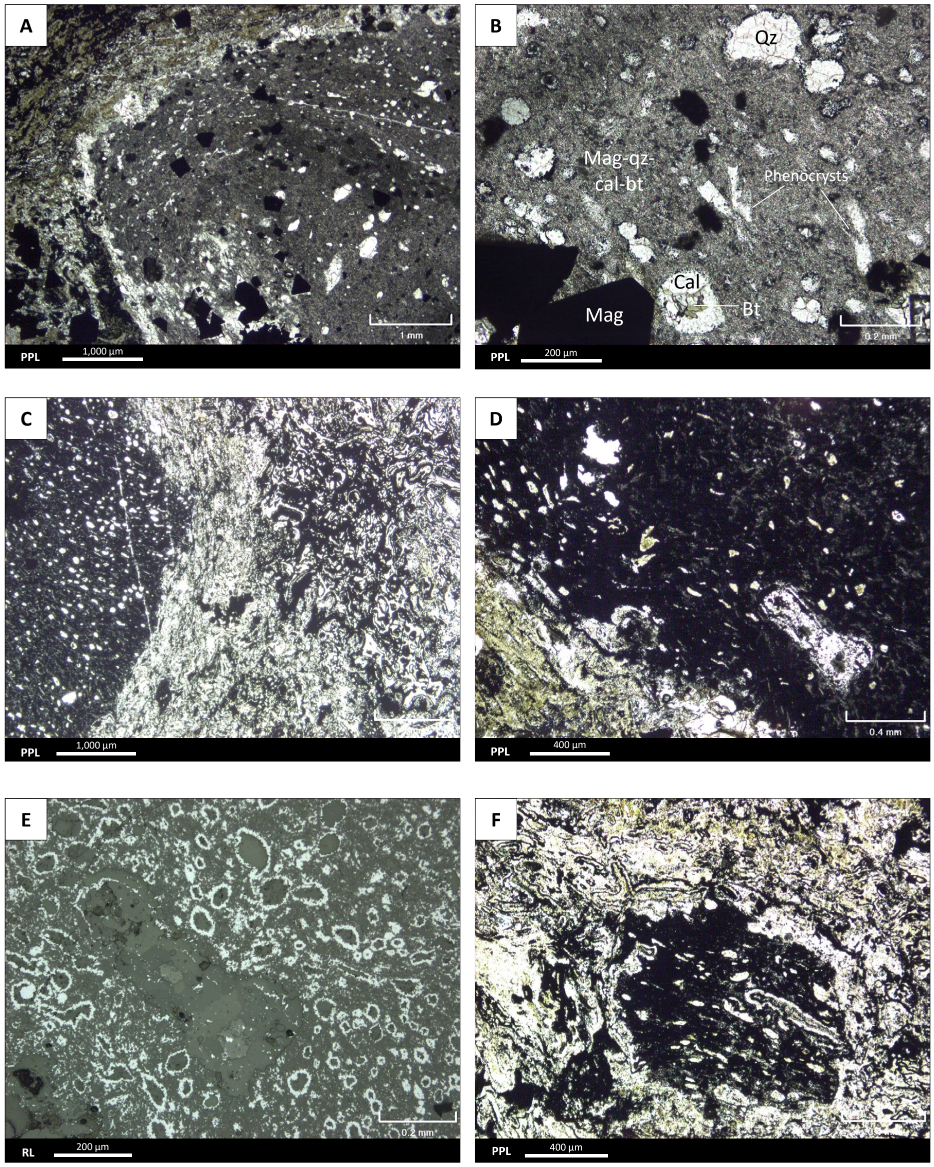

Fig. A2. 19 (A-E) Microphotographs of basaltic lapilli with relic plagioclase phenocrysts replaced by quartz, and ovoid features (amygdules?) composed of quartz, calcite, and lesser biotite. The groundmass of the lapilli is dominated by very fine-grained magnetite, and includes cryptocrystalline quartz, calcite, and biotite. The tuffaceous matrix is biotite and quartz, with lesser calcite, and chlorite. (A-B) Microphotographs of the paler lapilli. This lapilli has less magnetite than the darker lapilli. (C-E) Dark grey-black basalt lapilli. The RL image (E) highlights the texture of magnetite rimming ovoid features in the basalt lapilli, but magnetite is generally not within the relic lath shaped plagioclase phenocrysts. (F) The tuffaceous matrix includes tuff sized fragments of basalt with the same character as the lapilli fragments.

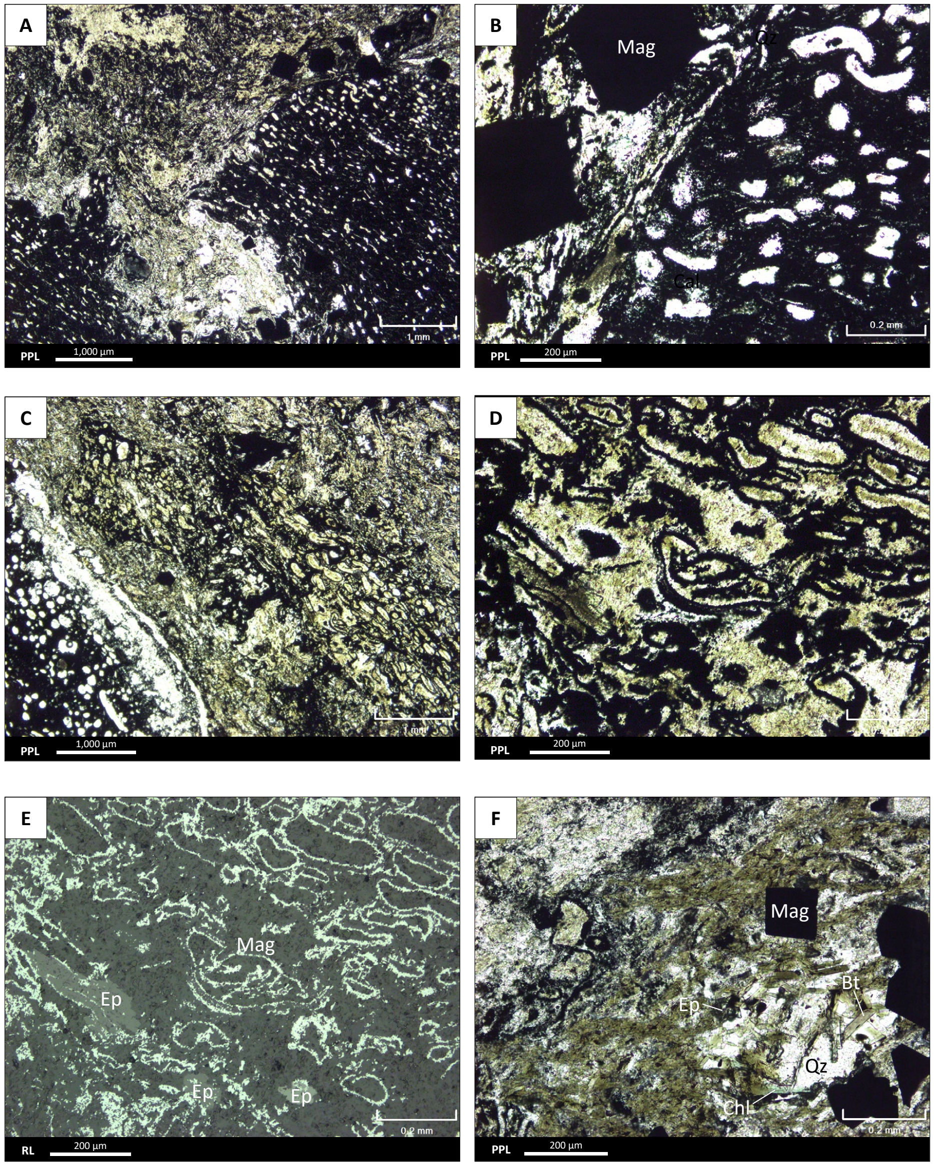

Fig. A2. 20 (A-E) Microphotographs of basaltic lapilli and tuffaceous matrix. (A) Irregular, cuspate, embayed margin of the basaltic lapilli. (B) Close up of the ovoid features within the basaltic lapilli. Some are deformed and U-shaped. (C-E) Lapilli with abundant ovoid features with less sharp margins compared to the darker lapilli. (D-E) Magnetite defines compact ovoid features that may be relic amygdules. (F) Tuffaceous matrix is very-fine grained aggregates of biotite, quartz, and chlorite with minor disseminated larger crystals of epidote and magnetite.

S037015 – Z-FeTiB

Sample ID: S037015

Surface Sample - UTM NAD 83 Zone 8N
Easting: 420134 m **Northing:** 6581924 m **Elevation:** 1203 m

Rock Name: Bt-chl-mag-ilm-ep, variolitic, sparsely plagioclase-phyric basalt
Geochemical Suite: Zone FeTi Basalt (Z-FeTiB)

Lithofacies and textures:
Variolitic, porphyritic

Hand sample description:
Dark grey green, vfg, moderately magnetic and chloritic basalt w/ 40% leucocratic varioles. Varioles are subround to splatter-shaped and locally coalesce. Most varioles are concentrically zoned with sericitic core and qz rim.

Petrographic description:
The groundmass is dominated by plagioclase microlites (typically 0.1 – 0.2 mm, but up to 0.5 mm) set in mesostasis with a cruddy brownish-green appearance in PPL. SEM work revealed that this mesostasis is mainly intersertal cryptocrystalline bt-chl (likely devitried glass) and dark glassy blebs that have amphibole-like spectra. The groundmass also contains minor apatite, and trace ep, amp, qz and py. Magnetite and ilmenite are typically restricted to the groundmass. Magnetite is spongey with Inclusions of ap, ank, chl, ilm or glass. Mag edges are commonly embayed and may be resorption features or could be a result of rapid growth due to undercooling. Ilmenite needles are disseminated, some of which form masses in the shape of larger (up to 60 um), boxy, skeletal crystals with hollow cores filled with bt-chl-ep-pl. Sparse, larger pl phenocrysts up to 1.5 mm are typically lath-shaped and partially replaced by ab, ms, chl, bt and minor ep. Plag microlite and phenocrysts have average andesine composition (An_{35}).

Varioles range from ~0.5 mm to 3.67 mm, and are most commonly zoned, with an outer rim of annealed polycrystalline qz with triple junctions at grain boundaries. The cores are typically plagioclase with variable ms, ep, chl, amp replacement. Chloritic cores with amphibole are less common. BSE images show a few varioles that may have nucleated on a lath-shaped plagioclase phenocryst (partially replaced by ep-ms) and have fibrous bits of pl radiating out from core like bicycle spokes with interstices composed of qz and Fe-Mg-Ti minerals like chl, amp, mag. The recrystallization and greenschist facies metamorphism obscure primary textures, but these interstitial Fe-Mg-Ti minerals could have been primarily glassy components between the pl fibers that formed by spherulitic growth. Some of the smallest varioles (0.5 mm) are nearly wholly qz with trace tiny disseminated xls between the qz grains of pl, amp, chl, bt and the odd py or mag. Py is rare in groundmass, but some varioles contain py and one larger variole has large py xl with ccp inclusion and hematite rim surrounded by amphibole needles and chl-bt. The largest variole has a diameter of 3.67mm.

A few ovoid chloritic features (0.4 – 2.9 mm) may be amygdules. These “amygs” are typically not zoned like the white varioles. They are composed of massive chl with trace bt, ep, amp (up to

0.17 mm), and mag. Distinct bt-mag rims are common. Locally the leucocratic varioles are partially composed of the same chloritic features, or they are impinged upon and altered this way? If these chloritic features were primary vesicles, and the varioles are spherulites, then this may indicate that some spherulitic crystallization nucleated on vesicles.

Mineral	Residence	%	Size max (μm)	Habit	Comments
Plagioclase	Phenocryst	2%	1000	Subhedral-euhedral, blocky to lath	Some are very subtle, the largest one is offset along a fracture and is ~6mm long. The others are mainly about 0.5-1.5mm. Partially replaced by alb, chl, bt, and ep.
Plagioclase	Groundmass	50%	350	Anhedral-subhedral, microlites, interstitial	Average Andesine composition (An35). Partially replaced by biotite-chlorite
Biotite	Groundmass	20%	60	Flakes, intersertal	Predominant component of groundmass - interstitial. Interwoven w/ chl.
Chlorite	Groundmass	10%	30	Flakes, intersertal	Anomalous brown in XPL. Interwoven w/ bt.
Magnetite	Groundmass	7%	80	Euhedral, spongey	Generally restricted to the groundmass and not disseminated in fsp phenocrysts. Inclusions of ap, chl, ilm, glass and ank.
Ilmenite	Groundmass	5%	20	Anhedral-euhedral, needle, lath, skeletal	Disseminated needles in groundmass and locally manifest as several interconnected xls forming larger, blocky, skeletal masses with cores of bt-plag-ep-chl-glass. Some blocky xls have tiny inclusions of apatite.
Apatite	Groundmass	1%	10	Subhedral-euhedral	Disseminated.
Epidote	Groundmass	Tr	100	Subhedral-euhedral, lath	Partially replacing larger pl phenos or pl in groundmass.
Amphibole	Groundmass	Tr		Subhedral to euhedral	Disseminated
Allanite	Epidote core	Rare	25	Subhedral	A rare ep xl has aln core.
Quartz	Groundmass	Rare	10	Interstitial	Tr interstitial bits in groundmass.
Pyrite	Groundmass	Rare	4000	Euhedral	Disseminated. Up to 4mm in hand sample.
Ankerite	Magnetite inclusion	Rare	< 1	Inclusion, bleb	Inclusion within spongey mag

Mineral	Residence	%	Size max (μm)	Habit	Comments
Plagioclase	Variole	5 - 20%		Relic blocky/lath.	Forms core of variole, relic blocky to lath shapes may suggest spherulitic growth nucleated on primary phenocryst. Predominantly andesine but varies from oligoclase to labradorite. Labradorite (up to An_{65}) is restricted to the cores of a few varioles. Partially to wholly replaced by ms, ep, alb, bt, and chl.
Quartz	Variole	30 - 90%	0.05	Annealed, recrystallized, triple junctions	Equant and interlocking grains with triple junctions (polygonal) form rims of varioles of varied thickness, or locally makeup the entire variole, especially the smaller ones. Qz xls are generally 0.01-0.03mm, locally up to 0.05mm.
Muscovite	Variole	2-50%		Replacing plagioclase.	Vfg - sericite. Some have Ba in spectra.
Chlorite	Variole	Trace		Replacing plagioclase.	Within the core of some varioles.
Epidote	Variole	Trace		Replacing plagioclase.	Within the core of some varioles. Some spongey, ragged. Likely replacing pl.
Amphibole	Variole	Trace		Replacing plagioclase.	Within the core of some varioles.
Magnetite	Variole	Trace	10		
Pyrite	Variole	Rare	100	Euhedral	Rare cubes in a few varioles.
Zircon	Variole	Rare	10		One ~10 um crystal identified with SEM near core of variole.
Chalcopyrite	Variole	Rare	20		Rare in core of variole surrounded by py which is rimmed with hematite, and then all that is surrounded by amp-qz-chl-bt.

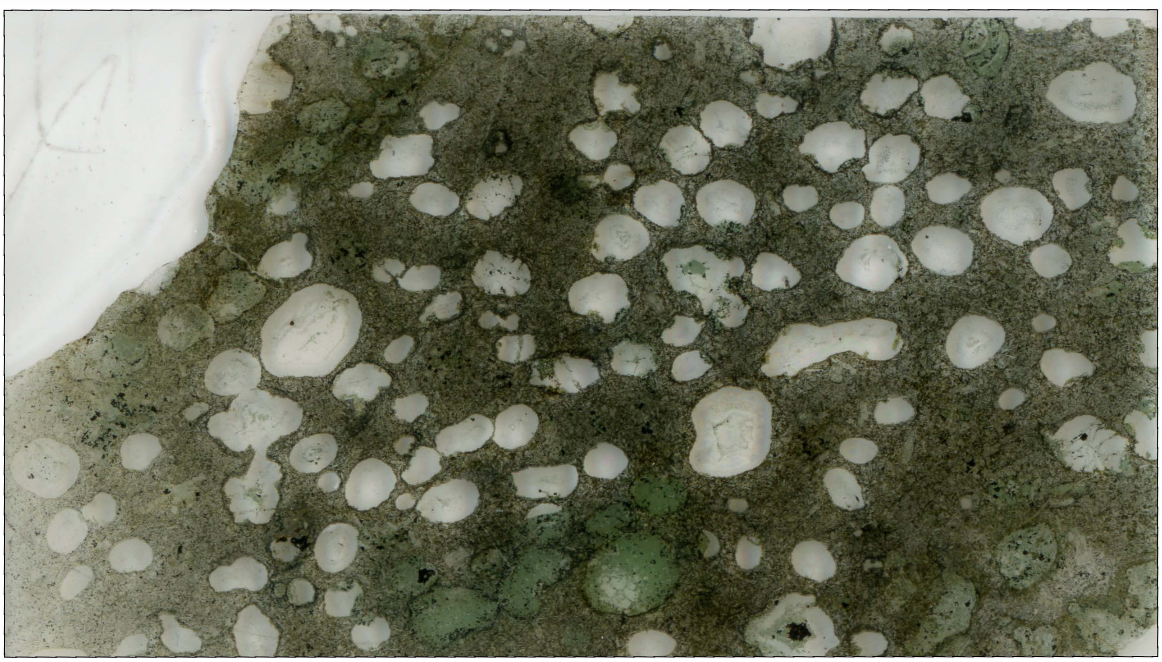

Fig. A2. 21 Hand sample photograph (above) and thin section scan (below) of sample S037015.

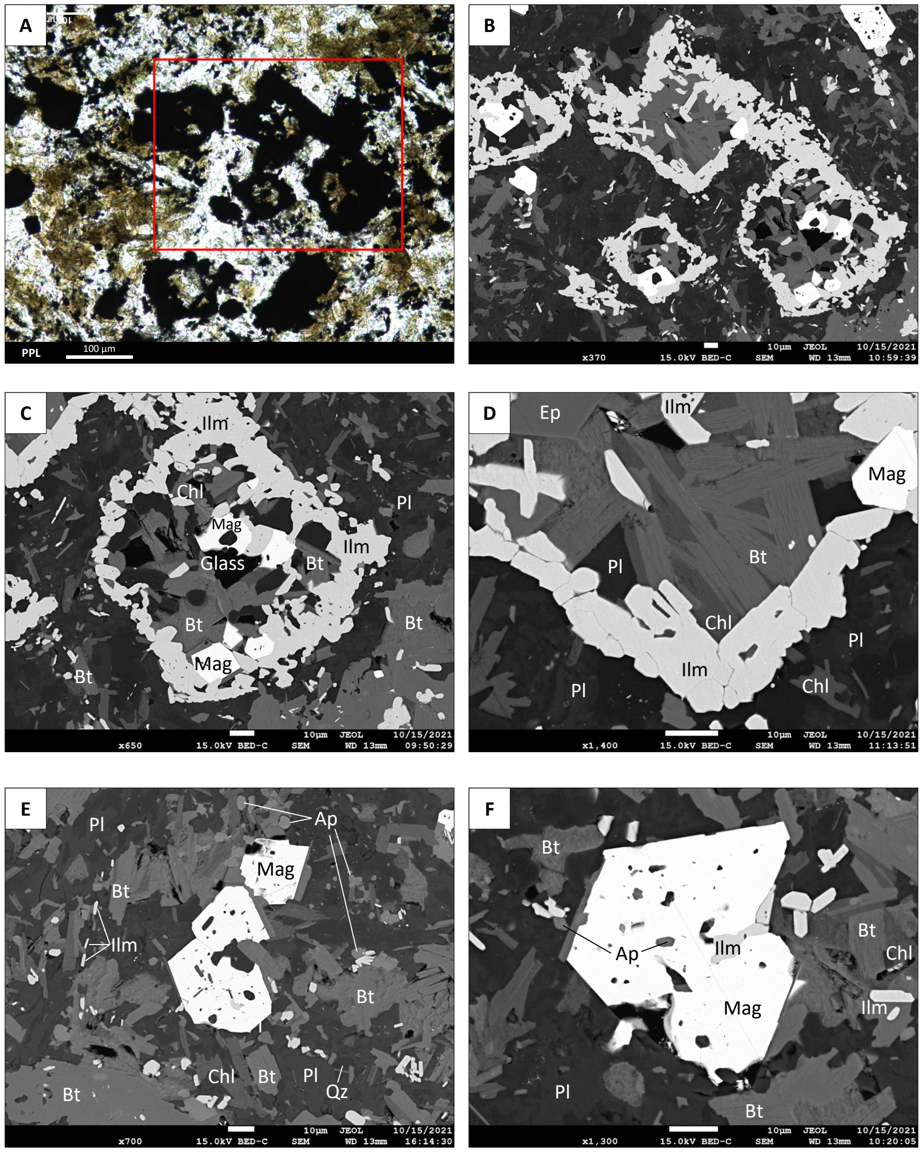

Fig. A2. 22 Microphotographs of the groundmass of sample S037015. (A) Blocky opaque FeTi oxide minerals disseminated in a groundmass composed of plagioclase microlites and a greenish brown mesostasis (PPL). The red box outlines the area of (B). (B-D) BSE images showing that the opaque minerals are ilmenite and magnetite, and the mesostasis is composed of biotite, chlorite, and minor epidote. Acicular ilmenite crystals and magnetite are interconnected to form larger blocky, skeletal crystals. (E-F) Disseminated magnetite crystals commonly have embayed margins and spongey interiors with inclusions of groundmass minerals. Apatite is an accessory phase and trace quartz is interstitial.

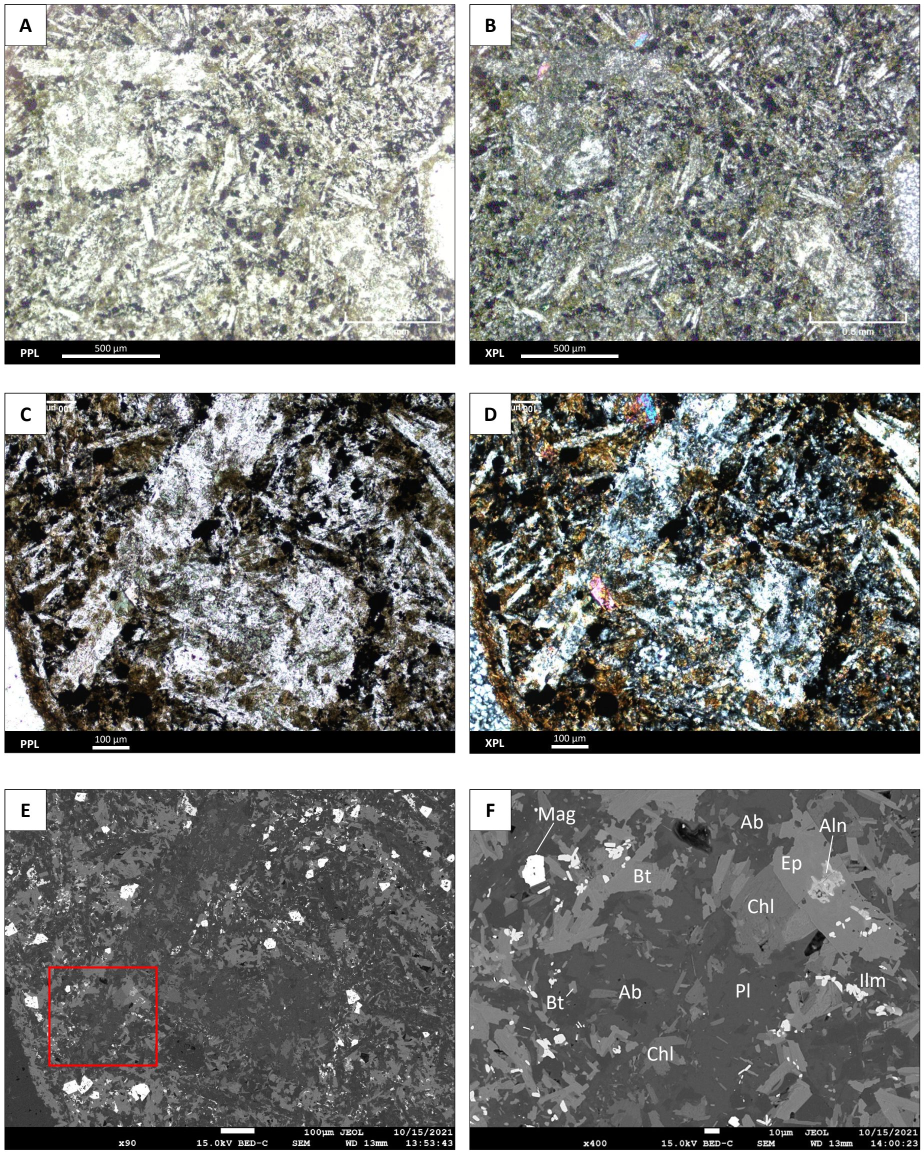

Fig. A2. 23 Microphotographs of plagioclase phenocrysts in sample S037015. (A-B) Twinned plagioclase phenocrysts (top left) and one lath-shaped plagioclase phenocryst (bottom right) in PPL (A) and the same view in XPL (B). (C-D) Close-up of the twinned plagioclase phenocrysts in PPL (C) and XPL (D) at a different orientation than A-B. The same FOV is shown in the BSE image in (E), with the red box denoting the area shown in (F). The plagioclase phenocrysts are partially replaced by albite, chlorite, biotite, and epidote. The brighter core of the epidote crystal is allanite. Note that magnetite and ilmenite (brighter minerals in BSE image) are generally restricted to the groundmass.

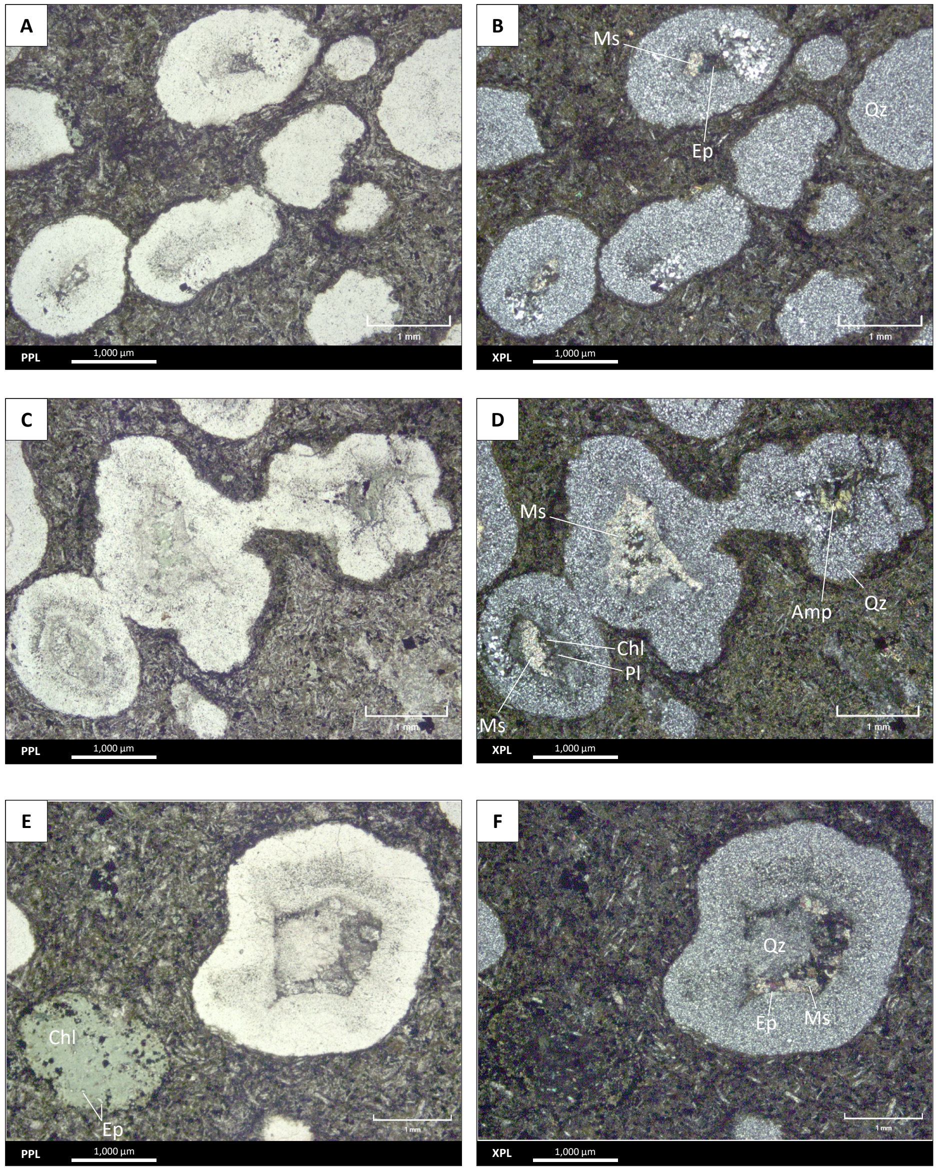

Fig. A2. 24 Microphotographs of varioles in sample S037015. (A-F) Larger varioles have cores of plagioclase variably replaced by albite, muscovite, epidote, chlorite, amphibole, and biotite. The outer rims of the varioles are composed of recrystallized quartz. Some of the smaller varioles are composed predominantly of quartz with no defined core. Varioles locally coalesce (C-D). Ovoid chloritic features that lack concentric zoning are interpreted to be amygdules (E-F).

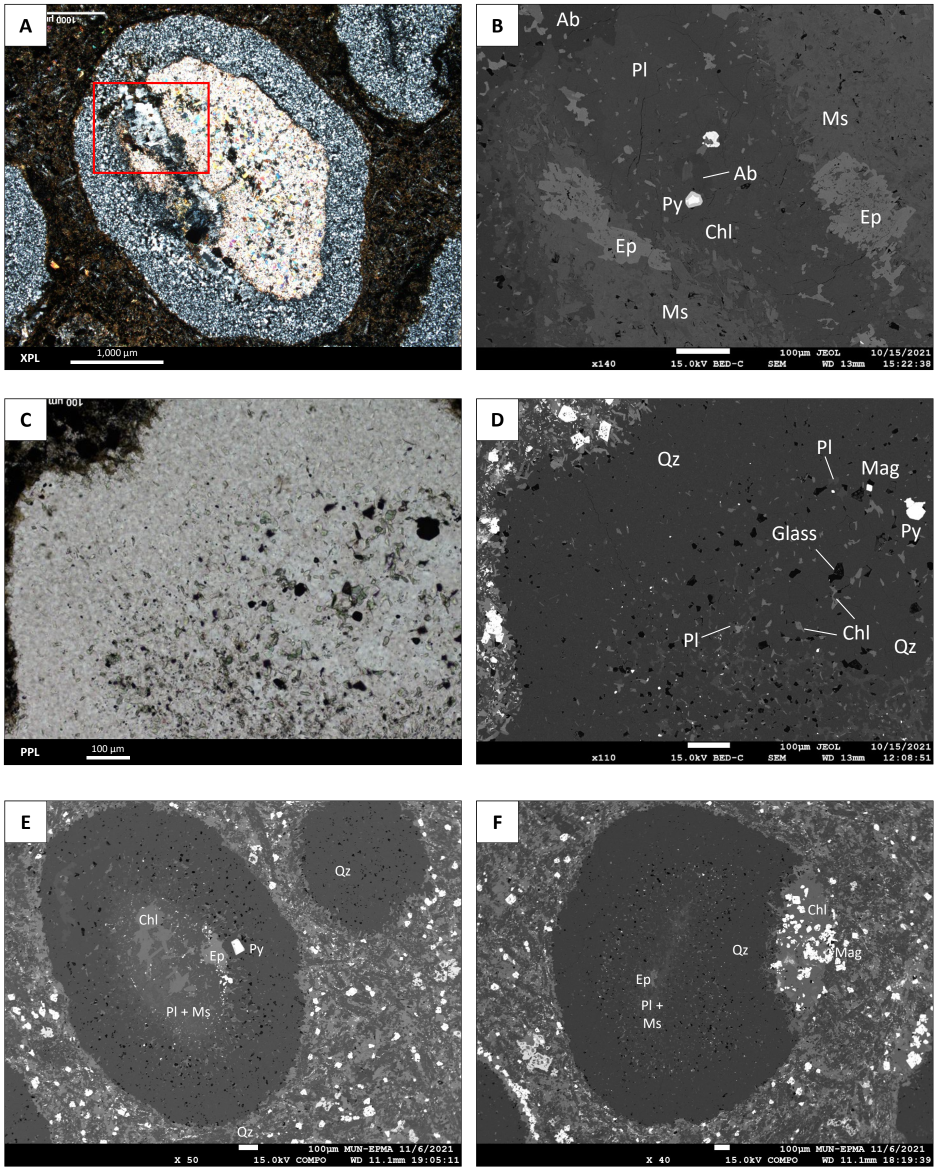

Fig. A2. 25 Microphotographs of varioles in sample S037015. (A) Larger variole with distinct quartz rim and muscovite-rich interior (XPL). Relic plagioclase is within the red box and this area is shown in (B). (B) BSE image showing plagioclase partially replaced by muscovite, epidote, albite, and chlorite. Pyrite is minor and locally has oxidation rims. Spectra for the muscovite show a slight barium peak, suggesting some of the muscovite is barium rich. (C-D) A smaller quartz-rich variole that lacks concentric zoning in PPL (C) and an BSE image (D). Tiny (<1 µm to 10 µm) crystals of chlorite, plagioclase, biotite, magnetite, and pyrite occupy the spaces in between the larger grains of quartz. Dark blebs are glass with amphibole-like spectra. (E-F) More examples of varioles with plagioclase cores partially replaced by muscovite and epidote. The variole in (F) has a chlorite- and magnetite-rich component (right) that may be an amygdule. The variole zoning is deflected parallel to this chlorite-magnetite feature.

W605318 – FeR

Sample ID: W605318

Drill hole: CMR18-109 **Drill hole depth (m):** 242.4m

Rock Name: Ms-qz-brt-py, pumiceous (?), globule-bearing rhyolitic lapilli tuff
Geochemical Suite: Ferrorhyolite (FeR)

Lithofacies and textures:
Foliated
Matrix-supported, very-poorly sorted
Pumice (?)- and globule-bearing

Hand sample description:
Strongly qz-ms-py-brt altered lapilli tuff with disseminated bleb of tan sph and sparse gn. Patchy/selective(?) alteration obscures boundaries "matrix" and "clasts." "Clasts" are darker grey with qz-py dominant alteration, >3-5cm, and some have ovoid-shaped (relic amyg?) features that are replaced by qz-brt. "Matrix" is white-coloured, vfg-mg ms-brt-sph-py-gn. Disseminated sp is pale, tan.

Petrographic description:

Matrix:
Strong foliation is defined by aligned wisps of ms. Lesser interstitial qz. Ms-rich matrix is presumably altered felsic (fsp-rich) tuffaceous component. Disseminated py is euhedral to subhedral, grains up to 0.8mm, but most under 0.5mm. Both ms and py are more abundant in matrix compared to clasts. Allanite is sparse, and always connected to py grains. Minor gn common along py edges. Rare vfg ccp blebs within py. Rare vfg bleb tetrahedrite (grey with brownish tint in RL) along py margin. Euhedral zircon crystals occur in both clasts and matrix. They are commonly fractured and rimmed with mnz, brt +/- gn. Mnz along zrn rims is bead-like. Some zrn have spongey interiors with inclusions of gn, mnz and felsic glassy material (SEM spectra contains Na, K, Al, Si). Some portions that are flooded with interlocking larger grains of brt, qz and sph may also be recrystallized matrix? Here larger grains of sp have ccp disease and gn discontinuously along margins. Barite is bladed, with blades up to 1.3 mm long.

Clasts:
Qz-brt-ms-sp clasts up to at least 1 cm are deformed, locally with cuspate to winged margins. Clasts are predominantly qz with minor brt, sp, py, and ms. Pyrite is generally <5% in clasts. Barite commonly has bladed texture. Rare, sub-micron ccp inclusions in sp (ccp disease). One clast is ~ 3 mm and is composed of vfg ms with a rare zircon grain and contains somewhat ovoid aggregates of polycrystalline qz that may be relic vesicles (altered pumice clast?). Sph locally has ccp-disease with <0.5% cpy (observed in larger bleb).

Globules:

Trace, discrete ovoid features up to 150 microns are composed of rutile, monazite, zircon, and locally galena, and rare apatite. In PPL, some globules can be identified by their dark reddish-brown hue, likely imparted by rutile. Rutile forms anhedral masses and commonly contains a Nb SEM spectra peak. Rutile is intergrown with vermicular zircon and monazite (symplectic texture). Locally, the sub-micron zrn or mnz crystals are arranged in chain-like successions with dendritic patterns that impart an overall "feathery" to "lace-like" appearance. Galena typically occurs as larger discrete masses but can be intergrown with zircon. The arrangement of minerals is disorderly and random within the globules.

Mineral	Residence	%	Size max (μm)	Habit	Comments
Muscovite	Matrix, clasts	50%	50	Flakes, fibrous	Defines strong foliation predominant in the vfg matrix. Some with Ba in spectra.
Quartz	Clasts, matrix	30%	500	Interstitial	Interstitial to ms in matrix.
Pyrite	Matrix, clasts	10%	800	Subhedral-euhedral	Most < 0.5 mm.
Barite	Clasts, matrix	3%	1300	Bladed	Largest blades are in parts of sample flooded w/ recrystallized brt-qz (matrix??). Smaller blades in qz-rich clasts too.
Sphalerite	Clasts, matrix	2%	2200	Anhedral-subhedral	Brown in PPL. Locally has galena blebs at margins. Grains are typically < 0.5 mm. Ccp disease observed in one larger bleb. Typically, more abundant in the more qz-brt rich parts interpreted to be clasts.
Galena	Grain boundaries, globules	1%	800	Anhedral-subhedral	Typically, along grain boundaries of py, zrn, and sp. Locally forms anhedral masses within globules.
Allanite	Py edges	Trace		100	Occurs along some py grains and some grains enclose py xls up to 10 micron.
Zircon	Clasts, matrix, globules	Trace	120	Anhedral to Euhedral	Larger grains are commonly fractured and rimmed with mnz, +/- brt. Gn is common in fractures and as inclusions in one spongey grain. Occur in sericitic-py matrix, qz-barite-rich clasts, and globules. In globules, zrn has a vermicular or "lace-like" texture.
Monazite	Rims zircon; part of globules	Trace	< 1	Anhedral	Blebs locally rimming zircon grains, giving a "doily" appearance. Vermicular textures within globules intergrown w/ rt and zrn.
Rutile	Globules	Trace		Subhedral-anhedral.	Most common as anhedral masses within globules intergrown w/ vermicular zrn and mnz. Some lath-shaped grains observed proximal to globules. Local reddish-brown hue (PPL) of globules is likely derived from rutile.
Apatite	Matrix, globule	Trace	80	Subhedral, spongey	Some spongey w/ felsic glassy inclusions. Rare in globules (P-phase is typically mnz in globules).
Chalcopyrite	Inclusions in py, sp	Rare	< 5	Blebs	Ccp disease in a few sp and py grains.
Tetrahedrite	Grain boundaries	Rare	< 1	Anhedral	Grey with brownish tint in RL. Rare vfg bleb along py margin.

Fig. A2. 26 Hand sample photograph (above) and thin section scan (below) of sample W605318.

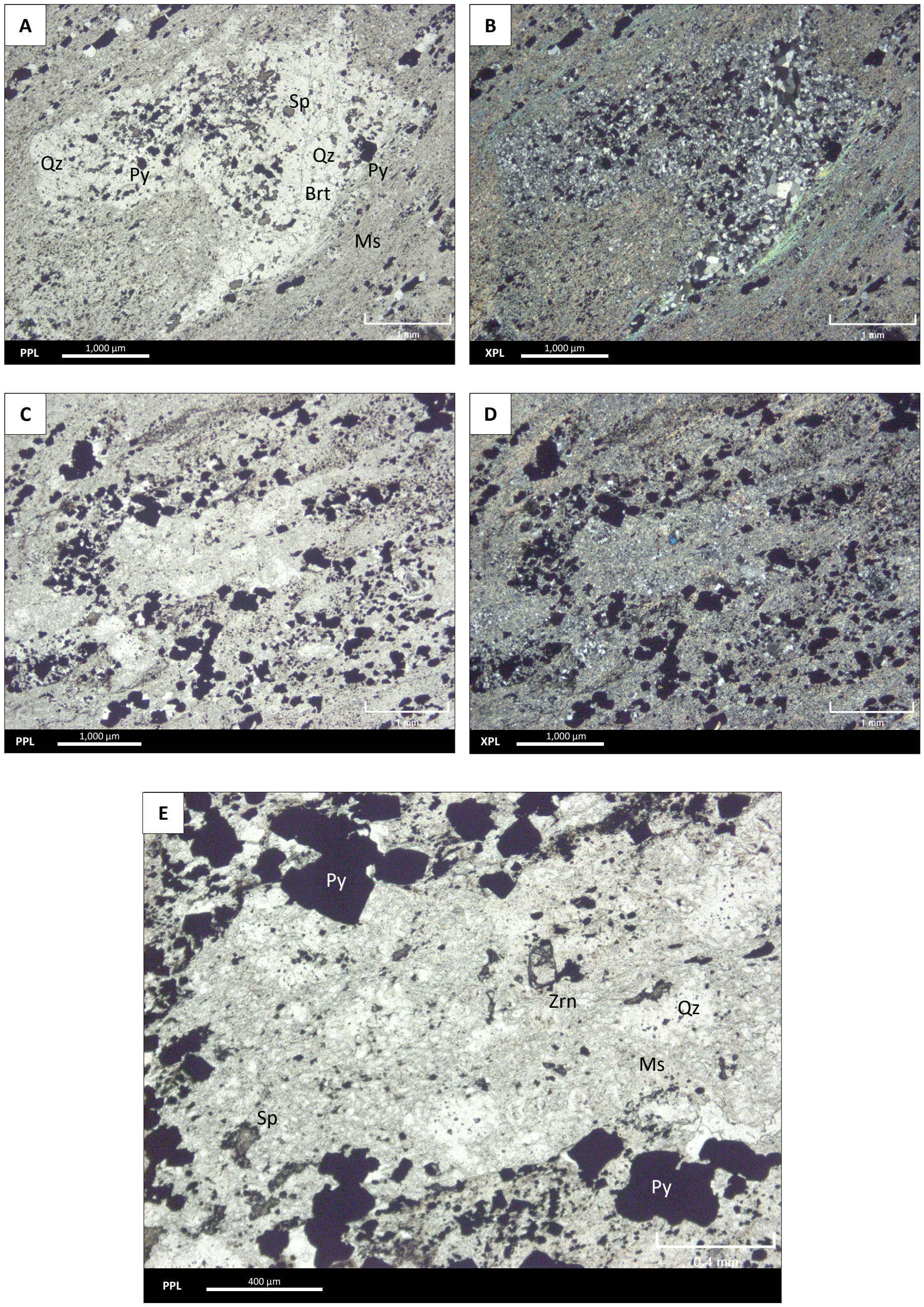

Fig. A2. 27 Microphotographs of lapilli. (A-B) Irregular-shaped clast with cuspate and winged margins shown in PPL (A) and XPL (B). The clast is quartz with minor muscovite and contains a disaggregated band of barite. Brown-colored (PPL) sphalerite and euhedral pyrite are disseminated in the clast. The matrix surrounding the clast is composed mostly of very fine-grained, muscovite (defining foliation), disseminated pyrite and minor quartz. (C-E) Possible pumice clast with a zircon crystal. The clast is composed of very fine-grained muscovite and quartz and ovoid aggregates of polycrystalline qz that may be relic vesicles. Pyrite is more abundant in the matrix and helps to define clast boundary.

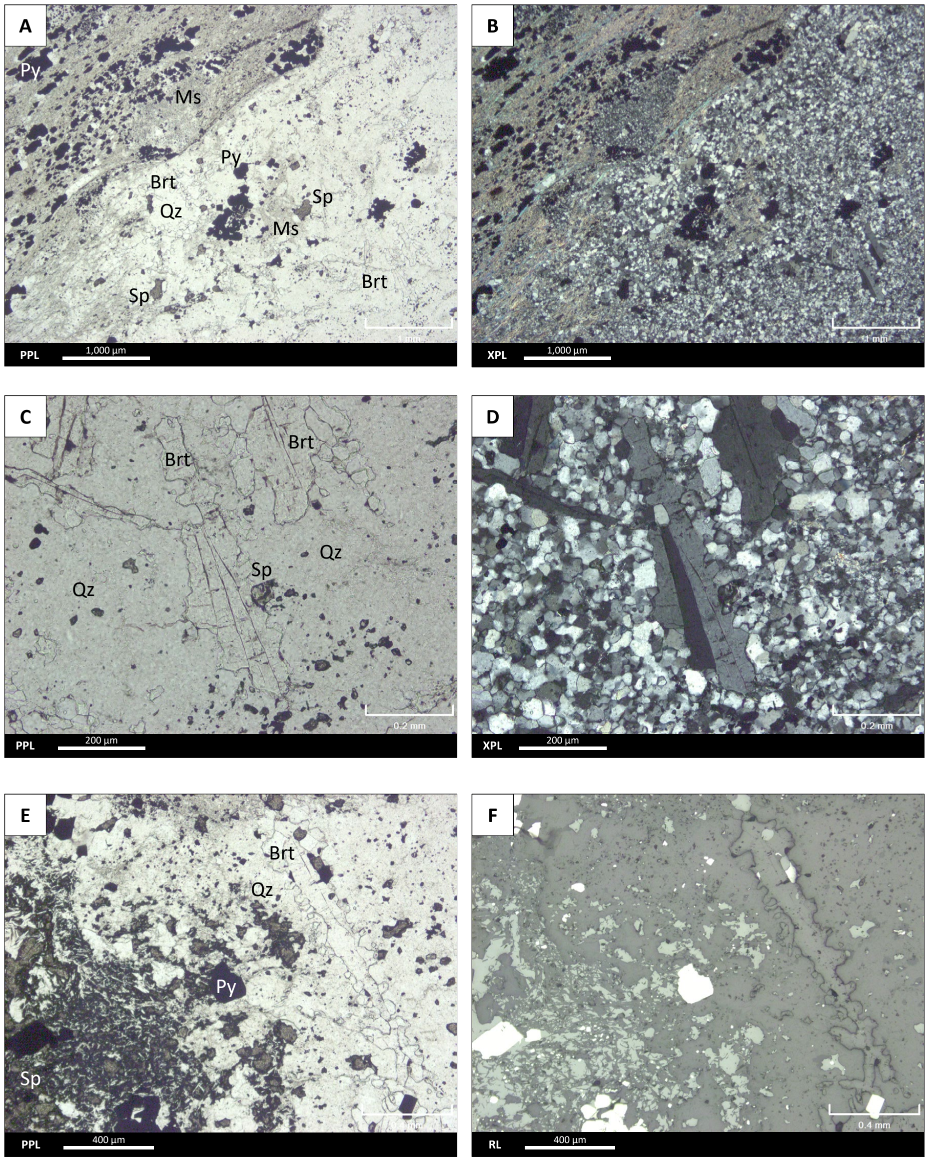

Fig. A2. 28 (A-D) Microphotographs of contact between lapilli and matrix showing bladed barite within the clast. (A-B) The matrix (top left FOV) is muscovite- and pyrite-rich compared to the quartz-rich clast with disseminated sphalerite, pyrite, and bladed barite (lower right FOV). (C-D) Close-up of the bladed barite texture in PPL (C) and XPL (D). (E-F) Another example of bladed barite in a sphalerite-rich section of the rock in PPL (E) and RL (F). Barite has a high relief.

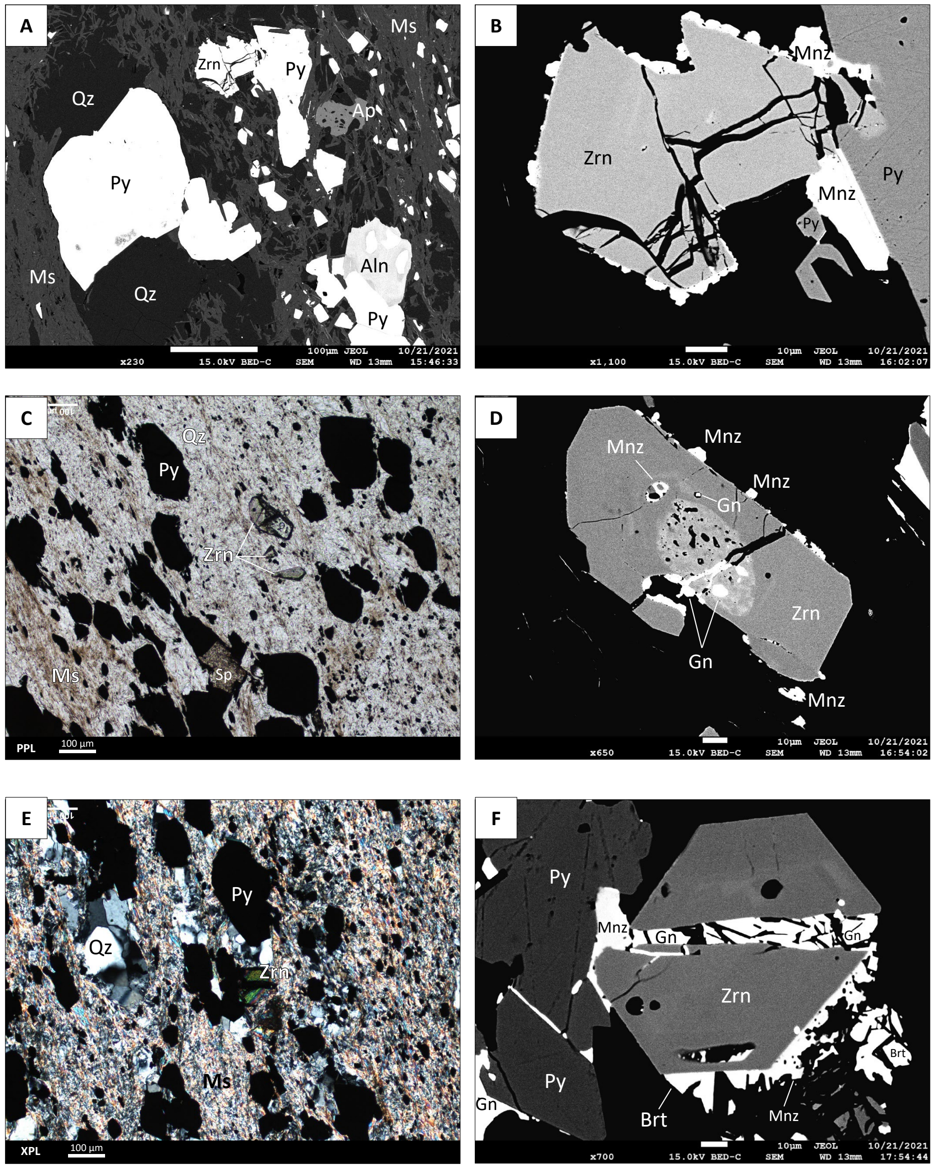

Fig. A2. 29 Microphotographs of zircon crystals (A-E). (A-B) BSE images of a zircon crystal along the edge of a pyrite grain within muscovite-quartz matrix. The BSE image in (B) is a close-up of the labeled zircon grain in (A) with a high contrast highlighting the boundaries between the heavier mineral phases (e.g., the quartz-muscovite matrix is black). The euhedral zircon grain is fractured and rimmed by beads of monazite. This texture is affectionately coined the monazite "doily" by the Piercey research group. (C) A cluster of zircon crystals in a muscovite-quartz matrix (PPL) and an BSE image of the larger zircon crystal in (D). The euhedral zircon crystal has beads of monazite along its edges and a spongey interior with inclusions of monazite, galena and felsic glass with Na, K, Al, Si spectra peaks. (E-F) A fractured zircon crystal shown in XPL (E) and a close-up BSE image (F) of the same crystal. The euhedral zircon crystal is rimmed with monazite and barite and the fracture is filled with galena.

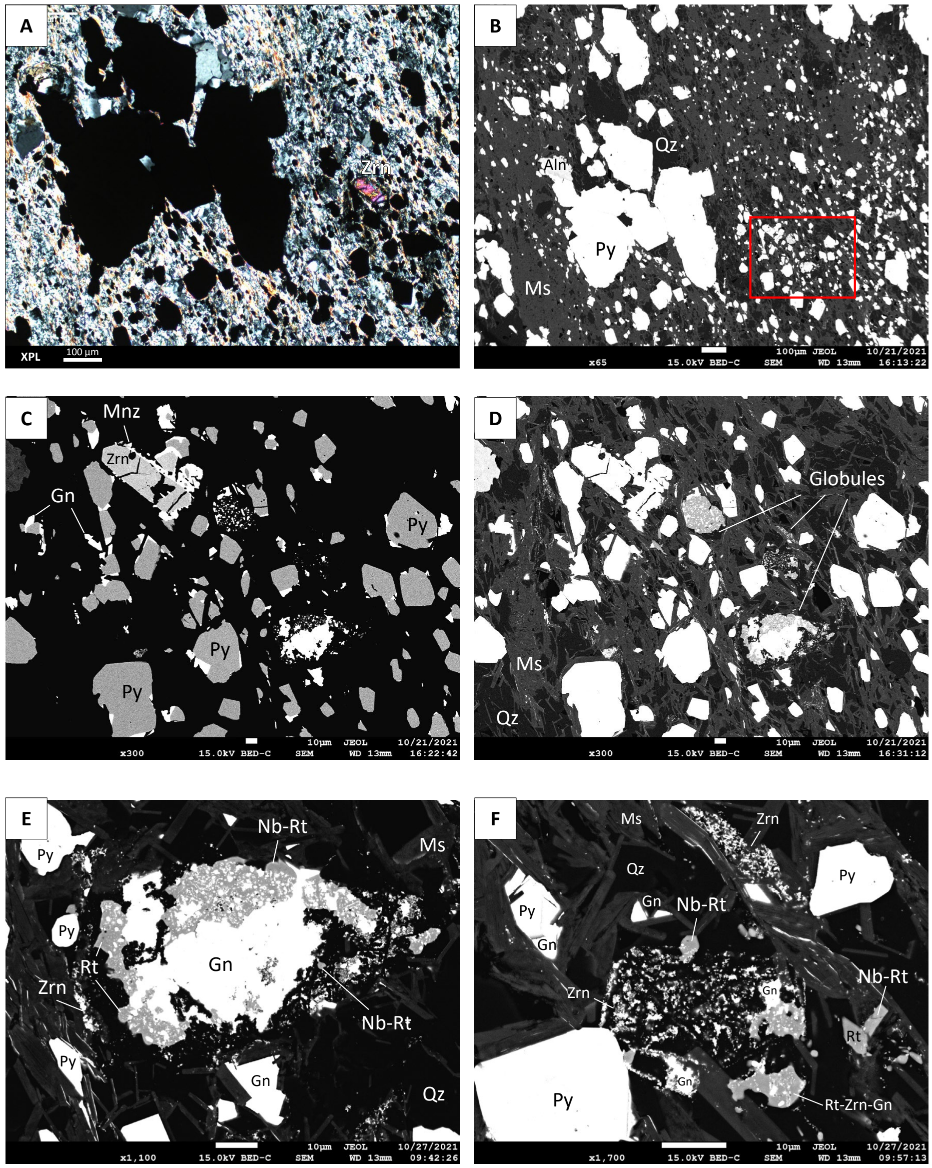

Fig. A2. 30 Microphotographs of an area containing globules near a broken zircon crystal (A-F). (A-B) Similar FOV in XPL and BSE image of muscovite and quartz matrix with disseminated pyrite. Allanite is along pyrite edge. The red box in (B) outlines the area shown in (C; high contrast) and (D; lower contrast). (C) The high contrast shows galena (white shade) discontinuously concentrated along pyrite grains (grey shade). Monazite (also white) is concentrated along margins of the zircon crystal. (D) Three globules occur near the broken zircon grain within the same foliated layer. (E-F) Close up of the globules shown in (D). (E) The globule is composed of galena but also has a titanium oxide mineral (rutile or anatase) that locally has a Nb spectra peak. Cryptocrystalline zircon crystals are disseminated in and around the globule. (F) Globule composed of feathery zircon crystals with blebs to crystals of galena, and Nb-bearing rutile.

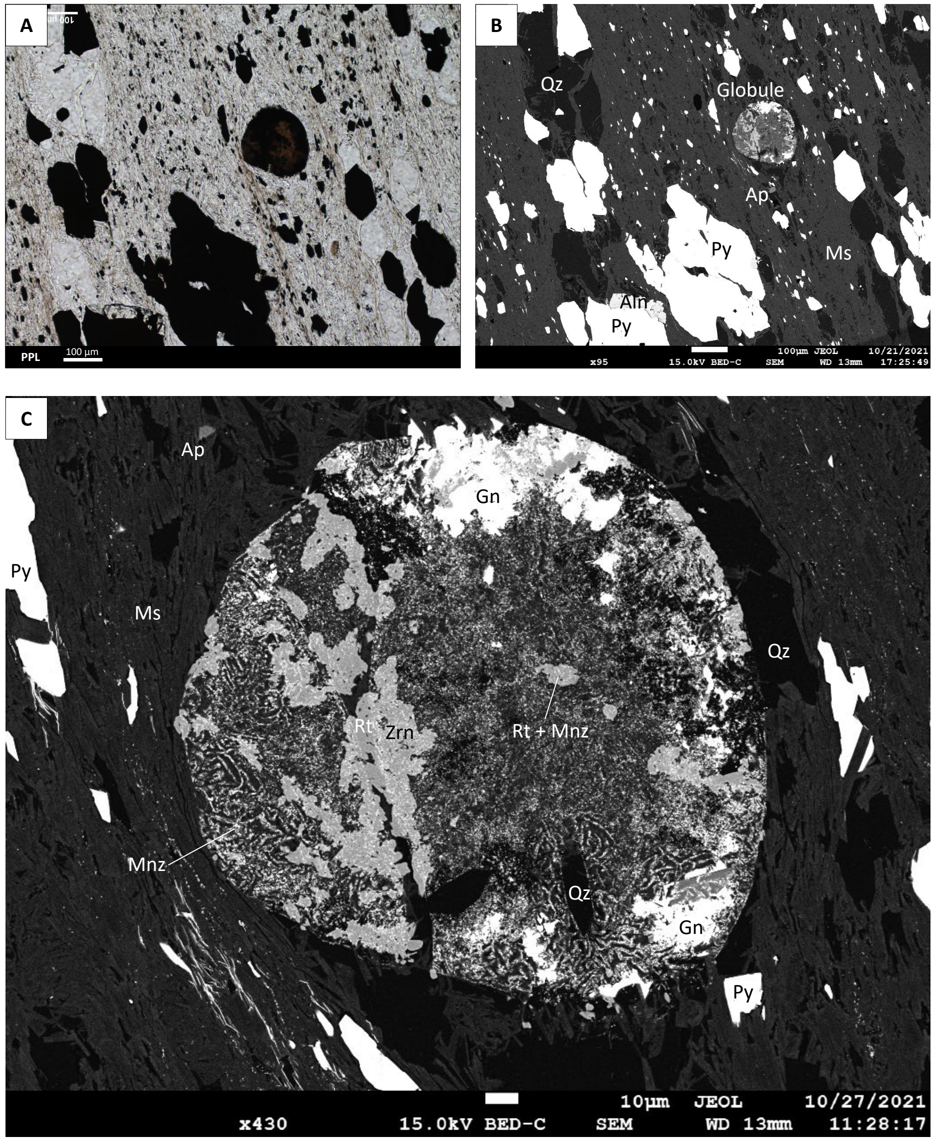

Fig. A2. 31 Microphotographs of a 150-micron globule (A-C). In PPL (A) the globule has a dark reddish-brown colour, imparted by rutile. (B) BSE image of the same FOV of as (A). (C) Close-up of the globule showing symplectic textures of rutile, zircon, and monazite. Anhedral masses of rutile are intergrown with zircon and monazite. Some of the rutile has Nb spectra peaks. The zircon and monazite crystals form vermicular textures. Patches of galena occur near the margins of the globule.

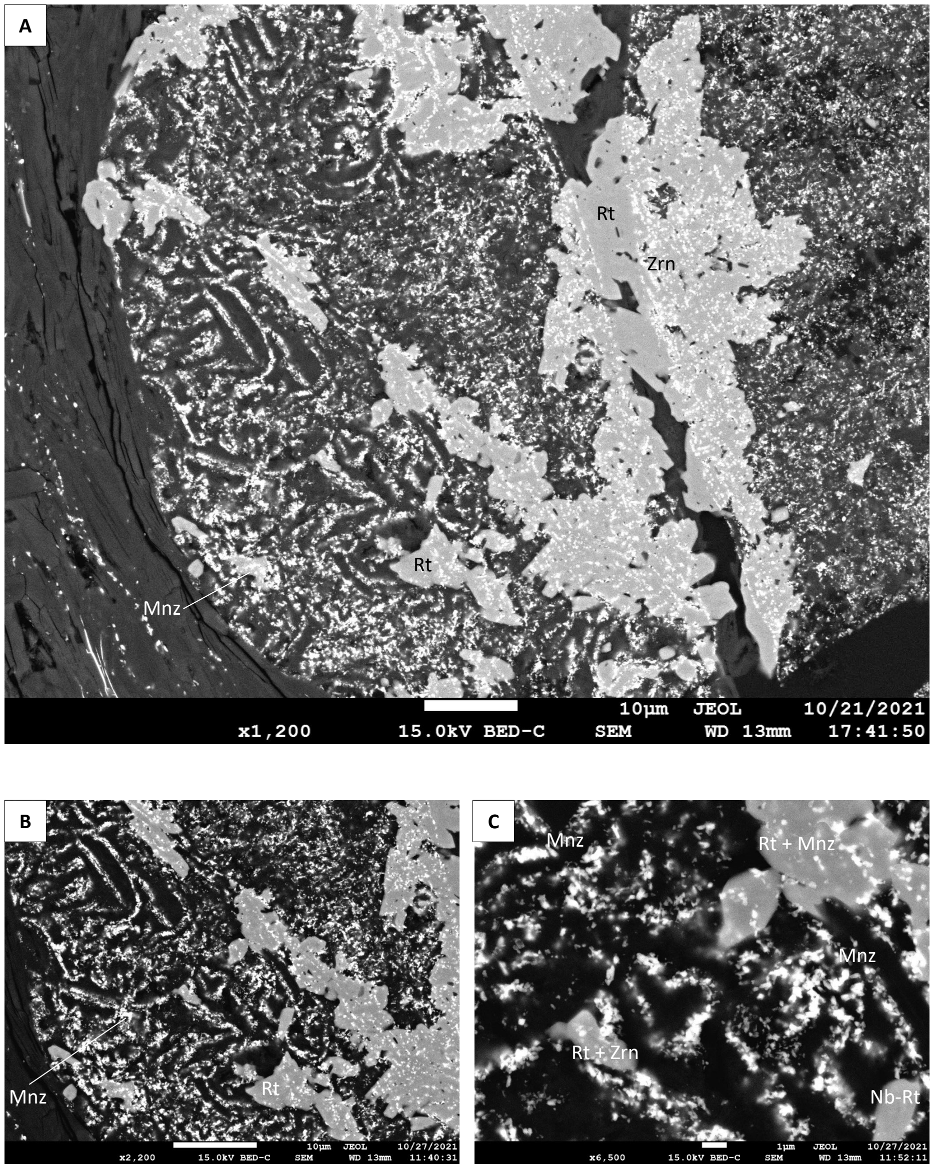

Fig. A2. 32 BSE images at different scales of the same globule as above (A-C). (A) Monazite and zircon (white) form vermicular textures within the globule. Rutile (grey) occurs as anhedral masses. (B-C) Close-up BSE images of the vermicular texture of sub-micron-sized zircon and monazite. The texture is reminiscent of ice crystals freezing on a windshield.

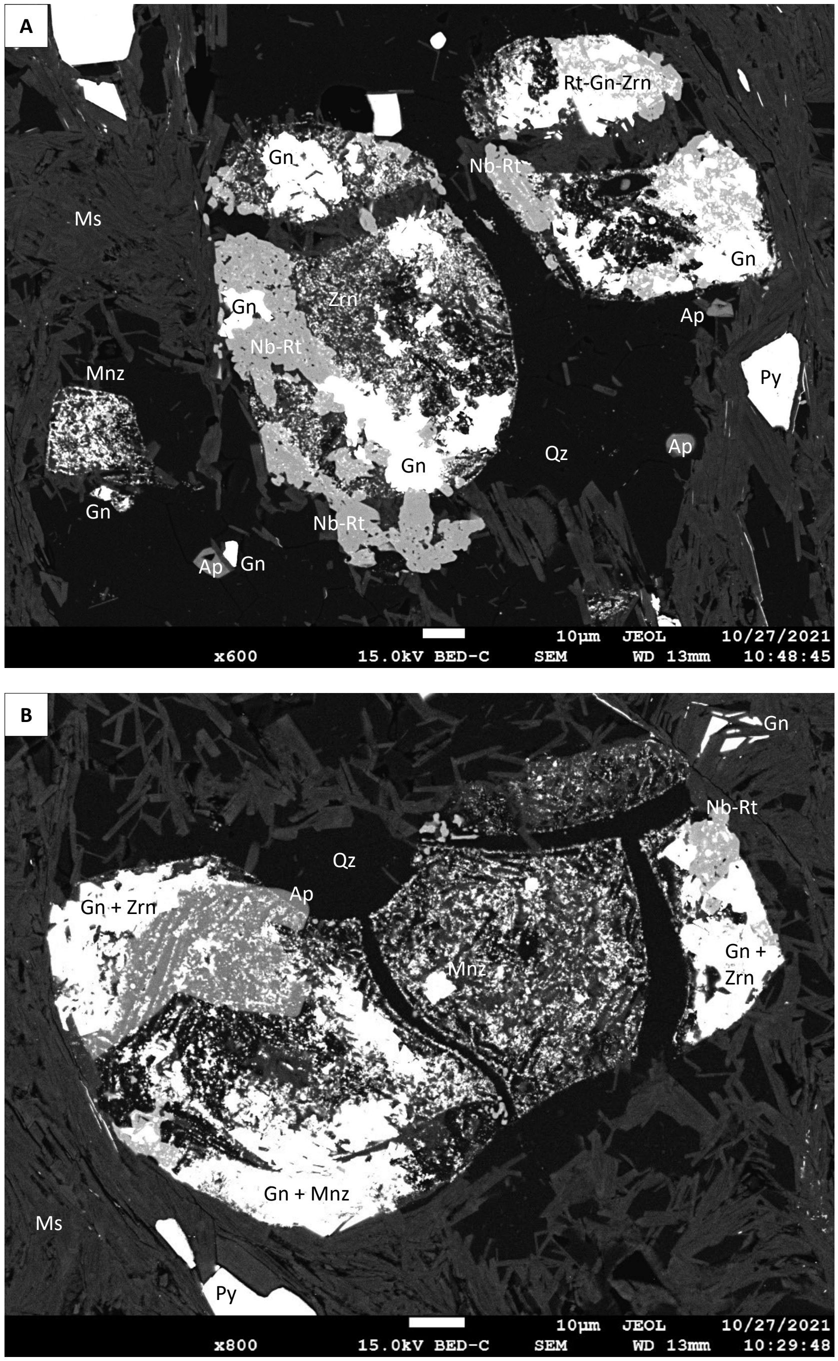

Fig. A2. 33 BSE images of examples of other globules in sample W605318 (A-B). (A) Three discrete globules composed of rutile, zircon, monazite, and galena. (B) Globule that looks fractured into four distinct parts. The larger anhedral bleb of monazite in the middle of the globule has Dy and Th spectra peaks. The apatite grain has a F spectra peak.

99-362 – FW-FeB

Sample ID: 99-362

Drill hole: CMR17-99 **Drill hole depth (m):** 362 m

Rock Name: Chl-qz-alb-cal-mag, plagioclase-phyric, amygdaloidal basalt
Geochemical Suite: Footwall ferrobasalt (FW-FeB)

Lithofacies and textures:
Porphyritic, amygdaloidal

Hand sample description:
Fg green, chl-cal groundmass w/ 10% diss fg mag. Plagioclase phenocrysts are white, soft (ms-replaced), subhedral laths 2-5mm. Tr fg py in clots.

Petrographic description:
The groundmass is mainly qz, chl, fsp (both pl and ab), and calcite with ~ 8% disseminated skeletal titaniferous magnetite. Ap and ep are accessory phases. Pl phenocrysts (~ 5%) are generally 2 – 3 mm long, but reach lengths up to 5 mm. They are typically lath-shaped, but some are equant and boxy. They are partially replaced by muscovite and lesser ab, chl and ep. Ms replacement locally has a cleavage and rim texture giving the muscovite a cross-hatched appearance. The larger pl phenocrysts are more strongly altered than the pl in the groundmass. Both pl phenocrysts and interstitial pl in groundmass have average andesine compositions, with pl phenocrysts having average anorthite content of 32% and (An_{32}) and pl in groundmass having average anorthite content of 39% (An_{39}). Probe work and stoichiometry distinguish between titaniferous magnetite, magnetite, and ilmenite. Titaniferous magnetite is the most abundant FeTi oxide mineral and is commonly skeletal. Tiny ilmenite crystals are rare. FeTi grains closer to stoichiometric magnetite compositions (Ulvospinel content ~ 4%) are also rare. Sparse (~25), relict amygdules are 0.5 – 1.3 mm. Some are deformed/flattened. They are composed of chlorite, calcite and quartz that are coarser-grained crystals than the groundmass.

Mineral	Residence	%	Size max (µm)	Habit	Comments
Chlorite	Groundmass, amyg	40	100	Subhedral-euhedral fibrous flakes	Some patches rim fsp phenocrysts.
Quartz	Groundmass, amyg	30	40	Anhedral-euhedral, interstitial	Recrystallized grains occupy interstitial space between other groundmass grains.
Titaniferous magnetite	Groundmass	8	200	Subhedral-euhedral, Skeletal	Shreddy margins, skeletal forms w/ hollow parts composed of groundmass minerals.
Plagioclase	Groundmass	5	100	Subhedral, interstitial, relic microlites?	Some may be relic microlites.
Albite	Replaces Pl	5	50	Anhedral, interstitial	Patchy replacement of pl in phenos, groundmass
Calcite	Groundmass, amyg	3	100	Subhedral, interstitial	Coarser grains with triple junctions are more common in amygs
Epidote	Groundmass	2	200	Subhedral-euhedral, Skeletal	Skeletal texture and embayed edges common. Minor partial replacement of some fsp phenocrysts. Can be lath-shaped in places.

Muscovite	Replaces Pl mainly in phenocrysts	4	50	Subhedral-euhedral fibrous flakes	Partially replace fps phenocrysts. Local cross-hatched texture (cleavage and rim replacement of primary twinning?). Some has minor Ba peak in SEM spectra.
Plagioclase	Phenocryst	1	5000	Subhedral, euhedral, lath	Pseudomorphs of pl are 5% of that, pl maybe accounts for 1% of rock?
Apatite	Groundmass	Tr	10	Subhedral	
Ilmenite	Groundmass, Ti-mag	Rare	8	Blebs	Rare in groundmass, or as bleb intergrown w/ Ti-mag.
Magnetite	Groundmass, Ti-mag	Rare	10	Euhedral	Rare in groundmass, or as bleb intergrown w/ Ti-mag. Generally smooth and not skeletal or ragged like Ti-mag.
Pyrite	Groundmass, amyg	Rare	100	Subhedral	Rare grain next to amyg
Chalcopyrite	Groundmass	Rare	10	Subhedral-euhedral	

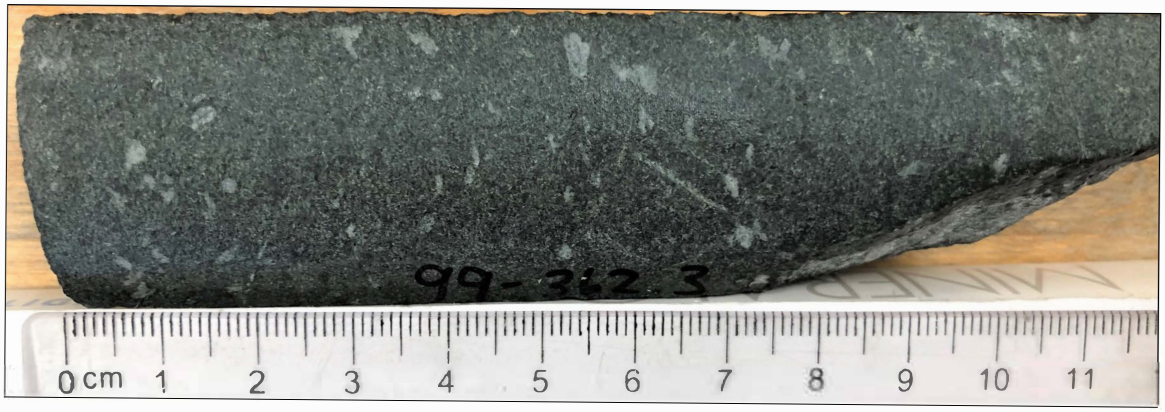

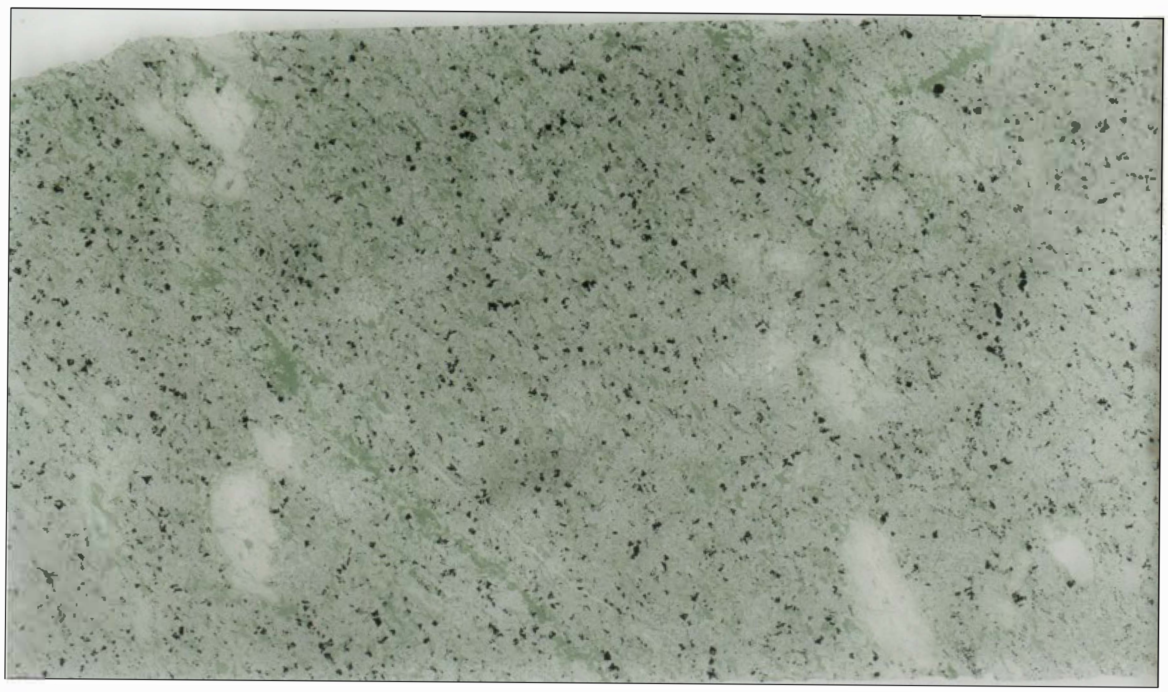

Fig. A2. 34 Hand sample photograph (above) and thin section scan (below) of sample 99-362.

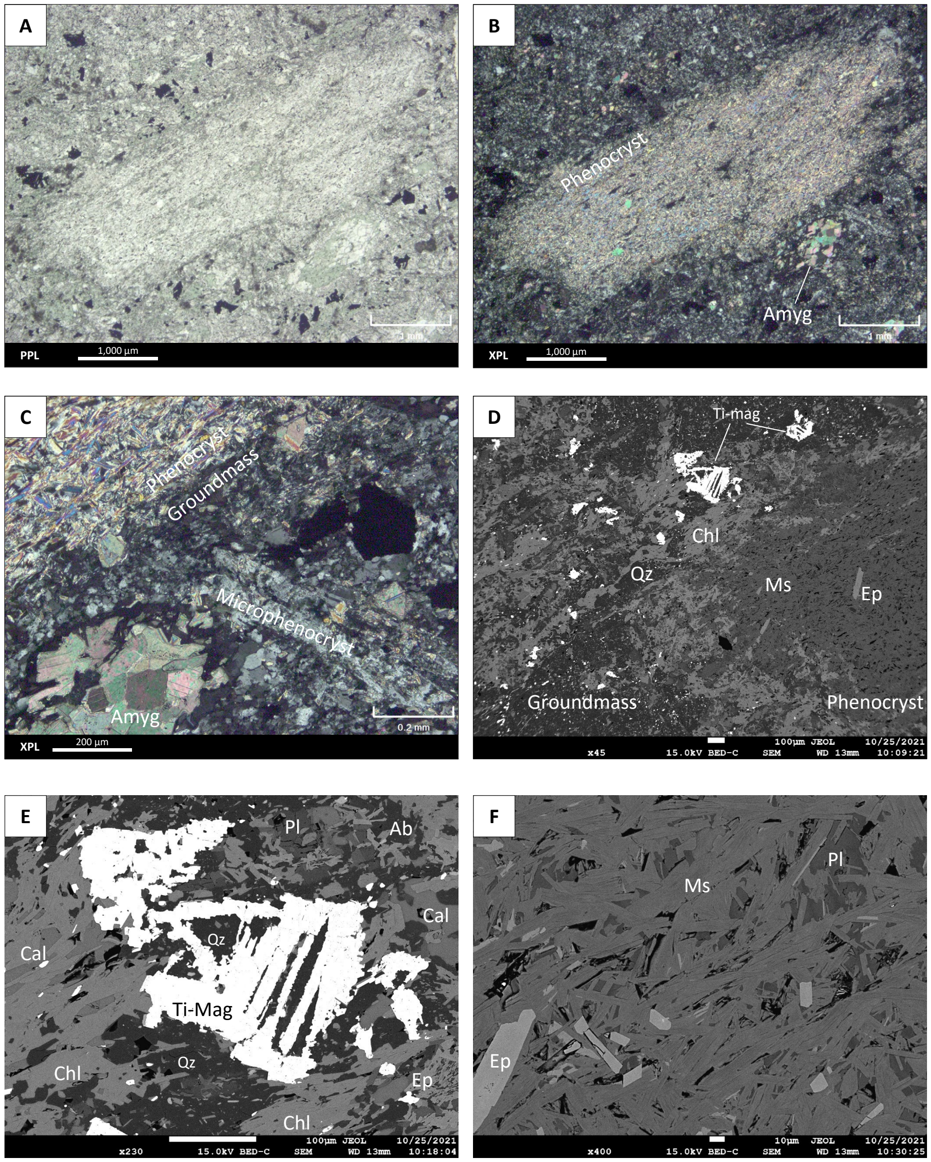

Fig. A2. 35 (A-E) Microphotographs and BSE images of a plagioclase phenocryst in groundmass. (A-B) Overview of plagioclase phenocryst that is nearly wholly replaced by muscovite in PPL (A) and XPL (B). An amygdule is composed of coarse recrystallized calcite (to bottom right of the phenocryst in the FOV). (C) Close up of the same phenocryst near the calcite amygdule in XPL. A Microphenocryst of plagioclase in the groundmass is less altered than the larger plagioclase phenocryst that has cross-hatched textured muscovite replacing it. (D) BSE image of the upper left edge of the same phenocryst in (A-B). Groundmass is chlorite and quartz with disseminated skeletal crystals of titaniferous magnetite. A few epidote grains also partially replace the plagioclase phenocryst. Chlorite is concentrated along the boundary between the phenocryst and groundmass. (E) Close-up BSE image of the same titaniferous magnetite crystal at the edge of the plagioclase phenocryst in (D). (F) Close up BSE image of the interior of the same plagioclase phenocryst that is nearly wholly replaced by muscovite and minor epidote.

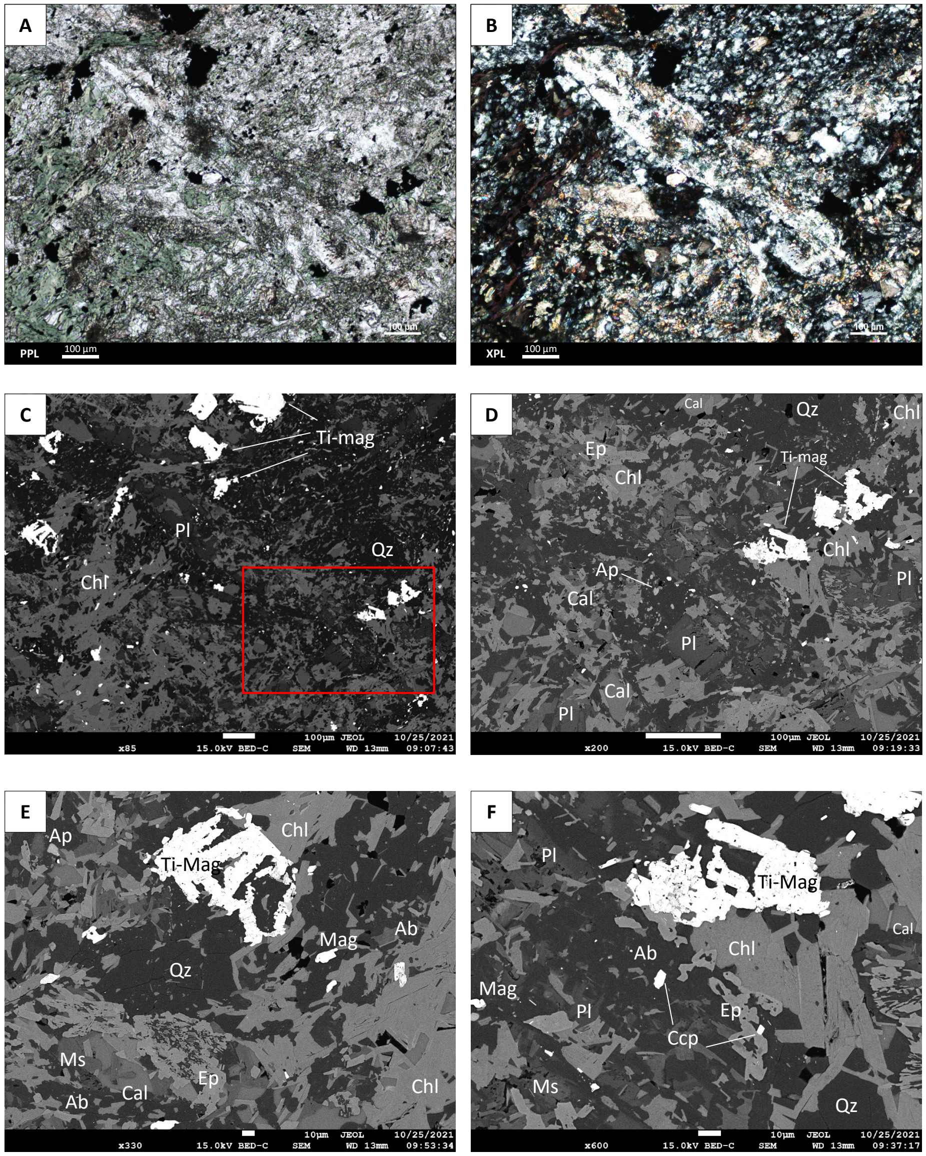

Fig. A2. 36 (A-E) Microphotographs and BSE images of the groundmass and relic plagioclase phenocrysts. (A-D) Plagioclase phenocryst in chlorite and quartz dominated groundmass. Titaniferous magnetite is disseminated.

Appendix 3. Whole rock geochemical data

Table A3. 1 Summary of Analytical Methods

ALS Code	Sample Decomposition	Analytical Method	# Analytes	Analytes
ME-XRF26	Li-borate fusion disk	XRF	15	Al_2O_3, BaO, CaO, Cr_2O_3, Fe_2O_3, K_2O, MgO, MnO, Na_2O, P_2O_5, SiO_2, SrO, TiO_2, LOI, Total
ME-IR08	LECO induction furnace	IR	2	C, S
ME-MS81	Li-borate fusion + 3-acid	ICP-MS	31	Ba, Ce, Cr, Cs, Dy, Er, Eu, Ga, Gd, Ge, Hf, Ho, La, Lu, Nb, Nd, Pr, Rb, Sm, Sn, Sr, Ta, Tb, Th, Tm, U, V, W, Y, Yb, Zr
ME-MS42	Aqua Regia	ICP-MS	9	As, Bi, Hg, In, Re, Sb, Se, Te, Tl
ME-4ACD81	4-acid	ICP-AES	10	Ag, Cd, Co, Cu, Li, Mo, Ni, Pb, Sc, Zn
Au-ICP21	Fire assay fusion	ICP - AES	1	Au
ME-OG62*	4-acid	ICP-AES	2	Pb, Zn

ICP-AES: Inductively Coupled Plasma - Atomic Emission Spectroscopy
ICP-MS: Inductively Coupled Plasma - Mass Spectrometry
IR: Infrared Spectroscopy
XRF: X-Ray Fluorescence Spectroscopy
4-acid: $HF\text{-}HNO_3\text{-}HClO_4$ acid digestion with HCl leach
3-acid: $HF\text{-}HNO_3\text{-}HCl$ acid digestion

*Samples with Zn and Pb values that exceeded the upper detection limits (10,000 ppm) of the ME-4ACD81 method were analyzed using ALS method ME-OG62. The prepared sample is digested in the same four acids and then evaporated to incipient dryness. HCl and de-ionized water is added for further digestion, and the sample is heated. The sample is then cooled to room temperature and transferred to a volumetric flask (100 mL), diluted to volume with de-ionized water, homogenized and analyzed by ICP-AES.

Table A3. 1 Whole rock lithogeochemical data of twenty-two drill core samples from the AG stratigraphy and six standard reference materials (ALS laboratory certificate #VA20253932). Three samples are duplicates of samples in the company database.

Sample	W812851	W812852	W812853	W812854	W812855	W812856	W812857	W812858	W812859	W812860
Hole		109	109	109	109	110		110	110	110
From-To (m)		250 - 251.3	269.8 - 270.9	352.3 - 352.8	391.9 - 392.3	33.6 - 34.2		120.2 - 120.5	141.8 - 142.5	167.4 - 168
Unit	Orca-1	FeR	FeA(?)	FW-FeB	FW-FeB	Argillite	LK-NIP 1	Trachyte dyke	Sed/Tuff	HW-FeTiB
Texture		Lapilli tuff	Flow margin breccia	Massive, Fsp-phyric, amygdaloidal	Massive; Fsp-phyric; amygdaloidal	Laminated		Fsp-porphyritic (25% fsp-phenocrysts)	Laminated	Lapilli tuff
Alteration		Qz-ser-py-brt	Qz-ser-py	Chl-ser-cal-mag-py	Chl-ep-cal-mag	Calcareous, trace py			Qz-ep	Mag-qz-ser
QAQC	SRM						SRM	DUP of W604724		
SiO_2 (wt %)	74.77	56.01	40.25	46.67	49.64	41.41	49.46	55.89	75.75	51.6
Al_2O_3	12.75	7.87	23.32	13.17	13.19	3.89	15.6	19.31	6.98	12.08
Fe_2O_3	2.91	6.75	12.88	16.61	16.93	5.61	13.78	4.82	4.33	23.8
TiO_2	0.29	0.21	2.61	1.95	1.88	0.18	1.18	0.53	0.4	2.39
MnO	0.06	0.04	0.02	0.24	0.25	0.09	0.19	0.13	0.07	0.03
MgO	0.48	0.55	1.7	2.68	4.31	4.54	7.4	1.3	1.37	2.09
CaO	1.15	0.87	0.49	7.63	6.97	24.2	10.45	4.6	5.12	1.58
K_2O	2.14	2.23	7.15	2.02	0.11	0.01	0.46	2.34	1.39	4.51
Na_2O	4.61	0.05	0.36	0.87	2.25	-0.01	2.39	6.49	0.06	0.13
P_2O_5	0.05	0.03	0.33	0.39	0.34	0.11	0.11	0.22	0.15	0.07
BaO	0.05	13.35	1.25	0.07	0.03	0.01	0.03	0.9	0.12	0.13
Cr_2O_3	0.01	0.01	0.02	-0.01	-0.01	-0.01	0.02	-0.01	0.01	-0.01
SrO	0.01	0.38	0.02	0.03	0.04	0.03	0.02	0.18	0.02	0.01
S	0.01	7.67	9.54	1.08	0.2	1	0.04	0.16	0.08	0.01
C	0.02	0.15	0.01	1.38	0.48	5.18	0.02	0.65	0.86	0.3
LOI	0.61	5.11	9.14	5.78	3.74	18.5	-0.11	3.28	3.64	1.46
Total	99.94	110	110	101	100.3	101.15	101.25	100.45	99.65	99.99
Se (ppm)	0.2	1.2	1	0.4	0.3	2.3	0.3	0.2	2.4	0.3
Li	10	-10	20	10	10	10	10	10	10	10
Sc	7	3	59	39	39	6	31	3	7	33
V	14	44	625	316	355	129	295	95	60	140
Cr	80	-10	90	10	10	40	160	20	100	30
Co	3	2	81	35	44	3	56	6	5	25
Ni	4	-1	44	4	8	13	151	3	17	27
Cu	12	366	215	82	32	16	167	8	31	-1
Zn	59	8590	1525	161	167	122	105	80	51	121
Ga	16.5	16.4	33.3	20.1	18.8	6	19.2	26.1	11.8	19.4
Ge	-5	-5	-5	-5	-5	-5	-5	-5	-5	5
As	1	41.2	109	5.7	2.6	0.6	0.9	0.7	2.6	1.4
Mo	4	3	4	1	1	1	1	-1	2	1
Ag	-0.5	5.7	6	-0.5	-0.5	-0.5	-0.5	-0.5	-0.5	-0.5
Cd	-0.5	31.5	5.2	0.6	0.5	0.5	-0.5	-0.5	-0.5	-0.5
In	0.023	0.066	0.078	0.012	0.011	0.019	0.015	0.006	0.009	0.015
Sn	4	3	1	1	1	-1	1	1	1	1
Sb	0.12	4.18	29.6	0.45	0.38	0.37	-0.05	0.25	0.18	0.55
Te	-0.01	-0.01	0.01	0.01	-0.01	0.06	-0.01	-0.01	0.15	-0.01
W	2	3	8	1	1	1	1	2	1	1
Re	0.001	0.001	0.005	0.002	0.001	0.003	0.001	-0.001	0.001	-0.001
Hg	0.005	0.336	0.15	0.005	-0.005	-0.005	-0.005	-0.005	0.006	0.011
Tl	0.02	0.84	0.65	0.08	0.04	0.03	0.08	0.39	0.04	1.21
Bi	0.05	0.08	0.07	0.03	0.02	0.1	0.02	0.06	0.12	0.02
Rb	52.9	42	134	30.3	2.3	0.3	12.2	62.2	24.9	133
Sr	71.6	3100	117.5	222	349	285	164	1690	148.5	102.5
Cs	0.56	0.73	2.15	0.42	0.16	0.05	0.6	1.17	0.26	4.56
Ba	392	10000	10000	615	126.5	24.2	140.5	9130	1085	1060
Pb	5	2970	1475	15	11	6	7	9	10	-2
Th	5.27	8.45	2	1.21	0.96	1.59	1.48	27.6	2.62	1.31
U	1.41	3.68	1.47	0.43	0.36	3.21	0.44	13	0.67	0.24
Y	72.4	65.7	61.7	45.1	39.9	37.5	21	31.8	17.3	18.7
Zr	264	359	172	138	119	98	86	374	82	183
Nb	11.4	23.1	15.3	11.3	10.2	3.1	4.6	24.5	6.5	15.3
Hf	8	9.1	4.5	3.6	3	1.6	2.2	8.2	3	3.4
Ta	1.1	1.4	0.9	0.8	0.7	0.3	0.4	1.3	0.5	1
La	29.1	32.6	21.3	12.8	11.2	12.8	8.4	108	19.9	15.2
Ce	64.9	64	42.8	29.2	25.4	16.7	18.6	198	28.6	33
Pr	8.76	7.74	5.66	4.28	3.48	2.88	2.44	22.7	5.25	4.32
Nd	37.3	31.5	25.9	19.6	16.2	12.7	11.3	84.5	24.2	19.6
Sm	9.82	9.26	7.59	5.64	5.1	3.04	3.07	14.55	5.57	5.05
Eu	1.34	0.57	1.67	1.7	1.51	0.63	1.05	3.36	1.13	1.61
Gd	10.5	9.31	9.57	6.66	6.28	4.81	3.72	9.55	5.02	5.12
Tb	1.79	1.78	1.72	1.2	1.06	0.83	0.61	1.22	0.65	0.83
Dy	11.7	11.5	11.45	7.68	7.01	5.27	3.85	6.17	3.52	4.92
Ho	2.56	2.43	2.46	1.66	1.56	1.17	0.89	1.16	0.66	1.01
Er	7.9	7.29	7.29	5.06	4.61	3.43	2.41	3.02	1.69	3.23
Tm	1.17	1.09	1.11	0.76	0.67	0.48	0.32	0.43	0.23	0.46
Yb	7.99	7.51	6.76	4.82	4.32	2.62	2.08	2.83	1.44	3.15
Lu	1.26	1.13	1.03	0.75	0.66	0.39	0.32	0.46	0.22	0.48
Au	0.013	0.03	0.078	0.006	0.002	0.004	NSS	-0.001	0.003	0.002
Pb (wt %)										
Zn (wt %)										

Table A3. 1 continued

Sample	W812861	W812862	W812863	W812864	W812865	W812866	W812867	W812868	W812869	W812870
Hole	110	110		110	110	110	110	110		110
From-To (m)	189 - 189.6	224.24 - 224.9		233.7 - 234.7	272.4 - 273.4	290.3 - 291.1	319.7 - 320.3	332.5 - 333		337.6 - 338
Unit	HW-FeTiB	HW-FeTiB	Orca-1	Argillite	Mineralized heterolithic fragmental	FeR block(?) in heterolithic fragmental	FeR	FeA	LK-NIP 1	Mafic dyke
Texture	Agglomerate lapilli tuff	Lapilli tuff		Laminated	Chaotic; Lapilli tuff	Lapilli tuff	Lapilli tuff	Massive; amygdaloidal		Massive; felted
Alteration	Mag-qz-ser-chl-jasper	FeCarb-cal-mag-chl-qz-jasper		Calcareous, trace py	Py-brt-sph-ser-qz	Qz-py-chl-cal-FeCarb	Qz-ser-py-mag-chl	Chl-FeCarb-cal-mag		Chl-ep
QAQC			SRM						SRM	
SiO_2 (wt %)	55.86	32.19	74.71	41.06	29.97	76.82	48.5	53.01	49.18	47.17
Al_2O_3	13	10.16	12.74	5.83	9.46	3.25	17.14	15.27	15.48	13.28
Fe_2O_3	17.6	15.19	2.91	8.99	25.47	7.12	17.13	13.6	13.6	9.95
TiO_2	2.52	1.7	0.29	0.29	0.93	0.11	0.6	2	1.16	0.77
MnO	0.03	0.3	0.06	0.78	0.03	0.11	0.05	0.1	0.19	0.19
MgO	2.22	5.6	0.47	6.26	0.55	1.26	2.44	3.44	7.33	10.2
CaO	1.14	14.4	1.15	14.95	0.15	3.47	1.91	6.65	10.35	11.75
K_2O	4.85	3.08	2.15	1.31	2.68	0.56	3.07	1.87	0.46	0.23
Na_2O	0.2	0.17	4.62	0.14	0.08	0.31	0.72	0.09	2.38	2.23
P_2O_5	0.08	0.5	0.05	0.19	0.02	0.02	0.04	0.33	0.11	0.12
BaO	0.07	0.23	0.05	0.58	8.19	0.45	0.36	0.14	0.03	0.02
Cr_2O_3	-0.01	-0.01	0.01	0.01	-0.01	-0.01	-0.01	-0.01	0.02	0.1
SrO	0.01	0.05	0.01	0.02	0.09	0.02	0.02	0.06	0.02	0.04
S	0.01	0.02	0.01	2.74	23.7	4.58	7.65	0.31	0.03	0.03
C	0.2	4.2	0.02	5.73	0.02	1.01	0.12	0.31	0.02	0.56
LOI	1.67	16.32	0.65	15.81	17.86	5.35	7.81	3.53	-0.06	4.24
Total	99.4	100.05	99.91	102.8	110	109.65	110	101.05	100.45	100.45
Se (ppm)	0.2	0.2	-0.2	4.2	33.3	0.3	0.4	0.9	-0.2	-0.2
Li	10	10	10	-10	10	10	20	20	10	10
Sc	34	26	7	7	11	2	9	29	31	40
V	492	442	12	166	109	18	61	239	339	327
Cr	40	30	70	90	10	10	10	10	180	780
Co	27	24	3	8	10	1	11	32	57	40
Ni	23	16	5	26	2	1	2	4	154	74
Cu	1	1	11	36	1010	10	11	34	171	5
Zn	127	95	56	27	10000	167	122	226	106	129
Ga	22.6	16.4	17.2	7.7	18.6	4.8	34.4	26	20.9	14.8
Ge	-5	-5	-5	-5	-5	-5	-5	6	-5	-5
As	1.5	2.1	0.6	79.7	250	108.5	12.3	5.1	1	2.7
Mo	1	-1	5	2	16	4	18	1	1	2
Ag	-0.5	-0.5	-0.5	2.4	86.1	0.7	-0.5	-0.5	-0.5	-0.5
Cd	-0.5	1.4	-0.5	0.5	89.3	0.7	-0.5	-0.5	-0.5	0.5
In	0.014	0.026	0.024	0.008	0.056	0.01	0.02	0.012	0.018	0.009
Sn	1	1	4	-1	1	1	6	2	1	1
Sb	1.01	2.7	0.11	10.25	250	3.44	0.71	1.24	-0.05	0.45
Te	-0.01	-0.01	-0.01	0.06	0.01	-0.01	-0.01	0.01	-0.01	-0.01
W	-1	1	1	2	24	-1	1	2	1	1
Re	-0.001	-0.001	0.001	0.026	0.019	0.001	0.003	0.002	0.001	0.001
Hg	-0.005	-0.005	-0.005	0.02	1.44	0.316	0.016	0.006	-0.005	-0.005
Tl	1.89	4.18	0.02	1.36	3.76	7.33	1.38	0.64	0.07	0.14
Bi	0.01	0.01	0.04	0.1	0.03	0.03	0.09	0.02	0.02	0.01
Rb	153	96.6	56	27.3	56.2	13.9	64.6	38.2	13.8	3.7
Sr	86	424	74	191	704	125.5	214	518	181	382
Cs	5.24	2.99	0.6	0.31	1.11	0.55	1.87	0.7	0.59	0.18
Ba	575	2260	406	5760	10000	4570	3650	1260	155	111
Pb	2	8	6	13	10000	56	8	66	2	7
Th	1.94	1.6	5.13	1.51	1.81	3.29	17.75	4.26	1.57	1.51
U	0.28	0.61	1.3	2.33	8.47	1.58	3.29	3.5	0.46	0.79
Y	28.5	45.6	72.4	27.9	26.2	14.5	83.7	61	22.7	17.6
Zr	152	165	270	51	133	90	708	283	86	61
Nb	17.3	12.4	11.8	3.9	9.6	11	60.6	18.5	4.9	3.2
Hf	3.7	3.6	7.9	1.4	3.3	2.6	19	6.5	2.4	1.8
Ta	1	0.8	1	0.3	0.5	0.6	3.1	1	0.4	0.2
La	15.9	17.4	27.7	13.9	24.7	12	70.5	26.5	8.8	8.1
Ce	34.6	39.8	63.9	17	46.1	23.8	155.5	57	19.5	17.7
Pr	4.6	5.29	8.44	3.04	5.78	2.56	17.95	7.28	2.67	2.43
Nd	19.8	22.5	35.1	12.4	23.5	8.5	69.2	30.6	11.8	10.6
Sm	5.06	5.82	9.65	2.6	6.34	1.65	17.05	8.12	3.3	2.98
Eu	1.74	1.78	1.3	0.62	2.27	0.34	2.72	2.23	1.1	0.98
Gd	5.73	6.58	10.3	3	5.26	1.79	16.7	9.94	4.1	3.32
Tb	0.98	1.17	1.87	0.5	0.93	0.41	2.9	1.76	0.67	0.53
Dy	5.6	7.1	11.85	3.46	5.38	2.7	17.25	11.35	4.01	3.2
Ho	1.13	1.56	2.54	0.78	1.12	0.6	3.54	2.42	0.84	0.66
Er	3.32	4.88	8.25	2.49	3.36	2.14	10.75	7.31	2.49	1.98
Tm	0.47	0.72	1.22	0.35	0.53	0.35	1.6	1.1	0.37	0.28
Yb	3.1	4.61	8.42	2.44	3.25	2.42	10.4	7.29	2.24	1.85
Lu	0.47	0.76	1.22	0.37	0.46	0.36	1.47	1.06	0.33	0.28
Au	0.001	-0.001	0.003	0.016	0.088	-0.001	0.001	0.002	0.009	-0.001
Pb (wt %)					1.145					
Zn (wt %)					2.4					

Table A3. 1 continued

Sample	W812871	W812872	W812873	W812874	W812875	W812876	W812877	W812878
Hole	110	110	120	120	120		112	
From-To (m)	367.7 - 368.1	377.8 - 378.2	301.1 - 302	323.1 - 323.4	330.9 - 331.7		536.4 - 536.9	
Unit	HSR	Calc-alkaline andesitic dyke	Jasper-magnetite exhalite	Z-FeTiB	FeA	Orca-1	FeD (least altered)	LK-NIP 1
Texture	Massive	Fsp- and Amp-phyric	Splotchy	Amygdaloidal; variolitic	Massive, amygdaloidal		Amygdaloidal	
Alteration	Qz-ep-chl(?)	Chl-ep-cal	Qz-Mag-cal	Mag-chl-cal	Chl-mag-cal-jasper		Chl-qz-ep	
QAQC	DUP of W604709	DUP of W604712				SRM		SRM
SiO_2 (wt %)	67.86	53.41	32.22	42.25	50.44	74.82	65.63	49.45
Al_2O_3	14.74	17.86	0.23	13.71	12.2	12.76	11.79	15.54
Fe_2O_3	3.58	8.14	15.02	16.78	13.59	2.92	8.93	13.74
TiO_2	0.15	0.66	0.01	3.04	1.64	0.29	0.85	1.18
MnO	0.03	0.12	0.29	0.22	0.11	0.06	0.1	0.19
MgO	0.97	3.87	0.42	4.48	4.53	0.48	2.14	7.41
CaO	4.27	8.25	29.1	8.74	7.91	1.15	3.44	10.4
K_2O	3.56	0.88	0.03	3.04	2.09	2.14	1.04	0.46
Na_2O	0.37	3.11	-0.01	1.4	0.43	4.61	3.71	2.41
P_2O_5	0.04	0.15	0.04	0.93	0.56	0.05	0.32	0.11
BaO	0.25	0.07	0.1	0.09	0.18	0.05	0.03	0.03
Cr_2O_3	-0.01	-0.01	-0.01	-0.01	-0.01	0.01	-0.01	0.02
SrO	0.02	0.1	0.04	0.05	0.05	0.01	0.03	0.02
S	0.04	0.2	0.12	0.01	0.19	0.02	0.07	0.03
C	0.5	0.21	6.27	0.98	0.97	0.01	0.25	0.02
LOI	3.68	3.04	22.36	4.96	5.49	0.64	1.6	-0.11
Total	99.64	100.25	100.2	99.84	99.84	100.05	99.85	101.1
Se (ppm)	-0.2	0.3	-0.2	0.2	0.4	-0.2	0.2	-0.2
Li	10	20	-10	20	20	10	10	10
Sc	1	16	-1	35	25	7	10	32
V	5	254	59	358	195	13	18	330
Cr	-10	10	10	20	10	90	10	170
Co	2	24	3	27	24	4	9	59
Ni	2	5	3	10	4	5	-1	159
Cu	9	24	4	1	41	11	16	180
Zn	99	78	10	182	152	56	101	109
Ga	36.8	21.4	0.8	23.1	20.1	17.7	18.5	20.3
Ge	-5	-5	-5	5	5	-5	-5	-5
As	0.6	2.5	0.9	1.5	1.9	0.9	0.9	0.9
Mo	1	1	5	2	1	5	2	1
Ag	-0.5	-0.5	-0.5	-0.5	-0.5	-0.5	-0.5	-0.5
Cd	-0.5	-0.5	0.8	0.7	0.5	-0.5	-0.5	0.9
In	0.02	0.005	-0.005	0.013	0.009	0.022	0.007	0.016
Sn	9	1	-1	2	2	4	4	1
Sb	0.99	0.42	0.19	0.2	0.36	0.12	0.18	-0.05
Te	0.01	0.01	0.01	-0.01	0.01	-0.01	-0.01	0.01
W	1	1	1	1	1	1	1	1
Re	-0.001	-0.001	-0.001	-0.001	-0.001	-0.001	-0.001	0.001
Hg	-0.005	-0.005	-0.005	-0.005	-0.005	-0.005	-0.005	-0.005
Tl	0.19	0.22	-0.02	0.42	0.39	0.02	0.17	0.07
Bi	0.01	0.01	0.03	-0.01	0.01	0.04	0.01	0.02
Rb	54.5	20.1	0.7	93.2	58.3	58.2	28.4	13.6
Sr	179	938	377	403	399	76.3	332	175
Cs	1.24	1	0.03	3.33	1.95	0.62	0.99	0.57
Ba	2540	611	869	749	1670	418	231	145.5
Pb	7	17	4	5	-2	-2	5	2
Th	13.95	3.11	0.08	2.25	3.09	5.33	6.41	1.55
U	3.52	1.28	0.97	1.94	1.63	1.39	2.96	0.48
Y	135	14.5	2.6	91.3	57.5	74.8	56.7	21.8
Zr	414	95	31	201	240	281	335	83
Nb	79.5	5.2	0.6	20.7	13.5	12.3	19	4.7
Hf	14.9	2.7	0.3	4.6	4.5	8.3	8	2.4
Ta	4.8	0.4	0.1	1.2	0.8	1.1	1.2	0.3
La	111.5	15.9	0.9	28.2	21.9	28.3	27.9	8.7
Ce	240	31.7	1.4	60.4	48.1	65.7	57.2	19
Pr	28.4	4.05	0.2	8.13	6.39	8.66	6.87	2.55
Nd	111.5	16.2	0.9	35.9	27	36.1	27.3	11.1
Sm	28.3	3.77	0.22	10.1	7.38	9.68	6.99	3.26
Eu	5.03	1.08	0.08	3.08	2.04	1.42	1.61	1.11
Gd	28.8	3.19	0.33	12.7	8.65	11	7.56	3.94
Tb	5.15	0.46	0.06	2.2	1.56	1.98	1.4	0.66
Dy	29.5	2.55	0.33	14.05	9.96	11.9	9.31	3.93
Ho	5.7	0.52	0.09	3.08	2.16	2.6	2.08	0.83
Er	17.25	1.55	0.28	9.82	6.9	8.53	6.9	2.48
Tm	2.63	0.24	0.04	1.35	1.04	1.32	1.04	0.37
Yb	18.15	1.55	0.37	9.17	7.29	8.6	7.22	2.16
Lu	2.63	0.25	0.06	1.4	1.1	1.28	1.06	0.35
Au	-0.001	0.001	0.047	-0.001	0.003	-0.001	-0.001	0.021
Pb (wt %)								
Zn (wt %)								

Appendix 4. Quality control and quality assurance (QAQC)

Researcher: Kei Quinn

Principal Investigator: Steve Piercey

Lab Name: ALS

Certificate #: VA20253932

Method: See Table A3. 1 for a summary of analytical methods

For this study, six in-house reference materials (three LK-NIP-1 diabase and three ORCA-1 rhyolite) and three blind duplicates were analyzed at ALS Laboratories in North Vancouver to monitor analytical accuracy and precision (Appendix 4). These reference materials were chosen as they represented the matrix of materials in the project area and the broad range of analytes. The ALS lab also inserted and analyzed 37 lab-chosen standards and 16 blanks during the run.

The LK-NIP-1 diabase (a sill from the Kitto Township, south of Beardmore, Ontario, Canada) and the ORCA-1 rhyolite (calc-alkaline rhyolite collected from Pontiac Township, 35 km northeast of Kirkland Lake, Ontario, Canada) samples were assessed for both accuracy and precision using percent relative difference (%RD) and percent relative standard deviation (%RSD) (Abzalov, 2008; Piercey, 2014). Precision was also estimated using the average coefficient of variation (CV_{avg}) from duplicate samples (Abzalov, 2008; Piercey, 2014). Quality ratings for accuracy and precision are summarized in Table A4. 1 (Jenner, 1996). Results are summarized in Table A4. 2 to Table A4. 4.

The accuracy of all analytes reported in the provisional data sheet for the standard reference materials was tested by calculating the percent relative difference:

$$\% \, RD = 100 \, x \, \frac{\mu_i - STD_i}{STD_i}$$

Where μ_i is the mean value of element i in the standard over a number of analytical runs, and STDi is the certified value of element i in the standard reference material. Most major elements returned absolute percent relative difference (% RD) values < 2%, except P_2O_5 (<12%) and MnO (<5% for LK-NIP-1). Most trace elements gave %RD values <10%, with many below 5%. Most trace elements gave %RD values <10%, with many below 5%. Trace elements with %RD > 10% included Cr (for ORCA-1), Cs (for LK-NIP-1), Ta (for LK-NIP-1), As (for ORCA-1), Bi (for ORCA-1), Re (for ORCA-1), Se (LK-NIP-1), Te (LK-NIP-1), Cd (LK-NIP-1), Mo (ORCA-1), Ni (ORCA-1), Pb (both ORCA-1 and LK-NIP-1), and Au (both ORCA-1 and LK-NIP-1), Co (for ORCA-1), Li (for ORCA-1), Mo (for LK-NIP-1), Ni (ORCA-1), Pb (both ORCA-1 and LK-NIP-1), Sc (LK-NIP-1), and Zn (ORCA-1). For the most part, the results were within a reasonable magnitude compared to the accepted value, and elevated % RD values were associated with analytes with concentrations at or near the lower detection limit.

To evaluate the reproducibility of the analytical results, the relative standard deviation (% RSD) was calculated as follows:

$$\% \, RSD = 100 \, x \, \frac{s_i}{\mu_i}$$

Where μ_i is the mean value of element i in the standard over a number of analytical runs, and s_i is the standard deviation of the mean from the analytical runs for element i. Most major elements returned absolute percent relative standard deviation (% RSD) values < 1%, except MgO (<2% for ORCA-1). Most trace elements gave %RSD values <10%, with many below 5%. Trace elements with %RSD > 10% include Cr (for ORCA-1), Ta (for LK-NIP-1), W (for ORCA-1), V (for ORCA-1), Zr (for ORCA-1), Tl (for both ORCA-1 and LK-NIP-1), Co (for ORCA-1), Li (for ORCA-1), Mo (for LK-NIP-1), Ni (ORCA-1), Pb (both ORCA-1 and LK-NIP-1), and Au (both ORCA-1 and LK-NIP-1). Results with elevated % RSD values are generally attributed to analytes with concentrations at or near the lower detection limit.

A total of three duplicate samples were collected. The original samples were collected by Company geologists as half-core samples and analyzed in 2018. The duplicate samples were quartered portions of the remaining core and analyzed using the same methods in 2020. Relatively homogeneous samples (massive high-silica rhyolite, a trachyte dyke, and a basaltic-andesite calc-alkaline dyke) were selected because any inherent inhomogeneity in samples makes them less ideal for assessing precision. The pairs were assessed using the average coefficient of variation for all analytes determined. The average coefficient of variation (CV_{avg}) is defined as:

$$CVavg\ (\%) = 100\ x\ \sqrt{\left(\frac{2}{N}\right)\sum_{i=1}^{N}\left(\frac{(a_i-b_i)^2}{(a_i+b_i)^2}\right)},$$

where a_i = the original sample and b_i = the duplicate sample of i pairs, and N is the total number of duplicate pairs. The average coefficient of variation is a robust and efficient method to assess the precision of duplicate data. It applies to datasets with a normal or non-normal distribution of errors. The CV_{avg} for three duplicate pairs returned results of all majors less than 10%, except for BaO (<23.22%) and P_2O_5 (< 10.09%). All HFSE were < 10% except for Ta (13.61%). The CV_{avg} for all REE was <10%. Other trace elements with CV_{avg} >10% include Ba, Cr, As, Bi, In, Sb, Sc, Tl, Co, Cu, Ni, and Pb. Poor precision was common for analytes near the lower limit of detection.

Table A4. 1 Summary of precision and accuracy quality ranking system proposed by Jenner (1996).

% RD (±) for accuracy	% CV_{avg} or % RSD for precision	Quality
0–3	0–3	Excellent
3–7	3–7	Very good
7–10	7–10	Good
>10	>10	Poor

Table A4. 2 Whole rock lithogeochemical data and summary of percent relative difference (% RD) and percent relative standard deviation (% RSD) results for the LK-NIP-1 standard reference materials.

					QAQC - LK-NIP-1									
ALS Method	**Analyte**		**LOD**	**3.3 LOD = LOQ**	**LK-NIP 1 accepted values**	**W812851**	**W812863**	**W812876**	**Avg**	**Stdev**	**%RSD**	**%RD**	**Comments on precision**	**Comments on accuracy**
ME-XRF26	SiO_2	%	0.01	0.03	49.65	49.46	49.18	49.45	49.36	0.16	0.32	-0.58		
ME-XRF26	Al_2O_3	%	0.01	0.03	15.84	15.6	15.48	15.54	15.54	0.06	0.39	-1.89		
ME-XRF26	Fe_2O_3	%	0.01	0.03	13.79	13.78	13.6	13.74	13.71	0.09	0.69	-0.60		
ME-XRF26	CaO	%	0.01	0.03	10.46	10.45	10.35	10.4	10.40	0.05	0.48	-0.57		
ME-XRF26	MgO	%	0.01	0.03	7.38	7.4	7.33	7.41	7.38	0.04	0.59	0.00		
ME-XRF26	Na_2O	%	0.01	0.03	2.43	2.39	2.38	2.41	2.39	0.02	0.64	-1.51		
ME-XRF26	K_2O	%	0.01	0.03	0.47	0.46	0.46	0.46	0.46	0.00	0.00	-2.13		
ME-XRF26	Cr_2O_3	%	0.01	0.03		0.02	0.02	0.02	0.02	0.00	0.00			
ME-XRF26	TiO_2	%	0.01	0.03	1.18	1.18	1.16	1.18	1.17	0.01	0.98	-0.56		
ME-XRF26	MnO	%	0.01	0.03	0.2	0.19	0.19	0.19	0.19	0.00	0.00	-5.00		
ME-XRF26	P_2O_5	%	0.01	0.03	0.1	0.11	0.11	0.11	0.11	0.00	0.00	10.00		In the ballpark
ME-XRF26	SrO	%	0.01	0.03		0.02	0.02	0.02	0.02	0.00	0.00			
ME-XRF26	BaO	%	0.01	0.03		0.03	0.03	0.03	0.03	0.00	0.00			
OA-GRA05	LOI	%	0.01	0.03	0.17	-0.11	-0.06	-0.11	-0.09	0.03	-30.93	-154.90	Near LOQ	Near LOQ
TOT-ICP06	Total	%	0.01	0.03		101.25	100.45	101.1	100.93	0.43	0.42			
C-IR07	C	%	0.01	0.03		0.02	0.02	0.02	0.02	0.00	0.00			
S-IR08	S	%	0.01	0.03	0.02	0.04	0.03	0.03	0.03	0.01	17.32	66.67	Near LOQ	Near LOQ
ME-MS81	Ba	ppm	0.5	1.65	142.3	140.5	155	145.5	147	7.37	5.01	3.30		
ME-MS81	Ce	ppm	0.1	0.33	20.59	18.6	19.5	19	19.0	0.45	2.37	-7.56		
ME-MS81	Cr	ppm	10	33.00	183	160	180	170	170	10.00	5.88	-7.10		Consistently lower
ME-MS81	Cs	ppm	0.01	0.03	0.69	0.6	0.59	0.57	0.59	0.02	2.60	-14.98		Near LOQ
ME-MS81	Dy	ppm	0.05	0.17	4.238	3.85	4.01	3.93	3.93	0.08	2.04	-7.27		
ME-MS81	Er	ppm	0.02	0.07	2.553	2.41	2.49	2.48	2.46	0.04	1.77	-3.64		
ME-MS81	Eu	ppm	0.02	0.07	1.174	1.05	1.1	1.11	1.1	0.03	2.96	-7.44		
ME-MS81	Ga	ppm	0.1	0.33	19.8	19.2	20.9	20.3	20.1	0.86	4.28	1.68		
ME-MS81	Gd	ppm	0.05	0.17	4.072	3.72	4.1	3.94	3.9	0.19	4.87	-3.73		
ME-MS81	Ge	ppm	5	16.50		-5	-5	-5	-5	0.00	0.00			
ME-MS81	Hf	ppm	0.5	1.65	2.5	2.2	2.4	2.4	2.3	0.12	4.95	-6.67		
ME-MS81	Ho	ppm	0.01	0.03	0.888	0.89	0.84	0.83	0.85	0.03	3.77	-3.90		
ME-MS81	La	ppm	0.1	0.33	9.27	8.4	8.8	8.7	8.6	0.21	2.41	-6.87		
ME-MS81	Lu	ppm	0.01	0.03	0.352	0.32	0.33	0.35	0.33	0.02	4.58	-5.30		
ME-MS81	Nb	ppm	0.1	0.33	4.9	4.6	4.9	4.7	4.7	0.15	3.23	-3.40		
ME-MS81	Nd	ppm	0.1	0.33	12.5	11.3	11.8	11.1	11.4	0.36	3.16	-8.80		
ME-MS81	Pr	ppm	0.02	0.07	2.776	2.44	2.67	2.55	2.55	0.12	4.51	-8.02		
ME-MS81	Rb	ppm	0.2	0.66	14.04	12.2	13.8	13.6	13.2	0.87	6.60	-5.98		
ME-MS81	Sm	ppm	0.03	0.10	3.33	3.07	3.3	3.26	3.21	0.12	3.83	-3.60		
ME-MS81	Sn	ppm	1	3.30		1	1	1	1	0.00	0.00			
ME-MS81	Sr	ppm	0.1	0.33	176.9	164	181	175	173	8.62	4.97	-2.02		
ME-MS81	Ta	ppm	0.1	0.33	0.3	0.4	0.4	0.3	0.4	0.06	15.75	22.22	Near LOQ	In the ballpark; near LOQ
ME-MS81	Tb	ppm	0.01	0.03	0.682	0.61	0.67	0.66	0.65	0.03	4.97	-5.18		
ME-MS81	Th	ppm	0.05	0.17	1.65	1.48	1.57	1.55	1.53	0.05	3.08	-7.07		
ME-MS81	Tm	ppm	0.01	0.03	0.368	0.32	0.37	0.37	0.35	0.03	8.17	-3.99		
ME-MS81	U	ppm	0.05	0.17	0.485	0.44	0.46	0.48	0.46	0.02	4.35	-5.15		
ME-MS81	V	ppm	5	16.50	306	295	339	330	321	23.25	7.23	5.01		
ME-MS81	W	ppm	1	3.30		1	1	1	1	0.00	0.00			
ME-MS81	Y	ppm	0.1	0.33	23.37	21	22.7	21.8	21.83	0.85	3.90	-6.58		
ME-MS81	Yb	ppm	0.03	0.10	2.36	2.08	2.24	2.16	2.16	0.08	3.70	-8.47		
ME-MS81	Zr	ppm	2	6.60	84	86	86	83	85.00	1.73	2.04	1.19		
ME-MS42	As	ppm	0.1	0.33		0.9	1	0.9	0.93	0.06	6.19			
ME-MS42	Bi	ppm	0.01	0.03		0.02	0.02	0.02	0.02	0.00	0.00			
ME-MS42	Hg	ppm	0.005	0.02		-0.005	-0.005	-0.005	-0.01	0.00	0.00			
ME-MS42	In	ppm	0.005	0.02		0.015	0.018	0.016	0.02	0.00	9.35			
ME-MS42	Re	ppm	0.001	0.00		0.001	0.001	0.001	0.00	0.00	0.00			
ME-MS42	Sb	ppm	0.05	0.17		-0.05	-0.05	-0.05	-0.05	0.00	0.00			
ME-MS42	Se	ppm	0.2	0.66		0.3	-0.2	-0.2	-0.03	0.29	-866.03		Near LOQ	
ME-MS42	Te	ppm	0.01	0.03		-0.01	-0.01	0.01	0.00	0.01	-346.41		Near LOQ	
ME-MS42	Tl	ppm	0.02	0.07	0.11	0.08	0.07	0.07	0.07	0.01	7.87	-33.33	Near LOQ	
ME-4ACD81	Ag	ppm	0.01	0.03		-0.5	-0.5	-0.5	-0.5	0.00	0.00			
ME-4ACD81	Cd	ppm	0.02	0.07		-0.5	-0.5	0.9	0.0	0.81	-2424.87		Near LOQ	
ME-4ACD81	Co	ppm	0.1	0.33	60.6	56	57	59	57	1.53	2.66	-5.39		
ME-4ACD81	Cu	ppm	0.2	0.66	165.3	167	171	180	173	6.66	3.86	4.46		
ME-4ACD81	Li	ppm	0.2	0.66	n/a	10	10	10	10	0.00	0.00			
ME-4ACD81	Mo	ppm	0.05	0.17	1.42	1	1	1	1	0.00	0.00	-29.58		Very low concentration
ME-4ACD81	Ni	ppm	0.2	0.66	160.5	151	154	159	155	4.04	2.61	-3.63		
ME-4ACD81	Pb	ppm	0.5	1.65	3.3	7	2	2	4	2.89	78.73	11.11	Not great for W812851 - possible carry-over from previous batch??	Not great for W812851 - possible carry-over from previous batch??
ME-4ACD81	Sc	ppm	0.1	0.33	34.9	31	31	32	31	0.58	1.84	-10.22		
ME-4ACD81	Zn	ppm	2	6.60	98	105	106	109	107	2.08	1.95	8.84		Consistently higher than accepted value
Au-ICP21	Au	ppm	0.001	0.00	99	NSS	0.009	0.021	0	0.01	56.57	-99.98	Near LOQ	Near LOQ

Table A4. 3 Whole rock lithogeochemical data and summary of percent relative difference (% RD) and percent relative standard deviation (% RSD) results for the ORCA-1 standard reference materials.

					QAQC - ORCA 1									
ALS Method	Analyte		LOD	3.3 LOD = LOQ	Orca-1 accepted values	W812851	W812863	W812876	Avg	Stdev	%RSD	%RD	Comments on precision	Comments on accuracy
ME-ICP06	SiO_2	%	0.01	0.03	49.65	49.46	49.18	49.45	49.36	0.16	0.32	-0.58		
ME-ICP06	Al_2O_3	%	0.01	0.03	15.84	15.6	15.48	15.54	15.54	0.06	0.39	-1.89		
ME-ICP06	Fe_2O_3	%	0.01	0.03	13.79	13.78	13.6	13.74	13.71	0.09	0.69	-0.60		
ME-ICP06	CaO	%	0.01	0.03	10.46	10.45	10.35	10.4	10.40	0.05	0.48	-0.57		
ME-ICP06	MgO	%	0.01	0.03	7.38	7.4	7.33	7.41	7.38	0.04	0.59	0.00		
ME-ICP06	Na_2O	%	0.01	0.03	2.43	2.39	2.38	2.41	2.39	0.02	0.64	-1.51		
ME-ICP06	K_2O	%	0.01	0.03	0.47	0.46	0.46	0.46	0.46	0.00	0.00	-2.13		
ME-ICP06	Cr_2O_3	%	0.01	0.03		0.02	0.02	0.02	0.02	0.00	0.00			
ME-ICP06	TiO_2	%	0.01	0.03	1.18	1.18	1.16	1.18	1.17	0.01	0.98	-0.56		
ME-ICP06	MnO	%	0.01	0.03	0.2	0.19	0.19	0.19	0.19	0.00	0.00	-5.00		
ME-ICP06	P_2O_5	%	0.01	0.03	0.1	0.11	0.11	0.11	0.11	0.00	0.00	10.00		in the ballpark
ME-ICP06	SrO	%	0.01	0.03		0.02	0.02	0.02	0.02	0.00	0.00			
ME-ICP06	BaO	%	0.01	0.03		0.03	0.03	0.03	0.03	0.00	0.00			
OA-GRA05	LOI	%	0.01	0.03	0.17	-0.11	-0.06	-0.11	-0.09	0.03	-30.93	-154.90	Near LOQ	Near LOQ
TOT-ICP06	Total	%	0.01	0.03		101.25	100.45	101.1	100.93	0.43	0.42			
C-IR07	C	%	0.01	0.03		0.02	0.02	0.02	0.02	0.00	0.00			
S-IR08	S	%	0.01	0.03	0.02	0.04	0.03	0.03	0.03	0.01	17.32	66.67	Near LOQ	Near LOQ
ME-MS81	Ba	ppm	0.5	1.65	142.3	140.5	155	145.5	147	7.37	5.01	3.30		
ME-MS81	Ce	ppm	0.1	0.33	20.59	18.6	19.5	19	19.0	0.45	2.37	-7.56		
ME-MS81	Cr	ppm	10	33.00	183	160	180	170	170	10.00	5.88	-7.10		Consistently lower
ME-MS81	Cs	ppm	0.01	0.03	0.69	0.6	0.59	0.57	0.59	0.02	2.60	-14.98		Near LOQ
ME-MS81	Dy	ppm	0.05	0.17	4.238	3.85	4.01	3.93	3.93	0.08	2.04	-7.27		
ME-MS81	Er	ppm	0.02	0.07	2.553	2.41	2.49	2.48	2.46	0.04	1.77	-3.64		
ME-MS81	Eu	ppm	0.02	0.07	1.174	1.05	1.1	1.11	1.1	0.03	2.96	-7.44		
ME-MS81	Ga	ppm	0.1	0.33	19.8	19.2	20.9	20.3	20.1	0.86	4.28	1.68		
ME-MS81	Gd	ppm	0.05	0.17	4.072	3.72	4.1	3.94	3.9	0.19	4.87	-3.73		
ME-MS81	Ge	ppm	5	16.50		-5	-5	-5	-5	0.00	0.00			
ME-MS81	Hf	ppm	0.5	1.65	2.5	2.2	2.4	2.4	2.3	0.12	4.95	-6.67		
ME-MS81	Ho	ppm	0.01	0.03	0.888	0.89	0.84	0.83	0.85	0.03	3.77	-3.90		
ME-MS81	La	ppm	0.1	0.33	9.27	8.4	8.8	8.7	8.6	0.21	2.41	-6.87		
ME-MS81	Lu	ppm	0.01	0.03	0.352	0.32	0.33	0.35	0.33	0.02	4.58	-5.30		
ME-MS81	Nb	ppm	0.1	0.33	4.9	4.6	4.9	4.7	4.7	0.15	3.23	-3.40		
ME-MS81	Nd	ppm	0.1	0.33	12.5	11.3	11.8	11.1	11.4	0.36	3.16	-8.80		
ME-MS81	Pr	ppm	0.02	0.07	2.776	2.44	2.67	2.55	2.55	0.12	4.51	-8.02		
ME-MS81	Rb	ppm	0.2	0.66	14.04	12.2	13.8	13.6	13.2	0.87	6.60	-5.98		
ME-MS81	Sm	ppm	0.03	0.10	3.33	3.07	3.3	3.26	3.21	0.12	3.83	-3.60		
ME-MS81	Sn	ppm	1	3.30		1	1	1	1	0.00	0.00			
ME-MS81	Sr	ppm	0.1	0.33	176.9	164	181	175	173	8.62	4.97	-2.02		
ME-MS81	Ta	ppm	0.1	0.33	0.3	0.4	0.4	0.3	0.4	0.06	15.75	22.22	Near LOQ	In the ballpark; near LOQ
ME-MS81	Tb	ppm	0.01	0.03	0.682	0.61	0.67	0.66	0.65	0.03	4.97	-5.18		
ME-MS81	Th	ppm	0.05	0.17	1.65	1.48	1.57	1.55	1.53	0.05	3.08	-7.07		
ME-MS81	Tm	ppm	0.01	0.03	0.368	0.32	0.37	0.37	0.35	0.03	8.17	-3.99		
ME-MS81	U	ppm	0.05	0.17	0.485	0.44	0.46	0.48	0.46	0.02	4.35	-5.15		
ME-MS81	V	ppm	5	16.50	306	295	339	330	321	23.25	7.23	5.01		
ME-MS81	W	ppm	1	3.30		1	1	1	1	0.00	0.00			
ME-MS81	Y	ppm	0.1	0.33	23.37	21	22.7	21.8	21.83	0.85	3.90	-6.58		
ME-MS81	Yb	ppm	0.03	0.10	2.36	2.08	2.24	2.16	2.16	0.08	3.70	-8.47		
ME-MS81	Zr	ppm	2	6.60	84	86	86	83	85.00	1.73	2.04	1.19		
ME-MS42	As	ppm	0.1	0.33		0.9	1	0.9	0.93	0.06	6.19			
ME-MS42	Bi	ppm	0.01	0.03		0.02	0.02	0.02	0.02	0.00	0.00			
ME-MS42	Hg	ppm	0.005	0.02		-0.005	-0.005	-0.005	-0.01	0.00	0.00			
ME-MS42	In	ppm	0.005	0.02		0.015	0.018	0.016	0.02	0.00	9.35			
ME-MS42	Re	ppm	0.001	0.00		0.001	0.001	0.001	0.00	0.00	0.00			
ME-MS42	Sb	ppm	0.05	0.17		-0.05	-0.05	-0.05	-0.05	0.00	0.00			
ME-MS42	Se	ppm	0.2	0.66		0.3	-0.2	-0.2	-0.03	0.29	-866.03		Near LOQ	
ME-MS42	Te	ppm	0.01	0.03		-0.01	-0.01	0.01	0.00	0.01	-346.41		Near LOQ	
ME-MS42	Tl	ppm	0.02	0.07	0.11	0.08	0.07	0.07	0.07	0.01	7.87	-33.33	Near LOQ	
ME-4ACD81	Ag	ppm	0.01	0.03		-0.5	-0.5	-0.5	-0.5	0.00	0.00			
ME-4ACD81	Cd	ppm	0.02	0.07		-0.5	-0.5	0.9	0.0	0.81	-2424.87		Near LOQ	
ME-4ACD81	Co	ppm	0.1	0.33	60.6	56	57	59	57	1.53	2.66	-5.39		
ME-4ACD81	Cu	ppm	0.2	0.66	165.3	167	171	180	173	6.66	3.86	4.46		
ME-4ACD81	Li	ppm	0.2	0.66	n/a	10	10	10	10	0.00	0.00			
ME-4ACD81	Mo	ppm	0.05	0.17	1.42	1	1	1	1	0.00	0.00	-29.58		Very low concentration
ME-4ACD81	Ni	ppm	0.2	0.66	160.5	151	154	159	155	4.04	2.61	-3.63		
ME-4ACD81	Pb	ppm	0.5	1.65	3.3	7	2	2	4	2.89	78.73	11.11	Not great for W812851 - possible carry-over from previous batch??	Not great for W812851 - possible carry-over from previous batch??
ME-4ACD81	Sc	ppm	0.1	0.33	34.9	31	31	32	31	0.58	1.84	-10.22		
ME-4ACD81	Zn	ppm	2	6.60	98	105	106	109	107	2.08	1.95	8.84		Consistently higher than accepted value
Au-ICP21	Au	ppm	0.001	0.00	99	NSS	0.009	0.021	0	0.01	56.57	-99.98	Near LOQ	Near LOQ

Table A4. 4 Summary of average coefficient of variation for three duplicate pairs.

					Duplicate pair 1		Duplicate pair 2		Duplicate pair 3		
			Sample		W604709	W812871	W604712	W812872	W604724	W812858	
			ALS Certificate		KL18175066	VA20253932	KL18175066	VA20253932	KL18175066	VA20253932	
ALS Method	**Analyte**		**LOD**	**LOQ**	**High-silica rhyolite**		**Mafic Dyke**		**Trachyte Dyke**		**Cv_{avg}**
ME-XRF26	SiO_2	%	0.01	0.03	67.01	67.86	53.17	53.41	53.38	55.89	1.95
ME-XRF26	Al_2O_3	%	0.01	0.03	14.80	14.74	17.53	17.86	18.59	19.31	1.74
ME-XRF26	Fe_2O_3	%	0.01	0.03	3.87	3.58	8.08	8.14	5.32	4.82	5.14
ME-XRF26	CaO	%	0.01	0.03	4.09	4.27	8.30	8.25	5.50	4.60	7.49
ME-XRF26	MgO	%	0.01	0.03	1.04	0.97	3.89	3.87	1.58	1.30	8.43
ME-XRF26	Na_2O	%	0.01	0.03	3.59	3.56	0.88	0.88	2.41	2.34	1.25
ME-XRF26	K_2O	%	0.01	0.03	0.35	0.37	3.04	3.11	5.84	6.49	4.95
ME-XRF26	Cr_2O_3	%	0.01	0.03	-0.01	-0.01	-0.01	-0.01	-0.01	-0.01	0.00
ME-XRF26	TiO_2	%	0.01	0.03	0.15	0.15	0.65	0.66	0.55	0.53	1.64
ME-XRF26	MnO	%	0.01	0.03	0.03	0.03	0.12	0.12	0.16	0.13	8.45
ME-XRF26	P_2O_5	%	0.01	0.03	0.05	0.04	0.16	0.15	0.24	0.22	10.09
ME-XRF26	SrO	%	0.01	0.03	0.02	0.02	0.10	0.10	0.19	0.18	2.21
ME-XRF26	BaO	%	0.01	0.03	0.24	0.25	0.04	0.07	0.77	0.90	23.22
OA-GRA05	LOI	%	0.01	0.03	3.59	3.68	3.15	3.04	3.83	3.28	6.56
TOT-ICP06	Total	%	0.01	0.03	98.94	99.64	99.66	100.25	98.77	100.45	0.78
C-IR07	C	%	0.01	0.03	0.48	0.50	0.28	0.21	0.88	0.65	17.01
S-IR08	S	%	0.01	0.03	0.02	0.04	0.20	0.20	0.14	0.16	27.76
ME-MS81	Ba	ppm	0.5	1.65	2410	2540	556	611	7090	9130	11.17
ME-MS81	Ce	ppm	0.1	0.33	252.00	240.00	31.20	31.70	172.50	198.00	6.00
ME-MS81	Cr	ppm	10	33.00	-10	-10	10	10	10	20	27.22
ME-MS81	Cs	ppm	0.01	0.03	1.36	1.24	1.16	1.00	1.25	1.17	7.62
ME-MS81	Dy	ppm	0.05	0.17	32.50	29.50	2.55	2.55	5.22	6.17	7.87
ME-MS81	Er	ppm	0.02	0.07	18.00	17.25	1.41	1.55	2.67	3.02	6.57
ME-MS81	Eu	ppm	0.02	0.07	5.11	5.03	0.97	1.08	3.22	3.36	4.76
ME-MS81	Ga	ppm	0.1	0.33	35.9	36.8	20.4	21.4	24.4	26.1	3.52
ME-MS81	Gd	ppm	0.05	0.17	29.60	28.80	2.88	3.19	8.62	9.55	6.01
ME-MS81	Ge	ppm	5	16.50	-5	-5	-5	-5	-5	-5	0.00
ME-MS81	Hf	ppm	0.5	1.65	15.6	14.9	2.4	2.7	7.3	8.2	7.00
ME-MS81	Ho	ppm	0.01	0.03	6.29	5.70	0.54	0.52	0.98	1.16	8.10
ME-MS81	La	ppm	0.1	0.33	119.0	111.5	15.5	15.9	94.3	108.0	6.22
ME-MS81	Lu	ppm	0.01	0.03	2.76	2.63	0.25	0.25	0.43	0.46	3.38
ME-MS81	Nb	ppm	0.1	0.33	81.9	79.5	4.6	5.2	20.7	24.5	8.58
ME-MS81	Nd	ppm	0.1	0.33	122.5	111.5	16.5	16.2	74.7	84.5	6.37
ME-MS81	Pr	ppm	0.02	0.07	31.00	28.40	3.82	4.05	19.75	22.70	7.12
ME-MS81	Rb	ppm	0.2	0.66	52.6	54.5	18.9	20.1	63.8	62.2	3.08
ME-MS81	Sm	ppm	0.03	0.10	29.40	28.30	3.69	3.77	13.25	14.55	4.22
ME-MS81	Sn	ppm	1	3.30	9	9	1	1	1	1	0.00
ME-MS81	Sr	ppm	0.1	0.33	182	179	931	938	1650	1690	1.23
ME-MS81	Ta	ppm	0.1	0.33	5.0	4.8	0.3	0.4	1.1	1.3	13.61
ME-MS81	Tb	ppm	0.01	0.03	5.29	5.15	0.43	0.46	1.01	1.22	8.24
ME-MS81	Th	ppm	0.05	0.17	14.10	13.95	3.05	3.11	24.70	27.60	4.62
ME-MS81	Tm	ppm	0.01	0.03	2.89	2.63	0.22	0.24	0.37	0.43	8.06
ME-MS81	U	ppm	0.05	0.17	3.85	3.52	1.29	1.28	11.95	13.00	5.03
ME-MS81	V	ppm	5	16.50	5	5	225	254	111	95	8.04
ME-MS81	W	ppm	1	3.30	1	1	1	1	2	2	0.00
ME-MS81	Y	ppm	0.1	0.33	139.5	135.0	14.3	14.5	28.8	31.8	4.30
ME-MS81	Yb	ppm	0.03	0.10	18.45	18.15	1.38	1.55	2.72	2.83	5.05
ME-MS81	Zr	ppm	2	6.60	439.00	414.00	92.00	95.00	320.00	374.00	6.91
ME-MS42	As	ppm	0.1	0.33	0.4	0.6	2.2	2.5	0.9	0.7	19.95
ME-MS42	Bi	ppm	0.01	0.03	0.01	0.01	0.01	0.01	0.09	0.06	16.33
ME-MS42	Hg	ppm	0.005	0.02	0.01	-0.01	-0.01	-0.01	-0.01	-0.01	
ME-MS42	In	ppm	0.005	0.02	0.03	0.02	0.01	0.01	0.01	0.01	28.75
ME-MS42	Re	ppm	0.001	0.00	-0.001	-0.001	-0.001	-0.001	-0.001	-0.001	0.00
ME-MS42	Sb	ppm	0.05	0.17	0.16	0.99	0.30	0.42	0.28	0.25	60.66
ME-MS42	Se	ppm	0.2	0.66	0.3	0.3	3.8	2.6	1.6	0.7	35.43
ME-MS42	Te	ppm	0.01	0.03	-0.01	0.01	-0.01	0.01	0.01	-0.01	
ME-MS42	Tl	ppm	0.02	0.07	0.23	0.19	0.26	0.22	0.53	0.39	16.16
ME-4ACD81	Ag	ppm	0.01	0.03	-0.5	-0.5	-0.5	-0.5	-0.5	-0.5	0.00
ME-4ACD81	Cd	ppm	0.02	0.07	-0.5	-0.5	-0.5	-0.5	-0.5	-0.5	0.00
ME-4ACD81	Co	ppm	0.1	0.33	1	2	25	24	8	6	29.66
ME-4ACD81	Cu	ppm	0.2	0.66	11	9	30	24	17	8	31.83
ME-4ACD81	Li	ppm	0.2	0.66	10	10	20	20	10	10	0.00
ME-4ACD81	Mo	ppm	0.05	0.17	-1	1	-1	1	-1	-1	
ME-4ACD81	Ni	ppm	0.2	0.66	1	2	6	5	3	3	28.21
ME-4ACD81	Pb	ppm	0.5	1.65	7	7	7	17	13	9	37.12
ME-4ACD81	Sc	ppm	0.1	0.33	1	1	16	16	6	3	27.22
ME-4ACD81	Zn	ppm	2	6.60	115	99	78	78	97	80	9.94

Appendix 4 References

Abzalov, M., 2008, Quality control of assay data: a review of procedures for measuring and monitoring precision and accuracy: Exploration and Mining Geology, v. 17, p. 131–144.

Jenner, G., 1996, Trace element geochemistry of igneous rocks: geochemical nomenclature and analytical geochemistry: Geological Association of Canada, Short Course Notes, p. 51–77.

Piercey, S.J., 2014, A review of quality assurance and quality control (QA/QC) procedures for lithogeochemical data: Geoscience Canada, v. 41, p. 75–88.

Appendix 5. U-Pb geochronology

Sample collection

Two samples of felsic rocks from the AG stratigraphy were collected from drill hole 110 to constrain the timing of VMS mineralization at AG based on their stratigraphic location, lithology, and geochemical attributes. Sample 110-322 is a hydrothermally altered FeR lapilli tuff collected at a downhole depth of 322 m (Fig. A5. 1); this FeR lapilli tuff is along strike of exhalative VMS mineralization and underlies hydrothermally altered and mineralized heterolithic fragmental rocks and overlies FeA flows. Sample 110-368 is massive high-silica rhyolite (HSR) with patchy epidote, chlorite, and calcite alteration collected at a downhole depth of 368 m (Fig. A5. 2); this HSR intrudes the FeA flows downhole of the ferrorhyolite lapilli tuffs. The samples were collected during the summer of 2020 and sent to the Boise State University Isotope Geology Laboratory (BSU IGL) in Idaho in the Spring of 2021.

Analytical methodology

Mineral separation and extraction, imaging, laser ablation inductively coupled plasma mass spectrometry (LA-ICPMS), and chemical abrasion isotope dilution thermal ionization mass spectrometry (CA-ID-TIMS) were all performed by Dr. James Crowley and his team at the BSU IGL Isotope Geology Laboratory. Dr. James Crowley of the Boise State University Isotope Geology Laboratory provided the following text for analytical methods:

LA-ICPMS methodology

Zircon grains were separated from rocks using standard techniques, annealed at 900°C for 60 hours in a muffle furnace, and mounted in epoxy and polished until their centers were exposed. Cathodoluminescence (CL) images were obtained with a JEOL JSM-300 scanning electron microscope and Gatan MiniCL. Zircon was analyzed by laser ablation inductively coupled plasma mass spectrometry (LA-ICPMS) using an iCAP RQ Quadrupole ICP-MS and Teledyne Photon Machines Analyte Excite+ 193 nm excimer laser ablation system with HelEx II Active two-volume ablation cell. In-house analytical protocols, standard materials, and data reduction software were used for acquisition and calibration of U-Pb dates and a suite of high field strength elements (HFSE) and rare earth elements (REE). Zircon was ablated with a laser spot of 20 µm wide using fluence and pulse rates of 2.5 J/cm^2 and 10 Hz, respectively, during a 25 second analysis (15 sec gas blank, 10 sec ablation) that excavated a pit ~8 µm deep. Ablated material was carried by a 0.25 L/min He gas stream in the inner cell and a 1.25 L/min He gas stream in the outer cell. Dwell times are given in Table A5. 1 and Table A5. 2. Background count rates for each analyte were obtained prior to each spot analysis and subtracted from the raw count rate for each analyte. Ablations pits that appear to have intersected glass or mineral inclusions were identified based on Ti and P. U-Pb dates from these analyses are considered valid if the U-Pb ratios appear to have been unaffected by the inclusions. Analyses that appear contaminated by common Pb were rejected based on mass 204 being above baseline. For concentration calculations, background-subtracted count rates for each analyte were internally normalized to ^{29}Si and calibrated with respect to NIST SRM-610 and -612 glasses as the primary standards. Temperature was calculated from the Ti-in-zircon thermometer (Watson et al., 2006). Because there are no constraints on the activity of TiO_2, an average value in crustal rocks of 0.6 was used.

Data was obtained in two experiments in March 2022. For U-Pb and $^{207}Pb/^{206}Pb$ dates, instrumental fractionation of the background-subtracted ratios was corrected, and dates were calibrated with respect to interspersed measurements of zircon standards and reference materials. The primary standard Plešovice zircon (Sláma et al., 2008) was used to monitor time-dependent instrumental fractionation based on two analyses for every 12 analyses of unknown zircon. A secondary correction to the $^{206}Pb/^{238}U$ dates was made based on results from the zircon standards

Seiland (531 Ma, Kuiper et al., 2022) and 91500 (1065 Ma, Wiedenbeck et al., 1995), which were treated as unknowns and measured once for every 12 analyses of unknown zircon. These results (Table A5. 6; Table A5. 5) showed a linear age bias of several percent that is related to the ^{206}Pb count rate. The secondary correction is thought to mitigate matrix-dependent variations due to contrasting compositions and ablation characteristics between the Plešovice zircon and other standards (and unknowns).

Radiogenic isotope ratio and age error propagation for all analyses includes uncertainty contributions from counting statistics and background subtraction. Errors without and with the standard calibration uncertainty are shown in Table A5. 3 and Table A5. 4. This uncertainty is the local standard deviation of the polynomial fit to the interspersed primary standard measurements versus time for the time-dependent, relatively larger U/Pb fractionation factor, and the standard error of the mean of the consistently time-invariant and smaller $^{207}Pb/^{206}Pb$ fractionation factor. These uncertainties are shown in Table A5. 1 and Table A5. 2. Errors on single analyses without the standard calibration uncertainty are given below. Age interpretations are based on $^{206}Pb/^{238}U$. Discordance, defined as the relative difference between the $^{207}Pb/^{235}U$ and $^{206}Pb/^{238}U$ dates, outside of uncertainty of 5% is flagged with strikethrough font in Table A5. 3 and Table A5. 4. Discordant results were not used to interpret age. Errors are at 2□.

CA-ID-TIMS U-Pb geochronology method

U-Pb dates were obtained by the chemical abrasion isotope dilution thermal ionization mass spectrometry (CA-ID-TIMS) method from analyses composed of single zircon grains (Table 2.4), modified after Mattinson (2005). Zircon was removed from the epoxy mounts for dating based on CL images (Fig. A5. 3, Fig. A5. 4) and LA-ICPMS data (Table A5. 3, Table A5. 4).

Zircon was put into 3 ml Teflon PFA beakers and loaded into 300 μl Teflon PFA microcapsules. Fifteen microcapsules were placed in a large-capacity Parr vessel and the zircon partially dissolved in 120 μl of 29 M HF for 12 hours at 190°C. Zircon was returned to 3 ml Teflon PFA beakers, HF was removed, and zircon was immersed in 3.5 M HNO_3, ultrasonically cleaned for an hour, and fluxed on a hotplate at 80°C for an hour. The HNO_3 was removed, and zircon was rinsed twice in ultrapure H_2O before being reloaded into the 300 μl Teflon PFA microcapsules (rinsed and fluxed in 6 M HCl during sonication and washing of the zircon) and spiked with the Boise State University mixed ^{233}U-^{235}U-^{205}Pb tracer solution (BSU-1B). Zircon was dissolved in Parr vessels in 120 μl of 29 M HF with a trace of 3.5 M HNO_3 at 220°C for 48 hours, dried to fluorides, and re-dissolved in 6 M HCl at 180°C overnight. U and Pb were separated from the zircon matrix using an HCl-based anion-exchange chromatographic procedure (Krogh, 1973), eluted together and dried with 2 μl of 0.05 N H_3PO_4.

Pb and U were loaded on a single outgassed Re filament in 5 μl of a silica-gel/phosphoric acid mixture (Gerstenberger and Haase, 1997), and U and Pb isotopic measurements made on a GV Isoprobe-T or IsotopX Phoenix multicollector thermal ionization mass spectrometer equipped with an ion-counting Daly detector. Pb isotopes were measured by peak-jumping all isotopes on the Daly detector for 160-250 cycles and corrected for 0.18 ± 0.03%/a.m.u. (1 σ) mass fractionation for analyses done on the GV Isoprobe-T and 0.24 ± 0.03%/a.m.u. (1 σ) mass fractionation for analyses done on the IsotopX Phoenix. Transitory isobaric interferences due to high-molecular weight organics, particularly on ^{204}Pb and ^{207}Pb, disappeared within approximately 60 cycles, while ionization efficiency averaged 10^4 cps/pg of each Pb isotope. Linearity (to ≥1.4 x 10^6 cps) and the associated deadtime correction of the Daly detector were determined by analysis of NBS982. Uranium was analyzed as UO_2^+ ions in static Faraday mode on 10^{12} ohm resistors for 200-300 cycles and corrected for isobaric interference of $^{233}U^{18}O^{16}O$ on $^{235}U^{16}O^{16}O$ with an $^{18}O/^{16}O$ of 0.00206. Ionization efficiency averaged 20 mV/ng of each U isotope. U mass fractionation was corrected using the known $^{233}U/^{235}U$ ratio of the Boise State University tracer solution.

U-Pb dates and uncertainties were calculated using the algorithms of Schmitz and Schoene (2007), calibration of BSU-1B tracer solution of $^{235}U/^{205}Pb$ of 77.93 and $^{233}U/^{235}U$ of 1.007066 for, U decay constants recommended by Jaffey et al., (1971), and $^{238}U/^{235}U$ of 137.818 (Hiess et al., 2012). $^{206}Pb/^{238}U$ ratios and dates were corrected for initial ^{230}Th disequilibrium using $D_{Th/U} = 0.20 \pm 0.05$ (1 σ) and the algorithms of Crowley et al. (2007), resulting in an increase in the $^{206}Pb/^{238}U$ dates of ~0.09 Ma. All common Pb in analyses was attributed to laboratory blank and subtracted based on the measured laboratory Pb isotopic composition and associated uncertainty. U blanks are estimated at 0.013 pg.

Weighted mean $^{206}Pb/^{238}U$ dates are calculated from equivalent dates (probability of fit >0.05) using Isoplot 3.0 (Ludwig, 2003) with error at the 95% confidence interval. Error is computed as the internal standard deviation multiplied by the Student's t-distribution multiplier for a two-tailed 95% critical interval and n-1 degrees of freedom when the reduced chi-squared statistic, mean squared weighted deviation (MSWD) (Wendt and Carl, 1991), takes a value less than its expectation value plus its standard deviation at the same confidence interval, which is when MSWD is <1+2*sqrt[2/(n-1)]. This error is expanded via multiplication by the sqrt (MSWD) when the MSWD is ≥1+2*sqrt[2/(n-1)] to accommodate unknown sources of over dispersion. Errors on the weighted mean dates are given as ± x / y / z, where x is the internal error based on analytical uncertainties only, including counting statistics, subtraction of tracer solution, and blank and initial common Pb subtraction, y includes the tracer calibration uncertainty propagated in quadrature, and z includes the ^{238}U decay constant uncertainty propagated in quadrature. Internal errors should be considered when comparing our dates with $^{206}Pb/^{238}U$ dates from other laboratories that used the same tracer solution or a tracer solution that was cross calibrated using EARTHTIME gravimetric standards. Errors including the uncertainty in the tracer calibration should be considered when comparing our dates with those derived from other geochronological methods using the U-Pb decay scheme (e.g., laser ablation ICPMS). Errors including uncertainties in the tracer calibration and ^{238}U decay constant (Jaffey et al., 1971) should be considered when comparing our dates with those derived from other decay schemes (e.g., $^{40}Ar/^{39}Ar$, ^{187}Re-^{187}Os). Errors on dates from individual analyses are 2 σ.

Results

Dr. James Crowley of the Boise State University Isotope Geology Laboratory provided the following text for results:

Eleven zircon grains from CMR-110-322 analyzed by LA-ICPMS yield dates of 212 ± 6 to 194 ± 5 Ma. Seven zircon grains were analyzed by CA-ID-TIMS. The three youngest dates yield a weighted mean date of 210.35 ± 0.27 (random) / 0.27 (+ tracer) / 0.35 (+ decay constant) Ma (MSWD = 1.1, probability of fit = 0.32). Four other grains that yield dates of 211.03 ± 0.32 to 210.68 ± 0.17 Ma are interpreted as containing inherited components.

Forty-nine zircon grains from CMR-110-368 analyzed by LA-ICPMS yield dates of 213 ± 5 to 189 ± 4 Ma. Six zircon grains analyzed by CA-ID-TIMS yield a weighted mean date of 210.52 ± 0.08 / 0.10 / 0.25 Ma (MSWD = 1.2, probability of fit = 0.29). This is the interpreted igneous crystallization age.

Table A5. 1 Metadata for LA-ICPMS U-Pb analyses for sample 110-322.

Laboratory and Sample Preparation	**Sample 110-322**
Laboratory name	Boise State University Isotope Geology Laboratory
Sample type/mineral	Zircon
Sample preparation	Conventional mineral separation, 1 inch resin mount, 0.3 μm polish to finish
Imaging	CL, JEOL T300, 10 nA, 17 mm working distance
Laser ablation system	
Make, Model and type	Teledyne (Photon Machines) Analyte Excite+
Ablation cell and volume	HelEx II active 2-volume ablation cell
Laser wavelength (nm)	193 nm ArF excimer
Pulse width (ns)	4 ns
Fluence (J cm^{-2})	energy stabilization mode, set daily at ~2.5 J cm^{-2} using in-cell EPC utility
Repetition rate (Hz)	10 Hz
Ablation duration (s)	10 s
Ablation pit depth / ablation rate	10 μm pit depth, measured using an optical microscope, equivalent to 0.1 μm/pulse
Spot diameter (μm)	20 μm
Sampling mode / pattern	Static spot ablation
Cell carrier gas flow (l min^{-1})	0.25 L min^{-1} He cup flow, 1.25 L min^{-1} He cell flow
ICP-MS Instrument	
Make, Model and type	ThermoElectron, iCAP-RQ, single quadrupole mass spectrometer
Sample introduction	190 cm long, 1 cm i.d. PFA tubing with Glass Expansion sample mixing chamber, 2.5 mm quartz injector; Ni cones, high-sensitivity skimmer insert
RF power (W)	1400 W
Make-up gas flow (l min^{-1})	~0.65 l min^{-1} Ar and 2 mL min^{-1} N_2 gas introduced in mixing bulbs between cell and torch
Detection system	single ion-counting SEM
Masses measured and dwell times per peak (ms)	89,91,177(2); 31,93,140,146,147,157,159,163,165,166,169,172,175,181(5); 29,139,141,202,204,232,238(10); 206(40); 207(60);49(100)
Total integration time (s)	~ 0.371 s
'Sensitivity' as useful yield	0.8% U [(#ions detected/#atoms sampled)*100; Schaltegger et al. 2015]
IC Dead time (ns)	44 ns
Data Processing	
Gas blank	15 s on-peak zero subtracted.
Calibration strategy	Mean of ratios; mass discrimination from interspersed zircon standard materials.
Common-Pb correction	No common-Pb correction applied; sweeps with mass 204 signals above background rejected.
Data processing packages	ThermoElectron Qtegra TRA software for integrated cps acquisition; in-house Microsoft VBA coded spreadsheet for data normalisation, concentration calibration, uncertainty propagation and age calculation.
Uncertainty level and propagation	Ages quoted at 2*s* absolute; propagation is by quadratic addition. Systematic errors from reproducibility of primary reference material propagated where appropriate.
Discordance criteria	Discordance is the relative difference between the measured $^{207}Pb/^{235}U$ and $^{206}Pb/^{238}U$ dates; discordance outside of uncertainty of 5% is flagged with strikethrough font in Table S2.
Interpreted age transition	The transition from preferred interpretation of $^{207}Pb/^{206}Pb$ to $^{206}Pb/^{238}U$ dates is set at 1500 Ma; preferred date is flagged with bold font in Table S2.
Mass discrimination corrections	$^{207}Pb/^{206}Pb$ fractionation error (from PL): 0.40% (1 sigma) [Zircon_08March2022_Miscellaneous_1]
	$^{206}Pb/^{238}U$ fractionation error (from PL): 0.62% (1 sigma) [Zircon_08March2022_Miscellaneous_1]
	$^{208}Pb/^{232}Th$ fractionation error (from PL): 1.81% (1 sigma) [Zircon_08March2022_Miscellaneous_1]
Quality control & validation standards	Plešovice (PL) (Slama et al. 2008); 336.9 Ma
	91500 (Wiedenbeck et al., 1995); 1065.4 Ma
	Seiland (Kuiper et al. 2022); 530.6 Ma
Quality control & validation results	Zircon_08March2022_Miscellaneous_1: 91500 ($^{206}Pb/^{238}U$) = 1088 ± 13 (95% c.i., MSWD = 0.9, pof = 0.53, n = 9)
	Zircon_08March2022_Miscellaneous_1: 91500 ($^{207}Pb/^{206}Pb$) = 1057 ± 36 (95% c.i., MSWD = 0.9, pof = 0.53, n = 9)
	Zircon_08March2022_Miscellaneous_1: Seiland ($^{206}Pb/^{238}U$) = 527 ± 7 (95% c.i., MSWD = 0.6, pof = 0.77, n = 10)

Table A5. 2 Metadata for LA-ICPMS U-Pb analyses for sample 110-368.

Laboratory and Sample Preparation	**Sample 110-368**
Laboratory name	Boise State University Isotope Geology Laboratory
Sample type/mineral	Zircon
Sample preparation	Conventional mineral separation, 1 inch resin mount, 0.3 μm polish to finish
Imaging	CL, JEOL T300, 10 nA, 17 mm working distance
Laser ablation system	
Make, Model and type	Teledyne (Photon Machines) Analyte Excite+
Ablation cell and volume	HelEx II active 2-volume ablation cell
Laser wavelength (nm)	193 nm ArF excimer
Pulse width (ns)	4 ns
Fluence (J cm^{-2})	energy stabilization mode, set daily at ~2.5 J cm^{-2} using in-cell EPC utility
Repetition rate (Hz)	10 Hz
Ablation duration (s)	10 s
Ablation pit depth / ablation rate	10 μm pit depth, measured using an optical microscope, equivalent to 0.1 μm/pulse
Spot diameter (μm)	20 μm
Sampling mode / pattern	Static spot ablation
Cell carrier gas flow (l min^{-1})	0.25 L min^{-1} He cup flow, 1.25 L min^{-1} He cell flow
ICP-MS Instrument	
Make, Model and type	ThermoElectron, iCAP-RQ, single quadrupole mass spectrometer
Sample introduction	190 cm long, 1 cm i.d. PFA tubing with Glass Expansion sample mixing chamber, 2.5 mm quartz injector; Ni cones, high-sensitivity skimmer insert
RF power (W)	1400 W
Make-up gas flow (l min^{-1})	~0.65 l min^{-1} Ar and 2 mL min^{-1} N_2 gas introduced in mixing bulbs between cell and torch
Detection system	single ion-counting SEM
Masses measured and dwell times per peak (ms)	89,91,177(2); 31,93,140,146,147,157,159,163,165,166,169,172,175,181(5); 29,139,141,202,204,232,238(10); 206(40); 207(60);49(100)
Total integration time (s)	~ 0.371 s
'Sensitivity' as useful yield	0.8% U [(#ions detected/#atoms sampled)*100; Schaltegger et al. 2015]
IC Dead time (ns)	44 ns
Data Processing	
Gas blank	15 s on-peak zero subtracted.
Calibration strategy	Mean of ratios; mass discrimination from interspersed zircon standard materials.
Common-Pb correction	No common-Pb correction applied; sweeps with mass 204 signals above background rejected.
Data processing packages	ThermoElectron Qtegra TRA software for integrated cps acquisition; in-house Microsoft VBA coded spreadsheet for data normalisation, concentration calibration, uncertainty propagation and age calculation.
Uncertainty level and propagation	Ages quoted at 2*s* absolute; propagation is by quadratic addition. Systematic errors from reproducibility of primary reference material propagated where appropriate.
Discordance criteria	Discordance is the relative difference between the measured $^{207}Pb/^{235}U$ and $^{206}Pb/^{238}U$ dates; discordance outside of uncertainty of 5% is flagged with strikethrough font in Table S2.
Interpreted age transition	The transition from preferred interpretation of $^{207}Pb/^{206}Pb$ to $^{206}Pb/^{238}U$ dates is set at 1500 Ma; preferred date is flagged with bold font in Table S2.
Mass discrimination corrections	$^{207}Pb/^{206}Pb$ fractionation error (from PL): 0.40% (1 sigma) [Zircon_08March2022_Miscellaneous_1]
	$^{206}Pb/^{238}U$ fractionation error (from PL): 0.62% (1 sigma) [Zircon_08March2022_Miscellaneous_1]
	$^{208}Pb/^{232}Th$ fractionation error (from PL): 1.81% (1 sigma) [Zircon_08March2022_Miscellaneous_1]
	$^{207}Pb/^{206}Pb$ fractionation error (from PL): 0.35% (1 sigma) [Zircon_08March2022_Miscellaneous_2]
	$^{206}Pb/^{238}U$ fractionation error (from PL): 0.67% (1 sigma) [Zircon_08March2022_Miscellaneous_2]
	$^{208}Pb/^{232}Th$ fractionation error (from PL): 1.61% (1 sigma) [Zircon_08March2022_Miscellaneous_2]
Quality control & validation standards	Plešovice (PL) (Slama et al. 2008); 336.9 Ma
	91500 (Wiedenbeck et al., 1995); 1065.4 Ma
	Seiland (Kuiper et al., 2022); 530.6 Ma
Quality control & validation results	Zircon_08March2022_Miscellaneous_1: 91500 ($^{206}Pb/^{238}U$) = 1088 ± 13 (95% c.i., MSWD = 0.9, pof = 0.53, n = 9)
	Zircon_08March2022_Miscellaneous_1: 91500 ($^{207}Pb/^{206}Pb$) = 1057 ± 36 (95% c.i., MSWD = 0.9, pof = 0.53, n = 9)
	Zircon_08March2022_Miscellaneous_1: Seiland ($^{206}Pb/^{238}U$) = 527 ± 7 (95% c.i., MSWD = 0.6, pof = 0.77, n = 10)
	Zircon_08March2022_Miscellaneous_2: 91500 ($^{206}Pb/^{238}U$) = 1088 ± 11 (95% c.i., MSWD = 1.1, pof = 0.37, n = 11)
	Zircon_08March2022_Miscellaneous_2: 91500 ($^{207}Pb/^{206}Pb$) = 1019 ± 33 (95% c.i., MSWD = 0.5, pof = 0.93, n = 11)
	Zircon_08March2022_Miscellaneous_2: Seiland ($^{206}Pb/^{238}U$) = 527 ± 6 (95% c.i., MSWD = 0.9, pof = 0.56, n = 12)

Table A5. 3 LA-ICPMS U-Pb geochronologic analyses, trace element concentrations, and Ti-in-zircon thermometer results for sample 110-322.

		Composition							Corrected isotope ratios											
LA-ICPMS labe	CA-TIMS label	U ppm	Th ppm	Pb ppm	Th/U	^{206}Pb cps	$^{206}Pb/^{204}Pb$	±1s	$^{208}Pb/^{232}Th$	±2s (%)	$^{207}Pb/^{235}U$	±2s (%)	$^{206}Pb/^{238}U$	±2s (%)	error corr	$^{238}U/^{206}Pb$	±2s (%)	$^{207}Pb/^{206}Pb$	±2s (%)
215	z7	786	423	31.4	0.538	28542	11988	342	0.00937	5.107	0.2285	4.0	0.03336	3.0	0.715682	29.97	3.0	0.04967	2.7
215	z5	205	62	7.5	0.302	7068	7068	127	0.01072	13.5628	0.2074	9.0	0.03197	3.4	0.365987	31.28	3.4	0.04705	8.3
219	z8	236	88	8.7	0.373	9377	451	5	0.01002	7.323322	0.2051	9.9	0.03189	4.1	0.400905	31.36	4.1	0.04756	9.1
212		327	121	12.0	0.370	11409	786	19	0.00935	7.824923	0.2239	6.7	0.03184	3.9	0.443876	31.41	3.9	0.05100	7.9
213	z4	533	224	19.6	0.421	19041	1593	14	0.00853	6.084147	0.2176	6.7	0.03178	2.2	0.307025	31.47	2.2	0.04965	6.3
218		206	56	7.3	0.271	8051	8051	109	0.00943	12.03806	0.2200	10.0	0.03169	4.1	0.401683	31.56	4.1	0.05035	9.1
222	z6	327	123	11.8	0.377	13105	579	5	0.00873	10.95345	0.2314	5.8	0.03142	2.5	0.407236	31.82	2.5	0.05342	5.2
220		208	64	7.4	0.305	8217	329	2	0.00958	10.65899	0.2126	7.4	0.03133	3.5	0.456522	31.92	3.5	0.04923	6.6
216		206	56	7.3	0.274	7730	922	17	0.01011	12.87218	0.2154	9.3	0.03132	2.6	0.264623	31.93	2.6	0.04987	8.8
221	z1	216	64	7.6	0.298	8405	415	5	0.00956	14.76081	0.2203	7.9	0.03112	3.2	0.388375	32.13	3.2	0.05136	7.2
217	z9	452	192	16.2	0.426	16386	724	33	0.00882	8.424681	0.2241	7.5	0.03058	2.7	0.351616	32.70	2.7	0.05313	6.9

		Dates (Ma)														207-method		208-method	
LA-ICPMS labe	CA-TIMS label	$^{208}Pb/^{232}Th$	±2s (Ma)	±2s sys (Ma)	$^{207}Pb/^{206}Pb$	±2s (Ma)	±2s sys (Ma)	$^{207}Pb/^{235}U$	±2s (Ma)	±2s sys (Ma)	$^{206}Pb/^{238}U$	±2s (Ma)	±2s sys (Ma)	disc (%)	±2s (%)	$^{206}Pb^*/^{238}U^*$	±2s (Ma)	$^{208}Pb^*/^{238}U^*$	±2s (Ma)
215	z7	188.5198	10	11.9	179.7	62	65	209	8	8.00	211.57	**6**	**6.66**	**-1.25**	4.7	211.5	6	213.28	7
215	z5	215.5462	29	30.2	52.3	198	199	191	16	15.85	202.87	**7**	**7.17**	**-5.99**	8.3	201.9	7	200.47	7
219	z8	201.5586	15	16.5	76.8	215	216	193	17	17.64	202.37	**8**	**8.46**	**-4.98**	10.4	201.5	8	200.77	9
212		188.0647	15	16.3	240.7	179	180	205	16	16.40	202.05	**8**	**8.22**	**1.50**	9.7	200.4	8	201.37	6
213	z4	171.7709	10	12.2	178.9	147	148	200	12	12.37	201.67	**4**	**4.99**	**-0.80**	6.5	200.9	4	202.72	5
218		189.6277	23	23.8	211.3	211	212	202	18	18.48	201.10	**8**	**8.45**	**0.40**	9.9	199.4	8	199.89	8
222	z6	175.7421	19	20.3	346.5	118	120	211	11	11.40	199.45	**5**	**5.45**	**5.64**	5.4	197.3	5	199.51	5
220		192.785	21	21.8	158.6	154	155	198	13	13.48	198.85	**7**	**7.23**	**-1.58**	7.7	197.4	7	197.46	7
216		203.3825	26	27.1	198.9	208	209	199	17	16.95	198.81	**5**	**5.60**	**-0.39**	9.9	197.2	5	196.91	5
221	z1	192.3779	28	29.2	256.4	165	166	202	14	14.64	197.56	**6**	**6.58**	**2.28**	7.6	195.7	6	196.15	7
217	z9	177.5282	15	16.3	334.5	157	158	205	14	14.14	194.20	**5**	**5.75**	**5.40**	6.9	192.4	5	194.22	6

		Concentrations (ppm)																					
LA-ICPMS label	CA TIMS label	P	Ti	Y	Zr	Nb	La	Ce	Pr	Nd	Sm	Eu	Gd	Tb	Dy	Ho	Er	Tm	Yb	Lu	Hf	Ta	Th	U	Ti-in-zircon T(°C)
215	z7	253.70	8	2771.94	585319	22		23.906	0.1	2.838	7.13	1.4	51.71	20.9	271.8	105	455	93	834	134	11513	6	423.2	786	743.54
215	z5	151.38	5	1064.85	582897	4		3.781	0.0	0.434	2.06	0.4	16.21	6.6	86.6	38	175	38	356	63	10232	1	51.9	205	739.85
219	z8	135.09	5	1180.61	588700	4		4.266	0.0	0.879	2.81	0.6	15.80	8.0	107.5	44	203	44	406	70	10775	2	88.0	236	745.12
212		155.46	6	2662.10	583610	6		6.135	0.1	2.327	6.62	1.8	51.96	19.8	246.7	96	444	92	774	132	10409	2	121.0	327	746.43
213	z4	215.20	4	5108.58	585604	9	0.0	7.920	0.2	3.761	17.22	2.8	112.66	40.9	499.2	187	831	157	1476	247	10110	3	224.5	533	719.41
218		139.01	5	1415.50	583861	4	0.0	3.622	0.1	1.270	2.70	0.8	29.34	10.6	133.2	53	243	53	487	88	10943	1	55.7	206	724.45
222	z6	164.62	5	2359.85	586734	5		5.413	0.1	1.615	5.06	1.4	46.84	17.8	218.3	89	398	84	734	125	10285	2	123.2	327	740.05
220		145.69	5	1372.14	574067	4		3.799	0.0	0.603	2.30	0.5	18.07	7.4	95.8	39	184	40	361	64	11145	2	54.2	208	744.36
216		104.90	6	1223.77	582363	4		2.900	0.1	1.045	3.09	0.5	21.61	8.2	103.0	45	215	45	436	75	10381	2	56.4	206	746.84
221	z1	146.11	5	1346.89	572460	6		6.263	0.0	1.069	2.97	0.8	24.76	9.7	125.9	52	233	51	455	80	11035	2	64.4	216	734.77
217	z9	202.48	7	3876.24	575799	8		9.114	0.2	3.704	11.11	2.5	86.56	29.5	385.1	145	629	130	1119	190	10818	2	162.4	452	758.08

Table A5. 4 LA-ICPMS U-Pb geochronologic analyses, trace element concentrations, and Ti-in-zircon thermometer results for sample 110-368. Data from experiment "Zircon_08March2022_Miscellaneous_1" is in black text and "Zircon_08March2022_Miscellaneous_2" is in blue text. Discordance, defined as the relative difference between the $^{207}Pb/^{235}U$ and $^{206}Pb/^{238}U$ dates, outside of uncertainty of 5% is flagged with strikethrough font and was not interpreted for age.

		Composition							Corrected isotope ratios										
LA-ICPMS label	CA-TIMS label	U ppm	Th ppm	Pb ppm	Th/U	^{204}Pb cps	$^{206}Pb/^{204}Pb$	±1s	$^{208}Pb/^{232}Th$	±2s (%)	$^{207}Pb/^{235}U$	±2s (%)	$^{206}Pb/^{238}U$	±2s (%)	error corr	$^{238}U/^{206}Pb$	±2s (%)	$^{207}Pb/^{206}Pb$	±2s (%)
245		230	54.3	7.50	0.272	8671	359	5	0.01040	7.750822	0.2224	9.4	0.03364	2.4	0.244404	29.72	2.4	0.04794	9.1
240		415	170	16.3	0.409	17651	988	9	0.00964	6.709631	0.2329	5.5	0.03354	3.8	0.572138	29.82	3.8	0.05038	5.3
248		269	97.1	10.3	0.361	11503	11503	152	0.00993	9.746988	0.2386	6.7	0.03306	3.5	0.506605	30.24	3.5	0.05233	5.7
233	z6	310	130	12.0	0.419	13383	12758	174	0.00982	7.162692	0.2104	8.1	0.03299	2.6	0.310715	30.31	2.6	0.04628	7.7
237		509	291	20.5	0.572	22586	1982	15	0.00966	4.04244	0.2254	5.7	0.03295	2.8	0.483359	30.35	2.8	0.04861	4.6
~~244~~		~~311~~	~~97.9~~	~~12.0~~	~~0.314~~	~~14134~~	~~1093~~	~~16~~	~~0.01169~~	~~11.6938~~	~~0.2659~~	~~7.9~~	~~0.03287~~	~~2.7~~	~~0.324862~~	~~30.42~~	~~2.7~~	~~0.05556~~	~~7.5~~
239		657	300	25.7	0.457	28856	1965	22	0.01022	6.538093	0.2151	5.7	0.03282	2.6	0.434237	30.47	2.6	0.04753	5.1
256		364	134	13.5	0.368	15804	15804	110	0.00873	7.228431	0.2060	8.4	0.03255	3.1	0.360509	30.72	3.1	0.04591	7.8
235		672	236	25.2	0.351	29097	4040	49	0.00980	7.145042	0.2155	5.5	0.03245	1.8	0.295051	30.82	1.8	0.04816	5.2
~~270~~		~~413~~	~~184~~	~~16.9~~	~~0.445~~	~~18026~~	~~659~~	~~9~~	~~0.01377~~	~~8.756956~~	~~0.3423~~	~~5.8~~	~~0.03241~~	~~3.8~~	~~0.562165~~	~~30.86~~	~~3.8~~	~~0.07661~~	~~5.6~~
272		607	325	23.6	0.535	25561	565	17	0.00938	6.556491	0.2240	7.7	0.03241	4.4	0.557609	30.86	4.4	0.05014	6.4
252		357	133	14.0	0.371	15114	928	10	0.01270	6.751987	0.2929	7.1	0.03232	3.1	0.41565	30.94	3.1	0.06573	6.5
~~230~~		~~278~~	~~94.9~~	~~10.6~~	~~0.342~~	~~11510~~	~~11510~~	~~134~~	~~0.01255~~	~~8.798886~~	~~0.2704~~	~~7.3~~	~~0.03228~~	~~2.8~~	~~0.371683~~	~~31.00~~	~~2.8~~	~~0.06080~~	~~6.7~~
~~246~~	z3	~~339~~	~~110~~	~~13.2~~	~~0.324~~	~~14297~~	~~2621~~	~~18~~	~~0.01419~~	~~13.53548~~	~~0.3044~~	~~12.9~~	~~0.03217~~	~~2.6~~	~~0.198186~~	~~31.09~~	~~2.6~~	~~0.06863~~	~~12.6~~
238		687	390	26.9	0.568	28667	10795	135	0.00964	4.874625	0.2134	5.3	0.03213	1.8	0.314113	31.12	1.8	0.04817	5.0
253		434	175	16.3	0.404	17804	749	6	0.01003	5.23473	0.2246	5.2	0.03197	2.5	0.463264	31.28	2.5	0.05098	4.5
264		557	245	21.1	0.440	23571	1414	24	0.01011	4.518947	0.2306	7.4	0.03189	2.8	0.368067	31.36	2.8	0.05245	6.9
~~227~~		434	~~200~~	~~16.7~~	~~0.462~~	~~15736~~	~~284~~	4	~~0.01081~~	~~5.607482~~	~~0.2612~~	~~7.3~~	~~0.03474~~	~~3.1~~	~~0.402315~~	~~31.50~~	~~3.1~~	~~0.05867~~	~~6.7~~
266		212	73.4	7.57	0.347	8766	818	13	0.00932	12.30015	0.2187	7.7	0.03169	3.7	0.47245	31.56	3.7	0.05005	6.8
255		231	65.1	8.23	0.295	9501	614	7	0.00877	10.34853	0.2128	10.0	0.03167	3.5	0.337604	31.58	3.5	0.04874	9.4
243		449	194	16.6	0.433	19631	1045	20	0.00866	6.438212	0.2126	6.2	0.03163	1.5	0.216731	31.61	1.5	0.04874	6.0
236		540	257	20.3	0.475	23217	23217	309	0.00920	6.093761	0.2237	5.6	0.03162	2.1	0.355861	31.63	2.1	0.05131	5.2
265		545	241	20.3	0.442	22132	6113	75	0.00955	4.616934	0.2192	6.8	0.03160	3.5	0.498424	31.64	3.5	0.05031	5.8
257		377	130	13.7	0.345	15932	432	5	0.01027	8.332779	0.2062	8.0	0.03159	4.2	0.511661	31.66	4.2	0.04734	6.8
267		1046	730	41.6	0.698	43459	4541	41	0.00925	3.718324	0.2286	5.2	0.03154	3.2	0.603153	31.70	3.2	0.05257	4.1
242		651	324	24.8	0.497	27051	1407	12	0.00984	4.741957	0.2213	5.5	0.03151	2.9	0.518855	31.73	2.9	0.05093	4.7
~~250~~		~~468~~	~~207~~	~~18.5~~	~~0.416~~	~~20235~~	~~689~~	~~8~~	~~0.00934~~	~~5.368792~~	~~0.2453~~	~~4.5~~	~~0.03149~~	~~2.0~~	~~0.414704~~	~~31.76~~	~~2.0~~	~~0.05650~~	~~4.0~~
241		236	84.5	8.60	0.358	10105	860	12	0.00944	7.657926	0.2305	8.3	0.03146	3.1	0.363521	31.78	3.1	0.05313	7.7
263		306	105	11.1	0.345	12303	12303	272	0.00977	6.591801	0.2206	5.5	0.03145	3.2	0.473334	31.80	3.2	0.05087	5.7
269		327	105	11.8	0.322	13850	447	5	0.01024	6.893992	0.2236	6.0	0.03138	3.2	0.387708	31.88	3.2	0.05171	7.3
254		326	111	11.8	0.341	13524	1172	13	0.00977	9.922537	0.2051	6.1	0.03134	2.7	0.511446	31.91	2.7	0.04747	4.3
~~228~~		~~253~~	~~80.9~~	~~9.74~~	~~0.320~~	~~10360~~	~~8749~~	~~167~~	~~0.01627~~	~~9.320712~~	~~0.3168~~	~~6.6~~	~~0.03124~~	~~3.3~~	~~0.478335~~	~~32.01~~	~~3.3~~	~~0.07425~~	~~5.7~~
258		483	227	17.8	0.470	15605	1621	60	0.00912	6.782473	0.2138	7.1	0.03124	3.1	0.425166	32.01	3.1	0.04963	6.4
225	z2	429	152	15.5	0.354	16979	549	5	0.00959	5.13066	0.2212	4.8	0.03120	2.7	0.530758	32.06	2.7	0.05144	4.0
247		514	274	19.4	0.534	21565	1836	35	0.00940	3.340196	0.2079	6.5	0.03115	2.4	0.361544	32.10	2.4	0.04840	6.0
251	z1	378	142	13.7	0.375	16084	2347	38	0.00976	5.701844	0.2130	5.2	0.03110	2.5	0.465414	32.16	2.5	0.04967	4.5
246	z5	806	455	30.7	0.565	33831	33831	234	0.00969	3.560068	0.2171	3.5	0.03099	2.3	0.613906	32.27	2.3	0.05081	2.7
~~232~~		~~734~~	~~344~~	~~29.6~~	~~0.468~~	~~30341~~	~~432~~	~~9~~	~~0.01482~~	~~4.307214~~	~~0.3383~~	~~6.6~~	~~0.03098~~	~~2.7~~	~~0.456895~~	~~32.28~~	~~2.7~~	~~0.07516~~	~~4.6~~
229	z4	296	113	10.8	0.383	11659	445	7	0.01065	8.154272	0.2128	6.0	0.03097	3.3	0.395909	32.29	3.3	0.04986	7.3
223		452	187	16.5	0.413	17416	3620	56	0.01029	5.354761	0.2317	7.3	0.03079	2.6	0.342223	32.48	2.6	0.05458	6.9
260		579	262	21.1	0.453	23239	558	5	0.00938	6.344329	0.2198	6.4	0.03065	2.0	0.286837	32.63	2.0	0.05202	6.1
261		246	73.2	8.62	0.298	9797	1169	19	0.01038	9.45102	0.2254	7.6	0.03065	3.5	0.454091	32.63	3.5	0.05334	6.7
271		358	132	12.7	0.365	14803	1130	11	0.00949	8.917217	0.2255	5.6	0.03063	2.5	0.42387	32.65	2.5	0.05339	5.0
262		855	362	30.9	0.423	35208	35208	604	0.00954	4.025701	0.2069	5.4	0.03062	3.4	0.605376	32.65	3.4	0.04899	4.2
266		595	284	21.8	0.477	23987	1673	14	0.00959	7.215663	0.2091	6.2	0.03060	2.0	0.297947	32.68	2.0	0.04957	5.9
259		660	249	23.3	0.378	26895	664	9	0.00875	5.776636	0.2050	5.1	0.03055	2.6	0.472354	32.74	2.6	0.04868	4.5
224		308	125	11.0	0.405	11493	11493	80	0.01056	7.314643	0.2238	7.2	0.03015	1.7	0.20487	33.16	1.7	0.05382	7.0
~~226~~		~~649~~	~~308~~	~~24.1~~	~~0.475~~	~~25144~~	~~649~~	~~7~~	~~0.01185~~	~~5.701436~~	~~0.2415~~	~~6.1~~	~~0.02986~~	~~2.1~~	~~0.243201~~	~~33.50~~	~~2.1~~	~~0.05866~~	~~7.8~~
~~234~~		~~381~~	~~132~~	~~13.6~~	~~0.337~~	~~15329~~	~~2130~~	~~46~~	~~0.01052~~	~~7.935141~~	~~0.2295~~	~~6.1~~	~~0.02982~~	~~2.3~~	~~0.432806~~	~~33.54~~	~~2.3~~	~~0.05582~~	~~4.5~~

Table A5. 4 continued.

LA-ICPMS label	CA-TIMS label	Dates (Ma) $^{208}Pb/^{232}Th$	±2s (Ma)	±2s-sys (Ma)	$^{207}Pb/^{206}Pb$	±2s (Ma)	±2s-sys (Ma)	$^{207}Pb/^{235}U$	±2s (Ma)	±2s-sys (Ma)	$^{206}Pb/^{238}U$	±2s (Ma)	±2s-sys (Ma)	disc (%)	±2s (%)	207-method $^{206}Pb^*/^{238}U^*$	±2s (Ma)	208-method $^{206}Pb^*/^{238}U^*$	±2s (Ma)
245		209	16.1	17.5	96.4	215	216	204	17.4	17.8	213	5.04	5.74	-4.6	5.3	214	5.21	213	5.30
240		154	11.0	12.6	212	123	124	213	12.5	12.9	213	7.96	8.41	0.3	7.0	213	8.04	214	8.51
248		220	18.4	20.4	300	131	132	217	13.1	13.4	210	7.16	7.66	3.5	6.7	209	7.23	210	7.63
233	z6	189	14.2	15.5	11.0	185	186	194	14.4	14.8	209	5.40	6.03	-7.9	8.5	210	5.53	210	5.84
237		200	8.05	10.2	177	114	115	206	10.6	10.9	209	5.80	6.39	-1.3	5.9	209	5.87	210	6.39
~~244~~		~~235~~	~~27.8~~	~~28.8~~	~~587~~	~~162~~	~~163~~	~~243~~	~~17.1~~	~~17.4~~	~~209~~	~~5.48~~	~~6.10~~	~~14.1~~	~~6.5~~	206	5.57	207	5.92
239		226	13.4	14.9	75.6	121	122	199	10.2	10.5	208	5.25	5.90	-5.2	6.1	209	5.34	209	5.73
256		176	12.6	14.3	-7.29	188	189	190	14.6	14.8	206	6.35	6.83	-8.6	8.0	206	6.49	207	6.77
235		187	14.0	15.3	107	123	124	198	9.86	10.2	206	3.56	4.43	-3.9	5.5	207	3.65	207	3.84
~~270~~		~~276~~	~~24.0~~	~~26.2~~	~~1111~~	~~112~~	~~114~~	~~296~~	~~17.7~~	~~18.1~~	~~206~~	~~7.76~~	~~8.48~~	~~31.2~~	~~4.8~~	198	7.66	199	8.54
272		189	12.3	14.2	201	148	149	205	14.4	14.5	206	8.87	9.22	-0.2	8.2	205	8.96	207	9.70
~~252~~		~~265~~	~~17.1~~	~~19.0~~	~~788~~	~~436~~	~~436~~	~~261~~	~~16.4~~	~~16.6~~	~~206~~	~~6.16~~	~~6.71~~	~~21.4~~	~~5.5~~	201	6.17	202	5.61
230		252	22.0	23.7	632	145	146	243	15.8	16.2	205	5.72	6.25	15.8	6.0	201	6.77	201	6.15
249	z3	285	38.3	39.4	888	261	261	273	30.5	20.7	204	5.32	5.93	24.4	8.8	199	5.67	200	5.93
238		184	9.41	11.2	108	117	118	196	9.42	9.79	204	3.60	4.45	-3.8	5.3	205	3.68	205	4.03
253		202	10.6	12.4	239	104	106	206	9.83	10.0	203	4.98	5.63	1.4	5.2	203	5.04	203	5.35
264		223	9.14	11.9	305	155	157	211	14.1	14.4	202	5.67	6.18	4.3	7.0	201	5.75	202	5.11
~~227~~		~~219~~	~~12.2~~	~~14.4~~	~~592~~	~~144~~	~~145~~	~~236~~	~~15.4~~	~~15.7~~	~~201~~	~~6.06~~	~~6.56~~	~~14.5~~	~~6.1~~	198	6.10	199	6.56
269		187	22.9	24.0	197	157	158	201	14.1	14.3	201	7.40	7.79	-0.1	7.9	200	7.49	200	7.91
259		177	18.2	19.4	135	220	221	196	17.8	18.0	201	6.86	7.28	-2.6	10.0	200	7.00	201	7.23
243		174	11.2	12.5	135	141	142	196	11.0	11.4	201	2.98	3.95	-2.6	6.0	201	3.09	203	3.28
236		185	11.2	12.6	255	120	121	205	10.4	10.8	201	4.18	4.91	2.1	5.4	200	4.25	202	4.59
265		182	8.83	11.4	209	134	136	201	12.3	12.5	201	6.84	7.27	0.3	7.0	200	6.92	200	7.38
257		227	17.1	18.8	86.3	162	163	190	13.8	14.1	200	8.20	8.56	-5.3	9.8	200	8.31	199	8.70
267		186	6.89	9.81	310	92.8	94.6	209	9.84	10.2	200	6.39	6.85	4.2	5.4	200	6.43	203	7.18
242		156	9.34	11.3	238	107	109	203	10.1	10.5	200	5.79	6.34	1.5	5.7	200	5.85	200	6.31
~~250~~		~~189~~	~~10.0~~	~~11.7~~	~~472~~	~~88.9~~	~~90.2~~	~~223~~	~~9.56~~	~~9.44~~	~~200~~	~~3.06~~	~~4.08~~	~~10.3~~	~~4.0~~	198	3.93	201	4.21
241		180	14.5	15.7	334	173	176	211	15.9	16.1	200	6.12	6.64	5.2	7.7	199	6.22	200	6.53
263		186	12.9	14.8	225	132	133	202	12.0	12.3	200	6.27	6.73	1.4	6.6	198	6.34	198	6.66
268		206	14.1	16.1	273	168	169	205	14.8	15.1	199	6.27	6.73	2.8	7.7	197	6.37	197	6.64
254		167	18.4	20.4	73.1	103	105	186	8.85	9.22	199	5.31	5.90	-5.0	5.6	199	5.38	199	5.69
~~229~~		~~326~~	~~30.2~~	~~32.2~~	~~1048~~	~~416~~	~~417~~	~~282~~	~~16.2~~	~~16.6~~	~~198~~	~~6.35~~	~~6.80~~	~~29.6~~	~~4.6~~	191	6.28	190	6.83
258		183	12.4	14.2	178	149	150	197	12.7	13.0	198	6.10	6.56	-0.8	7.2	198	6.19	198	6.64
225	z2	183	9.85	12.0	260	90.8	92.7	203	8.76	9.18	198	5.17	5.72	2.4	4.9	197	5.22	197	5.49
247		189	6.29	8.74	119	142	143	192	11.3	11.8	198	4.76	5.41	-3.1	6.6	198	4.85	199	5.21
251	z1	156	11.1	12.8	179	105	107	196	9.26	9.63	197	4.89	5.51	-0.7	5.4	197	4.95	197	5.23
246	z5	155	6.91	9.32	232	62.5	64.6	199	6.41	6.96	197	4.42	5.10	1.4	3.9	197	4.45	197	4.87
~~232~~		~~207~~	~~12.7~~	~~16.3~~	~~1177~~	~~86.2~~	~~87.6~~	~~209~~	~~14.2~~	~~14.6~~	~~197~~	~~5.10~~	~~5.74~~	~~33.5~~	~~2.7~~	189	5.12	189	5.66
228	z4	214	17.4	18.9	188	169	170	196	14.2	14.5	197	6.31	6.76	-0.3	8.0	195	6.41	194	6.79
223		207	11.0	13.2	395	153	154	212	14.0	14.3	195	5.07	5.61	7.6	6.6	193	5.15	194	5.45
260		189	11.9	13.9	286	138	140	202	11.7	12.0	195	3.81	4.49	3.5	5.9	194	3.90	194	4.18
261		209	15.6	21.1	343	152	153	206	14.2	14.5	195	6.80	7.20	5.7	7.3	192	6.86	192	7.18
271		181	16.9	18.4	346	114	115	206	10.5	10.9	195	4.81	5.36	5.9	5.3	193	4.86	193	5.19
262		182	7.69	10.5	147	99.2	101	191	9.41	9.75	194	6.45	6.88	-1.9	6.1	195	6.51	195	6.91
266		183	13.9	15.6	175	137	138	193	10.9	11.2	194	3.84	4.51	-0.8	6.0	194	3.92	194	4.27
255		176	10.1	12.1	132	105	107	185	8.69	9.25	194	4.89	5.43	-2.4	5.5	194	4.95	195	5.22
224		212	15.4	17.1	333	156	159	205	13.4	13.5	192	3.16	3.94	6.6	6.3	189	3.28	189	3.51
~~226~~		~~228~~	~~12.6~~	~~16.9~~	~~555~~	~~471~~	~~472~~	~~226~~	~~16.0~~	~~16.3~~	~~190~~	~~2.08~~	~~4.62~~	~~13.7~~	~~6.6~~	187	4.10	185	4.42
231		211	16.7	18.2	445	99.6	101	210	9.58	9.99	189	4.36	4.95	9.7	4.6	187	4.39	187	4.68

LA-ICPMS label	CA-TIMS label	Concentrations (ppm) P	Ti	Y	Zr	Nb	La	Ce	Pr	Nd	Sm	Eu	Gd	Tb	Dy	Ho	Er	Tm	Yb	Lu	Hf	Ta	Th	U	Ti-in-zircon T(°C)
245		404	3.66	1817	550147	19.4	0.023	8.95	0.085	1.27	3.57	0.820	30.0	12.4	175	71.5	324	58.7	526	112	15067	5.37	54.3	200	706.56
240		3556	4.61	3656	534759	42.3	300	816	120	615	188	16.4	273	51.6	457	147	566	115	971	161	14162	13.4	170	415	721.76
248		213	3.23	2831	547402	12.0	0.179	12.6	0.161	2.77	9.38	1.99	63.0	23.5	304	117	506	106	911	156	14876	4.97	97.1	269	690.84
233	z6	221	5.13	2290	556278	25.4		15.7	0.08	1.52	5.40	1.24	42.8	18.2	221	84.3	394	81.4	725	118	13294	7.89	130	310	731.34
237		319	5.97	2635	546127	36.0	0.017	22.2	0.132	2.45	8.04	1.83	61.4	23.7	296	115	493	102	912	147	12570	10.3	291	509	745.44
~~244~~		314	5.57	2590	513506	66.3	0.761	27.0	0.372	3.91	6.50	1.64	51.1	19.3	254	100	443	92.2	831	136	13446	10.6	97.9	311	738.95
239		420	89.7	6024	545010	47.2	0.1	40.6	0.469	7.66	16.8	3.58	131	49.7	619	245	1040	214	1820	297	12896	11.4	300	657	1043.60
256		243	2.70	3116	550874	27.2		20.5	0.112	3.74	7.55	1.72	63.8	24.4	318	125	563	117	1017	175	15518	9.24	134	364	675.98
235		358	4.03	4174	557547	89.1	0.0	40.4	0.176	3.04	8.45	2.09	77.8	31.8	402	161	708	151	1311	213	14393	20.0	236	672	709.87
~~270~~		267	4.13	3063	566137	34.3	0.014	22.7	0.149	2.65	8.46	2.06	82.2	25.3	328	127	557	114	976	167	14259	10.8	164	413	711.96
272		336	5.06	4375	558150	60.2		40.5	0.184	3.72	12.2	2.62	92.1	36.7	435	175	743	145	1295	220	14339	15.3	325	507	729.94
~~252~~		333	4.21	2529	553735	26.0	1.81	22.5	0.941	7.64	8.06	1.88	68.6	22.9	292	117	514	110	967	155	14330	7.75	139	357	713.71
230		217	3.23	1984	577019	26.7		14.4	0.074	1.74	4.20	1.14	33.6	13.8	187	75.4	334	72.4	617	108	15813	8.28	94.9	278	691.63
249	z3	256	6.36	2504	550723	33.3	0.154	21.6	0.185	2.72	5.40	1.39	42.7	18.0	240	93.3	414	87.6	792	133	14422	10.2	110	339	735.17
238		1385	4.87	3865	544002	61.5	69.9	225	29.0	148	49.8	6.29	123	35.6	400	152	631	129	1104	178	14163	17.4	390	687	726.65
253		275	4.02	2744	546956	37.2		24.2	0.122	2.10	6.06	1.54	48.9	20.6	266	106	471	97.3	853	145	14243	12.0	175	434	709.57
264		331	2.71	5745	560891	29.7	0.092	30.6	0.351	7.42	18.2	4.56	141	50.5	640	239	1032	206	1736	297	14584	8.03	245	657	676.22
~~227~~		9775	5.92	3789	565913	34.7	426	1187	166	960	283	36.9	367	74.3	572	168	633	117	939	161	15525	11.9	200	434	744.59
269		234	3.17	2828	577409	8.37	2.72	17.0	1.20	9.04	8.45	2.09	66.5	22.5	294	113	482	96.7	860	142	15121	3.82	73.4	212	689.19
259		208	3.73	2145	586911	30.1	0.1	16.9	0.080	1.84	5.03	1.04	38.3	16.6	220	88.0	388	84.2	742	127	15507	10.5	89.1	231	703.20
243		334	5.65	3476	526636	39.5	0.236	25.1	0.237	3.11	9.06	2.31	71.8	27.4	356	136	592	126	1087	181	14264	11.6	194	449	740.28
236		349	4.01	6709	533394	31.2	0.05	26.1	0.454	8.53	20.5	5.07	151	59.1	706	273	1151	230	1593	315	12530	6.84	257	540	709.32
265		341	3.39	5536	567062	29.2		22.6	0.319	6.41	14.7	3.72	121	45.3	603	230	986	211	1720	288	15567	7.79	241	645	694.85
257		234	3.80	2996	579217	33.1		22.1	0.06	2.49	7.40	1.65	63.3	20.9	278	109	462	101	865	151	15241	11.0	130	377	704.76
267		478	5.64	7334	563862	88.8	0.016	61.3	0.493	8.85	22.7	6.16	182	63.3	814	294	1258	249	2025	341	14117	19.5	720	1048	740.12
242		301	4.70	3415	551799	51.4	0.0	32.0	0.129	3.32	6.56	2.16	71.4	26.1	340	131	573	120	1037	171	15665	15.8	324	551	725.97
~~250~~		377	3.57	3337	555059	51.5	1.41	37.1	0.724	5.29	6.46	1.53	54.1	25.0	318	127	546	114	1006	167	14562	16.0	207	496	699.45
241		201	2.90	2773	560362	8.96		10.7	0.1	2.44	7.24	1.51	64.1	22.4	274	111	476	98.3	628	141	14306	3.81	64.5	236	681.99
263		229	3.24	2167	572060	29.3		19.0	0.079	2.00	5.52	1.22	44.6	17.0	231	91.0	402	80.7	737	128	16336	10.2	105	206	691.00
268		236	3.16	2774	570734	34.8		24.0	0.137	2.60	5.93	1.31	58.4	21.8	283	113	492	104	900	153	15029	11.2	105	327	689.08
254		190	3.32	2831	531086	22.2	0	19.0	0.136	3.43	7.16	1.76	59.0	22.2	281	109	463	99.2	874	145	13633	7.57	111	326	693.08
~~229~~		221	3.53	1680	554060	24.3	0.015	13.7	0.054	1.20	4.01	1.12	32.1	12.8	166	67.6	301	62.9	582	99.1	16315	8.45	60.9	253	699.19
258		263	3.88	2682	566904	39.7		23.5	0.06	2.38	5.67	1.60	63.1	20.3	266	105	467	95.1	852	141	15893	11.6	227	483	706.45
225	z2	283	3.49	3130	582233	39.8		27.7	0.109	2.22	7.93	2.06	80.5	23.9	314	128	550	115	979	168	15412	14.2	152	429	697.43
247		290	4.61	3424	540446	42.4		28.4	0.170	2.38	10.1	2.22	69.2	26.7	340	132	567	116	1023	171	12565	12.6	274	514	721.70
251	z1	275	4.75	3233	539526	35.5	0.0	24.2	0.139	3.48	7.16	1.55	55.5	25.1	321	125	548	114	1011	166	12570	11.2	142	378	724.50
246	z5	409	5.01	4264	544464	67.4		40.3	0.173	3.42	11.2	2.84	67.1	33.5	431	161	694	143	1239	198	12559	16.9	465	606	746.07
~~232~~		314	4.56	3668	565741	65.7		39.2	0.102	2.73	9.85	1.84	75.4	28.4	379	145	630	128	1083	187	15206	19.1	344	734	720.64
228	z4	202	2.86	2617	576045	13.8	0.027	13.1	0.245	3.93	12.4	2.88	86.2	30.9	390	147	641	131	1079	190	15325	5.00	113	296	680.64
223		267	3.81	4759	582734	26.0	0.250	22.0	0.268	5.70	15.3	3.80	111	40.1	501	192	822	167	1426	240	14612	7.75	187	452	704.90
260		320	4.13	3079	570019	45.0	0.018	29.6	0.118	2.74	8.10	2.23	67.0	24.8	316	126	550	115	972	164	15872	15.7	252	579	712.08
261		214	3.45	2000	582979	25.5	0.012	16.2	0.062	1.54	4.77	1.30	37.2	15.2	197	81.5	365	78.6	598	113	15567	8.19	73.2	246	696.63
271		264	3.06	2163	564243	30.4	0.02	19.6	0.099	1.99	6.18	1.36	45.2	16.9	236	91.4	412	66.6	754	128	15545	10.4	132	358	686.81
262		352	3.52	6008	545921	82.6		62.8	0.163	4.77	13.0	2.87	103	41.8	538	209	927	182	1567	268	14643	22.8	362	855	698.13
266		291	4.04	2650	566199	45.4	0.015	27.0	0.128	2.36	6.25	1.58	59.8	22.9	298	121	518	106	903	160	15472	14.8	284	595	709.96
255		353	5.23	4467	575673	71.3		43.6	0.159	3.75	10.2	3.19	97.6	36.1	484	183	826	170	1444	243	14633	16.7	249	560	733.17
224		3435	4.16	3592	572429	16.1	131	346	52.9	417	110	9.38	158	38.2	456	153	623	121	1035	174	16302	4.82	125	308	713.14
~~226~~		378	4.30	3599	573750	52.3	0.344	35.6	0.530	4.20	8.67	2.28	72.7	27.4	368	142	602	130	1093	185	15618	17.5	308	649	715.48
231		272	3.34	3131	560178	41.4		28.8	0.110	2.77	5.98	1.70	61.9	23.7	302	123	544	111	962	167	15714	13.1	132	391	693.74

Table A5. 5 LA-ICPMS U-Pb isotope ratios and trace element concentrations for standard data collected during sample 110-322 analyses.

Analysis	Composition: U ppm	Th ppm	Pb ppm	Th/U	206Pb cps	206Pb/204Pb	±1s	Corrected isotope ratios: 208Pb/232Th	±2s (%)	207Pb/235U	±2s (%)	206Pb/238U	±2s (%)	error corr.	238U/206Pb	±2s (%)	207Pb/206Pb	±2s (%)
Primary standards																		
PL 298	428.1	35.6	24.59	0.083	25527	1429	18	0.01640	11.4	0.3919	6.8	0.05338	3.2	0.46	18.73	3.2	0.05324	6.0
PL 299	463.5	41.4	27.56	0.089	32670	1016	18	0.01846	9.3	0.3993	6.0	0.05492	3.0	0.48	18.21	3.0	0.05273	5.2
PL 300	641.8	60.7	38.14	0.095	39234	31659	212	0.01579	11.7	0.4018	5.8	0.05490	2.6	0.43	18.22	2.6	0.05308	5.2
PL 301	611.1	54.1	35.28	0.088	35975	836800627	21857631	0.01680	9.3	0.4000	5.0	0.05328	3.1	0.60	18.77	3.1	0.05444	3.9
PL 306	720.4	64.9	40.97	0.090	41250	770	8	0.01628	11.2	0.3915	5.2	0.05241	3.9	0.74	19.08	3.9	0.05418	3.4
PL 307	717.2	76.1	41.71	0.106	41830	2067	28	0.01697	8.1	0.3814	4.7	0.05342	3.3	0.68	18.72	3.3	0.05178	3.3
PL 314	510.9	42.8	28.08	0.084	28759	12079	185	0.01612	11.6	0.3891	6.6	0.05087	3.6	0.54	19.66	3.6	0.05547	5.5
PL 315	423.6	35.5	24.28	0.084	24395	1277	21	0.01630	10.5	0.3796	5.6	0.05334	2.9	0.50	18.75	2.9	0.05162	4.8
PL 319	573.7	43.2	33.51	0.075	37047	1482	16	0.01812	6.6	0.3839	6.3	0.05419	4.1	0.63	18.46	4.1	0.05139	4.8
PL 323	1009.4	117.9	60.22	0.117	72411	60820	1119	0.01822	5.9	0.3927	5.6	0.05391	4.6	0.80	18.55	4.6	0.05283	3.3
PL 326	600.3	47.9	36.03	0.080	44487	7413	151	0.01702	8.9	0.3957	6.4	0.05556	4.1	0.63	18.00	4.1	0.05165	5.0
PL 327	581.8	44.0	34.39	0.076	43354	1457	31	0.01795	10.8	0.4276	4.3	0.05444	2.8	0.62	18.37	2.8	0.05697	3.3
PL 330	744.8	62.9	42.34	0.084	50098	1026	15	0.01680	9.7	0.3870	6.4	0.05230	5.3	0.83	19.12	5.3	0.05367	3.5
PL 331	704.1	62.2	41.34	0.088	49290	2760	36	0.01736	11.0	0.3960	5.1	0.05399	3.6	0.70	18.52	3.6	0.05319	3.6
PL 334	756.1	66.1	43.51	0.087	51493	1201	16	0.01582	7.4	0.3991	5.4	0.05292	3.4	0.61	18.90	3.4	0.05471	4.2
PL 335	713.7	62.3	40.41	0.087	49203	2175	32	0.01595	8.5	0.3688	4.7	0.05224	3.8	0.78	19.14	3.8	0.05119	2.9
PL 338	453.3	42.9	26.51	0.095	25807	3097	80	0.01524	18.7	0.3864	5.4	0.05436	2.5	0.43	18.40	2.5	0.05156	4.8
PL 339	432.8	35.8	24.89	0.083	24808	321	8	0.01635	10.4	0.3907	6.4	0.05346	4.6	0.71	18.71	4.6	0.05300	4.4
PL 342	741.3	70.9	42.78	0.096	43508	3035	32	0.01686	8.0	0.4004	6.1	0.05298	4.9	0.80	18.87	4.9	0.05481	3.5
PL 343	697.2	67.7	40.35	0.097	41823	1952	43	0.01655	10.2	0.3973	5.4	0.05321	3.9	0.70	18.79	3.9	0.05415	3.8
PL 346	436.6	40.2	25.87	0.092	25553	25553	731	0.01682	15.8	0.3987	6.5	0.05497	2.9	0.44	18.19	2.9	0.05260	5.8
PL 347	460.6	44.9	27.69	0.097	27248	1635	39	0.01919	15.8	0.4080	7.0	0.05540	3.8	0.53	18.05	3.8	0.05341	5.9
PL 350	588.9	51.3	33.68	0.087	34598	34598	639	0.01558	10.1	0.3978	5.8	0.05290	4.5	0.76	18.90	4.5	0.05454	3.7
PL 351	565.8	49.8	32.38	0.088	34797	1008	14	0.01860	11.5	0.3759	6.5	0.05282	3.3	0.49	18.93	3.3	0.05161	5.6
PL 354	564.7	50.5	32.56	0.090	33654	5654	86	0.01525	7.8	0.3768	6.7	0.05354	3.0	0.44	18.68	3.0	0.05105	5.9
PL 355	555.4	49.9	32.14	0.090	33662	764	9	0.01786	6.5	0.4062	5.9	0.05331	4.1	0.68	18.76	4.1	0.05527	4.3
Secondary standards																		
91500 382	66.8	23.2	14.86	0.347	12957	12957	257	0.05650	10.1	1.9973	6.2	0.18949	3.7	0.58	5.28	3.7	0.07645	5.0
91500 383	68.5	23.2	14.40	0.339	13045	10526	130	0.04982	7.0	1.8329	6.2	0.18124	4.0	0.63	5.52	4.0	0.07335	4.8
91500 387	66.9	23.2	14.39	0.346	12494	750	16	0.04886	9.6	1.9428	8.1	0.18546	3.8	0.45	5.39	3.8	0.07598	7.2
91500 390	73.0	25.5	15.79	0.350	14293	14293	238	0.05194	9.1	1.9160	7.1	0.18544	5.8	0.81	5.39	5.8	0.07494	4.1
91500 391	71.2	24.8	15.14	0.348	14813	1033	23	0.05269	7.8	1.9208	6.6	0.18155	3.8	0.56	5.51	3.8	0.07674	5.4
91500 394	70.6	23.6	14.52	0.334	13357	1395	22	0.04884	9.1	1.7840	7.8	0.17763	4.0	0.50	5.63	4.0	0.07284	6.7
91500 395	72.7	24.4	15.60	0.336	14837	3116	48	0.05493	10.3	1.7998	7.4	0.18421	4.7	0.63	5.43	4.7	0.07086	5.7
91500 398	73.3	25.2	15.64	0.344	14539	370	5	0.04928	9.2	1.8632	7.5	0.18397	3.6	0.47	5.44	3.6	0.07345	6.6
91500 399	70.1	24.1	15.19	0.343	15245	557	6	0.05090	11.2	1.9394	6.5	0.18624	3.2	0.48	5.37	3.2	0.07553	5.6
Seiland 358	64.3	53.4	6.99	0.830	4934	822	13	0.02476	7.6	0.5732	14.9	0.08481	5.9	0.40	11.79	5.9	0.04901	13.6
Seiland 359	61.3	52.3	6.87	0.855	4788	571	16	0.02583	10.1	0.7032	7.6	0.08587	2.8	0.36	11.64	2.8	0.05939	7.0
Seiland 362	62.6	52.0	6.93	0.830	4264	123	3	0.02772	6.4	0.6434	13.4	0.08385	4.4	0.33	11.93	4.4	0.05565	12.6
Seiland 363	61.9	50.0	6.88	0.807	4611	94315	1902	0.02658	7.5	0.6437	12.1	0.08586	5.2	0.43	11.65	5.2	0.05437	10.9
Seiland 366	64.1	51.8	6.99	0.809	5109	858	12	0.02407	8.3	0.6652	14.0	0.08569	4.7	0.33	11.67	4.7	0.05630	13.1
Seiland 367	61.3	51.0	7.12	0.831	5034	351	9	0.02560	12.0	0.8195	10.2	0.08974	5.5	0.53	11.14	5.5	0.06623	8.6
Seiland 370	67.8	58.9	7.34	0.869	5481	4604	103	0.02284	10.1	0.6338	10.4	0.08464	4.5	0.42	11.81	4.5	0.05431	9.4
Seiland 375	67.8	55.8	7.42	0.823	5608	5608	207	0.02688	10.1	0.6686	14.0	0.08331	4.9	0.34	12.00	4.9	0.05821	13.2
Seiland 378	69.4	58.0	7.71	0.836	5475	307	9	0.02768	9.2	0.5875	12.2	0.08452	3.3	0.26	11.83	3.3	0.05041	11.7
Seiland 379	66.8	56.4	7.40	0.844	5697	342	9	0.02633	7.5	0.6835	10.2	0.08442	5.0	0.48	11.85	5.0	0.05872	8.8

Analysis	Dates (Ma): 208Pb/232Th	±2s (Ma)	±2s-sys (Ma)	207Pb/206Pb	±2s (Ma)	±2s-sys (Ma)	207Pb/235U	±2s (Ma)	±2s-sys (Ma)	206Pb/238U	±2s (Ma)	±2s-sys (Ma)	disc. (%)	±2s (%)
Primary standards														
PL 298	329	37.3	39.1	339	136	137	336	19.5	20.0	335	10.6	11.3	0.2	6.6
PL 299	370	34.0	36.4	317	119	120	341	17.5	18.0	345	10.1	10.9	-1.0	6.0
PL 300	317	36.8	38.5	332	118	119	343	17.0	17.5	345	8.9	9.8	-0.5	5.6
PL 301	337	31.1	33.3	389	87	89	342	14.5	15.1	335	10.1	10.9	2.0	5.1
PL 306	326	36.2	38.1	379	76	78	335	14.8	15.4	329	12.7	13.3	1.8	5.8
PL 307	340	27.2	29.9	276	77	79	328	13.1	13.8	335	10.7	11.5	-2.3	5.2
PL 314	323	37.2	39.1	431	121	123	334	18.6	19.1	320	11.4	12.0	4.1	6.3
PL 315	327	34.0	36.1	269	109	111	327	15.5	16.1	335	9.4	10.2	-2.5	5.7
PL 319	363	23.7	27.3	258	110	112	330	17.7	18.2	340	13.5	14.1	-3.1	6.9
PL 323	365	21.4	25.4	322	75	77	336	16.1	16.6	338	15.0	15.6	-0.6	6.6
PL 326	341	30.3	32.8	270	114	115	339	18.6	19.0	349	14.0	14.6	-3.0	7.0
PL 327	360	38.6	40.9	490	73	75	361	13.2	13.9	342	9.3	10.1	5.5	4.3
PL 330	337	32.2	34.6	357	78	81	332	18.0	18.5	329	17.0	17.5	1.1	7.4
PL 331	348	38.1	40.2	337	81	83	339	14.7	15.3	339	12.0	12.7	-0.1	5.6
PL 334	317	23.3	26.1	400	95	96	341	15.8	16.4	332	11.1	11.9	2.5	5.6
PL 335	320	26.8	29.3	249	66	68	319	13.0	13.6	328	12.1	12.7	-3.0	5.7
PL 338	306	56.8	57.9	266	110	112	332	15.3	15.9	341	8.2	9.2	-2.9	5.4
PL 339	328	33.8	35.8	329	100	102	335	18.2	18.7	336	15.1	15.6	-0.3	7.1
PL 342	338	26.7	29.3	405	79	81	342	17.6	18.1	333	16.0	16.5	2.7	6.9
PL 343	332	33.7	35.7	377	85	87	340	15.7	16.3	334	12.7	13.3	1.6	5.9
PL 346	337	52.9	54.2	312	131	132	341	18.7	19.2	345	9.9	10.7	-1.3	6.3
PL 347	384	60.0	61.5	346	132	134	347	20.5	20.9	348	12.7	13.4	0.0	6.9
PL 350	313	31.2	33.0	393	83	85	340	16.7	17.3	332	14.5	15.0	2.3	6.4
PL 351	373	42.4	44.2	268	128	129	324	17.9	18.4	332	10.6	11.3	-2.4	6.5
PL 354	306	23.6	25.9	243	136	138	325	18.5	19.0	336	10.0	10.8	-3.5	6.7
PL 355	358	22.9	26.0	423	95	97	346	17.4	17.9	335	13.4	14.1	3.3	6.2
Secondary standards														
91500 382	1111	109.1	116.0	1107	99	100	1115	41.8	43.0	1119	38.0	40.0	-0.4	5.1
91500 383	983	67.1	75.8	1024	97	98	1057	41.0	42.1	1074	39.4	41.3	-1.6	5.4
91500 387	964	90.0	96.7	1095	144	145	1096	54.5	55.4	1097	38.1	40.1	-0.1	6.1
91500 390	1023	90.6	98.2	1067	83	85	1087	47.7	48.7	1097	58.9	60.2	-0.9	7.0
91500 391	1038	79.4	88.1	1114	108	109	1088	44.1	45.2	1075	37.4	39.4	1.2	5.3
91500 394	964	85.3	92.3	1010	136	137	1040	50.9	51.8	1054	39.0	40.8	-1.4	6.2
91500 395	1081	108.4	115.3	953	116	117	1045	48.1	49.0	1090	47.3	48.9	-4.3	6.6
91500 398	972	87.3	94.0	1026	133	134	1068	49.7	50.6	1089	36.2	38.3	-1.9	5.8
91500 399	1003	109.7	115.4	1083	113	114	1095	43.3	44.5	1101	32.6	34.9	-0.6	5.0
Seiland 358	494	37.0	41.0	148	320	320	460	55.1	55.3	525	29.9	30.6	-14.1	15.1
Seiland 359	516	51.2	54.4	581	152	153	541	31.7	32.3	531	14.3	15.6	1.8	6.3
Seiland 362	553	35.0	40.4	438	281	282	504	53.2	53.6	519	22.1	22.9	-2.9	11.7
Seiland 363	530	39.4	43.9	386	244	245	505	48.0	48.3	531	26.6	27.4	-5.2	11.3
Seiland 366	481	39.2	43.1	464	291	292	518	56.6	56.9	530	23.9	24.7	-2.4	12.1
Seiland 367	511	60.4	63.3	814	180	181	608	46.8	47.3	554	29.3	30.0	8.8	8.5
Seiland 370	456	45.6	48.7	384	212	213	498	41.1	41.5	524	22.5	23.3	-5.1	9.8
Seiland 375	536	53.5	56.9	538	288	289	520	57.1	57.5	516	24.1	24.9	0.8	11.8
Seiland 378	552	50.3	54.0	214	272	272	469	45.7	46.1	523	16.4	17.6	-11.5	11.4
Seiland 379	525	38.7	43.0	557	193	194	529	41.9	42.3	522	25.1	25.8	1.2	9.1

Analysis	Concentrations (ppm): P	Ti	Y	Nb	La	Ce	Pr	Nd	Sm	Eu	Gd	Tb	Dy	Ho	Er	Tm	Yb	Lu	Hf	Ta	Th	U
Primary standards																						
PL 298	191.3	53.52	267	2.60		1.28	0.045	0.23	1.930	0.523	6.83	2.54	29.8	8.67	28.6	5.5	38	4.8	14820	1.43	35.6	428.1
PL 299	69.1	67.16	387	3.48		1.46	0.105	1.41	2.324	0.609	10.13	3.08	36.5	10.82	37.1	6.5	46	5.9	11201	1.84	41.4	463.5
PL 300	363.8	75.24	500	3.77		1.97	0.144	2.35	3.511	1.252	14.68	5.55	54.5	14.39	52.8	8.9	69	8.3	13164	2.33	60.7	641.8
PL 301	299.4	68.99	419	4.17	0.0	1.77	0.128	1.63	2.849	0.524	11.11	4.16	48.6	14.16	45.4	8.2	62	7.3	13962	2.27	54.1	611.1
PL 306	338.0	79.06	513	3.95		2.23	0.143	0.88	3.597	1.043	14.50	5.66	57.8	16.47	56.1	9.6	74	8.7	14361	2.51	64.9	720.4
PL 307	295.1	73.38	427	5.17		2.07	0.130	1.16	4.067	0.925	12.57	5.15	51.9	14.37	45.6	8.4	59	7.4	13825	2.30	76.1	717.2
PL 314	228.3	54.33	325	3.22		1.66	0.122	1.11	2.097	0.583	9.39	3.56	36.7	10.49	36.4	6.5	52	5.8	14365	1.82	42.8	510.9
PL 315	179.0	47.01	259	2.23		1.47	0.102	0.36	1.291	0.301	6.66	2.75	28.2	7.87	28.7	5.0	37	4.6	14904	1.14	35.5	423.6
PL 319	281.7	61.08	332	3.36		1.66	0.120	1.17	2.639	0.639	9.33	3.97	40.0	11.34	38.6	7.1	52	5.7	12007	2.37	43.2	573.7
PL 323	355.1	63.97	458	4.10	0.0	2.70	0.214	3.76	4.801	1.436	18.78	6.10	61.8	15.76	51.4	8.6	67	6.5	12415	2.52	117.9	1009.4
PL 326	234.9	57.29	395	3.23		1.79	0.156	0.63	2.391	0.638	9.08	3.56	39.5	11.02	38.8	6.5	55	5.7	13135	2.11	47.9	600.3
PL 327	245.9	57.77	307	3.46	0.0	1.81	0.100	1.37	2.251	0.646	9.75	3.64	37.7	10.22	34.6	6.7	55	5.8	12682	2.30	44.0	581.8
PL 330	373.5	71.87	482	3.85		1.99	0.129	1.67	3.656	0.721	15.14	5.30	56.0	16.35	52.6	10.3	73	8.9	14442	2.75	62.9	744.8
PL 331	326.5	72.37	458	3.63	0.0	1.88	0.168	1.32	3.387	0.731	14.44	5.16	56.8	16.24	51.8	10.1	72	8.7	14204	2.62	62.2	704.1
PL 334	345.0	74.98	458	3.95	0.0	1.91	0.186	1.90	2.931	1.253	14.67	5.44	58.3	16.29	54.7	10.4	76	9.0	15017	2.55	66.1	756.1
PL 335	338.8	70.03	466	3.78		1.82	0.146	1.52	3.553	0.783	14.68	5.42	56.9	15.15	54.0	9.9	72	8.5	14326	2.63	62.3	713.7
PL 338	168.4	35.73	276	1.65		1.85	0.058	0.83	1.627	0.308	7.44	2.99	30.2	8.81	32.4	6.3	49	6.9	15805	1.48	42.9	453.3
PL 339	139.3	40.25	237	2.02		1.75	0.046	0.70	1.559	0.301	5.00	2.28	26.7	7.87	28.5	4.8	37	5.3	16619	1.41	35.8	432.8
PL 342	366.9	70.63	499	3.66	0.0	2.21	0.115	1.82	2.705	0.902	14.71	5.91	60.5	16.42	57.8	10.4	76	8.9	15382	2.68	70.9	741.3
PL 343	330.9	68.71	469	3.77	0.0	1.86	0.144	1.11	3.051	0.829	13.37	5.13	54.3	15.46	54.2	9.7	65	9.1	15810	2.45	67.7	697.2
PL 346	191.0	38.44	272	1.64		1.45	0.047	1.04	1.962	0.440	7.53	2.68	28.5	8.50	32.4	6.1	47	6.8	16202	1.66	40.2	436.6
PL 347	212.4	32.14	288	2.05		1.78	0.080	1.11	2.127	0.473	6.50	2.93	31.8	9.36	33.8	6.5	52	7.3	16538	1.51	44.9	460.6
PL 350	244.6	59.53	392	3.58		1.55	0.099	1.60	1.880	0.617	8.36	4.33	42.2	12.81	47.0	8.3	57	7.7	16879	2.29	51.3	588.9
PL 351	249.8	58.59	381	3.22		1.34	0.065	1.51	2.564	0.589	10.31	3.85	42.2	12.84	44.2	7.9	55	8.0	16114	2.10	49.8	565.8
PL 354	246.4	58.90	390	3.10	0.0	1.63	0.071	0.76	1.502	0.699	11.32	4.07	43.1	12.15	45.8	8.3	58	8.0	16292	2.36	50.5	564.7
PL 355	237.4	58.19	351	3.28		1.59	0.095	1.27	1.495	0.726	10.74	4.20	42.0	12.78	41.0	7.5	58	7.5	15664	1.98	49.9	555.4
Secondary standards																						
91500 382	82.6	3.85	115	0.56		2.07				0.082	1.19	0.58	8.8	3.57	21.5	4.9	55	11.4	8189	0.40	23.2	66.8
91500 383	49.4	4.18	108	0.67		2.08		0.17	0.398	0.223	1.85	0.61	8.0	3.64	21.7	5.4	53	10.3	7921	0.34	23.2	68.5
91500 387	62.6	3.69	112	0.45		2.01			0.344	0.187	1.40	0.74	8.6	4.03	20.3	5.2	55	11.0	7875	0.36	23.2	66.9
91500 390	65.6	3.47	113	0.54		2.50				0.157	1.70	0.58	9.0	4.27	22.7	6.0	57	11.5	8542	0.56	25.5	73.0
91500 391	54.2	3.55	110	0.55		2.12	0.012	0.13	0.413	0.133	1.95	0.62	8.8	3.93	22.1	5.5	56	11.1	8614	0.44	24.8	71.2
91500 394	80.2	3.48	108	0.45		2.27				0.075	1.85	0.60	8.9	3.89	21.0	5.5	59	11.2	8485	0.46	23.6	70.6
91500 395	70.0	3.33	113	0.49		1.94		0.15	0.249	0.249	1.03	0.68	8.6	4.09	21.7	5.6	57	11.2	8649	0.44	24.4	72.7
91500 398	38.2	4.19	112	0.53		2.48			0.186	0.114	1.50	0.86	9.4	3.94	22.0	5.8	59	12.1	8470	0.37	25.2	73.3
91500 399	56.3	4.37	112	0.61		2.39		0.18	0.245	0.079	1.45	0.56	9.3	4.23	21.1	5.0	52	11.4	8624	0.49	24.1	70.1
Seiland 358	78.3	1.80	280	1.46		3.60		0.19	0.309	0.746	3.55	1.78	26.1	9.76	52.6	11.9	122	22.1	7595	1.15	53.4	64.3
Seiland 359	27.8	1.58	283	1.65		3.67	0.009		0.497	0.629	3.99	1.81	24.2	9.90	50.2	12.3	115	21.7	7596	1.10	52.3	61.3
Seiland 362	86.6	1.88	261	1.47		3.45			0.586	0.679	4.44	1.58	26.1	10.85	51.2	12.1	120	21.8	7493	1.21	52.0	62.6
Seiland 363	85.0	1.74	266	1.61		3.86		0.28	0.630	0.570	3.04	1.53	24.7	10.21	48.3	11.3	116	20.7	7336	0.85	50.0	61.9
Seiland 366	58.0	1.24	284	1.57		3.52		0.06	0.451	0.520	4.56	1.68	24.8	10.74	48.1	11.8	120	20.4	7412	1.11	51.8	64.1
Seiland 367	66.6	0.78	279	1.31		3.45	0.010		0.258	0.824	5.21	1.51	25.9	9.52	49.5	12.2	119	20.9	7338	1.16	51.0	61.3
Seiland 370	70.3	1.00	305	1.50		3.87		0.31	0.708	0.600	5.20	1.84	24.4	11.21	56.0	12.6	127	24.3	8588	1.14	58.9	67.8
Seiland 375	70.8	1.09	290	1.63		4.03		0.17	0.564	0.658	4.46	2.18	28.0	10.48	53.1	12.3	128	22.9	7982	1.13	55.8	67.8
Seiland 378	63.6	1.73	289	1.87		4.23		0.14	0.510	0.778	4.75	2.11	27.2	11.39	53.7	13.3	125	23.7	7940	1.23	58.0	69.4
Seiland 379	78.3	1.16	271	1.51		3.88			0.713	0.700	4.61	2.01	25.9	10.14	52.3	12.1	127	22.1	7529	1.15	56.4	66.8

Table A5. 6 LA-ICPMS U-Pb isotope ratios and trace element concentrations for standard data collected during sample 110-368 analyses. Experiment “Zircon_08March2022_Miscellaneous_1” is in black text and “Zircon_08March2022_Miscellaneous_2” is in blue text.

	Composition							Corrected isotope ratios												Dates (Ma)														
	U	Th	Pb		206Pb	206Pb		208Pb	±2s	207Pb	±2s	206Pb	±2s	error	238U	±2s	207Pb	±2s	208Pb	±2s	±2s-sys	207Pb	±2s	±2s-sys	207Pb	±2s	±2s-sys	206Pb	±2s	±2s-sys	disc.	±2s
Analysis	ppm	ppm	ppm	Th/U	cps	204Pb	±1s	232Th	(%)	235U	(%)	238U	(%)	corr.	206Pb	(%)	206Pb	(%)	232Th	(Ma)	(Ma)	206Pb	(Ma)	(Ma)	235U	(Ma)	(Ma)	238U	(Ma)	(Ma)	(%)	(%)
Primary standards																																
PL 298	428	35.6	24.6	0.083	25527	1429	18	0.01640	11.4	0.3919	6.8	0.05338	3.2	0.46	18.73	3.2	0.05324	6.0	329	37.3	39.1	339	136	137	336	19.5	20.0	335	10.6	11.3	0.2	6.6
PL 299	463	41.4	27.6	0.089	32670	1016	18	0.01846	9.3	0.3993	6.0	0.05492	3.0	0.48	18.21	3.0	0.05273	5.2	370	34.0	36.4	317	119	120	341	17.5	18.0	345	10.1	10.9	-1.0	6.0
PL 300	642	60.7	38.1	0.095	39234	31659	212	0.01579	11.7	0.4018	5.8	0.05490	2.6	0.43	18.22	2.6	0.05308	5.2	317	36.8	38.5	332	118	119	343	17.0	17.5	345	8.86	9.78	-0.5	5.6
PL 301	611	54.1	35.3	0.088	35975	836800627	21857631	0.01680	9.3	0.4000	5.0	0.05328	3.1	0.60	18.77	3.1	0.05444	3.9	337	31.1	33.3	389	87.5	89.3	342	14.5	15.1	335	10.1	10.9	2.0	5.1
PL 306	720	64.9	41.0	0.090	41250	770	8	0.01628	11.2	0.3915	5.2	0.05241	3.9	0.74	19.08	3.9	0.05418	3.4	326	36.2	38.1	379	76.0	78.1	335	14.8	15.4	329	12.7	13.3	1.8	5.8
PL 307	717	76.1	41.7	0.106	41830	2067	28	0.01697	8.1	0.3814	4.7	0.05342	3.3	0.68	18.72	3.3	0.05178	3.3	340	27.2	29.9	276	76.6	78.8	328	13.1	13.8	335	10.7	11.5	-2.3	5.2
PL 314	511	42.8	28.1	0.084	28759	12079	185	0.01612	11.6	0.3891	6.6	0.05087	3.6	0.54	19.66	3.6	0.05547	5.5	323	37.2	39.1	431	121	123	334	18.6	19.1	320	11.4	12.0	4.1	6.3
PL 315	424	35.5	24.3	0.084	24395	1277	21	0.01630	10.5	0.3796	5.6	0.05334	2.9	0.50	18.75	2.9	0.05162	4.8	327	34.0	36.1	269	109	111	327	15.5	16.1	335	9.40	10.2	-2.5	5.7
PL 319	574	43.2	33.5	0.075	37047	1482	16	0.01812	6.6	0.3839	6.3	0.05419	4.1	0.63	18.46	4.1	0.05139	4.8	363	23.7	27.3	258	110	112	330	17.7	18.2	340	13.5	14.1	-3.1	6.9
PL 323	1009	118	60.2	0.117	72411	60820	1119	0.01822	5.9	0.3927	5.6	0.05391	4.6	0.80	18.55	4.6	0.05283	3.3	365	21.4	25.4	322	74.7	76.9	336	16.1	16.6	338	15.0	15.6	-0.6	6.6
PL 326	600	47.9	36.0	0.080	44487	7413	151	0.01702	8.9	0.3957	6.4	0.05556	4.1	0.63	18.00	4.1	0.05165	5.0	341	30.3	32.8	270	114	115	339	18.6	19.0	349	14.0	14.6	-3.0	7.0
PL 327	582	44.0	34.4	0.076	43354	1457	31	0.01795	10.8	0.4276	4.3	0.05444	2.8	0.62	18.37	2.8	0.05697	3.3	360	38.6	40.9	490	73.0	75.1	361	13.2	13.9	342	9.26	10.1	5.5	4.3
PL 330	745	62.9	42.3	0.084	50098	1026	15	0.01680	9.7	0.3870	6.4	0.05230	5.3	0.83	19.12	5.3	0.05367	3.5	337	32.2	34.6	357	78.5	80.5	332	18.0	18.5	329	17.0	17.5	1.1	7.4
PL 331	704	62.2	41.3	0.088	49290	2760	36	0.01736	11.0	0.3960	5.1	0.05399	3.6	0.70	18.52	3.6	0.05319	3.6	348	38.1	40.2	337	81.2	83.2	339	14.7	15.3	339	12.0	12.7	-0.1	5.6
PL 334	756	66.1	43.5	0	51493	1201	16	0.01582	7.4	0.3991	5.4	0.05292	3.4	0.61	18.90	3.4	0.05471	4.2	317	23.3	26.1	400	94.7	96.4	341	15.8	16.4	332	11.1	11.9	2.5	5.6
PL 335	714	62.3	40.4	0	49203	2175	32	0.01595	8.5	0.3688	4.7	0.05224	3.8	0.78	19.14	3.8	0.05119	2.9	320	26.8	29.3	249	65.9	68.4	319	13.0	13.6	328	12.1	12.7	-3.0	5.7
PL 338	453	42.9	26.5	0.095	25807	3097	80	0.01524	18.7	0.3864	5.4	0.05436	2.5	0.43	18.40	2.5	0.05156	4.8	306	56.8	57.9	266	110	112	332	15.3	15.9	341	8.21	9.20	-2.9	5.4
PL 339	433	35.8	24.9	0.083	24808	321	8	0.01635	10.4	0.3907	6.4	0.05346	4.6	0.71	18.71	4.6	0.05300	4.4	328	33.8	35.8	329	100	102	335	18.2	18.7	336	15.1	15.6	-0.3	7.1
PL 342	741	70.9	42.8	0.096	43508	3035	32	0.01686	8.0	0.4004	6.1	0.05298	4.9	0.80	18.87	4.9	0.05481	3.5	338	26.7	29.3	405	79.3	81.4	342	17.6	18.1	333	16.0	16.5	2.7	6.9
PL 343	697	67.7	40.3	0.097	41823	1952	43	0.01655	10.2	0.3973	5.4	0.05321	3.9	0.70	18.79	3.9	0.05415	3.8	332	33.7	35.7	377	85.1	87.1	340	15.7	16.3	334	12.7	13.3	1.6	5.9
PL 346	437	40.2	25.9	0.092	25553	25553	731	0.01682	15.8	0.3987	6.5	0.05497	2.9	0.44	18.19	2.9	0.05260	5.8	337	52.9	54.2	312	131	132	341	18.7	19.2	345	9.88	10.7	-1.3	6.3
PL 347	461	44.9	27.7	0.097	27248	1635	39	0.01919	15.8	0.4080	7.0	0.05540	3.8	0.53	18.05	3.8	0.05341	5.9	384	60.0	61.5	346	132	134	347	20.5	20.9	348	12.7	13.4	0.0	6.9
PL 350	589	51.3	33.7	0.087	34598	34598	639	0.01558	10.1	0.3978	5.8	0.05290	4.5	0.76	18.90	4.5	0.05454	3.7	313	31.2	33.0	393	82.8	84.8	340	16.7	17.3	332	14.5	15.0	2.3	6.4
PL 351	566	49.8	32.4	0.088	34797	1008	14	0.01860	11.5	0.3759	6.5	0.05282	3.3	0.49	18.93	3.3	0.05161	5.6	373	42.4	44.2	268	128	129	324	17.9	18.4	332	10.6	11.3	-2.4	6.5
PL 354	565	50.5	32.6	0.090	33654	5654	86	0.01525	7.8	0.3768	6.7	0.05354	3.0	0.44	18.68	3.0	0.05105	5.9	306	23.6	25.9	243	136	138	325	18.5	19.0	336	9.99	10.8	-3.5	6.7
PL 355	555	49.9	32.1	0.090	33662	764	9	0.01786	6.5	0.4062	5.9	0.05331	4.1	0.68	18.76	4.1	0.05527	4.3	358	22.9	26.0	423	94.9	96.6	346	17.4	17.9	335	13.4	14.1	3.3	6.2
Secondary standards																																
91500 382	66.8	23.2	14.9	0.347	12957	12957	257	0.05650	10.1	1.9973	6.2	0.18949	3.7	0.58	5.28	3.7	0.07645	5.0	1111	109	116	1107	99.0	100	1115	41.8	43.0	1119	38.0	40.0	-0.4	5.1
91500 383	68.5	23.2	14.4	0.339	13045	10526	130	0.04982	7.0	1.8329	6.2	0.18124	4.0	0.63	5.52	4.0	0.07335	4.8	983	67.1	75.8	1024	97.1	98.5	1057	41.0	42.1	1074	39.4	41.3	-1.6	5.4
91500 387	66.9	23.2	14.4	0.346	12494	750	16	0.04886	9.6	1.9428	8.1	0.18546	3.8	0.45	5.39	3.8	0.07598	7.2	964	90.0	96.7	1095	144	145	1096	54.5	55.4	1097	38.1	40.1	-0.1	6.1
91500 390	73.0	25.5	15.8	0.350	14293	14293	238	0.05194	9.1	1.9160	7.1	0.18544	5.8	0.81	5.39	5.8	0.07494	4.1	1023	90.6	98.2	1067	83.0	84.5	1087	47.7	48.7	1097	58.9	60.2	-0.9	7.0
91500 391	71.2	24.8	15.1	0.348	14813	1033	23	0.05269	7.8	1.9208	6.6	0.18155	3.8	0.56	5.51	3.8	0.07674	5.4	1038	79.4	88.1	1114	108	109	1088	44.1	45.2	1075	37.4	39.4	1.2	5.3
91500 394	70.6	23.6	14.5	0.334	13357	1395	22	0.04884	9.1	1.7840	7.8	0.17763	4.0	0.50	5.63	4.0	0.07284	6.7	964	85.3	92.3	1010	136	137	1040	50.9	51.8	1054	39.0	40.8	-1.4	6.2
91500 395	72.7	24.4	15.6	0.336	14837	3116	48	0.05493	10.3	1.7998	7.4	0.18421	4.7	0.63	5.43	4.7	0.07086	5.7	1081	108	115	953	116	117	1045	48.1	49.0	1090	47.3	48.9	-4.3	6.6
91500 398	73.3	25.2	15.6	0.344	14539	370	5	0.04928	9.2	1.8632	7.5	0.18397	3.6	0.47	5.44	3.6	0.07345	6.6	972	87.3	94.0	1026	133	134	1068	49.7	50.6	1089	36.2	38.3	-1.9	5.8
91500 399	70.1	24.1	15.2	0.343	15245	557	6	0.05090	11.2	1.9394	6.5	0.18624	3.2	0.48	5.37	3.2	0.07553	5.6	1003	110	115	1083	113	114	1095	43.3	44.5	1101	32.6	34.9	-0.6	5.0
Seiland 358	64.3	53.4	6.99	0.830	4934	822	13	0.02476	7.6	0.5732	14.9	0.08481	5.9	0.40	11.79	5.9	0.04901	13.6	494	37.0	41.0	148	320	320	460	55.1	55.3	525	29.9	30.6	-14.1	15.1
Seiland 359	61.3	52.3	6.87	0.855	4788	571	16	0.02583	10.1	0.7032	7.6	0.08587	2.8	0.36	11.64	2.8	0.05939	7.0	516	51.2	54.4	581	152	153	541	31.7	32.3	531	14.3	15.6	1.8	6.3
Seiland 362	62.6	52.0	6.93	0.830	4264	123	3	0.02772	6.4	0.6434	13.4	0.08385	4.4	0.33	11.93	4.4	0.05565	12.6	553	35.0	40.4	438	281	282	504	53.2	53.6	519	22.1	22.9	-2.9	11.7
Seiland 363	61.9	50.0	6.88	0.807	4611	94315	1902	0.02658	7.5	0.6437	12.1	0.08586	5.2	0.43	11.65	5.2	0.05437	10.9	530	39.4	43.9	386	244	245	505	48.0	48.3	531	26.6	27.4	-5.2	11.3
Seiland 366	64.1	51.8	6.99	0.809	5109	858	12	0.02407	8.3	0.6652	14.0	0.08569	4.7	0.33	11.67	4.7	0.05630	13.1	481	39.2	43.1	464	291	292	518	56.6	56.9	530	23.9	24.7	-2.4	12.1
Seiland 367	61.3	51.0	7.12	0.831	5034	351	9	0.02560	12.0	0.8195	10.2	0.08974	5.5	0.53	11.14	5.5	0.06623	8.6	511	60.4	63.3	814	180	181	608	46.8	47.3	554	29.3	30.0	8.8	8.5
Seiland 370	67.8	58.9	7.34	0.869	5481	4604	103	0.02284	10.1	0.6338	10.4	0.08464	4.5	0.42	11.81	4.5	0.05431	9.4	456	45.6	48.7	384	212	213	498	41.1	41.5	524	22.5	23.3	-5.1	9.8
Seiland 375	67.8	55.8	7.42	0.823	5608	5608	207	0.02688	10.1	0.6686	14.0	0.08331	4.9	0.34	12.00	4.9	0.05821	13.2	536	53.5	56.9	538	288	289	520	57.1	57.5	516	24.1	24.9	0.8	11.8
Seiland 378	69.4	58.0	7.71	0.836	5475	307	9	0.02768	9.2	0.5875	12.2	0.08452	3.3	0.26	11.83	3.3	0.05041	11.7	552	50.3	54.0	214	272	272	469	45.7	46.1	523	16.4	17.6	-11.5	11.4
Seiland 379	66.8	56.4	7.40	0.844	5697	342	9	0.02633	7.5	0.6835	10.2	0.08442	5.0	0.48	11.85	5.0	0.05872	8.8	525	38.7	43.0	557	193	194	529	41.9	42.3	522	25.1	25.8	1.2	9.1

	Concentrations (ppm)																					
Analysis	P	Ti	Y	Nb	La	Ce	Pr	Nd	Sm	Eu	Gd	Tb	Dy	Ho	Er	Tm	Yb	Lu	Hf	Ta	Th	U
Primary stanc																						
PL 298	191	53.5	267	2.60		1.28	0.045	0.231	1.93	0.523	6.83	2.54	29.8	8.67	28.6	5.50	38.1	4.77	14820	1.43	35.6	428
PL 299	69.1	67.2	387	3.48		1.46	0.105	1.41	2.32	0.609	10.1	3.08	36.5	10.8	37.1	6.52	46.3	5.90	11201	1.84	41.4	463
PL 300	364	75.2	500	3.77		1.97	0.144	2.35	3.51	1.25	14.7	5.55	54.5	14.4	52.8	8.93	68.9	8.34	13164	2.33	60.7	642
PL 301	299	69.0	419	4.17	0.027	1.77	0.128	1.63	2.85	0.524	11.1	4.16	48.6	14.2	45.4	8.25	61.7	7.27	13962	2.27	54.1	611
PL 306	338	79.1	513	3.95		2.23	0.143	0.875	3.60	1.04	14.5	5.66	57.8	16.5	56.1	9.64	73.8	8.66	14361	2.51	64.9	720
PL 307	295	73.4	427	5.17		2.07	0.130	1.16	4.07	0.925	12.6	5.15	51.9	14.4	45.6	8.37	59.1	7.45	13825	2.30	76.1	717
PL 314	228	54.3	325	3.22		1.66	0.122	1.11	2.10	0.583	9.39	3.56	36.7	10.5	36.4	6.54	52.2	5.79	14365	1.82	42.8	511
PL 315	179	47.0	259	2.23		1.47	0.102	0.364	1.29	0.301	6.66	2.75	28.2	7.87	28.7	5.04	37.0	4.64	14904	1.14	35.5	424
PL 319	282	61.1	332	3.36		1.66	0.120	1.17	2.64	0.639	9.33	3.97	40.0	11.3	38.6	7.13	52.0	5.70	12007	2.37	43.2	574
PL 323	355	64.0	458	4.10	0.05	2.70	0.214	3.76	4.80	1.44	18.8	6.10	61.8	15.8	51.4	8.62	66.5	6.46	12415	2.52	118	1009
PL 326	235	57.9	347	3.71		1.68	0.137	1.56	2.39	0.638	9.08	3.56	39.5	11.0	38.8	6.54	54.9	5.68	13135	2.11	47.9	600
PL 327	246	57.8	307	3.46	0.025	1.81	0.100	1.37	2.25	0.646	9.75	3.64	37.7	10.2	34.6	6.73	54.7	5.82	12682	2.30	44.0	582
PL 330	374	71.9	482	3.85		1.99	0.129	1.67	3.66	0.721	15.1	5.30	56.0	16.4	52.6	10.3	73.2	8.91	14442	2.75	62.9	745
PL 331	326	72.4	458	3.63	0.012	1.88	0.168	1.32	3.39	0.731	14.4	5.16	56.8	16.2	51.8	10.1	71.7	8.71	14204	2.62	62.2	704
PL 334	345	75.0	458	3.95	0.023	1.91	0.186	1.90	2.93	1.25	14.7	5.44	58.3	16.3	54.7	10.4	75.9	9.02	15017	2.55	66.1	756
PL 335	339	70.0	466	3.78		1.82	0.146	1.52	3.55	0.783	14.7	5.42	56.9	15.1	54.0	9.88	71.8	8.46	14326	2.63	62.3	714
PL 338	168	35.7	276	1.65		1.85	0.058	0.832	1.63	0.308	7.44	2.99	30.2	8.81	32.4	6.26	49.5	6.91	15805	1.48	42.9	453
PL 339	139	40.2	237	2.02		1.75	0.046	0.703	1.56	0.301	5.00	2.28	26.7	7.87	28.5	4.78	36.6	5.29	16619	1.41	35.8	433
PL 342	367	70.6	499	3.66	0.018	2.21	0.115	1.82	2.70	0.902	14.7	5.91	60.5	16.4	57.8	10.4	76.0	8.87	15382	2.68	70.9	741
PL 343	331	68.7	469	3.77	0.018	1.86	0.144	1.11	3.05	0.829	13.4	5.13	54.3	15.5	54.2	9.72	65.0	9.14	15810	2.45	67.7	697
PL 346	191	38.4	272	1.64		1.45	0.0	1.04	1.96	0.440	7.53	2.68	28.5	8.50	32.4	6.13	47.2	6.78	16202	1.66	40.2	437
PL 347	212	32.1	288	2.05		1.78	0.080	1.11	2.13	0.473	6.50	2.93	31.8	9.36	33.8	6.52	51.8	7.32	16538	1.51	44.9	461
PL 350	245	59.5	392	3.58		1.55	0.099	1.60	1.88	0.617	8.36	4.33	42.2	12.8	47.0	8.28	56.8	7.73	16879	2.29	51.3	589
PL 351	250	58.6	381	3.22		1.34	0.065	1.51	2.56	0.589	10.3	3.85	42.2	12.8	44.2	7.87	54.8	7.99	16114	2.10	49.8	566
PL 354	246	58.9	390	3.10	0.02	1.63	0.071	0.765	1.50	0.699	11.3	4.07	43.1	12.1	45.8	8.30	58.5	7.96	16292	2.36	50.5	565
PL 355	237	58.2	351	3.28		1.59	0.095	1.27	1.50	0.726	10.7	4.20	42.0	12.8	41.0	7.48	58.3	7.53	15664	1.98	49.9	555
Secondary standards																						
91500 382	82.6	3.85	115	0.559		2.07				0.08	1.19	0.578	8.82	3.57	21.5	4.92	55.1	11.4	8189	0.404	23.2	66.8
91500 383	49.4	4.18	108	0.671		2.08		0.167	0.398	0.223	1.85	0.611	8.03	3.64	21.7	5.36	53.3	10.3	7921	0.336	23.2	68.5
91500 387	62.6	3.69	112	0.447		2.01			0.344	0.187	1.40	0.739	8.61	4.03	20.3	5.17	55.3	11.0	7875	0.356	23.2	66.9
91500 390	65.6	3.47	113	0.539		2.50				0.157	1.70	0.585	8.96	4.27	22.7	5.98	57.1	11.5	8542	0.558	25.5	73.0
91500 391	54.2	3.55	110	0.553		2.12	0.012	0.127	0.413	0.133	1.95	0.617	8.79	3.93	22.1	5.48	56.3	11.1	8614	0.438	24.8	71.2
91500 394	80.2	3.48	108	0.445		2.27				0.08	1.85	0.598	8.90	3.89	21.0	5.49	59.3	11.2	8485	0.464	23.6	70.6
91500 395	70.0	3.33	113	0.494		1.94		0.150	0.249	0.249	1.03	0.680	8.62	4.09	21.7	5.65	57.5	11.2	8649	0.444	24.4	72.7
91500 398	38.2	4.19	112	0.526		2.48			0.186	0.114	1.50	0.858	9.37	3.94	22.0	5.76	58.7	12.1	8470	0.371	25.2	73.3
91500 399	56.3	4.37	112	0.613		2.39		0.179	0.245	0.079	1.45	0.560	9.26	4.23	21.1	5.02	52.1	11.4	8624	0.489	24.1	70.1
Seiland 358	78.3	1.80	280	1.46		3.60		0.192	0.309	0.746	3.55	1.78	26.1	9.76	52.6	11.9	122	22.1	7595	1.15	53.4	64.3
Seiland 359	27.8	1.58	283	1.65		3.67	0.009		0.497	0.629	3.99	1.81	24.2	9.90	50.2	12.3	115	21.7	7596	1.10	52.3	61.3
Seiland 362	86.6	1.88	261	1.47		3.45			0.586	0.679	4.44	1.58	26.1	10.8	51.2	12.1	120	21.8	7493	1.21	52.0	62.6
Seiland 363	85.0	1.74	266	1.61		3.86		0.276	0.630	0.570	3.04	1.53	24.7	10.2	48.3	11.3	116	20.7	7336	0.853	50.0	61.9
Seiland 366	58.0	1.24	284	1.57		3.52		0.06	0.451	0.520	4.56	1.68	24.8	10.7	48.1	11.8	120	20.4	7412	1.11	51.8	64.1
Seiland 367	66.6	0.784	279	1.31		3.45	0.010		0.258	0.824	5.21	1.51	25.9	9.52	49.5	12.2	119	20.9	7338	1.16	51.0	61.3
Seiland 370	70.3	0.998	305	1.50		3.87		0.310	0.708	0.600	5.20	1.84	24.4	11.2	56.0	12.6	127	24.3	8588	1.14	58.9	67.8
Seiland 375	70.8	1.09	290	1.63		4.03		0.175	0.564	0.658	4.46	2.18	28.0	10.5	53.1	12.3	128	22.9	7982	1.13	55.8	67.8
Seiland 378	63.6	1.73	289	1.87		4.23		0.135	0.510	0.778	4.75	2.11	27.2	11.4	53.7	13.3	125	23.7	7940	1.23	58.0	69.4
Seiland 379	78.3	1.16	271	1.51		3.88			0.713	0.700	4.61	2.01	25.9	10.1	52.3	12.1	127	22.1	7529	1.15	56.4	66.8

Table A5. 6 continued.

	Composition							Corrected isotope ratios											Dates (Ma)													
Analysis	U ppm	Th ppm	Pb ppm	Th/U	206Pb cps	206Pb/204Pb	±1s	208Pb/232Th	±2s (%)	207Pb/235U	±2s (%)	206Pb/238U	±2s (%)	error corr.	238U/206Pb	±2s (%)	207Pb/206Pb	±2s (%)	208Pb/232Th	±2s (Ma)	±2s-sys (Ma)	207Pb/206Pb	±2s (Ma)	±2s-sys (Ma)	207Pb/235U	±2s (Ma)	±2s-sys (Ma)	206Pb/238U	±2s (Ma)	±2s-sys (Ma)	disc. (%)	±2s (%)
Primary standards																																
PL 302	692	63.5	41.0	0.092	47409	47409	813	0.01690	7.3	0.3906	4.9	0.05474	3.9	0.79	18.27	3.9	0.05175	2.9	339	24.4	26.5	274	66.1	68.0	335	13.8	14.5	344	13.0	13.8	-2.6	5.8
PL 303	609	51.8	35.5	0.085	44181	10530	110	0.01642	11.8	0.4050	5.7	0.05373	4.0	0.69	18.61	4.0	0.05467	4.1	329	38.7	40.0	399	91.0	92.4	345	16.8	17.3	337	13.3	14.0	2.3	6.1
PL 304	756	70.6	43.6	0.093	52146	5038	71	0.01683	7.4	0.3766	6.2	0.05303	3.7	0.58	18.86	3.7	0.05150	5.0	337	24.8	26.9	263	114	115	325	17.1	17.6	333	11.9	12.6	-2.7	6.5
PL 305	634	57.0	37.1	0.090	44911	44911	343	0.01745	8.2	0.4076	3.6	0.05387	2.7	0.72	18.56	2.7	0.05488	2.4	350	28.4	30.4	407	54.5	56.8	347	10.7	11.6	338	8.95	9.93	2.6	4.0
PL 308	423	33.2	23.7	0.078	28657	28657	313	0.01577	10.1	0.3761	7.0	0.05210	3.6	0.51	19.19	3.6	0.05236	6.0	316	31.6	33.2	301	136	137	324	19.4	19.8	327	11.5	12.3	-1.0	7.0
PL 309	470	39.2	26.5	0.083	31732	2701	41	0.01556	10.1	0.3865	5.5	0.05217	3.6	0.63	19.17	3.6	0.05373	4.2	312	31.4	32.9	360	95.5	96.8	332	15.7	16.3	328	11.5	12.2	1.2	5.8
PL 316	399	32.5	23.0	0.081	27927	1094	12	0.01561	10.7	0.3942	5.0	0.05330	3.1	0.61	18.76	3.1	0.05364	3.9	313	33.3	34.8	356	89.2	90.6	337	14.5	15.1	335	10.2	11.1	0.8	5.2
PL 317	420	33.7	23.7	0.080	27836	1244	15	0.01862	9.2	0.3901	7.0	0.05202	3.3	0.46	19.22	3.3	0.05439	6.2	373	34.1	36.3	387	139	140	334	20.0	20.4	327	10.5	11.3	2.3	6.6
PL 320	639	51.2	37.9	0.080	45218	2536	21	0.01825	7.6	0.3970	5.6	0.05479	4.1	0.73	18.25	4.1	0.05256	3.8	366	27.6	30.2	310	85.9	87.4	339	16.1	16.7	344	13.8	14.5	-1.3	6.3
PL 321	778	89.8	47.9	0.115	58766	5877	56	0.01792	6.4	0.4130	5.3	0.05622	4.4	0.83	17.79	4.4	0.05328	2.9	359	22.7	25.6	341	65.4	67.3	351	15.7	16.3	353	15.1	15.8	-0.4	6.2
PL 324	705	61.7	41.6	0.088	46951	4216	47	0.01911	7.9	0.3997	5.0	0.05423	3.5	0.67	18.44	3.5	0.05345	3.7	383	29.9	32.5	348	83.0	84.5	341	14.6	15.3	340	11.5	12.3	0.3	5.4
PL 325	591	46.1	35.0	0.078	45485	4549	44	0.01978	8.7	0.3968	6.1	0.05461	3.2	0.51	18.31	3.2	0.05270	5.2	396	34.1	36.5	316	119	120	339	17.7	18.2	343	10.7	11.6	-1.0	6.1
PL 328	731	66.3	42.0	0.091	54973	13554	260	0.01512	6.1	0.3894	4.8	0.05296	3.9	0.80	18.88	3.9	0.05333	2.8	303	18.5	21.1	343	62.6	64.6	334	13.6	14.3	333	12.6	13.4	0.4	5.6
PL 329	663	61.0	38.9	0.092	52582	21483	482	0.01643	9.2	0.4086	5.1	0.05391	3.9	0.74	18.55	3.9	0.05496	3.4	329	30.1	32.0	411	75.1	76.8	348	15.1	15.7	339	12.8	13.5	2.7	5.6
PL 332	673	61.0	39.1	0.091	50371	1286	25	0.01710	9.3	0.3858	5.6	0.05346	4.1	0.73	18.70	4.1	0.05233	3.8	343	31.5	33.5	300	85.8	87.3	331	15.7	16.3	336	13.4	14.1	-1.4	6.3
PL 333	691	62.1	39.1	0.090	52547	9393	181	0.01515	7.5	0.3687	4.8	0.05236	3.5	0.72	19.10	3.5	0.05108	3.2	304	22.7	24.9	244	74.6	76.3	319	13.1	13.8	329	11.3	12.1	-3.2	5.5
PL 336	727	68.2	41.8	0.094	53626	3031	67	0.01723	7.4	0.3784	3.7	0.05288	3.4	0.89	18.91	3.4	0.05190	1.5	345	25.2	27.7	281	35.1	38.6	326	10.3	11.2	332	10.9	11.8	-1.9	4.7
PL 337	659	59.7	36.6	0.091	51231	3489	60	0.01542	10.4	0.3907	4.7	0.05099	3.5	0.73	19.61	3.5	0.05558	3.2	309	32.1	33.6	436	70.5	72.2	335	13.4	14.1	321	10.9	11.7	4.3	5.0
PL 340	413	35.3	23.8	0.086	24833	5918	153	0.01694	12.2	0.3787	6.5	0.05351	3.1	0.47	18.69	3.1	0.05133	5.7	340	41.2	42.6	256	131	132	326	18.1	18.6	336	10.2	11.1	-3.0	6.5
PL 341	565	51.7	33.4	0.091	35119	3044	85	0.01685	9.7	0.4101	5.9	0.05453	4.1	0.68	18.34	4.1	0.05454	4.3	338	32.5	34.3	394	95.6	96.9	349	17.5	18.1	342	13.7	14.4	1.9	6.3
PL 344	518	48.0	30.6	0.09	31644	31644	448	0.01527	11.4	0.4136	6.1	0.05458	3.8	0.61	18.32	3.8	0.05495	4.8	306	34.7	36.1	410	106	108	351	18.1	18.7	343	12.7	13.5	2.5	6.2
PL 345	400	33.8	22.8	0.084	25342	25342	519	0.01535	13.2	0.3810	5.2	0.05282	2.8	0.51	18.93	2.8	0.05231	4.4	308	40.2	41.4	299	100	102	328	14.5	15.2	332	8.90	9.94	-1.2	5.2
PL 348	563	52.0	32.5	0.092	37868	5415	83	0.01717	10.8	0.3838	5.0	0.05321	4.3	0.85	18.79	4.3	0.05231	2.6	344	36.8	38.3	299	58.2	60.4	330	14.0	14.7	334	13.9	14.6	-1.3	6.0
PL 349	550	49.7	31.9	0.090	35947	12851	317	0.01781	10.1	0.3988	5.6	0.05330	4.1	0.72	18.76	4.1	0.05427	3.8	357	35.9	37.5	382	85.6	87.1	341	16.1	16.7	335	13.3	14.0	1.8	6.1
PL 352	517	46.9	30.6	0.091	32415	3197	60	0.01600	12.2	0.4081	5.5	0.05473	4.8	0.85	18.27	4.8	0.05408	2.8	321	38.9	40.1	374	63.0	65.0	348	16.3	17.0	344	16.0	16.7	1.2	6.5
PL 353	509	46.1	28.8	0.091	31213	2705	69	0.01754	8.9	0.3773	5.1	0.05219	2.8	0.54	19.16	2.8	0.05243	4.2	352	31.0	32.8	304	96.1	97.4	325	14.1	14.8	328	9.06	10.1	-0.9	5.2
PL 356	527	47.4	30.4	0.090	34012	6080	128	0.01814	7.4	0.3929	5.5	0.05297	3.5	0.62	18.88	3.5	0.05379	4.2	363	26.6	28.8	362	95.6	96.9	336	15.7	16.3	333	11.3	12.1	1.1	5.7
PL 357	532	48.5	32.0	0.091	33694	973	20	0.01731	10.7	0.4014	6.4	0.05545	5.0	0.77	18.03	5.0	0.05250	4.0	347	37.0	38.4	307	91.6	93.0	343	18.7	19.3	348	17.1	17.7	-1.5	7.5
Secondary standards																																
91500 384	67.0	22.6	14.5	0.338	13431	14777	379	0.04819	9.5	1.8862	6.8	0.18680	2.6	0.36	5.35	2.6	0.07323	6.3	951	87.9	92.8	1020	127	128	1076	45.1	46.2	1104	26.1	29.3	-2.6	4.9
91500 385	64.2	21.1	13.9	0.329	12762	529	24	0.05342	7.6	1.8365	8.3	0.18642	5.2	0.62	5.36	5.2	0.07145	6.5	1052	78.3	85.0	970	132	133	1059	54.5	55.4	1102	52.7	54.4	-4.1	7.3
91500 388	65.8	23.8	14.2	0.362	13654	5138	59	0.04877	7.6	1.9194	7.6	0.18376	4.7	0.61	5.44	4.7	0.07576	6.0	962	71.6	78.0	1089	121	122	1088	51.0	52.0	1087	47.1	48.9	0.0	6.4
91500 389	68.1	24.7	14.9	0.363	13936	914	24	0.04891	7.9	1.8668	6.2	0.18745	3.4	0.53	5.33	3.4	0.07223	5.2	965	74.7	81.0	992	105	106	1069	40.7	41.9	1108	34.2	36.8	-3.6	5.1
91500 392	63.0	20.1	13.6	0.319	13445	808	37	0.05507	6.2	1.8847	7.7	0.18518	6.1	0.79	5.40	6.1	0.07381	4.7	1083	65.1	74.1	1036	94.5	95.6	1076	50.8	51.8	1095	61.0	62.5	-1.8	7.4
91500 393	65.0	22.3	13.9	0.343	14170	324	6	0.04576	7.6	1.8225	7.0	0.18487	4.6	0.66	5.41	4.6	0.07150	5.2	904	67.7	73.9	972	107	108	1054	45.8	46.9	1094	46.6	48.5	-3.8	6.3
91500 397	64.4	21.8	13.3	0.339	15089	853	16	0.04630	6.3	1.8354	6.4	0.17819	3.0	0.45	5.61	3.0	0.07470	5.7	915	56.5	63.9	1061	115	116	1058	42.3	43.5	1057	28.9	31.8	0.1	4.8
91500 400	64.9	22.7	13.8	0.349	14879	894	25	0.05327	6.0	1.8091	6.5	0.18047	3.9	0.59	5.54	3.9	0.07270	5.2	1049	61.5	69.9	1006	105	106	1049	42.5	43.6	1070	38.6	40.9	-2.0	5.5
91500 401	67.6	22.8	13.6	0.338	14308	1986	21	0.04976	9.7	1.7686	6.6	0.17172	3.3	0.49	5.82	3.3	0.07470	5.7	982	92.8	97.9	1060	115	116	1034	43.0	44.2	1022	31.5	34.0	1.2	5.1
91500 404	59.7	19.3	12.9	0.324	15419	15419	694	0.05726	8.2	1.8382	5.3	0.18472	2.4	0.43	5.41	2.4	0.07217	4.8	1125	90.1	96.3	991	96.7	97.8	1059	35.0	36.4	1093	23.9	27.6	-3.2	4.1
91500 405	65.8	22.2	13.9	0.337	15399	1335	18	0.05498	8.4	1.8192	7.9	0.17966	4.7	0.59	5.57	4.7	0.07344	6.3	1082	88.6	94.4	1026	127	128	1052	51.5	52.5	1065	46.2	48.1	-1.2	6.6
Seiland 360	64.3	53.8	6.89	0.837	5367	1323	20	0.02318	7.3	0.6634	8.4	0.08312	3.8	0.45	12.03	3.8	0.05789	7.5	463	33.2	36.2	525	164	165	517	34.1	34.6	515	19.0	20.0	0.4	7.5
Seiland 361	61.4	51.8	6.92	0.845	5372	301	6	0.02387	4.7	0.6252	11.3	0.08826	4.0	0.35	11.33	4.0	0.05137	10.6	477	22.3	26.8	258	244	244	493	44.3	44.7	545	21.1	22.2	-10.6	10.8
Seiland 364	61.6	51.1	6.79	0.830	5899	496	12	0.02496	8.6	0.6362	10.8	0.08510	5.0	0.45	11.75	5.0	0.05423	9.6	498	42.5	45.5	380	216	217	500	42.8	43.2	526	25.1	26.0	-5.3	10.3
Seiland 365	62.1	52.5	6.98	0.846	6455	923	21	0.02401	9.4	0.7298	9.7	0.08698	3.6	0.36	11.50	3.6	0.06085	9.0	479	44.6	47.2	634	194	195	556	41.5	42.0	538	18.4	19.6	3.4	7.9
Seiland 368	60.8	50.1	6.57	0.824	5949	2239	33	0.02365	9.1	0.6780	10.2	0.08384	4.7	0.45	11.93	4.7	0.05865	9.1	472	42.3	45.1	554	198	199	526	41.9	42.4	519	23.3	24.2	1.2	9.0
Seiland 369	61.9	52.0	6.68	0.840	5458	173	4	0.02284	7.5	0.6679	11.5	0.08406	5.3	0.46	11.90	5.3	0.05762	10.2	456	33.9	37.1	515	224	225	519	46.9	47.2	520	26.6	27.4	-0.2	10.4
Seiland 372	65.4	57.1	7.16	0.874	5953	284	3	0.02362	9.4	0.6804	12.7	0.08419	3.9	0.30	11.88	3.9	0.05862	12.1	472	44.0	46.7	553	264	265	527	52.4	52.7	521	19.6	20.7	1.1	10.5
Seiland 373	63.4	54.5	6.94	0.860	6335	477	10	0.02244	6.4	0.6321	11.0	0.08585	3.3	0.29	11.65	3.3	0.05340	10.5	449	28.5	32.2	346	236	237	497	43.1	43.5	531	16.7	18.0	-6.7	9.8
Seiland 376	63.7	54.3	7.18	0.853	5652	317	7	0.02454	8.5	0.7567	9.4	0.08659	4.9	0.51	11.55	4.9	0.06339	8.1	490	40.9	43.9	721	171	172	572	41.2	41.7	535	25.0	26.0	6.4	8.0
Seiland 377	62.0	51.1	6.73	0.824	5631	5631	174	0.02592	8.7	0.5814	11.0	0.08303	3.9	0.35	12.04	3.9	0.05078	10.3	517	44.6	47.7	231	238	239	465	41.2	41.6	514	19.4	20.5	-10.5	10.6
Seiland 380	62.5	52.2	6.81	0.836	6437	7082	166	0.02441	7.9	0.6344	8.4	0.08427	4.1	0.48	11.87	4.1	0.05460	7.3	487	38.1	41.1	396	165	165	499	33.2	33.7	522	20.6	21.7	-4.6	8.1
Seiland 381	61.7	50.2	6.79	0.814	6486	144	5	0.02500	9.9	0.6332	10.2	0.08520	4.3	0.41	11.74	4.3	0.05390	9.3	499	48.7	51.2	367	210	211	498	40.3	40.8	527	21.6	22.6	-5.8	9.6

	Concentrations (ppm)																					
Analysis	P	Ti	Y	Nb	La	Ce	Pr	Nd	Sm	Eu	Gd	Tb	Dy	Ho	Er	Tm	Yb	Lu	Hf	Ta	Th	U
Primary standards																						
PL 302	414	80.9	487	3.75		2.10	0.137	1.83	3.91	1.14	14.4	5.62	58.4	15.9	52.0	9.72	73.0	8.63	13742	2.44	63.5	692
PL 303	307	70.3	412	4.16	0.012	1.93	0.110	1.52	3.51	0.877	10.2	4.36	47.6	13.4	45.5	8.39	60.9	7.28	13078	2.05	51.8	609
PL 304	449	83.8	565	4.58	0.032	2.09	0.149	2.46	4.22	1.46	15.3	6.29	63.0	18.5	59.5	10.8	76.9	9.40	12708	2.43	70.6	756
PL 305	338	71.8	451	3.69	0.0	1.86	0.109	1.26	2.88	0.960	13.0	5.09	50.9	14.0	47.4	8.89	61.2	7.73	12882	2.21	57.0	634
PL 308	206	47.0	237	2.68		1.20	0.046	0.464	1.23	0.232	6.44	2.30	25.7	7.24	26.2	4.78	36.4	4.09	13965	1.31	33.2	423
PL 309	207	54.9	314	2.81		1.32	0.051	1.15	1.91	0.399	8.78	2.97	31.9	9.65	32.3	5.90	44.4	5.30	13860	1.60	39.2	470
PL 316	198	46.7	229	2.07	0.005	1.31	0.058	0.976	1.07	0.209	5.29	2.09	26.0	7.16	24.3	4.62	32.3	4.20	13529	1.32	32.5	399
PL 317	194	40.2	210	2.10	0.055	1.38	0.056	0.812	1.18	0.293	5.57	2.08	23.8	6.80	22.5	4.53	31.1	3.74	14393	1.39	33.7	420
PL 320	340	68.6	400	3.87		1.79	0.104	1.87	2.88	0.855	10.8	4.20	45.2	12.6	42.9	8.40	59.8	6.70	12013	2.36	51.2	639
PL 321	335	68.4	442	4.19		1.92	0.162	1.69	4.01	0.893	16.3	5.76	56.8	14.9	47.8	8.34	60.9	6.88	12078	2.24	89.8	778
PL 324	357	77.7	452	3.78		1.99	0.122	1.85	3.68	0.982	12.7	5.18	53.2	13.3	47.0	8.39	66.9	7.76	12378	2.54	61.7	705
PL 325	305	66.4	358	3.48	0.02	1.78	0.092	1.48	2.63	0.819	10.4	3.88	42.3	12.0	38.0	7.28	57.7	6.40	11153	2.21	46.1	591
PL 328	386	83.2	537	4.07	0.008	2.01	0.165	1.61	3.47	0.921	15.3	5.91	61.5	17.2	54.1	10.8	82.2	9.61	13456	2.55	66.3	731
PL 329	389	75.8	505	3.67		2.04	0.144	1.84	2.90	0.950	13.6	4.74	54.7	15.7	56.2	9.05	73.2	9.09	13313	2.17	61.0	663
PL 332	355	74.3	475	4.02	0.02	1.96	0.144	1.82	3.03	0.927	13.3	4.77	52.3	14.6	50.5	8.95	69.4	8.60	13820	2.49	61.0	673
PL 333	351	78.2	491	3.73	0.014	2.17	0.148	1.63	3.18	0.926	14.1	5.17	54.2	16.2	53.7	10.1	72.9	8.64	12545	2.43	62.1	691
PL 336	375	84.5	535	4.00	0.018	2.31	0.142	2.06	4.01	1.19	13.9	5.61	59.3	16.7	56.9	9.71	75.1	9.30	14349	2.71	68.2	727
PL 337	340	74.2	448	3.82	0.03	1.94	0.139	1.73	2.50	0.685	12.7	5.10	52.1	14.4	49.6	8.92	65.9	8.10	12963	2.32	59.7	659
PL 340	209	50.4	263	2.41		1.43	0	0.464	0.901	0.378	5.86	2.69	28.3	8.21	28.1	5.08	40.3	4.98	14972	1.38	35.3	413
PL 341	285	64.2	393	3.89		1.71	0	1.53	2.08	0.692	11.4	4.05	44.1	12.1	43.0	7.98	57.4	7.70	14049	2.06	51.7	565
PL 344	268	61.5	373	3.14		1.65	0.080	1.32	2.70	0.751	10.2	3.83	40.9	11.8	40.1	7.22	51.6	6.85	14637	2.13	48.0	518
PL 345	196	49.1	258	2.20		1.15	0.062	0.966	1.12	0.519	6.37	2.25	27.0	7.66	27.6	4.81	36.5	4.75	14665	1.54	33.8	400
PL 348	281	64.6	430	3.38		1.90	0.121	1.35	2.91	0.753	10.3	4.16	43.6	12.8	45.5	8.00	59.5	7.84	14788	2.23	52.0	563
PL 349	268	63.2	412	3.25	0.020	1.69	0.105	1.07	3.07	0.645	9.47	4.02	44.0	12.4	44.8	7.83	55.8	7.36	14301	2.17	49.7	550
PL 352	254	62.6	389	3.16		1.63	0.099	1.15	2.25	0.630	9.45	4.12	40.0	11.3	42.9	7.91	52.7	6.78	14286	1.81	46.9	517
PL 353	246	60.9	360	3.16	0.025	1.46	0.092	1.19	1.88	0.575	9.16	3.70	40.0	11.5	41.6	7.50	51.3	6.84	14234	2.25	46.1	509
PL 356	280	63.5	395	2.92		1.86	0.123	1.07	2.59	0.752	9.81	3.89	41.9	12.1	42.2	8.04	55.6	7.24	13988	1.79	47.4	527
PL 357	297	62.9	400	3.35	0.0	1.69	0.105	1.25	2.01	0.741	9.86	3.87	42.2	12.6	42.4	8.25	52.8	7.20	13567	1.96	48.5	532
Secondary standards																						
91500 384	49.1	4.83	115	0.545		2.39				0.223	1.76	0.556	8.95	3.81	21.0	5.16	57.7	11.5	7895	0.388	22.6	67.0
91500 385	72.1	3.59	100	0.412		2.16			0.099	0.058	1.32	0.624	8.27	3.26	18.1	4.89	50.7	10.5	7717	0.423	21.1	64.2
91500 388	47.6	4.25	113	0.596		2.26	0.008			0.157	1.45	0.592	9.67	3.65	20.5	5.19	55.3	10.2	7510	0.256	23.8	65.8
91500 389	62.6	5.17	117	0.530		1.97	0.01		0.489	0.191	1.80	0.725	8.09	4.08	20.6	5.00	58.4	10.6	7867	0.460	24.7	68.1
91500 392	58.7	3.93	108	0.465		2.32			0.252	0.233	1.31	0.496	8.38	3.54	19.0	4.61	53.7	10.4	7671	0.300	20.1	63.0
91500 393	29.5	3.90	109	0.529		1.86	0.010			0.133	1.30	0.695	7.24	3.50	18.9	5.05	52.6	10.3	7299	0.454	22.3	65.0
91500 397	54.2	3.80	111	0.498		2.26			0.183	0.165	1.74	0.561	8.75	4.10	19.3	5.22	52.0	10.5	7369	0.434	21.8	64.4
91500 400	69.3	4.44	112	0.467		2.32	0.0	0.041	0.309	0.098	1.76	0.685	8.13	4.26	21.9	5.03	54.8	10.6	7934	0.427	22.7	64.9
91500 401	60.8	4.12	115	0.469		2.03		0.145	0.216	0.139	2.23	0.608	10.1	4.27	20.9	5.21	56.1	10.6	7601	0.391	22.8	67.6
91500 404	40.5	3.71	98.9	0.389		1.88				0.157	1.19	0.541	8.01	3.09	18.4	4.62	50.2	9.90	7459	0.319	19.3	59.7
91500 405	30.0	3.66	109	0.658		2.24	0.013		0.242	0.177	1.87	0.557	9.05	3.49	20.1	5.19	55.8	10.8	7818	0.385	22.2	65.8
Seiland 360	69.5	1.18	287	1.76		4.05			0.762	0.697	4.37	1.90	25.3	10.7	51.3	12.2	115	22.7	7278	0.979	53.8	64.3
Seiland 361	52.2	0.974	285	1.51		3.86		0.200	0.499	0.557	4.67	1.82	25.4	10.7	49.7	12.1	117	22.4	7382	0.998	51.8	61.4
Seiland 364	77.8	1.67	282	1.68		3.47			0.690	0.685	3.68	1.56	24.6	10.3	50.6	11.4	120	21.4	6942	0.958	51.1	61.6
Seiland 365	69.1	1.25	291	1.53		3.68			0.797	0.607	3.92	1.92	24.8	10.2	50.9	12.0	116	21.5	7227	1.00	52.5	62.1
Seiland 368	32.7	0.976	276	1.33		3.34			0.659	0.572	4.36	1.78	24.9	9.64	47.6	12.1	117	21.1	6924	1.02	50.1	60.8
Seiland 369	42.8	1.58	276	1.65		4.02	0.016	0.171	0.617	0.595	5.16	1.55	25.3	9.75	47.8	12.2	119	21.1	7179	1.09	52.0	61.9
Seiland 372	59.1	1.63	312	1.72		4.36		0.264	0.724	0.556	4.82	1.99	26.9	10.5	55.0	12.4	126	22.8	7613	0.968	57.1	65.4
Seiland 373	47.6	1.15	286	1.88		3.68		0.441	0.585	0.628	4.41	2.00	25.9	9.92	53.1	12.8	122	22.4	7582	1.28	54.5	63.4
Seiland 376	55.3	0.995	300	1.73		3.75		0.07	0.714	0.640	4.68	1.71	27.2	10.0	48.8	11.5	122	22.3	7060	1.03	54.3	63.7
Seiland 377	21.2	0.840	281	1.46		4.02		0.422	0.152	0.576	5.29	1.75	22.9	10.2	46.8	11.1	115	20.0	6814	1.01	51.1	62.0
Seiland 380	74.3	0.973	271	1.54		4.00		0.218	0.347	0.691	4.76	1.84	26.1	9.47	48.8	12.3	117	21.2	7089	1.08	52.2	62.5
Seiland 381	62.8	1.57	256	1.56		3.84	0.011	0.167	0.332	0.648	4.02	2.00	24.4	10.1	48.8	11.7	115	19.8	6909	1.21	50.2	61.7

Fig. A5. 1 Sample 110-322 of ferrorhyolite (FeR) lapilli tuff with strong quartz, sericite, and pyrite alteration.

Fig. A5. 2 Sample 110-368 of massive FIIIb high-silica rhyolite (HSR) with patchy epidote, calcite, and chlorite alteration.

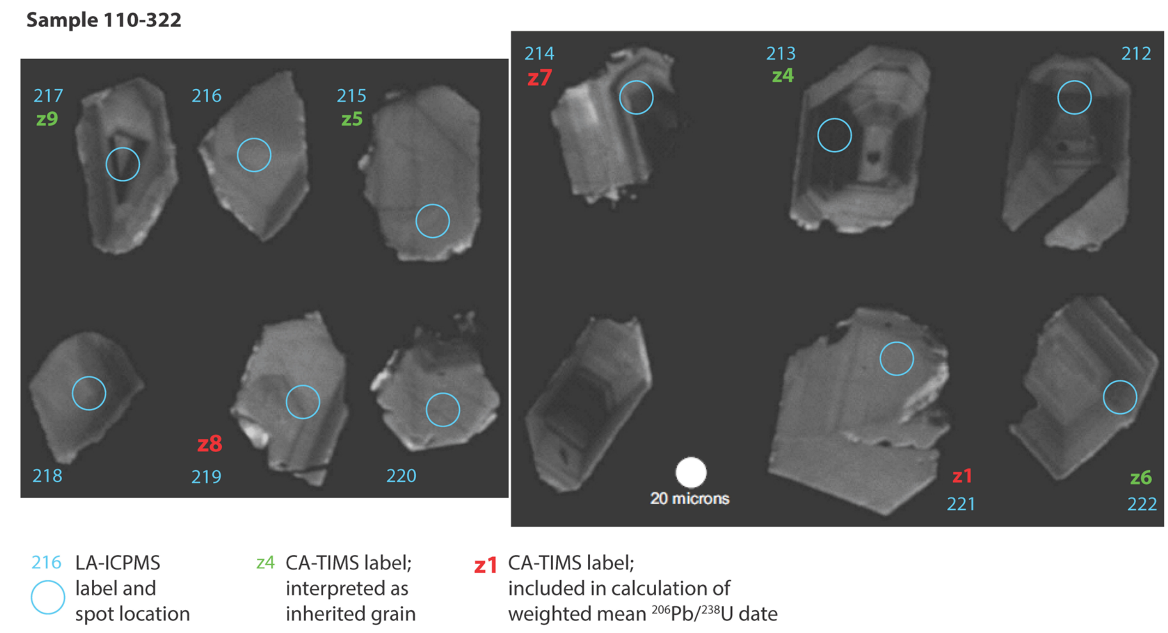

Fig. A5. 3 Cathodoluminescence (CL) images of zircon grains in sample 110-322. LA-ICPMS labels and spot locations are shown as blue text and circles, respectively. CA-ID-TIMS labels are also shown. Grains with red CA-ID-TIMS labels were used in the calculation of the weighted mean $^{206}Pb/^{238}U$ date. Grains with green CA-ID-TIMS labels were not used in the calculation of the weighted mean $^{206}Pb/^{238}U$ date; they are interpreted as inherited zircon grains.

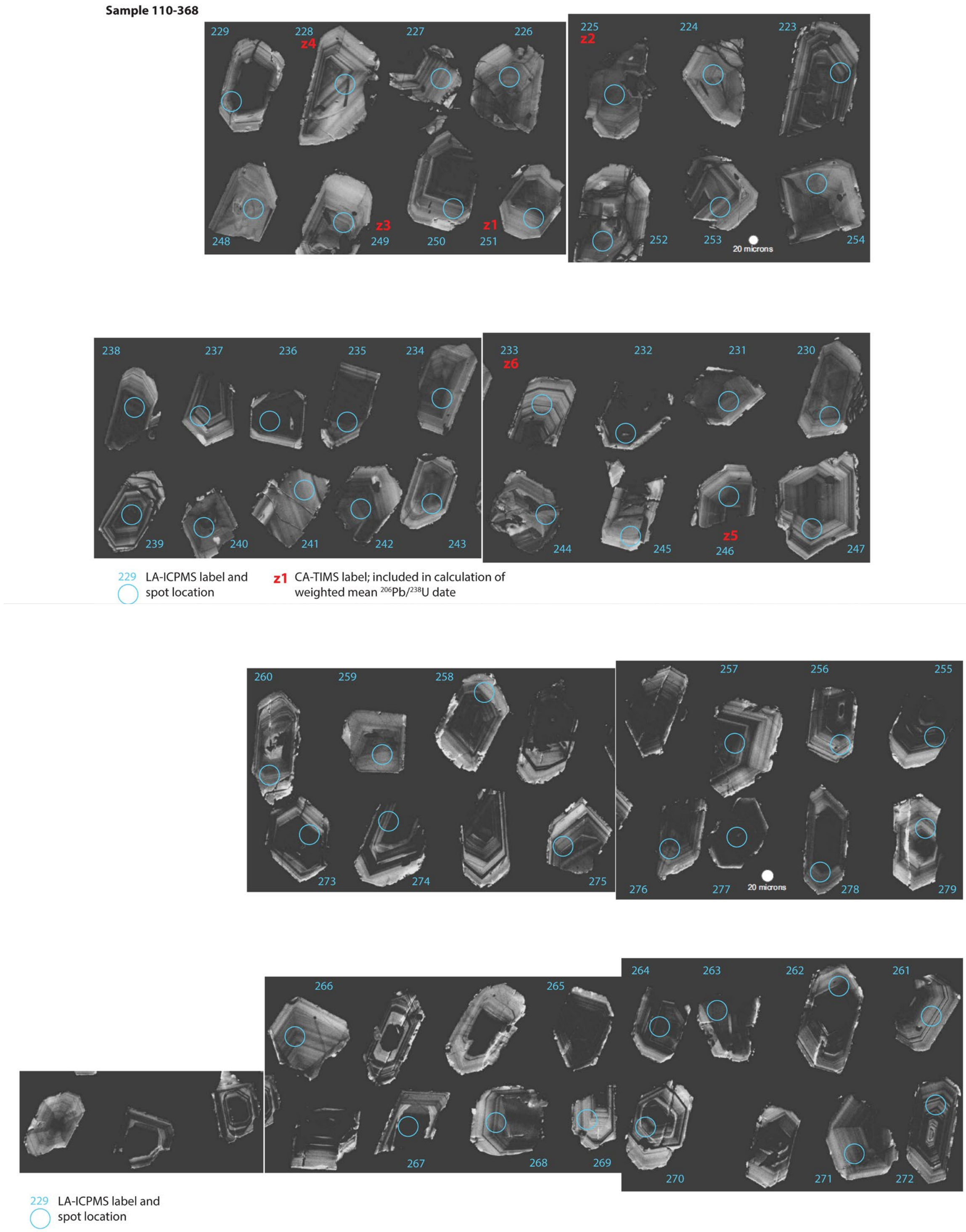

Fig. A5. 4 Cathodoluminescence (CL) images of zircon grains in sample 110-368. LA-ICPMS labels and spot locations are shown as blue text and circles, respectively. CA-ID-TIMS labels are also shown. Grains with red CA-ID-TIMS labels were used in the calculation of the weighted mean $^{206}Pb/^{238}U$ date.

Appendix 5 References

Crowley, J.L., Schoene, B., and Bowring, S.A., 2007, U-Pb dating of zircon in the Bishop Tuff at the millennial scale: Geology, v. 35, p. 1123–1126.

Gerstenberger, H., and Haase, G., 1997, A highly effective emitter substance for mass spectrometric Pb isotope ratio determinations: Chemical Geology, v. 136, p. 309–312.

Hiess, J., Condon, D.J., McLean, N., and Noble, S.R., 2012, $^{238}U/^{235}U$ systematics in terrestrial uranium-bearing minerals: Science (American Association for the Advancement of Science), v. 335, p. 1610–1614.

Jaffey, A.H., Flynn, K.F., Glendenin, L.E., Bentley, W.C., and Essling, A.M., 1971, Precision measurement of half-lives and specific activities of ^{235}U and ^{238}U: Physical Review C, v. 4, p. 1889–1906.

Krogh, T.E., 1973, A low-contamination method for hydrothermal decomposition of zircon and extraction of U and Pb for isotopic age determinations: Geochimica et Cosmochimica Acta, v. 87, p. 485–494.

Kuiper, Y.D., Murray, D.P., Ellison, S., and Crowley, J.L., 2022, U-Pb detrital zircon analysis of sedimentary rocks of the southeastern New England Avalon terrane in the U.S. Appalachians: evidence for a separate crustal block: Geological Society of America Special Paper 554, p. 93–119.

Ludwig, K.R., 2003, User's manual for Isoplot 3.00: Berkeley, USA, Berkeley Geochronology Center, 70 p.

Mattinson, J.M., 2005, Zircon U-Pb chemical abrasion (“CA-TIMS”) method: combined annealing and multi-step partial dissolution analysis for improved precision and accuracy of zircon ages: Chemical Geology, v. 220, p. 47–66.

Schmitz, M.D., and Schoene, B., 2007, Derivation of isotope ratios, errors, and error correlations for U-Pb geochronology using ^{205}Pb-^{235}U-(^{233}U)-spiked isotope dilution thermal ionization mass spectrometric data: Geochemistry, Geophysics, Geosystems, v. 8, p. 1–20.

Sláma, J., Košler, J., Condon, D.J., Crowley, J.L., Gerdes, A., Hanchar, J.M., Horstwood, M.S.A., Morris, G.A., Nasdala, L., Norberg, N., Schaltegger, U., Schoene, B., Tubrett, M.N., and Whitehouse, M.J., 2008, Plešovice zircon - a new natural reference material for U-Pb and Hf isotopic microanalysis: Chemical Geology, v. 249, p. 1–35.

Watson, E.B., Wark, D.A., and Thomas, J.B., 2006, Crystallization thermometers for zircon and rutile: Contributions to Mineralogy and Petrology, v. 151, p. 413–433.

Wendt, I., and Carl, C., 1991, The statistical distribution of the mean squared weighted deviation: Chemical Geology, v. 86, p. 275–285.

Appendix 6. Electron probe microanalyzer data

Analytical methods

Plagioclase and FeTi oxide mineral chemistry was investigated using a JEOL JXA-8230 electron probe microanalyzer (EPMA) equipped with four energy dispersive spectrometers (EDS) at the University of Memorial in St. John's, Newfoundland. Four hundred and ninety-nine spot analyses were conducted across eight polished, carbon-coated thin sections. The EPMA conditions are summarized in Table A6. 1 and Table A6. 2. Standard ZAF techniques with the JEOL software were used to correct the raw X-ray intensities. Astimex standards of plagioclase, rutile, and magnetite were used to assess the quality of the analyses (Table A6. 3, Table A6. 4, and Table A6. 5).

A total of 145 spot analyses were completed on plagioclase crystals on six thin sections. The feldspar end-members anorthite (An), albite (Ab), and orthoclase (Or) were calculated following the method of Deer et al. (2013), assuming eight oxygens per formula unit. The results are presented in Table A6. 6.

A total of 354 spot analyses were conducted on magnetite, ilmenite, and rutile grains (72 ilmenite, 82 rutile, and 200 magnetite spot analyses). Since the EPMA cannot detect the two oxidation states of iron, iron was measured as FeO (Fe^{2+}), and the method of Droop (1987) was used to estimate the relative abundance of Fe^{2+} and Fe^{3+}. The ulvospinel content of the FeTi oxides within the magnetite-ulvospinel series was calculated using the method of Stormer (1983) with a modified version of the ILMAT Microsoft Excel spreadsheet template created by Lepage (2003). Mineral formulae were calculated following the method of Deer et al. (2013), assuming 32, six, and two oxygens per formula unit for magnetite, ilmenite, and rutile, respectively.

Results

The plagioclase and FeTi oxide mineral chemistry data are yet to be thoroughly evaluated. However, the plagioclase mineral chemistry in the sample of Z-FeTiB (S037015) is discussed briefly here because it has important implications for understanding how the varioles in the Z-FeTiB may have formed. Variole is a non-genetic definition referring to "globular and spherical centimeter-scale, generally leucocratic masses visible on the weathered surfaces of mafic rock," and they may be products of spherulitic crystallization, magma mingling, liquid immiscibility, or superficial alteration (Fowler et al., 2002). Sample S037015 has larger plagioclase phenocrysts with a mean composition of andesine (An_{36}); this overlaps with the mean composition, An_{35}, of the plagioclase microlites and interstitial plagioclase in the groundmass, although these groundmass phases span a wider variety, including some oligoclase (Fig. A6. 1). The plagioclase in the varioles has a mean composition of An_{33}, although a few analyses of plagioclase preserved (e.g., not replaced by muscovite or epidote) in the core of the varioles have more Ca-rich compositions, reaching anorthite contents up to An_{65} (labradorite; Fig. A6. 1). Since spherulites are organized clusters of crystal fibers that originate from a common point or line (Lofgren, 1971; McPhie et al., 1993; Fowler et al., 2002), the plagioclase mineral chemistry in sample S037015 lends support to the interpretation that the varioles may have formed by spherulitic crystallization, whereby the more Ca-rich plagioclase cores crystallized before the outer, more Na-rich plagioclase parts (Lofgren, 1974). Spherulites can develop through primary magmatic crystallization (undercooling) or can be secondary and form due to devitrification (McPhie et al., 1993). Several petrologic features in the Z-FeTiB (see petrographic description for S037015 in Appendix 2) are consistent with high degrees of undercooling, including (1) the presence of magnetite crystals with embayed edges that may be resorption features, but could also result from rapid growth due to high degrees of undercooling (Winter, 2010; p.41), (2) the high abundance of plagioclase microlites (McPhie et al., 1993; p. 23), (3) the glassy groundmass (devitried to biotite, chlorite, and lesser epidote), and (4) the coexistence of tabular plagioclase crystals and spherulites that is favored at higher degrees of undercooling (Lofgren, 1974). The petrographic features of the Z-FeTiB support the interpretation that they formed by high degrees of undercooling and their plagioclase mineral chemistry suggests that their variolitic texture is a result of spherulitic crystallization.

Table A6. 1 Summary of electron microprobe operating conditions for plagioclase analysis.

Element	X-ray	Crystal	Spectro-meter	Accelerating voltage (kV)	Beam size (μm)	Current (nA)	Peak position	Background lower (mm)	Background upper (mm)
Ba	Lα	LIFL	2	15	1	10	192.8	4.0	2.0
K	Kα	PETL	3	15	1	10	119.8	3.0	7.0
Ca	Kα	PETL	3	15	1	10	107.5	3.0	2.0
Sr	Lα	PETL	3	15	1	10	219.9	11.7	3.7
Na	Kα	TAP	4	15	1	10	129.4	4.7	6.2
Al	Kα	TAP	4	15	1	10	90.6	5.5	3.3
Si	Kα	TAP	4	15	1	10	77.4	3.3	4.1

Table A6. 2 Summary of electron microprobe operating conditions for FeTi oxide analysis.

Element	X-ray	Crystal	Spectro-meter	Accelerating voltage (kV)	Beam size (μm)	Current (nA)	Peak position	Background lower (mm)	Background upper (mm)
Nb	Lα	PETJ	1	15	1	100	183.1	4.8	8.1
Zn	Kα	LIFL	2	15	1	100	99.6	2.0	2.0
Cu	Kα	LIFL	2	15	1	100	107.0	3.0	3.0
Ni	Kα	LIFL	2	15	1	100	115.1	2.0	2.0
Co	Kα	LIFL	2	15	1	100	124.2	5.8	5.0
Fe	Kα	LIFL	2	15	1	100	134.5	3.5	3.0
K	Kα	PETL	3	15	1	100	119.8	3.0	7.0
Ca	Kα	PETL	3	15	1	100	107.5	3.0	2.0
Sn	Lα	PETL	3	15	1	100	115.2	2.3	2.5
Zr	Lα	PETL	3	15	1	100	194.4	4.0	6.0
P	Kα	PETL	3	15	1	100	197.2	6.5	4.0
Al	Kα	TAP	4	15	1	100	90.6	5.5	3.3
Si	Kα	TAP	4	15	1	100	77.4	7.0	5.6
Mg	Kα	TAP	4	15	1	100	107.5	6.0	5.0
Mn	Kα	LIFH	5	15	1	100	146.3	6.0	3.3
Cr	Kα	LIFH	5	15	1	100	159.3	2.5	3.0
V	Kα	LIFH	5	15	1	100	174.1	2.0	3.0
Ti	Kα	LIFH	5	15	1	100	191.2	3.0	3.0

Table A6. 3 Electron microprobe results for the Astimex plagioclase standard.

Probe ID	Astimex plag	Astimex plag	Astimex plag	Astimex plag	Astimex plag	Astimex plag	Astimex plag	Astimex plag	Astimex plag	Astimex plag	Astimex plag	Astimex plag	Astimex plag	Astimex plag	Astimex plag	Astimex plag	Astimex plag
BaO wt%	0.09	-0.10	0.00	0.00	-0.10	-0.02	-0.04	-0.05	0.01	0.09	0.09	0.02	-0.03	-0.02	-0.03	0.03	0.01
K_2O wt%	0.34	0.34	0.37	0.34	0.35	0.36	0.34	0.34	0.34	0.34	0.35	0.35	0.35	0.35	0.33	0.04	0.35
CaO wt%	11.89	12.01	11.89	11.92	11.66	11.97	11.90	11.85	11.87	11.93	11.87	11.88	11.97	11.84	11.76	0.70	11.82
SrO wt%	0.14	0.20	0.07	0.21	0.16	0.20	0.18	0.27	0.21	0.17	0.13	0.19	0.19	0.18	0.15	0.29	0.24
Na_2O wt%	4.37	4.39	4.47	4.35	4.30	4.12	4.36	4.22	4.34	4.51	4.38	4.20	4.30	4.25	4.29	4.86	4.32
Al_2O_3 wt%	29.85	29.55	29.65	29.78	29.62	29.84	29.72	29.67	30.02	29.87	30.18	29.65	29.70	29.51	29.52	16.87	29.81
SiO_2 wt%	52.15	52.07	52.46	51.83	52.35	52.05	52.49	52.48	52.42	52.45	52.48	51.94	52.12	52.32	52.16	67.96	52.56
Total wt%	98.82	98.47	98.91	98.44	98.33	98.51	98.95	98.79	99.22	99.37	99.47	98.23	98.60	98.43	98.17	90.75	99.11

Table A6. 4 Electron microprobe results for the Astimex rutile standard.

Probe ID	Astimex rutile	Astimex rutile	Astimex rutile	Astimex rutile	Astimex rutile	Astimex rutile	Astimex rutile	Astimex rutile	Astimex rutile	Astimex rutile	Astimex rutile	Astimex rutile	Astimex rutile
SiO_2 wt%	0.00	0.01	0.01	0.00	0.00	0.00	0.01	0.00	0.01	0.00	0.00	0.00	0.01
TiO_2 wt%	101.06	101.04	100.80	101.01	100.83	100.96	101.56	101.63	101.61	101.00	100.77	101.22	100.93
Al_2O_3 wt%	0.05	0.02	0.24	0.04	0.04	0.06	0.05	0.05	0.04	0.04	0.05	0.04	0.04
Cr_2O_3 wt%	0.02	0.00	0.00	0.00	0.01	0.00	-0.01	-0.01	0.00	0.00	-0.01	0.00	0.00
FeO wt%	0.02	0.03	0.02	0.00	0.02	0.02	0.00	0.00	0.01	0.02	0.02	0.01	0.02
MnO wt%	0.02	-0.01	0.00	-0.01	-0.01	0.01	-0.02	0.01	0.00	0.00	0.00	0.00	0.00
MgO wt%	0.00	0.00	-0.01	0.00	0.00	0.00	0.00	0.00	0.00	0.00	0.00	0.00	0.00
CaO wt%	0.00	0.00	0.01	0.01	0.00	0.00	0.00	0.00	0.00	0.00	0.00	0.00	0.00
K_2O wt%	-0.01	0.00	0.00	0.00	0.00	0.00	0.00	0.00	0.00	0.00	0.00	0.00	0.00
Nb_2O_5 wt%	0.04	0.01	-0.01	-0.03	0.00	0.00	0.01	-0.02	-0.01	0.01	-0.02	0.02	0.02
ZnO wt%	0.00	0.01	0.01	0.01	0.00	0.01	0.00	0.00	0.01	0.00	0.03	0.01	0.02
CuO wt%	0.00	0.02	0.01	-0.01	0.00	0.01	0.00	0.00	0.02	0.00	0.02	0.01	0.00
NiO wt%	0.01	0.02	0.01	0.00	-0.01	-0.01	0.00	0.01	0.01	0.01	0.01	0.00	0.00
CoO wt%	0.00	-0.01	0.00	-0.01	-0.01	0.00	0.00	0.00	0.00	-0.01	0.01	-0.01	-0.01
SnO_2 wt%	0.00	0.00	-0.01	0.00	0.00	0.00	0.00	0.01	0.00	0.00	0.01	0.01	0.00
ZrO_2 wt%	0.00	-0.02	-0.01	0.00	-0.03	-0.01	-0.02	-0.01	0.00	0.02	0.00	0.00	-0.01
P_2O_5 wt%	0.00	0.00	0.00	-0.01	0.00	0.00	0.00	0.00	0.00	0.00	0.00	0.00	0.00
V_2O_3 wt%	0.76	0.73	0.75	0.74	0.74	0.75	0.76	0.77	0.77	0.76	0.71	0.76	0.75
Total wt%	101.97	101.82	101.82	101.74	101.59	101.80	102.33	102.44	102.47	101.86	101.60	102.06	101.78

Probe ID	Astimex rutile	Astimex rutile	Astimex rutile
SiO_2 wt%	0.01	0.01	0.01
TiO_2 wt%	101.04	100.85	101.44
Al_2O_3 wt%	0.04	0.04	0.05
Cr_2O_3 wt%	0.00	0.00	0.00
FeO wt%	0.00	0.00	0.02
MnO wt%	0.00	0.01	-0.01
MgO wt%	0.00	0.00	0.00
CaO wt%	0.00	0.00	0.01
K_2O wt%	0.00	0.00	0.00
Nb_2O_5 wt%	0.01	0.01	0.01
ZnO wt%	0.02	0.01	0.02
CuO wt%	0.00	0.00	0.00
NiO wt%	-0.01	0.00	0.00
CoO wt%	-0.01	-0.01	0.01
SnO_2 wt%	0.00	0.00	-0.01
ZrO_2 wt%	-0.01	-0.02	0.00
P_2O_5 wt%	0.00	-0.01	0.00
V_2O_3 wt%	0.76	0.75	0.76
Total wt%	101.86	101.66	102.31

Table A6. 5 Electron microprobe results for the Astimex magnetite standard.

Probe ID	Astimex magnetite	Astimex magnetite	Astimex magnetite	Astimex magnetite	Astimex magnetite	Astimex magnetite	Astimex magnetite	Astimex magnetite	Astimex magnetite	Astimex magnetite	Astimex magnetite	Astimex magnetite	Astimex magnetite
SiO_2 wt%	0.02	0.00	0.02	0.01	0.01	-0.01	0.02	0.00	0.01	0.01	0.02	0.01	0.00
TiO_2 wt%	0.03	0.04	0.05	0.06	0.04	0.05	0.25	0.07	0.10	0.12	0.04	0.05	0.05
Al_2O_3 wt%	0.06	0.05	0.05	0.08	0.08	0.07	0.08	0.06	0.69	0.05	0.04	0.03	0.06
Cr_2O_3 wt%	-0.01	-0.01	0.01	-0.01	0.00	0.00	0.00	-0.01	0.01	0.01	-0.01	0.00	0.00
FeO wt%	91.10	91.19	91.22	90.85	90.97	90.73	90.97	91.64	91.02	91.65	91.62	91.56	92.00
MnO wt%	0.30	0.25	0.23	0.28	0.26	0.29	0.37	0.34	0.31	0.35	0.20	0.25	0.26
MgO wt%	0.01	0.01	0.02	0.01	0.01	0.01	0.01	0.01	0.01	0.01	0.01	0.01	0.01
CaO wt%	0.00	0.00	0.00	0.00	-0.01	0.00	0.01	0.00	0.00	0.00	0.00	0.00	0.00
K_2O wt%	-0.01	0.00	0.00	0.00	0.00	0.00	0.00	0.00	0.00	0.00	0.00	0.00	0.00
Nb_2O_5 wt%	0.01	-0.01	0.01	0.03	0.02	0.02	0.00	0.01	0.01	-0.01	0.02	0.02	0.00
ZnO wt%	0.01	0.01	0.00	0.01	0.03	0.01	0.03	0.02	0.40	0.01	0.01	0.03	0.00
CuO wt%	0.02	-0.01	0.01	0.02	0.00	0.01	0.02	0.00	0.00	0.01	-0.02	0.00	0.00
NiO wt%	0.00	0.01	0.00	0.01	0.00	-0.01	0.00	0.02	-0.01	0.00	0.01	-0.01	0.01
CoO wt%	0.11	0.13	0.13	0.13	0.12	0.14	0.11	0.11	0.11	0.08	0.14	0.13	0.11
SnO_2 wt%	-0.07	-0.15	-0.01	-0.22	-0.02	0.00	-0.08	-0.01	-0.24	-0.05	-0.09	-0.01	-0.01
ZrO_2 wt%	-0.01	0.00	-0.01	0.01	0.00	0.00	-0.01	0.00	-0.02	0.00	0.01	-0.01	0.01
P_2O_5 wt%	0.00	-0.01	0.00	0.00	0.00	0.00	0.00	-0.01	0.00	0.00	0.00	-0.01	0.00
V_2O_3 wt%	0.03	0.01	0.02	0.02	0.01	0.02	0.01	0.01	0.03	0.02	0.03	0.01	0.02
Total wt%	91.60	91.51	91.74	91.29	91.52	91.31	91.78	92.27	92.45	92.26	92.02	92.07	92.53

Probe ID	Astimex magnetite	Astimex magnetite	Astimex magnetite	Astimex magnetite	Astimex magnetite	Astimex magnetite	Astimex magnetite	Astimex magnetite	Astimex magnetite	Astimex magnetite	Astimex magnetite	Astimex magnetite	Astimex magnetite
SiO_2 wt%	0.01	0.01	0.03	0.00	0.01	0.00	0.01	0.02	0.00	0.01	0.01	0.01	0.00
TiO_2 wt%	0.09	0.05	0.05	0.04	0.03	0.08	0.07	0.07	0.31	0.06	0.04	0.05	0.04
Al_2O_3 wt%	0.16	0.14	0.06	0.08	0.06	0.06	0.04	0.05	0.06	0.07	0.06	0.06	0.05
Cr_2O_3 wt%	-0.01	-0.01	0.01	0.00	-0.01	-0.01	-0.01	0.00	0.00	0.00	0.01	-0.01	-0.01
FeO wt%	91.61	90.84	91.31	91.98	92.05	91.60	91.26	91.67	90.88	91.73	91.82	91.33	91.88
MnO wt%	0.30	0.27	0.24	0.23	0.25	0.36	0.33	0.30	0.48	0.29	0.27	0.27	0.19
MgO wt%	0.01	0.01	0.01	0.01	0.00	0.02	0.02	0.02	0.01	0.01	0.02	0.01	0.01
CaO wt%	0.00	0.00	0.00	0.00	0.00	0.00	0.00	0.00	0.01	0.01	0.00	0.00	0.00
K_2O wt%	0.00	0.00	0.00	0.00	0.00	0.00	-0.01	0.00	0.00	0.00	-0.01	0.00	0.00
Nb_2O_5 wt%	0.03	0.05	-0.01	0.02	-0.01	-0.03	-0.01	-0.01	0.04	0.02	0.01	0.00	0.01
ZnO wt%	0.05	0.06	0.03	-0.01	0.02	0.01	-0.01	0.02	-0.01	0.01	0.01	0.00	-0.01
CuO wt%	-0.01	-0.01	-0.01	0.01	0.01	0.01	0.00	0.01	-0.01	0.00	0.02	0.00	0.01
NiO wt%	-0.01	0.00	-0.01	0.01	-0.01	0.00	0.00	-0.01	-0.01	-0.01	0.01	0.01	0.00
CoO wt%	0.13	0.13	0.14	0.14	0.13	0.11	0.13	0.14	0.13	0.13	0.12	0.10	0.14
SnO_2 wt%	-0.24	-0.01	-0.01	-0.01	-0.14	-0.02	-0.01	-0.20	0.00	-0.07	-0.02	-0.03	-0.16
ZrO_2 wt%	0.01	0.00	0.01	0.00	0.00	0.00	0.00	-0.01	0.00	-0.01	-0.01	0.01	0.00
P_2O_5 wt%	0.00	0.00	0.00	0.00	0.00	0.00	-0.01	0.00	0.00	0.00	0.00	0.00	0.00
V_2O_3 wt%	0.01	0.01	0.02	0.01	0.01	0.02	0.01	0.02	0.02	0.02	0.02	0.02	0.03
Total wt%	92.14	91.52	91.87	92.52	92.41	92.21	91.82	92.09	91.91	92.27	92.38	91.83	92.20

Table A6. 6 Electron microprobe results for plagioclase mineral chemistry and calculated mineral formulae based on eight oxygens.

	Probe ID	W605013_4_P1	W605013_1_P2	W605013_1_P4	W605013_1_P8	W605013_1_P7	W605013_1_P5	W605013_1_P6	W605013_1_P9	W605013_1_P10	W605013_1_P11	W605013_1_P12	W605013_2_P13	S037015_2_P14	S037015_2_P15	S037015_2_P16	S037015_2_P17
	Sample	W605013	W605013	W605013	W605013	W605013	W605013	W605013	S037015	S037015	S037015	S037015	S037015	S037015	S037015	S037015	S037015
	Rocktype	Iron formation	Iron formation	Iron formation	Iron formation	Iron formation	Iron formation	Iron formation	Z-FeTiB	Z-FeTiB	Z-FeTiB	Z-FeTiB	Z-FeTiB	Z-FeTiB	Z-FeTiB	Z-FeTiB	Z-FeTiB
	Feature	Interstitial	Interstitial	Interstitial	Interstitial	Interstitial	Interstitial	Interstitial	Variole	Variole	Variole	Variole	Variole	Variole	Variole	Variole	Groundmass
Probe data	**BaO wt%**	-0.02	0.09	0.07	-0.01	0.02	-0.05	-0.02	-0.07	0.00	-0.04	0.03	-0.03	-0.07	0.05	0.04	-0.02
	K_2O wt%	0.05	0.04	0.02	0.04	0.05	0.04	0.05	0.08	0.07	0.08	0.08	0.06	0.10	0.08	0.05	0.65
	CaO wt%	0.43	0.69	0.16	0.55	0.89	0.94	0.96	5.66	6.20	5.85	6.29	5.77	6.06	6.68	5.66	5.88
	SrO wt%	0.01	-0.02	0.12	-0.02	0.07	0.07	0.09	0.09	0.12	0.06	0.07	0.11	0.08	0.20	0.16	0.08
	Na_2O wt%	11.56	11.44	7.21	10.46	10.91	10.69	11.03	8.42	8.18	8.39	8.01	8.30	8.27	7.73	8.38	7.16
	Al_2O_3 wt%	20.67	20.67	11.60	20.61	20.76	20.83	20.75	24.93	25.46	24.91	25.47	25.31	25.15	25.92	25.22	24.60
	SiO_2 wt%	70.08	69.38	81.83	70.02	69.22	68.23	69.10	61.55	60.72	61.34	60.88	62.28	60.99	60.13	62.22	58.31
	Total wt%	102.79	102.30	101.01	101.64	101.93	100.75	101.96	100.68	100.75	100.60	100.83	101.81	100.57	100.80	101.72	96.67
Calc.	**An %**	2	3	1	3	4	5	5	27	29	28	30	28	29	32	27	30
	Ab %	98	97	99	97	95	95	95	73	70	72	69	72	71	67	73	66
	Or %	0	0	0	0	0	0	0	0	0	0	0	0	1	0	0	4

	Probe ID	S037015_2_P18	S037015_2_P19	S037015_2_P20	S037015_2_P21	S037015_2_P22	S037015_2_P23	S037015_2_P24	S037015_2_P25	S037015_2_P26	S037015_6_P27	S037015_6_P28	S037015_6_P29	S037015_6_P30	S037015_6_P31	S037015_6BR_P32	S037015_7_P33
	Sample	S037015	S037015	S037015	S037015	S037015	S037015	S037015	S037015	S037015	S037015	S037015	S037015	S037015	S037015	S037015	S037015
	Rocktype	Z-FeTiB	Z-FeTiB	Z-FeTiB	Z-FeTiB	Z-FeTiB	Z-FeTiB	Z-FeTiB	Z-FeTiB	Z-FeTiB	Z-FeTiB	Z-FeTiB	Z-FeTiB	Z-FeTiB	Z-FeTiB	Z-FeTiB	Z-FeTiB
	Feature	Groundmass	Groundmass	Phenocryst	Phenocryst	Phenocryst	Phenocryst	Phenocryst	Phenocryst	Phenocryst	Variole	Variole	Variole	Variole	Variole	Variole	Groundmass /microlites
Probe data	**BaO wt%**	0.02	-0.04	-0.03	0.01	0.04	0.00	0.03	-0.03	-0.05	0.05	0.03	-0.04	-0.01	-0.02	-0.01	0.05
	K_2O wt%	0.07	0.11	0.06	0.05	0.04	0.10	0.07	0.02	0.06	0.06	0.08	0.08	0.07	0.09	0.08	0.07
	CaO wt%	7.97	6.05	7.48	0.53	6.83	0.88	7.99	0.06	7.77	6.46	2.95	7.89	7.23	5.99	10.33	8.23
	SrO wt%	0.08	0.09	0.06	0.06	0.10	0.08	0.13	0.02	0.15	0.07	0.16	0.11	0.02	0.12	0.13	0.14
	Na_2O wt%	6.97	8.30	7.33	11.31	7.67	11.51	7.01	0.19	7.06	8.13	9.90	7.20	7.39	8.41	5.63	6.95
	Al_2O_3 wt%	26.97	24.86	26.63	20.04	25.97	20.41	27.11	0.67	26.64	25.67	22.67	26.95	26.14	25.23	29.03	27.22
	SiO_2 wt%	58.05	60.36	58.61	72.97	60.29	69.82	57.99	98.61	58.77	60.24	66.06	58.09	59.08	61.10	55.06	57.63
	Total wt%	100.13	99.73	100.14	104.97	100.94	102.81	100.34	99.54	100.41	100.68	101.83	100.29	99.93	100.92	100.24	100.28
Calc.	**An %**	39	29	36	3	33	4	39	15	38	30	14	38	35	28	50	39
	Ab %	61	71	64	97	67	95	61	79	62	69	85	62	65	71	49	60
	Or %	0	1	0	0	0	1	0	6	0	0	0	0	0	1	0	0

	Probe ID	S037015_7_P34	S037015_7_P35	S037015_7_P36	S039313_5_P37	S039313_5_P38	S039313_5_P39	S039313_5_P40	99362_2_P41	99362_2_P42	99362_2_P43	99362_2_P44	99362_2_P45	99362_2_P46	99362_2_P47	99362_2_P48	99362_2_P49
	Sample	S037015	S037015	S037015	S039313	S039313	S039313	S039313	99-362	99-362	99-362	99-362	99-362	99-362	99-362	99-362	99-362
	Rocktype	Z-FeTiB	Z-FeTiB	Z-FeTiB	HW-FeTiB	HW-FeTiB	HW-FeTiB	HW-FeTiB	FW-FeB	FW-FeB	FW-FeB	FW-FeB	FW-FeB	FW-FeB	FW-FeB	FW-FeB	FW-FeB
	Feature	Groundmass /microlites	Groundmass /microlites	Groundmass /microlites	Scoria groundmass	Scoria groundmass	Scoria groundmass	Scoria groundmass	Groundmass	Groundmass	Groundmass	Groundmass	Groundmass	Groundmass	Groundmass	Groundmass	Phenocryst
Probe data	**BaO wt%**	0.02	0.08	0.00	0.06	0.00	0.05	-0.05	-0.04	0.10	0.00	0.00	0.02	0.09	0.02	-0.09	0.01
	K_2O wt%	0.06	0.06	0.06	0.11	0.08	0.05	0.04	0.08	0.48	0.07	0.06	0.08	0.07	0.04	0.03	0.11
	CaO wt%	8.25	8.45	0.25	0.64	1.46	0.80	0.67	8.70	8.69	8.41	5.30	8.39	8.32	0.84	0.57	5.24
	SrO wt%	0.11	0.16	0.01	0.20	0.70	0.37	0.29	0.04	0.03	0.04	0.08	0.09	0.11	0.10	0.01	0.19
	Na_2O wt%	6.93	6.63	10.76	10.24	10.76	10.97	8.52	6.66	6.00	6.49	8.31	6.77	6.81	11.50	5.92	8.61
	Al_2O_3 wt%	27.32	27.36	20.84	18.58	21.61	20.70	16.32	27.03	26.39	26.77	23.99	26.62	26.35	20.71	10.58	24.45
	SiO_2 wt%	57.70	57.53	72.54	71.25	67.02	68.62	66.09	57.03	55.57	56.94	64.83	57.33	57.27	67.45	86.61	60.93
	Total wt%	100.39	100.26	104.46	101.09	101.63	101.54	91.89	99.50	97.27	98.73	102.56	99.31	99.01	100.67	103.62	99.54
Calc.	**An %**	40	41	1	3	7	4	4	42	43	42	26	40	40	4	5	25
	Ab %	60	58	98	96	93	96	96	58	54	58	74	59	59	96	95	74
	Or %	0	0	0	1	0	0	0	0	3	0	0	0	0	0	0	1

	Probe ID	99362_2_P50	99362_2_P51	99362_2_P52	99362_2_P53	99362_2_P54	99362_2_P55	99362_2_P56	99362_2_P57	99362_2_P58	99362_2_P59	99362_2_P60	99362_2_P61	99362_2_P62	99362_2_P63	99362_2_P64	99362_2_P65
	Sample	99-362	99-362	99-362	99-362	99-362	99-362	99-362	99-362	99-362	99-362	99-362	99-362	99-362	99-362	99-362	99-362
	Rocktype	FW-FeB	FW-FeB	FW-FeB	FW-FeB	FW-FeB	FW-FeB	FW-FeB	FW-FeB	FW-FeB	FW-FeB	FW-FeB	FW-FeB	FW-FeB	FW-FeB	FW-FeB	FW-FeB
	Feature	Phenocryst	Phenocryst	Phenocryst	Phenocryst	Groundmass	Groundmass	Groundmass	Groundmass	Groundmass	Phenocryst	Phenocryst	Phenocryst	Groundmass	Groundmass	Groundmass	Groundmass
Probe data	**BaO wt%**	0.02	0.10	-0.01	0.04	0.02	-0.01	-0.01	0.08	-0.04	0.00	0.03	0.05	-0.05	-0.04	-0.05	0.00
	K_2O wt%	0.12	0.08	0.09	0.12	3.42	0.09	1.76	0.05	0.07	0.15	0.08	0.09	0.04	0.05	0.06	0.06
	CaO wt%	6.18	1.64	2.00	3.06	1.50	8.73	5.28	8.14	7.09	6.89	8.44	7.41	0.38	8.32	6.32	8.23
	SrO wt%	0.11	0.10	0.09	0.12	0.11	0.14	0.08	0.04	0.13	0.19	0.06	0.08	0.04	0.12	0.12	0.01
	Na_2O wt%	8.01	10.96	10.81	9.75	5.92	6.51	5.98	6.99	7.54	7.63	6.68	6.87	11.52	6.78	7.86	6.78
	Al_2O_3 wt%	25.44	21.44	21.76	22.83	27.17	26.79	27.11	26.34	25.81	25.72	27.12	25.60	20.50	26.77	25.18	26.69
	SiO_2 wt%	59.78	67.35	66.94	64.76	60.86	56.44	58.26	57.09	58.94	59.13	57.12	56.88	70.32	57.01	59.92	57.22
	Total wt%	99.65	101.67	101.67	100.69	99.01	98.69	98.47	98.74	99.53	99.72	99.52	96.98	102.74	99.01	99.42	99.00
Calc.	**An %**	30	8	9	15	9	42	29	39	34	33	41	37	2	40	31	40
	Ab %	70	92	90	85	66	57	59	61	66	66	59	62	98	59	69	60
	Or %	1	0	0	1	25	1	12	0	0	1	0	1	0	0	0	0

	Probe ID	99362_2_P6 6	99362_2_P6 7	99362_2_P6 8	W605041_3 _P69	W605318_9 _P70	W605318_9 _P71	W605318_9 _P72	W605318_9 _P73	W605318_9 _P74	W605318_9 _P75	S037015_A _P76	S037015_A _P77	S037015_A _P78	S037015_A _P79	S037015_A _P80	S037015_A _P81
	Sample	99-362	99-362	99-362	W605041	W605318	W605318	W605318	W605318	W605318	W605318	S037015	S037015	S037015	S037015	S037015	S037015
	Rocktype	FW-FeB	FW-FeB	FW-FeB	HSR	FeR	FeR	FeR	FeR	FeR	FeR	Z-FeTiB	Z-FeTiB	Z-FeTiB	Z-FeTiB	Z-FeTiB	Z-FeTiB
	Feature	Groundmass	Phenocryst	Groundmass	Groundmass	Groundmass	Groundmass	Groundmass	Groundmass	Groundmass	Groundmass	Groundmass	Groundmass	Groundmass	Groundmass	Variole	Variole
Probe data	**BaO wt%**	-0.02	0.01	0.01	0.11	0.20	0.74	0.60	0.73	0.00	0.14	0.01	0.00	-0.03	-0.02	-0.05	-0.03
	K_2O wt%	0.05	0.15	0.12	4.60	1.11	2.35	1.87	2.15	0.03	0.52	0.06	0.08	0.06	0.09	0.04	0.06
	CaO wt%	1.00	8.47	9.75	0.78	0.01	0.01	0.13	0.00	0.00	0.01	4.34	4.80	6.64	7.13	8.08	8.02
	SrO wt%	0.06	0.00	0.08	0.06	0.04	0.06	0.00	-0.04	-0.04	-0.01	0.08	0.10	0.17	0.18	0.13	0.09
	Na_2O wt%	8.92	6.78	5.79	6.15	0.04	0.12	0.22	0.10	0.00	0.03	8.98	8.94	7.92	7.55	7.04	7.06
	Al_2O_3 wt%	20.59	26.56	27.86	24.39	3.66	7.86	5.85	7.10	0.05	1.71	23.90	24.77	25.81	26.35	27.24	26.96
	SiO_2 wt%	59.06	56.72	55.58	60.87	94.15	89.38	84.47	88.76	98.50	96.26	63.29	63.00	60.19	59.80	58.29	58.36
	Total wt%	89.65	98.69	99.18	96.96	99.22	100.51	93.14	98.81	98.55	98.67	100.65	101.70	100.76	101.08	100.77	100.52
Calc.	**An %**	6	40	48	4	1	0	5	0	4	1	21	23	32	34	39	38
	Ab %	94	59	51	64	6	7	15	7	12	9	79	77	68	65	61	61
	Or %	0	1	1	32	94	93	81	93	84	90	0	0	0	0	0	0

	Probe ID	S037015_A _P82	S037015_A _P83	S037015_A _P84	S037015_B _P85	S037015_B _P86	S037015_B _P87	S037015_B _P88	S037015_B _P89	S037015_B _P90	S037015_B _P91	S037015_B _P92	S037015_B _P93	S037015_B _P94	S037015_C _P95	S037015_C _P96	S037015_C _P97
	Sample	S037015	S037015	S037015	S037015	S037015	S037015	S037015	S037015	S037015	S037015	S037015	S037015	S037015	S037015	S037015	S037015
	Rocktype	Z-FeTiB	Z-FeTiB	Z-FeTiB	Z-FeTiB	Z-FeTiB	Z-FeTiB	Z-FeTiB	Z-FeTiB	Z-FeTiB	Z-FeTiB	Z-FeTiB	Z-FeTiB	Z-FeTiB	Z-FeTiB	Z-FeTiB	Z-FeTiB
	Feature	Variole	Variole	Variole	Groundmass	Groundmass	Groundmass	Groundmass	Groundmass	Groundmass	Groundmass	Groundmass	Groundmass	Groundmass	?	Variole	Variole
Probe data	**BaO wt%**	0.01	-0.09	-0.07	0.00	-0.03	-0.05	0.00	-0.02	0.07	-0.02	-0.03	0.00	0.06	0.01	0.05	0.59
	K_2O wt%	0.05	0.05	0.05	0.08	0.08	0.07	0.07	0.77	0.12	0.07	0.05	0.07	0.10	0.21	0.07	9.33
	CaO wt%	8.68	7.10	6.37	8.60	4.36	6.93	2.49	8.00	0.81	0.65	3.95	5.69	1.12	9.33	13.19	0.75
	SrO wt%	0.16	0.11	0.07	0.12	0.16	0.11	0.10	0.12	-0.02	0.05	0.14	0.07	0.05	0.16	0.12	0.04
	Na_2O wt%	6.66	7.67	7.39	6.72	9.02	7.67	9.84	6.55	11.47	11.30	9.71	7.38	4.61	5.98	3.92	0.62
	Al_2O_3 wt%	27.53	26.43	24.19	27.68	24.04	25.99	22.61	26.93	21.37	21.13	23.50	23.70	22.42	28.38	31.53	31.60
	SiO_2 wt%	57.74	59.56	63.73	57.29	64.64	59.71	66.74	56.36	71.72	71.81	64.85	63.38	73.07	56.06	51.92	48.39
	Total wt%	100.84	100.83	101.73	100.49	102.26	100.43	101.86	98.71	105.54	104.98	102.16	100.30	101.42	100.14	100.81	91.31
Calc.	**An %**	42	34	32	41	21	33	12	39	4	3	18	30	12	46	65	6
	Ab %	58	66	68	58	79	66	87	57	96	97	81	70	87	53	35	9
	Or %	0	0	0	0	0	0	0	4	1	0	0	0	1	1	0	86

	Probe ID	S037015_C _P98	S037015_C _P99	S037015_C _P100	S037015_C _P101	S037015_C _P102	S037015_C _P103	S037015_C _P104	S037015_D _P105	S037015_D _P106	S037015_D _P107	S037015_D _P108	S037015_D _P109	S037015_D _P110	S037015_D _P111	S037015_D _P112	S037015_D _P113
	Sample	S037015	S037015	S037015	S037015	S037015	S037015	S037015	S037015	S037015	S037015	S037015	S037015	S037015	S037015	S037015	S037015
	Rocktype	Z-FeTiB	Z-FeTiB	Z-FeTiB	Z-FeTiB	Z-FeTiB	Z-FeTiB	Z-FeTiB	Z-FeTiB	Z-FeTiB	Z-FeTiB	Z-FeTiB	Z-FeTiB	Z-FeTiB	Z-FeTiB	Z-FeTiB	Z-FeTiB
	Feature	Variole	Variole	Variole	Variole	Variole	Variole	Variole	Variole	Phenocryst	Phenocryst	Phenocryst	Phenocryst	Phenocryst	Phenocryst	Phenocryst	Phenocryst
Probe data	**BaO wt%**	0.01	0.04	0.03	0.08	0.01	0.04	-0.02	0.03	0.00	0.03	-0.01	-0.04	0.00	-0.02	-0.01	-0.01
	K_2O wt%	0.24	0.05	0.06	0.06	0.06	0.06	0.07	0.07	0.08	0.08	0.04	0.09	0.06	0.07	0.12	0.06
	CaO wt%	12.22	6.78	8.10	7.89	7.37	7.11	7.87	8.08	7.73	7.44	7.63	7.11	0.14	0.16	0.47	0.08
	SrO wt%	0.12	0.12	0.08	0.16	0.06	0.13	0.07	0.10	0.12	0.10	0.13	0.11	0.03	0.10	0.04	-0.03
	Na_2O wt%	4.41	7.64	7.01	7.18	7.36	7.46	7.25	7.05	7.33	7.41	7.39	7.46	11.05	11.47	11.54	11.97
	Al_2O_3 wt%	31.04	25.91	27.09	27.09	26.15	26.26	27.06	27.17	26.83	26.42	26.66	26.12	20.78	20.24	20.97	20.58
	SiO_2 wt%	52.67	60.03	57.61	58.35	58.84	59.12	58.32	58.08	58.82	59.14	58.47	58.70	73.23	71.55	72.01	72.14
	Total wt%	100.70	100.55	99.98	100.80	99.85	100.18	100.61	100.58	100.91	100.61	100.32	99.55	105.30	103.57	105.14	104.78
Calc.	**An %**	60	33	39	38	36	34	37	39	37	36	36	34	1	1	2	0
	Ab %	39	67	61	62	64	65	62	61	63	64	63	65	99	99	97	99
	Or %	1	0	0	0	0	0	0	0	0	0	0	0	0	0	1	0

	Probe ID	S037015_D _P114	S037015_D _P115	S037015_D _P116	S037015_D _P117	S037015_D _P118	S037015_D _P119	S037015_E _P120	S037015_E _P121	S037015_E _P122	S037015_E _P123	S037015_E _P124	S037015_E _P125	S037015_E _P126	S037015_E _P127	S037015_F _P128	S037015_F _P129
	Sample	S037015	S037015	S037015	S037015	S037015	S037015	S037015	S037015	S037015	S037015	S037015	S037015	S037015	S037015	S037015	S037015
	Rocktype	Z-FeTiB	Z-FeTiB	Z-FeTiB	Z-FeTiB	Z-FeTiB	Z-FeTiB	Z-FeTiB	Z-FeTiB	Z-FeTiB	Z-FeTiB	Z-FeTiB	Z-FeTiB	Z-FeTiB	Z-FeTiB	Z-FeTiB	Z-FeTiB
	Feature	Groundmass	Groundmass	Groundmass	Groundmass	Groundmass	Groundmass	Variole	Variole	Variole	Variole	Variole	Groundmass	Groundmass	Groundmass	Variole	Variole
Probe data	**BaO wt%**	0.06	-0.02	0.02	-0.01	0.05	0.00	0.05	-0.10	0.05	0.05	0.04	0.05	-0.02	-0.06	-0.03	0.00
	K_2O wt%	0.08	0.05	0.06	0.08	0.08	0.08	0.06	0.06	0.06	0.06	0.06	0.05	0.07	0.19	0.05	0.04
	CaO wt%	7.95	0.20	4.95	7.57	6.71	6.86	4.78	5.88	6.44	7.11	6.57	6.64	3.50	7.84	5.23	9.81
	SrO wt%	0.05	0.05	0.13	0.16	0.02	0.07	0.11	0.17	0.08	0.10	0.14	0.05	0.08	0.13	0.14	0.16
	Na_2O wt%	6.83	11.90	8.97	7.02	7.77	7.81	7.20	8.35	7.86	7.34	7.91	7.94	9.70	7.03	8.70	5.86
	Al_2O_3 wt%	26.92	20.63	24.45	26.54	25.62	25.84	21.72	25.43	25.78	26.35	25.72	25.69	23.86	26.75	24.51	28.59
	SiO_2 wt%	58.01	72.03	62.78	57.35	60.79	59.89	66.67	61.84	60.79	58.87	60.06	60.69	65.05	58.38	62.30	55.96
	Total wt%	99.90	104.84	101.37	98.71	101.03	100.53	100.60	101.64	101.06	99.88	100.50	101.13	102.24	100.25	100.89	100.43
Calc.	**An %**	39	1	23	37	32	33	27	28	31	35	31	32	17	38	25	48
	Ab %	61	99	76	62	67	67	73	72	69	65	68	68	83	61	75	52
	Or %	0	0	0	0	0	0	0	0	0	0	0	0	0	1	0	0

	Probe ID	S037015_F _P130	S037015_F _P131	S037015_F _P132	S037015_F _P133	S037015_F _P134	S037015_F _P135	S037015_F _P136	S037015_F _P137	S037015_H _P138	S037015_H _P139	S037015_H _P140	S037015_H _P141	S037015_H _P142	S037015_H _P143	S037015_H _P144	S037015_H _P145
	Sample	S037015	S037015	S037015	S037015	S037015	S037015	S037015	S037015	S037015	S037015	S037015	S037015	S037015	S037015	S037015	S037015
	Rocktype	Z-FeTiB	Z-FeTiB	Z-FeTiB	Z-FeTiB	Z-FeTiB	Z-FeTiB	Z-FeTiB	Z-FeTiB	Z-FeTiB	Z-FeTiB	Z-FeTiB	Z-FeTiB	Z-FeTiB	Z-FeTiB	Z-FeTiB	Z-FeTiB
	Feature	Variole	Variole	Variole	Variole	Groundmass	Groundmass	Groundmass	Groundmass	Variole	Variole	Variole	Variole	Groundmass	Groundmass	Groundmass	Groundmass
Probe data	**BaO wt%**	-0.05	0.01	0.03	-0.01	0.08	-0.04	-0.07	0.04	0.00	0.06	-0.07	0.05	0.02	-0.03	0.04	-0.07
	K_2O wt%	0.06	0.06	0.05	0.06	1.90	0.07	0.07	0.07	0.06	0.41	0.07	0.04	0.06	0.09	0.06	0.06
	CaO wt%	7.41	5.71	7.50	6.54	6.22	7.00	6.59	5.88	7.41	5.99	5.60	6.93	9.29	3.88	8.11	8.35
	SrO wt%	0.15	0.11	0.13	0.05	0.11	0.06	0.14	0.08	0.07	0.07	0.09	0.19	0.13	0.20	0.11	0.09
	Na_2O wt%	7.17	8.20	7.57	7.82	6.01	7.64	7.89	8.35	7.45	7.90	8.67	7.79	6.36	9.87	7.13	7.05
	Al_2O_3 wt%	26.60	24.95	26.68	25.38	25.08	26.02	26.00	25.27	26.64	25.16	25.03	26.10	27.87	23.79	27.18	27.33
	SiO_2 wt%	59.24	60.33	58.53	59.53	55.27	59.63	60.81	61.30	59.01	59.90	61.47	59.28	56.60	65.58	58.12	57.91
	Total wt%	100.58	99.37	100.49	99.38	94.68	100.38	101.43	100.99	100.63	99.48	100.87	100.39	100.33	103.38	100.76	100.71
Calc.	**An %**	36	28	35	31	32	33	31	28	35	29	26	33	44	18	38	39
	Ab %	63	72	64	68	56	66	68	72	64	69	73	67	55	82	61	60
	Or %	0	0	0	0	12	0	0	0	0	2	0	0	0	0	0	0

Table A6. 7 Electron microprobe results for magnetite mineral chemistry and calculated mineral formulae based on 32 oxygens.

	Probe ID	9431_1_M 113	9431_1_M 114	9431_1_M 117	9431_1_M 118	9431_1_M 119	9431_1_M 120	9431_2_M 123	9431_2_M 124	9431_2_M 125	9431_2_M 126	9431_3_M 127	9431_3_M 128	9431_3_M 129	9431_3_M 130	9431_3_M 131	9431_3_M 132
	Sample	94-31	94-31	94-31	94-31	94-31	94-31	94-31	94-31	94-31	94-31	94-31	94-31	94-31	94-31	94-31	94-31
	Rocktype	HW-FeTiB	HW-FeTiB	HW-FeTiB	HW-FeTiB	HW-FeTiB	HW-FeTiB	HW-FeTiB	HW-FeTiB	HW-FeTiB	HW-FeTiB	HW-FeTiB	HW-FeTiB	HW-FeTiB	HW-FeTiB	HW-FeTiB	HW-FeTiB
Probe data	SiO_2 wt%	0.03	0.75	0.40	54.23	0.05	0.06	0.09	0.05	0.04	0.00	0.03	0.02	0.00	0.00	0.00	0.00
	TiO_2 wt%	0.01	0.29	2.42	0.26	0.02	0.40	0.30	0.51	0.34	0.28	0.10	-0.01	0.00	0.01	0.01	0.00
	Al_2O_3 wt%	0.02	0.29	0.14	0.01	0.03	0.01	0.03	0.01	0.01	0.01	0.00	-0.01	-0.01	0.00	-0.01	-0.01
	Cr_2O_3 wt%	0.00	0.01	0.01	0.00	0.04	0.02	0.00	0.00	0.00	0.00	0.03	0.00	0.00	0.02	0.02	0.03
	FeO wt%	91.09	89.34	3.50	42.42	90.82	90.68	91.07	91.22	91.09	90.97	91.48	91.25	91.97	91.84	91.58	91.39
	MnO wt%	-0.01	0.00	1.19	0.00	0.03	0.00	0.00	0.00	0.00	-0.02	0.00	0.01	-0.01	-0.01	0.01	0.01
	MgO wt%	0.00	0.22	1.21	0.01	0.00	0.00	0.00	0.00	0.00	0.00	0.01	0.01	0.00	0.01	0.01	0.00
	CaO wt%	0.26	0.28	59.03	0.39	0.90	0.18	0.03	0.13	0.01	0.01	0.27	0.18	0.15	0.04	0.24	0.65
	K_2O wt%	0.00	0.13	0.14	0.03	0.02	0.02	0.08	0.02	0.04	0.06	0.00	0.01	-0.01	0.00	0.00	0.00
	Nb_2O_5 wt%	0.00	0.03	-0.02	0.01	0.02	0.05	0.00	0.01	-0.01	0.02	0.03	0.04	0.00	0.00	-0.03	0.01
	ZnO wt%	0.01	0.01	0.00	-0.01	0.00	0.01	0.00	0.01	0.00	-0.01	-0.02	0.00	0.01	0.01	0.00	0.00
	CuO wt%	0.01	0.00	0.01	0.00	0.00	-0.01	0.01	0.00	0.01	0.00	0.00	-0.01	0.00	0.01	0.00	0.00
	NiO wt%	0.00	-0.01	-0.01	0.01	0.01	0.01	0.01	0.00	0.00	0.01	0.01	0.00	0.01	-0.01	-0.01	0.00
	CoO wt%	0.14	0.12	0.01	0.06	0.11	0.13	0.14	0.11	0.14	0.14	0.13	0.13	0.09	0.13	0.14	0.14
	SnO_2 wt%	-0.05	-0.01	-0.03	-0.10	-0.22	-0.08	-0.01	-0.01	-0.02	-0.01	-0.02	-0.22	-0.19	-0.01	-0.14	-0.10
	ZrO_2 wt%	0.00	-0.01	-0.01	0.09	-0.01	-0.01	0.04	0.01	0.00	0.00	0.00	-0.01	-0.03	0.00	-0.01	0.00
	P_2O_5 wt%	0.00	0.00	0.03	-0.01	0.00	0.00	0.00	0.00	-0.01	-0.01	0.00	0.00	0.00	0.00	0.00	0.00
	V_2O_3 wt%	0.24	0.20	0.03	0.09	0.23	0.23	0.25	0.25	0.22	0.24	0.23	0.24	0.27	0.24	0.26	0.25
	Total wt%	91.75	91.63	68.04	97.49	92.06	91.69	92.03	92.34	91.86	91.70	92.26	91.64	92.25	92.28	92.08	92.38
Calculated	Fe_2O3_%	67.68	65.21	3.50	0.00	68.03	66.71	67.11	66.96	67.11	67.18	67.82	67.74	68.25	68.09	68.08	68.32
	FeO_%	30.20	30.67	0.00	42.42	29.60	30.65	30.67	30.97	30.70	30.52	30.45	30.29	30.56	30.57	30.32	29.91
	Total_%	98.61	98.19	68.11	97.62	99.11	98.48	98.77	99.06	98.62	98.47	99.11	98.69	99.35	99.14	99.10	99.34
	Ti mol %	0.01	0.36	3.03	0.33	0.03	0.50	0.38	0.64	0.43	0.35	0.12	0.00	0.01	0.01	0.02	0.01
	Fe^{2+} mol %	42.03	42.69	0.00	59.04	41.21	42.67	42.70	43.11	42.73	42.48	42.39	42.16	42.53	42.55	42.21	41.63
	Fe^{3+} mol %	42.38	40.83	2.19	0.00	42.60	41.78	42.03	41.93	42.03	42.07	42.47	42.42	42.74	42.64	42.63	42.78
	Usp Mol%	0.03	0.86	-15.08	-0.82	0.06	1.17	0.89	1.49	1.01	0.83	0.28	0.00	0.01	0.02	0.04	0.01
	Ilm Mol%	0.00	0.00	0.00	0.00	0.00	0.00	0.00	0.00	0.00	0.00	0.00	0.00	0.00	0.00	0.00	0.00

	Probe ID	9431_3_M 133	9431_3_M 135	9431_3_M 136	9431_4_M 137	9431_4_M 138	9431_4_M 139	99362_2_I 33	99362_2_I 35	99362_2_I 36	99362_2_I 37	99362_2_I 38	99362_2_I 39	99362_2_I 40	99362_2_I 41	99362_2_I 43	99362_2_I 44
	Sample	94-31	94-31	94-31	94-31	94-31	94-31	99-362	99-362	99-362	99-362	99-362	99-362	99-362	99-362	99-362	99-362
	Rocktype	HW-FeTiB	HW-FeTiB	HW-FeTiB	HW-FeTiB	HW-FeTiB	HW-FeTiB	FW-FeB	FW-FeB	FW-FeB	FW-FeB	FW-FeB	FW-FeB	FW-FeB	FW-FeB	FW-FeB	FW-FeB
Probe data	SiO_2 wt%	0.02	0.05	0.23	0.00	0.41	0.06	0.23	0.05	0.19	3.69	0.56	1.46	0.04	0.04	0.16	0.49
	TiO_2 wt%	0.00	0.02	0.03	0.00	0.02	0.06	1.66	19.17	25.36	20.98	21.16	24.65	11.98	14.10	15.31	22.72
	Al_2O_3 wt%	0.00	0.00	0.14	-0.01	0.17	0.05	0.16	0.01	0.11	0.04	0.02	0.03	0.03	0.03	0.00	0.37
	Cr_2O_3 wt%	0.01	0.00	0.00	0.00	0.00	0.02	0.03	0.01	0.00	0.01	0.04	-0.01	0.00	0.01	0.03	-0.01
	FeO wt%	91.81	90.48	90.58	91.97	91.16	91.24	89.71	73.82	67.73	68.58	71.45	68.71	81.21	79.28	77.72	69.02
	MnO wt%	0.00	0.00	0.01	0.00	0.00	-0.01	0.05	0.91	1.34	1.07	1.05	1.26	0.60	0.75	0.76	1.64
	MgO wt%	0.00	0.01	0.00	0.01	0.15	0.03	0.02	0.01	0.04	0.01	0.01	0.00	0.00	0.00	0.00	0.15
	CaO wt%	0.23	0.01	0.61	0.01	0.03	0.01	0.02	0.05	0.05	0.10	0.02	0.07	0.01	0.01	0.02	0.08
	K_2O wt%	0.00	0.00	0.07	0.00	0.00	0.00	0.03	0.01	0.00	0.02	0.01	0.00	0.00	0.00	0.00	0.01
	Nb_2O_5 wt%	-0.02	0.01	0.04	0.01	0.02	0.03	0.01	0.03	0.00	0.05	0.01	0.01	0.00	-0.01	0.04	0.00
	ZnO wt%	0.00	0.01	0.00	0.01	0.02	0.00	0.01	0.01	0.02	0.02	0.02	0.01	0.01	0.03	0.03	0.01
	CuO wt%	0.00	0.00	-0.01	-0.01	-0.01	0.00	0.01	0.00	0.00	-0.01	0.00	0.00	0.00	0.01	0.00	0.00
	NiO wt%	0.00	-0.01	0.00	0.00	-0.01	0.01	0.01	-0.01	0.00	0.00	0.00	-0.01	0.01	0.00	0.00	0.00
	CoO wt%	0.13	0.12	0.11	0.13	0.13	0.13	0.14	0.13	0.09	0.10	0.08	0.11	0.11	0.10	0.11	0.08
	SnO_2 wt%	-0.09	-0.06	-0.13	-0.27	-0.18	-0.01	-0.03	-0.06	0.00	0.00	-0.16	-0.12	-0.03	-0.01	0.00	-0.16
	ZrO_2 wt%	0.00	-0.01	-0.02	-0.02	0.01	0.01	0.00	0.00	-0.01	0.19	0.00	0.01	0.00	-0.01	-0.01	0.01
	P_2O_5 wt%	0.00	-0.01	-0.01	0.00	0.00	0.00	-0.01	0.00	0.00	0.01	0.00	-0.01	0.01	0.00	0.00	0.00
	V_2O_3 wt%	0.27	0.27	0.25	0.25	0.26	0.25	0.38	0.42	0.42	0.39	0.43	0.41	0.41	0.42	0.42	0.38
	Total wt%	92.36	90.89	91.91	92.10	92.20	91.86	92.43	94.55	95.33	95.26	94.70	96.59	94.39	94.77	94.57	94.78
Calculated	Fe_2O3_%	68.21	66.93	67.30	68.15	66.91	67.39	63.91	29.70	17.02	16.96	24.45	16.40	44.49	40.37	37.39	21.23
	FeO_%	30.43	30.25	30.02	30.65	30.95	30.60	32.20	47.09	52.42	53.31	49.44	53.96	41.17	42.95	44.07	49.92
	Total_%	99.31	97.68	98.81	99.24	99.10	98.64	98.87	97.60	97.05	96.97	97.31	98.38	98.87	98.84	98.34	97.08
	Ti mol %	0.00	0.03	0.03	0.01	0.02	0.08	2.07	24.01	31.75	26.27	26.50	30.86	15.00	17.66	19.16	28.44
	Fe^{2+} mol %	42.36	42.11	41.78	42.66	43.08	42.59	44.83	65.55	72.96	74.21	68.83	75.11	57.31	59.79	61.35	69.49
	Fe^{3+} mol %	42.71	41.91	42.15	42.68	41.90	42.20	40.02	18.60	10.66	10.62	15.31	10.27	27.86	25.28	23.41	13.29
	Usp Mol%	0.00	0.07	0.07	0.01	0.05	0.18	4.95	55.90	74.60	70.68	62.99	74.69	34.71	40.75	44.61	67.92
	Ilm Mol%	0.00	0.00	0.00	0.00	0.00	0.00	0.00	0.00	0.00	0.00	0.00	0.00	0.00	0.00	0.00	0.00

	Probe ID	99362_2_I45	99362_2_I46	99362_2_I48	99362_2_I49	99362_2_I50	99362_2_I52	99362_2_I53	99362_2_I55	99362_2_I58	99362_2_I59	99362_2_I60	99362_2_I61	S037015_A_M140	S037015_A_M141	S037015_A_M142	S037015_A_M143
	Sample	99-362	99-362	99-362	99-362	99-362	99-362	99-362	99-362	99-362	99-362	99-362	99-362	S037015	S037015	S037015	S037015
	Rocktype	FW-FeB	FW-FeB	FW-FeB	FW-FeB	FW-FeB	FW-FeB	FW-FeB	FW-FeB	FW-FeB	FW-FeB	FW-FeB	FW-FeB	Z-FeTiB	Z-FeTiB	Z-FeTiB	Z-FeTiB
Probe data	**SiO_2 wt%**	0.58	0.07	0.47	0.14	0.19	0.22	0.05	0.07	0.09	1.25	3.75	1.56	0.10	0.06	0.57	0.30
	TiO_2 wt%	30.45	15.40	9.18	17.86	6.48	20.76	0.95	7.67	14.78	7.09	6.07	22.47	0.09	0.04	0.06	0.08
	Al_2O_3 wt%	0.44	0.03	0.38	0.03	0.06	0.16	0.02	0.04	0.04	0.13	0.05	0.59	0.07	0.03	0.05	0.16
	Cr_2O_3 wt%	0.00	0.02	0.01	0.00	0.03	0.01	0.02	0.03	0.00	0.00	-0.01	-0.01	-0.01	0.05	0.00	0.04
	FeO wt%	62.65	77.03	81.74	76.11	85.45	71.64	90.65	84.23	77.89	84.20	82.94	67.90	92.27	92.14	91.14	91.50
	MnO wt%	1.68	0.78	0.51	0.79	0.13	1.62	0.05	0.39	0.83	0.36	0.31	1.10	0.00	0.00	0.02	0.00
	MgO wt%	0.24	0.01	0.15	0.01	0.00	0.05	0.00	0.00	0.01	0.05	0.01	0.06	0.02	0.00	0.05	0.11
	CaO wt%	0.02	0.05	0.05	0.01	0.05	0.07	0.15	0.05	0.07	0.04	0.04	0.14	0.04	0.01	0.01	0.01
	K_2O wt%	0.03	0.01	0.06	0.00	0.01	0.02	0.00	0.01	0.01	0.01	0.00	0.09	0.00	0.00	0.04	0.02
	Nb_2O_5 wt%	0.05	0.05	0.02	0.09	0.03	0.00	0.02	0.03	0.07	0.00	0.00	0.05	0.01	-0.01	-0.02	0.03
	ZnO wt%	0.03	0.00	0.02	0.01	0.01	0.02	0.00	-0.01	0.00	0.01	0.00	0.02	0.00	0.00	-0.02	0.00
	CuO wt%	0.00	0.00	-0.01	0.01	0.00	0.00	-0.01	0.01	0.01	0.00	0.01	-0.01	0.00	0.00	0.00	0.00
	NiO wt%	0.00	0.00	0.00	-0.02	0.02	0.00	-0.01	-0.01	0.00	0.00	0.00	0.00	0.00	0.00	0.00	-0.01
	CoO wt%	0.08	0.08	0.11	0.12	0.11	0.08	0.14	0.13	0.10	0.12	0.10	0.08	0.12	0.14	0.13	0.13
	SnO_2 wt%	-0.03	-0.01	-0.05	0.00	-0.01	-0.02	-0.01	0.00	-0.01	-0.20	-0.10	0.01	-0.02	-0.24	-0.17	-0.01
	ZrO_2 wt%	0.16	0.01	-0.01	0.00	0.01	-0.01	0.02	0.00	0.00	0.00	-0.01	-0.01	0.00	0.01	0.01	0.00
	P_2O_5 wt%	0.00	0.01	0.00	0.00	0.00	0.01	0.00	0.00	0.00	0.00	0.00	0.00	0.00	-0.01	0.00	0.00
	V_2O_3 wt%	0.44	0.39	0.56	0.48	0.42	0.43	0.29	0.49	0.39	0.36	0.34	0.41	0.47	0.45	0.44	0.46
	Total wt%	96.83	93.94	93.19	95.65	92.96	95.05	92.33	93.14	94.28	93.41	93.52	94.46	93.18	92.66	92.31	92.83
Calculated	**Fe_2O3_%**	5.98	36.90	47.94	32.74	54.36	26.26	65.93	52.28	38.41	51.00	46.94	18.42	67.99	68.02	66.52	67.16
	FeO_%	57.26	43.83	38.60	46.64	36.53	48.02	31.33	37.19	43.33	38.31	40.70	51.32	31.09	30.93	31.28	31.07
	Total_%	97.47	97.65	98.07	98.95	98.43	97.72	98.96	98.39	98.14	98.72	98.34	96.33	100.02	99.74	99.18	99.58
	Ti mol %	38.13	19.28	11.50	22.36	8.11	25.99	1.19	9.61	18.51	8.88	7.60	28.13	0.11	0.06	0.08	0.10
	Fe^{2+} mol %	79.71	61.01	53.73	64.93	50.85	66.84	43.60	51.77	60.31	53.33	56.66	71.44	43.28	43.06	43.54	43.25
	Fe^{3+} mol %	3.75	23.11	30.02	20.50	34.04	16.44	41.28	32.74	24.05	31.93	29.39	11.54	42.57	42.59	41.65	42.05
	Usp Mol%	91.55	45.03	27.59	51.72	19.21	60.69	2.80	22.54	43.00	21.63	20.43	71.65	0.26	0.13	0.19	0.25
	Ilm Mol%	0.00	0.00	0.00	0.00	0.00	0.00	0.00	0.00	0.00	0.00	0.00	0.00	0.00	0.00	0.00	0.00

	Probe ID	S037015_A_M144	S037015_A_M145	S037015_A_M146	S037015_A_M147	S037015_A_M148	S037015_A_M149	S037015_A_M150	S037015_B_M151	S037015_B_M152	S037015_B_M153	S037015_B_M154	S037015_B_M155	S037015_B_M156	S037015_B_M157	S037015_B_M158	S037015_C_M159
	Sample	S037015	S037015	S037015	S037015	S037015	S037015	S037015	S037015	S037015	S037015	S037015	S037015	S037015	S037015	S037015	S037015
	Rocktype	Z-FeTiB	Z-FeTiB	Z-FeTiB	Z-FeTiB	Z-FeTiB	Z-FeTiB	Z-FeTiB	Z-FeTiB	Z-FeTiB	Z-FeTiB	Z-FeTiB	Z-FeTiB	Z-FeTiB	Z-FeTiB	Z-FeTiB	Z-FeTiB
Probe data	**SiO_2 wt%**	0.02	0.33	0.09	0.04	0.05	0.06	0.13	0.24	8.68	0.98	0.06	0.17	0.03	0.09	0.49	0.16
	TiO_2 wt%	0.11	0.16	0.16	0.18	0.12	0.14	0.14	-0.01	0.02	0.04	0.14	0.17	0.42	0.88	2.74	0.03
	Al_2O_3 wt%	0.04	0.12	0.01	0.01	0.04	0.02	0.06	0.00	0.01	0.47	0.00	0.05	0.03	0.00	0.01	0.02
	Cr_2O_3 wt%	0.05	0.01	0.01	0.04	0.00	0.05	0.06	-0.01	0.00	0.00	0.00	0.00	0.01	0.00	0.01	0.01
	FeO wt%	91.77	91.08	91.38	91.84	91.73	90.74	90.18	90.30	84.21	88.65	91.53	91.40	91.37	90.36	89.17	91.23
	MnO wt%	0.00	0.01	0.01	0.00	-0.01	0.01	-0.01	-0.01	-0.01	0.00	-0.01	-0.01	0.00	-0.01	0.03	0.00
	MgO wt%	0.00	0.08	0.01	0.00	0.00	0.00	0.00	0.00	0.00	0.34	0.00	0.04	0.00	0.01	0.00	0.01
	CaO wt%	0.01	0.01	0.07	0.02	0.03	0.13	0.08	0.01	0.02	0.06	0.01	0.05	0.06	0.05	0.05	0.00
	K_2O wt%	0.01	0.09	0.01	0.02	0.01	0.01	0.01	0.01	0.00	0.02	0.06	0.04	0.06	0.03	0.01	0.00
	Nb_2O_5 wt%	-0.02	0.02	0.02	-0.01	0.03	0.05	0.02	0.02	0.00	0.05	0.04	-0.02	-0.02	0.01	0.03	0.04
	ZnO wt%	0.00	0.02	-0.01	0.01	0.02	0.00	0.02	0.00	0.03	-0.01	0.01	0.01	0.03	0.01	-0.01	0.00
	CuO wt%	-0.01	0.00	0.00	0.00	-0.01	0.00	0.01	0.00	0.00	0.00	-0.02	-0.01	0.01	0.00	0.01	0.00
	NiO wt%	0.00	0.01	0.00	0.00	0.00	0.00	0.00	0.01	0.00	-0.01	-0.01	0.01	0.02	-0.01	0.00	-0.01
	CoO wt%	0.12	0.14	0.13	0.14	0.11	0.13	0.11	0.14	0.14	0.11	0.14	0.10	0.12	0.11	0.14	0.15
	SnO_2 wt%	-0.01	-0.01	-0.27	-0.01	-0.01	-0.01	-0.10	-0.02	-0.05	-0.04	-0.01	-0.15	-0.01	-0.02	-0.20	0.00
	ZrO_2 wt%	0.01	0.00	0.07	0.01	0.00	0.01	-0.01	0.01	0.00	0.00	0.00	0.00	-0.01	-0.02	0.70	0.01
	P_2O_5 wt%	0.00	0.00	0.02	0.00	0.00	0.01	0.00	-0.01	0.01	0.00	0.00	0.00	-0.01	-0.01	0.05	0.00
	V_2O_3 wt%	0.44	0.38	0.40	0.43	0.41	0.39	0.65	0.07	0.14	0.17	0.35	0.41	0.36	0.38	0.29	0.36
	Total wt%	92.54	92.45	92.12	92.71	92.52	91.76	91.36	90.75	93.19	90.84	92.30	92.25	92.47	91.86	93.51	92.00
Calculated	**Fe_2O3_%**	67.71	66.93	67.23	67.72	67.64	66.91	66.28	66.54	47.05	64.15	67.59	67.29	67.28	65.69	60.87	67.19
	FeO_%	30.84	30.86	30.89	30.90	30.86	30.53	30.54	30.43	41.87	30.93	30.70	30.85	30.83	31.25	34.40	30.77
	Total_%	99.36	99.17	99.13	99.52	99.33	98.48	98.11	97.47	97.97	97.33	99.12	99.18	99.25	98.51	99.82	98.75
	Ti mol %	0.14	0.20	0.21	0.22	0.15	0.18	0.18	0.00	0.02	0.05	0.18	0.21	0.53	1.11	3.44	0.04
	Fe^{2+} mol %	42.92	42.95	42.99	43.01	42.96	42.50	42.51	42.35	58.28	43.05	42.74	42.94	42.92	43.50	47.88	42.83
	Fe^{3+} mol %	42.40	41.91	42.10	42.41	42.36	41.90	41.50	41.67	29.46	40.17	42.33	42.13	42.13	41.13	38.12	42.08
	Usp Mol%	0.33	0.49	0.48	0.53	0.34	0.43	0.42	0.00	0.08	0.11	0.41	0.50	1.24	2.62	8.18	0.09
	Ilm Mol%	0.00	0.00	0.00	0.00	0.00	0.00	0.00	0.00	0.00	0.00	0.00	0.00	0.00	0.00	0.00	0.00

	Probe ID	S037015_C_M160	S037015_C_M161	S037015_C_M162	S037015_D_M163	S037015_D_M164	S037015_D_M165	S037015_D_M166	S037015_D_M167	S037015_D_M168	S037015_E_M169	S037015_E_M170	S037015_E_M171	S037015_E_M172	S037015_E_M173	S037015_E_M174	S037015_E_M175
	Sample	S037015	S037015	S037015	S037015	S037015	S037015	S037015	S037015	S037015	S037015	S037015	S037015	S037015	S037015	S037015	S037015
	Rocktype	Z-FeTiB	Z-FeTiB	Z-FeTiB	Z-FeTiB	Z-FeTiB	Z-FeTiB	Z-FeTiB	Z-FeTiB	Z-FeTiB	Z-FeTiB	Z-FeTiB	Z-FeTiB	Z-FeTiB	Z-FeTiB	Z-FeTiB	Z-FeTiB
Probe data	SiO_2 wt%	0.17	0.16	0.22	0.08	0.18	0.06	3.26	0.10	0.06	2.10	0.45	0.68	0.15	0.05	0.02	0.01
	TiO_2 wt%	0.03	0.00	0.01	0.29	0.16	0.26	0.19	0.19	0.41	0.00	0.03	1.11	1.46	1.86	0.04	0.05
	Al_2O_3 wt%	0.02	0.01	0.03	0.03	0.04	0.04	0.04	0.03	0.00	1.16	0.02	0.06	0.02	0.00	0.03	0.01
	Cr_2O_3 wt%	0.03	0.00	0.04	0.00	0.03	-0.01	0.04	0.00	0.01	0.00	0.00	0.02	-0.01	0.01	0.03	0.03
	FeO wt%	90.32	90.03	90.19	91.46	91.67	91.45	88.22	91.08	91.12	87.25	90.27	90.61	91.50	91.21	91.75	91.90
	MnO wt%	0.00	-0.01	0.01	-0.01	0.00	0.00	-0.02	0.00	0.01	0.03	0.00	0.02	0.00	0.02	0.00	0.01
	MgO wt%	0.00	0.00	0.01	0.00	0.04	0.00	0.00	0.00	0.00	0.94	0.00	0.18	0.01	0.00	-0.01	0.00
	CaO wt%	0.01	0.01	0.01	0.08	0.07	0.06	0.05	0.06	0.07	0.01	0.01	0.02	0.04	0.01	0.01	0.05
	K_2O wt%	0.00	0.00	0.00	0.07	0.03	0.02	0.05	0.01	0.03	0.01	0.00	0.02	0.04	0.03	0.00	0.00
	Nb_2O_5 wt%	0.05	0.03	0.02	0.02	0.01	0.03	0.01	0.02	0.02	0.03	0.03	0.05	0.00	0.05	0.01	0.02
	ZnO wt%	0.01	0.01	0.00	0.00	0.02	0.01	0.02	0.01	0.01	0.01	0.00	0.00	-0.01	0.00	-0.02	0.01
	CuO wt%	-0.01	0.00	0.00	0.00	0.01	0.00	0.01	-0.01	0.01	0.00	0.00	0.01	0.00	0.00	-0.01	-0.01
	NiO wt%	-0.01	0.00	-0.01	0.01	0.00	-0.01	0.00	0.01	0.00	-0.01	0.00	0.00	0.01	0.01	0.01	0.00
	CoO wt%	0.13	0.13	0.13	0.11	0.15	0.13	0.14	0.08	0.11	0.11	0.14	0.13	0.11	0.14	0.11	0.14
	SnO_2 wt%	-0.01	0.00	-0.04	-0.03	-0.15	-0.02	-0.07	0.00	-0.09	-0.11	-0.11	-0.02	-0.05	-0.05	-0.01	-0.16
	ZrO_2 wt%	-0.01	-0.01	-0.01	0.06	0.01	0.00	0.01	0.00	0.01	-0.02	-0.01	-0.01	0.13	0.01	-0.01	0.00
	P_2O_5 wt%	0.00	0.01	0.00	0.00	0.01	0.00	0.00	0.00	0.00	0.00	0.00	0.00	0.00	-0.01	0.00	-0.01
	V_2O_3 wt%	0.43	0.41	0.50	0.37	0.39	0.37	0.36	0.41	0.37	0.17	0.22	0.35	0.36	0.35	0.43	0.38
	Total wt%	91.14	90.79	91.11	92.52	92.68	92.40	92.30	92.02	92.13	91.69	91.05	93.22	93.76	93.67	92.40	92.46
Calculated	Fe_2O3_%	66.44	66.33	66.30	67.36	67.46	67.34	59.44	67.01	66.92	61.61	66.02	64.63	65.55	65.03	67.78	67.96
	FeO_%	30.54	30.34	30.52	30.84	30.97	30.86	34.73	30.78	30.90	31.82	30.86	32.45	32.51	32.70	30.76	30.75
	Total_%	97.84	97.46	97.81	99.32	99.59	99.19	98.34	98.75	98.92	98.00	97.80	99.73	100.39	100.25	99.25	99.44
	Ti mol %	0.03	0.00	0.02	0.37	0.20	0.32	0.23	0.24	0.52	0.00	0.03	1.39	1.83	2.32	0.05	0.07
	Fe^{2+} mol %	42.51	42.23	42.49	42.93	43.10	42.96	48.34	42.85	43.01	44.29	42.96	45.17	45.26	45.52	42.81	42.80
	Fe^{3+} mol %	41.60	41.54	41.52	42.18	42.24	42.17	37.22	41.96	41.91	38.58	41.34	40.47	41.05	40.72	42.45	42.56
	Usp Mol%	0.08	0.01	0.04	0.86	0.48	0.76	0.62	0.57	1.22	0.01	0.08	3.29	4.26	5.40	0.11	0.16
	Ilm Mol%	0.00	0.00	0.00	0.00	0.00	0.00	0.00	0.00	0.00	0.00	0.00	0.00	0.00	0.00	0.00	0.00

	Probe ID	S037015_F_M176	S037015_F_M177	S037015_F_M178	S037015_F_M179	S037015_F_M180	S037015_G_M181	S037015_G_M182	S037015_G_M183	S037015_H_M184	S037015_H_M185	S037015_H_M186	S037015_H_M188	S037015_H_M189	S037015_H_M190	S037015__1B_M25	S037015__1B_M26
	Sample	S037015	S037015	S037015	S037015	S037015	S037015	S037015	S037015	S037015	S037015	S037015	S037015	S037015	S037015	S037015	S037015
	Rocktype	Z-FeTiB	Z-FeTiB	Z-FeTiB	Z-FeTiB	Z-FeTiB	Z-FeTiB	Z-FeTiB	Z-FeTiB	Z-FeTiB	Z-FeTiB	Z-FeTiB	Z-FeTiB	Z-FeTiB	Z-FeTiB	Z-FeTiB	Z-FeTiB
Probe data	SiO_2 wt%	0.20	0.21	0.05	0.39	0.07	0.05	0.03	0.10	0.14	0.34	0.09	0.44	0.01	0.60	0.09	2.65
	TiO_2 wt%	0.00	-0.01	0.71	1.46	0.35	0.09	0.08	0.07	0.00	0.01	0.01	1.23	1.58	0.09	0.62	1.96
	Al_2O_3 wt%	0.03	-0.01	0.03	0.04	0.02	0.07	0.07	0.04	0.02	0.16	0.04	0.15	0.01	0.04	0.05	0.02
	Cr_2O_3 wt%	0.00	0.00	0.04	0.01	0.01	-0.01	0.00	0.00	0.05	0.00	0.05	0.00	0.00	0.02	0.00	0.04
	FeO wt%	90.77	59.14	91.49	90.50	90.54	92.30	92.19	91.85	91.57	90.84	91.15	91.20	91.39	90.82	91.43	87.61
	MnO wt%	0.00	-0.01	0.00	0.02	0.01	0.00	-0.01	-0.02	0.00	-0.01	-0.01	0.02	0.01	-0.03	0.01	0.05
	MgO wt%	0.00	0.01	0.00	0.00	0.00	0.00	0.00	-0.01	0.00	0.02	0.01	0.00	0.00	0.00	0.00	0.00
	CaO wt%	0.02	0.00	0.03	0.06	0.27	0.01	0.00	0.00	0.02	0.04	0.07	0.06	0.03	0.12	0.02	0.01
	K_2O wt%	0.01	0.07	0.01	0.02	0.02	0.00	0.00	0.00	0.01	0.04	0.01	0.02	0.02	0.05	0.02	0.03
	Nb_2O_5 wt%	0.02	-0.06	0.00	0.01	0.04	0.03	0.00	0.01	0.01	0.01	0.01	0.02	0.01	0.03	0.04	0.03
	ZnO wt%	-0.01	-0.02	0.01	0.02	0.00	-0.01	0.00	0.01	0.00	0.00	-0.01	0.00	0.02	0.00	0.00	0.01
	CuO wt%	0.00	0.01	0.00	0.00	-0.01	0.00	-0.01	0.00	0.04	0.01	0.00	0.00	-0.01	0.00	-0.01	-0.01
	NiO wt%	0.00	0.01	0.01	0.00	0.02	0.00	0.00	0.00	0.00	0.01	0.01	0.00	-0.01	0.02	0.01	0.01
	CoO wt%	0.12	0.09	0.11	0.11	0.15	0.13	0.15	0.14	0.11	0.11	0.11	0.13	0.13	0.10	0.13	0.13
	SnO_2 wt%	-0.01	0.00	-0.22	-0.10	-0.16	0.00	0.00	-0.05	-0.01	-0.17	-0.06	-0.01	-0.03	-0.03	-0.18	-0.01
	ZrO_2 wt%	0.00	-0.03	-0.01	0.05	0.00	-0.01	0.01	0.00	-0.01	-0.01	-0.01	0.00	0.03	0.00	0.01	0.00
	P_2O_5 wt%	0.00	0.00	0.00	0.00	-0.01	0.01	-0.01	0.00	0.01	0.00	0.00	0.00	0.00	0.00	0.00	0.01
	V_2O_3 wt%	0.18	0.00	0.36	0.29	0.38	0.24	0.19	0.20	0.44	0.43	0.41	0.37	0.32	0.35	0.39	0.34
	Total wt%	91.34	59.42	92.63	92.88	91.69	92.89	92.70	92.34	92.39	91.83	91.89	93.64	93.50	92.18	92.60	92.89
Calculated	Fe_2O3_%	66.92	43.75	66.75	64.45	66.70	68.10	68.16	67.77	67.53	66.69	67.36	65.12	65.63	66.25	66.71	57.62
	FeO_%	30.55	19.78	31.43	32.50	30.51	31.02	30.86	30.86	30.80	30.83	30.54	32.60	32.33	31.21	31.40	35.76
	Total_%	98.06	63.93	99.55	99.43	98.56	99.75	99.56	99.22	99.18	98.69	98.72	100.18	100.12	98.87	99.49	98.68
	Ti mol %	0.00	0.00	0.89	1.83	0.44	0.11	0.10	0.09	0.00	0.02	0.01	1.53	1.97	0.11	0.77	2.46
	Fe^{2+} mol %	42.52	27.53	43.75	45.24	42.48	43.18	42.96	42.96	42.88	42.92	42.50	45.38	45.01	43.44	43.70	49.78
	Fe^{3+} mol %	41.91	27.39	41.80	40.36	41.77	42.64	42.68	42.44	42.29	41.76	42.18	40.78	41.10	41.48	41.78	36.08
	Usp Mol%	0.01	0.00	2.08	4.33	1.04	0.26	0.23	0.22	0.00	0.04	0.02	3.64	4.58	0.26	1.81	6.38
	Ilm Mol%	0.00	0.00	0.00	0.00	0.00	0.00	0.00	0.00	0.00	0.00	0.00	0.00	0.00	0.00	0.00	0.00

	Probe ID	S037015_2_M27	S037015_2_M28	S037015_2_M29	S037015_2_M30	S037015_2_M31	S037015_2_M32	S037015_2_M33	S037015_2_M34	S037015_2_M35	S037015_2_M36	S037015_2_M37	S037015_2_M38	S037015_2_M39	S037015_4_M40	S037015_4_M41	S037015_5_M44
	Sample	S037015	S037015	S037015	S037015	S037015	S037015	S037015	S037015	S037015	S037015	S037015	S037015	S037015	S037015	S037015	S037015
	Rocktype	Z-FeTiB	Z-FeTiB	Z-FeTiB	Z-FeTiB	Z-FeTiB	Z-FeTiB	Z-FeTiB	Z-FeTiB	Z-FeTiB	Z-FeTiB	Z-FeTiB	Z-FeTiB	Z-FeTiB	Z-FeTiB	Z-FeTiB	Z-FeTiB
Probe data	SiO_2 wt%	0.17	0.28	26.21	29.58	0.27	1.18	0.21	0.16	0.05	0.10	0.08	0.04	0.07	0.07	0.06	0.12
	TiO_2 wt%	0.04	0.07	0.00	0.00	0.04	0.02	0.00	0.01	0.25	0.24	0.23	0.09	0.19	0.06	0.10	0.03
	Al_2O_3 wt%	0.05	0.10	9.20	11.52	0.09	0.04	0.05	0.04	0.03	0.05	0.03	0.03	0.02	0.04	0.09	0.04
	Cr_2O_3 wt%	0.04	0.00	0.02	0.00	0.03	0.00	0.00	0.02	0.00	0.00	0.06	0.01	-0.01	-0.01	0.00	0.04
	FeO wt%	90.53	90.14	52.29	51.96	89.75	89.34	90.21	90.20	91.43	91.08	91.41	91.34	90.49	92.08	91.76	92.41
	MnO wt%	-0.01	0.01	-0.01	0.00	0.00	0.00	-0.01	0.00	-0.01	0.00	-0.01	0.00	-0.01	0.00	0.00	-0.01
	MgO wt%	0.00	0.00	0.00	0.00	0.01	0.01	0.02	0.00	0.00	0.00	-0.01	0.00	0.00	0.01	0.01	0.00
	CaO wt%	0.01	0.03	2.41	2.23	0.03	0.04	0.03	0.05	0.06	0.09	0.03	0.02	0.07	0.02	0.01	0.01
	K_2O wt%	0.00	0.00	0.07	0.02	0.01	0.00	0.01	0.00	0.03	0.01	0.02	0.02	0.04	0.00	0.00	0.00
	Nb_2O_5 wt%	0.00	0.05	0.05	0.03	0.03	-0.02	0.00	0.02	0.00	-0.03	0.04	0.04	0.03	0.02	0.03	0.00
	ZnO wt%	0.01	0.04	0.00	0.01	0.00	-0.01	-0.02	-0.01	0.00	0.00	0.02	0.02	-0.02	-0.01	0.00	0.00
	CuO wt%	0.01	0.00	-0.01	-0.01	0.00	0.01	0.00	0.01	0.01	0.00	0.01	0.00	0.01	0.01	0.01	0.00
	NiO wt%	0.01	0.00	0.00	-0.01	0.00	0.00	-0.01	0.01	0.00	-0.01	0.00	0.01	0.01	-0.01	0.00	0.00
	CoO wt%	0.13	0.11	0.07	0.08	0.12	0.12	0.11	0.13	0.13	0.14	0.12	0.14	0.12	0.13	0.12	0.13
	SnO_2 wt%	-0.01	-0.17	-0.03	-0.01	-0.12	-0.02	-0.19	-0.02	-0.20	-0.02	-0.13	-0.02	0.00	-0.01	0.00	-0.02
	ZrO_2 wt%	-0.01	-0.01	0.01	0.00	-0.01	0.01	-0.01	0.00	0.00	-0.01	0.04	0.00	0.01	0.00	0.00	0.00
	P_2O_5 wt%	-0.01	0.00	0.01	0.01	0.00	0.00	0.00	0.00	0.00	0.00	0.00	0.00	0.00	0.00	0.00	0.01
	V_2O_3 wt%	0.39	0.25	0.19	0.20	0.26	0.30	0.32	0.31	0.40	0.42	0.43	0.41	0.36	0.32	0.25	0.41
	Total wt%	91.37	90.89	90.47	95.62	90.50	91.02	90.71	90.92	92.15	92.09	92.37	92.16	91.39	92.72	92.43	93.14
Calculated	Fe_2O3_%	66.66	66.14	0.00	0.00	65.93	64.08	66.46	66.50	67.39	67.03	67.17	67.46	66.74	67.98	67.69	68.13
	FeO_%	30.54	30.62	52.29	51.96	30.42	31.68	30.41	30.36	30.79	30.77	30.97	30.64	30.43	30.91	30.85	31.11
	Total_%	98.07	97.70	90.52	95.65	97.24	97.50	97.61	97.61	99.13	98.86	99.25	98.94	98.11	99.57	99.22	100.01
	Ti mol %	0.05	0.09	0.00	0.00	0.05	0.02	0.00	0.01	0.31	0.30	0.29	0.12	0.23	0.07	0.12	0.03
	Fe^{2+} mol %	42.51	42.62	72.78	72.33	42.34	44.10	42.32	42.26	42.86	42.83	43.11	42.65	42.36	43.03	42.95	43.30
	Fe^{3+} mol %	41.74	41.42	0.00	0.00	41.29	40.13	41.62	41.64	42.20	41.97	42.06	42.24	41.80	42.57	42.38	42.66
	Usp Mol%	0.12	0.21	0.00	0.00	0.12	0.05	0.00	0.03	0.73	0.71	0.68	0.28	0.56	0.17	0.29	0.07
	Ilm Mol%	0.00	0.00	0.00	0.00	0.00	0.00	0.00	0.00	0.00	0.00	0.00	0.00	0.00	0.00	0.00	0.00

	Probe ID	S037015_5_M45focus	S037015_6_M47	S037015_7_M48	S037015_7_M49	S037015_7_M50	S037015_5_M45	S039313_1_I20	S039313_4_I24	S039313_4_I25	S039313_4_I26	S039313_1_M51	S039313_1_M52	S039313_1_M53	S039313_1_M54	S039313_1_M55	S039313_3_M56
	Sample	S037015	S037015	S037015	S037015	S037015	S037015_nonfocus	S039313	S039313	S039313	S039313	S039313	S039313	S039313	S039313	S039313	S039313
	Rocktype	Z-FeTiB	Z-FeTiB	Z-FeTiB	Z-FeTiB	Z-FeTiB	Z-FeTiB	HW-FeTiB	HW-FeTiB	HW-FeTiB	HW-FeTiB	HW-FeTiB	HW-FeTiB	HW-FeTiB	HW-FeTiB	HW-FeTiB	HW-FeTiB
Probe data	SiO_2 wt%	0.34	0.06	0.09	0.08	0.11	0.33	7.41	1.14	0.37	2.31	0.02	0.02	1.40	0.00	0.02	0.02
	TiO_2 wt%	0.03	0.34	0.06	0.09	0.67	0.04	7.39	8.30	8.94	7.31	0.02	0.02	0.42	0.10	0.03	0.02
	Al_2O_3 wt%	0.10	0.04	0.02	0.04	0.02	0.09	0.02	0.60	0.06	0.01	0.01	0.02	0.02	0.03	0.03	0.02
	Cr_2O_3 wt%	0.03	0.04	0.00	0.01	0.04	0.00	0.00	0.00	0.01	0.02	-0.01	0.00	0.00	0.00	0.01	0.01
	FeO wt%	91.62	91.95	91.07	91.41	91.59	91.62	76.98	80.24	79.68	80.24	91.69	91.79	35.82	92.44	89.42	92.53
	MnO wt%	0.01	-0.01	0.00	0.00	0.01	0.00	0.01	0.00	0.00	0.00	-0.01	0.01	0.22	0.00	0.00	-0.02
	MgO wt%	0.03	-0.01	0.00	0.00	0.00	0.03	0.00	0.01	0.01	0.00	0.00	0.00	0.38	0.00	0.00	-0.01
	CaO wt%	0.01	0.06	0.13	0.07	0.05	0.01	0.02	0.01	0.02	0.02	0.19	0.25	26.52	0.00	0.00	0.00
	K_2O wt%	0.03	0.02	0.05	0.03	0.04	0.03	0.00	0.22	0.02	0.01	0.02	0.01	0.09	0.00	0.00	0.00
	Nb_2O_5 wt%	0.01	-0.01	0.03	0.02	0.00	0.01	-0.02	0.00	0.02	0.06	0.02	-0.01	-0.02	-0.01	0.01	0.03
	ZnO wt%	0.01	0.01	-0.02	0.02	-0.01	0.00	0.00	0.02	0.01	0.01	0.00	-0.01	-0.01	0.03	-0.01	0.00
	CuO wt%	0.01	0.00	0.00	0.00	-0.01	0.00	0.00	0.01	-0.02	0.01	0.00	0.01	-0.01	0.00	0.01	-0.01
	NiO wt%	-0.01	0.02	0.00	0.00	0.01	0.01	0.00	0.01	0.00	0.01	0.01	0.01	0.00	0.00	0.01	0.00
	CoO wt%	0.14	0.14	0.10	0.11	0.12	0.11	0.11	0.08	0.12	0.11	0.11	0.12	0.04	0.13	0.12	0.13
	SnO_2 wt%	-0.27	-0.01	-0.18	-0.09	-0.03	-0.21	-0.01	-0.02	-0.01	0.00	-0.01	-0.20	0.00	-0.12	-0.11	-0.14
	ZrO_2 wt%	-0.01	-0.01	0.02	0.01	0.12	0.02	0.07	0.00	0.00	0.00	0.01	-0.01	0.00	0.00	0.01	-0.02
	P_2O_5 wt%	0.00	-0.01	0.04	0.00	0.00	-0.01	0.00	0.00	0.00	0.01	0.00	0.00	0.02	0.00	0.00	0.01
	V_2O_3 wt%	0.41	0.32	0.39	0.39	0.36	0.41	0.64	0.30	0.28	0.28	0.12	0.13	0.03	0.14	0.15	0.13
	Total wt%	92.49	92.94	91.81	92.21	93.10	92.50	92.61	90.93	89.51	90.41	92.21	92.16	64.93	92.73	89.68	92.71
Calculated	Fe_2O3_%	67.25	67.66	67.26	67.51	66.78	67.24	33.87	46.68	46.45	45.53	68.12	68.24	35.82	68.40	66.20	68.46
	FeO_%	31.11	31.06	30.54	30.67	31.50	31.12	46.50	38.24	37.88	39.28	30.39	30.38	0.00	30.90	29.85	30.93
	Total_%	99.52	99.77	98.75	99.06	99.84	99.45	96.04	95.63	94.20	94.97	99.06	99.21	64.98	99.72	96.44	99.76
	Ti mol %	0.04	0.43	0.08	0.12	0.83	0.05	9.25	10.39	11.20	9.15	0.03	0.03	0.53	0.12	0.04	0.02
	Fe^{2+} mol %	43.30	43.24	42.51	42.69	43.85	43.32	64.72	53.22	52.73	54.67	42.30	42.29	0.00	43.01	41.55	43.05
	Fe^{3+} mol %	42.11	42.37	42.12	42.27	41.82	42.10	21.21	29.23	29.09	28.51	42.66	42.73	22.43	42.83	41.46	42.87
	Usp Mol%	0.10	1.00	0.18	0.27	1.95	0.12	30.39	26.88	27.86	24.30	0.06	0.07	-0.56	0.29	0.08	0.05
	Ilm Mol%	0.00	0.00	0.00	0.00	0.00	0.00	0.00	0.00	0.00	0.00	0.00	0.00	0.00	0.00	0.00	0.00

	Probe ID	S039313_3_M57	S039313_3_M58	S039313_4_M59	S039313_5_M60	S039313_5_M61	W605013_4_C	W605013_4_R	W605013_2_M10	W605013_3_M13	W605013_1_M15focus	W605013_1_M15	W605013_1_M16focus	W605013_1_M16	W605013_1_M17	W605013_1_M22	W605013_1_M23
	Sample	S039313	S039313	S039313	S039313	S039313	W605013	W605013	W605013	W605013	W605013	W605013	W605013	W605013	W605013	W605013	W605013
	Rocktype	HW-FeTiB	HW-FeTiB	HW-FeTiB	HW-FeTiB	HW-FeTiB	Iron formation	Iron formation	Iron formation	Iron formation	Iron formation	Iron formation	Iron formation	Iron formation	Iron formation	Iron formation	Iron formation
Probe data	SiO_2 wt%	0.03	0.34	0.15	0.07	0.04	0.27	0.14	0.05	0.15	0.20	0.15	0.03	0.03	0.41	0.30	0.50
	TiO_2 wt%	0.04	0.05	0.05	0.14	0.26	0.01	0.00	0.02	0.01	0.01	0.01	0.01	0.02	0.01	0.00	0.00
	Al_2O_3 wt%	0.03	0.21	0.08	0.01	0.00	0.07	0.05	0.01	0.01	0.01	0.01	-0.01	0.00	0.03	0.01	0.01
	Cr_2O_3 wt%	0.00	0.00	0.01	0.00	0.00	0.00	0.01	0.02	0.01	0.01	0.01	-0.01	0.01	0.00	0.00	0.01
	FeO wt%	92.29	91.68	91.67	91.73	91.84	91.45	91.49	90.95	91.72	91.77	91.61	91.17	91.30	91.36	91.83	91.42
	MnO wt%	0.00	-0.02	-0.01	0.01	-0.01	0.03	0.03	0.04	0.04	0.04	0.04	0.03	0.01	0.04	0.06	0.06
	MgO wt%	0.00	0.00	0.02	0.00	0.00	0.00	0.03	0.00	0.01	0.03	0.04	0.01	0.00	0.09	0.00	0.01
	CaO wt%	0.00	0.00	0.01	0.00	0.05	0.00	0.00	0.01	0.00	0.00	0.00	0.01	0.00	0.01	0.00	0.01
	K_2O wt%	0.01	0.12	0.00	0.03	0.00	0.01	0.05	0.00	0.00	0.00	0.00	0.00	0.00	-0.01	-0.01	0.00
	Nb_2O_5 wt%	0.03	0.00	0.03	-0.01	0.04	0.02	-0.02	0.03	0.02	0.00	0.01	-0.01	-0.02	0.04	0.03	0.01
	ZnO wt%	0.02	0.01	0.02	0.01	0.02	0.01	0.00	0.01	0.02	0.00	0.01	0.01	0.01	0.02	0.00	0.02
	CuO wt%	0.00	0.00	-0.01	0.00	-0.01	0.01	-0.01	0.00	0.00	0.00	0.00	0.01	0.00	0.00	0.00	0.01
	NiO wt%	0.01	0.01	0.00	0.01	0.01	0.00	0.00	0.01	0.03	0.01	0.00	0.00	0.00	-0.02	0.00	-0.01
	CoO wt%	0.11	0.12	0.13	0.12	0.13	0.11	0.12	0.14	0.12	0.13	0.13	0.09	0.13	0.14	0.12	0.14
	SnO_2 wt%	-0.02	-0.15	-0.12	-0.09	-0.04	-0.01	-0.06	0.00	-0.02	-0.01	-0.16	0.00	-0.14	-0.14	-0.17	0.00
	ZrO_2 wt%	0.00	-0.01	0.00	-0.01	0.00	0.00	0.00	-0.02	-0.01	-0.01	-0.01	-0.01	0.00	0.01	0.00	0.00
	P_2O_5 wt%	-0.01	0.00	-0.01	0.00	0.01	0.00	0.00	0.00	0.00	0.00	0.00	0.00	0.01	0.00	0.00	0.00
	V_2O_3 wt%	0.14	0.14	0.13	0.10	0.12	0.07	0.06	0.20	0.05	0.04	0.05	0.03	0.06	0.05	0.05	0.04
	Total wt%	92.67	92.51	92.15	92.13	92.48	92.04	91.88	91.44	92.15	92.23	91.91	91.38	91.43	92.05	92.19	92.22
Calculated	Fe_2O3_%	68.29	67.54	67.59	67.80	67.66	67.31	67.78	67.31	67.78	67.75	67.73	67.59	67.64	67.12	67.57	66.98
	FeO_%	30.85	30.90	30.85	30.72	30.96	30.88	30.50	30.38	30.73	30.81	30.67	30.35	30.44	30.96	31.02	31.15
	Total_%	99.55	99.46	99.07	99.03	99.31	98.80	98.77	98.21	98.97	99.05	98.86	98.18	98.37	98.94	99.17	98.95
	Ti mol %	0.04	0.07	0.07	0.17	0.33	0.01	0.00	0.02	0.02	0.02	0.01	0.01	0.03	0.02	0.00	0.01
	Fe^{2+} mol %	42.94	43.02	42.95	42.76	43.09	42.98	42.46	42.28	42.77	42.88	42.69	42.25	42.37	43.10	43.18	43.36
	Fe^{3+} mol %	42.76	42.29	42.32	42.46	42.37	42.15	42.44	42.15	42.44	42.42	42.41	42.32	42.36	42.03	42.32	41.94
	Usp Mol%	0.10	0.16	0.16	0.40	0.77	0.03	0.00	0.05	0.04	0.04	0.02	0.03	0.07	0.04	0.00	0.01
	Ilm Mol%	0.00	0.00	0.00	0.00	0.00	0.00	0.00	0.00	0.00	0.00	0.00	0.00	0.00	0.00	0.00	0.00

	Probe ID	W605013_4_M4	W605013_4_M5	W605013_4_M7	W605013_2_M8	W605013_2_M9	W605041_1_M62	W605041_1_M63	W605041_1_M64	W605041_1_M65	W605041_1_M66	W605041_1_M67	W605041_1_M68	W605041_1_M69	W605041_1_M70	W605041_1_M71	W605041_1_M72
	Sample	W605013	W605013	W605013	W605013	W605013	W605041	W605041	W605041	W605041	W605041	W605041	W605041	W605041	W605041	W605041	W605041
	Rocktype	Iron formation	Iron formation	Iron formation	Iron formation	Iron formation	HSR	HSR	HSR	HSR	HSR	HSR	HSR	HSR	HSR	HSR	HSR
Probe data	SiO_2 wt%	0.01	0.07	0.27	0.05	0.10	0.20	0.23	2.55	0.60	0.10	0.07	0.43	0.05	0.09	3.04	0.22
	TiO_2 wt%	0.00	0.00	0.00	0.01	0.01	0.02	0.01	0.06	0.04	0.01	0.01	0.04	0.01	0.01	0.04	0.04
	Al_2O_3 wt%	0.00	0.01	0.01	-0.01	0.00	0.01	-0.01	1.47	0.20	0.02	0.00	0.15	0.01	0.00	2.15	0.02
	Cr_2O_3 wt%	0.01	0.00	0.00	0.00	0.00	-0.01	0.01	0.00	0.00	-0.01	0.00	0.00	-0.01	0.01	0.00	0.00
	FeO wt%	91.61	90.98	90.17	91.34	91.02	91.25	90.86	85.72	90.46	91.31	91.58	89.89	91.25	91.64	85.93	91.38
	MnO wt%	-0.01	0.04	0.02	0.03	0.03	-0.01	0.00	0.00	-0.01	0.01	0.00	0.00	0.01	0.01	0.00	-0.01
	MgO wt%	0.00	0.01	0.00	0.00	0.00	0.00	0.00	0.53	0.05	0.00	0.00	0.06	0.01	0.00	0.26	0.00
	CaO wt%	0.00	0.01	0.00	0.00	0.00	0.01	0.01	0.08	0.01	0.01	0.01	0.02	0.11	0.01	0.06	0.00
	K_2O wt%	0.00	0.03	0.01	0.00	0.00	0.03	0.03	0.42	0.14	0.01	0.02	0.10	0.00	0.01	0.84	0.01
	Nb_2O_5 wt%	0.04	0.02	0.02	0.04	-0.02	0.02	0.02	0.00	0.01	0.05	0.01	0.01	-0.01	0.00	-0.01	0.00
	ZnO wt%	0.03	-0.01	0.01	0.01	0.01	-0.01	0.01	0.05	0.00	-0.02	0.00	0.00	0.00	0.01	0.00	0.02
	CuO wt%	-0.01	0.00	0.00	0.00	0.01	0.00	0.00	0.00	0.00	0.00	0.00	-0.01	0.00	-0.01	0.00	0.00
	NiO wt%	-0.01	0.01	0.01	0.00	0.00	0.00	0.01	-0.01	0.00	0.00	0.01	-0.01	-0.01	0.01	0.01	0.00
	CoO wt%	0.14	0.13	0.15	0.11	0.14	0.10	0.10	0.11	0.14	0.15	0.14	0.14	0.15	0.12	0.10	0.13
	SnO_2 wt%	-0.01	-0.19	-0.23	-0.02	-0.13	-0.28	-0.02	-0.01	-0.02	-0.04	-0.04	-0.04	-0.07	-0.02	-0.05	0.00
	ZrO_2 wt%	-0.01	0.00	-0.01	0.00	-0.01	-0.01	-0.01	0.00	0.00	-0.01	0.00	0.01	0.00	0.00	0.00	-0.01
	P_2O_5 wt%	-0.01	0.00	0.00	0.00	0.00	0.00	0.01	0.00	-0.01	0.00	0.00	0.00	0.00	0.00	0.00	0.00
	V_2O_3 wt%	0.07	0.06	0.03	0.21	0.19	0.01	0.01	0.01	-0.01	0.00	0.01	0.01	0.00	0.01	-0.01	0.01
	Total wt%	91.86	91.17	90.45	91.76	91.33	91.34	91.26	90.97	91.59	91.60	91.82	90.82	91.52	91.89	92.37	91.83
Calculated	Fe_2O3_%	67.88	67.47	66.44	67.55	67.32	67.35	67.00	60.18	66.37	67.55	67.86	66.18	67.73	67.84	59.97	67.37
	FeO_%	30.53	30.27	30.38	30.55	30.44	30.65	30.57	31.57	30.73	30.52	30.51	30.34	30.30	30.59	31.96	30.76
	Total_%	98.71	98.13	97.36	98.57	98.25	98.41	98.01	97.02	98.30	98.45	98.66	97.50	98.40	98.72	98.45	98.60
	Ti mol %	0.01	0.00	0.01	0.01	0.01	0.03	0.01	0.07	0.04	0.02	0.01	0.05	0.02	0.01	0.05	0.05
	Fe^{2+} mol %	42.49	42.13	42.29	42.52	42.37	42.66	42.55	43.94	42.78	42.49	42.47	42.23	42.18	42.59	44.49	42.82
	Fe^{3+} mol %	42.50	42.25	41.61	42.30	42.16	42.17	41.96	37.69	41.56	42.30	42.50	41.44	42.41	42.48	37.56	42.19
	Usp Mol%	0.01	0.00	0.01	0.03	0.02	0.07	0.03	0.19	0.11	0.04	0.03	0.11	0.04	0.03	0.13	0.12
	Ilm Mol%	0.00	0.00	0.00	0.00	0.00	0.00	0.00	0.00	0.00	0.00	0.00	0.00	0.00	0.00	0.00	0.00

	Probe ID	W605041 _1_M73	W605041 _1_M74	W605041 _1_M75	W605041 _1_M76	W605041 _1_M77	W605041 _1_M78	W605041 _1_R23	W605282 _1_M100	W605282 _1_M101	W605282 _1_M102	W605282 _1_M103	W605282 _4_M104	W605282 _4_M105	W605282 _4_M106	W605282 _4_M107	W605282 _5_M108
	Sample	W605041	W605041	W605041	W605041	W605041	W605041	W605041	W605282	W605282	W605282	W605282	W605282	W605282	W605282	W605282	W605282
	Rocktype	HSR	HSR	HSR	HSR	HSR	HSR	HSR	Z-FeTiB	Z-FeTiB	Z-FeTiB	Z-FeTiB	Z-FeTiB	Z-FeTiB	Z-FeTiB	Z-FeTiB	Z-FeTiB
Probe data	**SiO_2 wt%**	0.31	0.08	0.16	0.11	0.17	0.23	13.28	0.00	0.00	0.01	0.01	0.00	0.01	0.00	0.02	0.05
	TiO_2 wt%	0.02	-0.01	0.00	0.01	0.04	0.02	0.00	0.05	0.03	0.04	0.01	0.05	0.05	0.04	0.04	0.04
	Al_2O_3 wt%	-0.01	0.00	0.00	0.01	0.02	0.02	0.06	0.04	0.03	0.01	0.00	0.06	0.05	0.04	0.03	0.03
	Cr_2O_3 wt%	0.02	0.00	-0.01	0.00	0.00	-0.01	0.00	0.07	0.00	0.04	0.04	0.06	0.04	0.03	0.06	0.04
	FeO wt%	90.81	91.04	91.37	91.33	91.31	91.18	81.48	91.68	91.61	90.90	85.79	91.81	91.60	91.81	91.78	92.07
	MnO wt%	-0.01	-0.01	0.01	0.02	0.01	0.00	0.00	-0.01	0.02	0.06	0.21	0.00	0.02	0.02	0.01	0.01
	MgO wt%	0.00	0.00	0.00	0.00	0.00	0.00	-0.01	0.00	-0.01	-0.01	0.05	0.00	0.00	0.00	-0.01	0.01
	CaO wt%	0.01	0.01	0.00	0.01	0.01	0.03	0.01	0.08	0.52	0.85	4.22	0.12	0.12	0.37	0.34	0.03
	K_2O wt%	0.04	0.05	0.04	0.02	0.00	0.01	0.05	0.00	0.00	0.00	0.00	0.01	0.01	0.00	0.00	0.00
	Nb_2O_5 wt%	-0.02	-0.01	0.03	0.01	0.04	0.03	0.00	-0.02	-0.01	0.02	0.03	0.00	0.02	0.05	0.03	-0.03
	ZnO wt%	0.00	0.00	-0.02	0.00	0.01	0.00	0.01	0.01	0.01	0.01	-0.01	0.00	-0.01	0.01	0.00	-0.01
	CuO wt%	-0.01	-0.02	0.00	0.00	0.01	0.00	0.00	-0.02	0.00	0.00	-0.01	0.00	0.00	-0.01	0.00	0.00
	NiO wt%	-0.01	0.00	0.01	0.00	0.02	0.00	0.00	-0.01	0.00	0.00	0.01	0.00	0.00	0.00	0.00	0.00
	CoO wt%	0.16	0.13	0.11	0.14	0.12	0.14	0.12	0.13	0.11	0.14	0.09	0.11	0.11	0.14	0.11	0.13
	SnO_2 wt%	-0.11	-0.04	0.00	-0.08	-0.01	-0.03	-0.03	-0.16	-0.10	-0.03	-0.01	-0.18	-0.19	0.00	-0.02	0.00
	ZrO_2 wt%	-0.01	0.00	0.00	0.00	0.00	0.04	0.01	-0.01	0.00	-0.01	0.00	-0.01	-0.01	0.01	0.00	-0.01
	P_2O_5 wt%	0.00	0.00	-0.01	0.00	0.00	-0.01	0.00	0.00	0.01	0.00	0.00	0.00	0.00	0.00	0.00	0.00
	V_2O_3 wt%	0.01	-0.01	0.00	0.00	0.00	0.00	0.01	0.62	0.52	0.49	0.46	0.67	0.64	0.62	0.64	0.35
	Total wt%	91.22	91.21	91.69	91.58	91.72	91.66	95.01	92.44	92.73	92.51	90.87	92.72	92.46	93.14	93.02	92.69
Calculated	**Fe_2O3_%**	66.92	67.53	67.57	67.62	67.35	67.21	37.03	67.76	68.21	67.99	67.63	67.89	67.70	68.11	68.02	68.04
	FeO_%	30.60	30.27	30.56	30.48	30.70	30.70	48.15	30.71	30.23	29.72	24.93	30.72	30.68	30.52	30.57	30.84
	Total_%	98.09	98.08	98.51	98.44	98.49	98.44	98.76	99.46	99.69	99.38	97.68	99.71	99.45	99.97	99.87	99.56
	Ti mol %	0.03	0.00	0.00	0.01	0.04	0.02	0.00	0.06	0.03	0.05	0.01	0.06	0.06	0.05	0.05	0.05
	Fe^{2+} mol %	42.59	42.14	42.55	42.43	42.74	42.74	67.03	42.74	42.09	41.37	34.71	42.76	42.70	42.48	42.55	42.93
	Fe^{3+} mol %	41.90	42.29	42.31	42.35	42.18	42.08	23.19	42.43	42.71	42.58	42.35	42.51	42.39	42.65	42.59	42.61
	Usp Mol%	0.06	0.00	0.01	0.02	0.10	0.06	0.00	0.13	0.07	0.11	0.01	0.15	0.14	0.10	0.11	0.11
	Ilm Mol%	0.00	0.00	0.00	0.00	0.00	0.00	0.00	0.00	0.00	0.00	0.00	0.00	0.00	0.00	0.00	0.00

	Probe ID	W605282 _5_M109	W605282 _5_M110	W605282 _5_M111	W605282 _5_M112	W605282 _1_M79	W605282 _1_M80	W605282 _1_M81	W605282 _1_M82	W605282 _1_M83	W605282 _1_M84	W605282 _1_M85	W605282 _1_M86	W605282 _1_M88	W605282 _1_M89	W605282 _1_M90	W605282 _1_M91
	Sample	W605282	W605282	W605282	W605282	W605282	W605282	W605282	W605282	W605282	W605282	W605282	W605282	W605282	W605282	W605282	W605282
	Rocktype	Z-FeTiB	Z-FeTiB	Z-FeTiB	Z-FeTiB	Z-FeTiB	Z-FeTiB	Z-FeTiB	Z-FeTiB	Z-FeTiB	Z-FeTiB	Z-FeTiB	Z-FeTiB	Z-FeTiB	Z-FeTiB	Z-FeTiB	Z-FeTiB
Probe data	**SiO_2 wt%**	0.01	0.04	0.03	0.05	0.00	0.03	-1.63	0.04	0.03	0.00	0.00	0.00	0.62	0.01	0.05	0.89
	TiO_2 wt%	0.04	0.04	0.05	0.04	0.03	0.07	0.06	0.00	0.03	0.05	0.02	0.02	0.06	0.04	0.04	-0.02
	Al_2O_3 wt%	0.03	0.05	0.05	0.02	0.05	0.02	-0.16	0.00	0.00	0.05	0.02	-0.01	0.27	-0.01	0.00	0.20
	Cr_2O_3 wt%	0.03	0.01	0.03	0.03	0.00	0.05	0.00	0.00	-0.01	0.01	0.06	0.06	0.05	-0.01	0.04	0.01
	FeO wt%	92.21	92.06	92.01	92.31	91.62	90.83	1.24	62.33	89.73	91.36	90.72	89.01	87.97	91.52	91.38	47.28
	MnO wt%	0.01	0.01	-0.01	0.01	0.01	0.06	0.02	0.07	0.07	0.02	0.06	0.11	0.04	0.05	0.02	0.01
	MgO wt%	0.00	0.00	0.01	0.00	0.00	0.00	-0.13	0.01	0.00	0.00	0.00	0.00	0.04	0.00	0.00	0.16
	CaO wt%	0.00	0.00	0.02	0.01	0.23	0.92	0.36	1.84	1.30	0.21	1.14	2.17	0.67	0.75	0.47	0.15
	K_2O wt%	0.00	0.00	0.00	0.01	0.00	0.01	0.01	0.00	0.01	0.00	0.00	0.00	0.11	0.00	0.00	0.13
	Nb_2O_5 wt%	0.04	0.02	0.01	0.03	-0.01	0.03	-0.47	0.03	0.00	0.00	0.01	0.03	0.00	0.01	0.01	-0.02
	ZnO wt%	0.00	0.02	0.04	0.00	0.00	-0.02	-0.09	0.02	0.00	0.02	0.00	0.02	0.01	0.00	0.00	1.07
	CuO wt%	0.00	0.00	0.01	0.00	-0.02	0.00	-0.02	-0.01	0.00	0.00	-0.01	-0.01	0.00	-0.01	0.00	19.51
	NiO wt%	-0.01	0.00	0.00	0.00	-0.01	0.01	-0.11	0.00	-0.01	0.00	0.00	-0.01	-0.01	-0.01	-0.01	0.18
	CoO wt%	0.12	0.11	0.11	0.10	0.10	0.11	2.43	0.08	0.13	0.13	0.10	0.10	0.13	0.13	0.12	0.32
	SnO_2 wt%	-0.01	-0.01	-0.07	-0.01	-0.07	-0.01	0.00	-0.06	-0.01	-0.05	-0.01	-0.01	-0.15	-0.18	-0.13	-0.04
	ZrO_2 wt%	0.01	0.00	0.00	-0.01	0.00	-0.01	0.08	-0.01	0.01	0.02	0.00	-0.01	0.01	-0.01	0.00	0.01
	P_2O_5 wt%	0.00	0.00	0.00	0.00	0.00	0.00	34.54	0.00	0.00	-0.01	0.00	0.00	0.03	0.00	-0.01	0.03
	V_2O_3 wt%	0.37	0.35	0.38	0.37	0.65	0.54	-0.01	0.37	0.51	0.64	0.53	0.66	0.52	0.52	0.57	-0.01
	Total wt%	92.85	92.69	92.66	92.97	92.58	92.64	36.12	64.72	91.80	92.43	92.63	92.11	90.35	92.82	92.55	69.88
Calculated	**Fe_2O3_%**	68.12	67.97	68.01	68.19	67.86	67.91	0.00	47.82	67.61	67.67	68.15	67.85	64.70	68.38	67.87	48.12
	FeO_%	30.90	30.89	30.82	30.95	30.56	29.71	1.24	19.30	28.89	30.47	29.40	27.96	29.75	29.99	30.31	3.98
	Total_%	99.70	99.52	99.56	99.82	99.50	99.48	38.75	69.59	98.61	99.27	99.50	98.97	96.99	99.89	99.51	74.78
	Ti mol %	0.05	0.05	0.06	0.05	0.04	0.08	0.07	0.01	0.04	0.06	0.02	0.02	0.08	0.05	0.05	0.00
	Fe^{2+} mol %	43.02	43.00	42.90	43.08	42.54	41.36	1.73	26.86	40.21	42.42	40.92	38.92	41.41	41.74	42.19	5.54
	Fe^{3+} mol %	42.66	42.56	42.59	42.70	42.50	42.53	0.00	29.94	42.34	42.37	42.68	42.49	40.51	42.82	42.50	30.13
	Usp Mol%	0.12	0.13	0.13	0.13	0.09	0.19	2.39	0.02	0.08	0.14	0.05	0.04	0.19	0.11	0.11	0.00
	Ilm Mol%	0.00	0.00	0.00	0.00	0.00	0.00	0.00	0.00	0.00	0.00	0.00	0.00	0.00	0.00	0.00	0.00

	Probe ID	W605282 _1_M92	W605282 _1_M93	W605282 _1_M94	W605282 _1_M95	W605282 _1_M96	W605282 _1_M97	W605282 _1_M98	W605282 _1_M99
	Sample	W605282	W605282	W605282	W605282	W605282	W605282	W605282	W605282
	Rocktype	Z-FeTiB	Z-FeTiB	Z-FeTiB	Z-FeTiB	Z-FeTiB	Z-FeTiB	Z-FeTiB	Z-FeTiB
Probe data	**SiO_2 wt%**	0.01	0.00	0.02	0.01	0.02	0.00	0.02	0.04
	TiO_2 wt%	0.03	0.01	0.03	0.10	0.03	0.05	0.03	0.04
	Al_2O_3 wt%	0.02	0.01	0.02	0.09	0.04	0.06	0.05	0.03
	Cr_2O_3 wt%	0.01	0.06	0.03	0.01	0.01	0.05	0.00	0.00
	FeO wt%	91.22	91.17	91.60	91.71	91.24	91.76	91.57	91.28
	MnO wt%	0.04	0.03	0.02	0.00	0.00	0.02	0.02	0.00
	MgO wt%	0.00	0.00	-0.01	-0.01	0.00	-0.01	0.00	0.00
	CaO wt%	0.36	0.57	0.26	0.05	0.31	0.11	0.16	0.05
	K_2O wt%	0.00	0.01	0.00	0.00	0.00	0.00	0.00	0.00
	Nb_2O_5 wt%	0.02	0.01	0.04	0.01	0.00	-0.01	0.03	0.00
	ZnO wt%	0.01	-0.01	0.00	0.00	0.00	-0.03	0.01	0.00
	CuO wt%	-0.01	-0.01	0.00	0.01	-0.01	-0.01	0.00	0.00
	NiO wt%	0.01	0.00	-0.02	0.00	0.00	-0.01	0.00	0.00
	CoO wt%	0.12	0.14	0.12	0.13	0.13	0.14	0.11	0.13
	SnO_2 wt%	-0.14	-0.15	-0.02	-0.02	-0.28	-0.08	-0.27	-0.09
	ZrO_2 wt%	0.00	-0.01	0.01	0.00	-0.01	0.00	0.00	0.00
	P_2O_5 wt%	0.00	0.00	0.00	0.00	0.00	0.01	-0.01	0.00
	V_2O_3 wt%	0.57	0.55	0.61	0.63	0.59	0.61	0.65	0.62
	Total wt%	92.27	92.39	92.71	92.72	92.08	92.66	92.37	92.09
Calculated	**Fe_2O3_%**	67.73	67.97	67.83	67.65	67.67	67.86	67.72	67.42
	FeO_%	30.27	30.01	30.56	30.83	30.34	30.70	30.63	30.62
	Total_%	99.21	99.38	99.56	99.53	99.16	99.59	99.43	98.95
	Ti mol %	0.04	0.02	0.04	0.12	0.04	0.06	0.04	0.05
	Fe^{2+} mol %	42.13	41.77	42.54	42.91	42.24	42.73	42.63	42.62
	Fe^{3+} mol %	42.42	42.56	42.48	42.37	42.38	42.49	42.41	42.22
	Usp Mol%	0.10	0.03	0.09	0.29	0.09	0.13	0.08	0.12
	Ilm Mol%	0.00	0.00	0.00	0.00	0.00	0.00	0.00	0.00

Table A6. 8 Electron microprobe results for magnetite mineral chemistry and calculated mineral formulae based on six oxygens.

	Probe ID	99362_2_I34	99362_2_I42	99362_2_I47	99362_2_I51	99362_2_I54	99362_2_I57	S037015_1B_I1	S037015_6_I10	S037015_E_I200	S037015_E_I201	S037015_F_I202	S037015_F_I203	S037015_F_I204	S037015_F_I205	S037015_F_I206	S037015_6_I11
	Sample	99-362	99-362	99-362	99-362	99-362	99-362	S037015	S037015	S037015	S037015	S037015	S037015	S037015	S037015	S037015	S037015
	Rocktype	FW-FeB	FW-FeB	FW-FeB	FW-FeB	FW-FeB	FW-FeB	Z-FeTiB	Z-FeTiB	Z-FeTiB	Z-FeTiB	Z-FeTiB	Z-FeTiB	Z-FeTiB	Z-FeTiB	Z-FeTiB	Z-FeTiB
Probe data	SiO_2 wt%	0.05	0.07	0.58	0.06	0.25	62.32	0.05	23.56	0.05	0.05	0.93	0.16	0.09	0.14	0.62	0.30
	TiO_2 wt%	49.75	51.42	49.74	51.09	49.68	0.05	52.15	6.43	52.37	50.87	51.97	52.01	52.51	52.07	50.99	52.23
	Al_2O_3 wt%	0.01	0.00	0.00	0.00	0.23	23.03	0.01	8.63	0.00	0.02	0.11	0.01	0.00	0.01	0.26	0.00
	Cr_2O_3 wt%	-0.01	0.00	-0.01	0.01	0.00	0.01	0.01	-0.01	0.00	0.01	0.01	0.01	-0.01	0.00	0.00	0.00
	FeO wt%	46.19	44.90	44.73	45.38	45.35	3.89	46.23	55.26	46.83	47.28	44.82	45.80	46.27	46.15	45.70	45.49
	MnO wt%	2.50	2.81	2.54	2.66	2.91	0.01	1.44	0.16	1.53	1.50	1.44	1.43	1.49	1.44	1.43	1.49
	MgO wt%	0.01	0.01	0.01	0.01	0.14	0.53	0.03	0.17	0.03	0.03	0.03	0.02	0.02	0.04	0.26	0.02
	CaO wt%	0.05	0.03	0.16	0.03	0.23	3.71	0.03	1.37	0.04	0.01	0.83	0.08	0.08	0.21	0.10	0.04
	K_2O wt%	0.00	0.00	0.01	0.00	0.00	0.90	0.02	0.25	0.03	0.00	0.01	0.02	0.02	0.05	0.01	0.02
	Nb_2O_5 wt%	0.05	0.06	0.07	0.08	0.01	-0.05	0.04	0.06	0.05	0.08	0.05	0.01	0.06	0.06	0.05	0.03
	ZnO wt%	0.05	0.06	0.02	0.03	0.01	0.00	0.04	0.00	0.07	0.00	0.04	0.05	0.01	-0.01	0.04	0.02
	CuO wt%	0.01	-0.01	0.00	0.00	0.02	0.00	0.00	-0.01	-0.01	-0.01	0.02	0.00	0.01	-0.01	0.02	0.00
	NiO wt%	0.01	0.01	0.01	-0.01	0.00	0.00	0.00	0.00	0.00	-0.01	0.00	0.01	0.00	0.00	0.00	0.01
	CoO wt%	0.06	0.05	0.06	0.07	0.07	0.01	0.06	0.08	0.05	0.07	0.06	0.07	0.06	0.05	0.06	0.05
	SnO_2 wt%	-0.02	-0.11	-0.01	-0.02	-0.01	0.01	-0.07	-0.10	-0.09	-0.04	0.00	-0.01	-0.03	-0.01	-0.01	-0.09
	ZrO_2 wt%	-0.01	0.00	0.00	0.00	0.00	0.05	-0.01	0.00	0.07	0.00	0.04	0.19	0.07	0.09	0.10	0.41
	P_2O_5 wt%	0.00	0.00	0.00	0.00	0.00	0.00	0.00	0.01	0.01	0.00	0.00	0.03	0.02	0.17	0.01	0.02
	V_2O_3 wt%	0.54	0.49	0.46	0.47	0.50	0.01	0.49	0.34	0.45	0.47	0.49	0.47	0.46	0.45	0.43	0.44
	Total wt%	99.25	99.80	98.38	99.85	99.37	94.49	100.52	96.20	101.48	100.33	100.85	100.37	101.11	100.92	100.06	100.49
Calculated	Fe_2O_3 %	4.54	1.70	2.38	2.33	4.39	0.00	1.03	26.97	1.54	3.37	0.00	0.47	0.66	0.76	1.30	0.00
	FeO %	42.10	43.37	42.59	43.28	41.40	3.89	45.30	30.99	45.45	44.25	44.82	45.37	45.67	45.46	44.53	45.49
	Total_%	99.75	100.10	98.63	100.12	99.83	94.54	100.71	99.02	101.73	100.72	100.85	100.43	101.22	101.02	100.20	100.59
	Ti mol %	62.29	64.39	62.27	63.96	62.20	0.07	65.29	8.05	65.56	63.69	65.07	65.12	65.74	65.20	63.84	65.39
	Fe^{2+} mol %	58.61	60.37	59.29	60.24	57.63	5.42	63.05	43.14	63.26	61.59	62.39	63.16	63.58	63.28	61.98	63.32
	Fe^{3+} mol %	2.84	1.07	1.49	1.46	2.75	0.00	0.65	16.89	0.97	2.11	0.00	0.30	0.41	0.48	0.81	0.00
	Usp Mol%	0.00	0.00	0.00	0.00	0.00	0.00	0.00	0.00	0.00	0.00	0.00	0.00	0.00	0.00	0.00	0.00
	Ilm Mol%	95.55	98.32	97.64	97.68	95.71	-5.97	99.09	53.53	98.54	96.72	100.46	99.51	99.37	98.99	98.72	100.25

	Probe ID	S037015_7_I12	S037015_7_I13	S037015_7_I14	S037015_7_I15	S037015_7_I16	S037015_1B_I2	S037015_1B_I3	S037015_2_I4	S037015_2_I5	S037015_2_I6	S037015_2_I7	S037015_2_I8	S037015_A_I84	S037015_A_I85	S037015_A_I86	S037015_A_I87
	Sample	S037015	S037015	S037015	S037015	S037015	S037015	S037015	S037015	S037015	S037015	S037015	S037015	S037015	S037015	S037015	S037015
	Rocktype	Z-FeTiB	Z-FeTiB	Z-FeTiB	Z-FeTiB	Z-FeTiB	Z-FeTiB	Z-FeTiB	Z-FeTiB	Z-FeTiB	Z-FeTiB	Z-FeTiB	Z-FeTiB	Z-FeTiB	Z-FeTiB	Z-FeTiB	Z-FeTiB
Probe data	SiO_2 wt%	0.11	3.33	0.10	11.75	0.11	0.05	0.50	1.64	33.86	3.57	12.33	9.56	0.06	0.11	0.73	0.08
	TiO_2 wt%	51.75	47.92	51.38	30.13	52.53	51.92	51.22	47.24	22.47	44.24	33.29	41.26	49.83	50.44	49.74	52.03
	Al_2O_3 wt%	0.01	1.63	0.02	7.92	0.01	0.01	0.00	1.17	11.84	2.34	5.73	3.67	0.01	0.00	0.04	0.00
	Cr_2O_3 wt%	0.01	0.01	-0.01	-0.01	-0.01	0.00	0.01	0.01	0.00	-0.01	0.01	-0.01	0.00	0.00	-0.01	0.01
	FeO wt%	46.11	42.26	44.01	34.25	44.84	45.89	45.55	45.05	20.13	43.74	35.73	35.78	46.81	47.09	46.49	46.39
	MnO wt%	1.40	1.29	1.49	0.84	1.41	1.43	1.44	1.40	0.63	1.28	0.98	1.25	1.44	1.39	1.54	1.52
	MgO wt%	0.02	1.05	0.02	5.73	0.02	0.02	0.03	0.81	0.01	1.55	3.64	0.71	0.02	0.03	0.03	0.02
	CaO wt%	0.04	0.44	0.69	0.28	0.03	0.18	0.07	0.07	2.81	0.11	0.11	1.90	0.08	0.00	0.03	0.04
	K_2O wt%	0.06	1.10	0.09	1.24	0.08	0.05	0.01	0.05	0.06	0.58	4.31	0.05	0.00	0.00	0.00	0.00
	Nb_2O_5 wt%	0.06	0.05	0.06	0.03	0.02	0.03	0.06	0.07	0.06	0.03	0.05	0.03	0.04	0.04	0.05	0.02
	ZnO wt%	0.02	0.04	0.03	0.02	0.02	0.01	0.02	0.04	-0.02	0.02	0.04	0.04	0.04	0.03	0.01	0.04
	CuO wt%	-0.01	0.01	0.00	0.00	0.00	0.01	0.00	0.02	-0.01	0.01	-0.02	0.00	0.00	-0.01	0.00	-0.01
	NiO wt%	-0.02	-0.01	0.00	0.00	-0.01	-0.01	0.00	0.01	-0.02	-0.01	0.01	0.00	0.00	0.00	-0.01	0.00
	CoO wt%	0.06	0.05	0.05	0.05	0.05	0.06	0.06	0.05	0.03	0.04	0.05	0.04	0.05	0.06	0.06	0.07
	SnO_2 wt%	-0.08	0.00	0.01	0.00	0.00	0.00	0.00	0.00	-0.04	0.00	-0.01	-0.04	0.00	-0.01	-0.01	-0.04
	ZrO_2 wt%	0.13	0.00	0.00	0.15	0.13	0.02	0.73	0.09	0.05	0.00	0.06	0.57	0.00	0.00	-0.01	0.05
	P_2O_5 wt%	0.01	0.22	0.49	0.09	0.01	0.00	0.04	0.00	0.01	0.00	0.01	1.20	0.36	0.00	0.00	0.01
	V_2O_3 wt%	0.43	2.92	0.47	0.26	0.46	0.48	0.49	0.44	0.20	0.41	0.31	0.34	0.49	0.44	0.49	0.47
	Total wt%	100.10	102.32	98.89	92.73	99.69	100.14	100.21	98.16	92.07	97.91	96.63	96.33	99.23	99.60	99.17	100.70
Calculated	Fe_2O_3 %	1.13	2.10	0.00	8.99	0.00	1.16	0.03	4.07	0.00	6.31	13.12	0.00	3.14	3.47	2.82	1.30
	FeO %	45.09	40.37	44.01	26.16	44.84	44.85	45.52	41.39	20.13	38.06	23.93	35.78	43.98	43.97	43.95	45.22
	Total_%	100.32	102.55	98.90	93.64	99.71	100.28	100.22	98.57	92.16	98.56	97.98	96.38	99.56	99.98	99.49	100.88
	Ti mol %	64.80	60.00	64.33	37.72	65.77	65.00	64.12	59.15	28.13	55.39	41.68	51.66	62.39	63.15	62.27	65.14
	Fe^{2+} mol %	62.76	56.20	61.26	36.41	62.42	62.42	63.36	57.61	28.02	52.98	33.31	49.80	61.22	61.20	61.18	62.94
	Fe^{3+} mol %	0.71	1.31	0.00	5.63	0.00	0.72	0.02	2.55	0.00	3.95	8.21	0.00	1.97	2.17	1.77	0.82
	Usp Mol%	0.00	0.00	0.00	0.00	0.00	0.00	0.00	0.00	0.00	0.00	0.00	0.00	0.00	0.00	0.00	0.00
	Ilm Mol%	98.98	101.22	99.86	92.59	101.10	99.08	99.45	95.92	216.26	95.34	101.99	110.71	96.12	96.66	97.23	98.76

	Probe ID	S037015_A_I88	S037015_A_I89	S037015_2_I9	S037015_A_I90	S037015_A_I91	S037015_A_I92	S037015_D_I93	S037015_D_I94	S037015_D_I95	S037015_D_I96	S037015_D_I97	S037015_E_I198	S037015_E_I199	S039313_1_I17	S039313_1_I19	S039313_1_I22
	Sample	S037015	S037015	S037015	S037015	S037015	S037015	S037015	S037015	S037015	S037015	S037015	S037015	S037015	S039313	S039313	S039313
	Rocktype	Z-FeTiB	Z-FeTiB	Z-FeTiB	Z-FeTiB	Z-FeTiB	Z-FeTiB	Z-FeTiB	Z-FeTiB	Z-FeTiB	Z-FeTiB	Z-FeTiB	Z-FeTiB	Z-FeTiB	HW-FeTiB	HW-FeTiB	HW-FeTiB
Probe data	SiO_2 wt%	0.21	0.31	9.06	0.15	0.17	0.16	0.05	0.16	0.35	0.16	0.23	0.07	0.06	79.01	75.91	34.28
	TiO_2 wt%	51.07	51.11	40.14	51.57	50.78	51.65	52.01	51.87	51.73	51.95	51.64	52.25	52.19	1.62	3.58	5.60
	Al_2O_3 wt%	0.10	0.00	4.35	0.00	0.02	0.00	0.00	0.00	0.03	0.00	0.02	0.01	-0.01	14.47	0.22	0.02
	Cr_2O_3 wt%	0.01	-0.01	-0.01	0.00	0.00	0.00	0.00	0.00	0.00	0.00	0.00	0.01	0.00	0.00	0.00	0.00
	FeO wt%	46.44	46.22	38.74	46.67	46.11	46.76	46.21	45.39	45.41	45.89	45.80	46.46	46.74	3.93	19.34	53.31
	MnO wt%	1.53	1.45	1.16	1.46	1.42	1.41	1.48	1.48	1.42	1.45	1.54	1.56	1.47	0.01	0.00	-0.01
	MgO wt%	0.07	0.03	2.60	0.03	0.03	0.03	0.02	0.01	0.02	0.02	0.02	0.02	0.02	0.51	0.02	0.00
	CaO wt%	0.09	0.06	0.15	0.08	0.25	0.06	0.06	0.11	0.33	0.05	0.15	0.04	0.01	0.01	0.01	0.01
	K_2O wt%	0.02	0.05	3.37	0.02	0.05	0.02	0.03	0.03	0.04	0.05	0.06	0.04	0.04	5.48	0.11	0.01
	Nb_2O_5 wt%	0.05	0.08	0.03	0.06	0.05	0.04	0.05	0.03	0.04	0.05	0.05	0.04	0.06	-0.04	-0.03	0.01
	ZnO wt%	0.03	0.03	0.02	0.02	0.00	0.04	0.02	0.02	0.04	0.04	0.04	0.05	0.05	0.01	0.01	0.00
	CuO wt%	0.00	0.02	0.01	0.00	0.00	0.00	0.00	0.00	0.00	-0.01	0.00	0.01	0.01	0.00	0.00	0.00
	NiO wt%	0.00	0.00	0.00	-0.01	0.00	-0.01	-0.01	-0.01	-0.01	-0.01	0.01	0.00	-0.01	0.01	0.00	0.00
	CoO wt%	0.05	0.07	0.04	0.06	0.06	0.08	0.06	0.05	0.05	0.06	0.05	0.05	0.06	0.00	0.03	0.07
	SnO_2 wt%	-0.06	-0.02	-0.12	0.00	-0.13	-0.09	-0.06	-0.02	-0.02	-0.03	-0.07	-0.04	-0.09	-0.01	-0.03	-0.02
	ZrO_2 wt%	0.00	0.35	-0.01	0.15	0.11	0.19	0.04	0.20	0.06	0.04	0.27	0.04	0.06	-0.01	0.00	0.00
	P_2O_5 wt%	0.00	0.01	0.01	0.01	0.03	0.01	0.01	0.03	0.01	0.00	0.02	0.00	0.00	0.00	-0.01	0.01
	V_2O_3 wt%	0.46	0.46	0.39	0.47	0.45	0.48	0.41	0.48	0.43	0.42	0.45	0.45	0.48	0.05	0.10	0.48
	Total wt%	100.05	100.20	99.92	100.75	99.40	100.84	100.36	99.85	99.93	100.13	100.28	101.05	101.15	105.04	99.25	93.76
Calculated	Fe_2O_3 %	2.33	1.57	9.00	1.89	2.29	1.85	1.16	0.18	0.53	0.79	0.95	1.32	1.56	0.00	0.00	8.17
	FeO %	44.34	44.80	30.64	44.97	44.05	45.10	45.17	45.23	44.93	45.18	44.95	45.27	45.34	3.93	19.34	45.96
	Total_%	100.35	100.39	100.96	100.95	99.76	101.12	100.56	99.90	100.02	100.26	100.45	101.22	101.42	105.11	99.33	94.62
	Ti mol %	63.94	63.99	50.25	64.57	63.58	64.67	65.11	64.94	64.77	65.04	64.66	65.42	65.35	2.03	4.48	7.02
	Fe^{2+} mol %	61.72	62.37	42.65	62.59	61.31	62.77	62.87	62.97	62.54	62.88	62.57	63.02	63.12	5.47	26.92	63.97
	Fe^{3+} mol %	1.46	0.98	5.64	1.18	1.43	1.16	0.72	0.11	0.33	0.49	0.59	0.82	0.97	0.00	0.00	5.12
	Usp Mol%	0.00	0.00	0.00	0.00	0.00	0.00	0.00	0.00	0.00	0.00	0.00	0.00	0.00	0.00	0.00	0.00
	Ilm Mol%	97.78	98.39	102.94	98.12	97.79	98.17	98.95	99.76	99.56	99.39	99.05	98.85	98.62	-34.87	-87.38	80.68

	Probe ID	S039313_5_I28	S039313_5_I29	S039313_5_I30	S039313_5_I31	S039313_5_I32	W605282_1_I62	W605282_1_I63	W605282_1_I64	W605282_1_I65	W605282_1_I66	W605282_1_I67	W605282_1_I68	W605282_1_I69	W605282_1_I70	W605282_1_I71	W605282_1_I72
	Sample	S039313	S039313	S039313	S039313	S039313	W605282	W605282	W605282	W605282	W605282	W605282	W605282	W605282	W605282	W605282	W605282
	Rocktype	HW-FeTiB	HW-FeTiB	HW-FeTiB	HW-FeTiB	HW-FeTiB	Z-FeTiB	Z-FeTiB	Z-FeTiB	Z-FeTiB	Z-FeTiB	Z-FeTiB	Z-FeTiB	Z-FeTiB	Z-FeTiB	Z-FeTiB	Z-FeTiB
Probe data	SiO_2 wt%	16.36	18.81	37.95	32.85	29.54	0.06	0.18	0.01	0.25	0.06	1.19	0.45	2.75	0.05	0.03	0.01
	TiO_2 wt%	7.48	5.07	6.29	4.03	4.86	51.65	51.81	51.59	51.79	50.75	49.59	51.24	47.24	51.77	51.79	52.09
	Al_2O_3 wt%	1.65	0.03	5.01	9.61	7.25	0.03	0.09	0.00	0.18	0.02	1.00	0.01	2.04	0.04	0.01	0.00
	Cr_2O_3 wt%	0.00	0.01	0.00	0.00	0.00	0.00	0.01	0.00	0.01	0.00	0.01	0.00	-0.01	0.00	0.00	0.01
	FeO wt%	68.66	63.35	45.74	44.46	16.92	44.79	45.28	45.78	45.73	45.55	44.70	45.56	42.27	45.52	45.48	45.87
	MnO wt%	-0.01	0.00	0.00	0.00	0.00	2.77	2.65	2.68	2.71	2.61	2.52	2.54	2.42	2.65	2.72	2.69
	MgO wt%	0.00	-0.01	0.00	0.01	0.02	0.01	0.03	0.01	0.03	0.01	0.09	0.02	0.06	0.01	0.01	0.02
	CaO wt%	0.10	0.05	0.47	0.69	0.55	1.02	0.09	0.45	0.04	0.30	0.20	0.34	0.92	0.21	0.06	0.09
	K_2O wt%	0.00	0.01	0.04	0.21	0.08	0.00	0.05	0.00	0.04	0.02	0.26	0.01	0.77	0.01	0.03	0.02
	Nb_2O_5 wt%	0.01	-0.02	0.02	0.00	0.01	0.06	0.04	0.07	0.06	0.09	0.05	0.08	0.04	0.06	0.06	0.04
	ZnO wt%	0.01	0.02	0.01	0.01	0.02	0.05	0.04	0.03	0.03	0.02	0.04	0.00	0.04	0.00	0.03	0.02
	CuO wt%	0.01	0.00	0.00	0.01	0.01	-0.02	0.01	0.00	0.01	0.01	0.01	0.01	0.00	0.00	0.00	-0.01
	NiO wt%	-0.01	-0.02	0.01	0.01	0.00	0.00	0.00	-0.01	0.00	0.00	0.00	-0.01	0.00	0.00	0.01	-0.02
	CoO wt%	0.10	0.10	0.06	0.06	0.02	0.07	0.05	0.07	0.08	0.06	0.06	0.05	0.05	0.05	0.05	0.07
	SnO_2 wt%	-0.01	-0.07	-0.03	-0.07	-0.02	0.00	-0.01	-0.03	0.00	-0.08	-0.01	-0.09	-0.01	-0.07	-0.11	0.00
	ZrO_2 wt%	0.00	0.01	0.00	-0.02	-0.02	0.00	-0.01	0.00	-0.01	0.00	0.00	0.00	0.00	0.00	-0.01	0.00
	P_2O_5 wt%	0.00	0.00	0.00	0.01	0.00	0.00	0.00	0.00	0.00	0.00	0.00	0.01	0.00	0.00	0.00	-0.01
	V_2O_3 wt%	0.70	0.70	0.42	0.34	0.17	0.47	0.51	0.51	0.52	0.50	0.50	0.48	0.47	0.49	0.45	0.49
	Total wt%	95.07	88.04	96.01	92.22	59.42	100.96	100.82	101.15	101.46	99.92	100.23	100.70	99.07	100.78	100.61	101.39
Calculated	Fe_2O_3 %	47.35	40.54	0.00	3.51	0.00	2.73	1.67	3.00	2.06	3.25	2.77	2.20	2.94	2.08	2.00	2.19
	FeO %	26.05	26.87	45.74	41.30	16.92	42.33	43.78	43.08	43.88	42.62	42.21	43.58	39.63	43.65	43.67	43.89
	Total_%	99.84	92.22	96.04	92.66	59.46	101.25	101.01	101.50	101.69	100.33	100.52	101.03	99.38	101.07	100.93	101.65
	Ti mol %	9.37	6.35	7.88	5.05	6.08	64.66	64.87	64.59	64.84	63.55	62.09	64.15	59.14	64.82	64.84	65.22
	Fe^{2+} mol %	36.27	37.40	63.68	57.50	23.55	58.92	60.94	59.97	61.07	59.33	58.75	60.66	55.16	60.76	60.79	61.10
	Fe^{3+} mol %	29.65	25.39	0.00	2.20	0.00	1.71	1.04	1.88	1.29	2.04	1.74	1.38	1.84	1.30	1.26	1.37
	Usp Mol%	0.00	0.00	0.00	0.00	0.00	0.00	0.00	0.00	0.00	0.00	0.00	0.00	0.00	0.00	0.00	0.00
	Ilm Mol%	38.42	37.88	116.09	90.92	639.84	97.33	98.56	97.08	98.14	96.83	98.13	97.84	99.68	97.99	98.13	97.96

	Probe ID	W605282_1_I73	W605282_1_I74	W605282_4_I75	W605282_4_I76	W605282_4_I77	W605282_4_I78	W605282_4_I79	W605282_5_I80
	Sample	W605282	W605282	W605282	W605282	W605282	W605282	W605282	W605282
	Rocktype	Z-FeTiB	Z-FeTiB	Z-FeTiB	Z-FeTiB	Z-FeTiB	Z-FeTiB	Z-FeTiB	Z-FeTiB
Probe data	**SiO_2 wt%**	0.05	0.22	0.14	0.07	0.30	0.02	0.39	0.28
	TiO_2 wt%	51.25	51.88	51.85	51.37	51.75	52.34	50.80	50.56
	Al_2O_3 wt%	0.01	0.13	0.10	0.02	0.23	0.00	0.21	0.21
	Cr_2O_3 wt%	0.00	0.00	0.00	-0.01	0.00	0.00	-0.01	0.02
	FeO wt%	44.98	45.32	45.54	45.67	45.58	44.79	45.78	46.11
	MnO wt%	2.79	2.71	2.73	2.51	2.62	2.80	2.63	2.16
	MgO wt%	0.07	0.01	0.02	0.04	0.01	0.01	0.02	0.11
	CaO wt%	0.33	0.19	0.45	0.32	0.25	0.50	0.22	0.03
	K_2O wt%	0.04	0.08	0.07	0.08	0.09	0.01	0.14	0.00
	Nb_2O_5 wt%	0.04	0.06	0.09	0.07	0.04	0.04	0.01	0.03
	ZnO wt%	0.01	0.05	0.04	0.04	0.01	0.03	0.04	0.00
	CuO wt%	0.00	-0.01	0.00	-0.01	-0.01	0.00	-0.01	0.00
	NiO wt%	0.00	0.00	0.00	-0.01	0.00	0.00	-0.02	0.00
	CoO wt%	0.07	0.06	0.05	0.08	0.07	0.07	0.05	0.05
	SnO_2 wt%	-0.05	-0.03	0.00	-0.03	0.00	-0.05	0.00	-0.01
	ZrO_2 wt%	0.00	-0.02	0.01	0.01	0.01	0.01	0.01	0.00
	P_2O_5 wt%	0.00	0.01	0.00	0.00	0.00	0.00	0.00	0.00
	V_2O_3 wt%	0.46	0.48	0.50	3.13	0.51	0.47	0.47	0.47
	Total wt%	100.04	101.13	101.60	103.34	101.47	101.07	100.75	100.01
Calculated	**Fe_2O_3 %**	2.61	1.87	2.56	2.98	2.20	1.41	3.45	3.04
	FeO %	42.62	43.64	43.24	42.98	43.60	43.52	42.68	43.37
	Total_%	100.36	101.37	101.86	103.70	101.71	101.26	101.13	100.33
	Ti mol %	64.17	64.95	64.91	64.32	64.79	65.53	63.60	63.30
	Fe^{2+} mol %	59.33	60.75	60.18	59.83	60.70	60.58	59.41	60.38
	Fe^{3+} mol %	1.64	1.17	1.60	1.87	1.38	0.88	2.16	1.90
	Usp Mol%	0.00	0.00	0.00	0.00	0.00	0.00	0.00	0.00
	Ilm Mol%	97.59	98.43	97.68	97.34	98.16	98.69	97.11	97.04

Table A6. 9 Electron microprobe results for rutile mineral chemistry and calculated mineral formulae based on two oxygens.

	Probe ID	9431_1_I8 1	9431_1_I8 2	9431_1_I8 3	9431_1_M 116	9431_1_R 71	9431_1_R 72	9431_1_R 73	9431_1_R 74	9431_1_R 75	9431_1_R 76	9431_1_R 77	9431_1_R 78	9431_1_R 79	9431_2_R 80	9431_2_R 81	9431_2_R 82
	Sample	94-31	94-31	94-31	94-31	94-31	94-31	94-31	94-31	94-31	94-31	94-31	94-31	94-31	94-31	94-31	94-31
	Rocktype	HW-FeTiB	HW-FeTiB	HW-FeTiB	HW-FeTiB	HW-FeTiB	HW-FeTiB	HW-FeTiB	HW-FeTiB	HW-FeTiB	HW-FeTiB	HW-FeTiB	HW-FeTiB	HW-FeTiB	HW-FeTiB	HW-FeTiB	HW-FeTiB
Probe data	SiO_2 wt%	0.01	4.00	1.61	0.03	52.35	7.42	3.53	6.30	8.65	22.60	0.09	1.58	7.12	3.30	0.24	3.23
	TiO_2 wt%	96.85	94.68	94.61	96.21	2.41	82.78	90.71	21.35	69.77	16.43	99.89	93.62	83.46	93.00	97.72	88.45
	Al_2O_3 wt%	0.00	0.10	0.30	0.03	7.93	1.10	1.06	2.37	4.82	17.96	0.01	1.10	3.68	2.29	0.06	2.55
	Cr_2O_3 wt%	-0.01	0.01	0.00	0.00	-0.03	-0.01	-0.01	0.00	0.00	-0.01	0.01	0.00	-0.01	0.01	0.00	0.00
	FeO wt%	0.86	0.82	0.77	1.44	2.22	1.25	1.63	3.60	2.05	17.85	0.71	2.43	1.89	1.53	2.11	3.43
	MnO wt%	-0.01	0.00	0.00	0.01	0.25	0.02	0.02	0.59	0.10	0.11	0.00	0.03	0.00	0.00	0.00	0.03
	MgO wt%	0.00	0.03	0.07	0.07	0.76	0.23	0.40	1.60	1.19	14.43	0.00	0.82	0.63	0.16	0.03	2.16
	CaO wt%	0.00	0.50	0.63	1.64	21.91	0.80	0.25	38.58	5.36	0.10	0.68	0.15	0.12	0.02	0.05	0.58
	K_2O wt%	0.00	0.10	0.18	0.25	1.89	0.72	0.51	2.05	2.26	0.56	0.04	0.04	1.70	0.95	0.06	0.23
	Nb_2O_5 wt%	0.07	0.09	0.05	0.08	0.00	0.05	0.05	0.00	0.06	0.05	0.07	0.05	0.06	0.49	0.12	0.01
	ZnO wt%	0.00	0.03	0.00	0.01	0.01	0.01	0.02	0.01	0.02	0.07	0.01	0.01	0.02	0.00	0.04	0.00
	CuO wt%	0.00	0.00	0.03	0.00	0.00	0.04	0.00	0.02	0.02	0.00	0.00	0.02	0.00	0.01	0.11	0.00
	NiO wt%	0.00	-0.01	0.01	-0.01	0.01	0.01	0.01	-0.01	0.00	0.01	0.00	0.00	0.00	0.00	0.01	0.00
	CoO wt%	0.00	0.00	0.00	-0.01	0.00	0.00	-0.01	0.00	0.00	0.03	0.00	0.01	0.00	-0.01	0.00	0.00
	SnO_2 wt%	0.00	0.00	0.01	0.00	-0.01	0.00	0.00	-0.01	0.00	-0.04	0.00	0.01	0.00	0.00	0.00	0.00
	ZrO_2 wt%	0.00	0.01	0.00	0.01	0.36	0.00	0.06	0.00	0.00	-0.01	0.05	0.03	0.00	-0.01	-0.01	0.01
	P_2O_5 wt%	0.00	0.00	0.01	0.00	4.78	0.02	0.02	0.05	0.02	0.00	0.00	0.00	0.00	0.00	0.00	0.01
	V_2O_3 wt%	0.95	0.98	0.94	0.95	0.07	0.83	0.90	0.26	0.75	0.20	1.04	0.94	0.92	1.01	1.07	0.93
	Total wt%	98.72	101.35	99.24	100.71	94.87	95.27	99.15	76.75	95.08	90.35	102.60	100.83	99.60	102.73	101.60	101.61
Calculated	Fe_2O_3 %	0.86	0.82	0.77	1.44	2.22	1.25	1.63	3.60	2.05	17.85	0.71	2.43	1.89	1.53	2.11	3.43
	FeO %	0.00	0.00	0.00	0.00	0.00	0.00	0.00	0.00	0.00	0.00	0.00	0.00	0.00	0.00	0.00	0.00
	Total_%	98.75	101.36	99.24	100.73	94.92	95.28	99.17	76.78	95.08	90.41	102.61	100.83	99.62	102.76	101.62	101.62
	Ti mol %	121.26	118.54	118.46	120.45	3.01	103.65	113.57	26.73	87.36	20.57	125.06	117.21	104.49	116.43	122.35	110.74
	Fe^{2+} mol %	0.00	0.00	0.00	0.00	0.00	0.00	0.00	0.00	0.00	0.00	0.00	0.00	0.00	0.00	0.00	0.00
	Fe^{3+} mol %	0.54	0.51	0.49	0.90	1.39	0.78	1.02	2.25	1.29	11.18	0.44	1.52	1.18	0.96	1.32	2.15

	Probe ID	9431_2_R 83	9431_2_R 84	9431_3_R 85	9431_3_R 86	9431_3_R 87	9431_3_R 88	9431_3_R 89	9431_3_R 90	9431_3_R 91	9431_4_R 92	9431_4_R 93	9431_4_R 94	S039313_1_R1	S039313_3_R10	S039313_3_R11	S039313_4_R12
	Sample	94-31	94-31	94-31	94-31	94-31	94-31	94-31	94-31	94-31	94-31	94-31	94-31	S039313	S039313	S039313	S039313
	Rocktype	HW-FeTiB	HW-FeTiB	HW-FeTiB	HW-FeTiB	HW-FeTiB	HW-FeTiB	HW-FeTiB	HW-FeTiB	HW-FeTiB	HW-FeTiB	HW-FeTiB	HW-FeTiB	HW-FeTiB	HW-FeTiB	HW-FeTiB	HW-FeTiB
Probe data	SiO_2 wt%	0.11	0.60	28.47	0.06	0.04	0.11	0.13	0.07	0.46	71.18	0.09	0.19	45.27	58.51	41.91	0.17
	TiO_2 wt%	99.73	97.84	73.95	99.52	99.37	98.95	82.64	99.97	98.64	30.38	99.79	99.05	48.40	43.10	54.95	93.70
	Al_2O_3 wt%	0.02	0.47	0.03	0.03	0.02	0.02	0.04	0.01	0.19	1.16	0.03	0.08	2.19	0.03	0.06	0.00
	Cr_2O_3 wt%	0.01	0.00	0.00	0.00	0.01	0.01	-0.01	0.00	0.00	0.01	0.02	0.01	0.00	0.00	0.00	0.01
	FeO wt%	0.92	1.11	0.48	0.80	0.81	0.68	0.54	0.71	1.04	0.66	0.81	0.94	2.52	0.76	3.48	5.79
	MnO wt%	0.02	0.01	0.01	0.00	0.01	-0.01	0.00	0.00	0.01	0.00	0.01	0.01	0.01	0.01	0.06	0.02
	MgO wt%	0.00	0.32	0.01	0.02	0.00	0.00	0.01	0.00	0.12	0.15	0.01	0.03	1.87	0.01	0.01	0.01
	CaO wt%	0.01	0.19	0.30	0.28	0.06	0.03	9.31	0.67	0.08	0.04	0.01	0.01	0.08	0.16	0.06	0.01
	K_2O wt%	0.13	0.10	0.08	0.09	0.18	0.16	0.17	0.08	0.12	0.50	0.15	0.15	0.03	0.05	0.03	0.02
	Nb_2O_5 wt%	0.09	0.03	-0.01	0.08	0.05	0.03	0.05	0.03	0.04	0.05	0.01	0.03	0.03	0.05	0.03	0.02
	ZnO wt%	0.01	0.00	-0.01	0.01	0.01	0.01	0.00	0.01	0.01	0.02	0.00	0.02	0.02	0.00	0.01	0.02
	CuO wt%	0.01	0.00	0.01	-0.01	0.01	0.00	0.00	0.00	0.01	0.02	0.01	0.00	0.00	0.02	0.00	0.00
	NiO wt%	0.01	0.00	0.00	0.01	0.01	-0.01	0.00	0.00	0.01	0.00	0.00	0.01	0.00	0.01	0.01	0.00
	CoO wt%	0.00	0.01	0.00	-0.01	0.00	0.00	-0.01	0.00	0.00	0.00	0.00	0.00	0.01	0.00	0.00	0.00
	SnO_2 wt%	0.00	0.00	0.01	0.01	0.00	-0.01	0.00	0.00	0.01	-0.01	-0.01	0.00	0.00	0.00	0.01	0.00
	ZrO_2 wt%	0.02	-0.01	-0.01	0.00	0.00	0.00	0.04	-0.02	0.00	0.05	0.00	0.00	0.04	0.04	0.02	-0.01
	P_2O_5 wt%	0.00	0.00	0.00	0.00	-0.01	0.00	8.07	0.00	0.00	0.00	0.00	0.00	0.01	0.03	0.01	0.00
	V_2O_3 wt%	1.01	1.02	0.76	1.07	1.01	1.00	0.84	1.07	1.08	0.33	0.99	1.10	0.46	0.38	0.48	0.80
	Total wt%	102.11	101.70	104.07	101.95	101.59	100.99	101.83	102.60	101.81	104.53	101.93	101.62	100.95	103.15	101.13	100.55
Calculated	Fe_2O_3 %	0.92	1.11	0.48	0.80	0.81	0.68	0.54	0.71	1.04	0.66	0.81	0.94	2.52	0.76	3.48	5.79
	FeO %	0.00	0.00	0.00	0.00	0.00	0.00	0.00	0.00	0.00	0.00	0.00	0.00	0.00	0.00	0.00	0.00
	Total_%	102.11	101.71	104.11	101.98	101.60	101.02	101.85	102.63	101.82	104.55	101.95	101.63	100.96	103.16	101.14	100.57
	Ti mol %	124.86	122.50	92.59	124.61	124.42	123.89	103.47	125.16	123.51	38.04	124.93	124.02	60.60	53.97	68.80	117.31
	Fe^{2+} mol %	0.00	0.00	0.00	0.00	0.00	0.00	0.00	0.00	0.00	0.00	0.00	0.00	0.00	0.00	0.00	0.00
	Fe^{3+} mol %	0.57	0.70	0.30	0.50	0.51	0.43	0.34	0.45	0.65	0.41	0.51	0.59	1.58	0.48	2.18	3.62

	Probe ID	S039313_4_R13	S039313_4_R14	S039313_4_R15	S039313_5_R16	S039313_5_R17	S039313_1_R2	S039313_1_R3	S039313_1_R4	S039313_1_R5	S039313_1_R6	S039313_1_R7	S039313_1_R8	S039313_3_R9	W605041_1_R18	W605041_1_R19	W605041_1_R20
	Sample	S039313	S039313	S039313	S039313	S039313	S039313	S039313	S039313	S039313	S039313	S039313	S039313	S039313	W605041	W605041	W605041
	Rocktype	HW-FeTiB	HW-FeTiB	HW-FeTiB	HW-FeTiB	HW-FeTiB	HW-FeTiB	HW-FeTiB	HW-FeTiB	HW-FeTiB	HW-FeTiB	HW-FeTiB	HW-FeTiB	HW-FeTiB	HSR	HSR	HSR
Probe data	SiO_2 wt%	51.22	56.57	55.64	32.77	32.92	26.86	7.22	41.58	27.36	72.19	54.10	57.02	26.59	50.94	19.70	46.44
	TiO_2 wt%	49.15	43.04	27.32	37.69	15.64	66.06	0.00	26.48	73.81	27.01	45.49	48.31	73.06	0.62	58.29	0.91
	Al_2O_3 wt%	0.35	0.04	14.54	18.53	10.07	6.68	0.10	20.70	0.12	0.00	0.01	0.01	0.00	28.89	9.12	26.62
	Cr_2O_3 wt%	-0.01	0.01	0.00	0.00	0.02	0.00	0.00	-0.01	0.01	0.00	0.00	0.00	0.01	-0.01	0.00	0.00
	FeO wt%	0.95	0.82	0.30	2.57	35.36	1.07	53.28	3.16	0.39	1.93	2.21	0.24	0.80	5.36	4.01	6.79
	MnO wt%	0.01	0.00	0.00	0.00	-0.01	-0.01	0.73	0.02	0.02	0.00	0.00	-0.01	0.01	0.19	0.00	0.27
	MgO wt%	0.00	0.00	0.01	0.69	0.00	0.29	0.56	0.96	0.08	0.00	-0.01	0.00	0.00	1.82	0.71	1.50
	CaO wt%	0.01	0.13	0.61	0.53	0.75	0.06	22.54	0.04	0.06	0.01	0.01	0.18	0.06	0.05	0.16	0.09
	K_2O wt%	0.20	0.02	0.16	5.43	0.06	2.68	0.06	6.47	0.08	0.01	0.01	0.01	0.02	6.16	4.13	5.50
	Nb_2O_5 wt%	0.06	0.05	-0.01	0.03	-0.02	0.27	0.02	0.01	0.02	0.00	0.03	0.01	0.09	7.31	5.06	12.76
	ZnO wt%	0.01	0.00	0.01	0.01	0.00	0.00	0.06	0.00	0.03	-0.01	0.00	-0.01	0.00	0.01	0.01	-0.01
	CuO wt%	0.00	0.00	0.00	0.02	0.00	-0.01	0.00	-0.01	0.00	-0.01	0.00	0.00	0.00	0.00	0.00	0.00
	NiO wt%	0.00	-0.01	0.01	0.00	0.00	0.01	-0.01	0.01	0.00	0.00	0.01	0.00	0.00	-0.01	-0.01	0.00
	CoO wt%	0.00	0.00	-0.01	0.00	0.05	0.00	0.07	0.00	0.00	-0.01	0.00	0.00	-0.01	0.01	0.01	0.01
	SnO_2 wt%	0.00	0.00	-0.01	0.00	-0.01	-0.01	-0.02	0.00	0.00	0.00	0.00	0.01	0.00	0.00	0.02	0.00
	ZrO_2 wt%	0.00	0.11	-0.01	0.03	0.00	0.01	0.00	0.00	0.02	0.00	-0.01	0.00	0.19	0.00	0.00	1.95
	P_2O_5 wt%	0.00	0.09	0.01	0.36	0.00	0.00	0.00	0.00	0.00	0.00	0.00	0.00	0.06	0.00	0.00	0.03
	V_2O_3 wt%	0.45	0.36	0.28	0.46	0.45	0.64	0.00	0.26	0.66	0.29	0.46	0.50	0.63	0.00	0.46	0.02
	Total wt%	102.41	101.23	98.86	99.12	95.27	104.60	84.64	99.68	102.66	101.43	102.34	106.28	101.50	101.35	101.67	102.87
Calculated	Fe_2O_3 %	0.95	0.82	0.30	2.57	35.36	1.07	53.28	3.16	0.39	1.93	2.21	0.24	0.80	5.36	4.01	6.79
	FeO %	0.00	0.00	0.00	0.00	0.00	0.00	0.00	0.00	0.00	0.00	0.00	0.00	0.00	0.00	0.00	0.00
	Total_%	102.42	101.25	98.90	99.12	95.33	104.64	84.66	99.69	102.66	101.47	102.36	106.30	101.52	101.37	101.69	102.89
	Ti mol %	61.53	53.89	34.21	47.19	19.58	82.71	0.01	33.15	92.41	33.81	56.96	60.49	91.48	0.77	72.98	1.14
	Fe^{2+} mol %	0.00	0.00	0.00	0.00	0.00	0.00	0.00	0.00	0.00	0.00	0.00	0.00	0.00	0.00	0.00	0.00
	Fe^{3+} mol %	0.60	0.52	0.19	1.61	22.14	0.67	33.36	1.98	0.25	1.21	1.39	0.15	0.50	3.36	2.51	4.25

	Probe ID	W605041_1_R21	W605041_1_R22	W605041_1_R25	W605041_1_R26	W605041_1_R27	W605041_1_R30	W605041_1_R32	W605041_1_R33	W605041_1_R34	W605041_1_R35	W605041_1_R36	W605318_9_R37	W605318_9_R38	W605318_9_R39	W605318_9_R40	W605318_9_R41
	Sample	W605041	W605041	W605041	W605041	W605041	W605041	W605041	W605041	W605041	W605041	W605041	W605318	W605318	W605318	W605318	W605318
	Rocktype	HSR	HSR	HSR	HSR	HSR	HSR	HSR	HSR	HSR	HSR	HSR	FeR	FeR	FeR	FeR	FeR
Probe data	SiO_2 wt%	42.05	17.01	45.74	41.54	75.43	31.76	18.58	45.73	18.68	53.37	38.66	4.97	40.43	9.18	23.95	1.68
	TiO_2 wt%	17.93	49.07	1.13	0.13	4.53	4.55	3.17	0.99	2.46	36.39	0.17	84.21	8.56	55.71	43.94	87.95
	Al_2O_3 wt%	16.55	11.60	21.74	25.34	4.62	16.44	11.96	27.26	11.06	2.75	25.54	3.73	24.18	0.63	11.02	0.29
	Cr_2O_3 wt%	0.00	-0.01	-0.01	-0.01	0.01	0.00	0.00	0.01	-0.01	0.00	0.00	0.00	-0.05	-0.01	-0.02	0.00
	FeO wt%	2.47	9.87	7.69	9.26	0.79	11.28	12.81	7.35	12.47	2.45	9.39	1.16	0.66	0.69	1.82	1.01
	MnO wt%	0.03	0.07	0.27	0.17	0.01	0.51	1.34	0.31	1.20	0.01	0.19	0.00	0.03	0.00	0.10	0.00
	MgO wt%	0.94	3.46	1.08	0.35	0.21	0.12	1.22	2.04	1.01	0.40	0.09	0.35	2.30	0.05	8.68	0.01
	CaO wt%	14.57	0.14	5.17	16.79	0.25	15.70	0.05	0.04	0.11	0.47	21.75	0.21	0.10	0.04	0.01	0.05
	K_2O wt%	4.37	2.57	4.24	2.41	1.88	0.05	4.46	6.15	4.44	0.97	0.07	1.40	6.69	0.32	6.98	0.36
	Nb_2O_5 wt%	1.26	4.49	9.41	1.81	7.36	15.96	46.33	11.37	46.70	2.40	0.13	1.95	0.23	1.12	0.64	1.69
	ZnO wt%	0.01	0.05	0.00	-0.01	0.01	0.01	0.02	0.03	0.02	0.01	0.00	0.02	0.07	-0.01	0.08	0.00
	CuO wt%	0.01	0.00	0.00	0.01	-0.03	0.01	0.00	0.00	0.00	0.00	0.00	0.00	0.02	-0.01	0.00	0.00
	NiO wt%	0.00	0.00	0.01	0.00	-0.02	0.00	0.01	-0.01	0.01	-0.01	0.00	-0.01	0.01	-0.01	0.00	-0.01
	CoO wt%	0.01	0.02	0.04	0.02	0.18	0.04	0.07	0.01	0.01	0.00	0.04	0.00	0.00	0.03	0.00	0.04
	SnO_2 wt%	-0.02	0.00	0.00	-0.01	-0.02	0.00	-0.02	-0.01	-0.01	0.01	0.00	0.00	0.00	0.00	0.00	0.03
	ZrO_2 wt%	-0.01	-0.02	0.01	0.03	0.00	0.02	0.13	0.55	0.03	0.50	0.00	0.03	0.99	5.89	0.00	2.34
	P_2O_5 wt%	0.00	0.00	0.01	0.01	0.01	0.02	0.01	0.01	0.01	0.00	0.06	0.03	0.20	0.72	0.01	0.76
	V_2O_3 wt%	0.14	0.36	0.01	0.01	0.03	0.01	0.02	0.01	0.01	0.29	0.01	0.79	0.10	0.51	0.40	0.77
	Total wt%	100.29	98.67	96.55	97.83	95.27	96.49	100.16	101.85	98.19	100.02	96.12	98.85	84.49	74.86	97.62	96.97
Calculated	Fe_2O_3 %	2.47	9.87	7.69	9.26	0.79	11.28	12.81	7.35	12.47	2.45	9.39	1.16	0.66	0.69	1.82	1.01
	FeO %	0.00	0.00	0.00	0.00	0.00	0.00	0.00	0.00	0.00	0.00	0.00	0.00	0.00	0.00	0.00	0.00
	Total_%	100.33	98.70	96.56	97.86	95.34	96.49	100.17	101.87	98.21	100.04	96.12	98.86	84.54	74.89	97.65	96.99
	Ti mol %	22.44	61.44	1.41	0.16	5.67	5.70	3.97	1.24	3.08	45.57	0.21	105.43	10.72	69.75	55.02	110.11
	Fe^{2+} mol %	0.00	0.00	0.00	0.00	0.00	0.00	0.00	0.00	0.00	0.00	0.00	0.00	0.00	0.00	0.00	0.00
	Fe^{3+} mol %	1.54	6.18	4.81	5.80	0.50	7.07	8.02	4.60	7.81	1.53	5.88	0.73	0.42	0.43	1.14	0.63

	Probe ID	W605318 _3_R42	W605318 _3_R43	W605318 _3_R44	W605318 _3_R45	W605318 _3_R47	W605318 _3_R48	W605318 _3_R49	W605318 _3_R50	W605318 _3_R51	W605318 _3_R52	W605318 _3_R53	W605318 _3_R54	W605318 _3_R55	W605318 _3_R56	W605318 _3_R57	W605318 _3_R58
	Sample	W605318	W605318	W605318	W605318	W605318	W605318	W605318	W605318	W605318	W605318	W605318	W605318	W605318	W605318	W605318	W605318
	Rocktype	FeR	FeR	FeR	FeR	FeR	FeR	FeR	FeR	FeR	FeR	FeR	FeR	FeR	FeR	FeR	FeR
Probe data	SiO_2 wt%	4.07	41.63	58.68	27.41	16.00	28.28	62.08	27.95	0.80	0.96	2.27	0.64	2.05	2.03	0.55	3.54
	TiO_2 wt%	76.51	59.21	31.00	64.65	76.98	60.13	32.47	66.66	92.51	92.87	91.06	94.87	90.51	89.05	95.54	84.28
	Al_2O_3 wt%	0.09	0.24	0.35	0.06	0.36	6.98	1.42	0.12	0.17	0.05	1.27	0.10	1.02	0.82	0.35	0.92
	Cr_2O_3 wt%	-0.02	0.01	0.00	0.00	0.01	-0.01	0.00	0.00	0.00	-0.01	0.01	0.00	0.01	0.01	0.00	0.00
	FeO wt%	0.88	0.74	8.06	0.75	1.02	1.01	0.57	0.87	1.18	1.19	1.23	1.20	1.27	1.55	1.19	1.29
	MnO wt%	0.01	0.00	-0.01	0.00	0.00	0.00	0.00	0.01	0.00	0.00	-0.01	0.01	0.00	0.00	0.01	0.00
	MgO wt%	0.00	0.01	0.00	0.00	0.01	0.54	0.08	0.00	0.02	0.00	0.08	-0.01	0.06	0.09	0.02	0.14
	CaO wt%	0.12	0.02	0.00	0.13	0.05	0.01	0.00	0.05	0.03	0.04	0.01	0.03	0.05	0.04	0.01	0.05
	K_2O wt%	0.09	0.12	0.19	0.05	0.14	2.39	0.55	0.14	0.15	0.07	0.80	0.13	0.49	0.46	0.24	0.54
	Nb_2O_5 wt%	1.49	1.24	0.55	1.53	1.49	1.37	1.06	1.23	1.96	1.79	2.49	2.38	2.45	3.03	2.44	2.52
	ZnO wt%	0.03	0.03	0.01	0.01	0.00	0.00	0.00	-0.01	0.00	0.00	0.02	0.01	0.01	0.00	0.02	0.01
	CuO wt%	0.01	0.00	0.00	-0.01	-0.01	0.00	-0.01	-0.02	0.00	0.00	0.01	0.00	0.00	-0.02	0.00	0.00
	NiO wt%	-0.01	0.00	-0.01	0.00	0.00	0.00	-0.01	-0.01	-0.02	0.00	0.01	-0.01	-0.01	0.00	-0.01	-0.01
	CoO wt%	0.01	0.00	0.00	0.00	0.00	0.00	0.00	0.03	0.01	-0.01	-0.01	-0.01	0.01	0.02	0.00	0.05
	SnO_2 wt%	0.02	0.00	0.00	0.01	0.02	0.02	0.01	0.02	0.01	0.02	0.01	0.03	0.02	0.02	0.03	0.02
	ZrO_2 wt%	7.61	0.96	0.04	3.39	1.83	0.77	0.82	4.18	0.90	1.47	0.18	0.66	1.24	1.28	0.09	3.91
	P_2O_5 wt%	1.66	0.22	0.00	0.71	0.31	0.08	0.07	0.68	0.17	0.24	0.04	0.17	0.33	0.35	0.01	1.00
	V_2O_3 wt%	0.66	0.53	0.29	0.63	0.70	0.58	0.30	0.56	0.82	0.85	0.94	0.92	0.87	0.92	0.88	0.80
	Total wt%	93.24	104.95	99.15	99.34	98.92	102.17	99.44	102.46	98.69	99.54	100.42	101.12	100.38	99.65	101.38	99.05
Calculated	Fe_2O_3 %	0.97	0.74	8.06	0.75	1.02	1.01	0.57	0.87	1.18	1.19	1.23	1.20	1.27	1.55	1.19	1.29
	FeO %	0.01	0.00	0.00	0.00	0.00	0.00	0.00	0.00	0.00	0.00	0.00	0.00	0.00	0.00	0.00	0.00
	Total_%	93.37	104.96	99.17	99.35	98.93	102.18	99.45	102.51	98.72	99.56	100.43	101.15	100.39	99.67	101.39	99.08
	Ti mol %	95.80	74.13	38.81	80.94	96.38	75.29	40.65	83.46	115.82	116.28	114.01	118.78	113.32	111.50	119.62	105.52
	Fe^{2+} mol %	0.01	0.00	0.00	0.00	0.00	0.00	0.00	0.00	0.00	0.00	0.00	0.00	0.00	0.00	0.00	0.00
	Fe^{3+} mol %	0.61	0.46	5.05	0.47	0.64	0.63	0.36	0.54	0.74	0.74	0.77	0.75	0.79	0.97	0.75	0.81

	Probe ID	W605318 _3_R59	W605318 _5_R60
	Sample	W605318	W605318
	Rocktype	FeR	FeR
Probe data	SiO_2 wt%	9.41	1.86
	TiO_2 wt%	86.09	90.33
	Al_2O_3 wt%	0.43	0.06
	Cr_2O_3 wt%	0.01	0.00
	FeO wt%	1.03	1.19
	MnO wt%	0.00	0.02
	MgO wt%	0.02	0.00
	CaO wt%	0.01	0.14
	K_2O wt%	0.39	0.22
	Nb_2O_5 wt%	2.09	1.96
	ZnO wt%	0.01	0.01
	CuO wt%	0.01	-0.02
	NiO wt%	0.00	0.01
	CoO wt%	0.00	0.02
	SnO_2 wt%	0.02	0.00
	ZrO_2 wt%	0.16	3.97
	P_2O_5 wt%	0.04	0.23
	V_2O_3 wt%	0.80	0.80
	Total wt%	100.50	100.82
Calculated	Fe_2O_3 %	1.03	1.19
	FeO %	0.00	0.00
	Total_%	100.51	100.84
	Ti mol %	107.79	113.10
	Fe^{2+} mol %	0.00	0.00
	Fe^{3+} mol %	0.65	0.75

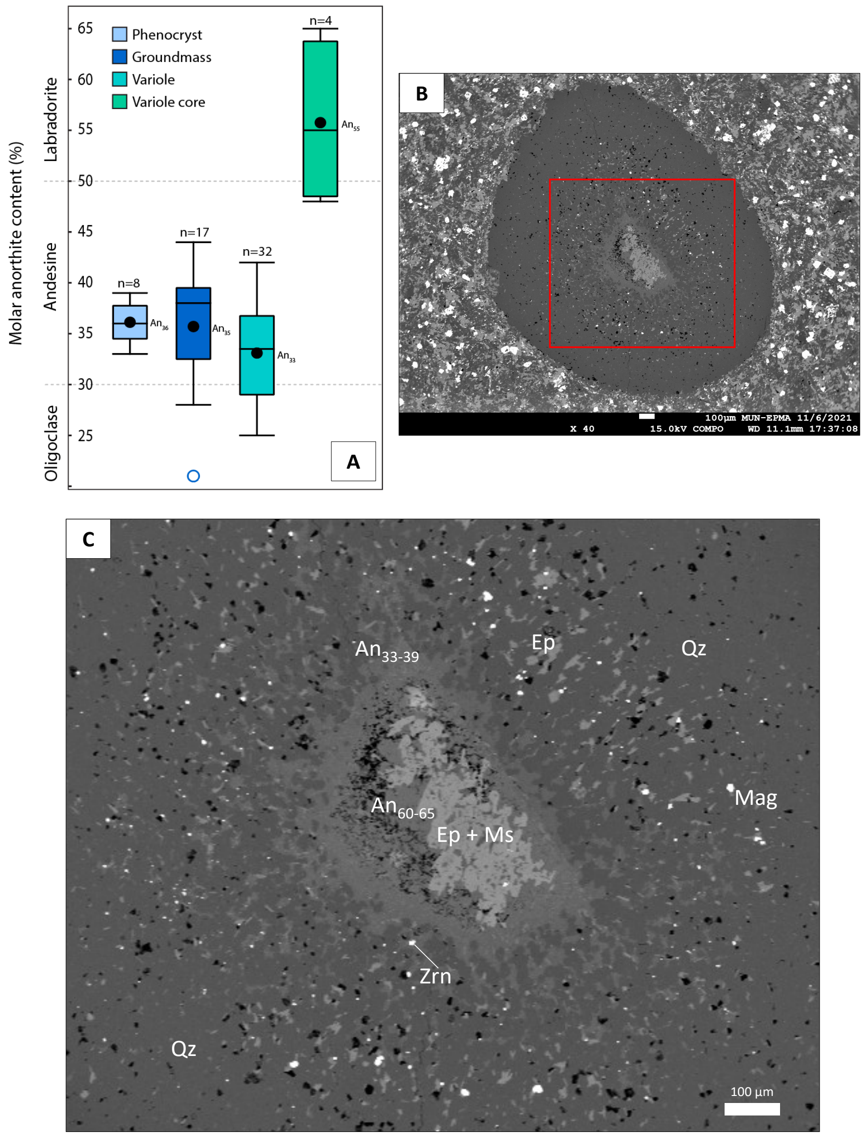

Fig. A6. 1 (A) A box plot showing the molar anorthite content (%) of the different plagioclase phases in sample S037015 of the Z-FeTiB. The most Ca-rich plagioclase phases were probed within the very core of a few varioles. Plagioclase in the outer cores have average andesine compositions, like the plagioclase microlites in the groundmass and larger plagioclase phenocrysts. (B) Backscattered electron (BSE) image of a variole with well-defined zoning from the core. The area within the red box is shown in (C). (C) The Ca-rich plagioclase core (labradorite composition) is partially replaced by muscovite and epidote. It has a relic lath shape with less Ca-rich fibrous blebs of plagioclase (andesine composition) radiating from the core like bicycle spokes. Interstices between the plagioclase fibers comprise quartz and Fe-, Mg-, and Ti-bearing minerals such as chlorite, amphibole, magnetite, and dark, glassy bits. The recrystallization and greenschist facies metamorphism obscure primary textures. Still, these interstitial Fe-Mg-Ti minerals could have been primarily glassy components between the plagioclase fibers formed by spherulitic growth and nucleated on a plagioclase phenocryst. Note the rare sub-micrometer zircon crystal identified during SEM/EPMA work.

Appendix 6 References

Deer, W.A., Howie, R.A., and Zussman, J., 2013, An introduction to the rock-forming minerals: London, England, Mineralogical Society of Great Britain and Ireland, 498 p.

Droop, G.T.R., 1987, A general equation for estimating Fe^{3+} concentrations in ferromagnesian silicates and oxides from microprobe analyses, using stoichiometric criteria: Mineralogical Magazine, v. 51, p. 431–435.

Fowler, A.D., Berger, B., Shore, M., Jones, M.I., and Ropchan, J., 2002, Supercooled rocks: development and significance of varioles, spherulites, dendrites and spinifex in Archaean volcanic rocks, Abitibi greenstone belt, Canada: Precambrian Research, v. 115, p. 311–328.

Lepage, L.D., 2003, ILMAT: An Excel worksheet for ilmenite-magnetite geothermometry and geobarometry: Computers and Geosciences, v. 29, p. 673–678.

Lofgren, G., 1971, Spherulitic textures in glassy and crystalline rocks: Journal of Geophysical Research, v. 76, p. 5635–5648.

Lofgren, G., 1974, An experimental study of plagioclase crystal morphology; isothermal crystallization: American Journal of Science, v. 274, p. 243–273.

McPhie, J., Doyle, M., and Allen, R.L., 1993, Volcanic textures: a guide to the interpretation of textures in volcanic rocks: Hobart, Australia, Centre for Ore Deposit Research University of Tasmania, 198 p.

Stormer, J.C., 1983, The effects of recalculation on estimates of temperature and oxygen fugacity from analyses of multicomponent iron-titanium oxides: American Mineralogist, v. 68, p.

586–594.

Winter, J.D., 2010, An introduction to igneous and metamorphic petrology: Upper Saddle River, Pearson Prentice Hall, 702 p.